The northwest extension of the West Cycladic Detachment System, Attica, Greece

Mark Coleman

A thesis submitted in partial fulfillment of the requirements
for the Doctorate in Philosophy degree in Earth Sciences

Department of Earth and Environmental Sciences
Faculty of Science
University of Ottawa

© Mark Coleman, Ottawa, Canada, 2024

Abstract

In the central Aegean of Greece, metamorphic rocks have been brought to the surface along multiple detachment faults producing a series of core complexes. The detachment faults have been grouped into several detachment systems including the North and West Cycladic Detachment Systems. The timing and magnitude of displacement along individual detachment faults is variable, the faults exhumed footwall rocks with a range of metamorphic grades from different crustal depths. Geochronology (zircon (U-Th)/He and white mica $^{40}Ar/^{39}Ar$ analyses) was conducted to investigate the timing of activity along a paired detachment system exposed in the bedrock of Mt. Hymittos, Attic Peninsula, Greece. Taken together the geochronometers indicate the detachments of Hymittos were active from the late Oligocene to the late Miocene with both faults active during the middle Miocene. The ductile-to-brittle deformation of the structures, top-SSW kinematics, morphology of the massif, and metamorphic grade indicate that these detachments are extensions of the West Cycladic Detachment System. Additionally, the overlap in timing between the structures indicates that paired detachment systems can be coeval. Coeval displacement along separate detachment branches has important implications for strain partitioning within the crust and the development of detachment systems. Detrital zircon U-Pb geochronology was conducted on samples from exposures of the West Cycladic Detachment System on the Attic Peninsula. The results are compared to unpublished data from the Attic Peninsula and the Western Cyclades including Santorini. The analyses confirm the correlation of the footwall rocks of Hymittos to the Cycladic Blueschist Unit as well as evaluate several paleogeographic correlations for the Cycladic Blueschist Unit. The samples herein record significant recycling of Variscan zircon from the Cycladic Basement, strongly suggesting the proto-Cycladic Blueschist Unit was deposited atop the Cycladic Basement. The Pindos Zone of the Hellenides is the most likely paleogeographic equivalent to the Cycladic Blueschist Unit.

Strengthening this correlation gives additional insight into the position of the proto-Cycladic Blueschist Unit which is important for understanding both the movement of Hellenic terranes through time, and the pre-subduction relationship(s) between the terranes that today comprise the Attic-Cycladic Complex. Finally, electron backscatter diffraction analysis was utilized to examine the mechanisms of deformation in a suite of calcitic and dolomitic marble mylonites from the detachments of Hymittos. This was used to shed light on the conditions under which these ductile-then-brittle structures deformed suggesting that dolomite deformed under lower to sub-greenschist facies conditions may be surprisingly weak when deforming by grain size sensitive processes. Dolomite is a major rock forming mineral and comprises significant parts of carbonate dominated terranes and (meta)sedimentary successions. The apparent weakness of dolomite reported herein suggests that under greenschist and sub-greenschist facies conditions dolomite may accommodate significant strain not predicted by experiments or commonly reported from the field. Together this thesis provides insight into detachment fault architecture, deformation processes and the pre-subduction dynamics and structural position of the geologic units exposed within the Attic-Cycladic Complex.

Acknowledgements

I will be forever grateful for efforts of the many people who contributed to this doctoral thesis and my associated education. Chiefly, David Schneider who provided measured, long-suffering critique and guidance. Dave provided support and encouragement for collaborating with other researchers and funded significant analyses as well as fieldwork both as part of the PhD as well as significant learning experiences. I would not be half the scientist I am now without his support.

I thank Bernhard Grasemann for his mentorship and contributions during fieldwork in Greece and laboratory analysis at the University of Vienna. Bernhard welcomed and taught me on multiple field excursions and is an excellent climbing partner and picture maker.

Konstantinos Soukis provided invaluable knowledge and support during fieldwork in Greece, and as an expert on the geology of Greece during the publishing process. Kostis is also a phenomenal cook and welcomed me into his home on multiple occasions; his zucchini flowers are to die for.

Glenn Poirier deserves recognition for his instruction and assistance in using the SEM and EMPA at the University of Ottawa Microanalysis Laboratory the results of which have been in every one of my publications and all the main chapters of this thesis. Alain Mauviel at the University of Ottawa also deserves thanks as he dealt with my many and occasionally last-minute requests for specific thin sections.

I am very thankful to Anna Rogowitz and Gerlinde Habler at the University of Vienna for guidance in collecting EBSD data. Many thanks to the team at University of Colorado's TRaIL specifically James Metcalf for his indefatigable good spirits in the face of many zircon helium aliquots. I am thankful to Riccardo Graziani and Sudip Shrestha for assistance and guidance while collecting data at the Fipke Laboratory for Trace Element Research. Cheers to Alfredo Camacho for his shocking insights into white mica $^{40}Ar/^{39}Ar$ analytical data.

Martijn Schetselaar deserves thanks for his important contribution to the collection, processing and interpretation of detrital zircon U-Pb analyses.

A special thank you to office mate Sandra W., Birendra S., Meghan M., Yannick M., Victor G., Megan R., Elyse G., Taylor D., Martijn, S. and too many other students to name at the University of Ottawa and Carleton University.

This project would not have been possible without funding and support from several agencies. Including the Natural Sciences and Engineering Research Council of Canada, the Ontario Graduate Scholarship through the Ontario Student Assistance Program which provided funding support for analysis fieldwork and presenting the results of this work at conferences. Fieldwork could not have been conducted without support from the Institute of Geology and Mineral Exploration, Greece which provided permits for and sampling and conducting research in the field areas.

Finally, I would like to thank the thesis review committee: Laurent Godin, Noah Phillips, Pascal Audet, and Brian O'Driscoll.

Table of Contents

Abstract ii

Acknowledgements iv

Table of Contents v

Chapter 1: Introduction 1

1.1 Low-angle detachment faults and metamorphic core complexes 2

1.2 Geology of Attica and the Cyclades 5

1.3 Regional geology of the Attic Peninsula 8

1.4 Thesis organization 11

Chapter 2: Lateral termination of a Cycladic-style detachment system 19

2.1 Abstract 20

2.2 Introduction 21

2.3 Geological Setting 23

2.3.1 Geodynamic evolution of the Central Aegean 23

2.3.2 Regional geology of the Attic Peninsula 26

2.4 Methodology 27

2.5 Hymittos Mountain 28

2.5.1 Upper Unit 28

2.5.2 Middle Unit 36

2.5.3 Lower Unit 38

2.5.4 Ductile-then-brittle faulting 39
2.5.5 White mica compositions 41
2.5.6 White mica 40Ar/39Ar geochronology 45
2.5.7 Zircon (U-Th)/He geochronology 48
2.6 Discussion 50
2.6.1 Upper Plate 51
2.6.2 Lower Plate 53
2.6.3 Tectonic history 59
2.6.4 Northwestern termination of the West Cycladic Detachment System 63
2.6.5 Cycladic-style detachment systems 64
2.7 Conclusion 66
2.8 Acknowledgements 67
Chapter 3: Detrital zircon geochronology of the Lower Cycladic Blueschist Nappe – Provenance of Neotethyan terranes in the western Cyclades 68
Abstract 69
3.1 Introduction 70
3.2 Regional Geology 73
3.2.1 Pelagonian Zone 73
3.2.2 Pindos Zone 74
3.2.3 Vardar Zone 75

3.2.4 Cycladic Islands and Attic Peninsula 76
3.5 Methodology 84
3.6 Results 90
3.6.1 Upper Plate 90
3.6.2 Lower Plate 91
3.7 Discussion 92
3.7.1 Applicability of maximum depositional ages 93
3.7.2 Precambrian zircon: A Peri-Gondwanan shared origin 93
3.7.3 Upper Plate: Pelagonian Zone 95
3.7.4 Lower plate: LCBN 96
3.7.5 Paleogeographic configuration 102
3.8 Conclusions 105
3.9 Acknowledgments, Samples, and Data 106
Chapter 4: Can dolomite be weaker than calcite at lower greenschist to subgreenschist facies conditions? 108
Abstract 109
4.1 Introduction 109
4.2 Geologic Setting & Field Evidence 112
4.3 Sampling Strategy and Methods 116
4.4 Sample characterization 118

4.4.1 Mineral composition 119

4.4.2 Lower Unit: Dolomitic rocks 119

4.4.3 Middle Unit: Calcitic rocks 125

4.5 Discussion 131

4.5.1 Deformation of the Lower Unit - dolomite 132

4.5.2 Deformation of the Middle Unit - calcite 135

4.5.3 Low temperature deformation of dolomite and calcite 136

4.5.5 Implications 140

4.6 Conclusion 141

4.7 Acknowledgements 142

Chapter 5: Conclusions 143

5.1 Architecture, timing and conditions of detachment faulting on Hymittos 144

5.2 Mica chemical composition and its relationship to $^{40}Ar/^{39}Ar$ ages 146

5.3 Provenance of the Cycladic Blueschist Unit and its reorganization by structural displacement 147

5.4 Future work 148

References 152

Supplementary information 178

SI Chapter 2 178

S2.1 Methodology 178

S2.1.1 Sampling Strategy 178

S2.1.2 Petrographic Methods 179

S2.1.3 White mica $^{40}Ar/^{39}Ar$ Geochronology 179

S2.1.4 Zircon (U-Th)/He Thermochronology 182

S2.1.5 EMPA methods 184

S2.2 eU vs age vs ESR 185

S2.3 Figures: 188

S2.4 Tables: 196

SI Chapter 3 204

S3.1. Methodology 204

S3.1.1 Zircon U-Pb geochronology 204

S3.1.2 SEM-CL imaging 206

S3.2 Detailed sample descriptions and results 206

3.2.1 Attic Peninsula samples 207

S3.2.2 Santorini samples 210

S3.3 Figures 215

S3.4 Tables 216

SI Chapter 4 243

S4.1 Tables: 243

Chapter 1: Introduction

1.1 Low-angle detachment faults and metamorphic core complexes

Crustal-scale boudinage is an important mechanism contributing to the evolution of strain localization during continental extension (Davis & Coney, 1979; Lacassin, 1988) and accounts for many of the common features associated with extension including metamorphic core complexes, half grabens and detachment faults. Continental detachment faults are low-angle extensional structures that accommodate significant displacement, frequently extending through the crust to the base of the lithosphere (Coney, 1980; Frisch et al., 2011; Gartrell, 1997; Wernicke, 1981, 1985; Wernicke & Burchfiel, 1982). Detachment faults are important because they represent major crustal breaks and localizers of deformation and displacement during the geologic evolution of the Earth particularly in extensional settings. Common models of detachment faults involve one or more fault branches of a low-angle fault system separating low metamorphic grade to unmetamorphosed hanging-wall rocks and extensional sedimentary basins from a footwall comprised of higher-grade metamorphic rocks (Collettini, 2011; Frisch et al., 2011; **Figure 1.1**). (Coleman et al., 2020).

Key features of detachment faults and their associated core complexes include: **(1)** A low metamorphic grade hanging wall structurally juxtaposed above a relatively higher metamorphic grade footwall with a generally elongate, dome-shaped architecture (Davis & Coney, 1979; Vanderhaeghe, 2004; Wernicke & Axen, 1988). The centres of the metamorphic domes may consist of augen gneisses, associated high metamorphic grade metasedimentary rocks and sometimes migmatites; or they may consist of highly deformed metasedimentary and metavolcanic rocks commonly intruded by granitoids and pegmatites (Compton et al., 1977; Coney, 1980; Davis & Coney, 1979). **(2)** The detachments separating the hanging wall and footwall are low-angle, knife sharp fault planes frequently associated with cataclasite and shear-sense indicators that

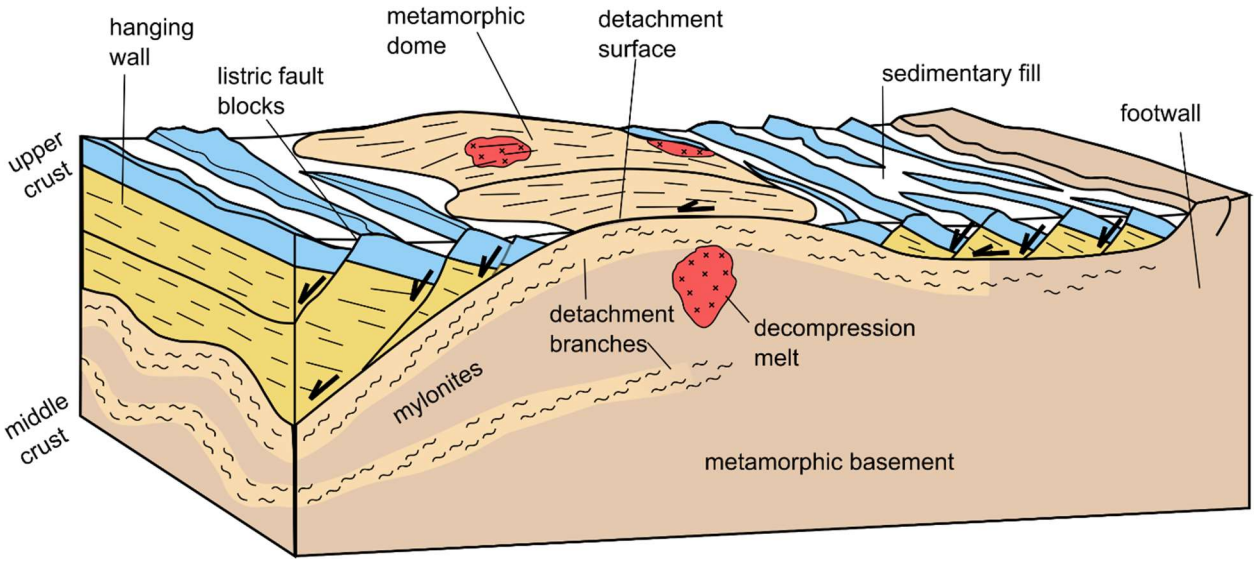

Figure 1.1. Schematic diagram of a metamorphic core complex. Modified after Frisch (2011).

record a consistent direction of displacement (Compton et al., 1977; Davis & Coney, 1979). The present day curvature of the fault plane leads to apparent thrust and apparent normal displacement kinematics across the structure; when the curvature of the fault surface is restored to a planar orientation the kinematic indicators suggest normal displacement (Wernicke, 1981). **(3)** The detachments are commonly spatially associated with mylonitic and ultramylonitic rocks within a footwall shear zone kinematically related to the detachment fault plane, commonly exhibiting decreasing shear strain as the structural distance from the plane increases (Collettini, 2011; Compton et al., 1977; Davis, 1983; Davis & Coney, 1979; Reynolds & Rehrig, 1980). **(4)** Fault blocks of hanging wall strata rotated as a result of displacement along the major detachment plane; these fault blocks are divided from one another by high-angle normal faults with similar slip sense to the detachment plane (Gartrell, 1997; Lister & Davis, 1989; Wernicke & Axen, 1988).

Displacement along lithospheric faults thins the lithosphere promoting asthenospheric rise and crustal weakening (Frisch et al., 2011; Wernicke, 1981, 1985; Wernicke & Burchfiel, 1982). Core complexes and their associated detachment systems are commonly zones of high heat flow

within the crust and steep thermal gradients (Coney, 1980; Davis & Coney, 1979). This heat flow may partially or fully reset geochronological systematics (Compton et al., 1977; Reynolds & Rehrig, 1980). Additionally, geochronometers may also be reset during deformation along a detachment wherein dynamic recrystallization of minerals can reset isotopic ratios (Freeman et al., 1997; Kellett et al., 2016). Resetting of geochronometers is useful for geochronologists as it allows for the dating of thermal events, displacement along the detachment plane and associated fluid flow. K-Ar and $^{40}Ar/^{39}Ar$ in hornblende, biotite and white mica, and zircon and apatite (U-Th)/He and fission track analyses are commonly used for this purpose (Dinter et al., 1995; Foster & Fanning, 1997; Heineke et al., 2019; Reynolds & Rehrig, 1980).

Granitic plutonism is often temporally and spatially associated with crustal extension and core complexes with many studies demonstrating that magmatism coincides with extensional deformation (Coney, 1980; Eskola, 1949; Foster & Fanning, 1997; Rabillard et al., 2018; Reynolds & Rehrig, 1980). In other instances highly extended detachment zones are observed without associated plutons (e.g. Wernicke, 1985). When plutons are present they have been suggested as a mechanism for relocalization of deformation and migration of detachment planes to different structural levels (Bessiere et al., 2018; Liati et al., 2009; Rabillard et al., 2018). Plutons associated with detachment faults are commonly I-type but may exhibit a broad range of compositions; in some cases, high positive $\varepsilon Nd_{(t)}$ and low initial $^{87}Sr/^{86}Sr$ ratios have been interpreted to indicate the involvement of mantle-derived basaltic melts in their formation (Dilek & Altunkaynak, 2007; Oner et al., 2010; Pe-Piper & Piper, 2002).

Field observations and simple shear models suggest that low-angle detachment faults form from progressively deforming structures at angles less than 30° (Brun et al., 1995; Lister et al., 1986; Wernicke, 1981). Other studies note that such simple shear models conflict with

Andersonian fault mechanisms and geophysical data suggesting that it is mechanically easier to form a more optimally oriented fault at approximately 60° rather than activate one dipping at 30° (Collettini & Sibson, 2001; Jackson & White, 1989). This apparent paradox led researchers to propose models wherein faults form at high angles before rotating to lower angles during progressive deformation (Brun et al., 1995; Davis, 1983; Jackson, 1987; Wernicke & Axen, 1988). Competing models for low-angle detachment formation continue to be applied (Axen, 2007; Clerc et al., 2018; Collettini, 2011). More recent studies have focused on time dependent strain localization and dating specific deformation events (Heineke et al., 2019), the mechanics by which these faults deform (Abers, 2009; Axen, 2004) and the mechanisms leading to the deactivation or creation of new detachment branches (Laurent et al., 2015; Rabillard et al., 2018). Unanswered questions remain regarding the mechanisms by which detachment faults accommodate strain, and why and how detachments localize and/or delocalize during extension-driven cooling resulting in temporal evolution of specific detachment faults and impacting the architecture of mechanically interlinked detachment systems.

1.2 Geology of Attica and the Cyclades

The bedrock of the Aegean region, mainland Greece and much of the Balkans are the product of Mesozoic and Cenozoic rifting, collision, and subduction between the Eurasian and African tectonic plates during closure of the Tethys ocean(s) and the Alpine and Variscan orogenies (Jolivet & Brun, 2010; Papanikolaou, 2021; Schmid et al., 2020). Amalgamation of microcontinents and closure of ocean basins built up a nappe stack termed the Hellenides (Jacobshagen, 1986; Ring et al., 2010). The Hellenides are comprised of the Phyllite-Quartzite, Ionian, Gavrovo-Tripolitza, Pindos, Pelagonian, Axios-Vardar, Serbo-Macedonian and Rhodope thrust units (**Figure 1.2a**; Jolivet & Brun, 2010). Following the Alpine orogeny, sections of the

Hellenides collapsed and extended along a series of low-angle detachment faults due to a decrease in the convergence rate between the African and Eurasian tectonic plates (Jolivet et al., 2013; Jolivet & Brun, 2010).

Due to the complex, geologically recent and well-preserved history of subduction, syn-orogenic exhumation and extension along detachment systems, the Cyclades (**Figure 1.2b**) are an excellent location to investigate geologic processes and have been heavily studied over the last fifty or more years (Jolivet et al., 2013; Jolivet & Brun, 2010; Pe-Piper & Piper, 2002). Published geologic research in Attica began with Lepsius (1893) who produced the first bedrock geology maps of the Attic Peninsula. Much of the more recent structurally-driven research began after the first recognition of core-complexes in the Aegean (Lister et al., 1984). Subsequent research expanded upon these initial observations in terms of timing of activity along the detachments (e.g. Chapter 2 and references therein) and linked core complexes whose detachment faults were co-active with similar kinematics into a series of detachment systems including the North Cycladic Detachment System (NCDS; Jolivet et al., 2010), West Cycladic Detachment System (WCDS; Grasemann et al., 2012), the Naxos-Paros Detachment (NPD; Urai et al., 1990) and the Santorini Detachment System (SDS; Schneider et al., 2018), Folegandros Detachment System (Bakowsky et al., 2023), and Evia detachment, which were unrecognized at the start of this project.

The footwalls of the Cycladic-style detachment systems are composed of Eocene high pressure blueschist and eclogite facies metamorphic rocks of the Cycladic Blueschist Unit (CBU; Altherr et al., 1979; Urai et al., 1990). A regionally recognized Oligo-Miocene greenschist facies metamorphic event associated with detachment faulting has partially overprinted footwall rocks with greenschist facies metamorphic mineral assemblages (Altherr et al., 1982; Bröcker et al.,

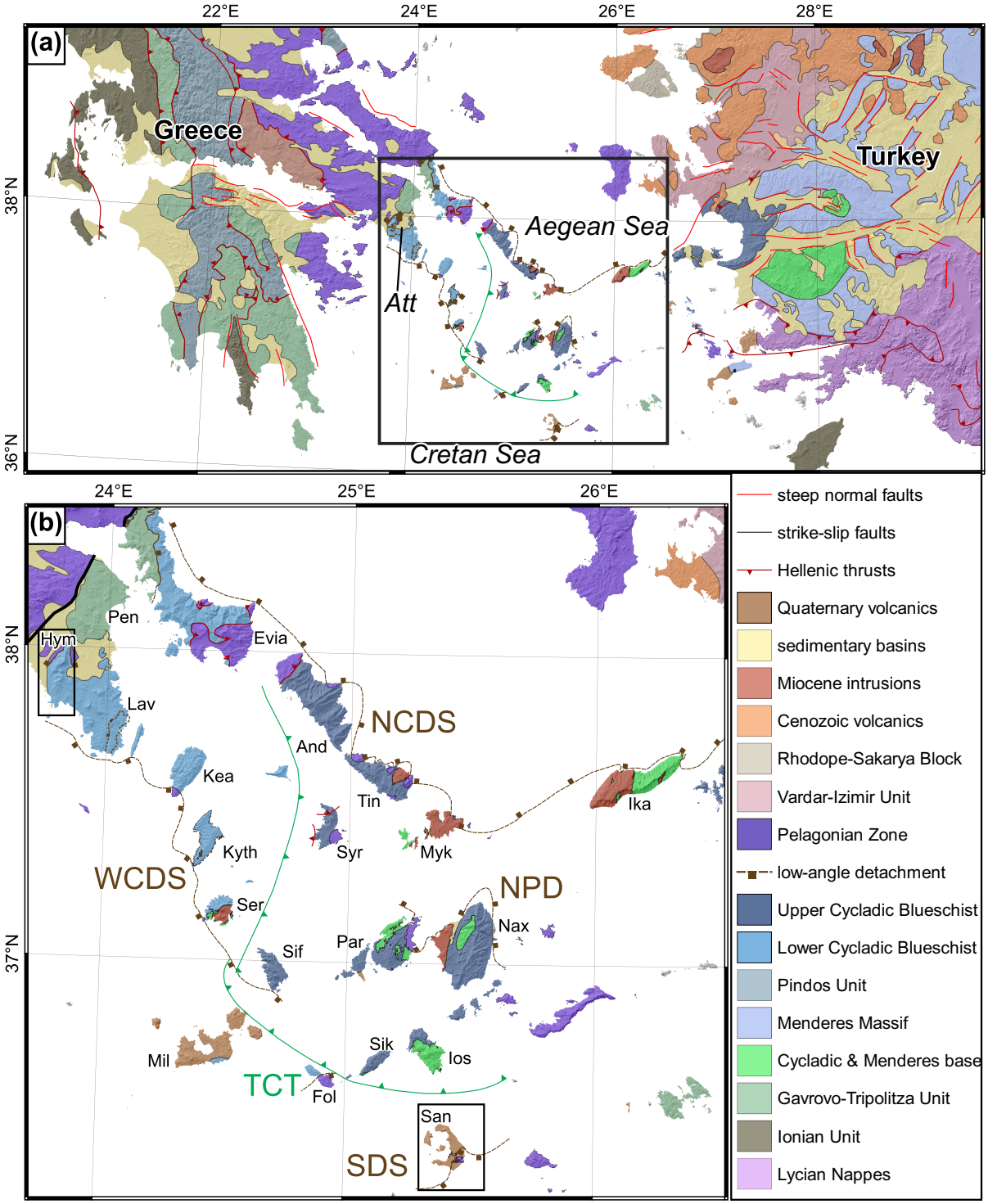

Figure 1.2. (a) Bedrock geological map of Hellenides in Greece and their equivalents in western Turkey. **(b)** Bedrock geological map of the Attic-Cycladic Complex denoting the detachment systems and the core complexes forming the islands and bedrock of the mainland. Black boxes denote the locations of Hymittos (Hym) and Santorini (San) the study areas of this thesis. Structures abbreviated: NCDS: North Cycladic Detachment System; NPD: Naxos-Paros Detachment; SDS: Santorini Detachment System; TCT: Trans-Cycladic Thrust; WCDS: West Cycladic Detachment System. Geographic entities abbreviated: Att: Attic Peninsula; And: Andros; Fol: Folegandros; Hym: Hymittos; Ika: Ikaria; Kyth: Kythnos; Lav: Lavrion; Mil: Milos; Myk: Mykonos; Nax: Naxos; Par: Paros; Pen: Pentelli; Ser: Serifos; Sif: Sifnos; Sik: Sikinos; Syr: Syros; Tin: Tinos.

1993, 2004; Coleman et al., 2019; Huet et al., 2015; Wijbrans et al., 1990). Notably in the Cyclades, metamorphic domes do not exhibit rocks of high metamorphic grade, save the core complexes of Naxos and Mykonos (Lister et al., 1984; Peillod, 2018; Urai et al., 1990). The protoliths of the metamorphic footwalls of the detachment systems are Permo-Carboniferous to latest Cretaceous siliciclastic, carbonate and volcanic rocks that deposited on the passive margin of a small-scale basin that initiated as a rift within peri-Gondwanan continental crust intruded by Variscan plutonic rocks (Bonneau, 1984; Keiter et al., 2011; Poulaki et al., 2019); the Red Sea has been invoked as a possible modern analog of this style of basin (Degnan & Robertson, 2006; Robertson & Dixon, 1984). The CBU is subdivided into the Upper Cycladic Blueschist Nappe (UCBN) and Lower Cycladic Blueschist Nappe (LCBN) on the basis of metamorphic grade inferring the existence of a syn-orogenic thrust emplacing the eclogites of the UCBN atop the blueschists of the LCBN; this thrust is termed the Trans-Cycladic Thrust (TCT; **Figure 1.2**; Grasemann et al., 2018). Owing to the number of detachment systems, recent geologic activity, good exposure and available metamorphic and geochronological datasets, the Attic-Cycladic complex is a common setting for research investigating fault mechanisms and the structural evolution of core complexes (e.g. Rabillard et al., 2018; Jolivet et al., 2010 and references therein).

1.3 Regional geology of the Attic Peninsula

Although the Cycladic Islands are extensively studied, the Attic Peninsula of mainland Greece has been rarely investigated (**Figure 1.2**). The WCDS, first identified on Serifos, Kea, and Kythnos (Grasemann et al., 2012; Grasemann & Petrakakis, 2007), appeared to follow a trend that would intersect with the peninsula (Figure 5a of Grasemann et al., 2012). In the Lavrion district of SE Attica, paired detachment faults had been identified and correlated to the WCDS (Berger et al., 2013; Scheffer et al., 2016; Seman, 2016). This concurred with previous research that correlated

the bedrock of the southern Attic Peninsula with the tectonostratigraphy and kinematics of the western Cyclades (Marinos & Petrascheck, 1956; Leleu & Neumann, 1969; Katsiavrias et al., 1991; Lekkas & Lozios, 2000; Photiades & Carras, 2001; Papanikolaou et al., 2004; Photiades & Saccani, 2006; Krohe et al., 2010; Lekkas et al., 2011; Berger et al., 2013; Scheffer et al., 2016; Seman et al., 2017). The bedrock of the Lavrion district exposes a tripartite tectonostratigraphy separated by a pair of top-SSW low-angle detachments correlated to the West Cycladic Detachment System (Lekkas et al., 2011; Scheffer et al., 2016; Coleman et al., 2019). The upper tectonic unit of Lavrion is correlated to the Pelagonian Zone, the middle and lower tectonostratigraphic units of Lavrion have been correlated to the LCBN (Coleman et al., 2019; Seman et al., 2017) and sometimes the Basal Unit (Ring et al., 2010; Spanos et al., 2015), a unit that structurally underlies much of the CBU (Dürr et al., 1978).

Mt. Hymittos stretches 25 km along a NNE-SSW trend and is 7 km at its widest point. Prior to this thesis the bedrock of Mt. Hymittos was originally divided into two tectonostratigraphic units of equivocal affinity. The upper unit of Hymittos is comprised of low metamorphic grade marble, and metasedimentary and metavolcanic phyllites termed the Alepovouni Unit (Baziotis et al., 2020; Seman, 2016; Papanikolaou et al., 2004). The lower unit is comprised of calcitic and Triassic dolomitic marbles, and metasedimentary and metavolcanic schist, sometimes referred to as the Kaissariani schist (Baziotis et al., 2020; Seman, 2016, Negris & Meunier, 1915). The contact between the two units was proposed to be a major fault with disputed kinematics; some authors thought microstructures related to the fault evinced top-NW shear (Papanikolaou et al., 2004; Papanikolaou & Papanikolaou, 2007), and others reported top-S kinematics (Seman, 2016). The basement of Mt. Hymittos is overlain by the Miocene to recent sedimentary strata of the Athens and Mesogea basins.

The provenance of the bedrock of the western Attic Peninsula including Hymittos and Penteli Mountains (northern Attica; **Figure 1.2**) is still under debate. Some authors suggest the crystalline rocks are extensions of the Attic-Cycladic Complex (Diamantopoulos et al., 2009a; Krohe et al., 2010), whereas others infer these rocks to be exposures of the Gavrovo-Tripolitza Unit (Ring et al., 2010), or the Cycladic Basal Unit (Baziotis et al., 2009; Baziotis & Mposkos, 2011; Liati et al., 2013). Similarly, the nature of the major tectonic boundary exposed on Hymittos and Penteli is not clear; previous investigations have interpreted the boundary as an Alpine thrust or a transpressional fault (Marinos & Petraschek, 1956; Clement, 1976; Xypolias et al., 2003; Papanikolau & Papanikolaou, 2007; Papanikolau & Royden, 2007) whereas other authors interpreted Mt. Hymittos and the Penteli mountains as a series of NNW-directed asymmetric metamorphic core complexes (Diamantopoulos et al., 2009a). The bedrock of the Penteli mountains north of Athens has also been interpreted as an isoclinally folded stratigraphy correlating to the middle and lower units of Lavrion, though with different P-T paths (Lozios et al., 2019).

Initial fieldwork by Mark Coleman, David Schneider, Bernhard Grasemann, and Konstantinos Soukis identified a second major fault zone on Mt. Hymittos, with striking similarities to the detachment system recognized in Lavrion. Given the structural position of Hymittos, its spatial proximity to the Attic-Cycladic complex and the jump in metamorphic grade from the Upper Unit to the Middle and Lower units we hypothesized that Hymittos exposed an extension of the WCDS. Firstly, bedrock mapping and structural analysis were conducted to establish the extent of the detachment faults of Hymittos, and determine the kinematics of the faults. Subsequently geochronology was conducted to determine the timing of metamorphism within the lower plate and displacement along the detachment branches. Together these data allow

for correlation of the detachments of Hymittos to the detachment systems of the Cyclades (**Figure 1.2**). This study expanded the extent of the Attic-Cycladic domain and presented novel findings on how detachment faults accommodate strain near the fault termini. The provenance of the lower plate of Hymittos was uncertain, we hypothesized that the lower plate likely correlated to the LCBN subdivision of the CBU based on metamorphic grade and structural position and limited paleontological evidence. Detrital zircon geochronology was applied to test this proposed correlation. Finally, the lower detachment of Hymittos displayed an extensive ductile shear zone that localized in dolomitic marble. This initial observation was surprising as calcitic marble horizons are present at other stratigraphic levels within the lower unit. Calcite is rheologically weaker than dolomite under most crustal conditions, so deformation would generally be expected to preferentially localize in the weaker phase. We applied microstructural analysis to examine the deformation conditions of the detachments and investigate this anomalous weakness in the dolomitic marble.

1.4 Thesis organization

The thesis is divided into three papers, and chapters two, three, and four have been structured as such. For each of the body chapters the research question and project design were refined through consultation with David Schneider with additional guidance from Bernhard Grasemann and Konstantinos Soukis. Analyses were conducted at the University of Ottawa (scanning electron microscopy (SEM), electron microprobe analysis and U-Pb geochronology), the University of Vienna (electron backscatter diffraction (EBSD) analysis), the University of British Columbia-Okanagan (EBSD analysis), the University of New Brunswick (U-Pb geochronology), the University of Manitoba ($^{40}Ar/^{39}Ar$ geochronology) and the University of Colorado at Boulder (zircon (U-Th)/He geochronology). The overarching goal of the thesis is to determine the timing,

kinematics and deformation conditions of the detachment faults exposed on Mt. Hymittos, and associate the detachment faults of Hymittos with one of the detachment systems of the Cyclades (if applicable). By doing so this thesis will answer unresolved questions about how branched detachment systems terminate, and localize shear strain between different detachment branches in extensional, cooling shear zones. Detrital zircon geochronology will be applied to determine the provenance of the bedrock of Mt. Hymittos this can then be compared to other exposures of detachment systems throughout the Cyclades and used to test paleogeographic correlations of the CBU to the different units of the Hellenides.

Chapter 2: Hymittos' location at the end of the WCDS presented the opportunity to answer several interesting research questions. The bedrock exposes a clear metamorphic discontinuity across multiple faults, one of which was previously unrecognized, yet the massif should be positioned close to the terminus of the detachment system wherein displacement would be expected to be minimal (**Figure 1.2**). Alternatively, the structures may have been related to the Pelagonian Zone of mainland Greece, in which case the faults would represent a previously unrecognized detachment system. In either case, previous studies disagreed on the kinematics and nature of this fault system.

Chapter two presents the results of new bedrock mapping, structural analyses, zircon (U-Th)/He and white mica $^{40}Ar/^{39}Ar$ geochronology, and associated wavelength dispersive spectroscopy (WDS) chemical compositional data from phengitic and muscovitic white mica. The goal of this chapter was to determine the kinematics and timing of the detachment system, and in so doing determine whether the detachment faults of Mt. Hymittos are related to the major detachment systems to the southeast or some other structure. For this chapter, bedrock mapping was conducted over two field seasons; structural analysis involved the synthesis and interpretation

of 1517 structural measurements. For geochronology, 37 samples were collected for analyses distributed between the three units of the tectonostratigraphy of Mt. Hymittos. Of these samples 21 were sufficiently zircon bearing for zircon (U-Th)/He analysis, and 25 were analyzed by the white mica $^{40}Ar/^{39}Ar$ method. The results support that Mt. Hymittos possesses low-angle faults that could be correlated to the WCDS to the southeast. Notably the top-SSW kinematics, ductile-then-brittle style of deformation and distribution of geochronologic analyses are strikingly similar to other exposures of the WCDS (Coleman et al., 2019; Grasemann et al., 2012).

The majority of paired detachment systems in the Cyclades are associated with syn-kinematic plutons, which intruded and cross-cut the detachment plane forcing deformation to re-localize to higher structural levels (Bessiere et al., 2018; Liati et al., 2009; Rabillard et al., 2018). Where the timing of detachments are constrained, the structurally higher detachment is generally active after the lower detachment (Grasemann et al., 2012; Liati et al., 2009). Notably the paired detachments of Hymittos developed without the involvement of a pluton and evince co-activity from $^{40}Ar/^{39}Ar$ and (U-Th)/He geochronology. Furthermore, this chapter also examines how the >100-km long Cycladic-style detachment systems terminate. The age patterns and metamorphic grade of the bedrock of Mt. Hymittos indicate significant extension yet the displacement along the detachment system must reach a minimum within a few kilometers of Mt. Hymittos as the Pelagonian Zone to the northwest (**Figure 1.2**) is not affected by the detachment faulting. This requires an extreme displacement gradient along the faults in central Attica. The geometry and coeval activity of the detachment faults of Mt. Hymittos support chapter two's conclusion that these detachment faults terminate as a vertically oriented horsetail structure accommodating the significant displacement gradient.

Chapter two is published in *Tectonics* (Coleman et al., 2020). Mark Coleman conducted fieldwork, processed samples, analyzed data and wrote the manuscript. Co-authors David Schneider engaged in fieldwork, provided guidance and contributed to editing of the manuscript, and Konstantinos Soukis, Bernhard Grasemann, Stylianos Lozios and Marianne Sophie Hollinetz conducted fieldwork and contributed during the writing and editing process.

Chapter 3: Multiple studies have assigned a range of different provenances for the bedrock of Mt. Hymittos. Existing detrital zircon U-Pb data from Mt. Hymittos (Seman, 2016) did not fully characterize the units of the massif, missing the lowest tectonostratigraphic unit. Chapter three reports detrital zircon U-Pb analyses from Attica and Santorini and synthesizes the result with previously existing data along the western Cyclades. Samples were collected from Hymittos and Lavrion on the Attic peninsula to compare to samples of the CBU from within the Cyclades (Bakowsky et al., 2023; Flansburg et al., 2019; Poulaki et al., 2019; Seman et al., 2017) and to unmetamorphosed paleogeographic equivalents to determine the provenance of the metasedimentary rocks.

A second set of samples are reported from the Santorini archipelago originally presented in Lion (2018). Attica and Santorini are at opposite ends of the Cycladic archipelago and the timing and setting of deposition within the proto-CBU basin may have been different, resulting in detrital zircon signatures reflecting the geologic history of the basin. Samples from the Upper Unit (dominantly the Pelagonian Zone), which occupies the hanging walls of Santorini and Attica, are also compared to other exposures of the Pelagonian Zone throughout the Cyclades. The sampling strategy for this project worked around the pre-existing dataset in order to fill in gaps and allow for better detrital zircon coverage of the massif. This existing dataset is only partly published (Seman et al., 2017) as such several unpublished samples have been included in diagrams and

discussion within this chapter to allow for a proper investigation of the metasedimentary bedrock of Hymittos.

In total, Chapter three reports data from six new samples from Attica, integrated with thirteen pre-existing samples from the peninsula and seven samples from Santorini. The detrital zircon data confirm the correlation between the footwall rocks of Mt. Hymittos and the Cycladic Blueschist. Furthermore the data support the conclusion that the hanging wall of the detachments in the Attic Peninsula correlates to the Upper Unit of the Attic-Cycladic Complex, which is mostly comprised of Pelagonian Zone rocks, but also includes Miocene sedimentary basins and ophiolites of Vardar affinity (Lamont et al., 2019). Together with previous investigations this work supports the hypothesis that the central and eastern Attic Peninsula are a mainland extension of the Attic-Cycladic complex. Some studies have proposed that the CBU of the Cyclades is correlated to the Vardar Zone (Meinhold et al., 2010; Zlatkin et al., 2018). Our study provides evidence of Late Cretaceous zircon that post-date closure of the Vardar Ocean, further supporting the commonly held correlation of the CBU to the Pindos Zone of the Hellenides. Variscan aged zircon identified in the lowest unit of Lavrion were derived through near-source recycling of Variscan-aged plutons identified within the Cycladic Basement.

Chapter three will be submitted for publication in *Tectonics*. Mark Coleman conducted fieldwork, processed samples, analyzed data and wrote the manuscript. David Schneider engaged in fieldwork, provided guidance and contributed to editing of the manuscript. Konstantinos Soukis conducted fieldwork and contributed during the writing and editing process along with Bernhard Grasemann. Allan Lion engaged in fieldwork and processed samples from Santorini and contributed to the writing and editing process.

Chapter 4: Despite its contribution to rock strength, the deformation of dolomite as a major rock forming mineral is understudied in comparison to calcite, quartz, and feldspar. On Mt. Hymittos dolomitic ultramylonites were observed to have accommodated major deformation and appeared more strained than nearby less deformed calcitic marbles. This was notable as generally calcite is expected to be significantly weaker than dolomite for most crustal conditions and thus would preferentially localize deformation (Davis et al., 2008, 2011; Kushnir et al., 2015). Interrogating the apparent weakness of dolomite in this instance is valuable for understanding how detachments localize strain during crustal-scale deformation in carbonate bearing terranes.

Six samples of variably deformed dolomitic marbles were collected from the Lower Unit of Hymittos. Petrographic and EBSD analysis were used to examine the conditions under which these dolomitic marble samples deformed. Within the lower package, dolomitic and calcitic rocks are both mylonitic to ultramylonitic with previously published P-T data suggesting metamorphism at ~470°C and 0.8 GPa (Baziotis et al., 2020). The dolomitic mylonite rocks deformed on the retrograde path of this event. EBSD analyses reveal a progressive fabric evolution from mylonites to ultramylonites interpreted to partly reflect the magnitude of strain and/or decreasing temperature of deformation. In mylonitic domains, average grain diameters range from 70 to 25 μm. The mylonitic dolomite exhibits low-angle grain boundaries, internal misorientation zones and textures suggestive of subgrain-rotation recrystallization. This mylonitic fabric is crosscut by finer-grained bands of dolomite with grain diameters of 15 to 5 μm, which overlaps with the dominant grain size of the subgrains formed within the mylonitic domains. The concentration of low-angle boundaries in the intermediate domains is interpreted to reflect dislocation creep leading to grain-size reduction of the original coarser grained protolith, supported by the similarities in grain size between the fine domain matrix, and the recrystallized subgrains in the intermediate domains. In

samples closer to the fault core, the fully recrystallized ultramylonite fabric is predominant though boudinaged veins, and relict mylonite zones with coarser grains may still be observed. Uniformly ultramylonitic dolomitic marbles exhibit grain diameters of 40 to 5 μm; the majority of grain diameters are less than 15 μm. The ultramylonite bands have low degrees of internal misorientation and an absence of low-angle grain boundaries that are more randomly oriented than the mylonitic dolomite domains. The increasing degree of randomness of dolomite crystal orientations at finer grain sizes was interpreted to be due to deformation accommodated via grain size sensitive grain-boundary sliding. Interstitial calcite grains within the mylonite rock may reflect creep cavitation processes interpreted to have occurred syn-kinematically with grain-boundary sliding. The change from subgrain-rotation recrystallization to grain-boundary sliding is interpreted to reflect the interplay of grain-size sensitive and insensitive processes during dynamic recrystallization.

The dolomitic marbles of the lower unit deformed on the retrograde path from the high-pressure, mid-temperature portion of the greenschist facies. Estimates of deformation temperature (Chapter Two) and structural position suggest the dolomite deformed at significantly lower temperatures than might be predicted by deformation experiments (Davis et al., 2008, 2011; Holyoke et al., 2014; Kushnir et al., 2015). Over most crustal conditions dolomite is expected to be stronger than calcite and quartz (Berger et al., 2016; Czaplińska et al., 2015; Davis et al., 2008; Leiss et al., 1994; Ma et al., 2022; Oesterling et al., 2007; Prikryl, 2001; Schmid, 1982). Given that dolomite is a major rock forming mineral, potential for low-temperature weakness should be accounted for when estimating the strength of the upper crust in carbonate dominated terranes.

Chapter four will be submitted for publication in *The Journal of Structural Geology*. Mark Coleman conducted fieldwork, processed samples, analyzed data and wrote the manuscript. David Schneider and Bernhard Grasemann engaged in fieldwork, provided guidance and contributed to

editing of the manuscript. Konstantinos Soukis conducted fieldwork and contributed during the writing and editing process. Riccardo Graziani and Anna Rogowitz conducted sample processing, data acquisition and contributed to the writing and editing process.

Chapter five concludes the manuscript summarizing the main findings of the research and tying together the different chapters, to draw conclusions from the total thesis dataset. The chapter finishes with some suggestions for future work within the region and how the work may answer unresolved questions about detachment systems.

Chapter 2: Lateral termination of a Cycladic-style detachment system

2.1 Abstract

The bedrock of Hymittos, Attic peninsula, Greece exposes a pair of low-angle crustal-scale ductile-then-brittle detachment faults. The uppermost detachment fault separates sub-greenschist facies phyllite and marble of a Pelagonian Zone hanging wall, from greenschist facies metasedimentary schist, calc-schist, and marble correlated to the Cycladic Blueschist Unit. A second, structurally lower detachment fault subdivides the metamorphic rocks of the Cycladic Blueschist Unit footwall into Middle and Lower units. There is a marked step in metamorphic grade between the sub-greenschist facies uppermost package, and the middle-to-upper greenschist facies middle and lower packages. A suite of new white mica $^{40}Ar/^{39}Ar$ and zircon (U-Th)/He dates indicates accommodation of deformation along these faults occurred from the late Oligocene to the late Miocene with both faults active during the middle Miocene. The structures have clear top-S/SSW kinematics determined from flanking folds, sigmoids, shear bands, stair-stepping of strain shadows on porphyroclasts, and SCC' fabrics. The ductile-to-brittle deformation of the structures, morphology of the massif and the increase in metamorphic grade suggest these low-angle structures are part of a major, crustal-scale extensional complex, located at the northwest end of the West Cycladic Detachment System that accommodated Miocene bivergent exhumation of Attic-Cycladic metamorphic core complexes in the central Aegean region. Taken together the above data suggest that multiple coeval detachment branches may form in highly strain partitioned regions to accommodate the mechanically necessary regional high strain at the termini of Cycladic-style detachment systems.

2.2 Introduction

In the Aegean Sea, high-pressure metamorphic rocks of the Attic-Cycladic Complex (ACC) have been exhumed along crustal-scale extensional detachment faults as a series of asymmetric metamorphic core complexes (**Figure 2.1;** Grasemann et al., 2012; Jolivet & Brun, 2010; Lister et al., 1984). Four major low-angle detachment systems have been identified accommodating the bivergent extension of the ACC: (1) the top-NNE North Cycladic detachment system (NCDS) is exposed on Andros, Tinos, Mykonos and Ikaria (Beaudoin et al., 2015; Jolivet et al., 2010); (2) the top-SSW West Cycladic detachment system (WCDS) exposed on Attica, Kea, Kythnos, Serifos, with a brittle manifestation on Sifnos and Folegandros (Augier et al., 2015; Coleman et al., 2019; Grasemann et al., 2012; Iglseder et al., 2011; Laurent et al., 2016); (3) the top-N Naxos-Paros detachment system (NPDS) exhumes amphibolite and granulite facies marble, gneiss and migmatite (Urai et al., 1990); and (4) the top-S Santorini detachment (SD; Schneider et al., 2018; **Figure 2.1**). Where syn-tectonic plutonism is absent, detachments are commonly a single cataclastic to brittle fault plane and a broad zone of penetrative, ductile deformation extends hundreds of meters into the footwall (Iglseder et al., 2011; Grasemann et al., 2012). In contrast, the effects of plutonism apparently generated multiple detachment fault planes that diachronously localize deformation (Laurent et al., 2015; Rabillard et al., 2015, 2018).

Extensional detachments are useful natural laboratories for studying fault processes that accommodate exhumation, as displacement along a low-angle normal fault exhumes footwall rocks. Typically, the center of a fault (lengthwise) exhibits the maximum displacement, with zero displacement at each of the fault terminations (Elliot, 1976). The ends of faults are often characterized by damage zones produced by the concentration of stress resulting in secondary faults or fractures mechanically linked to the main fault (Cowie & Scholz, 1992; Martel, 1997).

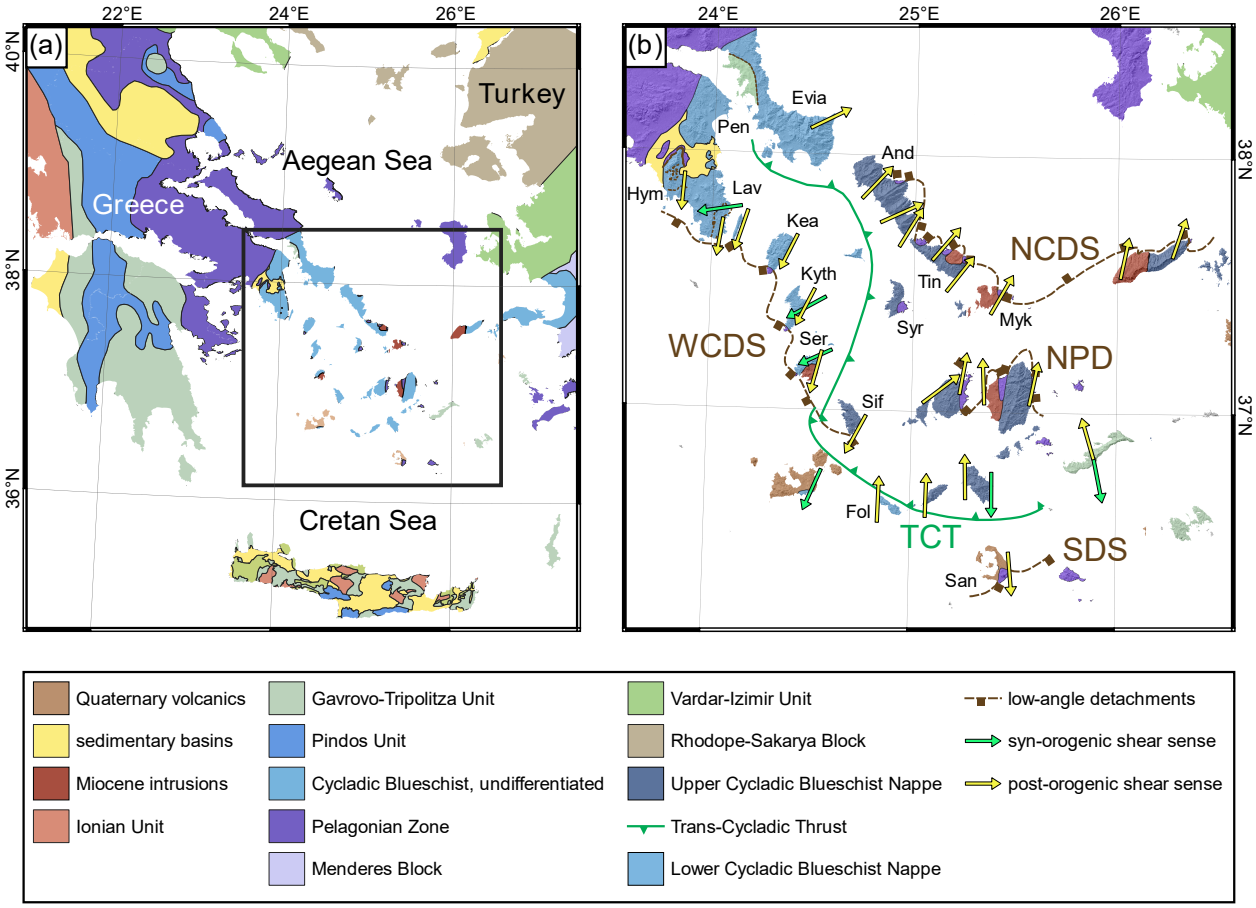

Figure 2.1. (a) Simplified bedrock geological map of the Hellenides in Greece, Turkey and Crete as well as the Aegean and Cretan seas. The Hellenides are a series of nappes recording the accretion of oceanic basins and microcontinents to the European continental margin. **(b)** Simplified bedrock geological map of Greece and the central Aegean region. Post-orogenic, Oligo-Miocene low-angle extensional detachments include the top-SSW West Cycladic Detachment System (WCDS; Grasemann et al., 2012), the top-NE North Cycladic Detachment System (NCDS; Jolivet et al., 2010), the top-NE Naxos-Paros Detachment (NPD; Buick, 1991; Urai et al., 1990) and the top-SSE Santorini Detachment System (SDS; Schneider et al., 2018). The Lower and Upper Cycladic Blueschist Nappes are subdivisions of the Cycladic Blueschist Unit; separated by the Eocene Trans-Cycladic Thrust (TCT; Grasemann et al., 2018). The Pelagonian Zone is the amphibolite facies to unmetamorphosed hanging wall of the Cycladic detachment systems. Post-orogenic shear sense indicates the directions of displacement along the low-angle detachment systems accommodating bivergent extension and exhumation of the Cycladic Blueschist Unit (Augier et al., 2015; Beaudoin et al., 2015; Brichau et al., 2007; Faure et al., 1991; Forster & Lister, 1999; Gautier & Brun, 1994; Grasemann et al., 2012; Huet et al., 2009; Jolivet et al., 2010; Jolivet & Patriat, 1999; Laurent et al., 2016; Lister et al., 1984; Mehl et al., 2005, 2007; Ring et al., 2011; Soukis & Stockli, 2013). And: Andros; Fol: Folegandros; Hym: Hymittos; Kyth: Kythnos; Lav: Lavrion; Myk: Mykonos; Pen: Pentelli; San: Santorini; Ser: Serifos; Sif: Sifnos; Syr: Syros; Tin: Tinos. The map is projected in the geographic coordinate system, using the World Geodetic System (WGS) 1984 datum.

2.3 Geological Setting

2.3.1 Geodynamic evolution of the Central Aegean

In the central Mediterranean, Late Jurassic to Cenozoic north-directed convergence at the Eurasian continental margin led to subduction of the Apulian microcontinent and accretion of numerous exotic terranes, building a nappe stack termed the Hellenides (Jacobshagen, 1986; Ring et al., 2010). The nappes comprising the Hellenides are the Pelagonian, Pindos, Gavrovo-Tripolitza, Phyllite-Quartzite, Ionian and pre-Apulian thrust units (**Figure 2.1**; Jolivet & Brun, 2010). The majority of central Aegean bedrock is correlated to the Cycladic Blueschist (proposed to be metamorphosed Pindos; e.g. Papanikolaou, 1984, 1987, 2009) and Pelagonian units. Within the Mediterranean, the Aegean Sea is one of a series of Cenozoic back-arc basins distributed along the Europe-Africa continental margin. The opening of the Aegean Sea initiated c. 35 Ma as a result of slab rollback and subsequent back-arc spreading (Jolivet & Faccenna, 2000; Royden, 1993). Extension began in the northern Aegean Sea and migrated southwards through time (Fytikas et al., 1984; Jolivet et al., 2003). In the southern Aegean region, extension was accompanied by greenschist facies deformation that overprinted Eocene-Oligocene high-pressure assemblages as a series of bivergent NNE-SSW oriented metamorphic core complexes (MCCs) (**Figure 2.1**; Lister et al., 1984; Jolivet & Brun, 2010; Grasemann et al., 2012).

The Pelagonian Zone is the remnant of a subducted microcontinent consisting of Paleozoic basement with a Paleozoic-Mesozoic carbonate cover sequence, overlain by a Triassic-Jurassic ophiolite (Auboin, 1959; Bonneau, 1984; Bonneau & Kienast, 1982; Jacobshagen, 1986). The package of rocks comprises the hanging wall of the Cycladic detachments on the islands, where it occurs as isolated klippen of metasedimentary, metabasic and ophiolitic rocks. Pelagonian metamorphic rocks within the Cyclades record middle Cretaceous high-pressure and Late

Cretaceous greenschist to amphibolite facies metamorphism (**Figure 2.1**; Altherr et al., 1994; Bonneau, 1984; Huet et al., 2015; Reinecke et al., 1982), equivalent to exposures of the Pelagonian Zone on Evia (Maluski et al., 1981) and the Greek mainland (Altherr et al., 1994; Dürr et al., 1978; Lips et al., 1998; Maluski et al., 1987; Patzak et al., 1994; Reinecke et al., 1982; Schermer et al., 1990). Pelagonian Zone rocks were thrust over the Pindos Unit during 55-30 Ma subduction and accretion at the European continental margin (Skourlis & Doutsos, 2003). The rocks of the Pindos Unit are Late Triassic to Paleocene pelagic limestone and siliciclastic rocks, overlain by a Maastrichtian-Eocene flysch sequence (Auboin, 1959; Brunn, 1956; Stampfli et al., 2003).

The Cycladic Blueschist Unit (CBU) of the Cyclades is the proposed paleogeographic equivalent of the passive margin Pindos Unit of the Hellenides (Bonneau, 1984; Bonneau & Kienast, 1982). Other proposed correlations include a Vardar Unit of the Hellenides affinity (Chatzaras et al., 2013; Doutsos et al., 1993), possibly deposited in a rift basin within or northeast of the Pelagonian Zone (Zlatkin et al., 2018). Some authors suggest that the proto-CBU formed as a Late Cretaceous back-arc basin above the subducting Pindos Ocean (Keiter et al., 2011); others suggest CBU is the southernmost margin of the Pelagonian microcontinent (Bonneau, 1984). Regardless of affinity, the CBU consists of a Permo-Carboniferous to latest Cretaceous marble, metapelite, and metavolcanic sequence (Dürr et al., 1978; Poulaki et al., 2019). Polyphase deformation and metamorphism have reworked the original CBU stratigraphy (Brun & Faccenna, 2008; Jolivet et al., 2003). The CBU experienced Eocene high-pressure metamorphism during collision and subduction of the Pindos ocean basin (Altherr et al., 1979; Okrusch & Bröcker, 1990; Tomaschek et al., 2003). Zircon U-Pb, white mica $^{40}Ar/^{39}Ar$ and garnet Sm-Nd and Lu-Hf ages suggest peak eclogite to blueschist facies metamorphism occurred at 52 Ma and continued until 40 Ma (Dragovic et al., 2015; Lagos et al., 2007; Laurent et al., 2017; Lister & Forster, 2005; Ring &

Layer, 2003; Schneider et al., 2011; Tomaschek et al., 2003). The Cycladic Blueschist Unit overlies the Cycladic Basement unit, which is a polymetamorphic terrane comprising pre-Carboniferous schist intruded by Carboniferous granitic rocks associated with the Variscan orogeny (Flansburg et al., 2019; Reischmann, 1998).

A c. 40-30 Ma Eocene-Oligocene metamorphic event linked to synorogenic exhumation driven by ductile extrusion has been identified by white mica $^{40}Ar/^{39}Ar$ and Rb-Sr dating (Gerogiannis et al., 2019; Huet et al., 2009; Jolivet et al., 2010; Ring, Will, et al., 2007; Scheffer et al., 2016; Schneider et al., 2011). Deeper levels of the CBU are suggested to have continued experiencing high-pressure metamorphism until 30 Ma (Lister & Forster, 2016; Wijbrans et al., 1990) even as the higher structural levels were partially exhumed and undergoing contemporaneous greenschist facies metamorphism (Ring et al., 2010). Other authors consider this an entirely greenschist facies metamorphic event (Cao et al., 2018). The CBU has been subdivided into the eclogite facies Upper (UCBN) and blueschist facies Lower Cycladic Blueschist nappes (UCBN), separated by the synorogenic Trans-Cycladic Thrust (**Figure 2.1**; Grasemann et al., 2018; Wind et al., 2020).

Subsequent post-orogenic slab rollback during the Oligo-Miocene drove back-arc extension leading to diachronous 25-18 Ma greenschist facies metamorphism (Altherr et al., 1982; Bröcker et al., 2004; Cossette et al., 2015; Iglseder et al., 2011; Parra, Vidal, & Jolivet, 2002; Wijbrans & McDougall, 1986) and exhumation of Attic-Cycladic metamorphic core complexes along a series of low-angle extensional detachment faults (Jolivet & Brun, 2010; Lister et al., 1984).

Cycladic detachments are frequently associated with I- and/or S-type granitoids (e.g. Serifos, Ikaria, Naxos, and Paros; **Figure 2.1**). Magmatism migrated from the northeast to the

southwest in the Aegean region and is associated with slab-tearing and clockwise rotation of the External Hellenides (Jolivet et al., 2015). Where detachments exhibit a spatial relationship with these granitoids, deformation was frequently accommodated by multi-plane detachment systems (Serifos, Tinos, Mykonos, Ikaria; Beaudoin et al., 2015; Brichau et al., 2010; Grasemann & Petrakakis, 2007; Iglseder et al., 2009; Tschegg & Grasemann, 2009). The multiple detachment branches are suggested to be produced by stalling of the rising granitic melt at the brittle-ductile transition (Rabillard et al., 2018). Cooling of the granitoid inhibited deformation along a structurally-lower detachment; simultaneously, thermal weakening of the crust above the pluton led to initiation of a new, structurally-higher detachment producing a multi-plane detachment system. On Cycladic islands where plutons are not observed, detachments frequently are a single fault plane with a zone of diffuse ductile deformation extending several hundreds of meters below the detachment core (e.g. Kea, Kythnos; Iglseder et al., 2011; Grasemann et al., 2012).

2.3.2 Regional geology of the Attic Peninsula

The tectonostratigraphy and structural style of the western Cycladic islands can be extended to the Lavrion District, southern Attic peninsula (Berger et al., 2013; Katsiavrias et al., 1991; Krohe et al., 2010; Lekkas & Lozios, 2000; Leleu & Neumann, 1969; Marinos & Petrascheck, 1956; Papanikolaou et al., 2004; Photiades & Carras, 2001; Photiades & Saccani, 2006; Scheffer et al., 2016; Seman et al., 2017). The bedrock of Lavrion exposes a tripartite tectonostratigraphy separated by a pair of top-SSW low-angle detachments correlated to the WCDS (Scheffer et al., 2016; Coleman et al., 2019). The upper tectonic unit of Lavrion is correlated to the Pelagonian Zone, the middle and lower tectonostratigraphic units have been correlated to the LCBN (Scheffer et al., 2016; Coleman et al., 2019).

The provenance of rocks exposed on the western Attic Peninsula including Hymittos and Penteli Mountains is uncertain. Some authors suggest the crystalline rocks are extensions of the ACC (Diamantopoulos et al., 2009b; Krohe et al., 2010), yet others infer these rocks to be exposures of the Gavrovo-Tripolitza Unit (Ring et al., 2010), or the Cycladic Basal Unit (Baziotis et al., 2009; Baziotis & Mposkos, 2011; Liati et al., 2013). Similarly, the nature of the major tectonic boundary separating crystalline rocks from the hanging wall is not yet clarified; previous investigations interpreted the boundary as an Alpine thrust or a transpressional fault (Marinos & Petrascheck, 1956; Papanikolaou & Papanikolaou, 2007; Papanikolaou & Royden, 2007; Xypolias et al., 2003) whereas other authors interpreted Hymittos and Penteli mountains as a series of asymmetric metamorphic core complexes formed by NNW-directed extensional faulting (Diamantopoulos et al., 2009b). Penteli has also been interpreted as an isoclinally folded stratigraphy correlative to that of the middle and lower units of Lavrion, though metamorphosed under different P-T conditions (Lozios et al., 2019).

2.4 Methodology

In order to investigate the tectonic history of Hymittos we combine bedrock mapping, structural and petrographic analysis, electron microprobe analyzer (EMPA) analysis, and multiple single-grain total-fusion white mica $^{40}Ar/^{39}Ar$ and zircon (U-Th)/He geochronology on samples from the Upper, Middle and Lower units of Hymittos. We focused on mica-bearing metasedimentary rocks, including calcitic and dolomitic marble, mica schist and calc-mica schist. White mica $^{40}Ar/^{39}Ar$ dating was conducted at the University of Manitoba using a multi-collector Thermo Fisher Scientific ARGUSVI mass spectrometer. Zircon (U-Th)/He dating was carried out at the University of Colorado-Boulder on a Balzers PrismaPlus QME 220 quadrupole mass spectrometer. EMPA mineral chemical analyses and associated EDS mapping were carried out

using a JEOL JXA-8230 SuperProbe and JEOL 6610LV SEM at the University of Ottawa. Detailed methodology, data tables and additional figures are available in the Supporting Information (**Chapter S2**).

2.5 Hymittos Mountain

New bedrock geology mapping of Hymittos identified a local tectonostratigraphy dominated by three tectonostratigraphic units (herein Upper, Middle and Lower units, local names after Lepsius [1893]) separated by ductile-then-brittle low-angle normal faults (**Figure 2.2; Figure 2.3**). Away from the massif these units are overlain and obscured by late Miocene to Pleistocene sedimentary rocks of the Athens and Mesogea basins (e.g. Lepsius, 1893; Marinos & Petrascheck, 1956; Marinos & Symeonidis, 1974; Papanikolaou et al., 2004 and references therein). The following sections synthesize field observations and structural and petrographic analyses conducted on rock samples from the Upper, Middle and Lower units of Hymittos. Detailed petrographic results are available in **Table S2.1**.

2.5.1 Upper Unit

The upper tectonostratigraphic package of Hymittos (herein Upper Unit; locally Alepovouni Unit) consists of low metamorphic grade metasiliciclastic phyllite, serpentinite, marble and ophiolitic rocks (**Figure 2.4a, b, c**). The Upper Unit is primarily exposed at the margins of the northern massif; there are smaller exposures preserved in a dextral pull-apart basin in the central massif and a graben in the southern foothills (**Figure 2.2**). Upper Unit calc-phyllite and phyllite typically have a calcite-sericite-chlorite-white mica-quartz-plagioclase feldspar ± tourmaline ± epidote mineralogy and are bedded on a 1-10 cm scale. Most mineral phases are anhedral to subhedral, frequently angular, and evince a shape-preferred orientation, elongate minerals are aligned into a foliation (**Figure 2.5a; Figure S2.4a**). Upper Unit marble display

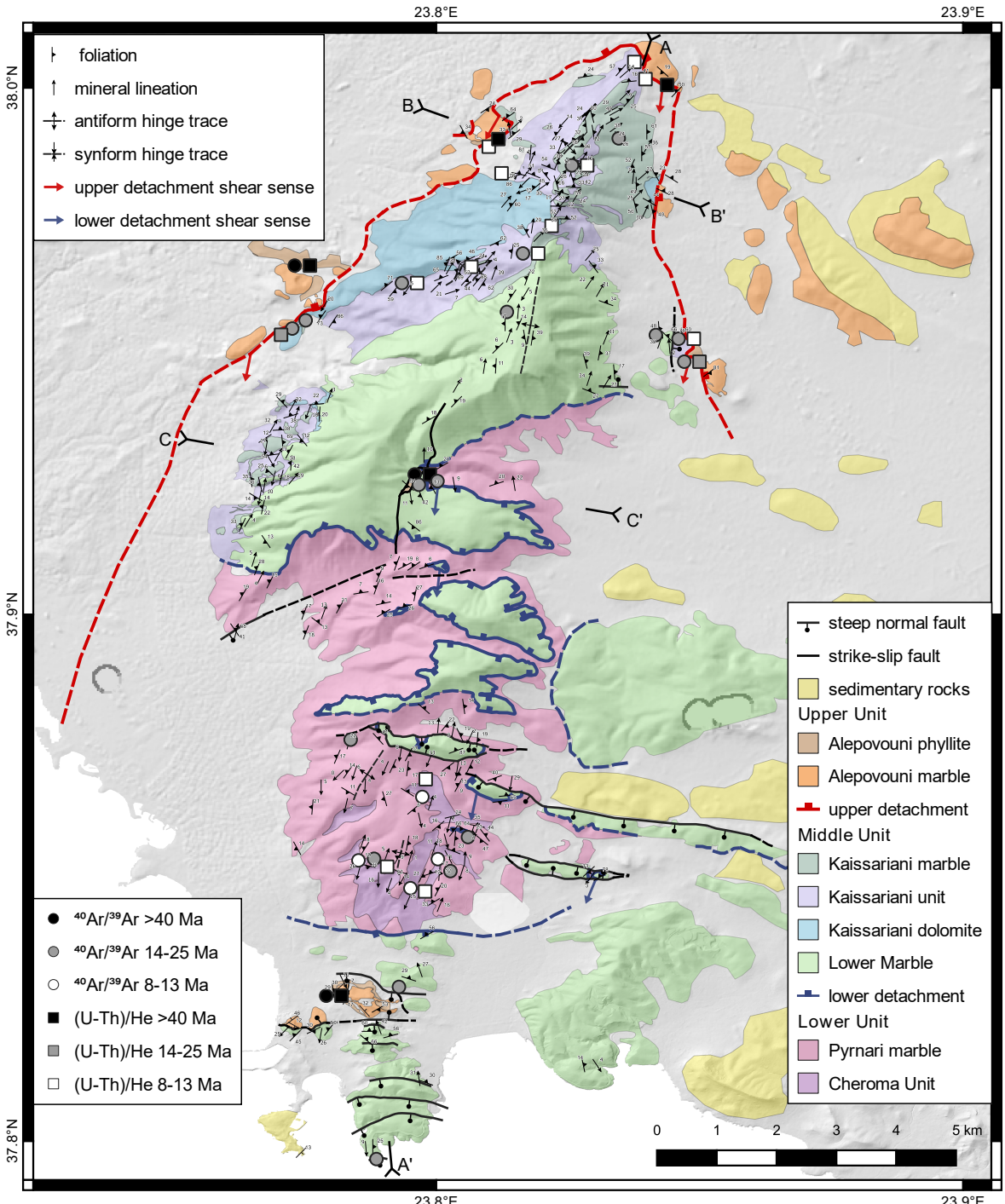

Figure 2.2. Geologic map of Mt. Hymittos, Greece based on new bedrock mapping and maps of Lepsius (1893), Lekkas and Lozios (2000), and Latsoudas (2003). Map shows structural measurements (foliation and lineation) and location of geochronology samples (with ages). See Figure S1 for more information. Cross-section markers correspond to the profiles in Figure 3. The unmetamorphosed rocks of the Mesogea and Athens basins as well as those underlying them have been grouped into the sedimentary rocks unit. Grey regions of the map represent areas of no or limited data, typically obscured by the city of Athens. The map is projected in the Universal Transverse Mercator (UTM) coordinate system, zone 35S, using the World Geodetic System (WGS) 1984 datum.

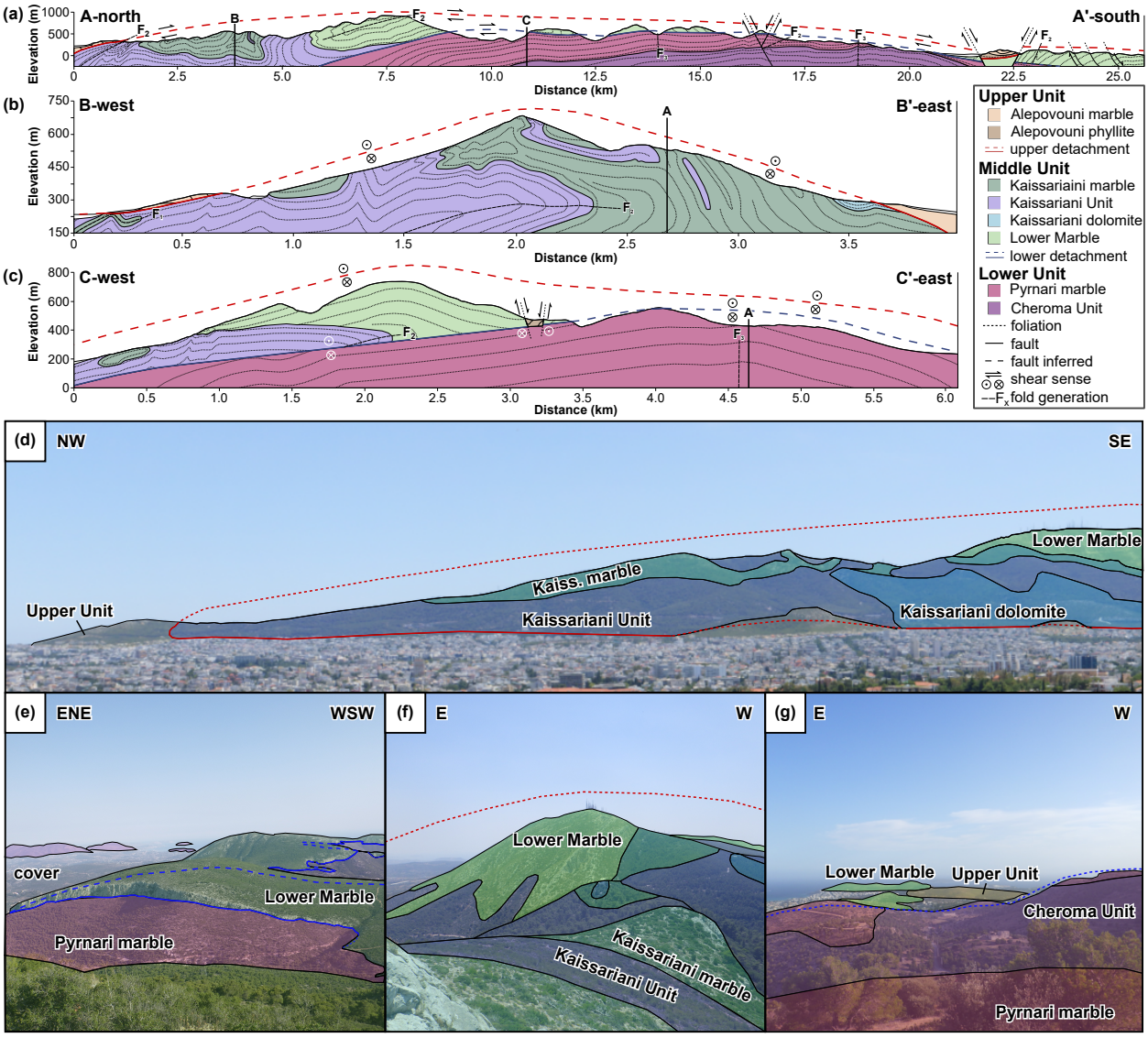

Figure 2.3. Refer to caption on next page.

Figure 2.3. (a) (previous page) N-S geological cross-section of Hymittos massif drawn at 1:1 scale. Structural styles differ across the massif. In north and central Hymittos, the detachments shape the topography producing a north-dipping dip slope and a series of klippen. Shear sense along both detachments is top-S. In southern Hymittos, a graben and asymmetric, listric, high-angle normal faults have developed. These faults cross-cut and offset the detachments as part of a graben. **(b)** W-E geological cross-section of the bedrock of northern Hymittos massif drawn at 1:1 scale. Middle Unit schist and marble are folded together as part of a km-scale recumbent fold. **(c)** W-E geological cross-section of the bedrock of central Hymittos massif drawn at 1:1 scale. Syn-orogenic structures preserved in the Middle Unit are truncated by the post-orogenic lower detachment. **(d)** Field photo of the upper detachment in northern Hymittos taken from (**38.023665°N, 23.76793°E**). The Upper Unit hanging wall (orange) is comprised of the phyllites and marbles of the Alepovouni Unit. The Middle Unit footwall is the intercalated schists and marbles of the Kaissariani Unit (blue), the Kaissariani dolomite (light blue), the Kaissariani calcitic marble (dark green) and the calcitic Lower Marble (light green). Lithology colours correspond to colours on the geology map (Figure 2). **(e)** Exposures of the lower detachment in central Hymittos; photo taken from (**37.94068°N, 23.8038°E**). The footwall is a Lower Unit (violet) dolomitic marble mylonite (Pyrnari Marble), the hanging wall is a Middle Unit (green) calcitic (Lower Marble) mylonite. **(f)** Folded and intercalated Middle Unit rocks in northern Hymittos including Kaissariani Unit schist (dark blue), marble (forest green) and the Lower Marble (light green). Photo taken from (**37.97992°N; 23.82409°E**). **(g)** Exposures of the Upper, Middle and Lower units in southern Hymittos; photo taken from (**37.85850°N, 23.80152°E**). Middle Unit is comprised of the Lower Marble (green), Lower Unit is valley-forming Cheroma Unit (purple) and ridge-capping Pyrnari Marble (violet).

Figure 2.4. (next page) **(a)** Roughly bedded, ankeritized Upper Unit Alepovouni marble, eight meters above the upper detachment (**37.95868°N; 23.77806°E**). **(b)** Upper Unit (Alepovouni Unit) low metamorphic grade, foliated, cataclased metasedimentary phyllites with sheared, flattened clasts. Upper Unit phyllites are commonly heavily weathered (**37.828016°N; 23.781051°E**). **(c)** Cataclased serpentinite and metasediment melange exposed along the Upper Detachment (**38.000546°N; 23.843805°E**). **(d_1)** Outcrop exposing brittle fault rocks of the lower detachment. The hanging wall is a cataclased calcitic marble mylonite; the footwall is a brittlely deformed, dolomitic marble ultramylonite. **(d_2)** The fault core is comprised of ultracataclasite cut by a sharp fault plane **(37.90942°N; 23.79802°E)**. **(e)** Recumbent (F_2) folds in Middle Unit calc-schist in NW Hymittos. Two generations of veins are visible, an initial generation predates foliation (S_2) development and is folded with the foliation; the second vein generation cross-cuts the folds. Outcrop is cut by an apparent thrust fault that produced fault drag folds (**37.98398°N; 23.81199°E**). **(f)** Apparent top-SW shear sense inferred from domino boudinage of a dolomitic interlayer within a calcitic Middle Unit marble mylonite (Lower Marble; **37.95949°N; 23.83243°E**). **(g)** Calcitic and dolomitic Lower Unit mylonitic marbles. Contact between the two is gradational over a few centimeters (**37.85974°N; 23.80189°E**). **(h)** Top-S shear sense inferred from A-type flanking fold developed along a boudinaged quartz vein in Lower Unit (Cheroma Unit) calc-schist. Vein offsets also indicate top-S shear (**37.85258°N; 23.79088°E**).

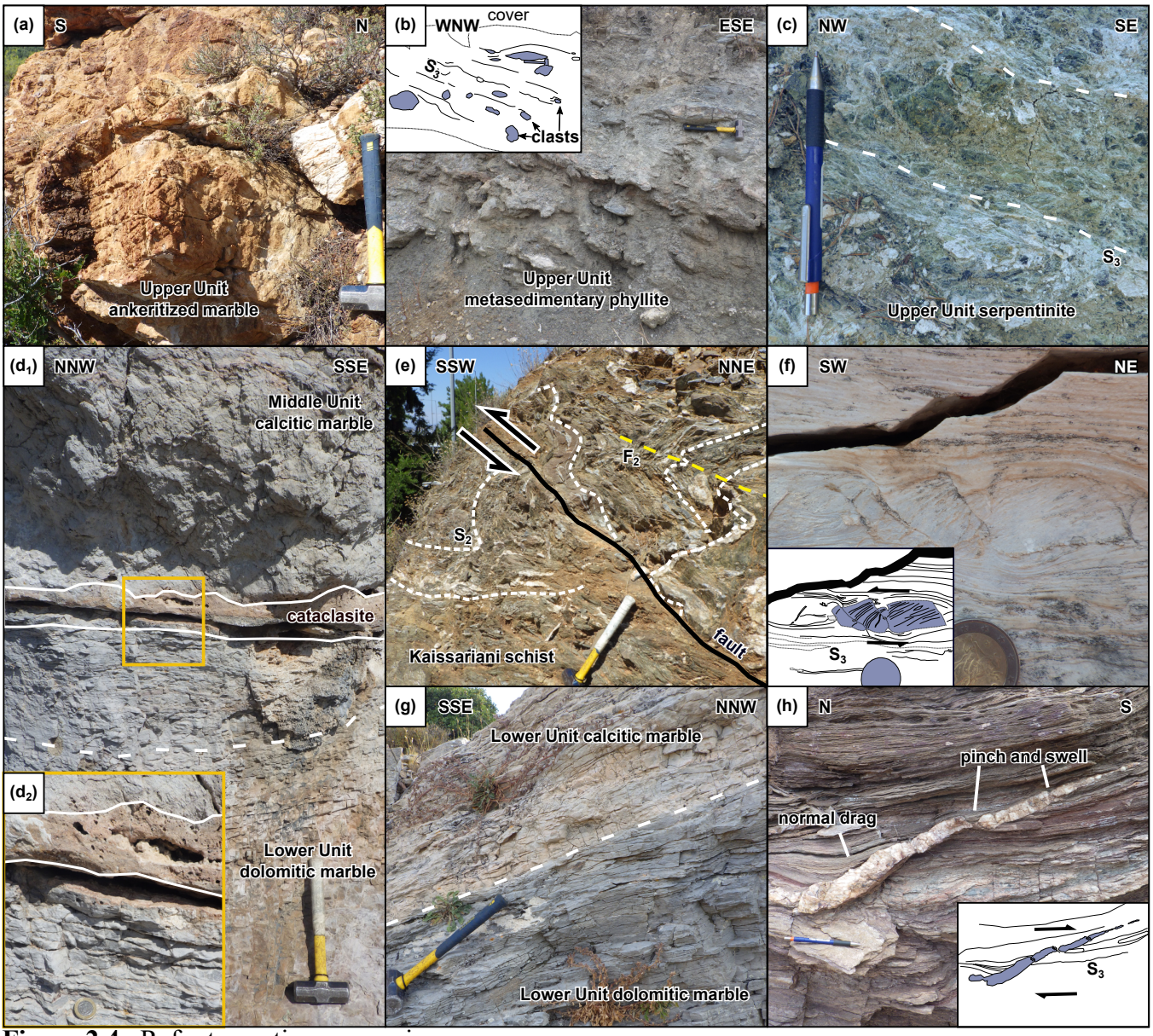

Figure 2.4. Refer to caption on previous page.

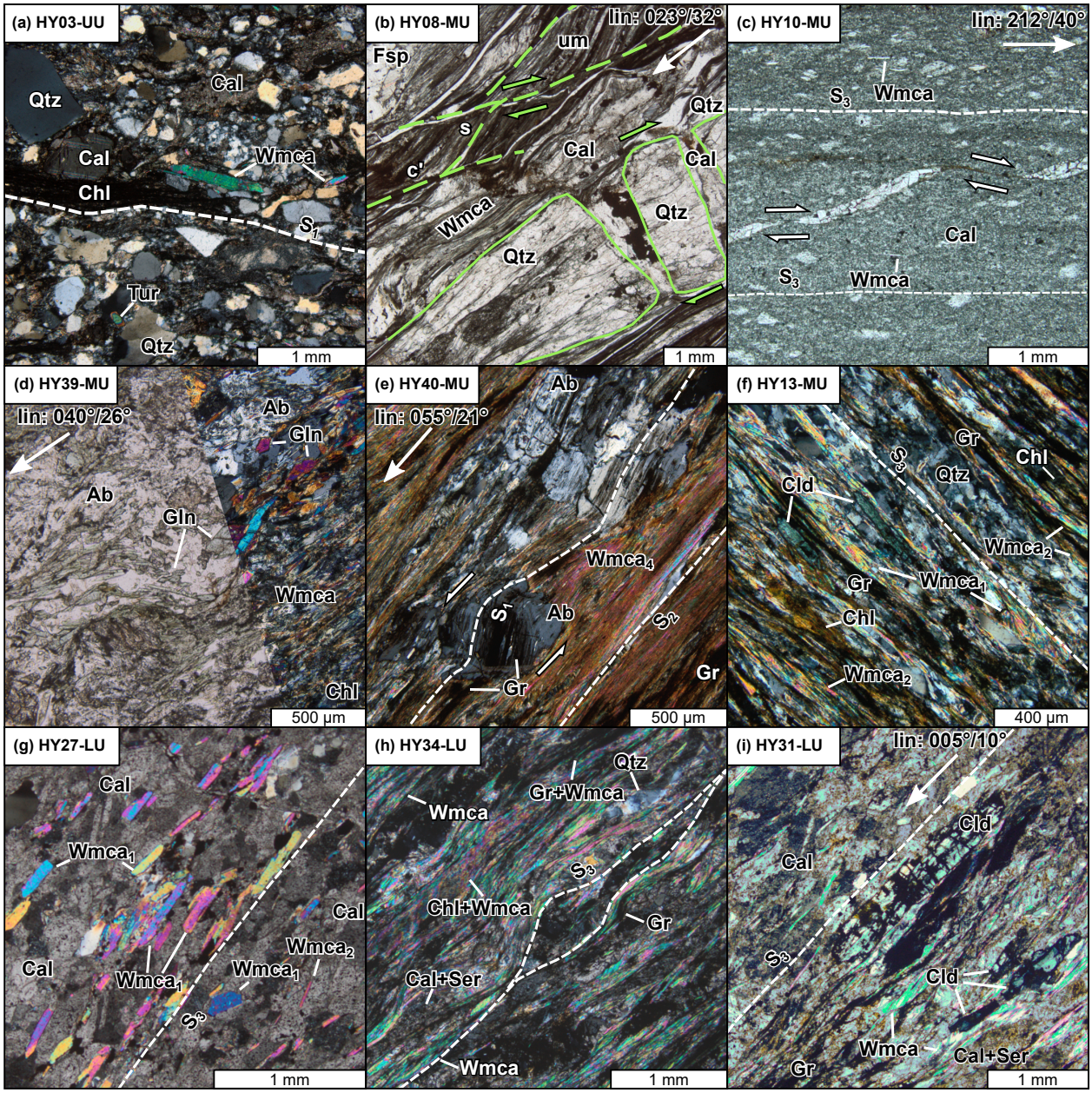

Figure 2.5. Refer to caption on next page.

Figure 2.5. (previous page) (**a: HY03: 37.82802°N; 23.78105°E**) XPL photomicrograph of Upper Unit metasedimentary phyllite white mica that form a single population of 100-1000 μm-long, brittlely deformed, kinked, subhedral to anhedral crystals. **(b: HY08: 37.955294°N; 23.774308°E)** PPL photomicrograph of Middle Unit white mica, calcite, feldspar, quartz, ultramylonitic schist. Top-S sense of shear inferred from S-C' fabrics in dark ultramylonite bands and rotation of domino boudinaged quartz microlithons. **(c: HY10: 37.954109°N; 23.842426°E)** PPL photomicrograph of Middle Unit calcitic marble mylonite. Top-S shear sense inferred from shear band boudinaged calcite vein. **(d: HY39: 37.963677°N; 23.807964°E)** Composite PPL and XPL photomicrograph of Middle Unit glaucophane-bearing metabasic schist. M_1 glaucophane is preserved as part of a relict S_1 foliation in albite porphyroblasts. **(e: HY40: 37.963923°N; 23.803121°E)** XPL photomicrograph of Middle Unit quartz graphite chlorite albite white mica schist. Albite porphyroblasts exhibit apparent top-N shear during top-N rotation. Graphite in albite porphyroblasts preserves an earlier generation of the foliation S_1, rotated during a second generation of deformation synchronous with metamorphism evinced by curved graphite foliation in the clearer rims of the albite porphyroblasts. The S_2 foliation is comprised of white mica, graphite and chlorite. **(f: HY13: 37.96293°N; 23.79347°E)** XPL photomicrograph of Middle Unit mylonitic metasedimentary schist, where white mica comprise two populations: $Wmca_1$ 100-250 μm-long subhedral crystals oriented oblique to foliation within quartz- and feldspar-rich microlithons. $Wmca_2$ elongate 100-500 μm-long, subhedral-to-anhedral, kinked crystals within shear bands; commonly interlayered with graphite, and/or chlorite. **(g: HY27: 37.85127°N; 23.80268°E)** XPL photomicrograph of Lower Unit calcitic marble mylonite, where white mica comprise two populations: $Wmca_1$ 200-800 μm-long euhedral crystals oriented parallel to the S_3 foliation. $Wmca_2$ 50-100 μm-long euhedral crystals oriented parallel to the foliation in calcitic and dolomitic marble mylonites. **(h: HY34: 37.85355°N; 23.80040°E)** XPL photomicrograph of Lower Unit mylonitic pelitic schist, where white mica are elongate 100-500 μm-long, extensively sheared and deformed subhedral-to-anhedral, crystals forming shear bands in mylonitic mica schist and calc-mica schist; commonly interlayered with graphite, and/or chlorite. **(i: HY31: 37.86536°N; 23.797344°E)** XPL photomicrograph of chloritoid-white mica calc-schist. Qtz: quartz, Cal: calcite, Wmca: white mica, Ser: Sericite, Chl: Chlorite, Fsp: Feldspar, Ab: Albite; Gr: Graphite, Cld: Chloritoid, Gn: Glaucophane, S_1: 1st foliation, S_2: 2nd foliation (mineral abbreviations from Siivola & Schmid, 2007).

several generations of calcite veining and elongate calcite ribbons (**Figure S2.4b**). Upper Unit serpentinite and serpentinized phyllite exhibit a calcite-talc-epidote-quartz-chlorite-serpentinite mineralogy (**Figure S2.4c**). Bedding thicknesses of Upper Unit marble range from 50 cm to >1 m and primary bedding is weakly expressed. Folded metachert layers at some outcrops indicate these units are deformed. Foliations are typically low-angle and mineral and elongation lineations show a large dispersion; at lower structural levels approaching the upper detachment, the lineations are oriented N-S (**Figure 2.6e, j**). The mineral assemblages of the Upper Unit suggest low-grade metamorphic conditions of prehnite-pumpellyite to lowest greenschist facies. Micro and

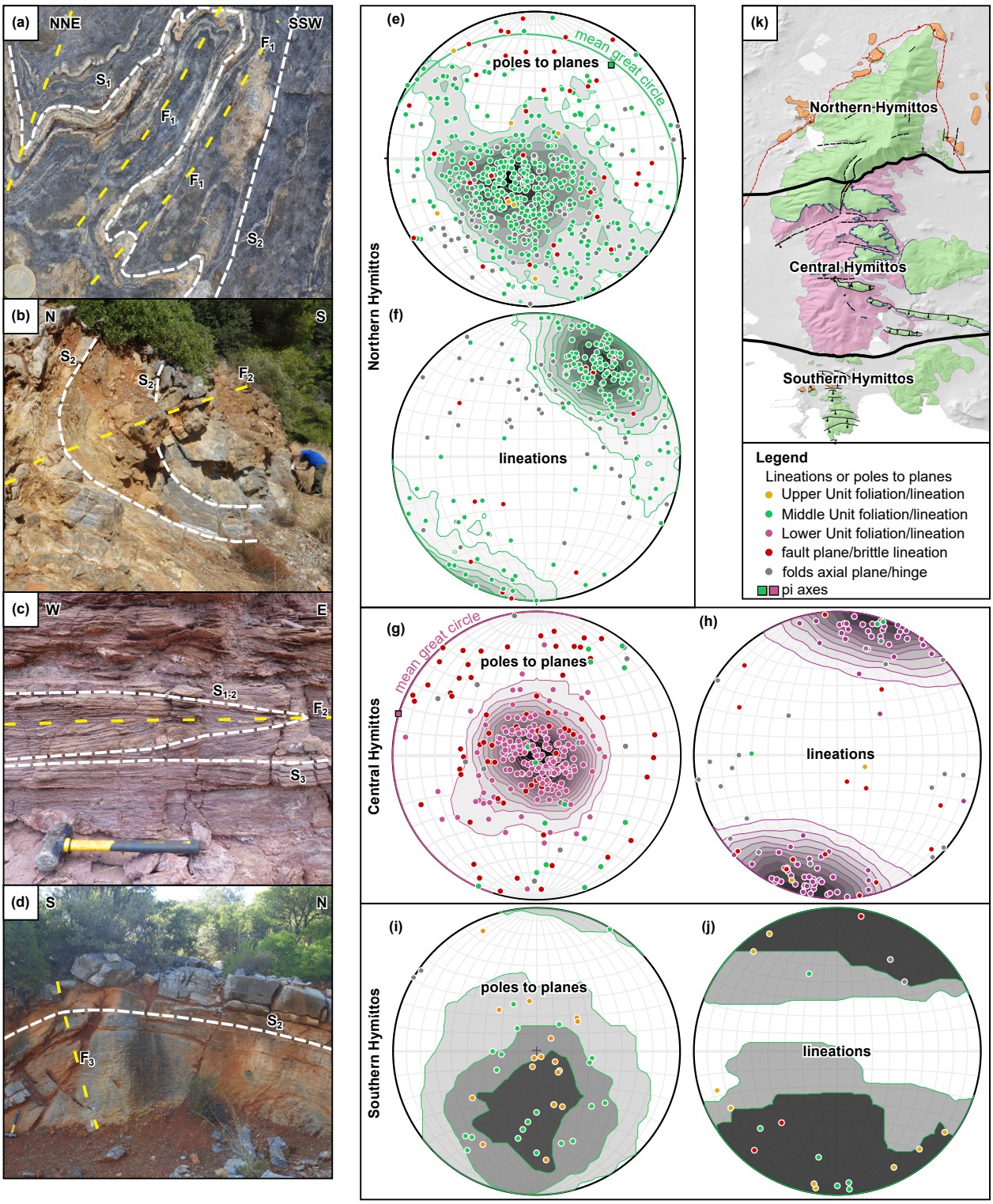

Figure 2.6. Refer to caption on next page.

Figure 2.6. (previous page) Outcrop images of structural elements (a-d) and equal-area lower hemisphere stereograms of planar and linear structural elements (e-j). **(a)** S_1 foliation refolded by F_1 folds and transposed into the S_2 foliation in Middle Unit calcitic marble (**37.98275°N; 23.82005 °E**). **(b)** S_2 foliated Middle Unit marble and calc-schist folded by recumbent F_2 folds in northern Hymittos (**37.96591°N; 23.80582°E**). **(c)** Isoclinally folded S_{1-2} foliation as a product of S_3 transposition foliation in Lower Unit quartz-mica schist (**37.85335°N; 23.78549°E**). **(d)** Foliated (S_2) and open F_3 folded calcitic Middle Unit marble in northern Hymittos (**37.99040°N; 23.834621°E**). **(e)** Stereogram of poles to planes of Upper and Middle unit planar elements in northern Hymittos. Ductile foliations have been contoured illustrating a broadly flat-lying foliation pattern related to reorientation of steeper dipping S_1 and S_2 foliations during D_3 deformation. Axial planes of folds are generally steeply to shallowly north dipping. Faults are moderate to steeply dipping with many orientations. **(f)** Stereogram of Upper and Middle unit linear elements in northern Hymittos. Note the dominant relatively shallow NE-SW post-orogenic lineation (L_3) overprinting most of the E-W and ENE-WSW synorogenic lineations **(g)** Stereogram of poles-to-planes of Upper, Middle and Lower unit planar elements in central Hymittos. S_3 deformation was more pervasive in these units and fully transposed most earlier structures, resulting in relatively little dispersion in measurements. **(h)** Stereogram of Upper, Middle and Lower unit linear elements in central Hymittos. Mineral and elongation lineations contoured populations are more uniform and rotated slightly counterclockwise compared to Middle Unit lineations in northern Hymittos. F_3 fold hinges are both E-W and N-S oriented. **(i)** Stereogram of poles-to-planes of Upper and Middle unit planar elements in southern Hymittos. While the pole to foliation contouring is imprecise due to relatively low measurements, the distribution has a similar orientation to measurements from the Middle Unit in northern Hymittos. **(j)** Stereogram of Upper and Middle unit linear elements in southern Hymittos. See inset diagram for delineation of northern, central and southern Hymittos. Poles to planes of folds (grey): axial planes, fold lineations (grey): hinges. Mean great circles were calculated using a cylindrical best fit. Stereograms plotted using Stereonet (Cardozo & Allmendinger, 2013).

macrostructures suggest a single episode of foliation development related to isoclinal folding (F_1; **Figure 2.4b, c**), followed by a generation of open folding (F_2) with shallowly north-plunging fold hinges and subvertical axial planes.

2.5.2 Middle Unit

The middle tectonostratigraphic package of Hymittos bedrock (herein Middle Unit comprising the Kaissariani Unit and Lower Marble [locally Kaissariani Schist, Upper Marble, and Lower Marble]) consists of the greenschist facies metasedimentary and metavolcanic schist (**Figure 2.4e; 2.5b, d**) and calcitic and dolomitic marbles (**Figure 2.4f; 2.5c**). The schistose lithotypes are a calcite-chlorite-graphite-quartz-white mica ± feldspar ± chloritoid

metasedimentary schist (**Figure 2.5f**) and epidote-chlorite-graphite-quartz-albite-white mica ± feldspar metavolcanic schist (**Figure 2.5d**). Quartz microlithons in Middle Unit metabasic schist uncommonly preserve glaucophane crystals and metapelitic calc-schist exhibit chloritoid, which is often replaced by chlorite and white mica (**Figure 2.5e**). This relationship suggests initial high-pressure metamorphism followed by greenschist facies retrogression. Schistose rocks form dm- to m-thick layers that are intercalated and folded together with blue-grey calcitic mylonitic marble. At higher structural levels, and to the east, the proportion of calcitic marble increases (**Figure 2.2; 2.3a, d**) and the mylonite are paler in colour. Within the interfolded mylonite are cm- to km-scale pervasively fractured dolomite blocks containing Triassic corals (Negris & Meunier, 1915), and rare quartzite and serpentinite. At the highest structural levels, along the upper detachment are exposures of a cataclased epidote-serpentinite mélange. Ultramylonitic bands are common in samples close to the upper detachment (**Figure 2.5b**). Middle Unit marbles exhibit a dominantly calcitic mineralogy with minor white mica. The calcitic marble are mylonitic with grain sizes ranging from 50-15 μm and display a 30-60° dipping $S_{1\text{-}2}$ foliation (**Figure 2.6a**). Middle Unit dolomitic blocks are commonly weakly to non-foliated and brittlely deformed and juxtaposed against calcitic marble by a tectonically reworked sedimentary contact. The Middle Unit is present as a series of steeply foliated (S_2) calcitic marble klippen above the lower detachment in central Hymittos and within the foothills east and south of the massif (**Figure 2.2; Figure 2.3a**).

The greenschist facies rocks of the Middle (and Lower) units exhibit a regional-scale foliation delineated by alternating marble and schist layers. In northern and north-central Hymittos, highly attenuated, tight to isoclinal folds are preserved within laterally extensive mylonitic layers suggesting an early F_1 folding event that reoriented an initial S_1 foliation (**Figure 2.6a**). These F_1 folds are overprinted and sheared into an S_2 foliation associated with rarely preserved WNW-ESE

mineral lineations (L_2) producing a regional-scale $S_{1\text{-}2}$ transposition foliation (**Figure 2.6a, f**). The schist and marble layers that define this variably dipping $S_{1\text{-}2}$ foliation are themselves folded (F_2) into km-scale recumbent folds with NNE-SSW hinges (**Figure 2.3b; Figure 2.6b**). $S_{1\text{-}2}$ foliation orientations vary across the massif as they have been reoriented by both F_2 and F_3 fold generations. Parasitic s-, z- and m-folds distributed along the margin of the Lower Marble-Kaissariani Unit contact indicate that the Kaissariani Unit is folded around the Lower Marble, underlying it in the southwest and occurring adjacent to and above it in the northwest. The weakly developed girdle illustrated in the contoured poles to Middle Unit foliation planes is the product of folding of S_2 foliations around the ~NNE-SSW fold hinge (**Figure 2.6e**). Middle Unit axial planes show a similar E-W dispersion (**Figure 2.6e**). Dolomitic (or high-Mg calcite) layers within the calcitic Middle Unit marble mylonites of the massif are boudinaged in E-W and N-S directions and have been rotated with a top-SSW sense of shear (**Figure 2.4f**).

At higher structural levels, close to the upper detachment ultramylonitic marble are more common with 10-3 μm sized calcite grains defining a subhorizontal S_3 foliation. Sheared calcite and quartz veins preserve a top-S sense of shear (**Figure 2.5c**). Schistose lithotypes at similar structural levels contain ultramylonitic bands with top-S S-C fabrics (**Figure 2.5b**).

2.5.3 Lower Unit

The lower tectonostratigraphic package of Hymittos bedrock (herein Lower Unit; locally Vari Schist, Pyrnari Marble) consists of greenschist facies pelitic schist, calc-schist, calcitic and dolomitic marbles, and rare quartzite (**Figure 2.4g, h; 2.5g, h, i**). In the central massif, exposures of the Lower Unit comprise >200 m thick, medium-to-dark grey, variably carbonaceous dolomitic marbles (Pyrnari Marble); at higher structural levels these marbles transition from largely undeformed to a strongly S_3-parallel foliated mylonite (50-20 μm grain size) and ultramylonite (5-

3 μm grain size). In southcentral Hymittos, the mylonitic marble is 20-30 m thick and variably calcitic to dolomitic in composition (**Figure 2.4g**).

Deeper structural levels expose intercalated metasiliciclastic rocks and marble of the Cheroma Unit. Historically termed the Vari Schist (Lepsius, 1893), we propose renaming this unit to avoid confusion with the Vari Unit on Syros (e.g. Aravadinou & Xypolias, 2017; Soukis & Stockli, 2013), as well as the presence of both marble and schistose lithotypes within the Vari Schist. Cheroma is the local term for the valley in southern Hymittos that best exposes the proposed type section. Cheroma schist and calc-schist have a calcite-chlorite-graphite-quartz-white mica ± chloritoid ± tourmaline mineralogy and are intercalated with fine-grained calcitic and dolomitic marble mylonite and rare quartzite (**Figure 2.5g, h, i**). Cheroma quartzite are fine- to medium-grained with a quartz-white mica-tourmaline-apatite mineralogy and display quartz fabrics indicative of subgrain rotation, incipient grain-boundary bulging and a grain-shape preferred orientation (S_3) the long axes of which are shallowly inclined towards the south. White mica, chlorite and graphite occur as top-S shear bands; quartz defines distinct microlithons that commonly contain chloritoid aligned in a N-S orientation. Cheroma marble are calcitic and dolomitic mylonite with grain sizes ranging from 50-20 μm and trace foliation-parallel coarse-grained white mica. Cheroma Unit rocks exhibit an F_2 refolded $S_{1\text{-}2}$ foliation most evident in schist and calc-schist.

2.5.4 Ductile-then-brittle faulting

The Upper, Middle and Lower units are separated by a pair of top-SSW, ductile then brittle, low-angle normal detachment faults (**Figure 2.2, 2.3**). The ductile deformation associated with the detachments commonly extends >100 m into the footwall and produced NNE-SSW lineated, subhorizontally foliated L-S tectonites, mylonite and ultramylonite in both marble and schist. The

structures have clear top-SSW sense of shear determined from flanking folds, sigmoids, delta clasts, stair-stepping of strain shadows on porphyroclasts, domino boudinage, and SCC' fabrics within this zone of ductile deformation (**Figure 2.4f, h; 2.5d, h, k**). Both detachment faults exhibit cataclastic fault cores that grade into the less deformed lithology of their respective hanging walls (**Figure 2.4d; S2.4j**); imbrication of clasts within the cataclasite bands gives a top-S sense of shear. The low metamorphic grade marble of the Upper Unit is heavily ankeritized close to the upper detachment, suggesting the detachments was a conduit for Fe-rich fluids (**Figure 2.4a**). Serpentinite and metavolcanic lenses are present within the fault zone of the upper detachment (**Figure 2.4c**).

Close to the upper detachment in the Middle Unit, and pervasively within the Lower Unit in central and southern Hymittos, the F_2 folded $S_{1\text{-}2}$ foliation is overprinted by a shallowly dipping mylonitic S_3 foliation with associated NNE-SSW oriented elongation and mineral lineations (L_3; **Figure 2.6f, h, j**) that increases in intensity with proximity to the detachments. The L_3 lineation is more strongly expressed and uniform than the S_3 foliation, the NNE-SSW oriented elongation and mineral lineations are uniformly present in the Lower Unit in almost all instances; these L_3 lineations are somewhat more dispersed in the Middle Unit than in the Lower Unit (**Figure 2.6f, h, j**). The S_3 foliation transposes previous folds and rotates fold hinges into a NNE-SSW orientation producing a second generation of isoclinal folds (**Figure 2.6c**). The S_3 foliations and all earlier structures are folded by F_3 domal open folds with vertical axial planes and both N-S and E-W hinges (**Figure 2.6d, e, g**).

Flanking structures in both the Middle and Lower units are dominantly top-SSW, though uncommon top-NNE structures are observed; consistent with a top-SSW regime, as antithetically rotating flanking structures may form under general shear (Wiesmayr & Grasemann, 2005).

Several generations of veins within Middle and Lower unit rocks preserve evidence of progressive shearing; earlier vein generations are fully transposed into the S_2 and S_3 foliations and are folded by F_2 and F_3 folds. Younger veins crosscut the S_2 foliation and F_2 folds and are only sheared and folded where S_3 and F_3 structures are evident.

Several orientations of steeply-dipping normal faults are observed across the massif (**Figure 2.2**). In north and central Hymittos, steeply-dipping E-W normal and N-S strike-slip faults have been identified in several instances; no definitive cross-cutting relationships have been observed. In southernmost Hymittos, displacement along E-W oriented normal faults have rotated foliated Middle Unit marble into a steep orientation (**Figure 2.3a**). These south-dipping faults are evident on satellite imagery and based on their orientation may root into the lower detachment.

2.5.5 White mica compositions

White mica $^{40}Ar/^{39}Ar$ geochronology requires characterizing the potential white mica populations in the sample. Through optical petrography, EDS mapping and EMPA analysis, multiple populations of white mica have been identified based on grain size, host lithotype, degree of crystal plastic deformation and geochemistry.

White mica from Upper Unit phyllites exhibit a single population of 100-1000 μm-long, brittlely deformed, kinked, subhedral to anhedral crystals with minimal undulatory extinction (**Figure 2.5a; S2.4d**). Where the phyllite possess a foliation, these crystals may display a weak preferential alignment. In some instances, chlorite-white mica intergrowths can be observed (**Figure S2.4d**). EDS chemical mapping and EMPA analysis were not conducted on white mica from Upper Unit samples as these samples are low metamorphic grade metasedimentary rocks from the hanging wall and are not expected to have experienced the Cenozoic metamorphic history of the CBU.

Optical petrography identified five white mica populations within samples from the Middle Unit rocks. Two populations are recognized in Middle Unit marble. (1) 50-250 μm-long euhedral crystals oriented parallel to the foliation in calcitic marble mylonite (**Figure 2.5c; S2.4e; S2.6b**). (2) In certain mica rich marble samples, white mica crystals are 200-500 μm-long, anhedral to euhedral and exhibit weak interlinked mica layers, and some kinks and undulose extinction, indicating some degree of deformation, but no significant shear strain (**Figure S2.4f**). Populations 1 and 2 are dominantly moderate-Si phengite, with minor muscovite intergrowths and rims though exceptions exist (**Figure S2.2; S2.6; Table S2.2**). The calc-mica schist and mica schist of the Middle Unit host an additional three populations. (3) Subhedral 100-250 μm-long crystals oriented oblique to the S_3 foliation within quartz- and feldspar-rich microlithons (**Figure 2.5f; S2.6e**); (4) elongate 100-500 μm-long, subhedral-to-anhedral, kinked muscovite crystals within shear bands; commonly interlayered with graphite, more rarely chlorite (**Figure 2.5f**); and (5) anhedral, 50-100 μm-long, phengitic or less commonly muscovitic crystals forming the cores of mica fish (**Figure 2.5f; S2.2**).

Optical petrography identified four white mica populations within samples from Lower Unit rocks. (1) Euhedral 200-1000 μm-long crystals oriented parallel to the foliation in calcitic marble mylonite (e.g. Hy27, **Figure S2.2; Figure 2.5g; S2.6c**), these crystals are dominantly moderate-Si phengite but exhibit muscovite-adjacent Si values (e.g. Hy 28; **Figure S2.2**). (2) Euhedral 50-100 μm-long phengitic crystals oriented parallel to the foliation in calcitic and dolomitic marble ultramylonites these crystals exhibit sparse muscovitic rims (e.g. Hy26, **Figure S2.2; Figure 2.5g**). (3) Elongate 100-500 μm-long, extensively sheared and deformed subhedral-to-anhedral crystals forming shear bands in mylonitic mica schist and calc-mica schist; commonly interlayered with graphite, and more rarely chlorite (**Figure 2.5h; S2.2; S2.6d**). (4) Subhedral-to-

anhedral, 100-700 μm-long, moderately deformed crystals in less mica rich calc-mica schists (**Figure 2.5i; S2.6a**).

White mica in Middle and Lower unit marble typically possess a phengitic composition (**Figure 2.7b**) trending from a median composition between Al-celadonite along the Tschermak substitution to a muscovite-rich end member (**Figure 2.7a, c; Table S2.2**); white mica in schistose rocks exhibit a slightly more muscovitic composition. Both in marble and schist, white mica shows a greater compositional heterogeneity in the Middle Unit (marble: 40-86% muscovite; schist: 49-89% muscovite, except one outlier; **Figure 2.7a; Table S2.2**) compared to the Lower Unit yielding more muscovitic analysis (marble: 56-82% muscovite, schist: 59-91% muscovite **Figure 2.7c; Table S2.2**). This is comparable to mica compositions in the middle and lower tectonic units of Lavrion (Coleman et al., 2019), though white mica from Hymittos show an overall greater range of compositions. The degree of pyrophyllitic substitution is higher in Middle Unit samples compared to Lower Unit samples, analogous to data from the upper and lower units of the nearby Penteli Mountains (Baziotis et al., 2020). Individual samples show a substantial degree of compositional heterogeneity. EDS maps combined with WDS point data reveal compositional zoning with phengitic, high-Si cores and muscovitic, low-Si rims fairly pronounced in Middle Unit rocks (e.g. Hy17; **Figure S2.2**) and to some extent also in Lower Unit rocks. In populations 2, 3, and 4 of the Middle Unit and 2, 3, 4 and 5 of the Lower Unit occasional intergrowths of chlorite and rare paragonite were observed. Compositional variability is particularly common in shear bands, where white mica is intergrown with chlorite and graphite (**Figure 2.5h; S2.2; S2.4; S2.6**).

The division between marble and schistose white mica populations is best evident on the Si (a.p.f.u.) versus relative Mg concentration $\left(X_{Mg} = \frac{Mg}{Fe+Mg}\right)$ binary diagrams (**Figure 2.7b, d**). White mica from Middle and Lower unit marbles exhibit X_{Mg} values larger than 0.8 (except one

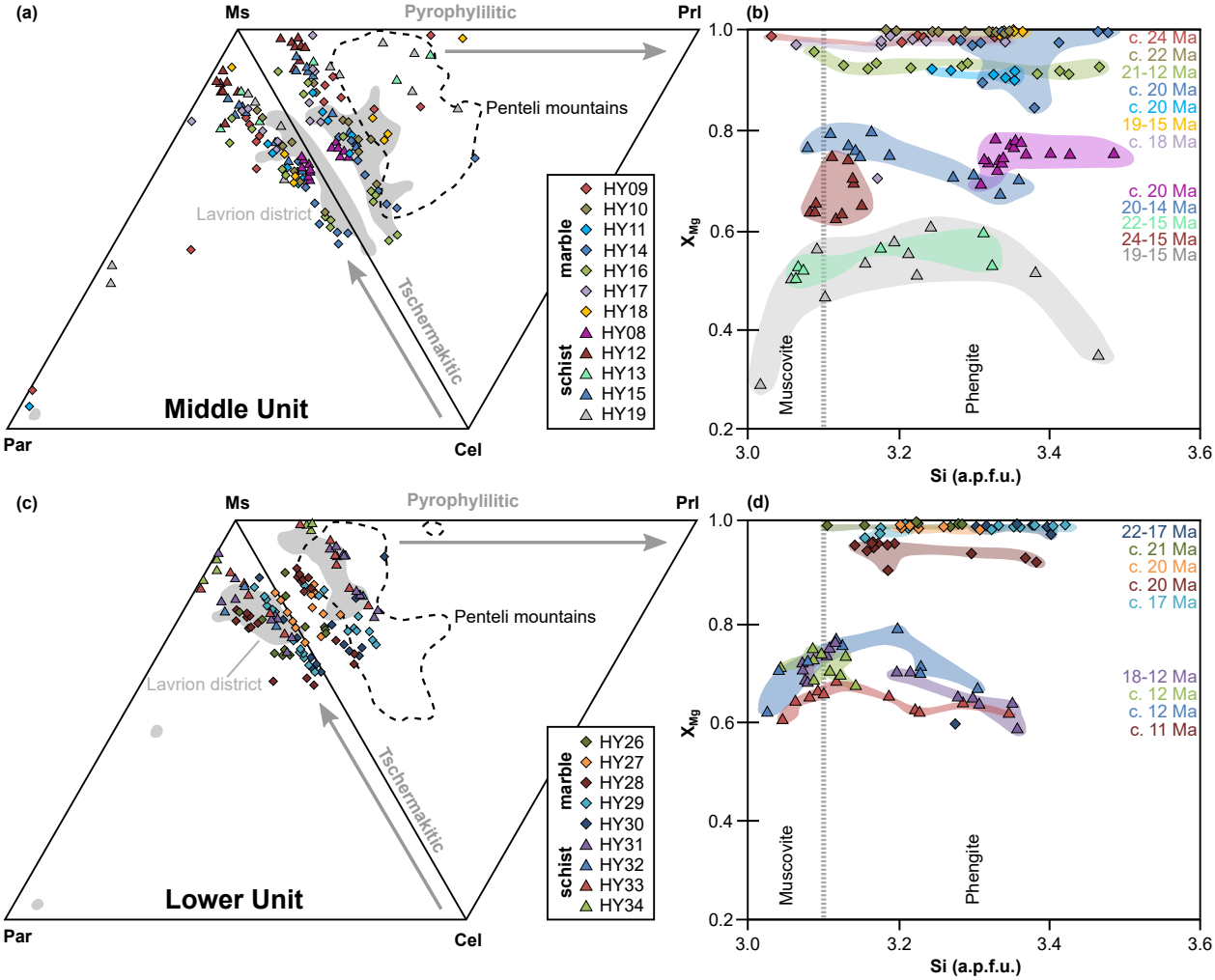

Figure 2.7. Mica chemical compositions. **(a)** Muscovite (Ms)-celadonite (Cel)-paragonite (Par) and muscovite-celadonite-pyrophyllite (Prl) chemistry ternary diagrams for the Middle Unit marble (diamonds) and schist (triangles) of Hymittos. Dashed field: white mica analyses from the upper tectonic unit of Penteli (Baziotis et al., 2019); grey field: analyses from the middle tectonic unit of the Lavrion district (Coleman et al., 2019). **(b)** Si (a.p.f.u.) vs. relative magnesium concentration (X_{Mg} = Mg/(Fe+Mg)) binary diagram for Middle Unit white mica. White mica analyses define two populations divided by lithotype. **(c)** Ms-Cel-Par and Ms-Cel-Prl chemistry ternary diagrams for marble and schist of the Lower Unit of Hymittos. White mica analyses are displayed from the lower tectonic unit of Penteli (dashed field, Baziotis, Proyer, et al., 2019) and the lower tectonic unit of the Lavrion district (grey field; Coleman et al., 2019). **(d)** Si (a.p.f.u) vs. XMg binary diagram for Lower Unit white mica. Mica form two populations divided by lithotype. Endmember calculations followed the methodology of Parra et al. (2002) and Vidal and Parra (2000). The mica nomenclature and compositional fields are from Rieder et al. (1998). The weighted average of $^{40}Ar/^{39}Ar$ total fusion analyses are listed for each sample in (d) and (e).

outlier) whereas X_{Mg} in Middle and Lower unit schists ranges from 0.4-0.8 (**Figure 2.7b, d**), with individual samples forming distinct populations with respect to X_{Mg}. As no overlap occurs between the schist and marble samples, and there is no observable trend between Si and X_{Mg}, the difference in X_{Mg} between schists and marbles and also individual samples is likely controlled by bulk-rock composition rather than changing metamorphic conditions. In contrast, Si (a.p.f.u.) values of schist and marbles largely overlap between 3.0-3.5. It is noted however, that in the Lower Unit white mica from schistose samples exhibit lower Si (a.p.f.u.) than white mica in marble samples (**Figure 2.7d**). Maximum Si (a.p.f.u) values reach up to 3.5 in the Middle Unit and 3.4 in the Lower Unit. Irrespective of lithology in the tectonic unit, considerable intrasample dispersion is observed in some cases. More or less continuous variation along the Tscherkmak substitution and evidence of multiple white mica populations suggests that the intra-sample dispersion in mineral composition is likely indicative of subtly changing P-T conditions during (neo/re)crystallization events (Parra, Vidal, & Jolivet, 2002).

2.5.6 White mica 40Ar/39Ar geochronology

Multiple single-grain total fusion white mica $^{40}Ar/^{39}Ar$ analyses were conducted on up to eight grains for each of 25 mica-bearing rock samples from Hymittos. Three Upper Unit, thirteen Middle Unit and nine Lower Unit samples were analyzed (**Figure 2.2; Figure S2.1** for sample locations). Weighted average ages are reported for samples where dispersion is low and age ranges for samples where dispersion is high (1σ; **Figure 2.8; Table S2.3**). Total fusion is a useful technique as it constrains age heterogeneity both within a sample and across multiple samples (e.g. Coleman et al., 2019; Schneider et al., 2018; Uunk et al., 2018). Total fusion has several major benefits over the step-heating technique, chiefly it allows for many more dates from

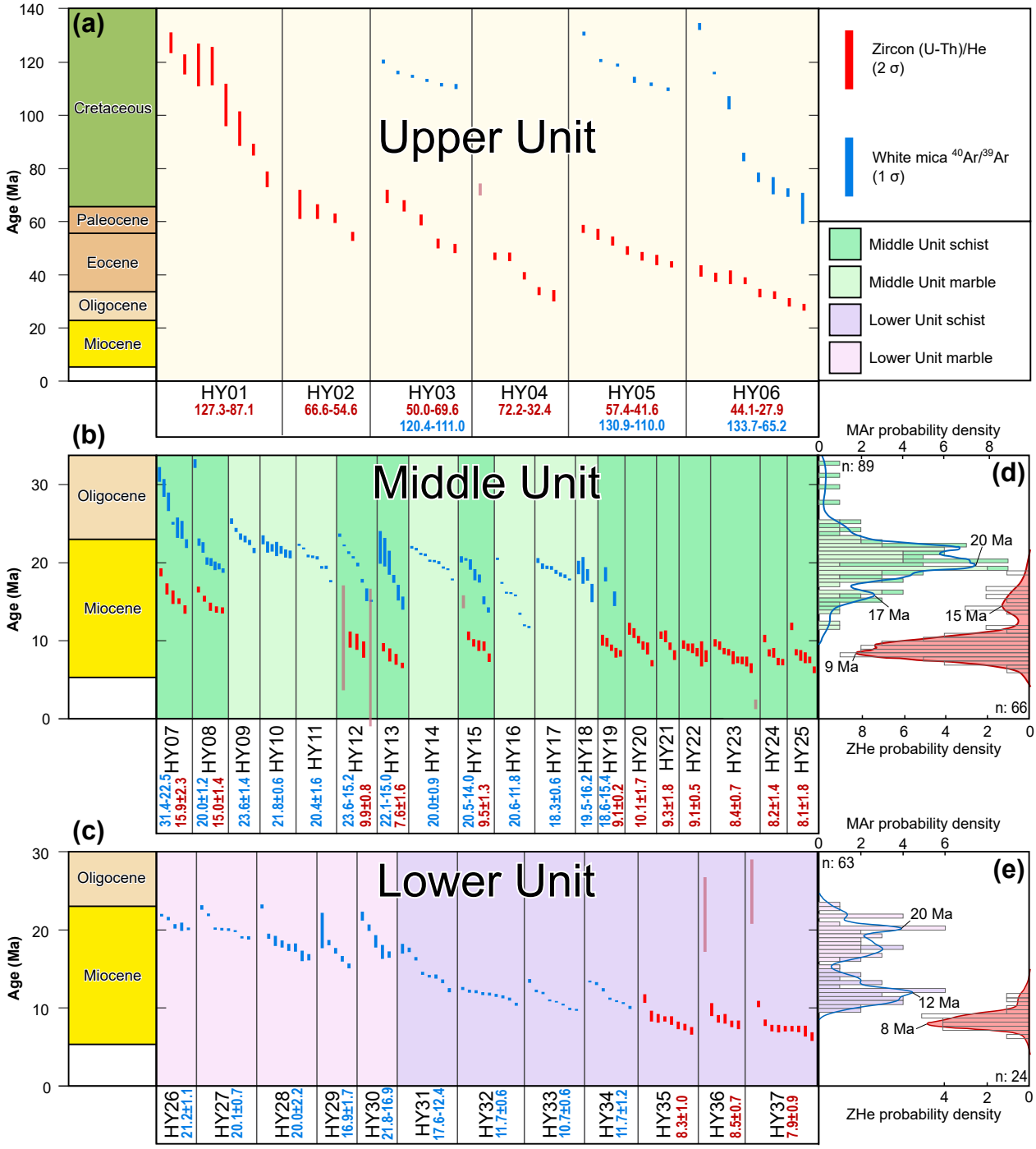

Figure 2.8. Summary of new geochronology from Hymittos. **(a, b, c)** Weighted distribution diagrams and **(d, e)** kernel density estimates for white mica 40Ar/39Ar total fusion (MAr; blue) and zircon (U-Th)/He (ZHe; red) ages. All ZHe ages are from (meta)siliciclastic rocks; MAr ages from marbles and schists. Grey bars are rejected analyses. Weighted average ages (when permissible) for both techniques are calculated for each sample. Two Devonian 40Ar/39Ar ages (337.5 ± 0.7 Ma, HY03 and 369.2 ± 1.7 Ma, HY05) and a single early Jurassic 40Ar/39Ar age (199.7 ± 0.8 Ma, HY05) are not displayed. See data repository for 40Ar/39Ar and (U-Th)/He analytical data tables (**Table S2.3; S2.4**) and sample locations (**Figure S2.1**).

polymetamorphic rocks for the same analytical budget, the technique produces a range of analytical dates better representing the total date range of mica from within a sample, and avoiding age bias due to a limited number of dates often one or two in the total fusion technique. In instances where the metamorphic history of a massif is unknown, total fusion is superior for examining the history of complexly deformed polyminerallic mica bearing samples.

Analysis of 23 single grains from three Upper Unit samples produced ages that range from the Late Devonian (369.3 ± 1.8 Ma) to the earliest Paleocene (65.2 ± 5.6 Ma). A Cretaceous to early Paleocene age population (n: 20; **Figure 2.8a**) is present in all three samples, but is dominated by ages between 133.7-104.9 Ma (n: 15), with a Late Cretaceous to earliest Paleocene component (n: 5) only evident in a single sample. Overall the population of Upper Unit white mica $^{40}Ar/^{39}Ar$ ages yields the greatest dispersion within individual samples 259.3 Myr, 226.6 m.y, and 68.5 Myr Elimination of three outliers drastically reduces much of the intra sample dispersion to 20.9 Myr, 9.5 Myr, and 68.5 Myr.

Total fusion white mica $^{40}Ar/^{39}Ar$ analyses of 89 single grains from thirteen Middle Unit samples yielded ages ranging from 52.1 ± 0.6 Ma to 11.8 ± 0.1 Ma. The dispersion within individual samples ranges from 38.1 Myr to 1.9 Myr. Removal of two outliers (52.1 ± 0.6 Ma, 32.7 ± 0.5 Ma) yields middle Oligocene to middle Miocene ages (n: 81) ranging from 31.4 ± 0.9 Ma to 11.8 ± 0.1 Ma (**Figure 2.8b, d**). Mica ages from marbles typically range from 25-16 Ma; sample HY16 possesses a younger age population extending to 11.8 ± 0.1 Ma (**Figure 2.8b**). Middle Unit schist single-grain ages are from 23.6 ± 0.1 to 14.0 ± 0.3 Ma; these schists typically have slightly larger errors and a greater degree of age dispersion than most marble samples (**Figure 2.8b**). Sparse early Oligocene single grain analyses concentrated in HY07 and HY08 may define an early Oligocene age population (32.7 ± 0.5 Ma to 27.9 ± 1.1 Ma, n: 4) within the highest levels

of the Middle Unit close to the upper detachment (**Figure 2.8b, c**). No uniform grain size control on white mica ages was observed in these analyses. Some samples exhibited both more tightly defined chemical compositions and age ranges (e.g. HY18), but this trend is not evident for most samples, which may suggest that white mica composition has an unpredictable control on age dispersion in these samples.

$^{40}Ar/^{39}Ar$ analysis of 63 single grains from nine Lower Unit samples yielded ages ranging from 23.1 ± 0.2 Ma to 9.8 ± 0.1 Ma with a single 78.1 ± 0.3 Ma outlier (**Figure 2.8c**). Removal of the single outlier reduces the range of intrasample dispersion to 6.5-1.7 Myr and Lower Unit $^{40}Ar/^{39}Ar$ white mica ages define two populations i) An early-to-middle Miocene 3.1-3.5 Si phengitic population in marbles ranging from 23.1 ± 0.2 Ma to 15.5 ± 0.2 Ma; and ii) a middle-to-late Miocene phengitic-to-muscovitic population in mica and calc-mica schists that ranges from 13.5 ± 0.1 Ma to 9.8 ± 0.1 Ma and 3.0-3.3 Si (**Figure 2.8d; 2.7d**) with a dominant population at c. 12 Ma. Sample HY31 is from a higher structural level, has a greater proportion of calcite and spans a range from 17.7 ± 0.6 Ma to 12.4 ± 0.2 Ma.

Though there are a range of grain sizes and ages in Middle and Lower unit marbles, there is no obvious grain size control on age. Mylonitic marbles with 50-100 μm-long grains produce statistically identical ages to samples with mica grain sizes up to 500 μm. Plotting ^{39}Ar as a proxy for grain size against age shows no uniform relationship (**Figure S2.6**).

2.5.7 Zircon (U-Th)/He geochronology

Zircon (U-Th)/He analysis was conducted on up to ten grains per sample for 21 zircon-bearing samples from Hymittos in order to elucidate the low-temperature (<200°C) geologic history of the massif. Weighted average ages are reported for samples where dispersion is low and age ranges for samples where dispersion is high (2σ; **Figure 2.8; Table S2.4**).

Upper Unit zircon (U-Th)/He analysis (single crystals n: 44) from six samples of metasiliciclastic rocks yielded widely dispersed ages. Typically, zircons are euhedral with tabular to elongate habits and range from 220-100 μm in length; rarer subhedral and anhedral grains are stubby to equant and may lack one or both terminations. Crystals contain minimal inclusions and exhibit a range of metamictization. The dispersion comprises dates from late Oligocene to Late Cretaceous from five samples (27.9-72.2 Ma; n: 31; **Figure 2.8a**). A second, more dispersed Late to Early Cretaceous age population is present in sample HY01 (76.2-127.3 Ma; **Figure 2.8a**).

Zircon from the Middle Unit range in size from 110-50 μm, and are commonly subrounded to rounded, clear and colourless to rosy and translucent with stubby to tabular habits. Zircon (U-Th)/He analyses from twelve samples (n: 74) identified a middle and a late Miocene population (**Figure 2.8b, d**). The middle Miocene population (15.4 ± 1.0 Ma, n: 10) is observed in two samples: a cataclased quartz-feldspar-white mica ultramylonitic schist and a cataclased serpentinite melange located within the upper detachment brittle fault zone (**Figure S2.1**). A dominant population of late Miocene ages are recorded in samples from structurally deeper levels (n: 56, 12.0 ± 0.31 to 6.5 ± 0.2 Ma; **Figure 2.8b**, **d**). Eight spurious analyses were discarded due to low He, low U or the presence of inclusions combined with anomalous ages (**Table S2.4**).

Lower Unit zircon from Cheroma Unit quartzite are typically subhedral and exhibit prismatic to tabular habits ranging in size from 380-105 μm. Grains from calc-schist and mica-schist range from 85-45 μm. Zircon (U-Th)/He analysis of Lower Unit samples HY35 (8.3 ± 1.0 Ma, n: 8), HY36 (8.5 ± 0.7 Ma, n: 5), and HY37 (7.9 ± 0.9 Ma, n: 10) produced late Miocene populations that are statistically identical (**Figure 2.8e**). Two anomalous analyses were discarded due to low U (**Table S2.4**).

2.6 Discussion

The significant differences in low-temperature geochronology, metamorphic grade, and degree of deformation between the Upper and Middle units supports the conclusion that the upper detachment is a major tectonic contact. The detachment fault cross-cutting the massif displays consistent top-SSW sense of shear, ductile-then-brittle deformation and is located along-strike of other exposures of the WCDS. The elongate north-south geomorphology of the massif (similar to exposures of other metamorphic domes within the western Cyclades; **Figure 2.1**), presence of a major tectonic contact and low-angle detachment faults prove that Hymittos is a Cycladic-style metamorphic core complex. We suggest that the Upper Unit (Alepovouni Unit) is an exposure of the Pelagonian Zone, based on its lithologies, low metamorphic grade, age, and structural position overlying crystalline rocks of the Middle and Lower units. The presence of a cataclased serpentinite melange within the upper detachment is observed elsewhere in the Cyclades separating the Pelagonian Zone and CBU (Selçuk Mèlange as reported in Okrusch & Brocker, 1990; Ring & Layer, 2003). The footwall to the upper detachment (Middle and Lower units) are exposures of the Lower Cycladic Blueschist Nappe evinced by the presence of a retrogressed blueschist facies mineral assemblage in metabasites of the Middle Unit and pelitic schists of the Middle and Lower units. To streamline the following discussion, we will consider the Middle and Lower units together as the Lower Plate; the Upper Unit and the overlying sedimentary basins are grouped into the Upper Plate.

The deformation of large blocks of rock is commonly heterogeneous and often diachronous (e.g. Chadwick, 1968), which complicates differentiating between different structural generations and correlating them across a region (Park, 1969). In geologic settings where deformation is relatively continuous (e.g. core complexes), structures that would traditionally be categorized as

different generations may occur over geologically short time periods under the same conditions; this is termed progressive deformation (Tobisch & Paterson, 1988). In such a setting structures produced during the early portion of progressive deformation are frequently reoriented, refolded, cannibalized or destroyed by the same conditions that created them producing composite structures (e.g. Grujic & Mancktelow, 1995; Platt & Behrmann, 1986; Turner & Weiss, 1963). We suggest that the ubiquitous overprinting of earlier structures by later generations is evidence that Hymittos underwent progressive deformation for >10 Myr as indicated by the dispersion of $^{40}Ar/^{39}Ar$ ages (further discussed in section 5.2.3). As a result, we define folds and foliations that are kinematically compatible and uniformly affect all previous structures (F_{x-1}, F_{x-2}) as part of the same generation (F_x and S_x respectively).

2.6.1 Upper Plate

The moderate upright folding, prevalence of N-S lineations, and cataclasite development in Upper Unit phyllites increases with proximity to the upper detachment. Calcite ribbons in calcitic rocks have been tentatively tied to intermediate strain at comparatively low temperature (Rybacki et al., 2003); likely all of these tectonic structures are a consequence of shallow crustal displacement along the detachment suggesting they correspond to the S_3 structures of the Middle and Lower units.

White mica within Upper Unit phyllites exhibit a range of grain sizes and morphologies, but overall show little evidence for ductile deformation or recrystallization (**Figure 2.5a**). Undulatory extinction is minimal and the host rocks are low metamorphic grade. Taken together, these observations suggest that the white mica within Alepovouni phyllites have a detrital origin. White mica $^{40}Ar/^{39}Ar$ ages in the Upper Unit of Hymittos are more dispersed and significantly older than white mica from the Lower Plate (**Figure 2.8**). White mica ages from samples HY03

and HY05 are c. 115 Ma similar to c. 116 Ma $^{40}Ar/^{39}Ar$ ages reported from phengite ages of the Pelagonian Zone (Makrotantalon Unit) on Andros Island, although the Makrotantalon Unit ages are much less dispersed and reflect 116 Ma metamorphism (Huet et al., 2015). The ages from the Upper Unit are also similar to white mica ages from the Pelagonian Zone in the hanging wall of the Santorini Detachment System (Schneider et al., 2018). Some of the age dispersion in the Upper Unit samples may reflect thermal heating during widespread late Cretaceous metamorphism and plutonism within the Pelagonian Zone (Altherr et al., 1982; Bröcker & Franz, 2006; Patzak et al., 1994) or could represent partial resetting during stacking of the Upper Unit atop the CBU during the Eocene (Huyskens & Bröcker, 2014). Overall, we suggest these Cretaceous to early Paleocene $^{40}Ar/^{30}Ar$ ages represent a detrital white mica population that may have been partially reset during HP-LT Cretaceous metamorphism of the Pelagonian Zone (Lips et al., 1998; Maluski et al., 1981; Schermer et al., 1990).

Cretaceous to Eocene zircon (U-Th)/He ages preserved in the Upper Unit metasedimentary rocks of Hymittos are interpreted as a partially reset detrital age signature based on the dispersion of the analyses (**Figure 2.8a**). We suggest this partial resetting occurred during the low-grade metamorphism of the Upper Unit, during which temperatures did not significantly exceed ~130 °C (lower limit of the ZHe partial retention zone; Reiners & Brandon, 2006) as this would have fully reset the zircon (U-Th)/He systematics.

The majority of the Upper Unit has been eroded from atop the massif (**Figure 2.2, 2.3**) and the late Miocene to Pleistocene terrestrial sedimentary rocks of the Athens and Mesogea basins contain clasts with a sub-Pelagonian Zone source and ZHe ages of 38-92 Ma (Krohe et al., 2010; Seman, 2016; **Figure S2.2**), indicating the Upper Unit was exposed and eroding during the Miocene. Presuming the partially reset ages reflect burial temperatures of ~130 °C it would be

necessary to remove ~5-8 km of material (based on an estimated 25°C/km geothermal gradient) between the Eocene and the present. A sample of unmetamorphosed Athens Schist (HY02) overlying the Pelagonian rocks of Hymittos produced zircon (U-Th)/He ages indistinguishable from analyses of Alepovouni Unit samples (**Figure 2.8a**). Paleontology suggests the Athens Schist Unit spans the Maastrichtian to Paleocene in age (Papanikolaou et al., 2004). We suggest that partially reset Paleocene to Eocene ZHe ages in the Upper Unit reflect shallow burial and a short residence time in the partial retention zone. Consequently, we envisage a scenario where the material from the Upper Unit was eroded during the Miocene to Pliocene, which led to deposition of Pelagonian-derived sediments in the Mesogea and Athens basins. Thus, the Athens Schist Unit may be in part recycled components of the Pelagonian Zone. Erosional removal of the Alepovouni Unit was perhaps driven by upward flexure of the metamorphic dome in the late Miocene.

2.6.2 Lower Plate

Our reinterpretation of the tectonostratigraphy of Hymittos differs from previous works (e.g. Lepsius, 1893; Marinos & Petraschek, 1956; Lekkas & Lozios, 2000; Krohe et al., 2010), which interpreted the dolomitic rocks in the northern massif as a graben, and proposed a succession based on primary sedimentary layering of calcareous and siliciclastic sediments. The km-scale folding (F_2) within the Middle Unit was hitherto unrecognized and explains previously unresolved field observations including s- and z-fold orientations, inconsistent 'stratigraphic' relationships and contacts. Despite the complex structure, elongation and mineral lineations are dominantly NNE-SSW and kinematics are dominantly top-S. We suggest that this is due to reorientation of S_1 and S_2 foliation surfaces and lineations during top-S shear associated with the development of the S_3 foliation.

2.6.2.1 High-pressure metamorphism

Mineralogy and mineral chemistry indicate relics of a high-pressure assemblage that was pervasively overprinted during greenschist facies metamorphism in the Lower Plate. High-pressure metamorphism (M_1) is evident from relict glaucophane uncommonly observed in Kaissariani metabasic schists (**Figure 2.5d**). Chloritoid in thin section typically appears metastable, retrogressing to white mica and chlorite (**Figure 2.5i**). The stability field for chloritoid in Fe- and Al-rich metapelites overlaps with the stability field for glaucophane in metabasites (El-Shazly & Liou, 1991; Spear & Cheney, 1989). Due to the commonly observed intergrowth of chloritoid, white mica and chlorite indicating retrogression, we suggest chloritoid growth occurred during M_1 metamorphism (Vidal et al., 1994). The absence of metabasic rocks within the Lower Unit of the massif prevents the unequivocal identification of more characteristic blueschist facies metamorphic assemblages.

White mica is used as both a thermobarometer and geochronometer because the mineral possesses a range of chemical composition strongly controlled by pressure and temperature (Parra, Vidal, & Agard, 2002; Vidal & Parra, 2000) and because of its elevated K content (McDougall & Harrison, 1999). When applied as a geobarometer, higher Si content has been correlated with elevated pressure (Massonne & Schreyer, 1987). Thus, the phengitic chemical compositions observed in marbles (**Figure 2.7b, d**), and the phengitic cores of zoned white mica in Kaissariani and Cheroma schist (**Figure S2.2**) are also compatible with a high-pressure metamorphic stage. This agrees with previous white mica-chlorite thermobarometry within the massif that identified a high-pressure metamorphic event in the Kaissariani schist (300 ± 25 °C, 1.4 ± 0.05 GPa; Baziotis et al., 2019b).

2.6.2.2 Greenschist facies metamorphism

High-Si phengitic mica have been partially chemically re-equilibrated to moderate-Si phengite and muscovitic compositions (**Figure 2.7a, b**), which we suggest occurred along the retrograde path of M_1 metamorphism at and below upper greenschist facies conditions of 470 ± 20 °C and 0.8 ± 0.1 GPa for the Middle Unit (M_2; Baziotis et al., 2019b). The new metamorphic conditions are further evinced by the muscovitic (Si-poor) rims on phengite-cored white mica crystals, zoned intergrowth of muscovitic and phengitic mica, growth of albite porphyroblasts, and the ubiquity of metamorphic chlorite and epidote. The thermal increase may be a result of higher heat flow relating to the emplacement of the metamorphic core complex (e.g. Roche et al., 2018).

Regrettably, there are currently no P-T estimates for the Lower Unit of Hymittos. We suggest that M_2 greenschist facies metamorphism was as hot (or slightly hotter) and associated deformation was more pervasive in the Lower Unit than in the Middle Unit based on the greater degree of compositional re-equilibration of white mica to a muscovitic composition (**Figure 2.7a, b, c, d**), complete resetting of $^{40}Ar/^{39}Ar$ systematics (**Figure 2.8c**), and the presence of ductilely deformed Lower Unit dolomite; Middle Unit dolomite is exclusively brittlely deformed. The trend of lower tectonostratigraphic units having relatively higher-grade metamorphism concurs with geothermobarometry on the LCBN from the Penteli Mountains and Lavrion elsewhere on Attica (Baziotis et al., 2009, 2019; Scheffer et al., 2016).

2.6.2.3 Thermal and deformation induced resetting of $^{40}Ar/^{39}Ar$ systematics

High-pressure metamorphism in the Cyclades occurred in the Eocene, yet white mica $^{40}Ar/^{39}Ar$ analyses on phengitic mica from Hymittos do not produce Eocene ages. The minor population of middle to early Oligocene white mica $^{40}Ar/^{39}Ar$ ages in Middle Unit schist that overlap with 33-21 Ma Rb-Sr phengite ages from Evia (Ring, Glodny, et al., 2007) and 36-22 Ma

white mica $^{40}Ar/^{39}Ar$ ages from the middle unit of Lavrion (Coleman et al., 2019) may correspond to diachronous Oligocene c. 30 Ma greenschist facies overprinting (Huet et al., 2014; Cao et al., 2018), the last gasp of blueschist facies metamorphism during syn-orogenic exhumation (Cliff et al., 2016; Laurent et al., 2017; Peillod et al., 2017; Ring, Glodny, et al., 2007). Alternatively, the ages are reflective of partial resetting of an original c. 50-40 Ma phengitic population produced during M_1 high-pressure metamorphism (Bröcker et al., 2004; Schneider et al., 2011). High-Si (>3.45; Bröcker et al., 2004) phengitic chemical compositions do not make up a major proportions of the Lower Plate analyses (**Figure 2.7b, d**), which may also explain the scarcity of early to middle Oligocene ages (**Figure 2.8b, c, d, e,**).

Peak temperatures during M_2 metamorphism (470 ± 20 °C; Baziotis, Proyer, et al., 2019) were sufficient to fully reset muscovite $^{40}Ar/^{39}Ar$ systematics (**Figure 2.8b**) but possibly not fully reset the high-Si phengite ages (Augier et al., 2005; Laurent et al., 2017; Di Vincenzo et al., 2001). That being said, the white mica $^{40}Ar/^{39}Ar$ ages in marbles occur over a relatively narrow age range (average intrasample dispersion is 4 Myr) and show no obvious relationship to white mica composition so it is likely that $^{40}Ar/^{39}Ar$ systematics were reset even if temperature was not the dominant controlling factor. We suggest that white mica $^{40}Ar/^{39}Ar$ systematics were reset by latest Oligocene to early Miocene greenschist facies metamorphism as a consequence of (re)crystallization enhanced by fluid flow during syn-metamorphic deformation. Consequently, we suggest that the c. 20 Ma peak in white mica $^{40}Ar/^{39}Ar$ ages (**Figure 2.8d, e**) is the timing of peak greenschist facies metamorphism for the Lower Plate rocks of Hymittos. The younger mid-Miocene ages yielded by mica from marble may indicate minor muscovite (neo)crystallization on the retrograde path of M_2 metamorphism (**Figure 2.8b, c**).

White mica in Lower Plate marble are typically subhedral to euhedral, relatively undeformed (**Figure 2.5c, g**) and preserve 25-16 Ma white mica $^{40}Ar/^{39}Ar$ ages with a distinct concentration at c. 20 Ma (**Figure 2.8b, c**). The <10 Myr range and subhedral to euhedral nature of the white mica in most Middle and Lower unit marbles suggests that were largely unaffected by progressive deformation at temperatures above 250 °C, the lower limit for crystal-plastic deformation of calcite (Kennedy & White, 2001). The youngest marble white mica ages are middle Miocene. Hence, we interpret that white mica $^{40}Ar/^{39}Ar$ isotopic systems closed in both Middle and Lower unit marbles c. 16 Ma. Ductile deformation of the marble mylonites likely ceased at temperatures close to 250 °C where the calcitic marble mylonite would have significantly increased in strength and decreased in permeability (Kennedy & White, 2001), we suggest this limited further recrystallization of white mica in marbles (Lewis et al., 1998).

White mica from Lower Plate schistose rocks have a variable muscovitic to moderate-Si phengitic composition (**Figure 2.7a, b**), chemical zonation, and exhibit a deformed appearance in thin section (**Figure 2.5f**). Compared to marble samples, Middle Unit schist show a greater dispersion of white mica $^{40}Ar/^{39}Ar$ ages ranging from early Oligocene to middle Miocene (**Figure 2.8d**). Schist generally exhibit a greater sensitivity to changing P-T conditions than marble, which commonly avoid extensive re-equilibration due to differences in permeability, more stable mineralogy, etc. (e.g. Ganor et al., 1989; Lewis et al., 1998; Lü et al., 2013). As the rocks of the Lower Plate cooled on the M_2 retrograde path, deformation would be preferentially accommodated by linked phyllosilicate layers. We speculate that the white mica $^{40}Ar/^{39}Ar$ ages from the Middle Unit schist record deformation-induced resetting of the latest Oligocene to early Miocene metamorphic population preserved in Middle Unit marble. The greater age dispersion is a result of partial substitution and incomplete chemical re-equilibration observed in the mineral chemistry

and chemical maps, as has been recognized in Lavrion and the Western Cyclades (Schneider et al., 2011; Iglseder et al., 2011; Grasemann et al., 2012; Cossette et al., 2015; Coleman et al., 2019). Lower Unit schistose rocks exhibit a smaller dispersion of white mica $^{40}Ar/^{39}Ar$ ages and compositions (**Figure 2.7d**) and are more pervasively deformed than equivalent samples from the Middle Unit. We suggest the majority of the white mica $^{40}Ar/^{39}Ar$ ages record complete recrystallization during pervasive c. 12 Ma S_3 deformation along the lower detachment (HY32; HY33; HY34; **Figure 2.8c**). HY31 contains a significant proportion of calcite (**Table S2.1**), the sample occurs at a higher structural level, its mica are less sheared and deformed than other schistose samples (**Figure 2.5i**), and consequently mica $^{40}Ar/^{39}Ar$ ages are slightly older. We suggest HY31 was only partially reset during late Miocene deformation along the lower detachment. $^{40}Ar/^{39}Ar$ systematics have been fully reset in many Cheroma schist samples, yet the white mica compositions are dispersed, which suggests that S_3 deformation-induced recrystallization did not fully chemically re-equilibrate white mica compositions. This further supports the conclusion that the degree of dispersion of white mica chemistry analyzed herein does not have a clear control on age dispersion in these samples.

2.6.2.4 Onset of brittle deformation

Samples HY07 and HY08 preserve the oldest zircon (U-Th)/He ages (c. 15 Ma) and white mica 40Ar/39Ar ages (early Oligocene) in the Lower Plate (**Figure 2.8b, d**). Furthermore, these are the only schistose samples to preserve 40Ar/39Ar ages that are uniformly older than ages from Middle Unit marbles. These samples are both located within the brittlely deformed fault zone of the upper detachment and are the structurally highest samples from within the Middle Unit. We suggest that these samples reflect preservation of a structurally higher portion of the LCBN within the fault zone c. 15 Ma even as the rest of the Lower Plate continued to exhume.

The dominant 10-8 Ma zircon (U-Th)/He ages in the Middle and Lower units of Hymittos are interpreted as reflecting relatively rapid cooling during late Miocene exhumation along the upper detachment. These data exhibit a limited dispersion, and flat age-eU and age-ESR trends (**Figure 2.8b, c, S2.4**), consistent with rapid cooling to temperatures below <130°C (Guenthner et al., 2013, 2014). The marked break in zircon (U-Th)/He cooling ages across the upper detachment suggests that this structure accommodated the majority of brittle late Miocene deformation.

2.6.3 Tectonic history

By integrating a new bedrock map with quantitative data, a metamorphic and deformation history may be resolved for Hymittos. We propose M_1 was a HP-LT metamorphic event recorded in the Middle and Lower units of the massif evinced by high-Si phengite preserved in marbles, phengite-cored white mica in schists, relict glaucophane in metabasites, and chloritoid in Middle and Lower unit schists and calc-schists. Syn-metamorphic (M_1) deformation within the subduction channel produced the S_1 foliations preserved in albite porphyroblasts and quartz-rich microlithons and as highly attenuated or rootless isoclinal folds (**Figure 2.5e; 2.9a**). Baziotis et al. (2019) estimates the conditions of this metamorphic event at 300 ± 25 °C, 1.4 ± 0.05 GPa based on chlorite-white mica thermobarometry. Eocene HP-LT metamorphism has been recognized regionally within the CBU (Altherr et al., 1979; Okrusch & Bröcker, 1990; Wijbrans & McDougall, 1986, 1988; Tomaschek et al., 2003; Schneider et al., 2011) and within the western Cyclades zircon U-Pb and white mica $^{40}Ar/^{39}Ar$ geochronology has documented c. 40 Ma metamorphism on Serifos (Schneider et al., 2011).

HP-LT metamorphism was followed by or overlapped with E-W compression and macroscopic folding of intercalated schist and marble layers producing the east-verging recumbent folds (F2) of the Middle Unit (Figure 2.9b). We suggest this occurred during the Eocene to early

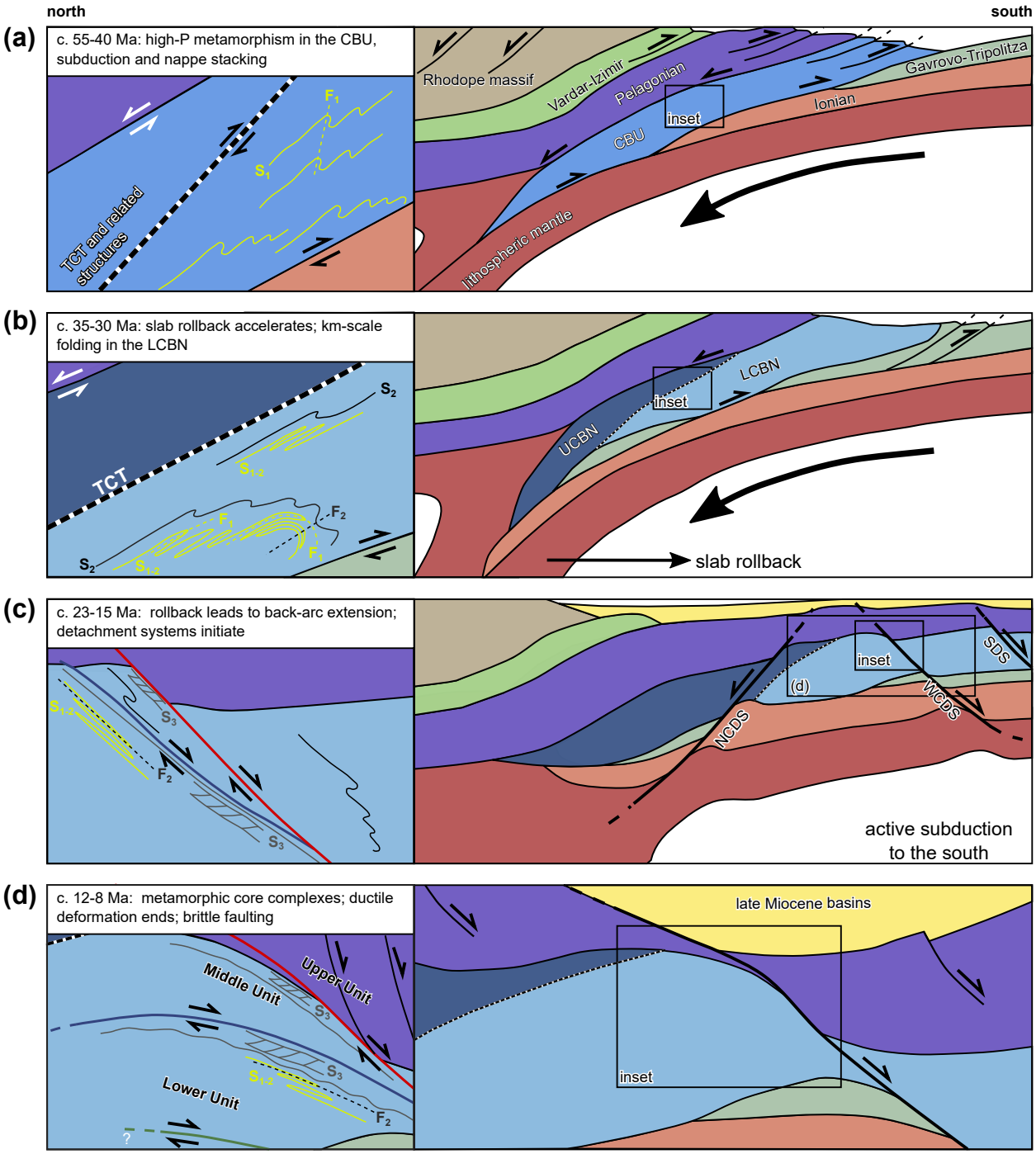

Figure 2.9. Refer to caption on next page.

Figure 2.9. (previous page) Unscaled, schematic diagram depicting the tectonic evolution of the proto-Aegean, Aegean and the units of the Hymittos massif. **(a)** At c. 55-40 Ma: subduction and nappe-stacking produces high-P metamorphism in the CBU, coeval with the onset of synorogenic exhumation within the subduction channel. S_1 foliations and F_1 folds are produced by progressive deformation **(b)** At c. 35-30 Ma: slab rollback accelerates, and synorogenic exhumation juxtaposes the LCBN and UCBN along the Trans-Cycladic Thrust. S_2 foliations and F_2 folds form, reorienting and exploiting earlier structures. **(c)** At c. 23-15 Ma: slab rollback has produced back-arc extension and crustal thinning, which initiated the detachment systems under greenschist facies conditions. Initial S_3 foliation develops, flattening and transposing older structures close to the detachments. Geochronology suggests the Hymittos detachments were coeval by the middle Miocene **(d)** At c. 12-8 Ma: metamorphic core complex development under waning greenschist facies conditions; the splays of the WCDS are an example of a horsetail structure accommodating the termination of a fault system as displacement approaches zero. Ductile deformation ceases on the Hymittos massif c. 8 Ma transitioning to brittle faulting and the formation of the Mesogea and Athens basins overlying the Upper Unit.

Oligocene at mid-crustal depth within the subduction channel, possibly during basal thrusting that has been associated with the syn-orogenic exhumation of the CBU (Forster & Lister, 2009; Huet et al., 2009; Jolivet & Brun, 2010; Ring et al., 2010; Ring, Glodny, et al., 2007). Progressive shear reoriented and flattened perturbations in the S_1 foliation producing tight-to-isoclinal folds and the $S_{1\text{-}2}$ foliation.

A pervasive greenschist facies (M_2) mineral assemblage in Middle and Lower unit rocks is recorded by muscovitic rims on zoned white mica, and the growth of chlorite, epidote, and albite porphyroblasts (**Figure 2.5e**). M_2 occurred during latest Oligocene to early Miocene coeval with exhumation of the Middle and Lower units through ductile top-SSW deformation along the detachments as recorded by white mica $^{40}Ar/^{39}Ar$ ages in Lower Plate marbles. The 25-16 Ma white mica $^{40}Ar/^{39}Ar$ ages are strikingly similar to regional c. 25-18 Ma dates for the dominant greenschist facies metamorphism that has been correlated to post-orogenic extension-related exhumation throughout the Cyclades (e.g. Altherr et al., 1982; Brocker et al., 1993, 2004; Bröcker & Franz, 1998; Wijbrans et al., 1990; Wijbrans & McDougall, 1986, 1988; Xypolias et al., 2012). We propose the M_2 greenschist facies metamorphic event on Hymittos is an expression of the widespread greenschist facies event, and the ages overlap with c. 21-14 Ma white mica $^{40}Ar/^{39}Ar$

ages reported from Kea and Kythnos (Grasemann et al., 2012; Igleseder et al., 2011; Cosette et al., 2015) and 18-14 Ma from the Lower Unit of Lavrion (Coleman et al., 2019).

Progressive syn- to post-M_2 deformation likely produced the S_3 mylonitic foliation observed in the footwalls of the detachments (**Figure 2.5e; 2.9c**). This deformation also formed the open F_3 folds with N-S and E-W oriented hinges. White mica in Middle and Lower unit schists are aligned and stretched into the L_3 orientation suggesting the late Oligocene to Miocene white mica $^{40}Ar/^{39}Ar$ deformation ages are the product of recrystallization as a result of M_2-related syn-to-post-metamorphic deformation (**Figure 2.8b, c**). Continued accommodation of deformation within the schists led to shear and flattening of the F_2 folds into isoclines (**Figure 2.6c**). Sparse NE-SW and E-W oriented lineations in the Middle Unit (**Figure 2.6f**) may correspond to earlier deformation predating or during 50-40° clockwise rotation of the Aegean microplate during the latest Oligocene to mid-Miocene (van Hinsbergen et al., 2005).

During the late Miocene, as the Middle and Lower units cooled, ductile deformation was succeeded by brittle deformation along the detachments. Within the Middle and Lower units, deformation produced structurally controlled N-S aligned brittle slip lineations along S_3 and earlier foliations. This top-SSW ductile-then-brittle deformation along the detachment faults led to the exhumation of LCBN rocks as the footwall of an asymmetric metamorphic core complex producing extension parallel and perpendicular folding (F_3; **Figure 2.9d**). Similar fold styles are commonly observed in other crustal-scale detachment faults (e.g. Aravadinou & Xypolias, 2017; Braathen et al., 2000; Fletcher & Bartley, 1994; Mancktelow & Pavlis, 1994), however the extension perpendicular F_3 folds suggests the conditions of deformation on Hymittos require further investigation. During the latest stages of extension, the massif was dissected up by east-west trending high-angle normal faults, and dextral and sinistral strike slip faults.

2.6.4 Northwestern termination of the West Cycladic Detachment System

It has been previously observed that low-temperature geochronology is consistent along-strike of the WCDS (Coleman et al., 2019). We suggest that these new data, along with the SW-directed kinematics, conclusively demonstrate that the detachments of Hymittos are exposures of the WCDS that were ductilely active in the early and middle Miocene before transitioning to a wholly brittle structure at c. 9-8 Ma represented by zircon (U-Th)/He cooling ages from Hymittos, Lavrion, Kea, Kythnos and Serifos (Grasemann et al., 2012; Berger et al., 2013; Seman, 2016). The overlap between Middle Unit zircon (U-Th)/He ages (15-9 Ma) and Lower Unit white mica $^{40}Ar/^{39}Ar$ ages (c. 12 Ma) suggests the lower detachment was ductilely deforming even as the upper detachment was brittlely active. Furthermore the 15 Ma zircon cooling ages provide a minimum bound for the onset of brittle faulting related to the WCDS on Hymittos.

Most Hymittos Middle Unit samples have similar white mica $^{40}Ar/^{39}Ar$ ages (23-15 Ma) compared to the lower tectonostratigraphic unit of Lavrion (18-14 Ma; Coleman et al., 2019). The only samples from Hymittos that have a similar age pattern to the middle unit of Lavrion are samples from the structurally highest levels of the Middle Unit of Hymittos (HY07, HY08; **Figure 2.8b**; Berger et al., 2013; Seman, 2016; Coleman et al., 2019). These samples are structurally higher portions of the CBU preserved in the detachment during faulting. Therefore, the lower and upper detachments of Lavrion may laterally join the upper detachment of Hymittos as a pair of splays.

The detachment systems of the Cyclades juxtapose CBU (LCBN and UCBN) footwalls against Pelagonian Zone hanging wall. To the west of Hymittos, the Pelagonian Zone is the dominant geological unit (**Figure 2.1a, b**). The absence of CBU to the west suggests the detachments of Hymittos have accommodated less displacement than detachments on islands

closer to the center of the WCDS (i.e. Kea and Kythnos; Grasemann et al., 2012), and represent exposures of the lateral terminus of a Cycladic-style detachment. The late Miocene white mica $^{40}Ar/^{39}Ar$ ages, and their similarity to ages from the lower detachment of Serifos indicate that ductile deformation at the two ends of the fault was occurring simultaneously, suggesting a ductile shear zone ~150 km in lateral extent, terminating a comparatively short distance northwest of Hymittos and southeast of Serifos.

The significant difference in metamorphic grade and white mica $^{40}Ar/^{39}Ar$ and zircon (U-Th)/He ages between the Upper and Middle units of Hymittos, as well as the evidence that the Lower Unit of the massif experienced somewhat higher temperature conditions suggests that displacement along the Hymittos detachments must be significant. Thus, the WCDS may carry on several km to the northwest beneath the rocks of the Pelagonian Zone on the Greek mainland (**Figure 2.1**) possibly continuing along structures recently identified via gravimetry measurements (Dilalos et al., 2019). Top-NNE kinematics have been reported for the Pelagonian Zone in this region, possibly pointing to a terminus or linkage of the NCDS and WCDS (Diamantopolos et al., 2009). The displacement gradients at the terminations of the structure must be extremely high, since the significant offset at Hymittos must be negligible within tens of kilometers to the northwest. This may in part be accommodated by the multi-plane detachments of Hymittos as a vertically oriented horsetail, serving the same mechanically necessary purpose as the horizontally oriented structures that are sometimes recognized as the termini of strike-slip faults (Kim & Sanderson, 2006).

2.6.5 Cycladic-style detachment systems

The consensus on the architecture and evolution of the detachment systems accommodating extension within the Cyclades has advanced significantly over the last two

decades. Multi-plane detachments are commonly associated with extension-triggered plutonism; in this model extension along a detachment fault produces crustal thinning, the rise of asthenosphere and melting of the lower crust (Liati et al., 2009; Lister & Davis, 1989). The melt rises before being arrested at the brittle-ductile transition, in so doing it deactivates the original fault, and thermally weakens the crust above the pluton, leading to localization of a new detachment plane that accommodates subsequent deformation (Rabillard et al., 2018). Granitoid crystallization ages from along the WCDS are similar c. 12-9 Ma for Serifos (Altherr et al., 1982; Iglseder et al., 2009) and Lavrion c. 9-8 Ma (Liati et al., 2009). These localities both expose multiple fault planes correlated to the WCDS, with youngest white mica $^{40}Ar/^{39}Ar$ ages suggesting the detachment branches that localized at the roof of these plutons were active at c. 10 Ma (Iglseder et al., 2009; Schneider et al., 2011; Grasemann et al., 2012; Berger et al., 2013; Coleman et al., 2019). This has been interpreted to indicate a sequence of fault deactivation and relocalization in these and other localities (e.g., Tinos, Mykonos and Ikaria; Brichau et al., 2010; Laurent et al., 2015; Beadoin et al., 2015; Rabillard et al., 2018). Where plutons are not present, detachments exhibit a single plane (i.e. Kea, Kythnos, Sifnos, Andros; Iglseder et al., 2011; Ring et al., 2011; Grasemann et al., 2012; Huet et al., 2014).

On Hymittos, multiple faults of the WCDS are observed without spatially associated plutonism. Local studies on mineralization and airborne gravimetry to characterize the subsurface of Athens found no evidence for a magmatic body (Dilalos et al., 2019; Stouraiti et al., 2019). The late Miocene white mica ages in the Cheroma schists overlap with the oldest portions of the late Miocene zircon (U-Th)/He ages in both the Middle and Lower units (**Figure 2.8b, c, d, e**). The lower detachment was ductilely deforming in the late Miocene as the upper detachment was brittlely deforming. Thus, another case for Cycladic-style detachments must be considered: multi-

plane detachments within the Cyclades may be co-active and plutonism cannot be the only mechanism driving (re)localization.

In a regional context, the NE-directed NCDS initiated before the SW-directed WCDS: 35-30 Ma and 26-22 Ma, respectively (Jolivet et al., 2010; Grasemann et al., 2012). Rb-Sr and $^{40}Ar/^{39}Ar$ constrain the latest ductile deformation along the NCDS to 20-18 Ma (Laurent et al., 2017). The youngest ages related to ductile deformation on Hymittos are c. 12 Ma, which is 6 Myr younger than c. 18 Ma ages of ductile deformation from Kea and Kythnos (Grasemann et al., 2012; Cossette et al., 2015) and are similar to 13-9 Ma white mica $^{40}Ar/^{39}Ar$ ages from a ductile-brittle branch of the WCDS on Serifos (Grasemann et al., 2012) and 14-10 Ma ages from the lower unit of Lavrion (Coleman et al., 2019). Thus, the WCDS continued to be active as a ductile structure c. 8 Myr after the NCDS began deforming brittlely. This suggests that extension within the Cyclades is diachronous and migrated southwards through time, agreeing with similar observations for the greater Aegean (Jolivet et al., 2003).

2.7 Conclusion

Bedrock mapping, white mica $^{40}Ar/^{39}Ar$ and zircon (U-Th)/He dates, and petrographic and structural analyses suggest the detachments of Hymittos are an extension of the Western Cycladic Detachment System (**Figure 2.1**). The Upper Unit is part of the Pelagonian Zone, and regional evidence and zircon (U-Th)/He data suggests the Upper Unit exhumed during Eocene to recent erosion. The Middle and Lower units of Hymittos are correlated to the LCBN of the Cyclades. Our work suggests a series of deformation and metamorphic events: M_1 high-pressure low-temperature metamorphism and associated deformation correlated to Eocene metamorphism recognized elsewhere within the Cyclades. Foliations associated with this syn-orogenic deformation are transposed and refolded as an $S_{1\text{-}2}$ foliation during west-verging folding. M_2 greenschist facies

metamorphism occurred during the late Oligocene to early Miocene as indicated by white mica $^{40}Ar/^{39}Ar$ ages in Middle and Lower unit marbles. Middle to late Miocene ductile deformation partially to fully transposed $S_{1\text{-}2}$ foliations into an S_3 transposition foliation and reset $^{40}Ar/^{39}Ar$ systematics in Middle and Lower unit schists. Finally, zircon (U-Th)/He cooling ages suggest the Middle and Lower units were exhuming under brittle conditions c. 8 Ma. Field evidence and the overlap in deformation ages suggests that the upper and lower detachments were coeval in the middle Miocene. Co-active multi-plane detachments suggest a new endmember for Cycladic-style detachment systems.

2.8 Acknowledgements

Funding was provided by the Natural Sciences and Engineering Research Council of Canada (to David Schneider) and the Austrian Academy of Sciences (Emil Suess-Erbschaft, to Bernhard Grasemann). I thank the Greek Institute for mining and Exploration in Athens for providing permission for fieldwork and technical support. Rebecca Flowers and James Metcalf (TRaIL) assisted with zircon (U-Th)/He analyses, Alfredo Camacho (University of Manitoba) for 40Ar/39Ar analyses, and Glenn Poirier (University of Ottawa-Canadian Museum of Nature MicroAnalysis Laboratory) for SEM and microprobe analyses; their contributions are greatly valued. The manuscript on which this chapter is based is published in *Tectonics*. In light of this we thank the editors Laurent Jolivet and Federico Rosssetti for editorial handling and Paraskevas Xypolias and Patrick Monié for constructive reviews.

Chapter 3: Detrital zircon geochronology of the Lower Cycladic Blueschist Nappe – Provenance of Neotethyan terranes in the western Cyclades

Abstract

Sections of presumed Cycladic Blueschist Unit exposed along the western Cyclades, Greece are of uncertain provenance and the paleogeographic relationship of the Cycladic Blueschist Unit to the greater Hellenides is unclear. Understanding the sediment sources of metasedimentary rocks within the Cycladic Blueschist Unit gives insight into the pre-subduction tectonic position and history of the basin in which the protoliths were deposited. This study presents new detrital zircon U-Pb analyses from the metasedimentary bedrock of the Attic Peninsula and integrated with results from the Santorini archipelago. These localities are at either end of the Lower Cycladic Blueschist Nappe, the structurally lowest subdivision of the Cycladic Blueschist Unit. Zircon U-Pb analysis of samples allow for correlations across the nappe, and throughout the greater Aegean region. Samples reported herein are divided into Proterozoic and Paleozoic end members, which represent zircon dominantly sourced from Gondwana and the European margin, respectively. Several samples display clear mixing between these two end members supporting a gradual evolution in sediment sources over time rather than an abrupt change wherein limited mixing would be observed. Variscan-aged zircon in samples of the Cycladic Upper Unit and Lower Cycladic Blueschist Nappe are interpreted to be sourced from a shared metamorphic basement. The recognition of a laterally extensive Proterozoic horizon across the Lower Cycladic Blueschist Nappe suggests a coherent stratigraphy for the lowest sections of the Cycladic Blueschist Unit. This study supports the correlation of the Cycladic Blueschist Unit to the Pindos Zone of the Hellenides on the basis of detrital zircon ages, regional geologic history, and tectonic position.

3.1 Introduction

The Alpine orogen contains numerous crustal blocks derived from the late Neoproterozoic to Cambrian Avalonian-Cadomian belt of northern Gondwana. Termed peri-Gondwanan terranes, the terranes are characterized by 640-570 Ma arc magmatism and contemporaneous basin development (Nance et al., 2008). Although they share a Gondwanan origin, these terranes are arrayed over hundreds of kilometers and have differentiable geologic signatures including the timing and composition of magmatism, ages of sedimentary strata, and grade of metamorphism (Zak et al., 2021). Determining the position and wandering of microcontinents from the northern and western margins of Gondwana is obscured by crustal reworking during Variscan and Alpine events leading to disruption of paleontological and paleomagnetic data (Dürr et al., 1978). Detrital zircon U-Pb geochronology may be useful for decoding the tectonic evolution of some of these terranes by examining the age of sedimentary sources (Dickinson & Gehrels, 2009; Gehrels, 2014), identifying the origin of allochthonous terranes (Krogh & Kepspie, 1990) and defining episodes of crustal growth and accretion (Keay & Lister, 2002; Moecher & Samson, 2006). Zircon is suitable for such a task as it is a physically and chemically robust mineral, and can normally withstand erosion, deformation and metamorphism, while preserving internal microstructures, primary crystallization date, chemical zoning and metamorphic overgrowths (Gehrels, 2014).

The Cycladic Blueschist Unit (CBU) is a polymetamorphosed sequence of Mesozoic rocks of equivocal affinity (**Figure 3.1a**). Based on the degree of Eocene high-pressure metamorphism the CBU has been subdivided into the Lower and Upper Cycladic Blueschist Nappes (LCBN and UCBN respectively; Grasemann et al., 2018). The CBU has been proposed as a paleogeographic equivalent of the Pindos Unit (Bonneau, 1984; Bonneau & Kienast, 1982), the Pelagonian Zone (Stampfli et al., 2003), or the Vardar-Izmir Unit (Chatzaras et al., 2013; Zlatkin et al., 2018). The

UCBN in the central, northern and eastern portions of the Cyclades has been the subject of numerous detrital zircon U-Pb studies (Bröcker et al., 2016; Flansburg et al., 2019; Keay & Lister, 2002; Löwen et al., 2015; Porkolab et al., 2019; Poulaki et al., 2019; Zlatkin et al., 2018). In contrast, significantly fewer studies have focused on exposures of the LCBN in the southern and western Cyclades, which represent different portions of the proto-CBU basin and possibly record different sedimentary sources (Seman et al., 2017). Exposures of the LCBN on Mt. Hymittos at the northwest end of the WCDS host significant metasedimentary sequences including >200 m thick packages of calcitic and dolomitic marble. This stratigraphy hosts far more carbonate rocks than other exposures of the LCBN from the western Cyclades (e.g., Santorini) which presents a greater proportion of metasiliciclastic and metavolcanic rocks. The difference in abundance of protolith types from the same metamorphic unit may be the product of spatial or temporal variation in the protolith's environment of deposition giving insight into the history of the basin. The aim of this study is to investigate the provenance of the metamorphic bedrock of the LCBN by sampling across the nappe, correlating the zircon U-Pb dates to the Pindos or Vardar zones and evaluating the evolution of sediment sources through time. Additionally, I investigated the zircon age spectra of the upper plate (Pelagonian Zone) for comparison to lower plate samples and integration into a regional tectonic model. In this study I report new detrital zircon U-Pb data from Attica combined with unpublished data from Attica and Santorini (Lion, 2018; Seman, 2016), that allow correlation between sedimentary sequences of the Greek mainland and the western Cycladic islands and address uncertainties regarding the affinity of terranes bracketing the proto-CBU basin.

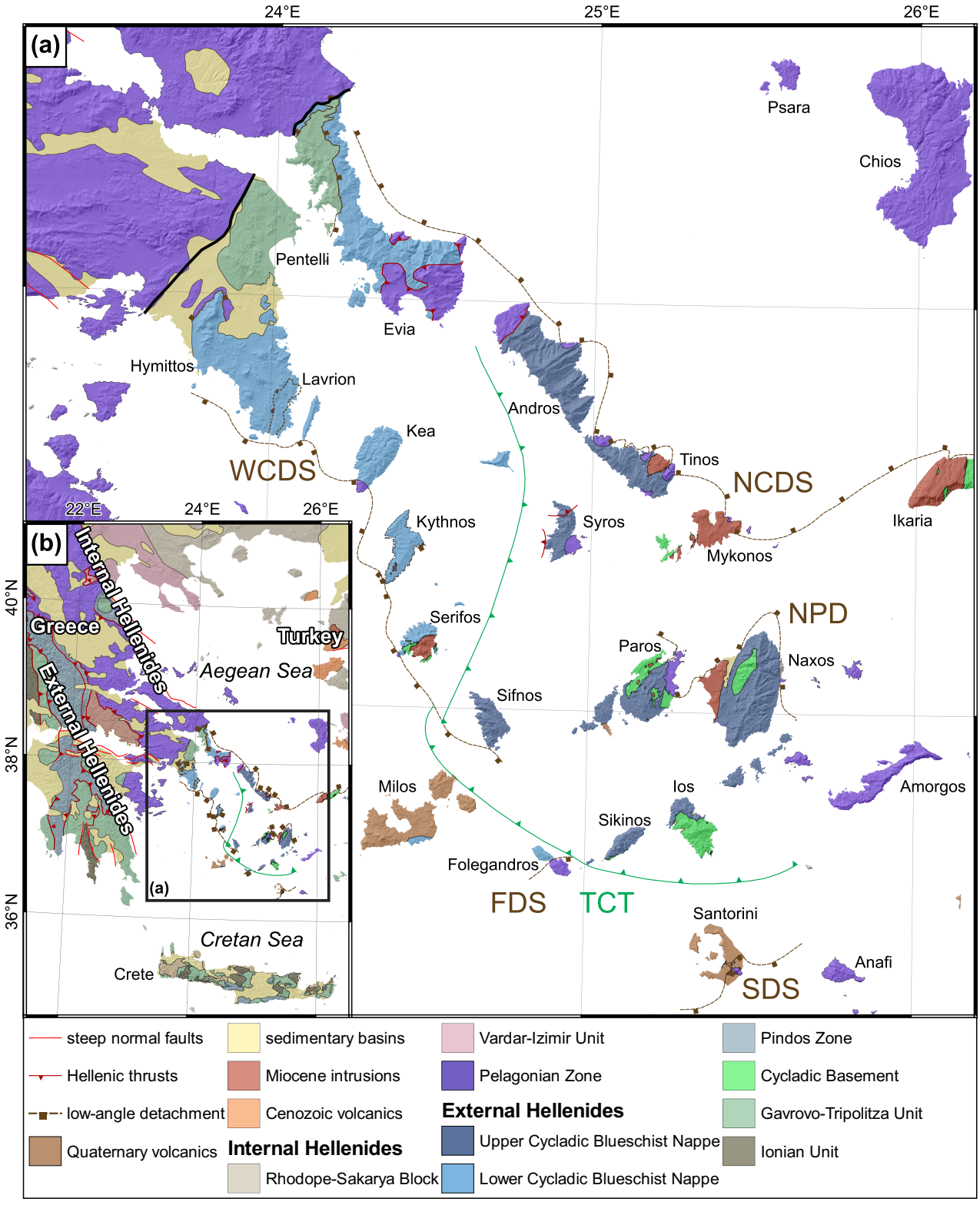

Figure 3.1. Refer to caption on next page.

Figure 3.1. (previous page) **(a)** Simplified bedrock geological map of the central Aegean. Extensional detachments include the West Cycladic Detachment System (WCDS; Grasemann et al., 2012), the North Cycladic Detachment System (NCDS; Jolivet et al., 2010), the Naxos-Paros Detachment (NPD; Buick, 1991; Urai et al., 1990), the Santorini Detachment System (SDS; Schneider et al., 2018) and the Folegandros Detachment System (FDS; Bakowsky et al., 2023). The Lower and Upper Cycladic Blueschist Nappes are subdivisions of the Cycladic Blueschist Unit, separated by the Trans-Cycladic Thrust (TCT; Grasemann et al., 2018). **(b)** Simplified bedrock geological map of the Hellenides in Greece, westernmost Turkey and Crete as well as the Aegean and Cretan seas. These maps are projected in the geographic coordinate system, using the World Geodetic System (WGS) 1984 datum.

3.2 Regional Geology

The bedrock of the Aegean region and mainland Greece are the product of Mesozoic and Cenozoic rifting, subduction, and collision between the Eurasian and African tectonic plates as a result of closure of the Tethys ocean(s) and during the Alpine orogeny (Jolivet & Brun, 2010; Papanikolaou, 2021; Schmid et al., 2020). Amalgamation of microcontinents and closure of ocean basins built up a nappe stack termed the Hellenides (Jacobshagen, 1986; Ring et al., 2010). The orogen has been subdivided into the External Hellenides that comprises the Phyllite-Quartzite, Ionian, Gavrovo-Tripolitza, and Pindos thrust units and the Internal Hellenides, which contains the Pelagonian, Axios-Vardar, Serbo-Macedonian and Rhodope thrust units (**Figure 3.1b**; Jolivet & Brun, 2010). In the following sections I characterize several proposed correlations of the CBU and discuss the bedrock geology of the Cyclades.

3.2.1 Pelagonian Zone

The Pelagonian Zone of the Hellenides (**Figure 3.1b**) has been interpreted as a fragment of the extended Cimmerian/Apulian microcontinent that rifted from Gondwana and divided the Paleo- and Neotethys ocean basins (Mountrakis, 1986). It comprises a Paleozoic-Mesozoic continental margin assemblage of volcano-sedimentary rocks, Triassic-Jurassic carbonates and local ophiolites (Bonneau, 1984; Yarwood & Aftalion, 1976) that overlie a crystalline basement

of Neoproterozoic gneisse, amphibolite and metapelite (Anders et al., 2006; Schenker et al., 2014). These Precambrian rocks have been dubbed the Florina Terrane and are correlated to the Pan-African or Cadomian orogenies (Anders et al., 2006; Schenker et al., 2014), but have also been suggested to be of Amazonian or Avalonian affinity (Zlatkin et al., 2014, 2017). This terrane separated from southern Eurasia (Anders et al., 2007) during the Triassic breakup of Pangea and before the Late Jurassic-Early Cretaceous closure of the Vardar Ocean obducted Triassic to Jurassic ophiolitic rocks atop the Pelagonian Zone (Ferrière et al., 2012; Maffione & van Hinsbergen, 2018). The uppermost portions of the Pelagonian stratigraphy comprise Cretaceous limestone that grade into a late Cretaceous-Paleocene turbidite sequence (Mountrakis et al., 1983). Geochronology identified a magmatic history comprising Precambrian, Carboniferous, Permo-Triassic and Early Cretaceous magmatism (Anders et al., 2006, 2007; Pe-Piper & Piper, 2002; Schenker et al., 2014; Yarwood & Aftalion, 1976; Zlatkin et al., 2014). Recently recognized Late Cretaceous magmatism is linked to the north-directed subduction of the Pindos Ocean beneath Pelagonia (Koutsovitis et al., 2021).

3.2.2 Pindos Zone

The Pindos Zone of the Hellenides is interpreted as an Early Triassic to Eocene ocean basin of Neotethyan affinity (Degnan & Robertson, 1998; Robertson, 2002). The Pindos stratigraphy consists of oceanic lithosphere overlain by Middle to Late Triassic immature siliciclastic rocks, Early Jurassic passive-margin carbonate platform rocks, debris flows, and turbidite deposits (Degnan & Robertson, 2006; Fleury, 1980; Robertson et al., 1991). The Middle to Late Jurassic marked a regional change to oxidized mudstones, clastic sandstones and chert (Jenkyns & Winterer, 1982) followed by Late Jurassic to Late Cretaceous carbonate deposition and a Paleocene to Eocene flysch sequence recording suturing of Neotethys (Degnan & Robertson, 1998;

Ricou et al., 1986). Rare individual thrust sheets within the zone expose a depositional contact between the overlying sedimentary succession and mafic to intermediate extrusive igneous rocks of oceanic affinity (Degnan & Robertson, 2006; Robertson et al., 1991). Similar sedimentary successions tectonically overlie the westernmost portions of the Pelagonian Zone (Smith, 1993; Smith et al., 1975). Pelitic sequences of the Pindos Zone contain radiolarites suggesting deposition in cooler, deeper waters; widths of 300 km to 500 km have been suggested for the ocean at its maximum extent (van Hinsbergen et al., 2005). The western margin of the basin evolved as a subsiding passive margin before east-directed subduction and accretion in the Eocene to Oligocene (Degnan & Robertson, 1998).

3.2.3 Vardar Zone

The Vardar Zone is classified as part of the Internal Hellenides, and represents a Mesozoic oceanic domain recorded by an ophiolite-bearing suture zone that separates the Pelagonian Zone to the southwest from the Serbo-Macedonian Massif to the northeast (**Figure 3.1b**; Papanikolaou, 2021; Pe-Piper & Piper, 2002). The Vardar Zone comprises Triassic to Jurassic variably-metamorphosed ophiolites and associated volcanic and sedimentary rocks (Anders et al., 2005). This oceanic stratigraphy is overlain by an Early Cretaceous flysch containing blocks of ophiolitic and high metamorphic grade metamorphic material (Mercier et al., 1975; Ricou et al., 1998). Subduction of the Vardar basin began in the Late Jurassic corresponding to obduction of ophiolites atop the Pelagonian Zone (Anders et al., 2005; Maffione & van Hinsbergen, 2018; Ricou et al., 1998). Alternative models suggest an Early Cretaceous closure of the Vardar Ocean and ophiolite obduction in eastern continental Greece (Scherreiks et al., 2014). In the Late Cretaceous the suture zone collapsed producing a Cenomanian sedimentary basin before Turonian northeast-directed

thrusting and compression led to basin inversion (Bailey et al., 2020) driven by subduction of the Pindos Ocean (Sharp & Robertson, 2006).

3.2.4 Cycladic Islands and Attic Peninsula

The Attic-Cycladic Complex is a series of Oligo-Miocene metamorphic core complexes that juxtapose a Cycladic Upper Unit hanging wall against a footwall comprised of CBU and the Cycladic Basement Unit (**Figure 3.1b**; Grasemann et al., 2012; Jolivet & Brun, 2010; Lister et al., 1984; Schneider et al., 2018; Coleman et al., 2020). Eocene thrusting and Oligo-Miocene extension has dissected and reorganized the original stratigraphy of the ancient basin (Aravadinou et al., 2016; Huet et al., 2009; Jolivet & Brun, 2010). Investigating the terrane dynamics and provenance of the Attic-Cycladic complex is further complicated by the pre-Cenozoic history of the region, as Variscan and Alpine tectonism further confound investigation (Dürr et al., 1978). My study specifically targeted rocks proposed to be LCBN, and so this structural unit is described in more detail below along with the Upper Unit and Cycladic Basement.

3.2.4.1 Upper Unit

The hanging walls of the Cycladic core complexes are mostly low metamorphic grade metasedimentary, metabasic and ophiolitic rocks (Dürr et al., 1978). Where these rocks are higher metamorphic grade, they record middle Cretaceous high-pressure, and/or Late Cretaceous greenschist to amphibolite facies metamorphism and I- and S-type plutonism (Altherr et al., 1982, 1994; Patzak et al., 1994; Reinecke et al., 1982). The metamorphic rocks of the Cycladic Upper Unit are correlated to the Pelagonian Zone of the Internal Hellenides (Bonneau, 1984; Coleman et al., 2020; Huet et al., 2015; Katzir et al., 2000; Schneider et al., 2018). The stratigraphically highest sections of these Pelagonian rocks are a Paleocene-Eocene metaflysch (Jacobshagen, 1986;

Papanikolaou, 2021; Porkolab et al., 2019). The Pelagonian stratigraphy is often overlain and obscured by Neogene syn-extensional basin sediments (**Figure 3.1b**; Bargnesi et al., 2013; Konstantinos & Papanikolaou, 2004; Krohe et al., 2010; Sanchez-Gomez et al., 2002).

3.2.4.2 Cycladic Blueschist Unit

The CBU largely occupies the footwalls of the Attic-Cycladic Complex and extends from the central Attic Peninsula (Coleman et al., 2020) as far south as Santorini (Schneider et al., 2018), the northernmost Dodecanese (Roche et al., 2019) and possibly to westernmost Turkey (Candan et al., 1997; Cetinkaplan et al., 2020). The stratigraphy consists of a sequence of Permo-Carboniferous to latest Cretaceous passive margin marbles and metapelites (Dürr et al., 1978; Papanikolaou, 1987a; Poulaki et al., 2019). The CBU metasediments are commonly intercalated with Triassic metavolcanic rocks (Bröcker & Pidgeon, 2007; Liati et al., 2013; Pe-Piper & Piper, 2002) comprising ancient flows, volcaniclastic sequences or isolated blocks in serpentinized mélange. The metavolcanic rocks have MORB-type geochemical signatures and frequently exhibit high-pressure mineral assemblages (Brocker, 1990; Schliestedt & Matthews, 1987; Seck et al., 1996).

The CBU experienced high-pressure metamorphism during Eocene subduction and accretion (52-40 Ma: Dragovic et al., 2015; Lagos et al., 2007; Laurent et al., 2017; Lister & Forster, 2005; Ring & Layer, 2003; Schneider et al., 2011). Eocene high pressure metamorphism in the LCBN is calculated to have reached peak temperatures of 400°C (Augier et al., 2015; Baltatzis, 1996; Baziotis et al., 2009, 2019; Grasemann et al., 2018; Katzir et al., 2000). Eocene metamorphic zircon rims reported on Serifos, Ios and Sikinos are correlated to this HP metamorphic event (Poulaki et al., 2021; Schneider et al., 2011). High-pressure metamorphism was followed by greenschist facies metamorphism (30-18 Ma) that coincided with Oligo-Miocene

post-orogenic slab rollback and back-arc extension (Altherr et al., 1982; Brocker et al., 2004; Iglseder et al., 2011).

A single detrital zircon study of the LCBN within the western Cyclades has divided U-Pb age distributions into Proterozoic and Paleozoic end members (Seman et al., 2017). The Proterozoic samples in that investigation have Triassic to Early Jurassic maximum depositional ages (MDAs) and are inferred to have been derived from the Gondwanan margin. The overlying Paleozoic samples have Late Jurassic to Cretaceous MDAs, interpreted to have been sourced from the Pelagonian Zone (Seman et al., 2017). The similarities in detrital zircon age spectra between disparate exposures of the CBU on Kea, Kythnos and Serifos suggests that on at least some of the Cycladic islands a resolvable stratigraphy may be recognized (Seman et al., 2017).

3.2.4.3 Cycladic Basement Unit

The Cycladic Basement Unit underlies the CBU. Principally exposed on the islands of Naxos, Ios, Sikinos and Serifos, the Cycladic Basement largely comprises S-type Carboniferous (300-330 Ma) Variscan orthogneiss (Engel & Reischmann, 1998; Poulaki et al., 2019; Zlatkin et al., 2018) linked to protracted magmatism during closure of the Paleotethys ocean. The orthogneiss crosscut a mylonitic sequence of metapelitic and metapsammitic gneiss and schist, which possess Gondwanan detrital zircon signatures and Neoproterozoic to early Paleozoic MDAs (Flansburg et al., 2019; Keay & Lister, 2002; Poulaki et al., 2019; Zlatkin et al., 2018). Bonneau & Kienast (1982) consider the Cycladic Basement to have been the northern most part of the Apulian microcontinent and it has been correlated with the basement of the Pelagonian Zone (Flansburg et al., 2019).

3.2.4.4 Attica: Hymittos & Lavrion

The bedrock of Mt. Hymittos and the Lavrion district have been correlated to the Attic-Cycladic Complex (Coleman et al., 2020; Seman et al., 2017). These settings are characterized by tripartite tectonostratigraphies divided by paired top-SSW Oligo-Miocene detachment systems that have been correlated to the West Cycladic Detachment System (**Figure 3.2**; Berger et al., 2013; Coleman et al., 2019, 2020; Grasemann et al., 2012). These structures extend from southern Lavrion to Hymittos in the north, and beneath Athens to the west (**Figure 3.2a;** Baziotis et al., 2019; Dilalos et al., 2019). The detachments have been associated with significant fluid flow and syn-kinematic mineralization (Skarpelis, 2002; Stouraiti et al., 2016, 2019; Voudouris et al., 2008).

The hanging walls to these detachments (herein referred to as the upper plate) comprise low metamorphic grade to unmetamorphosed chemical and siliciclastic sedimentary rocks (**Figure 3.3b**; Krohe et al., 2010; Scheffer et al., 2016). The basement rocks of the upper plate are poorly preserved, likely a result of erosion during activity along the detachment systems (Coleman et al., 2019, 2020; Krohe et al., 2010). In Lavrion a klippe of unmetamorphosed red chert, serpentinites and upper Cretaceous limestones have been correlated to the Pelagonian Zone (Marinos & Petrascheck, 1956; Photiades & Carras, 2001). On Hymittos, upper plate basement rocks comprise the Alepovouni Unit, a sequence of low metamorphic grade metasiliciclastic phyllite, serpentinite, and marble (Coleman et al., 2020). These probable Pelagonian rocks are of notably higher metamorphic grade than those exposed in Lavrion and may record Late Cretaceous metamorphism recognized elsewhere within the Pelagonian Zone (Coleman et al., 2020; Patzak et al., 1994). The metamorphic rocks of the upper plate are overlain and obscured by several sedimentary basins (Krohe et al., 2010).

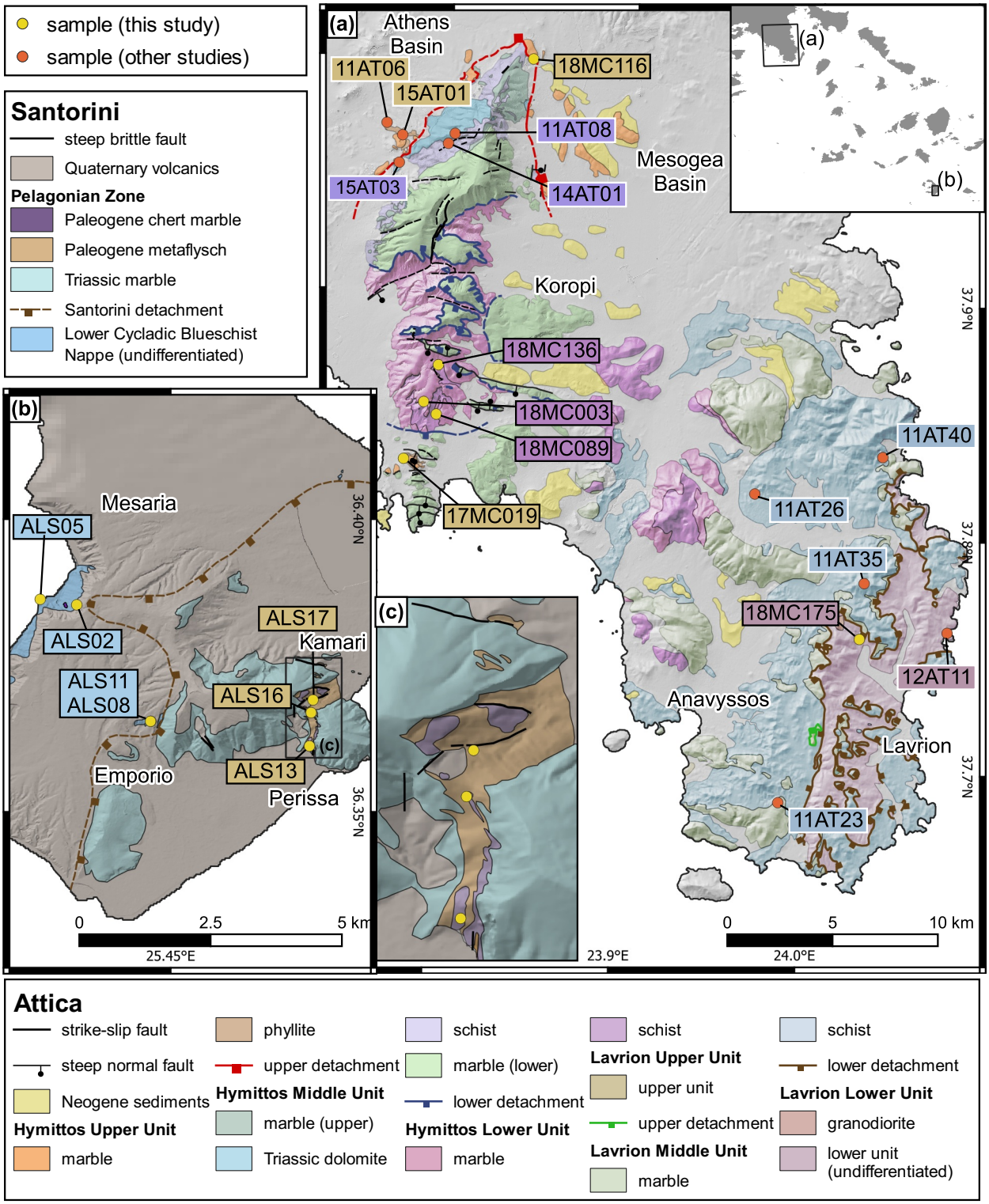

Figure 3.2. Maps of bedrock geology, structures, sample locations, sedimentary basins and geographic places for the study areas. **(a)** The Attic peninsula including Hymittos and Lavrion (after Coleman et al., 2019; 2020). Previously published detrital zircon U-Pb sample locations are also displayed (Seman, 2016; Seman et al., 2017). Grey regions of the map represent areas of no or limited data, typically obscured by the city of Athens. **(b, c)** Bedrock geological map of Santorini after Schneider et al. (2018). These maps are projected in the Universal Transverse Mercator (UTM) coordinate system, zone 35S using the WGS 1984 datum.

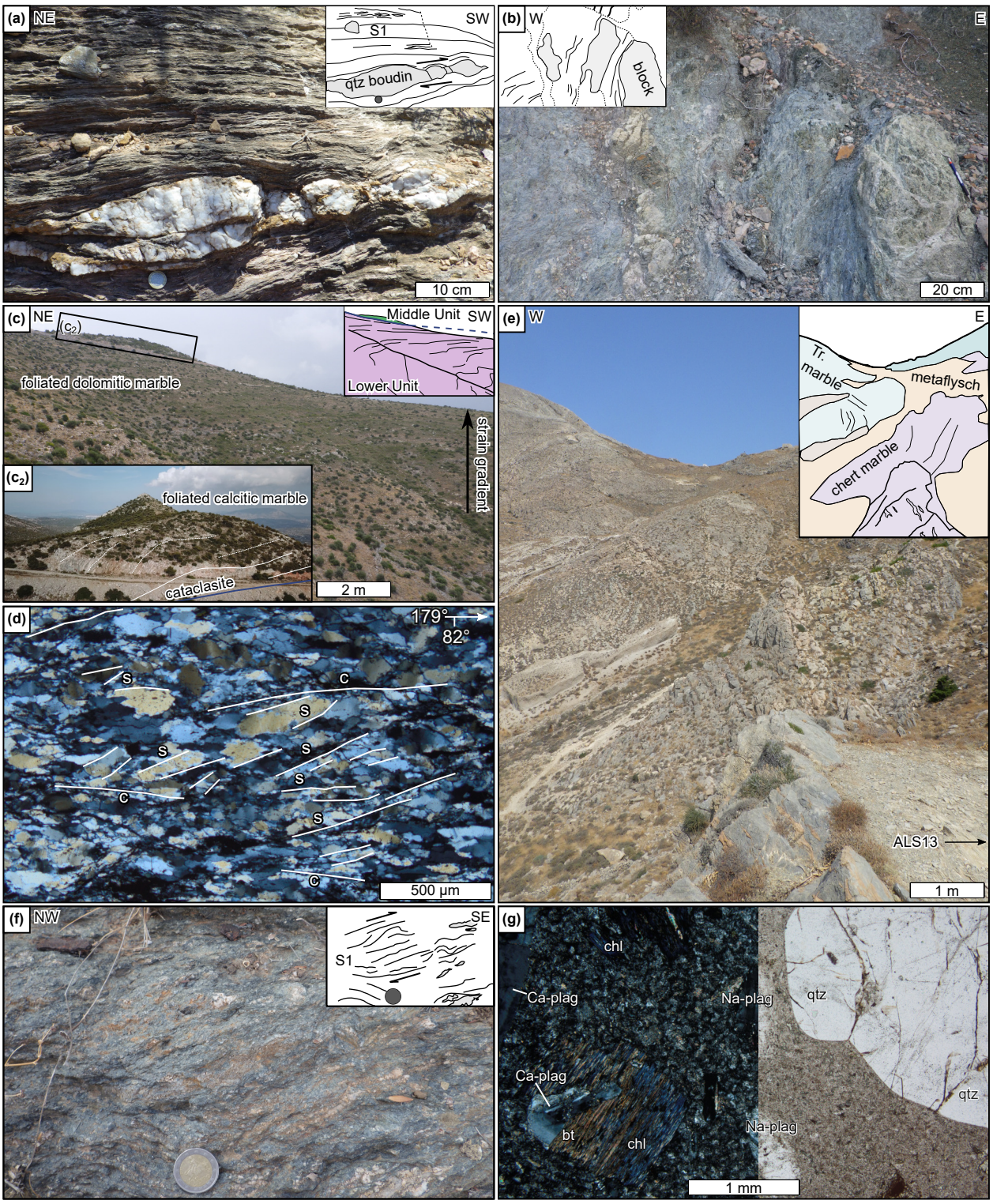

Figure 3.3. Refer to caption on next page.

Figure 3.3. (previous page) Field photos and sample localities from Hymittos, Lavrion, and Santorini. (**a**) Hymittos: Boudinaged quartz vein within Cheroma quartz-mica schist of the Lower Unit, S_1 foliation produced by top-SSW deformation along the lower detachment; sample location of 18MC089A1 (**4192574N, 746177E**). (**b**) Hymittos: Epidote-serpentinite blocks within a serpentinized groundmass, occurring as lenses of possible ophiolitic material along the upper detachment; sample location of 18MC116A1 (**4209692N; 749701E**). (**c**) Hymittos: Intercalated dolomitic marble, schist and calc-schist forming subhorizontal layering in the footwall of the lower detachment, location of subfigure c2 is shown by box. Inset (**c2**) depicts calcitic marble of the Middle Unit in the hanging wall of the lower detachment (**37.877176N, 23.783664E**). (**d**) Hymittos: Photomicrograph of quartz fabric formed by subgrain rotation. Alignment of quartz boundaries indicates top-S sense of shear during deformation; sample 18MC136A1 (**4194918N; 746129E**). **(e)** Santorini: Folded Paleogene metaflysch containing blocks of Triassic blue-grey calcitic chert marble (foreground) and associated dolomitic marble in the saddle of Profitis Ilias; sample location for ALS13 (**4025097N; 363067E**). (**f**) Lavrion: Metasedimentary Lower Unit schist in the footwall of the lower detachment exhibiting top-S S-C fabric and folding of more competent layers; sample location for 18MC175A1 (**4183016N, 238297E**). (**g**) Santorini: Thin section (XPL and PPL) photomicrographs of metarhyolitic sample ALS11 (**4025605N; 360636E**).

The Middle and Lower units of Hymittos and Lavrion are grouped into the lower plate. Lower plate rocks broadly comprise variably mylonitic, greenschist facies marbles, and metavolcanic and metasedimentary schist (**Figure 3.3a, c, d, f**). At Hymittos, the Middle Unit comprises cm- to m-scale interlayered greenschist facies metasiliciclastic and subordinate metaigneous schist and blue-grey calcitic marble mylonite (Kaissariani Unit) folded at the km-scale around a pale-grey to cream coloured sequence of calcitic marble mylonite with a maximum thickness >250 m (Lower Marble; Coleman et al., 2020). At higher structural levels and towards the north of the massif, the abundance of calcitic marble increases and dolomitic marble that host Triassic corals are present (Negris & Meunier, 1915). Quartz microlithons within Middle Unit metavolcanic schist preserve relict glaucophane attesting to a blueschist facies metamorphic event overprinted by greenschist facies metamorphism (Baziotis et al., 2020; Coleman et al., 2020). The Lower Unit of Hymittos consists of interlayered greenschist facies calc-schist, pelitic schist, calcitic and dolomitic marble mylonite and rare quartzite of the Cheroma Unit (**Figure 3.3a, d**).

Higher structural levels feature a >300 m sequence of interlayered dolomitic marble mylonite with subordinate calcite mylonite and rare schist lenses (**Figure 3.3c;** Coleman et al., 2020).

In Lavrion, the Middle Unit (locally Lavrion Schist) comprises metavolcanic-, metasiliciclastic- and calc-schist, overlying a calcitic marble (Marinos & Petrascheck, 1956). At higher structural levels the Lavrion schist preserve ophiolitic serpentinite and metabasalt with dominantly E- and N-MORB compositions (Photiades & Carras, 2001; Photiades & Saccani, 2006). The Lower Unit of Lavrion is composed of a pair of marble layers divided by a ~200 m thick sequence of the pelitic schist and Triassic volcanic rocks (Liati et al., 2009; Photiades & Carras, 2001) intruded by a Miocene granitoid (Liati et al., 2009). The lower plate of Lavrion preserves evidence of two tectono-metamorphic events: an initial HP/LT event reflecting syn-orogenic burial during subduction followed by greenschist facies metamorphism during syn- to post-orogenic exhumation (Baziotis et al., 2009; Scheffer et al., 2016).

3.2.4.5 Santorini

Santorini is located at the southernmost extent of the Attic-Cycladic Complex (**Figure 3.1**). The metamorphic bedrock of Santorini is largely obscured by Quaternary volcanic rocks and pumice deposits relating to the Plinian eruptions (**Figure 3.2;** Friedrich et al., 2006). Structural investigations identified a major low-angle detachment, the Santorini Detachment, separating a footwall correlated to the LCBN from a hanging wall correlated to the Pelagonian Zone (Schneider et al., 2018).

The upper plate of Santorini comprises metasedimentary and metavolcanic rocks largely exposed at Profitis Ilias. These rocks consist of a variably mylonitic marble sequence that hosts Triassic *Megalodon* fossils; the marble is folded around an early Paleocene metaflysch (Kilias et al., 1998), itself containing blocks of a distinct chert-bearing marble (**Figure 3.3e**). Folding of the

metaflysch within the Triassic marble is attributed to top-to-NW thrusting (Kilias et al., 1998). The upper unit was previously correlated to the Phyllite-Quartzite Unit and Tripolitza limestone of Crete (Craddock et al., 2009; Kilias et al., 1998).

The footwall of the Santorini Detachment comprises mylonitic quartz-rich phyllite, metaconglomerate, marble and metavolcanic rocks (**Figure 3.3g**; Schneider et al., 2018; Skarpelis & Liati, 1990). The intensity of ductile deformation increases approaching the detachment plane, which is strongly overprinted by cataclasis. The presence of glaucophane, phengite and crossite reflect a blueschist facies metamorphic assemblage (Davis & Bastas, 1978). Near Athinios, the basement is intruded by a Late Miocene I-type granitoid (Schneider et al., 2018).

Located at either end of the West Cycladic Detachment System, the bedrock of the Attic Peninsula and Santorini have been correlated to the LCBN based on metamorphic grade, structural style, similarities in lithotypes and limited detrital zircon geochronology (Coleman et al., 2019, 2020; Scheffer et al., 2016; Schneider et al., 2018; Seman et al., 2017). Additionally, Attica and Santorini both host better than average exposures of the Upper Unit hanging wall of the Cycladic detachments (**Figure 3.1; 3.2**). In consideration of the above factors, I strategically sampled units from these underexplored regions to assess their correlations to the LCBN, determine their relative positions within the tectonostratigraphy and make inferences about the source terranes for both the Upper Unit and LCBN.

3.5 Methodology

Following initial petrographic analysis, six samples were selected for LA-ICP-MS zircon U-Pb geochronology from exposures of the Cycladic Upper Unit and the LCBN, 5 samples are from the Upper and Lower units of Mt. Hymittos, and one sample is from the Lower Unit of Lavrion. Samples were selected from a range of structural levels and lithotypes to examine changes

in zircon populations with stratigraphic level. Zircon imaging and characterization were carried out at the University of Ottawa using a JEOL 6610LV SEM. Zircon U-Pb dating was carried out at the University of New Brunswick and the University of Ottawa. SEM images were used to position 24 μm diameter analytical laser spots, avoiding fractures, inclusions or other potential sources of common lead. Core and rim analyses were conducted on zircon that exhibited sufficiently thick overgrowths. A detailed methodology is available in the supporting information (**S3.1**).

The results of 1422 new laser spot analyses are presented as kernel density estimate (KDE) diagrams and their associated age histograms (**Figure 3.4; 3.5**). Preexisting data from Lion (2018) consisting of 616 zircon LA-ICP-MS dates have been re-plotted in a similar manner (**Figure 3.6; Table S3.2**). KDE diagrams have been argued to be more statistically robust for displaying U-Pb zircon dates (Vermeesch, 2012) than the more conventional probability density plot (PDP) as the latter can produce counterintuitive results and has little theoretical basis as a density estimator. To supplement my data from Attica, I include data previously reported from the area including six samples from the middle and upper units of Hymittos (**Figure 3.4**) and Lower Unit of Lavrion (**Figure 3.5**) from Seman (2016) and four samples from the Middle Unit of Lavrion (**Figure 3.5**) from Seman et al. (2017). Several unpublished samples (Seman, 2016) are presented only as PDP curves without associated zircon U-Pb age tables because the data were not present in the referenced document, in these cases the PDP curves have been reproduced without histogram bars. **Table 3.1** provides sample and zircon descriptions and synthesizes age analyses. Analyses that are >10% discordant, >5% reversely discordant or have >10% 2σ uncertainty are not considered in the following sections. Analyses younger than 900 Ma were not discordance filtered. The $^{206}Pb/^{238}U$ dates are considered for apparent ages <1000 Ma, and $^{207}Pb/^{206}Pb$ dates are used for

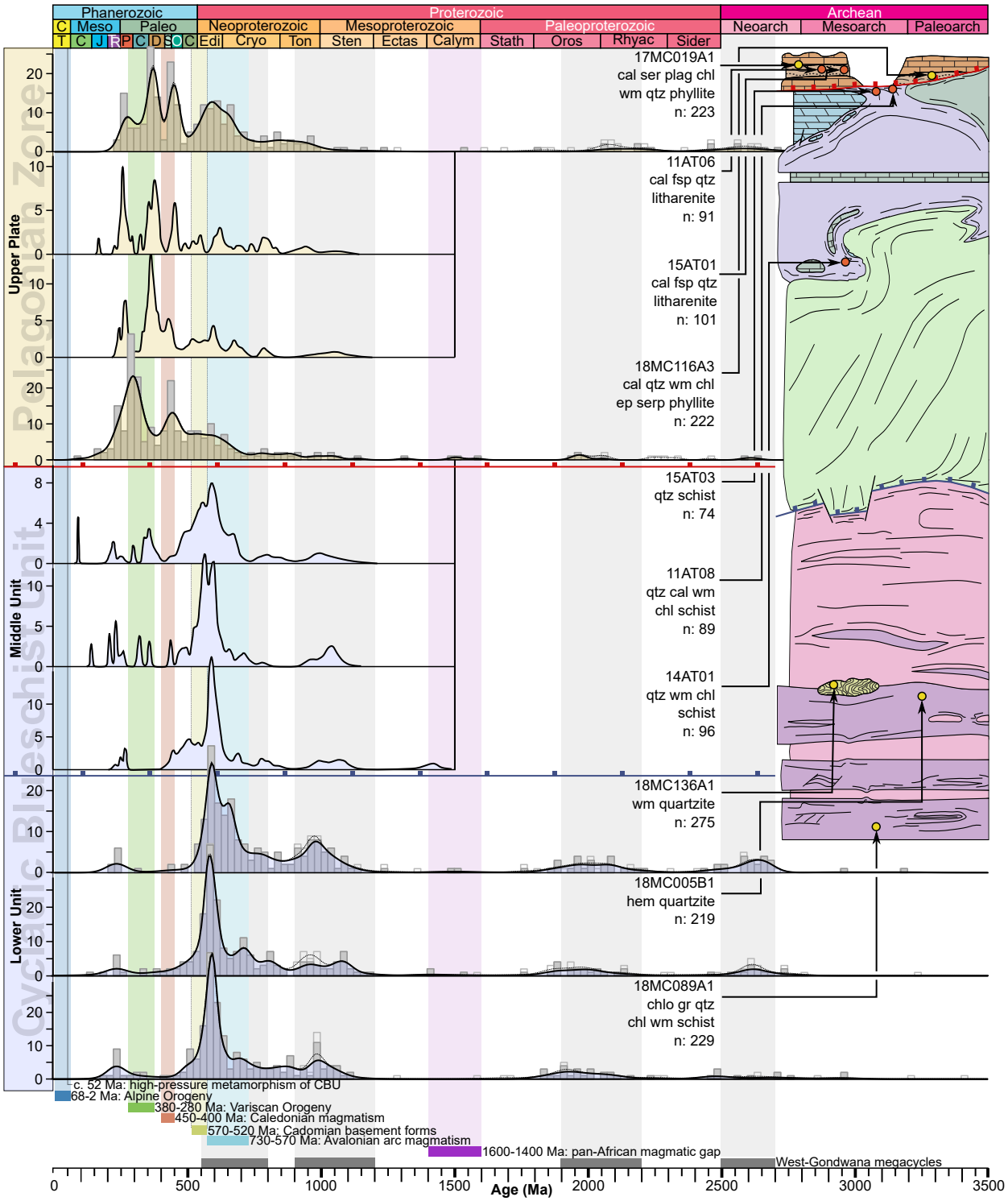

Figure 3.4. Refer to next page for figure caption.

Figure 3.4. (previous page) Kernel density estimates (KDE) and age histograms for Pelagonian Zone and LCBN samples from Mt. Hymittos. Relative sample positions are shown on the stratigraphic column, see Figure 2 for legend. Solid KDEs and histogram columns reflect the discordance elimination criterion reflected in the methodology; dashed KDEs and unfilled columns comprise all ages from the sample. Probability density plot curves have been extracted from unpublished data in the area (Seman, 2016). Select major tectonic events effecting the Mediterranean, Eurasia and Africa are displayed at the base of the figure. The histograms have a bin width of 25 Myr; the adaptive KDE curves have a bandwidth of 25 Myr; the area under the curve is normalized (Vermeesch, 2012). Abbreviations: cal: calcite; chl: chlorite; chlo: chloritoid; ep: epidote; fsp: feldspar; hem: hematite; qtz: quartz; ser: serpentinite; wm: white mica.

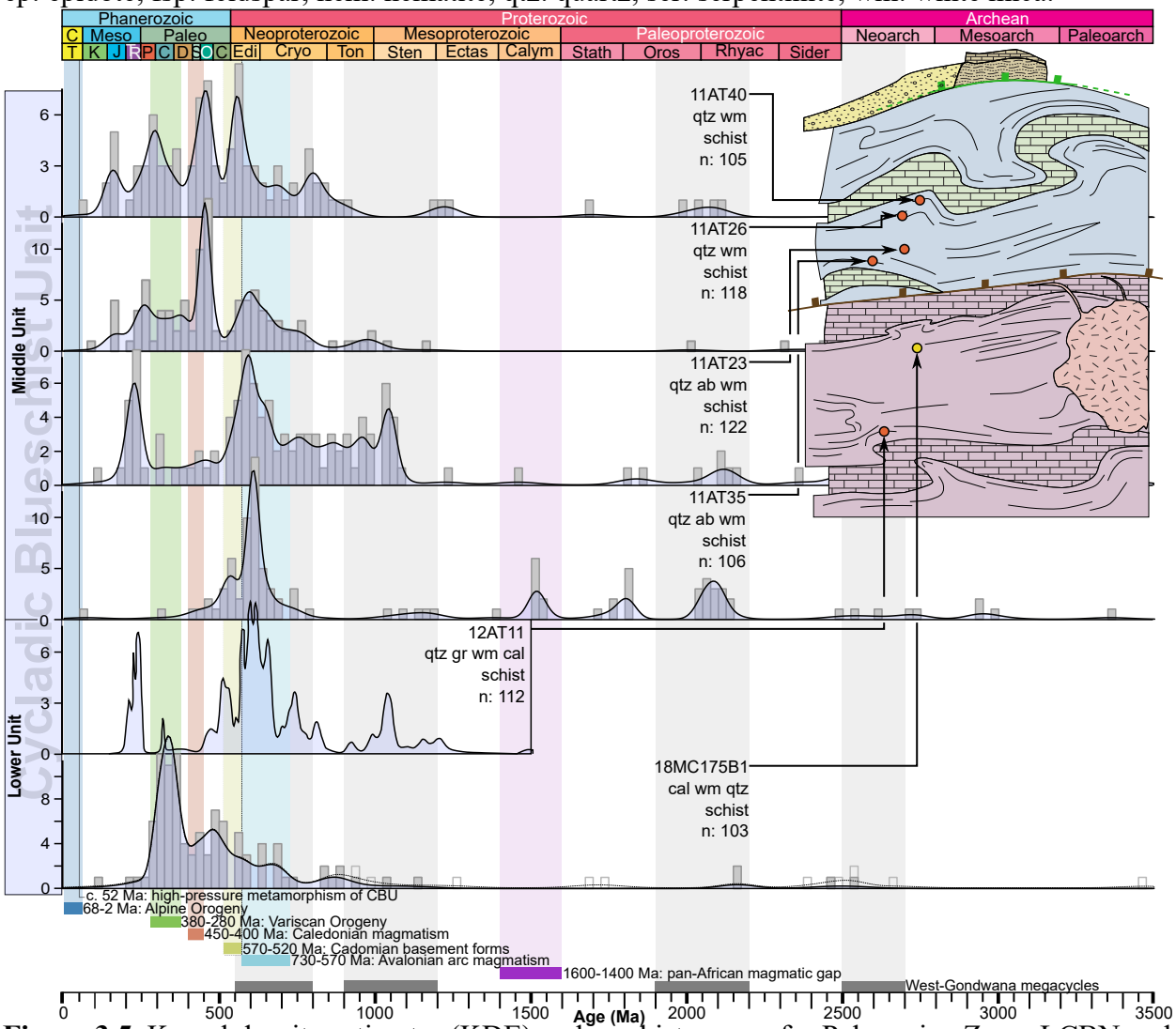

Figure 3.5. Kernel density estimates (KDE) and age histograms for Pelagonian Zone, LCBN and Cycladic Basement samples from Lavrion. Relative sample positions are shown on the stratigraphic column, see Figure 2 for legend. Solid KDEs and histogram columns reflect the discordance elimination criterion reflected in the methodology; dashed KDEs and unfilled columns comprise all ages from the sample. Probability density plot curves and recalculated KDE diagrams and associated histograms have been shown from published and unpublished data in the area (Seman, 2016; Seman et al., 2017). Select major tectonic events effecting the Mediterranean, Eurasia and Africa are displayed at the base of the figure. These data have been treated in the same manner as in Figure 4. Abbreviations: qtz: quartz, cal: calcite, wm: white mica, fsp: feldspar, ab: albite, gr: graphite.

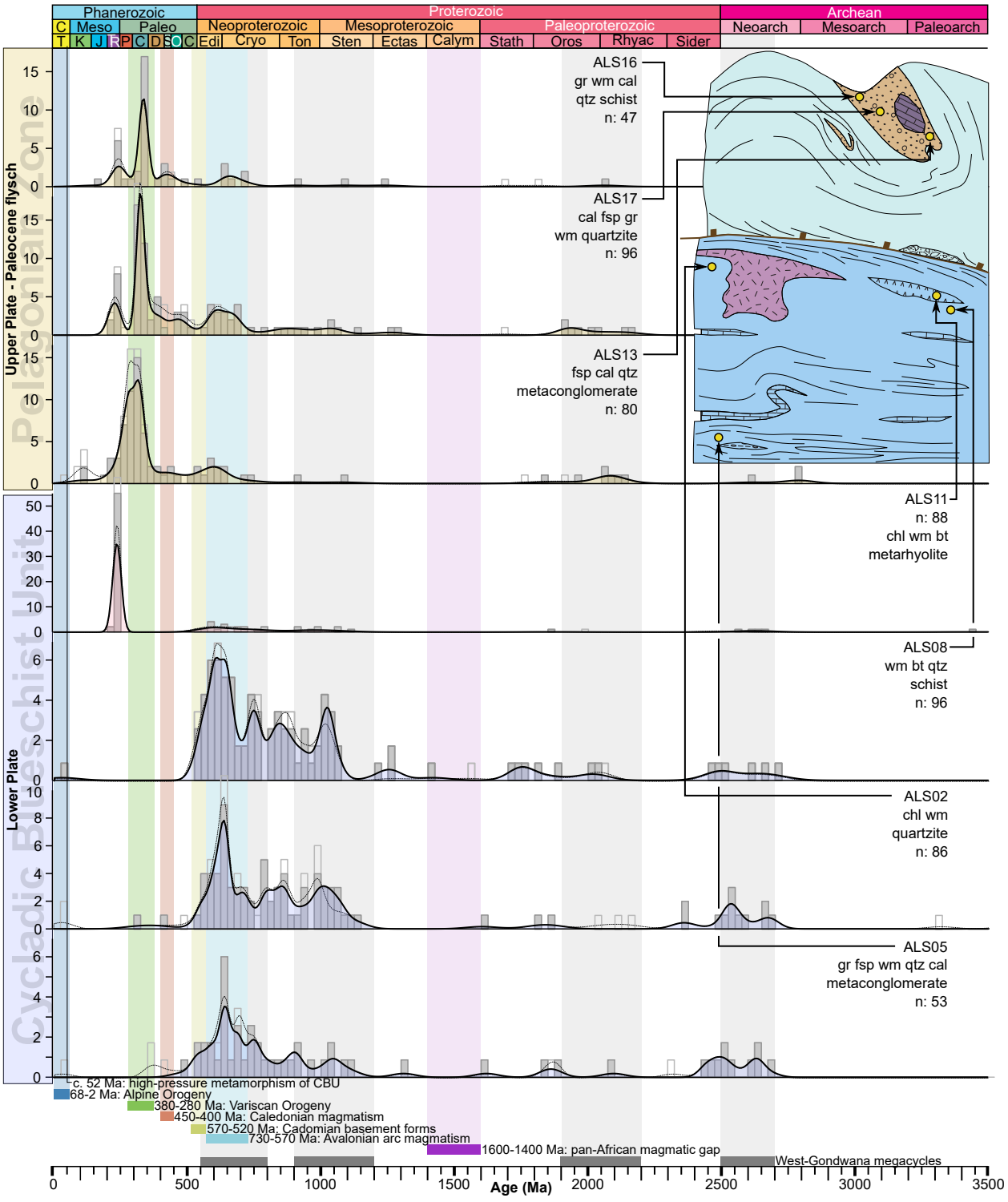

Figure 3.6. Refer to caption on next page.

Figure 3.6. (Previous page) Kernel density estimates (KDE) and age histograms for Pelagonian Zone and CBU samples from Santorini. Relative sample positions are shown on the stratigraphic column, see Figure 2 for legend. Solid KDEs and histogram columns reflect the discordance elimination criterion reflected in the methodology; dashed KDEs and unfilled columns comprise all ages from the sample. Select major tectonic events effecting the Mediterranean, Eurasia and Africa are displayed at the base of the figure. These data have been treated in the same manner as in Figure 3.4. Abbreviations: bt: biotite; chl: chlorite; cal: calcite; fsp: feldspar; gr: graphite; qtz: quartz; wm: white mica.

analyses >1000 Ma. In cases where $^{206}Pb/^{238}U$ and $^{207}Pb/^{206}Pb$ dates straddle 1000 Ma, the age with lower uncertainty is considered. Representative SEM-BSE images of zircon are displayed in **Figure 3.7** and zircon microstructures are described using the nomenclature of Corfu et al. (2003). Detailed analytical data and sample coordinates are incorporated into **Table S3.1,** and **Figures S3.1, S3.2** contain all the imaged zircon in this study.

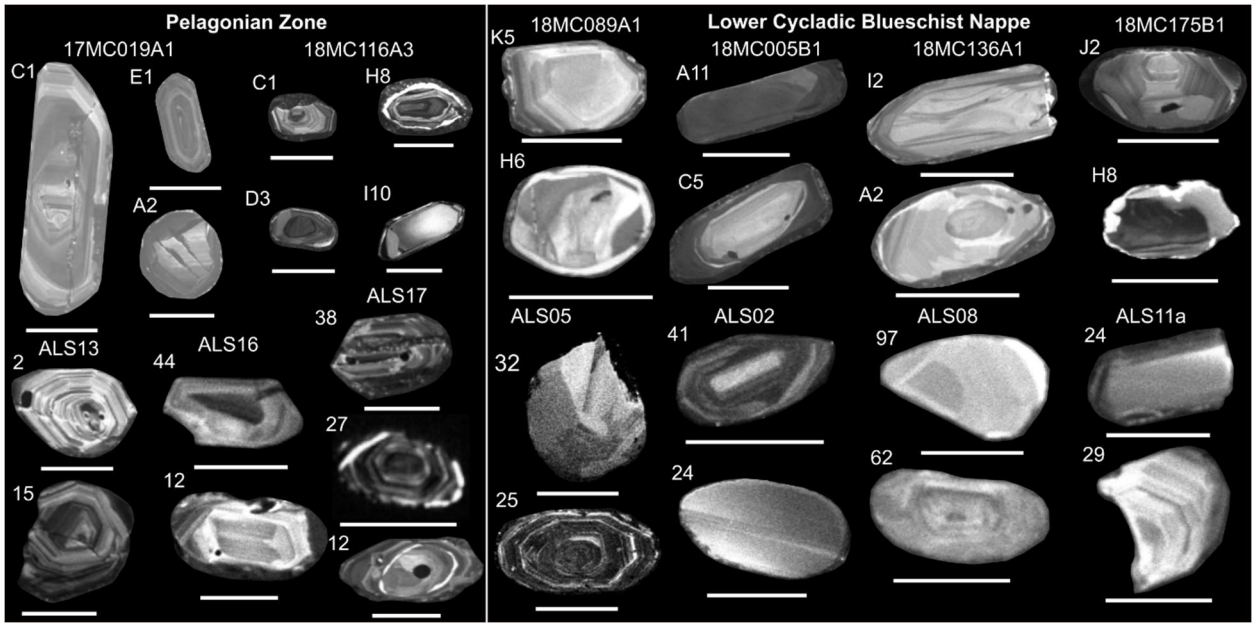

Figure 3.7. Photomicrographs of select zircon internal microstructures from samples of the Pelagonian Zone and Lower Cycladic Blueschist Nappe on Attica and Santorini. Scale bars are 100 mm. Grain identifiers correspond to tables S3.1, S3.2.

3.6 Results

3.6.1 Upper Plate

Samples of the metamorphosed upper plate of this study generally possess dominant Jurassic to Neoproterozoic or early Mesoproterozoic populations comprising 65-85% of the dates, with a distinct Variscan mode, though the specific peak may vary from the latest Devonian (17MC019; **Figure 3.4**) to Permo-Carboniferous (18MC116A3; **Figure 3.4**). Older zircon dates consist of minor distributions or sparse single analyses in the Neoarchean to early Paleoproterozoic and middle Paleoproterozoic.

A Variscan mode comprises the majority of zircon from the upper plate of Santorini, which typically exhibits a dominant Carboniferous population with secondary peaks in the Triassic and late Neoproterozoic (**Figure 3.6**); sample ALS13 exhibits a broader main mode due to a greater proportion of Permian zircon.

Zircon U-Pb age populations from samples of the upper plate of Attica exhibit a greater degree of inter-sample variability than samples from Santorini. Samples 17MC019A1, 11AT06 and 15AT01 exhibit age populations in the Permo-Triassic, Devono-Carboniferous and Ordovician-Silurian (**Figure 3.4**). The relative proportions of zircon within each of these peaks changes by sample, for example the Permo-Triassic peak is most dominant in 18MC116A3, whereas the Devono-Carboniferous and Ordovician-Silurian modes are a greater component of 17MC019A1 (**Figure 3.4**). Regardless of relative abundance these three peaks are present in all three samples and make up the main age distributions, along with a minor mode in the Ediacaran to late Cryogenian.

3.6.2 Lower Plate

All lower plate samples exhibit a small proportion of Paleoproterozoic zircon, which consist of minor distributions or sparse single analyses of Neoarchean to early Paleoproterozoic and middle Paleoproterozoic (**Figure 3.4; 3.5; 3.6**). Furthermore, all lower plate samples exhibit a major Ediacaran population, except 18MC175 from the Lower Unit of Lavrion, which yield only a few Ediacaran zircon (**Figure 3.5**).

Samples from the lower plate of Hymittos exhibit minimal inter-sample variability (**Figure 3.4**). All samples yield a distinct Ediacaran population, and a Stenian to Silurian or Devonian major distribution. All samples similarly exhibit a cluster of Triassic analyses and minor distributions and sparse analyses of middle Paleoproterozoic and Neoarchean dates. Samples 15AT03 and 11AT08, from the Middle Unit of Hymittos, present a small proportion of Jurassic and Cretaceous zircon unrecognized in structurally lower samples (**Figure 3.4**).

Samples from the lower plate of Lavrion present several distinct detrital zircon age spectra. Sample 18MC175B1 of the Lower Unit exhibits a dominant Variscan population. with a Triassic to Stenian distribution, this age spectra is dissimilar to other lower plate samples in this study (**Figure 3.5**). From the same Lower Unit, 12AT11 exhibits age spectra more similar to Middle Unit sample 12AT13, together these samples display a Triassic to Stenian distribution with major peaks in the Triassic, and Ediacaran and a smaller age peak in the Stenian. Sample 11AT35 is from the lowest portion of the Middle Unit, and its age spectrum is similar to spectra from the lower plate of Hymittos, sharing the Ediacaran peak and Stenian to Devonian distribution. Samples from higher levels within the Middle Unit of Lavrion (11AT40, 11AT26) exhibit more variable spectra, with a greater component of Paleozoic zircon (**Figure 3.5**). Samples 11AT40 and 11AT26 share a

Jurassic to Tonian main population with peaks in the Permian, Ordovician, and Ediacaran, with relatively less Ediacaran zircon in sample 11AT26.

Detrital zircon age spectra of metasedimentary samples from the lower plate of Santorini are relatively uniform. The three samples possess main populations from the Cambrian to the Stenian with a main peak in the Ediacaran, and minor peaks in the Cryogenian-Tonian and Stenian (**Figure 3.6**). The stratigraphically higher samples display a greater component of Ediacaran and Cryogenian zircon. Overall, these metasedimentary samples are similar in terms of dominant Ediacaran peak and main distribution to samples from the lower plate of Hymittos and 11AT35 from the Middle Unit of Lavrion. Metavolcanic sample ALS11 is a metarhyolite that presents a unimodal Triassic age distribution, with a few dispersed analyses that range from the Ediacaran to Stenian (**Figure 3.6**).

3.7 Discussion

All metasedimentary samples of both the upper and lower plate exhibit a similar component of Neoarchean to Paleoproterozoic zircon that are common to peri-Gondwanan terranes, a shared signal that will be interpreted together (section 3.7.2). Discussing these older zircon together will streamline addressing the dominant Mesoproterozoic to Mesozoic age spectrum that comprise the bulk of the U-Pb analyses. It is important to note that the PDP diagrams of the unpublished data (Seman, 2016) do not extend past the early Mesoproterozoic and so cannot be used to investigate older zircon populations. Subsequently, the detrital zircon age spectra of upper (section 3.7.3) and lower (section 3.7.4) plate samples will be synthesized and correlated to equivalent regional units. Finally, the data will be integrated with regional constraints to interrogate the suitability of paleogeographic equivalents and produce a tectonic model of the configuration of peri-Gondwanan terranes (section 3.7.5; **Figure 3.8**). This work does not rely on MDAs for its interpretations, I

recognize that these are commonly utilized in detrital zircon studies and have given my reasons for avoiding applying them below.

3.7.1 Applicability of maximum depositional ages

MDAs are commonly used to determine the depositional age of (meta)sedimentary rocks and aid in provenance analysis. Depending on the MDA calculation applied (Coutts et al., 2019; Vermeesch, 2021), the ages for the CBU of Santorini would range from the Cambrian to the Carboniferous, which would make these rocks the oldest rocks in the CBU by at least c. 50 Myr The presence of a Triassic metarhyolite (ALS11, c. 235 Ma; **Figure 3.6**) within the stratigraphically highest levels of LCBN on Santorini is strongly suggestive that the samples of the footwall on the island are Triassic in age. The metarhyolite was collected within a few meters of a schist (ALS08), which produced a Cambrian MDA. This apparently old MDA is probably a result of rare <500 Ma zircon in the source terranes for this portion of the CBU. Applying MDAs in situations such as this is unlikely to produce a reliable chronostratigraphy and care must be taken when using them to construct chronostratigraphic frameworks throughout the CBU in the absence of supporting dateable marker horizons or fossils. As such my work does not rely on MDAs for its interpretations as they may not be reliable.

3.7.2 Precambrian zircon: A Peri-Gondwanan shared origin

Precambrian zircon dates comprise a small proportion of all the data within upper and lower plate samples. All metasedimentary samples analyzed herein possess minor Neoarchean to Mesoproterozoic age populations reflecting distinct episodes of crustal growth in precursor terranes. Four Precambrian megacycles of crustal growth have been identified within the peri-Gondwanan terranes of Europe as displayed on **Figure 3.4, 3.5,** and **3.6** (Avigad et al., 2003;

Gebauer, 1993; Keay & Lister, 2002; Kolodner et al., 2006; Nance & Murphy, 1994). The similarity between the timing of the Gondwanan megacycles and the Neoarchean to Mesoproterozoic age distributions in Pelagonian Zone and LCBN samples herein suggests all samples in this study likely contain a component of Gondwanan-derived zircon.

The proto-CBU basin opened in the Permo-Triassic, and the presence of Gondwanan-derived zircon in my samples indicates a peri-Gondwanan source terrane or that a long-distance sediment routing system was delivering zircon of Gondwanan affinity. Gondwanan-derived zircon has been recognized in samples from the Cycladic Basement (Flansburg et al., 2019) and the LCBN of the central western Cyclades (Seman et al., 2017). Samples of the upper plate similarly exhibit a peri-Gondwanan signal (this study) thus both upper and lower plate samples are broadly peri-Gondwanan concurring with other detrital zircon provenance studies throughout the Cyclades (Laskari et al., 2022; Seman et al., 2017; Zlatkin et al., 2018).

The detrital zircon data from upper and lower plate samples exhibit significantly different distributions for the late Neoproterozoic and younger ages with most LCBN samples yielding major populations at the Ediacaran-Cryogenian boundary (**Figure 3.4; 3.5; 3.6**), largely unrepresented in upper plate rocks, which instead exhibit a greater proportion of Phanerozoic zircon (**Figure 3.4; 3.6**). Throughout the Cyclades, the Upper Unit always occupies the uppermost hanging wall of the Cycladic detachment systems (**Figure 3.1; 3.2**; Bonneau, 1984; Grasemann et al., 2012; Jolivet et al., 2010; Photiades & Carras, 2001). Despite the similarities in their Mesoproterozoic to Archean distributions, the structural position of the samples and dissimilarity of the bulk of their age spectra suggests that the Upper Unit and LCBN samples in this study have separate peri-Gondwanan source terranes. Given these distinct differences the Upper Unit and LCBN cannot be assigned to the same zone of the Hellenides.

3.7.3 Upper Plate: Pelagonian Zone

All samples from metamorphic rocks of the upper plate possess a significant component of Variscan-aged zircon, a Triassic minor population and generally an early Mesozoic to early Neoproterozoic distribution. Upper plate samples display varying amounts of Ediacaran- and Cryogenian-aged zircon, though both are always present and, in some cases, define a late Neoproterozoic minor peak (e.g., 17MC019; [**Figure 3.4**], ALS17 [**Figure 3.6**]). Samples from the upper plate of Hymittos are somewhat more variable than those from the upper plate of Santorini, exhibiting an additional Silurian-Ordovician population. Overall, these similarities between the metamorphic rocks of the upper plate suggest they probably reflect the same source terrane. The Triassic dates in all upper plate metamorphic samples likely correspond to regional Triassic volcanism recognized throughout the Cyclades and mainland Greece (Bröcker & Pidgeon, 2007; Pe-Piper & Piper, 2002).

At Hymittos, metasedimentary and metavolcanic phyllite of the Upper Unit are overlain by Triassic marble (Marinos & Petrascheck, 1956). The Paleocene metaflysch unit of Santorini was deposited atop a thick sequence of Triassic *Megalodon*-bearing marble (Kilias et al., 1998). As Triassic fossils are recognized in the Upper Unit of Hymittos, and the metaflysch sequence of Santorini is Paleocene, the two sequences represent exposures of different sections of the Cycladic Upper Unit stratigraphy. The variability in detrital zircon age spectra between these exposures of the upper plate can be explained by changes in sediment sourcing from the Triassic to the Paleocene.

A low metamorphic grade Cretaceous to Paleocene metaflysch is recognized in the upper plate of Folegandros (**Figure 3.1a**), where it rests a atop a Jura-Cretaceous marble sequence (Bakowsky et al., 2023). The metaflysch of Folegandros has been correlated to the Pelagonian

Zone and detrital zircon age data of a quartz-mica calc-schist possess a Variscan population, and Triassic and Ediacaran minor modes (CB21-14; Bakowsky et al., 2023), similar to samples of the upper plates of Hymittos and Santorini. Upper plate samples from Hymittos (17MC019, 18MC116) share the distinct Variscan mode, and minor Triassic and Silurian-Ordovician peaks with age-spectra from a Permo-Triassic sandstone on Chios (Meinhold et al., 2008). Age spectra of samples from the upper plate of Santorini (ALS16, ALS17) are indistinguishable to spectra derived from sedimentary rocks on Psara Island (CH19; Meinhold & Frei, 2008). The sedimentary rocks of Chios and Psara are unmetamorphosed exposures of the Pelagonian Zone, given the similarities between the age spectra of these samples and the upper plate samples herein it seems probably that these samples may be paleogeographic equivalents.

The metamorphic rocks from the upper plates of Santorini and Attica can be correlated to the Pelagonian Zone on the basis of their position in the hanging walls of the Cycladic detachment systems, stratigraphic ages, and zircon age spectra, agreeing with previous correlations for some portions of the Upper Unit (Jolivet et al., 2004). The upper plate of Hymittos is dominantly Triassic in age (Marinos & Petrascheck, 1956) whereas the clastic sedimentary rocks of Santorini are Paleocene (Kilias et al., 1998), thus the upper plate of Hymittos must correspond to a lower portion of the Pelagonian Zone stratigraphy than the upper plate of Santorini.

3.7.4 Lower plate: LCBN

The samples from the lower plate of Hymittos, Lavrion and Santorini have several commonalities including a distinct Ediacaran peak and main age distributions that generally range from the Stenian (except 11AT35; Lavrion Middle Unit) to the Paleozoic or Mesozoic.

The detrital zircon spectra of the lower plates can be divided into two main end members that characterize almost all samples. Samples from the lower plates of Hymittos and Santorini, and

one sample from the base of the Middle Unit of Lavrion (11AT35) are largely composed of Neoproterozoic zircon with age distributions ranging from the Stenian to the Cambrian (Santorini), or Devonian (Hymittos and Lavrion; **Figure 3.4; 3.5; 3.6**). At higher stratigraphic levels within the Middle Unit of Lavrion, Mesozoic- to Paleozoic-dominated spectrum can be observed in samples 11AT40 and 11AT26. These samples yield Tonian to early Cretaceous populations, and exhibit Ediacaran, Ordovician and Variscan-aged peaks (**Figure 3.5**). A pair of samples from the Middle (11AT23) and Lower (12AT11) units of Lavrion display Stenian to Jurassic populations and retain the dominant Ediacaran peak with additional peaks in the Stenian and Triassic. These two samples can generally be explained by intermixing of the sediment sources of the Neoproterozoic and Mesozoic-Paleozoic end members.

The similarity in detrital zircon age spectra between the Neoproterozoic zircon-dominated samples of lower plate of Hymittos and the lowest levels of the Middle Unit of Lavrion suggest that these rocks had the same source and were likely deposited synchronously, predating deposition of the overlying Mesozoic-Paleozoic dominated samples. Sample 12AT11, from the Lower Unit of Lavrion, evinces a mixed Mesozoic-Paleozoic-Neoproterozoic age spectra, but is located structurally lower than 11AT35. The position of this mixed spectra conflicts with the pattern observed at Hymittos and within the western Cyclades, where samples yielding Mesozoic-Paleozoic dominant age spectra overlie samples yielding Neoproterozoic age spectra (**Figure 3.4**; Seman et al., 2017). This which may indicate that the tectonostratigraphy of Lavrion is disrupted by Alpine thrusts. Additionally the Lavrion and Hymittos detachments exhumed rocks from different levels based on the different metamorphic conditions recorded in their footwalls, which may further complicate the tectonostratigraphy (Baziotis et al., 2009, 2020; Scheffer et al., 2016). The evidence for mixing between the Neoproterozoic and Mesozoic-Paleozoic dominated

sediment sources at multiple structural levels may indicate a gradual rather than abrupt change in the origin of the detritus depositing in the proto-CBU basin over time.

The lower plate samples of Santorini and Hymittos yield Neoproterozoic dominated zircon age populations. In contrast to Hymittos, the metasedimentary rocks of the lower plate of Santorini possess no Triassic and limited Paleozoic aged zircon despite hosting a Triassic metarhyolite (ALS11; 235 ± 5 Ma) (**Figure 3.5**). Triassic dates reflect the regionally extensive igneous activity reported within the LCBN (Liati et al., 2009, 2013; Seman et al., 2017) and the greater CBU (Bröcker & Pidgeon, 2007; Pe-Piper & Piper, 2002). In contrast, all samples from the lower plate of Hymittos exhibit a distinct Triassic-aged zircon population (**Figure 3.4**). It is possible that most of the lower plate rocks on Santorini were deposited earlier in the basin's history relative to lower plate rocks on Hymittos (**Figure 3.8**), which is supported by the presence of Triassic corals in dolomite within the Middle Unit of Hymittos (Negris & Meunier, 1915) and sparse Jurassic to Cretaceous-aged zircon at higher levels within the middle units of Hymittos and Lavrion.

Exposures of the lower plate on Attica contain more marble than on Santorini, and a greater proportion of coarser-grained and quartzitic lithotypes like metaconglomerate and quartzite (e.g., 18MC136A1, 18MC005B1), suggesting a shore-proximal setting. In contrast the lower plate of Santorini is dominantly comprised of fine-grained siliciclastic rocks most commonly mica schist, with limited quartz-carbonate pebble metaconglomerate, perhaps implying a deeper position within the proto-CBU basin at the time of deposition. On Attica the carbonate lithotypes thin towards the southeast (Coleman et al., 2019, 2020; Scheffer et al., 2016), possibly denoting a southeast deepening basin, where water depth limited carbonate development. If this is the case, then the protoliths of the lower plate of Santorini likely deposited outboard of the protoliths of Attica (**Figure 3.8**).

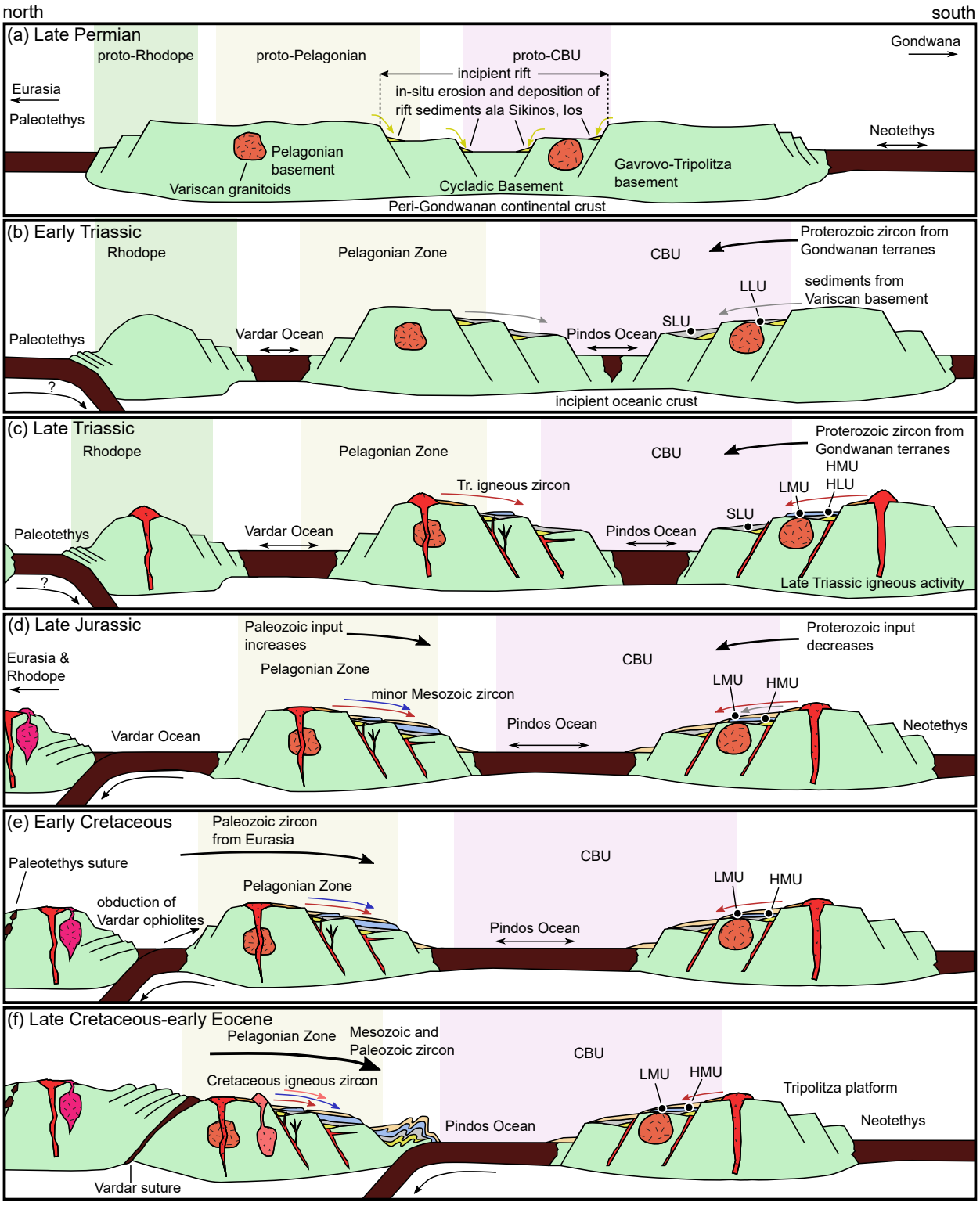

Figure 3.8. Refer to caption on next page.

Figure 3.8. (previous page) Schematic diagrams (not to scale) reflecting terrane positions, sediment sourcing and tectonic events related to the formation of the proto-CBU ocean basin. **(a)** Late Permian: small scale rifting within a metamorphic terrane of Variscan-affinity leads to local deposition of Cycladic Basement detritus at the lowest levels of the CBU. This terrane will later be the basement of the Pelagonian Zone and the Cycladic Basement. **(b)** Early Triassic: subduction of Paleotethys to the north of the Rhodope block leads to back-arc spreading and opening of the Vardar Ocean. Simultaneously, rifting continues in the Pindos Basin, and oceanic crust forms. The Pindos Basin is more connected allowing for deposition of sediment from more southerly Neoproterozoic peri-Gondwanan terranes forming the lower unit of Santorini. Eroded Cycladic Basement deposits as the Lower Unit of Lavrion. **(c)** Late Triassic: Igneous activity related to rifting develops in the Pelagonian Zone and proto-CBU basin due to continued crustal extension. Rhyolitic flows occur in the uppermost levels of the Lower Unit of Santorini, marking the upper limit of the stratigraphy preserved on the island. Zircon produced by this event are deposited within Pelagonian Zone and CBU strata, mixed Triassic igneous zircon and Neoproterozoic sediments deposit as the Lower and Middle units of Hymittos and lower portion of the Middle Unit of Lavrion (11AT35). **(d)** Late Jurassic: Proterozoic zircon deposit in the Middle Unit of Hymittos in between episodes of Carbonate development. Changes in sediment source through time lead to a significant increase in the proportion of Paleozoic zircon which deposit as the Middle Unit of Lavrion which represents mixing between the Proterozoic and Paleozoic end members. To the north, Paleotethys has closed, and the Vardar Ocean has begun north-directed subduction beneath Eurasia. **(e)** Early Cretaceous: Continued deposition of Paleozoic zircon, likely sourced from Eurasia. The Vardar Ocean has closed, and the Vardar ophiolites are obducted over the Pelagonian Zone. **(f)** Late Cretaceous-early Eocene: Increasing proportions of Mesozoic zircon in the Middle Units of Hymittos and Lavrion reflect incorporation of zircon from Europe, and the Vardar Ophiolites. Subduction of the Pindos Ocean beneath the Pelagonian Zone drives Cretaceous igneous activity which provides a source for Late Cretaceous zircon within the CBU. We follow the model of Stampfli et al. (2014) for the Vardar Ocean while acknowledging that multiple models exist for this domain but all agree that by the Late Cretaceous Vardar had closed. Abbreviations: SLU: Santorini Lower Unit, LLU: Lavrion Lower Unit, LMU: Lavrion Middle Unit, HLU: Hymittos Lower Unit, HMU: Hymittos Middle Unit.

The Neoproterozoic dominated samples of this study share similar zircon age spectra with rocks of the LCBN from Kea and the lower levels of Kythnos of the western Cyclades (Seman et al., 2017), defined by a Stenian to Cambrian-Devonian main population, common Ediacaran main peak and minor Triassic peak. The Middle Unit of Lavrion has already been correlated to the LCBN of Serifos and the upper levels of Kythnos (Seman et al., 2017). Similar Proterozoic distributions are also recognized in CBU of the Lower Schist of Iraklia (Laskari et al., 2022). The

structural positions of the lower plate of Attica and Santorini within the footwall of crustal-scale detachments strongly indicate these rocks belong to the CBU, consistent with most other footwall exposures within the western Cyclades (Grasemann et al., 2012, 2018; Iglseder et al., 2011). Moreover, blueschist facies metamorphic assemblages and phase equilibria modelling suggest high-pressure metamorphism did not exceed 450°C (Baziotis et al., 2009, 2020; Baziotis & Mposkos, 2011; Coleman et al., 2019, 2020), identifying these rocks as part of the lower CBU nappe (LCBN; Grasemann et al., 2018). My new detrital zircon data from the lower plate provide additional support for this correlation and demonstrate – at the scale of my sampling – that the LCBN is a coherent package of rock stretching across >200 km from northern Attica to the southern Cyclades.

One sample (18MC175) from the Lower Unit of Lavrion exhibits a dominant Carboniferous mode and Paleozoic to Neoproterozoic age distribution similar to the syn-intrusive metasediments of Ios' Cycladic Basement (Flansburg et al., 2019). The Neoproterozoic end-member samples from the lower plates of Hymittos and Santorini are likewise similar to samples from the pre-Variscan Cycladic Basement of Naxos and Ios. Given these similarities, it is possible that the lower structural levels of the LCBN contains a significant component of zircon recycled from the Cycladic Basement, a similar recycled component has been recognized on Sikinos (Poulaki et al., 2019). At higher structural levels, the stratigraphy of Lavrion reveals increasing proportions of Mesozoic and Variscan-aged zircon (**Figure 3.4; 3.5**). This evolution likely reflects the increasing proportion of zircon derived from the Pelagonian Zone or Eurasian continent. The Pelagonian Zone records Early Cretaceous metamorphism and volcanism corresponding to closure of the Vardar Ocean and accretion of Pelagonia to Eurasia, and Late Cretaceous igneous activity related to Pindos Ocean subduction (Altherr et al., 1994; Koutsovitis et al., 2021; Pe-Piper & Piper,

2002; Schenker et al., 2014). The Pelagonian Zone is a suitable source for Mesozoic and Variscan zircon as it was adjacent to the proto-CBU basin and rapidly eroding during the Early Cretaceous (**Figure 3.8e**; Schenker et al., 2015).

3.7.5 Paleogeographic configuration

The CBU has been proposed as a paleogeographic equivalent of the Pindos Zone (Bonneau, 1984; Bonneau & Kienast, 1982), the Pelagonian Zone (Stampfli et al., 2003) or the Vardar-Izmir Unit (Chatzaras et al., 2013; Zlatkin et al., 2018). I support the interpretation that the CBU of the western Cyclades correlates to the Pindos Zone for a number of reasons:

1. The Pindos Zone hosts a mid-Cretaceous flysch sequence (Terry & Mercier, 1971) that may be correlated to upper portions of the Middle Units of Lavrion and Hymittos (**Figure 3.4; 3.5**), and proposed mid-Cretaceous depositional ages of the CBU on Ios and Sikinos, (Poulaki et al., 2019). The detrital zircon U-Pb age spectrum of one sample from the Lower Plate of Lavrion (18MC175; **Figure 3.5**) is similar to a sample of the mid-Cretaceous flysch of the Pindos Zone (Faupl et al., 2006) including a prominent Variscan mode, sparse Mesozoic dates and Paleozoic-Neoproterozoic distribution. I acknowledge that given the paucity of U-Pb detrital zircon data from the Pindos Zone (sensu stricto) more analyses are necessary to strengthen this conclusion.
2. LCBN samples of this study contain Late Cretaceous zircon that are undocumented in exposures from the Vardar Zone (**Figure 3.4; 3.5**; Meinhold et al., 2009, 2010), which was already closed in the Late Cretaceous. Late Cretaceous zircon have similarly been reported from the UCBN of Tinos (Hinsken et al., 2016), and the Late Cretaceous dates provide more evidence that the LCBN and the broader CBU cannot be correlated to the Vardar Zone.

3. Ophiolites structurally overlying the Pelagonian Zone on Tinos and Evia are associated with the Vardar ophiolites of mainland Greece (Lamont et al., 2019; Scherreiks et al., 2014). These ophiolites structurally overlie both the CBU and Pelagonian Zone, suggesting they cannot be equivalents to the Pindos Zone. The structural position of the CBU sandwiched below the Pelagonian Zone and above the Gavrovo-Tripolitza Unit (Basal Unit of the Cyclades) matches the structural position of the Pindos Zone below the Pelagonian Zone on mainland Greece (**Figure 3.1b**; Papanikolaou, 2009).
4. The Pindos oceanic basin began subducting below the Pelagonian Zone in the Late Cretaceous (Degnan & Robertson, 1998, 2006; Koutsovitis et al., 2021) with final collision in the Tertiary. Subduction of the Vardar ocean began in the Late Jurassic and ceased by the Early Cretaceous corresponding to obduction of ophiolitic rocks atop the Pelagonian Zone (**Figure 3.8;** Clift, 1996; Ferrière et al., 2012; Robertson & Dixon, 1984; Scherreiks et al., 2000, 2014). The Eocene age of high-pressure metamorphism of the CBU is consistent with the timing of Pindos subduction (Kendall, 2016; Kotowski et al., 2021; Laurent et al., 2017; Poulaki et al., 2021).
5. Some authors have posited that the presence of 450-400 Ma zircon in the Cycladic Basement, but an absence of similar aged zircon in the Pelagonian Zone basement and cover, requires the opening of the CBU basin to have occurred north of the Pelagonian Zone (Zlatkin et al., 2018). The 450-400 Ma zircon within samples of the Pelagonian Zone (**Figure 3.4; 3.5**; Seman et al., 2017; Bakowsky et al., 2023) conflict with this model. As indicated by the data herein, it is not necessary that the proto-CBU basin (and basement) be located north of the Pelagonian Zone in order to incorporate such Ordovician-Silurian zircon.

On the basis of the observations above and other points within this discussion, I support the model that the proto-CBU/Pindos basin opened within the westernmost margins of the

Pelagonian microcontinent during the late Permian (**Figure 3.8a**; Bonneau, 1984; Flansburg et al., 2019; Grasemann et al., 2021; Laskari, Soukis, Lozios, et al., 2022; Poulaki et al., 2019; Stampfli et al., 2003). This incipient ocean basin incorporated locally eroded material from the underlying and adjacent continental basement shared between the Pelagonian Zone and proto-CBU. This eroded material deposited as the lower plate of Santorini and Lower Unit of Lavrion (18MC175; **Figure 3.8b**).

As the rift evolved into a small marine basin floored by oceanic crust, regional Triassic magmatism produced zircon grains that were ultimately shed into the proto-CBU basin, which were incorporated with the detritus from the continental basement likely including Proterozoic zircon originally from Gondwanan terranes (**Figure 3.8c**). As the basin expanded, longer distance sediment routing systems developed, leading to the incorporation of a greater proportion of Mesozoic Eurasian- and Variscan-derived detritus into younger sequences of the LCBN. Increasing proximity to the Eurasian margin was driven by north-directed subduction of the Vardar ocean basin (**Figure 3.8d**) and ending with accretion of Pelagonia to Eurasia. Closure of the Vardar ocean and obduction of ophiolites in the Early Cretaceous (**Figure 3.8e**) transported Vardar-derived sediments into nearby basins (Bailey et al., 2020). Finally, arc magmatism related to Late Cretaceous subduction of the Pindos ocean basin beneath the Pelagonian Zone (Koutsovitis et al., 2021) produced relatively limited Late Cretaceous detritus recognized at the highest levels of the Middle Units of Lavrion and Hymittos (**Figure 3.8f**).

The increase of Mesozoic zircon age populations at highest stratigraphic levels in the LCBN samples of this study likely reflect Eurasian-derived sediments from the eroding, obducted Vardar ophiolites mixed with sediments from the underlying Pelagonian Zone (Koutsovitis et al., 2021), which together comprise the Upper Unit of the Attic-Cycladic Complex. Furthermore,

sediments are also being derived from the Eurasian margin; the suturing of Pelagonia to Eurasia would allow for sediment routing systems to transport detritus directly from the continent. Since the Vardar basin is proximal to the Eurasian margin, there is likely a pronounced Eurasian signal. Determining differences between these two is likely impossible, except that Eurasian material continued to be deposited in the proto-CBU basin after the closure of the Vardar ocean.

3.8 Conclusions

This study presents new U-Pb detrital zircon analyses from the Attic Peninsula and Santorini archipelago. Episodes of crustal growth and zircon production associated with the Gondwana are recognized in the zircon U-Pb age spectra of all samples in the study, suggesting a peri-Gondwanan affinity for both the upper and lower plates of Attica and Santorini. Samples from Hymittos and Santorini possess a similar pattern of Neoproterozoic-dominated age spectra. Comparison to other studies across the Western Cyclades indicates the lower plates of Hymittos and Santorini are exposures of the lower nappe of the CBU (LCBN) and correlate with Kea and the lowermost portions of Kythnos. These Neoproterozoic age spectra likely contain recycled detritus of the Cycladic Basement and possibly incorporation of material from Gondwanan terranes. At higher stratigraphic levels the metasedimentary rocks of the lower plate of Attica record greater interconnectivity of the proto-CBU basin with increasing proportions of Paleozoic and Mesozoic zircon derived from the Pelagonian Zone, Vardar Zone and Eurasia reflecting increasing proximity to the Eurasian margin during the late Mesozoic. Regional Triassic magmatism produced zircon that are common in all metasedimentary samples from Attica yet are missing from the stratigraphy on Santorini. A Triassic metarhyolite from the highest levels of the lower plate of Santorini demonstrates that the majority of the lower plate of Santorini was deposited prior to this igneous event. I support the model that the LCBN and the greater CBU are

paleogeographic equivalents of the Pindos Zone based on comparison between detrital zircon age-spectra, Late Cretaceous zircon that correspond to closure of the Pindos Ocean, and structural position of the LCBN.

3.9 Acknowledgments, Samples, and Data

Funding was provided by the Natural Sciences and Engineering Research Council of Canada (to David Schneider) and the Austrian Academy of Sciences (Emil Suess-Erbschaft, to Bernhard Grasemann). I thank the Greek Institute for Mining and Exploration in Athens for providing permission for fieldwork and technical support. Sam Morfin and Martijn Schetselaar (University of Ottawa), and Chris McFarlane and Brandon Boucher (University of New Brunswick) assisted with zircon U-Pb analyses, and Glenn Poirier (University of the Ottawa-Canadian Museum of Nature MicroAnalysis Laboratory) for SEM and microprobe analyses; their contributions are greatly valued.

Table 3.1. Hand sample, zircon, and age descriptions.

		Sample	Northing Easting	Lithology	Zircon morphology	Notable textures	Condordant dates / Total number of dates	Zircon age distributions	Major peaks	Th/U ratios	Post-depositional metamorphic ages	Magmatic age (Ma), (dates used / total number of dates)
Attic Peninsula	Hymittos Upper Unit (Alepovouni Unit)	17MC019A1	4190378 744762 (34S)	Foliated, metasedimentary calcite-sericite-plagioclase feldspar-chlorite-white mica-quartz phyllite	euhedral-subrounded equant (1:1 L:W) to elongate (6:1), lengths 90-400 µm	Oscillatory zoning, commonly truncated by subrounded boundaries, rare 1-10 µm thick CL-white overgrowths.	223/264	Neoarchean-early Paleoproterozoic, middle Paleoproterozoic, late Mesoproterozoic-early Mesozoic, sparse late Paleoproterozoic and early Mesoproterozoic analyses	Ediacaran, Ordovician, Devonian	0.00-1.00; 13 analyses >1.5. Th/U ratios < 0.2 cluster in the Carboniferous-Silurian and Neoproterozoic	Metamorphic rims identified - no robust ages measured	na
		18MC116A3	4209692 749701 (34S)	Foliated, cataclased, calcite-quartz-white mica-chlorite-epidote-serpentinite phyllite	subhedral-rounded L:W ratios from 1:1 to 5:1, lengths 50-150 µm	Common two generations of CL-bright and CL-dark oscillatory zoning, occasional inherited cores. Subrounded and rounded grain boundaries truncate internal zoning. 1-8 µm thick CL-white overgrowths	222/241	early-middle Paleoproterozoic, late Mesoproterozoic to late Mesozoic, sparse Neoarchean, Mesoarchean and Cretaceous analyses	Orosirian, Ediacaran, Silurian, Permian	0.026-3.083; Th/U < 0.2 cluster in the Late Ordovician	Metamorphic rims identified - no robust ages measured	na
	Hymittos Lower Unit (Cheroma Schist)	18MC136A1	4194918 746129 (34S)	Foliated, L>S tectonite, white mica quartzite	subhedral-rounded L:W ratios from 1.2:1 to 4.1:1, lengths 50-200 µm	Oscillatory zoning, CL-bright or CL-dark inherited cores. Rare CL-white 1-5 µm thick rims.	275/288	Neoarchean-middle Paleoproterozoic, late Mesoproterozoic-Ordovician, sparse early Mesoproterozoic and Triassic ages	Stenian, Ediacaran	0.029-2.064; Th/U < 0.2 clustered in the Neoproterozoic and middle Paleoproterozoic	Metamorphic rims identified - no robust ages measured	na
		18MC005B1	4193129 745545 (34S)	Foliated, hematite quartzite	euhedral-subrounded L:W ratios from 1:1 to 5.5:1, lengths 90-190 µm	Common oscillatory zoning, rare CL-bright or CL-dark inherited cores. Grain boundaries truncate internal zoning. Uncommon CL-white rims	219/261	Neoarchean, middle Paleoproterozoic, Mesoproterozoic-early Paleozoic, sparse Calymmian, Mississippian, and Triassic analyses	Stenian, Tonian, Ediacaran	0.052-2.148; Th/U < 0.2 clustered in the Neoproterozoic c. 600 Ma	Metamorphic rims identified - no robust ages measured	na
		18MC089A1	4192574 746177 (34S)	Foliated, lineated, SCC' banded, chloritoid-graphite-quartz-chlorite-white mica schist	subhedral-anhedral L:W ratios from 1:1 to 5:1, lengths 65-190 µm	Common oscillatory zoning; uncommonly two generations and Cl-bright or CL-dark cores	229/255	Neoarchean-early Paleoproterozoic, middle Paleoproterozoic, late Mesoproterozoic-early Paleozoic, sparse Mesoarchean analyses	Tonian, Ediacaran	0.02-2.75; Th/U < 0.2 cluster in the Neoproterozoic	Metamorphic rims identified - no robust ages measured	na
	Lavrion Lower Unit (Kamariza Schist)	18MC175B1	4183016 238297 (35S)	Foliated, refolded, lineated, calcite-white mica-quartz schist	equant and anhedral to elongate and prismatic L:W ratios from 1:1 to 3:1, 70-170 µm	Common one or more generations of oscillatory zoning and CL-bright inherited corses; rounding of cores suggests erosion prior to further zircon growth. Discontinuous 1-5 µm thick, CL-white metamorphic rims and recrystallized domains visible at the margins of some euhedral zircon	70/113	late Neoarchean to middle Paleoproterozoic, Mesoproterozoic to Mesozoic	Mississippian, Silurian	0.00-1.87; Th/U < 0.2 cluster in the Carboniferous to Cambrian	Metamorphic rims identified - no robust ages measured	na
Santorini	Pelagonian Zone	ALS16	4025730 363102 (35S)	Graphite-white mica-calcite-quartz schist	euhedral-subhedral L:W ratios from 1.1:1 to 4.5:1, lengths 75-200 µm	Oscillatory, sector and patchy zoning, uncommon chaotic alteration patterns. Rare multi-stage zoning and CL-bright or CL-dark cores	47/52	late Neoproterozoic to early Mesozoic, sparse Proterozoic and Neoarchean analyses	Carboniferous, Triassic	0.07-1.64; Th/U <0.2 cluster in the Ordovician to Mississippian	Metamorphic rims identified - no robust ages measured	na
		ALS17	4025970 363135 (35S)	Foliated, calcite-alkali feldspar-graphite-white mica quartzite	rounded anhedral-euhedral prismatic L:W ratios from 2:1 to 4:1, lengths 55-180 µm	Dominantly oscillatory zoned, commonly multi-stage. Uncommon patchy zoning, sector zoning or chaotic alteration patterns. Rare parallel partings and CL-bright or CL-dark cores	96/112	middle Mesoproterozoic-early Mesozoic. Sparse Paleoproterozoic and Neoarchean analyses	Carboniferous, Triassic, Cryogenian	0.05-1.88; Th/U <0.2 cluster in the Silurian to Ediacaran	Metamorphic rims identified - no robust ages measured	na
		ALS13	4025097 363067 (35S)	Feldspar-calcite-quartz metaconglomerate	anhedral to blocky subhedral with rare euhedral prismatic crystals, L:W ratios from 1.5:1 to 4.5:1, lengths 50-120 µm	Oscillatory and patchy multi-stage zoning, resorption textures. Rare sector zoning, complex alteration patterns and CL-bright overgrowths	80/96	middle Neoproterozoic-early Mesozoic, Paleoproterozoic, sparse Neo- and Mesoarchean analyses	Permo-Carboniferous, Ediacaran	0.02-1.61	28.6 Ma	na
	Cycladic Blueschist Unit	ALS11	4025605 360636 (35S)	Foliated, lineated, chlorite-white mica-biotite metarhyolite	subhedral to euhedral crystals, prismatic to elongate or tabular, L:W ratios 1:1 to 3.5:1, lengths t75-200 µm	Common oscillatory, multi-stage, or sector zoning, resorption textures. Rare patchy zoning, parallel parting, and CL-bright or CL-dark inherited cores	88/96	late Stenian-Ediacaran, sparse Paleoproterozoic and Neoarchean analyses	Triassic	0.02-1.45; Th/U < 0.2 cluster in the Ediacaran to Cryogenian	Metamorphic rims identified - no robust ages measured	Triassic, 235 Ma (57/88)
		ALS08	4025605 360641 (35S)	Foliated, lineated white mica-biotite-quartz schist	blocky anhedral to elongate/prismatic subhedral crystals, L:W ratios from 1:1 to 3.5:1, lengths 75-195 µm	Common one or more generations of oscillatory or sector zoning. Uncommon patchy zoning and CL-bright inherited cores	96/100	late Neoarchean to Siderian, Orosirian to Stathian, Ectasian to Ediacaran	Ediacaran, Cryogenian, Stenian	0.02-2.85; Th/U < 0.2 cluster in the Cambrian to Cryogenian	27.9 Ma	na
		ALS02	4027830 359540 (35S)	Foliated, lineated chlorite-white mica quartzite	equant and rounded to elongate or prismatic subhedral crystals rare euhedral forms; L:W ratios from 1:1 to 4:1, lengths 65-255 µm	Common oscillatory, sector or patchy zoning. Unzoned CL-bright overgrowths and CL-bright or CL-dark inherited cores. Discontinuous 1-15 µm thick CL-white rims	86/98	late Neoarchean-early Paleoproterozoic, late Mesoproterozoic-early Paleozoic	Ediacaran, Cryogenian, Stenian	0.01-2.19; Th/U < 0.2 cluster in the Cryogenian to Tonian	29.0, 29.5 Ma	na
		ALS05	4027944 358981 (35S)	Foliated, lineated, graphite-feldspar-white mica-quartz-calcite metaconglomerate	equant or blocky to tabular euhedral and prismatic subhedral crystals, L:W ratios from 1:1 to 3:1, lengths 90-170 µm	Common one to two generations of oscillatory/patchy zoning, resorptions textures. CL-bright or CL-dark inherited cores. Partially abraded 1-10 µm thick CL-white rims	53/62	late Neoarchean-early Paleoproterozoic, Stenian-Cambrian	Ediacaran, Tonian, Stenian	0.01-1.51; Th/U < 0.2 clsuter in the Ordovician to Cryogenian	27.5 Ma	na

Chapter 4: Can dolomite be weaker than calcite at lower greenschist to subgreenschist facies conditions?

Abstract

The bedrock of Mt. Hymittos, Greece exposes a pair of Miocene extensional detachment faults. Ductile strain related to the upper detachment is primarily localized in mylonitic calcitic marble and schist. Deformation associated with the lower detachment is dominantly accommodated by a >100 m thick package of dolomitic mylonite. Field and geochronometric evidence indicate these structures deformed under middle greenschist to sub-greenschist facies conditions, therefore dolomite would generally be expected to be significantly stronger than calcite within this temperature range. Microstructures in the naturally deformed dolomitic and calcitic marble record dislocation creep of calcite and dolomite leading to subgrain rotation and grain size reduction of coarse domains (>50 μm). In finer domains (10-50 μm), dolomite of the lower detachment underwent grain boundary sliding facilitated by diffusion creep with minor dislocation creep activity. Calcite of the upper detachment deformed by paired grain boundary sliding and dislocation creep, structurally high samples were significantly annealed following deformation. In this instance the dolomitic ultramylonite marble is finer grained than nearby calcitic mylonite marble located in the same structural horizon and preferentially localized strain. Our work suggests that dolomitic marble can be weaker than calcitic marble at relatively low temperatures.

4.1 Introduction

The deformation mechanisms of major rock forming minerals (e.g., quartz, feldspar, calcite) are often studied, but the relative strengths of different major minerals during deformation is less well understood. Carbonates are common minerals that can form thick, relatively homogeneous packages of rock. Calcite ($CaCO_3$) is the most common rock forming carbonate mineral, and calcitic marble is typically considered relatively weak compared to other common major rock forming minerals (Brodie & Rutter, 2000). Under lower greenschist facies conditions,

calcite deforms predominantly by grain size sensitive creep (i.e., diffusion creep *s.l.*) assisted by dislocation creep which becomes more active at high temperatures (Bestmann et al., 2000; Brodie & Rutter, 2000; Leiss & Molli, 2003; Schulmann et al., 2023; Urai et al., 1990). The relative weakness, and sensitivity of calcite to grain size reduction and diffusion creep processes under greenschist facies conditions has caused calcitic marble to act as a 'lubricating layer' within metasedimentary sequences deformed at temperatures below 430°C (Rutter & Brodie, 1988; Ulrich et al., 2002). Intracrystalline deformation of calcite has been observed in micro-shear zones at temperatures <150°C (Bauer et al., 2018) suggesting deformation mechanisms generally associated with higher temperatures may be active in the upper crust.

Dolomite [$CaMg(CO_3)_2$] is a less common carbonate mineral than calcite. Dolomitic marble is typically considered rheologically stronger than rocks composed of other common (meta)sedimentary minerals such as phyllosilicates and calcite but weaker than homogeneous quartzite for most crustal conditions (Delle Piane et al., 2008, 2017; Schmid, 1983; Schulmann et al., 2023; Ulrich et al., 2020). Studies of experimentally and naturally deformed dolomite report a variety of deformation mechanisms for different temperatures. Delle Piane et al. (2008) reported boudinage of calcite marble within dolomitic marble deformed at temperatures >700°C and proposed a relative strength inversion between the two phases at temperatures >600°C. Below this temperature, dolomite is expected to be more viscous than calcite during deformation possessing a middle-to-upper greenschist facies lower limit of deformation by dislocation creep (Berger et al., 2016; Davis et al., 2008; Delle Piane et al., 2008; Holyoke et al., 2013; Parsons et al., 2016). Dolomite deformation by grain boundary migration followed by dislocation accommodated grain boundary sliding at temperatures >550°C has been reported from the Himalaya Main Central Thrust zone (Nania, 2021). Elsewhere in the Himalaya, dolomite deformation by grain boundary

migration and bulging is associated with temperatures of 300-600°C based on structural position, twinning and slip system activity (Parsons et al., 2016). Berger et al. (2016) report dolomite deformed by dislocation creep at 540°C on Naxos (Greece), with mixed diffusion and dislocation creep at temperatures >390°C. Grasemann and Tschegg (2012) documented ductile (~300°C) high strain deformation of dolomite-calcite marble containing fractured quartz boudins facilitated by reaction weakening and fluid flow in a greenschist facies viscous shear zone. Generally for low temperatures, field evidence, deformation experiments and flow law extrapolation suggest coarse grained dolomite is strong particularly in comparison to calcite (Bestmann et al., 2000; Davis et al., 2008; Schmid, 1982). Despite dolomite's generally assumed and reported strength, Newman and Mitra (1994) reported crystal plasticity and dynamic recrystallization of dolomite at temperatures <270°C. Herein we report on a major crustal-scale detachment system in which lower greenschist to subgreenschist facies ductile deformation was accommodated by a package of dolomitic mylonitic and ultramylonitic marble.

On Mt. Hymittos, Greece ductile deformation related to a paired extensional detachment system localized in calcitic and dolomitic marbles at different structural levels. The upper detachment primarily localized in calcitic marbles, whereas ductile deformation of the lower detachment was accommodated in dolomitic marbles. Preliminary field observations support the interpretation that the dolomitic mylonites accommodated pervasive high-shear strain deformation under lower greenschist to sub-greenschist facies conditions even though conventionally weaker calcitic marbles were present at similar structural levels. To interrogate this phenomenon, we apply microstructural analysis to a suite of highly sheared dolomitic and calcitic mylonite and ultramylonite samples from the footwalls of the detachment branches. Our findings suggest that under lower to subgreenschist facies temperatures dolomite may accommodate significant ductile

strain. Such low temperature weakness has notable implications for crustal strength and shear zone localization as dolomite may have accommodated significant unrecognized shear strain in other field areas.

4.2 Geologic Setting & Field Evidence

Mount Hymittos, Attic Peninsula, Greece, is an early to middle Miocene metamorphic core complex at the northwest end of the West Cycladic Detachment System (**Figure 4.1a**; Coleman et al., 2020; Grasemann et al., 2012), the footwall of which exposes paired detachment branches of this system. Ductile mylonites along the detachments record top-SSW shear sense, and at increasingly higher structural levels the mylonite transition into brittle overprinted mylonite and finer-grained ultramylonite capped by a cataclastic fault core and knife-sharp fault planes (**Figure 4.2a, f, g**). The highest structural levels of the massif (Upper Unit) consist of low metamorphic grade calcitic marble and metasedimentary phyllite. The Middle and Lower units expose intercalated sequences of lower greenschist facies schist and dolomitic and calcitic marbles of the Cycladic Blueschist Unit. These rocks record a history of polyphase metamorphism and deformation beginning with protracted Eocene high-pressure metamorphism related to subduction and syn-orogenic exhumation within the subduction channel (Dragovic et al., 2015; Kotowski et al., 2021; Laurent et al., 2017, 2018; Lister & Forster, 2005), followed by greenschist facies metamorphism during extensional detachment faulting (Baziotis et al., 2020; Coleman et al., 2020). Relict glaucophane in some Middle Unit schist attest to the episode of high-pressure metamorphism and contemporaneous deformation within the subduction channel that produced an S_1 mylonitic foliation, which was later transposed as an $S_{1\text{-}2}$ foliation during syn-orogenic exhumation (Coleman et al., 2020). Subsequently, the Middle and Lower units were extensively sheared during top-SSW deformation along the detachment branches producing an S_3 mylonitic to

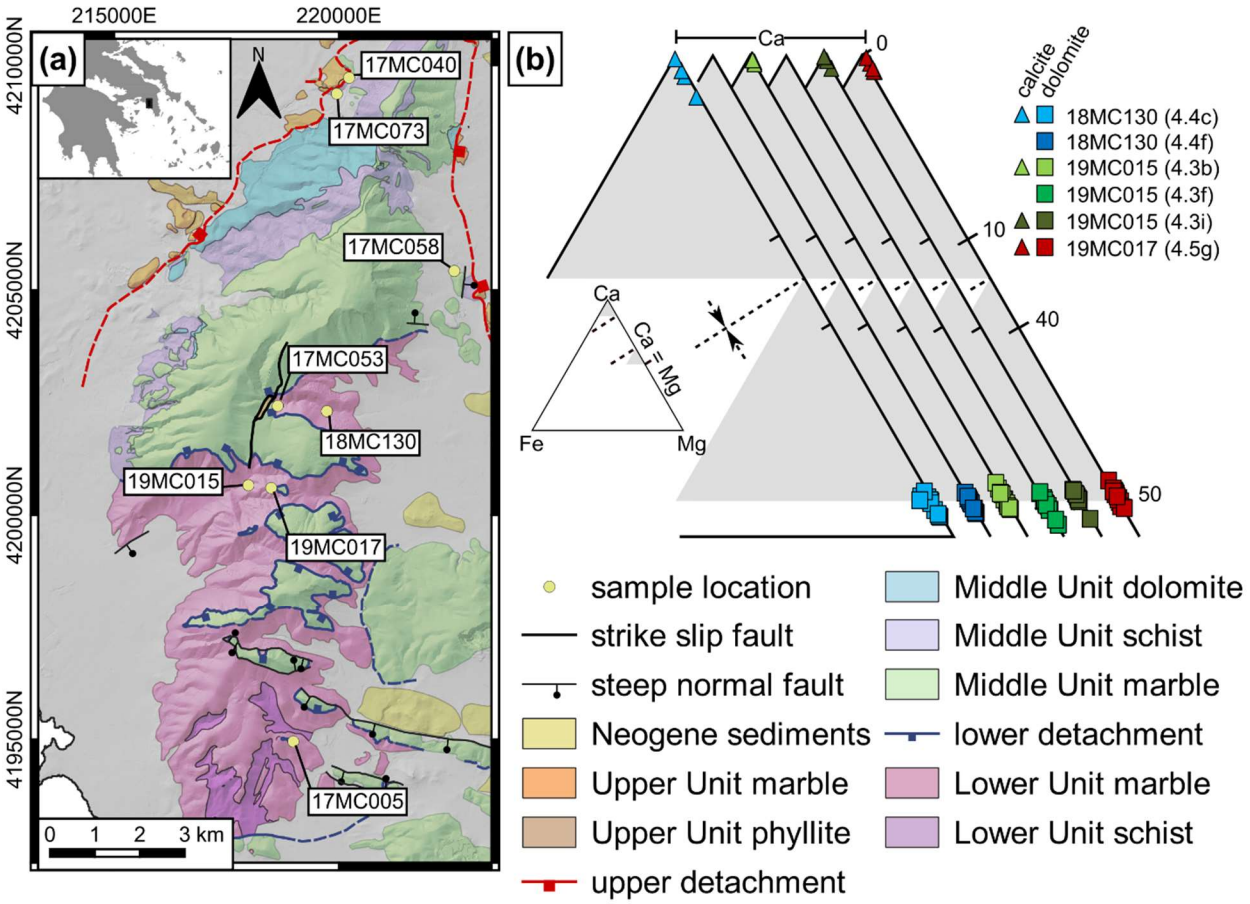

Figure 4.1. (a) Bedrock geology map, and sample locations from Mt. Hymittos, Greece; modified from Coleman et al. (2020). Grey regions of the map represent areas of no or limited data, typically obscured by the city of Athens. **(b)** Calcite and dolomite wavelength disperse spectroscopy ternary diagrams for the samples analyzed in this study. Due to the uniformity of their chemical compositions, dolomite and calcite analyses are plotted on expanded ternary diagrams wherein the boundaries of each grey triangle are 1/8 that of a standard ternary diagram. The map is projected to UTM zone 35S from the geographic coordinate system, using the World Geodetic System 1984 datum.

ultramylonitic foliation and NNE-SSW mineral and elongation lineation (Coleman et al., 2020). Notably, dolomitic marble within the Middle Unit shows little evidence of ductile deformation (**Figure 4.2b, c**) and hosts minimally deformed Triassic coral (Negris & Meunier, 1915), whereas Lower Unit dolomitic marble are mylonitic to ultramylonitic (**Figure 4.2e**). The Middle Unit of Hymittos (**Figure 4.1a**) records peak greenschist facies conditions of 470 ± 20°C at 0.8 ± 0.1 GPa

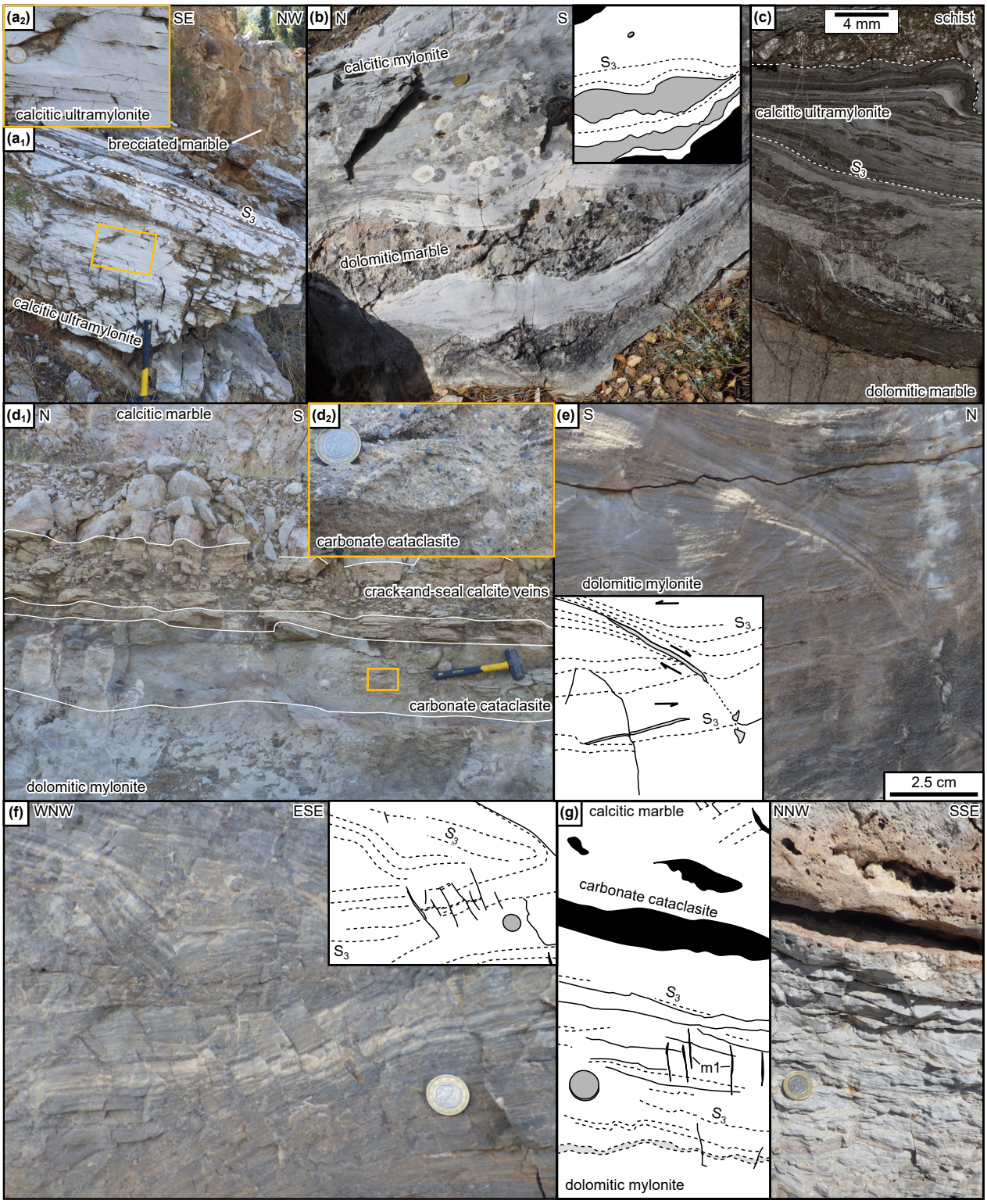

Figure 4.2. Refer to caption on next page.

Figure 4.2. (previous page) **(a_1)** Foliated calcitic ultramylonite in the Middle Unit of the footwall of the upper detachment. Brecciated marble overlying the ultramylonite fractured by brittle displacement along the detachment **(37.9550087°N, 23.7738712°E)**. **(a_2)** Inset, foliation in calcitic ultramylonite. **(b)** Boudinaged dolomitic marble preserved within Middle Unit mylonitic calcitic marble. During deformation the dolomitic marble acted as rheologically strong layers and was boudinaged within the calcitic marble **(37.9737665°N, 23.8218751°E)**. **(c)** Photomicrograph of thin section from the Middle Unit, calcitic ultramylonitic marble adjacent to dolomitic marble. The calcitic marble is extremely fine grained and strongly foliated, the dolomitic marble is fractured and shows no strong evidence it accommodated ductile strain. **(d_1)** Outcrop of the lower detachment in eastern Hymittos. Foliated Lower Unit dolomitic marble in the footwall is overprinted by cataclasis and carbonate veins **(37.8506050°N, 23.8296148°E)**. **(d_2)** Inset, close-up of polymictic carbonate cataclasite in fault core of the lower detachment. **(e)** Flanking structure in a Lower Unit dolomitic mylonite, top-S shear sense inferred from co-rotation of central vein element, counter shear along the vein displaced local foliations **(37.854367°N, 23.793738°E)**. **(f)** Dolomitic mylonite of the Lower Unit overprinted by complex brittle deformation due to displacement along the lower detachment. Ductile surfaces were reactivated by brittle slip during layer-parallel shear before the layers buckled and folded, or fractured during bookshelf rotation **(37.8742403°N, 23.7915233°E)**. **(g)** Brittlely overprinted, foliated dolomitic ultramylonite of the Lower Unit overlain by cataclasis and the surface plane of the lower detachment. m1: mode 1 extensional fractures. Location of sample 19MC017 **(37.909398°N, 23.798244°E)**.

and cooling to ~390°C at 0.7 ± 0.1 GPa based on Raman spectroscopy and multi-equilibrium thermobarometry on garnet-chloritoid-chlorite-phengite schists (Baziotis et al., 2020). The schistose rocks in the Lower Unit have similar metamorphic assemblages to the Middle Unit, but lack garnet (Coleman et al., 2020). White mica $^{40}Ar/^{39}Ar$ deformation ages and zircon (U-Th)/He cooling ages temporally overlap for samples collected from the Lower Unit, indicating the lower detachment was active as a ductile structure after metamorphism at temperatures approaching ~200°C (Coleman et al., 2020). In contrast, geochronologic analyses from the Middle Unit suggest that ductile deformation may have ceased in the middle Miocene and at somewhat higher temperatures before transitioning to a brittle structure and cooling below ~200°C in the late Miocene (Coleman et al., 2020). Calcitic marble from similar structural levels to the dolomitic mylonite are coarser grained and less recrystallized (Coleman et al., 2020).

4.3 Sampling Strategy and Methods

Dolomitic and calcitic marble samples (n: 47) were collected from across the massif taking into consideration chemical composition, observable (micro)structures, and structural position relative to the detachments. A subset of mylonitic samples (n: 8) were targeted for detailed analysis following thin section petrography, mylonites and ultramylonites were differentiated based on the clast-to-matrix ratio (Sibson, 1977), which has been invoked as a proxy for the degree of dynamic recrystallization provided coarse material is not reintroduced during, or following, recrystallization. The dolomitic marble samples in this study (n: 4; 19MC015, 18MC130, 17MC053, 19MC017) were specifically collected from the lower detachment footwall in central Hymittos, as this area has the best exposures of dolomitic mylonite with minimal schistose and calcitic intercalations. The selected samples reflect a trend of decreasing structural level within the Lower Unit toward the detachment surface, which approximately correspond to an increase in matrix-porphyroclast ratio (**Figure 4.1a**). Calcitic marble samples (n: 3; 17MC040, 17MC073, 17MC058) were collected from the footwall of the upper detachment in northern Hymittos as this is where the upper detachment is best exposed; an additional calcitic sample (17MC005) was collected from a klippe of the Middle Unit in the southern massif to assess the changing conditions of deformation of the upper detachment at deeper crustal levels. For the upper detachment the variability of recognizable microstructures in the calcitic mylonites and spatial distribution of the samples precludes assigning an obvious structural level with the same confidence as the dolomitic samples herein. Oriented samples were taken in the field, and polished thin sections (XZ plane of the kinematic reference frame) were examined under plain and crossed polarized light via a transmitted light microscope. Prior to further analyses, thin sections were chemo-mechanically

polished with an alkaline colloidal silica suspension to ensure accurate measurements of crystallographic orientation and carbon-coated (~20 nm thickness) to enhance conductivity.

Quantitative dolomite and calcite compositions were determined by wavelength dispersive spectroscopy via a JEOL JXA-8230 SuperProbe (University of Ottawa). Analyses were conducted with an accelerating voltage of 20 kV to focus and concentrate the beam diameter to 5 μm. Point data were collected from coarse, mylonitic and ultramylonitic dolomite, as well as calcite where it is present as an interstitial phase.

Calcite and dolomite crystal orientations for three samples (19MC015, 18MC130, 19MC017) were determined via electron backscatter diffraction (EBSD) mapping using a Tescan Mira 3 XMU Field Emission SEM equipped with an Oxford Instruments Nordlys EBSD detector (University of British Columbia, Okanagan). The instrument was operated at 20 kV, with a working distance of 15 mm sample tilt of 70° and a step size of 1-2 μm. EBSD maps of five additional samples (17MC053, 17MC040, 17MC073, 17MC005, 17MC058) were determined via an FEI Quanta 3D field emission gun scanning electron microscope (SEM) equipped with an EDAX Digiview IV EBSD camera (University of Vienna). The instrument was operated at 10 kV with a working distance of 13-17 mm and a step size of 0.5-1 μm. Data were processed using Aztec Cnahhel5 (Oxford Instruments) and Aztec Crystal (Oxford Instruments) for the initial data cleaning and pseudo-symmetry removal. The final post processing and were carried out using the MTEX toolbox (5.8.1, Bachmann et al., 2010) for MATLAB 2018a (www.mathworks.com). Crystal orientation data were cleaned via confidence index standardization at 5°. Grains with a size smaller than two pixels were removed, followed by neighbor orientation correlation at 0.1 confidence interval. Twining in dolomite commonly occurs by a rotation of 90° around the $1\bar{1}04$ axis and calcite twins by 52.5° rotation around the $1\bar{1}08$ axis (Barber & Wenk, 1979; Rybacki et

al., 2011). Dolomite pseudosymmetry is also recognized in several maps produced by a rotation of 180° around the $2\bar{1}\bar{1}0$. These twin and pseudosymmetry orientations can dominate statistical analyses and have been reintegrated with their parent grains by reversing the twin rotation prior to analyses where the presence of many twins would bias the result.

Data are presented as misorientation deviation maps, the axis has been limited to 10° in most maps to prevent a few highly misoriented grains from biasing the display. The deviation maps are overlain by grain boundary maps with a misorientation angle of 10° for grain boundaries and 2-10° for low-angle boundaries (Bachmann et al., 2011). Inset rose diagrams represent the distribution and orientation of the long axes of grains. Crystal preferred orientation (CPO) data are displayed by equal-area lower-hemisphere projections of a random sample of 1666 crystallographic orientations of the *c*-axes, *a*-axes, and poles to *r*-planes and *f*-planes out of a total of 37625-307195 measured orientations per map. Outsized grains can dominate CPO figures and have been mostly removed from crystallographic orientation calculations. Grain size is described in terms of equivalent grain diameter. Misorientation angle distributions are presented for neighbor-pairs (correlated), random-pairs (uncorrelated) and fully uniform misorientation distributions for an array of theoretical dolomite crystals. Crystallographic vorticity axis diagrams have been produced for the calcitic samples that exhibit the greatest proportion of low-angle boundaries.

4.4 Sample characterization

The grain size distribution of the samples described below is not uniform; to simplify the results and discussion, a series of microstructural domains have been standardized across samples. Coarse domains generally comprise large grains (>200 μm) occupying a significant proportion of the map, and the immediately adjacent or interstitial finer grains (50-100 μm). The coarse material

within these domains may be primary or authigenic coarse-grained dolomite, or more commonly one of several generations of variably deformed pre-to-syn-kinematic veins (**Figure 4.3a, f; 4.4d**). Fine domains (<50 μm) exhibit the most uniform grain sizes and grains exhibit relatively little internal deformation. Intermediate domains (50-100 μm) are between the previous two relative sizes and may exhibit a broader range of microstructures and grain sizes. Matrix generally refers to fine grains that make up the fine domain and the smaller grains within the intermediate domain; these grains may reflect either recrystallized coarser material, or an initial fine grain size.

4.4.1 Mineral composition

Mineral chemical analysis of Lower Unit dolomitic marble and interstitial calcite plotted on Ca-Mg-Fe ternary diagrams reveal minimal Ca-Mg exchange in all samples (**Figure 4.1b**). Dolomitic analyses are tightly clustered and analysis exhibits <4% calcite ($CaCO_3$) and <2% ankerite [$Ca(Fe_{0.6},Mg_{0.3},Mn_{0.1})(CO_3)_2$]. Analyses of interstitial calcite (where present) are similarly tightly clustered with <1% ankerite, and a maximum of 5% dolomite [$CaMg(CO_3)_2$]. These results demonstrate that the Lower Unit marbles consist of dolomite, rather than high-Mg calcite, which may appear similar to dolomite in the field. Consistency of mineral composition in matrix and veins across structural levels (>100 m) and preservation of deformation structures indicate that dolomite is not the product of post-deformation alteration or localized fluid flow along faults.

4.4.2 Lower Unit: Dolomitic rocks

The least deformed dolomitic sample of this study is a graphite-bearing, fine grained dolomitic marble with minor (<1% volume) white mica and quartz (19MC015, **Figure 4.3a**). Grain sizes vary with intermediate (50-90 μm diameter) to fine (<10-50 μm) domains of dolomite

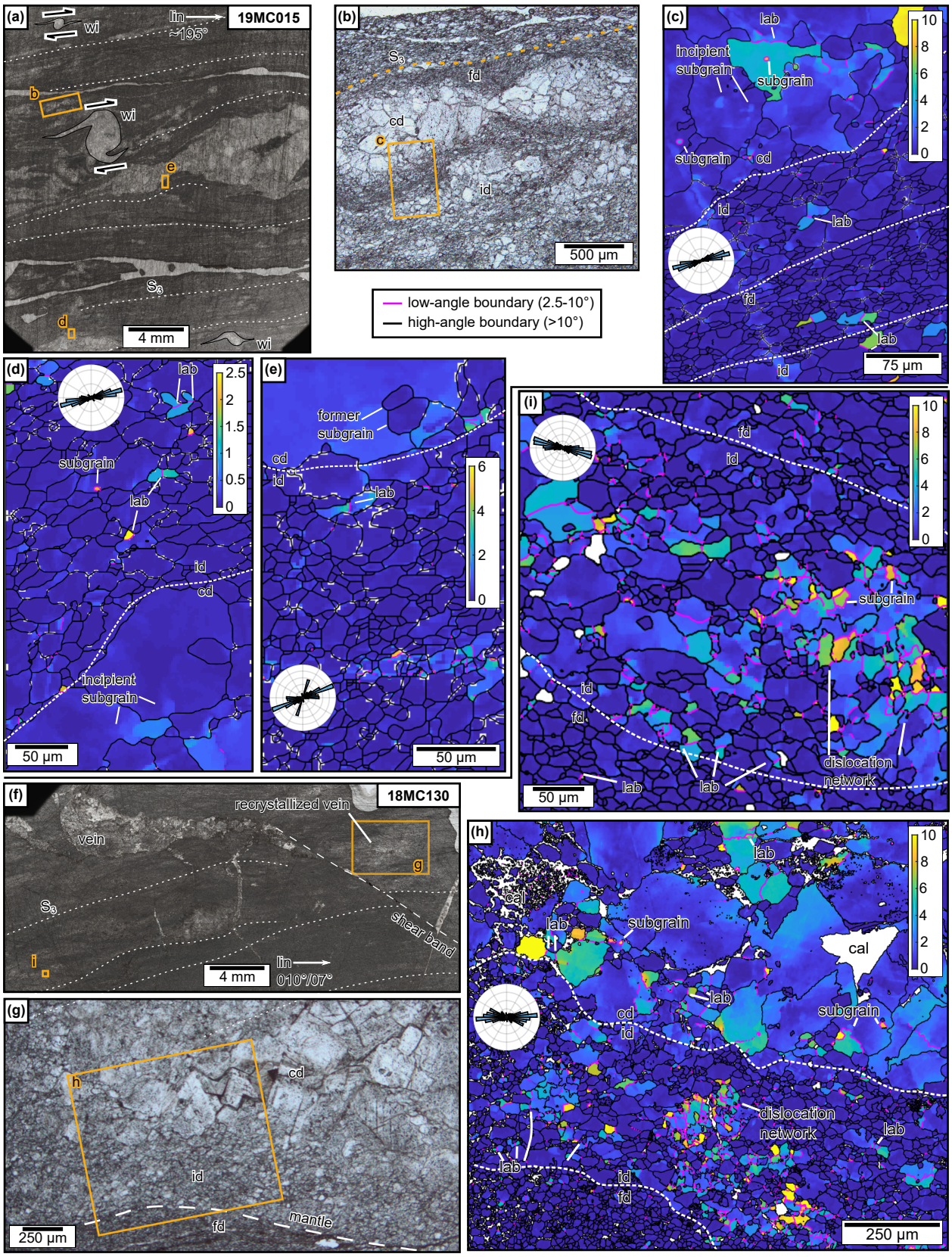

Figure 4.3. Refer to caption on next page.

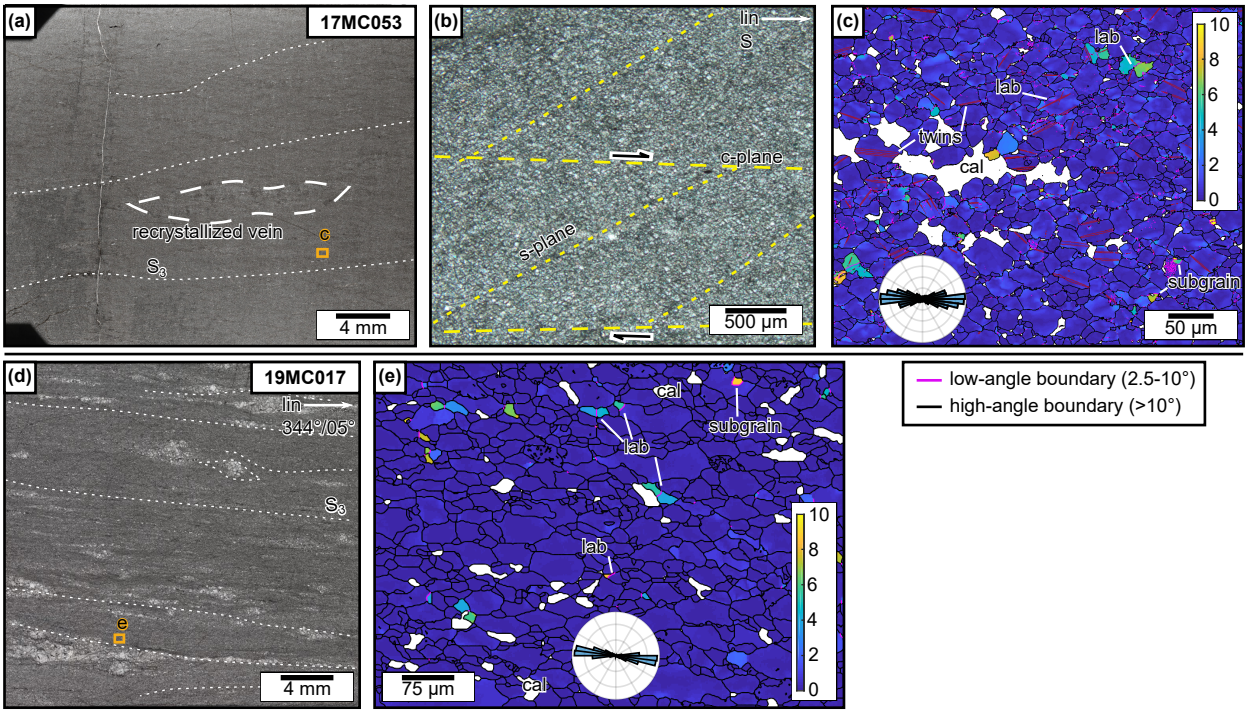

Figure 4.4. (a, d) Photomicrographs of sample 17MC053 displaying location of EBSD map (c) (218638E, 4202427N) and 19MC017 with location of map (e) (218493E, 4200601N). These dolomitic marbles exhibit a more homogeneous matrix and a greater proportion of interstitial calcite. **(b)** S-C fabric in sample 17MC053B1, the grain-shape preferred orientation is oblique to outcrop-scale foliation. **(c, e)** Misorientation deviation maps, with overlaid grain boundary maps, common twin boundary orientations (red) and grain-long axis rose diagrams. Abbreviations: cal: calcite, lab: low-angle boundary.

bordering coarse dolomite veins with average grain diameters of >200 μm. The intermediate and fine-grained domains exhibit a distinct grain shape preferred orientation parallel to the local foliation and is reflected in the rose diagrams of the long-axes of grains. Shear sense and deformation indicators such as flanking structures, boudinaged veins (**Figure 4.3a, b**) and winged inclusions (**Figure 4.3a**) are evident. The sense of shear indicated by some of these structures is consistent with the top-SSW kinematics derived from macroscopic field observations for the upper and lower detachments (**Figure 4.2**).

The EBSD maps of 19MC015 exhibit few low-angle grain boundaries and internal misorientation concentrated in coarse dolomite veins and intermediate recrystallized zones bordering the coarse domains (**Figure 4.3b, c**). In some grains, low-angle boundaries cross-cut grains delineating misoriented domains and may self-terminate or end against grain boundaries creating subgrains (**Figure 4.3c, d, e**). In the intermediate domains (**Figure 4.3c, d, e**), the low-angle boundaries subdivide grains commonly at high-angle to the SPO of the grain. The long axes of grains in the recrystallized matrix are approximately parallel to the contact with the relict veins. Correlated misorientation angle histograms show populations of <10° low-angle boundaries comprising 2-3% of all boundaries (**Figure 4.5b, d, f**). Outside of this low-angle population, uncorrelated misorientation curves match the uniform distribution except for one plot (**Figure 4.5f**), which is influenced by the presence of large grains. Pole figures (**Figure 4.5a, c, e**) exhibit a distinct CPO defined by a *c*-axis maxima normal to the foliation with a poorly developed girdle; one map area (**Figure 4.3e**) displays two-point maxima. The *a*-axes are dispersed as girdles with multiple weak sub-maxima and weak *f*-pole maxima are present in some maps (**Figure 4.3c, e**).

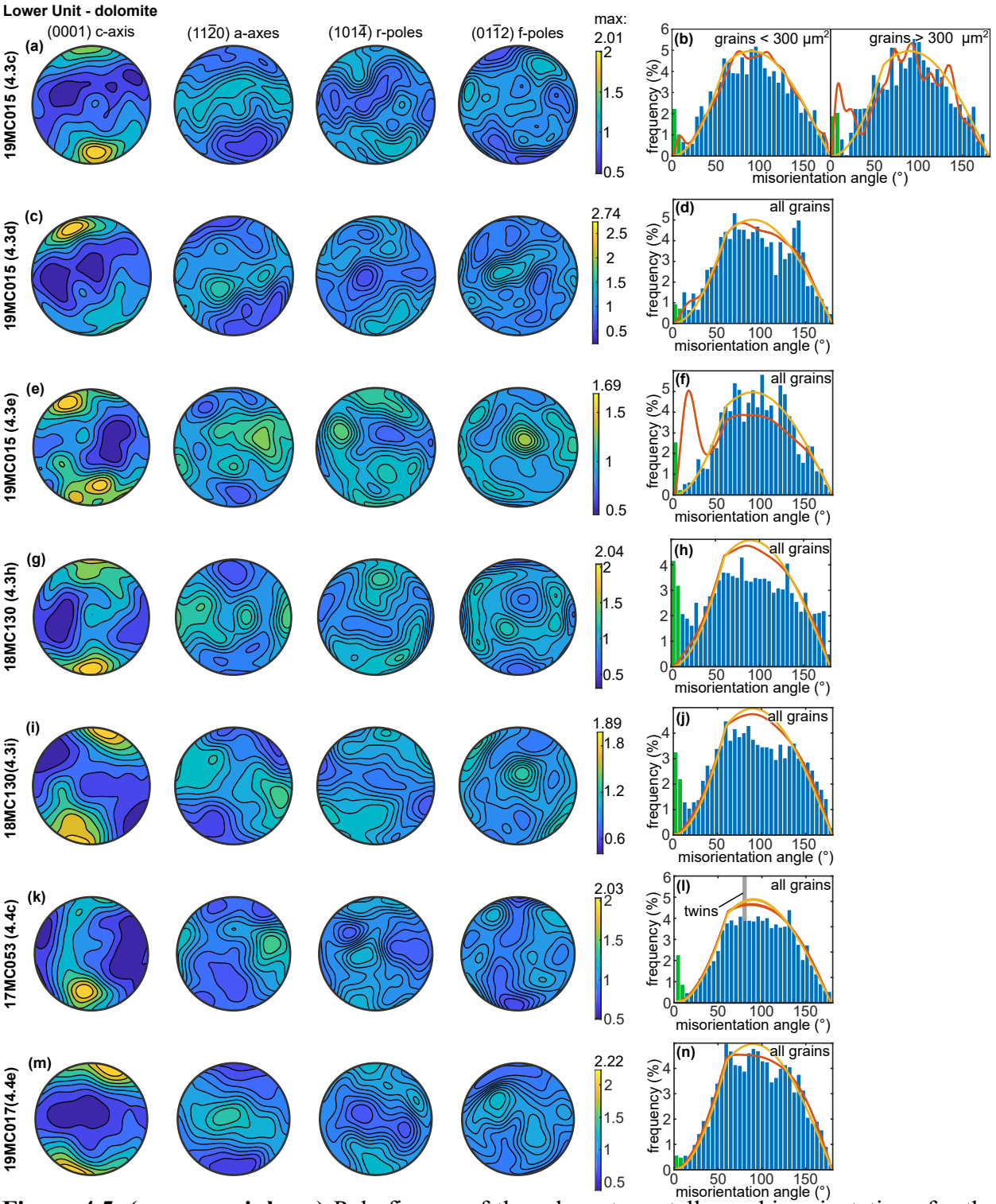

Figure 4.5. (a, c, e, g, i, k, m) Pole figures of the relevant crystallographic orientations for the dolomitic marble samples; textures show clear c-axis maxima orientated perpendicular to the foliation, and foliation-parallel a-axis girdles, m exhibits a weak a-axis maxima; c, e, and i present f-pol maxima parallel to the Y pole of the reference frame. **(b, d, f, h, j, l, n)** Misorientation angle diagrams for the corresponding EBSD maps on figures 4.3 and 4.4. Correlated distributions are divided into high-angle (blue) and low-angle (green) boundaries, compared to uniform distributions (orange) and uncorrelated distributions (red).

Sample 18MC130, closer to the detachment, exhibits a greater proportion of dolomitic matrix than the previous sample, coarse domains are disarticulated (**Figure 4.3f**) and core-mantle structures are evident (**Figure 4.3g**).

The recrystallized mantle bounding the relict veins (**Figure 4.3h**) in sample 18MC130 displays a greater concentration of low-angle boundaries than any other dolomitic sample. The microstructures are organized as complex networks of low-angle boundaries, terminating at high-angle grain boundaries (**Figure 4.3h, i**). The adjacent fine matrix domains host fewer low-angle grain boundaries, and most grains show minimal internal misorientation. The long axes of the grain SPOs are subparallel to the boundaries of coarse veins (**Figure 4.3h**). At greater distances from coarse domains the long axes define an oblique foliation (**Figure 4.3i**). Correlated misorientation angle histograms (**Figure 4.5h, j**) exhibit a significant proportion of low-angle boundaries (5-7% of all boundaries), and uncorrelated misorientation curves match with the expected uniform distribution. The *c*-axes define distinct foliation normal maxima with moderately developed girdles (**Figure 4.5g, i**) and *a*-axes are distributed as girdles with lineation parallel maxima; one map preserves weak *f*-pole maxima (**Figure 4.5i**).

Samples collected within five meters of the lower detachment fault plane (**Figure 4.2g**; 17MC053, 19MC017) exhibit a progression of microstructures toward homogeneity, showing fewer shear sense indicators and low-angle boundaries, more uniform grain size and fewer relict veins. The samples preserve minimal coarse material and generally consist of 5-50 μm grains comprising a matrix (>95% of 17MC053) that displays S-C fabrics (**Figure 4.4a, b**). Where present, coarse dolomite porphyroclasts are largely recrystallized or dissected (**Figure 4.4a, d**) exhibiting a reduction of, and uniformity in, grain size (**Figure 4.4b**).

EBSD maps of the dolomitic ultramylonite samples reveal dolomite grains with little internal misorientation, few low-angle grain boundaries compared to more heterogeneous samples, more interstitial calcite and, in sample 17MC053, a greater proportion of twins (**Figure 4.4c, e**). The microstructures and fabric of the grains in these maps are similar to the fine domains of the less recrystallized dolomitic samples. Low-angle boundaries and misorientations generally cross the narrowest portions of grains or delineate misoriented subgrains. Grain long axes are dominantly parallel to the main foliation, though some grains are parallel to the S-planes of S-C fabrics. Correlated misorientation histograms exhibit <10° misoriented boundaries that deviate from the uncorrelated distribution (1-3% of all boundaries; **Figure 4.5l, n**) though 19MC017 hosts fewer <10° misoriented boundaries than other samples. The ~80° population within sample 17MC053 (**Figure 4.5l**) is associated with twinning of dolomite by rotation around $1\bar{1}04$. Uncorrelated distributions are similar to uniform distributions. Pole figures exhibit *c*-axes foliation normal maxima and a distinct girdle in 17MC053 (**Figure 4.5k**). The *a*-axes exhibit lineation parallel maxima with weakly developed girdles. In 19MC017 the *c*-axis girdle is not well developed, and the maxima are oblique to the foliation normal. *a*-axes define a foliation parallel girdle with a lineation perpendicular maximum (**Figure 4.5m**).

4.4.3 Middle Unit: Calcitic rocks

Calcitic mylonite from the Middle Unit (**Figure 4.6)** exhibits a wider range of grain sizes and more mineralogical heterogeneity than the dolomitic samples described above. The sample closest to the upper detachment core (17MC040; **Figure 4.1a**) is a calcitic ultramylonite that exhibits the smallest and most uniform calcite grain size (<10-15 μm), with rare clasts up to 40 μm in diameter. Within this calcitic ultramylonite are dolomite and quartz clasts that have been fractured and distributed along discrete layers (**Figure 4.6a**, **b**). The fine domain matrix of the

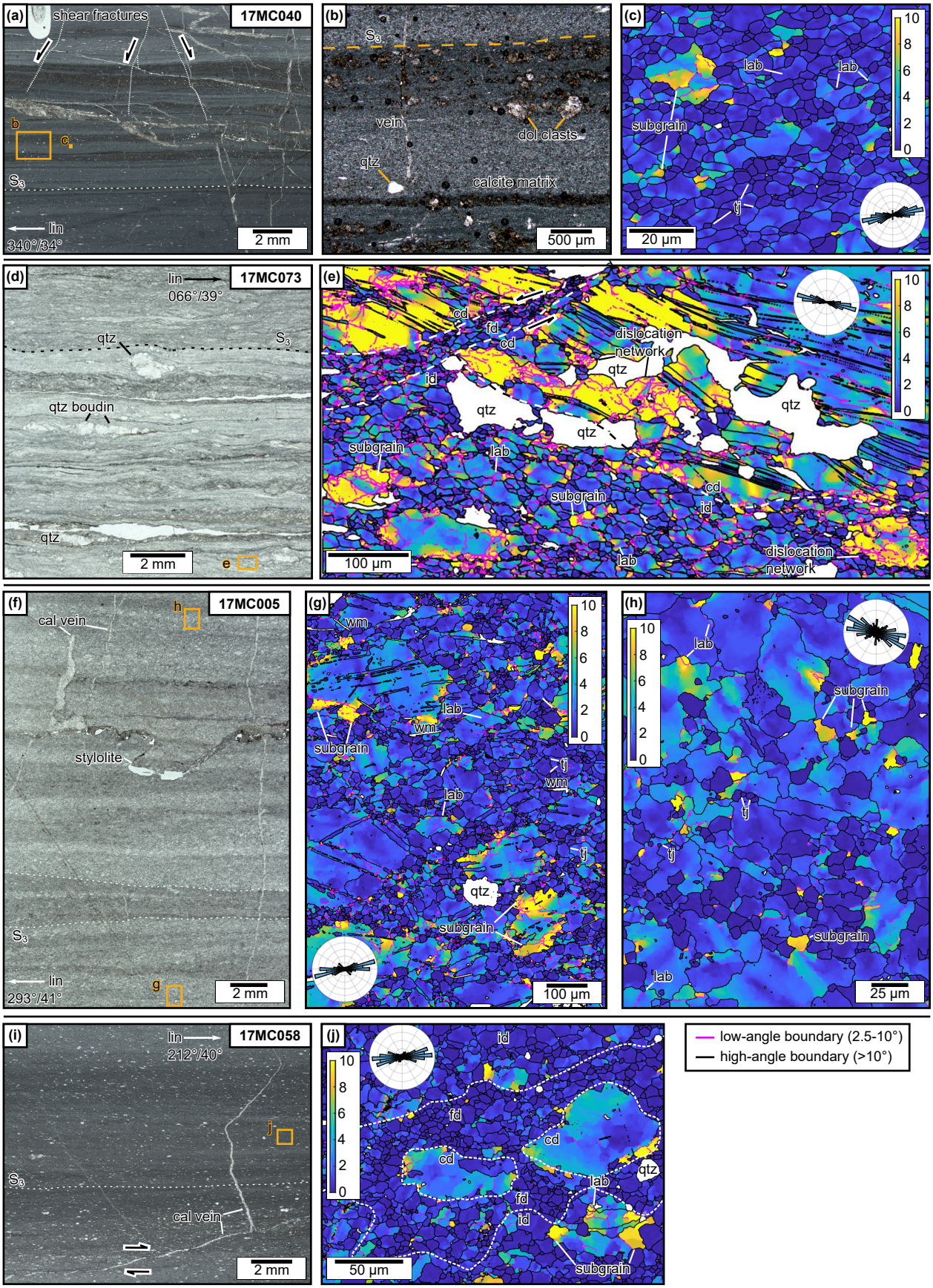

Figure 4.6. Refer to caption on next page.

Figure 4.6. (previous page) **(a, d, f, i)** Photomicrographs of sample 17MC040 displaying location of photomicrograph (b) and EBSD map (c) (220225E, 4209725N), 17MC073 with location of map (e) (219951E, 4209367N), 17MC005 with location of maps (g) and (h) (218984E, 4194950N) and 17MC058 with location of map (j) (222564E, 4205429N). These calcitic marbles exhibit a range of grain sizes and microstructures reflecting changing deformation conditions within the shear zone. **(b)** Photomicrograph of brittlely deformed dolomite clasts hosted in an ultramylonitic calcite matrix. **(c, e, g, h, j)** Misorientation deviation maps, with overlaid grain boundary maps, and grain-long axis rose diagrams. Abbreviations: cd: coarse domain, id: intermediate domain, fd: fine domain, lab: low-angle boundary; tj: triple junction, qtz: quartz, wm: white mica.

sample exhibits a distinct SPO, and conjugate veins that formed as shear fractures are evident at the micro-scale.

The EBSD map of 17MC040 displays a limited number of low-angle boundaries, and zones of significant internal misorientation are more common in coarser or more elongate grains (**Figure 4.6c**). In many instances, minimally misoriented grains exhibit polygonal triple junctions at grain boundaries. The grain misorientation histogram (**Figure 4.7b**) exhibits a small proportion of low-angle misoriented boundaries (2%) and twins; the remainder of the correlated distribution matches with the uncorrelated grain-grain distribution. The correlated and uncorrelated distributions exhibit a greater proportion of <60° boundaries than the expected distribution for a uniform calcite crystal. Pole figures (**Figure 4.7a**) exhibit a distinct *c*-axis single point maxima perpendicular to the SPO, *a*-axis girdles with a weak, lineation perpendicular sub-maxima, *r*-poles cluster at high angles to the foliation. The fine calcite grains, with minimal internal misorientation and pronounced foliation-parallel SPO exhibited in this map are microstructurally similar to the fine domains of the dolomitic mylonite samples described previously.

Twenty meters structurally lower than the previous sample, a marble sample (17MC073) preserves coarse (>500 μm) calcite domains bordered by intermediate (40-100 μm) domains forming core-mantle structures (**Figure 4.6d**). In some instances, the largest crystals are crosscut and offset by fine-grained top-SW C' shear bands with grain sizes <15 μm (**Figure 4.6e**). This

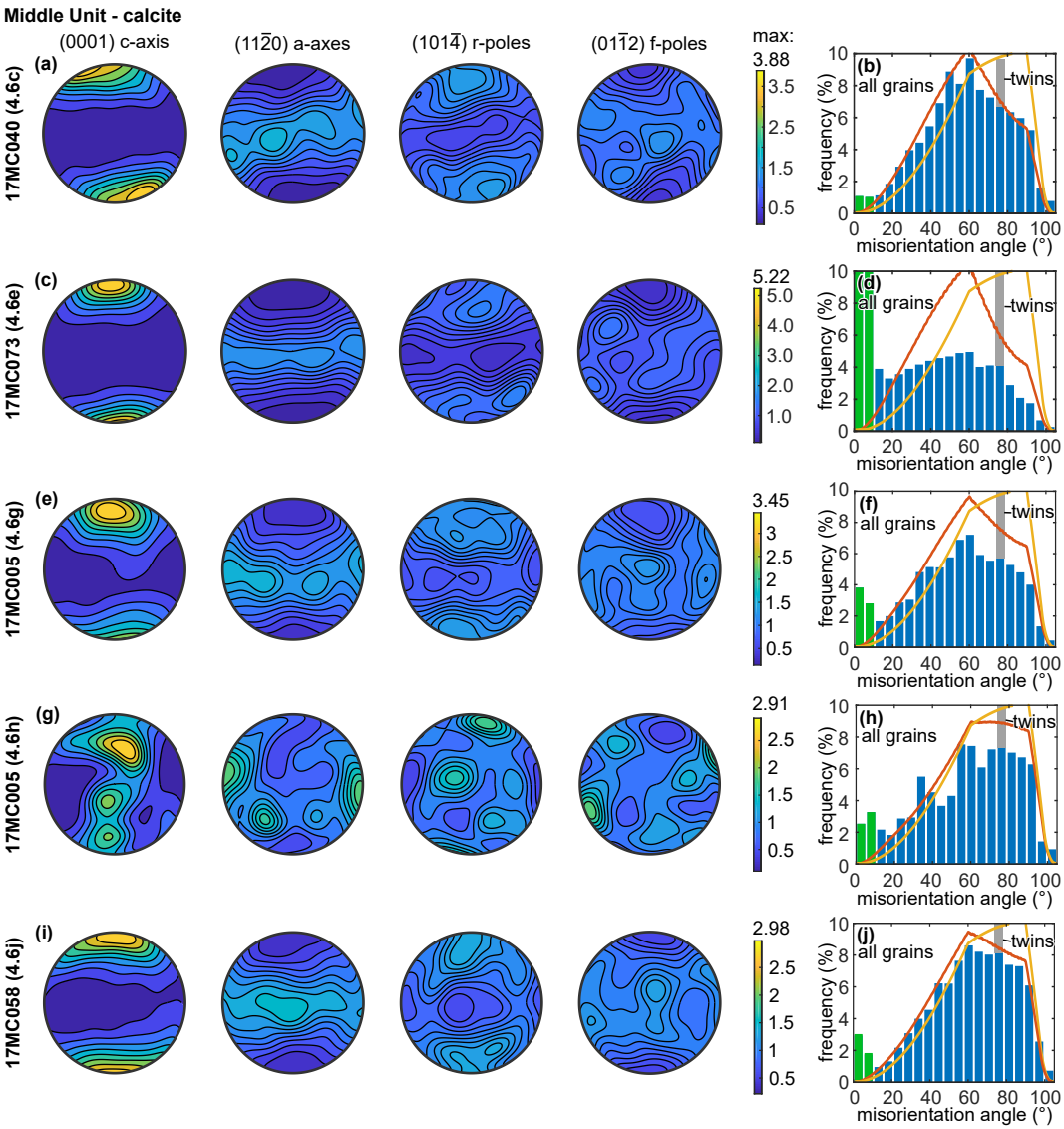

Figure 4.7. (a, c, e, g, i) Pole figures of the relevant crystallographic orientations for the calcitic marble samples; textures show: clear c-axis maxima orientated perpendicular to the foliation, with subfigure g displaying a c-axis girdle, foliation-parallel a-axis girdles, subfigure m exhibits a weak a-axis maxima, r-poles for subfigures a, c and e cluster near the foliation normal. **(b, d, f, h, j)** Misorientation angle diagrams for the corresponding EBSD maps on figures 4.3 and 4.4. Correlated distributions are divided into high-angle (blue) and low-angle (green) boundaries, compared to uniform distributions (orange) and uncorrelated distributions (red).

sample presents a significant proportion of quartz (~5%), largely introduced as a series of pre-kinematic veins that were subsequently boudinaged.

The EBSD map of sample 17MC073 (**Figure 4.6e**) displays the greatest concentration of dislocations of any sample in this study with abundant low angle boundaries in both the coarse and intermediate domains. All but the finest grain fractions present low-angle grain boundaries, and coarser calcite crystals display distinct twinning. The grain misorientation histogram (**Figure 4.7d**) displays a major proportion of low-angle boundaries (22% of all boundaries) and the remainder of the correlated distribution begins to match the uncorrelated distribution at angles >60°, and similar to the previous sample exhibits a greater proportion of <60° misoriented boundaries than a uniform calcite distribution. CPO figures (**Figure 4.7c**) present a sharp *c*-axis point maxima perpendicular to the main foliation in the sample, but at an oblique angle to the local SPO. The *a*-axes are oriented as a foliation-parallel girdle and *r*-poles cluster at high angles to the foliation. Notably the strength of this CPO fabric is greater than all other samples.

A calcitic marble sample from southern Hymittos (17MC005; **Figure 4.1a**) exhibits similar core-mantle structures to the previously described sample, though the grain size of the coarse grains (200-500 μm) is slightly smaller. This sample possesses layering that reflects differences in grain sizes and varying proportions of graphite, quartz and white mica (**Figure 4.6f)**. The ductile fabric is crosscut by a stylolite and associated calcite veins.

The EBSD maps of sample 17MC005 highlight the sample's heterogeneous grain sizes and their spatial distribution. The first map presents well developed core-mantle structures with coarser grains with highly misoriented subgrains and minimally misoriented matrix (**Figure 4.6g**). The second map (**Figure 4.6h**) reveals intermediate grains with common internal misorientation yet relatively few low-angle boundaries, in this map subgrain misorientation is accommodated by

diffuse zones of gradual misorientation change. 120° triple junctions are visible at the boundaries of some fine calcite grains. Misorientation histograms (**Figure 4.7f, h**) express a population of low-angle boundaries distinct from the uncorrelated distribution (5-7% of all grain boundaries). The rest of the distributions generally coincide with the uncorrelated curve and deviate from the uniform distribution at >60° misorientation angles. CPO diagrams (**Figure 4.7e, g**) display foliation perpendicular *c*-axis maxima with one map yielding a well-developed girdle (**Figure 4.7g**). The *a*-axes form foliation-parallel girdles though the two-point maxima in the second map may indicate a grain-size control on the CPO fabric of this sample.

In northeastern Hymittos, a flanking structure associated with the upper detachment exposes a Middle Unit calcitic mylonite (17MC058; **Figure 4.6i**) with variable grain sizes from 5 μm to 100 μm. This marble contains core-mantle structures though much of the groundmass is comprised of intermediate (40-80 μm) domains. Fine quartz grains (<2%) are present within the sample though it is not clear whether they originated as sedimentary clasts or vein material. Shear-band boudinaged calcite veins within the mylonite give a top-SSW sense of shear, veins inclined against the inferred shear direction are folded (**Figure 4.6i**).

EBSD mapping of sample 17MC058 exposed a series of microstructures similar to 17MC005, with a greater proportion of fine matrix and generally smaller grain size of the coarse domains (**Figure 4.6i**). Intermediate domains host both finer less-deformed grains and intermediate sized grains, which range from minimally to highly misoriented. In places these misoriented domains form subgrains delineated by low-angle boundaries (**Figure 4.6j**). In other locations, small grains with minimal misorientation are positioned at the boundaries of the most misoriented grains. More contiguous fine domains have distinctly smaller mean grain sizes with little internal deformation. Correlated misorientation histograms exhibit a proportion of low-angle

boundaries (5% of all boundaries) the remainder of the distribution generally fits the uncorrelated curve that deviates from the uniform distribution at misorientation angles >60° (**Figure 4.7j**). CPO figures display pronounced foliation normal *c*-axis maxima, and foliation parallel *a*-axis girdles with a possible weak *r*-pole maxima normal to the foliation (**Figure 4.7i**).

4.5 Discussion

The lower plate of Hymittos experienced Eocene high-pressure metamorphism (1.4 ± 0.05 GPa at 300 ± 25°C) followed by Oligo-Miocene greenschist facies metamorphism (0.8 ± 0.1 GPa at 470 ± 20°C) based on multi equilibrium thermobarometry and Raman spectroscopy of Middle Unit schist (Baziotis et al., 2020). Consistency of kinematic indicators and their structural position indicates that the mylonites of the Middle and Lower units of Hymittos developed during top-SSW shearing (S_3) as branches of the West Cycladic Detachment System (Coleman et al., 2020). White mica $^{40}Ar/^{39}Ar$ ages indicate that the calcitic mylonite of the Middle Unit deformed during the middle Miocene, and integration with pre-existing P-T data and comparison with metamorphic assemblages suggest deformation temperatures >300°C before ductile deformation ceased c. 15 Ma (Baziotis et al., 2020; Coleman et al., 2020). Within the Lower Unit, overlap between white mica $^{40}Ar/^{39}Ar$ deformation ages and zircon (U-Th)/He cooling ages indicates that the mylonites of the Lower Unit were deforming at temperatures <300°C in the late Miocene (Coleman et al., 2020). The mylonitic rocks of the lower detachment of Hymittos accommodated rapid exhumation of the footwall to upper crustal levels following greenschist facies metamorphism (Baziotis et al., 2020; Coleman et al., 2020), which minimized the time for the dolomitic mylonites of the Lower Unit to undergo significant post-deformation annealing, unlike the calcitic mylonites of the Middle Unit. As the two detachment branches deformed ductilely under different temperatures and at

separate times, the calcitic and dolomitic mylonites herein formed under different pressure and temperature conditions.

4.5.1 Deformation of the Lower Unit - dolomite

Monoclinic microstructures like oblique SPO, winged inclusions, S-C fabrics, and inclination of some *c*-axis maxima with respect to the foliation are indicative of non-coaxial deformation. The occurrence of winged inclusions suggests a minimum shear strain $\gamma \gtrapprox 10$ during top-SSW displacement of the detachment system as derived from numerical modelling (Grasemann & Dabrowski, 2015). The increasing proportion of matrix relative to clasts, more prominent core-mantle structures, and greater degree of disarticulation of coarse domains (**Figure 4.3f, g; 4.4d**) in structurally higher samples 18MC130 and 19MC017 compared to 19MC015 is interpreted to reflect a greater degree of recrystallization. Many of the coarse domains are the product of dolomite veins, some of which may have formed synkinematic to D_3 deformation of the detachment; as coarse material may be introduced during deformation, the ratio between clast and matrix likely does not reflect the total strain accommodated by any individual sample. The samples closest to the detachment cores (17MC053, 17MC040) exhibit a decrease in the number of shear sense indicators, fewer low-angle boundaries, more uniform grain sizes, and fewer relict veins which is inferred to reflect a greater volume of dynamically recrystallized material in samples proximal to the shear zone center (Janney & Wenk, 1994). Obliquity of some *c*-axes in the direction of inferred sense of shear is associated with progressive deformation and recrystallization under a component of simple shear (Leiss et al., 1999; Leiss & Barber, 1999).

The distribution of low-angle boundaries, similarity in size between subgrains and matrix, and misorientation to mean orientation maps evince subgrain rotation recrystallization and minor bulging (**Figure 4.3c; 4.3h, i**) that caused grain-size reduction of the coarser domains (Bestmann

& Prior, 2003; Lloyd et al., 1997). The coarse vein dolomite of sample 19MC015 and 18MC130 contains isolated portions of the fine domain matrix (**Figure 4.3; 4.4**) suggesting these veins are synkinematic to S_3 deformation related to shear along the detachment. The evidence of dislocation creep is best illustrated in the intermediate domains, which seem to record a transitional stage between the coarse vein-dolomite dominated domains, and the fine domains, which are almost entirely composed of recrystallized matrix (**Figure 4.4**). The minimally misoriented small grains at the boundaries of the more misoriented large grains are interpreted as the product of progressive dynamic recrystallization, which generated grains of similar size to the matrix (5-50 μm).

The foliation-perpendicular *c*-axis maxima, foliation parallel *a*-axis girdles and patterns of *r*- and *f*-poles (**Figure 4.5a, c, m**) observed in coarse and intermediate domains match modelled textures for deformation of dolomite at 200°C accommodated by *c*-slip on the basal plane with *a*-axes as the Burgers vector (Leiss et al., 1999). Such textures are similar to higher temperature natural examples produced by these same slip systems, though the higher temperature textures reflect a greater activation of *f*-slip (Barber et al., 1981; Barber & Wenk, 2001). *A*-axis maxima similar to those documented in 19MC017 and 17MC053 (**Figure 4.5k, m**) have been recognized in experimentally deformed high-strain dolomite ($\gamma \approx 8$; Delle Piane et al., 2008), supporting the evidence of high shear strain along the lower detachment extrapolated from winged inclusions. The consistent top-SSW kinematic indicators, geochronologic data (Coleman et al., 2020) and high degree of strain accommodation in the dolomitic samples supports the conclusion that these dolomitic mylonites clearly experienced grain-size reduction by dislocation creep during low-temperature ductile deformation as a branch of the West Cycladic Detachment System.

Within the fine domains, a low frequency of low-angle boundaries, limited intracrystalline misorientation, and approximately uniform correlated misorientation angles above 10° indicate

deformation via grain size sensitive creep (Barber & Wenk, 2001; Bestmann & Prior, 2003; Wenk & Christie, 1991). The approximately uniform correlated misorientation angles >10° points specifically to the activity of grain boundary sliding, which is known to randomize grain-grain orientations (Bestmann & Prior, 2003; Prior et al., 1999; Wheeler et al., 2001). Grain-boundary sliding facilitated by diffusion can result in the development of a distinct SPO (Davis et al., 2008) observable in the matrix of all samples (**Figure 4.3, 4.4**). Diffusion accommodated grain boundary sliding is further supported by the presence of interstitial calcite at grain triple junctions and voids (e.g., 17MC053; **Figure 4.3h, 4.4c**; White & White, 1980), furthermore the chemical uniformity of vein and host dolomite indicates that the veins may be produced by dissolution and reprecipitation of the dolomitic marble (**Figure 4.1**).

Although the S-C fabrics, chemical uniformity of vein and host, near-uniform misorientation angles, distinct SPO, and minor interstitial calcite all point toward grain-boundary sliding assisted by diffusion (*s.l.*), the occurrence of a CPO may conflict with this interpretation. Similarity between CPO from all grain size domains may indicate that the fabric in the matrix is inherited from the relatively larger domains. However, deformation via diffusion accommodated grain-boundary sliding is generally expected to randomize CPO (Casey & Mcgrew, 1999; Wenk & Christie, 1991). Therefore, we suggest that minor dislocation glide is co-active, resulting in the development of a weak CPO which concurs with the presence of uncommon low-angle boundaries in the fine domains of all samples (**Figure 4.3c, h; 4.4c**). The evolution of a CPO during dislocation accommodated grain boundary sliding has previously been observed in calcite marbles and has been shown to be an important strain accommodating mechanism at greenschist facies conditions (Bestmann et al., 2000; Rogowitz et al., 2016). A small component of dislocation creep activity concurs with the uncommon low-angle boundaries that can be observed in the finer sized

grain fractions in all dolomitic samples. The reduction in recrystallized grain size of the structurally highest dolomitic samples (17MC053, 17MC017) is reasoned to be due to increasing stress as temperature decreased and the shear zone narrowed.

4.5.2 Deformation of the Middle Unit - calcite

The calcitic mylonite of the Middle Unit of Hymittos exhibits a decrease in grain sizes and increase in brittle deformation indicators at higher structural levels (e.g., 17MC040 that overlies 17MC073). Extensional shear zones are known to narrow as they cool (Aravadinou & Xypolias, 2017; Parsons et al., 2018). Given the subhorizontal foliation related to the detachment, structurally deeper samples would have been closer to the margins of the shear zones and may preserve microstructures reflecting relatively higher temperatures of deformation. Sample 17MC073 is structurally lower than 17MC040 and is characterized by a greater proportion of coarse grains, a significant number of low-angle boundaries, well developed subgrains and bulges at the margins of coarse domains; together indicative of dislocation creep activity (Kerrich & Allison, 1978; Rutter & Casey, 1994; Schmid et al., 1987). Misoriented boundaries in the calcite matrix suggest that both grain size reduction of coarse domains and deformation of the recrystallized matrix was accommodated by dislocation creep. The pattern of pole figures (**Figure 4.7**), in particular the foliation normal *c*-axis maxima, is associated with slip on the basal plane, and alignment of *a*-axes as girdles or lineation parallel maxima are associated with $<2\bar{1}\bar{1}0>$ as the principal slip direction (Vauchez et al., 2015).

Structurally higher samples (e.g., 17MC040) exhibit fewer low-angle boundaries, and less internal misorientation and a somewhat weaker CPO fabric than sample 17MC073. In combination with the observed SPO in the matrix this likely indicates a component of grain-size sensitive grain-boundary sliding accommodating deformation of the finer domains, though the distinct CPO

indicates that dislocation creep is still accommodating much of deformation within the calcitic fine domains (**Figure 4.6e**).

The presence of ~120° triple junctions and polygonal grains in sample 17MC040 (**Figure 4.6c**), may indicate that some portions of the upper detachment experienced significant annealing and grain-boundary area reduction, which may erase dislocations within the fine domains while still retaining the CPO strength (Ohl et al., 2021). This fabric is only well developed in 17MC040, whereas calcitic mylonites from deeper structural levels of the Middle Unit and dolomitic mylonites of the Lower Unit do not exhibit evidence of pervasive annealing. Some samples (e.g., 17MC040; 17MC058) exhibit an apparent twin orientation on the misorientation histograms (**Figure 4.6d; 4.7j**), but show little evidence of twins in the EBSD map (**Figure 4.6c; 4.6j**), which may be explained by recrystallization of twin domains, in such instances adjacent grains could represent former domains of a larger twinned crystal (Bestmann & Prior, 2003).

Brittle deformation of the mylonitic fabric (**Figure 4.6a**), abundant calcite veins (some serving as shear sense indicators; **Figure 4.7h**) and stylolites (**Figure 4.7a**) taken together indicate the deformation of the calcitic mylonites continued at relatively low temperatures and that multiple episodes of dissolution and vein precipitation occurred during deformation along the upper detachment. Clear evidence of dissolution-precipitation and sheared veins (**Figure 4.6a, i**) may indicate that grain size sensitive creep was partly accommodated by dissolution-precipitation processes.

4.5.3 Low temperature deformation of dolomite and calcite

Within the calcite dominated Middle Unit, fine grained dolomite is brittlely deformed (**Figure 4.6a, b**), dolomite blocks within calcite marble are boudinaged (**Figure 4.2b**), exhibit minimal internal deformation (**Figure 4.2c**) and preserve primary features such as fossils

(Coleman et al., 2020). Based on the field evidence, within the Middle Unit of Hymittos, mylonitic deformation related to the upper detachment was dominantly accommodated within the calcitic marble, whereas in the Lower Unit mylonitic deformation associated with the lower detachment was accommodated predominantly within the dolomitic marble. Schistose lithotypes within the Middle and Lower units also accommodated detachment related strain, as discussed in Coleman et al (2020). The Lower Unit of Hymittos exposes both calcitic and dolomitic mylonites, the dolomitic mylonite are structurally positioned in the immediate footwall to the lower detachment (**Figure 4.2d, f, g**) suggesting they preferentially localized strain relative to calcite during the latest stages of ductile deformation. This observation is contrary to experimental investigations (Davis et al., 2008; Handin & Hager, 1958; Holyoke et al., 2013, 2014; Kushnir et al., 2015) and natural examples (Bestmann et al., 2000; Woodward et al., 1988) suggesting that calcite is the weaker phase at lower greenschist to subgreenschist facies conditions. In the following paragraphs we will expand on how dolomite accommodated low temperature strain.

Experimentally derived flow laws suggest that dislocation creep of dolomite requires high differential stress and is generally limited to high temperatures (>600°C for 100 μm diameter grains; **Figure 4.8**; Davis et al., 2008). Most natural examples of dislocation creep of dolomite have been observed at deformation temperatures >400°C (Berger et al., 2016; Nania, 2021; Parsons et al., 2016). Yet at lower temperatures (i.e., sub- to lower greenschist facies), the dolomitic marble of the Lower Unit hosts a major shear zone that evinces dislocation creep in the coarsest grain fraction (**Figure 4.3f, c**).

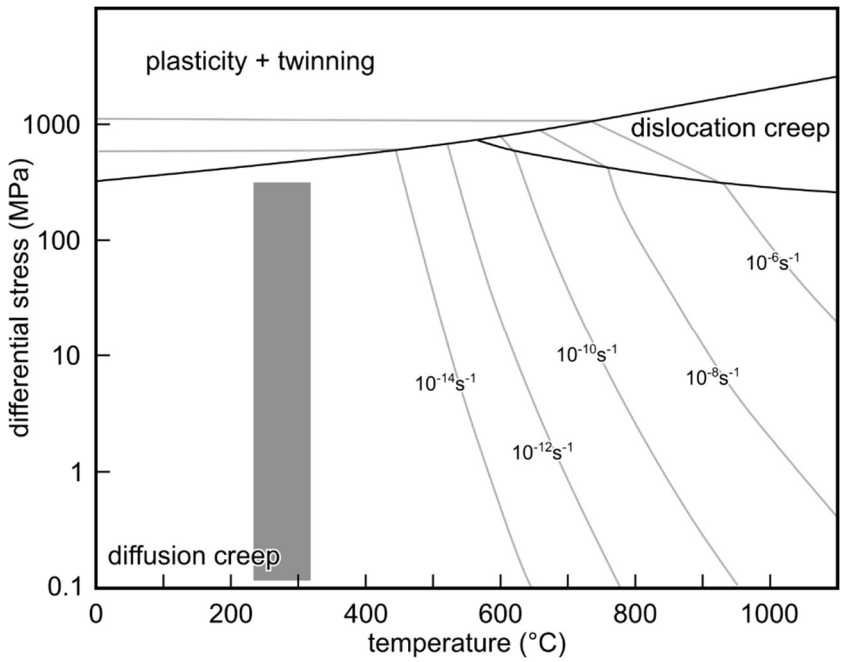

Figure 4.8. Deformation mechanism map for a 100 μm dolomite crystal in log(differential stress)-temperature space produced by integrating flow laws from Davis et al. (2008) and Delle Piane et al. (2008). Inferred temperatures of deformation based on metamorphic assemblages, white mica $^{40}Ar/^{39}Ar$ and zircon (U-Th)/He geochronology (Coleman et al., 2020). Grey box is the estimated temperature range under which these samples deformed, given for a wide range of differential stress.

Deformation experiments of polycrystalline dolomite (at 400-1000°C) record grain size reduction via dislocation creep at peak stresses followed by diffusion creep of original or recrystallized fine-grained material (Davis et al., 2008; Holyoke et al., 2014). The progression of deformation mechanisms agrees with that observed in our study except that the temperature of deformation in the natural samples is much lower. The temperatures of deformation determined for the lower detachment suggest that the samples should be deforming solely by diffusion creep at such low temperatures, yet the microstructures in the intermediate and coarse domains suggest clear evidence of dislocation creep. A study reporting on the experimental deformation of dry dolomite aggregates found an inversion in the activation energy of dislocation creep (145 kJ/mol) and diffusion creep (280 kJ/mol), which is unusual for most carbonate minerals, and suggests that dislocation creep may be favoured over diffusion creep at low temperatures or higher differential

stress (Holyoke et al., 2013). This finding was supported by the natural examples of Wells et al. (2019) which examined a pair of dolomitic shear zones and found that dislocation creep was favoured over diffusion creep at 240°C for fine grained dolomite whereas coarser grained dolomite deformed by mixed dislocation and diffusion creep. The microstructures herein suggest that dislocation creep is more active in the coarser grained dolomite fractions, and diffusion creep becomes more dominant at finer grain sizes and possibly lower temperatures though a small component of dislocation creep was still active. This is more in accordance with other experimental studies of dolomite that did not note the activation energy inversion (**Figure 4.8**; Davis et al., 2008; Delle Piane et al., 2008).

The Ca-Mg crystallographic layering of dolomite provides a more ordered lattice structure than calcite and magnesite; this has the effect of limiting grain-growth processes and strain-induced grain boundary migration (Davis et al., 2011). As such under most conditions dolomite is more susceptible to grain-size reduction than other carbonate minerals (Davis et al., 2008; Holyoke et al., 2014) and multiple deformation events may lead to significant grain-size contrast between calcitic and dolomitic marble thereby producing a change in rock strength (Rutter & Brodie, 1988). Davis et al. (2008) proposed that fine-grained dolomite that has deformed by diffusion creep will have low rheological contrast compared to calcite, which is clearly observed in field evidence from the Lower Unit, but not the Middle Unit of this study (**Figure 4.2b, c**). Prior to Oligo-Miocene extension, the bedrock of Hymittos was subjected to Eocene subduction and significant deformation under blueschist facies conditions (Baziotis et al., 2020; Coleman et al., 2020). Dolomite is comparatively weak when deformed under high pressure and more resistant to grain growth and recovery processes during and after deformation (Davis et al., 2008, 2011) which provides the opportunity to develop grain-size contrasts between the dolomitic and calcitic marbles

even if their protoliths were similarly coarse. Whether the fine-grained dolomitic marble herein possessed an original fine primary grain size, was recrystallized to finer grain sizes during deformation under blueschist facies metamorphic conditions or is the product of some combination of both is not consequential as the coarse-grained dolomite veins in several samples clearly recrystallized to finer grain sizes during deformation along the lower detachment (**Figure 4.3a, f, g**). The dolomitic mylonite of this study exhibits notably smaller grain sizes than calcitic mylonite from similar and structurally higher levels of the massif, and calcitic samples exhibit clear evidence for annealing and grain growth including the common triple junctions and polygonal grains in 17MC040, similar microstructures are not obvious in the dolomitic samples (Coleman et al., 2020). As a result of the grain size differences, yet potentially similar material strengths between calcite and dolomite, it stands to reason that during greenschist facies extensional thinning the finer-grained dolomite would have preferentially accommodated deformation as it would have been more susceptible to grain-size sensitive deformation processes (e.g. diffusion creep). This grain size and strength contrast would have been amplified by episodic deformation providing opportunities for coarsening of calcite relative to dolomite.

4.5.5 Implications

Dolomite can form in a number of different fashions including primary precipitation from evaporitic brines in lagoons (Clayton et al., 1968; Vasconcelos et al., 1995), authigenic alteration of calcite by seawater (Adams & Rhodes, 1960), and postdiagenetic replacement of carbonate minerals by fluids (Burns et al., 2000). Consequently, dolomite within the crust reflects a variety of potential sources, but is generally found in carbonate dominated terranes and as layers in sedimentary and metasedimentary sequences. Within the upper crust dolomite has been associated with the localization of brittle deformation as faults and significant seismicity (Doglioni, 1987;

Fondriest et al., 2012). The variability of dolomite and calcite microstructures reported herein reflect the control of the samples mechanical properties by the spatial distribution of strong and weak elements, specifically strong coarse grains hosted in weak fine grained matrix (Rutter & Brodie, 1988; Warren & Hirth, 2006). The unusual weakness of dolomite at lower greenschist to subgreenschist facies conditions has important implications for the understanding of crustal strength. In metasedimentary sequences, calcitic marble has been invoked as a lubricating layer that can accommodate significant shear strain within the middle and upper crust (Brodie & Rutter, 2000; Ulrich et al., 2002). If polydeformed dolomitic marble deformed under these same conditions is capable of accommodating major plastic strain due to grain-size sensitive deformation (diffusion creep), they may serve a similar purpose to conventionally weaker carbonate layers (Brodie & Rutter, 2000). Thus significant ductile deformation may be currently unrecognized in the upper and middle crust where conventionally dolomite would be expected to deform brittlely, or be rheologically strong and accommodate very limited ductile deformation.

4.6 Conclusion

Microstructural analyses of low-temperature, naturally deformed calcite and dolomite from a paired detachment system indicate dolomitic marble preferentially localized and accommodated strain along the lower detachment despite the presence of calcitic marble at a similar structural level. The coarser dolomite grains deformed via dislocation creep leading to subgrain rotation and grain size reduction. Deformation in finer dolomitic domains (<50 μm) was dominantly accommodated by grain boundary sliding facilitated by diffusion creep with a minor component of dislocation creep activity. Coarse and fine calcite mylonite of the upper detachment deformed by dislocation creep, though at finer grain sizes dislocation creep was balanced with grain boundary sliding. This study builds upon rare reports of low-temperature plastic deformation of

dolomite and highlights the importance of grain size sensitive and insensitive deformation mechanisms and the potential for strength inversion when recovery processes are hindered and grain-size contrasts develop. Importantly, under some natural conditions, dolomite appears to be anomalously weak and capable of accommodating significant displacement even in the presence of conventionally weaker lithotypes. The potential weakness of dolomite, a major rock forming mineral has significant implications for low-temperature strain localization in metasedimentary sequences of the middle and upper crust.

4.7 Acknowledgements

Funding was provided by the Natural Sciences and Engineering Research Council of Canada (to David Schneider), the Austrian Academy of Sciences (Emil Suess-Erbschaft) and the Austrian Science Foundation (Project Number I 5399-N, to Bernhard Grasemann and Anna Rogowitz). We thank the Greek Institute for Mining and Exploration in Athens for providing permission for fieldwork and technical support. Gerlinde Habler (University of Vienna) and Sudip Shrestha (University of British Columbia) assisted with EBSD analyses and Glenn Poirier (University of Ottawa) with SEM analysis; their contributions are greatly valued.

Chapter 5: Conclusions

The Cyclades are an ideal laboratory for research into detachment faulting and core complex development owing to the recent fault activity, extensive published data and good bedrock exposure. Recent advances in understanding detachment evolution have focused on the timing of the activity of different fault branches and discrete deformation events, the conditions under which displacement was accommodated, and the mechanisms driving strain (re)localization (Beaudoin et al., 2015; Bessiere et al., 2018; Heineke et al., 2019; Laurent et al., 2015; Rabillard et al., 2018; Rohrmeier et al., 2013). My thesis integrated multiple geochronometers (white mica $^{40}Ar/^{39}Ar$, and zircon (U-Th)/He and U-Pb analyses), (micro)structural analysis including EBSD, thin section petrography, and mineral chemistry to elucidate the macro- to grain-scale geologic evolution of Mt. Hymittos and its detachment faults, positioned at a critical tectonic boundary between two of the Hellenides. This thesis demonstrated that the bedrock of central Attica should be correlated to the Attic-Cycladic Complex and that the detachment faults of Hymittos are extensions of the West Cycladic Detachment System (WCDS).

5.1 Architecture, timing and conditions of detachment faulting on Hymittos

The zircon (U-Th)/He (ZHe) and white mica $^{40}Ar/^{39}Ar$ (MAr) analyses presented herein (Chapter 2) significantly improve the suite of geochronologic data of central Attica. Previous published analyses were limited to the Lavrion district in southeastern Attica (Berger et al., 2013; Coleman et al., 2019; Liati et al., 2009, 2013; Seman et al., 2017). These analyses are the first to examine the lower temperature evolution of the central part of the peninsula and demonstrate a clear relationship between the timing of metamorphism and detachment faulting within the Western Cyclades (Cossette et al., 2015; Grasemann et al., 2012; Tschegg & Grasemann, 2009) and the Greek mainland (Coleman et al., 2020).

Structural analysis and ZHe and MAr data presented in Chapter two indicate that the detachment faults of Hymittos accommodated the same crustal extension as the faults of Lavrion (Coleman et al., 2019) and are extension of the WCDS. Deformation-induced resetting of MAr and ZHe cooling ages demonstrate that the detachments of Hymittos were active from the Oligo-Miocene (~23.5 Ma) through to the Late Miocene (~9 Ma) with both detachments being co-active during the mid-Miocene (**Figure 2.8**). These ages are strikingly similar to results for the timing of activity of the detachment faults of Lavrion explored further in Chapter two (Coleman et al., 2019). The youngest MAr deformation ages overlap with the ZHe cooling ages indicating that white mica systematics were resetting at remarkably low temperatures, likely sub-greenschist facies; this has implications for dating shear zones hosted in significantly deformed mica schists (**Figure 2.8**). The minimum age range of activity for the faults (>10 Myr) and position at the end of the detachment system suggest that the detachment system did not propagate laterally significantly following the onset of faulting. The observation that the WCDS terminates as a vertically oriented horsetail-like splay of faults is similar to proposed models for new detachment fault propagation during core complex uplift, which has rarely been observed in the field (Lister & Davis, 1989). In contrast to these previously proposed models, ZHe and MAr geochronology demonstrate that the detachment faults of Hymittos young structurally downwards, with the most recent deformation recorded on the structurally deepest fault. The identification of km-scale boudinage of the major carbonate packages of Hymittos as a process driving detachment localization concurs with previous propositions that this process is a major driver of strain localization in extending terranes (Gartrell, 1997; Lacassin, 1988).

As mentioned above, ZHe and MAr data indicate that the lower detachment of Hymittos was deforming ductilely very close to the closure temperature of the ZHe system (**Figure 2.8**). Chapter

four examined dolomite marbles that accommodated some of this deformation. The marble are variably mylonitic to ultramylonitic with limited evidence for brittle deformation outside of the fault plane (**Figure 2.4**). The mylonitic fabric formed by accommodating low-temperature deformation of dolomite via grain-boundary sliding, enhanced by diffusion creep (*sensu lato*) and creep cavitation processes. The apparent weakness of the dolomite was due to the fine grain sizes a result of dislocation creep and subgrain rotation (**Figure 4.3; 4.4**). This weakness likely developed over multiple episodes of deformation events due to the comparative limitations on grain growth processes that dolomite exhibits as a result of its more ordered crystal structure relative to calcite (Davis et al., 2008; Kushnir et al., 2015). These natural observations conflict with the results predicted by forward modelling of deformation experiments on natural and synthetic dolomite and dolomite-calcite aggregates (Davis et al., 2008, 2011; Holyoke et al., 2013, 2014; Kushnir et al., 2015). The novel observation that dolomite at low temperatures can be weaker than calcite and accommodate major displacement has exciting implications for deformation localization in carbonate hosting terranes and the understanding of crustal strength.

5.2 Mica chemical composition and its relationship to $^{40}Ar/^{39}Ar$ ages

Microprobe analysis of white mica from the metamorphic basement of Hymittos identified a range of chemical compositions ranging from phengitic to muscovitic often within the same crystal (**Figure 2.7; S2.1**). Many schistose samples that exhibit a range of mica compositions record tightly constrained $^{40}Ar/^{39}Ar$ total fusion deformation ages (e.g. HY32, HY33; **Figure 2.7; 2.8**). Thus, at least in these samples it appears that deformation-induced resetting did not fully reequilibrate white mica crystals chemical compositions while still resetting $^{40}Ar/^{39}Ar$ systematics. Similar trends can be observed in marble samples that record thermal-induced resetting (e.g.

HY09, HY10; **Figure 2.7; 2.8**). It may be that chemical composition and the $^{40}Ar/^{39}Ar$ system are at least somewhat decoupled for samples from the metamorphic basement of Mt. Hymittos.

5.3 Provenance of the Cycladic Blueschist Unit and its reorganization by structural displacement

Prior to this thesis, the provenance of the bedrock of Mt. Hymittos was uncertain. Chapter three applied detrital zircon U-Pb geochronology to interrogate this disagreement. Previous authors suggested the crystalline rocks of Mt. Hymittos are extensions of the Attic-Cycladic Complex (Diamantopoulos et al., 2009a; Krohe et al., 2010), others infer these rocks to be exposures of the Gavrovo-Tripolitza Unit (Ring et al., 2010), or the Cycladic Basal Unit (Baziotis et al., 2009; Baziotis & Mposkos, 2011; Liati et al., 2013). Detrital zircon samples from the massif demonstrate that the Middle and Lower Units of Hymittos are exposures of the Lower Cycladic Blueschist Nappe and support the correlation of the Upper (Alepovouni) Unit to the Pelagonian Zone based on comparison with detrital zircon samples from Ios, Sikinos, Santorini, Serifos, Kea, Kythnos and Lavrion as well as unmetamorphosed Pelagonian Zone samples from the island of Chios (Meinhold et al., 2008). The CBU's paleogeographic equivalent has been disputed, as one of the Pelagonian Zone (Chatzaras et al., 2013, 2016), the Pindos Zone (Dürr et al., 1978), or the Vardar Zone (Zlatkin et al., 2018). Late Cretaceous detrital zircon from the basement of Mt. Hymittos support the hypothesis that Hymittos and the CBU cannot be correlated to the Vardar Zone, as the Vardar Ocean closed during the Early to Middle Cretaceous (Clift, 1996; Meinhold et al., 2010; Robertson & Dixon, 1984; Scherreiks et al., 2014). Furthermore, the Pelagonian Zone is a microcontinent and contains only small-scale basins, whereas the proto-CBU basin was large enough in size to have begun forming incipient oceanic crust (Kotowski et al., 2021). Thus, the most suitable paleogeographic correlation for the CBU is the Pindos Zone of the Hellenides. This

conclusion best fits the paleogeographic position of the CBU (**Figure 3.1**), the limited sedimentary evidence that can be derived from the metasedimentary sequence and the well understood south-directed synorogenic exhumation of the CBU within a ~north dipping subduction channel (Baziotis et al., 2020; Kotowski et al., 2021; Kotowski & Behr, 2019; Scheffer et al., 2016; Uunk et al., 2022).

5.4 Future work

This study provides insight into the timing of deformation along different branches of the WCDS using the ZHe and MAr geochronometers. Previous studies have produced similar datasets (including limited apatite (U-Th)/He - AHe) from the islands of Kea, Kythnos, Serifos, and the Lavrion district of southeast Attica (Berger et al., 2013; Coleman et al., 2019; Grasemann et al., 2012; Iglseder et al., 2011). Coleman et al. (2019) examined the timing of deformation for different detachments along the strike of the WCDS, this was expanded by Chapter two of this thesis. ZHe thermochronology has previously been mostly interpreted based on the concept of closure temperature (Dodson, 1973) wherein specific chronometers record cooling of a mineral below a temperature specific to that mineral-isotope system (i.e. ~180° for ZHe). Many terranes do not meet the assumptions required for applying this model. Newer models better account for the effects of diffusion, radiation damage and annealing (Guenthner et al., 2013). Time-temperature inverse models for the zircon and apatite (U-Th)/He system are often produced to provide insight into sample history in structurally complex terranes (Ehlers et al., 2005; Ketcham, 2005). Given the pre-existing ZHe and AHe data, thermal models from the hanging wall and footwall of each of the detachment branches might provide interesting insights into the evolution of the WCDS as a composite structure. If other detachments young with depth for the ~200-80°C range then HeFTy ZHe and AHe thermal models may produce time-temperature paths that give insight into the

activity of different fault branches (Ketcham, 2005; Ketcham & Brichau, 2008). Furthermore, QTQt provides tools for incorporating MAr analyses, though the kinetic variables governing diffusion of Ar in white mica are less well constrained than for the ZHe and AHe systems (Gallagher, 2012). Inverse modelling has been conducted on the upper and lower plate of Mt. Hymittos (**Figure 5.1**) and concluded that (U-Th)/He systematics in zircon sampled from the Upper Unit of Hymittos were fully reset during Cretaceous metamorphism of the Pelagonian Zone (Porkolab et al., 2019; Schenker et al., 2015). Cretaceous to Paleocene exhumation paths indicate the zircon grains were below 100°C at 55 Myr (resident in the upper crust), suggesting the upper plate samples were not meaningfully impacted by Eocene metamorphism during accretion of the lower plate (CBU). Comparison between zircon effective uranium, effective spherical radius, U-Pb dates and (U-Th)/He dates suggest that in samples from the Upper Unit, zircon populations have dissimilar diffusion kinetics likely as a result of incomplete annealing of radiation damage in Proterozoic zircon grains. Expanding these analyses to the entire WCDS would build an invaluable time-temperature model for detachment evolution.

SEM-CL images of zircon characterized in Chapter three exhibited thin CL-white rims interpreted as metamorphic overgrowths (**Figure S3.1, S3.2**). These overgrowths were too thin to be dated via conventional LA-ICP-MS techniques. Similar metamorphic overgrowths were identified on Serifos and yielded c. 40 Ma dates when analyzed via U-Pb SIMS depth profiling (Schneider et al., 2011). The ages reported by Schneider et al. (2011) were the first evidence for metamorphic zircon growth under blueschist facies conditions in the Cyclades. Serifos is located at the opposite end of the WCDS from Hymittos (**Figure 2.1**) and exhibits less of the greenschist facies overprint that obliterates most of the evidence for blueschist facies metamorphism on Hymittos. LA-ICP-MS U-Pb dating of metamorphic overgrowths on zircon collected from the

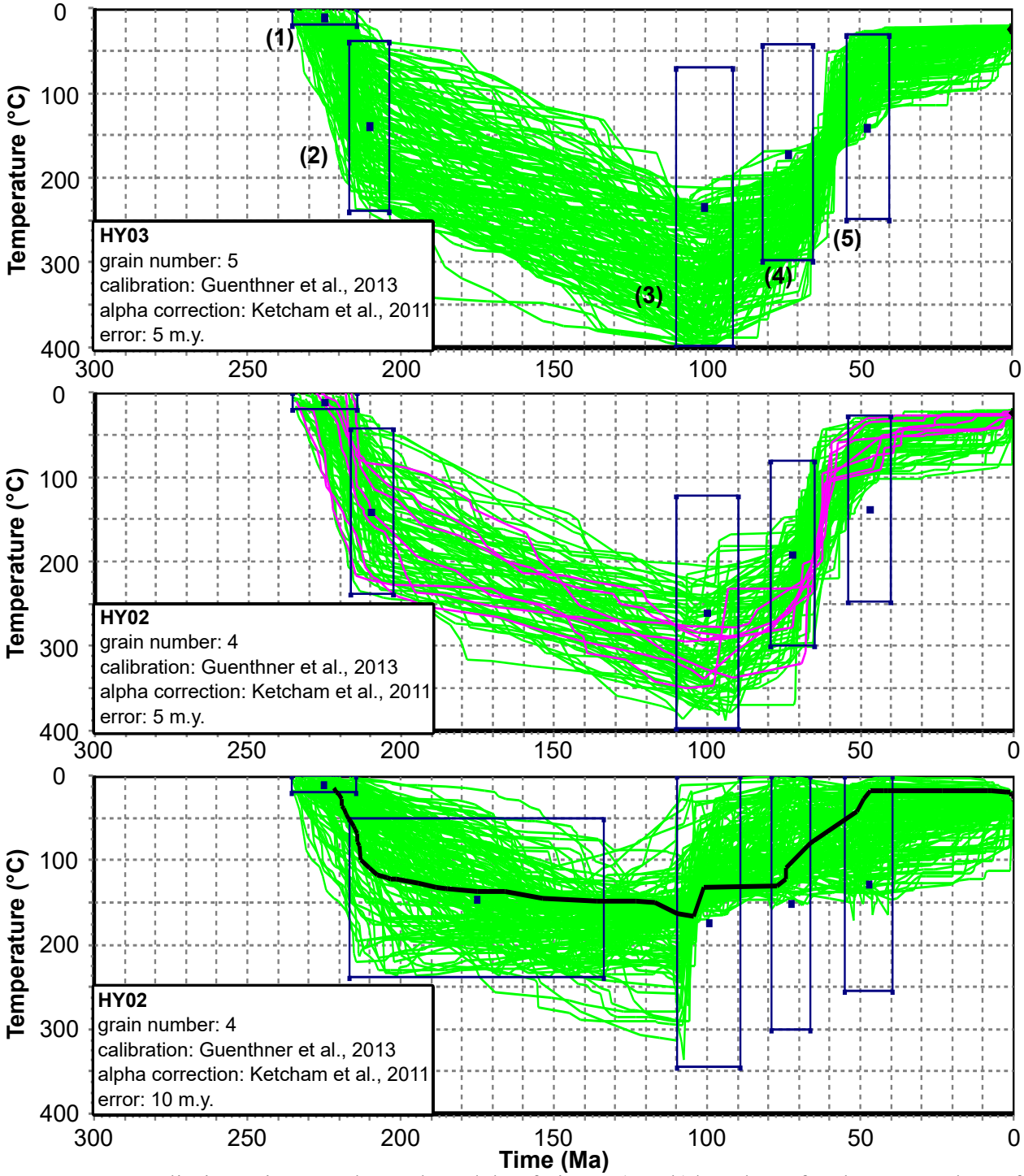

Figure 5.1. Preliminary inverse thermal models of zircon (U-Th)/He dates for the upper plate of Mt. Hymittos. Produced in HeFTy (Ketcham, 2005). The blue boxes represent temperature-time constraints. The leftmost two constraints (1, 2) reflect slow burial as a sedimentary sequence. The rightmost three constraints reflect: (3) mid Cretaceous high-pressure metamorphism recognized sparsely within the Pelagonian Zone (Lips et al., 1998; Schermer et al., 1990); (4) Regional greenschist to amphibolite facies metamorphism (Altherr et al., 1994); (5) Eocene high-pressure metamorphism related to accretion of the lower plate to the upper plate (Baziotis et al., 2020). Green paths represent possible time-temperature paths in the model (goodness of fit > 0.05), purple paths represent paths of best fit (goodness of fit >0.5).

hanging wall and footwall of the Santorini Detachment System produced dates of 29-28 Ma (Chapter three), the absence of 40 Ma dates and evidence for a younger event of zircon growth suggests that the conditions and/or timing of metamorphism on Santorini and Serifos were different. Considering this, depth profiling on the thin metamorphic overgrowths on zircon derived from the basement of Hymittos would provide valuable data to interpret the metamorphic history of the massif and the central peninsula as much of the evidence for the pre-greenschist history has been obscured by re-equilibration and post-orogenic deformation.

References

Abers, G. (2009). Slip on shallow-dipping normal faults. *Geology*, *37*(8), 767–768.

Adams, J. E., & Rhodes, M. L. (1960). Dolomitization by seepage refluion. *AAPG Bulletin*, *44*(12), 1912–1920.

Altherr, R., Schliestedt, M., Okrusch, M., Seidel, E., Kreuzer, H., Harre, W., et al. (1979). Geochronology of high-pressure rocks on Sifnos (Cyclades, Greece). *Contributions to Mineralogy and Petrology*, *70*, 245–255.

Altherr, R., Kreuzer, H., Wendt, I., Lenz, H., Wagner, G., Keller, J., et al. (1982). A late Oligocene/early Miocene high temperature belt in the Attic-Cycladic Crystalline Complex (SE Pelagonian, Greece). *Geologisches Jahrbuch*, *23*, 97–164.

Altherr, R., Kreuzer, H., Lenz, H., Wendt, I., Harre, W., & Dürr, S. (1994). Further evidence for a Late Cretaceous low-pressure/high-temperature terrane in the Cyclades, Greece. *Chemie Der Erde*, *54*, 319–328.

Anders, B., Reischmann, T., Poller, U., & Kostopoulos, D. (2005). Age and origin of granitic rocks of the eastern Vardar Zone, Greece: New constraints on the evolution of the Internal Hellenides. *Journal of the Geological Society*, *162*(5), 857–870.

Anders, B., Reischmann, T., Kostopoulos, D., & Poller, U. (2006). The oldest rocks of Greece: First evidence for a Precambrian terrane within the Pelagonian Zone. *Geological Magazine*, *143*(1), 41–58. https://doi.org/10.1017/S0016756805001111

Anders, B., Reischmann, T., & Kostopoulos, D. (2007). Zircon geochronology of basement rocks from the Pelagonian Zone, Greece: Constraints on the pre-Alpine evolution of the westernmost Internal Hellenides. *International Journal of Earth Sciences*, *96*(4), 639–661. https://doi.org/10.1007/s00531-006-0121-7

Aravadinou, E., & Xypolias, P. (2017). Evolution of a passive crustal-scale detachment (Syros, Aegean region): Insights from structural and petrofabric analyses in the hanging-wall. *Journal of Structural Geology*, *103*, 57–74. https://doi.org/10.1016/j.jsg.2017.09.008

Aravadinou, E., Xypolias, P., & Chatzaras, V. (2016). Ductile nappe stacking and refolding in the Cycladic Blueschist Unit: Insights from Sifnos Island (south Aegean Sea). *International Journal of Earth Sciences*, *105*(7), 2075–2096. https://doi.org/10.1007/s00531-015-1255-2

Auboin, J. (1959). Contribution à l'étude géologique de la Grèce septentrionale: Les confins de l'Epire et de la Thessalie. *Annales Géologiques Des Pays Helléniques*, *10*, 525.

Augier, R., Agard, P., Monié, P., Jolivet, L., Robin, C., & Booth-Rea, G. (2005). Exhumation, doming and slab retreat in the Betic Cordillera (SE Spain): in situ 40Ar/39Ar ages and P–T–d–t paths for the Nevado-Filabride complex. *Journal of Metamorphic Geology*, *23*, 357–381. https://doi.org/10.1111/j.1525-1314.2005.00581.x

Augier, R., Jolivet, L., Gadenne, L., Lagfid, A., Driussi, O., Lahfid, A., & Driussi, O. (2015). Exhumation kinematics of the Cycladic Blueschists unit and back-arc extension, insight from the Southern Cyclades (Sikinos and Folegandros Islands, Greece). *Tectonics*, *34*, 152–185. https://doi.org/10.1002/2014TC003664

Avigad, D., Kolodner, K., McWilliams, M., Persing, H., & Weissbrod, T. (2003). Origin of northern Gondwana Cambrian sandstone revealed by detrital zircon SHRIMP dating. *Geology*, *31*(3), 227–

230. https://doi.org/10.1130/0091-7613(2003)031<0227:OONGCS>2.0.CO;2

Axen, G. J. (2004). Mechanics of low-angle normal faults. In G. Karner, J. D. Morris, N. W. Driscoll, & E. A. Silver (Eds.), *Rheology and deformation of the lithosphere at continental margins*. New York: Columbia University Press.

Axen, G. J. (2007). Significance of large-displacement, low-angle normal faults. *Geology*, *35*(3), 287–288.

Bachmann, F., Hielscher, R., & Schaeben, H. (2010). Texture analysis with MTEX – free and open source software toolbox. *Solid State Phenomena*, *160*, 63–68.

Bachmann, F., Hielscher, R., & Schaeben, H. (2011). Grain detection from 2d and 3d EBSD data-Specification of the MTEX algorithm. *Ultramicroscopy*, *111*(12), 1720–1733. Retrieved from http://dx.doi.org/10.1016/j.ultramic.2011.08.002

Bailey, L. R., Schenker, F. L., Fellin, M. G., Cobianchi, M., & Adatte, T. (2020). Birth and closure of the Kallipetra Basin: Late Cretaceous reworking of the Jurassic Pelagonian – Axios/Vardar contact (northern Greece), 2463–2485.

Bakowsky, C., Schneider, D. A., Grasemann, B., & Soukis, K. (2023). Miocene ductile thinning below the Folegandros Detachment System, Cyclades, Greece. *Terra Nova*, 1–10.

Baltatzis, E. (1996). Blueschist-to-greenschist transition and the P-T path of prasinites from the Lavrion area, Greece. *Mineralogical Magazine*, *60*, 551–561.

Barber, D. J., & Wenk, H.-R. (1979). Deformation twinning in calcite, dolomite, and other rhombohedral carbonates. *Physics and Chemistry of Minerals*, *165*, 141–165.

Barber, D. J., & Wenk, H.-R. (2001). Slip and dislocation behaviour in dolomite. *European Journal of Mineralogy*, *13*, 221–243. https://doi.org/10.1127/0935-1221/01/0013-0221

Barber, D. J., Heard, H. C., & Wenk, H. R. (1981). Deformation of dolomite single crystals from 20-800° C. *Physics and Chemistry of Minerals*, *7*, 271–286.

Bargnesi, E. A., Stockli, D. F., Mancktelow, N., & Soukis, K. (2013). Miocene core complex development and coeval supradetachment basin evolution of Paros, Greece, insights from (U–Th)/He thermochronometry. *Tectonophysics*, *595–596*, 165–182. https://doi.org/10.1016/j.tecto.2012.07.015

Bauer, H., Rogowitz, A., Grasemann, B., & Decker, K. (2018). Intracrystalline deformation of calcite in the upper brittle crust. *Geology*, *46*(4), 375–378. https://doi.org/10.1130/G39990.1

Baziotis, I., & Mposkos, E. (2011). Origin of metabasites from upper tectonic unit of the Lavrion area (SE Attica, Greece): Geochemical implications for dual origin with distinct provenance of blueschist and greenschist's protoliths. *Lithos*, *126*, 161–173. https://doi.org/10.1016/j.lithos.2011.07.014

Baziotis, I., Proyer, A., & Mposkos, E. (2009). High-pressure/low-temperature metamorphism of basalts in Lavrion (Greece): Implications for the preservation of peak metamorphic assemblages in blueschists and greenschists. *European Journal of Mineralogy*, *21*(1), 133–148. https://doi.org/10.1127/0935-1221/2008/0020-1853

Baziotis, I., Proyer, A., Mposkos, E., Windley F., B., & Boukouvala, I. (2019). Exhumation of the high-pressure northwestern Cyclades, Aegean: New P-T constraints, and geodynamic evolution. *Lithos*, *324–325*, 439–453. https://doi.org/10.1016/j.lithos.2018.11.027

Baziotis, I., Evripides, M., Windley, B. F., & Lamont, T. N. (2020). Exhumation of Attica high-pressure

rocks in a subduction channel: New metamorphic PT constraints from Attica, NW Cyclades, Greece. *Lithos*, *354–355*, 1–9. https://doi.org/10.1016/j.lithos.2019.105266

Beaudoin, A., Augier, R., Laurent, V., Jolivet, L., Lahfid, A., Bosse, V., et al. (2015). The Ikaria high-temperature metamorphic core complex (Cyclades, Greece): Geometry, kinematics and thermal structure. *Journal of Geodynamics*, *92*, 18–41. https://doi.org/10.1016/j.jog.2015.09.004

Berger, A., Schneider, D. A., Grasemann, B., & Stockli, D. (2013). Footwall mineralization during Late Miocene extension along the West Cycladic Detachment System, Lavrion, Greece. *Terra Nova*, *25*(3), 181–191. https://doi.org/10.1111/ter.12016

Berger, A., Ebert, A., Ramseyer, K., Gnos, E., & Decrouez, D. (2016). Dolomite microstructures between 390° and 700 °C: Indications for deformation mechanisms and grain size evolution. *Journal of Structural Geology*, *89*, 144–152. https://doi.org/10.1016/j.jsg.2016.06.001

Bessiere, E., Rabillard, A., Précigout, J., Arbaret, L., Jolivet, L., Augier, R., et al. (2018). Strain localization within a syntectonic intrusion in a back-arc extensional context: The Naxos monzogranite (Greece). *Tectonics*, *37*(2), 558–587. https://doi.org/10.1002/2017TC004801

Bestmann, M., & Prior, D. J. (2003). Intragranular dynamic recrystallization in naturally deformed calcite marble: diffusion accommodated grain boundary sliding as a result of subgrain rotation recrystallization. *Journal of Structural Geology*, *25*, 1597–1613. https://doi.org/10.1016/S0191-8141(03)00006-3

Bestmann, M., Kunze, K., & Matthews, A. (2000). Evolution of a calcite marble shear zone complex on Thassos Island, Greece: microstructural and textural fabrics and their kinematic significance. *Journal of Structural Geology*, *22*, 1789–1807.

Bonneau, M. (1984). Correlation of the Hellenide nappes in the south-east Aegean and their tectonic reconstruction. *Geological Society Special Publication*, *17*, 517–527.

Bonneau, M., & Kienast, J. R. (1982). Subduction, collision et schistes bleus: exemple de l'Egée, Grece. *Bulletin de La Société Géologique de France*, *4*, 785–791.

Braathen, A., Nordgulen, O., Osmundsen, P., Andersen, T., Solli, A., & Roberts, D. (2000). Devonian, orogen-parallel, opposed extension in the Central Norwegian Caledonides. *Geology*, *28*(7), 615–618.

Brichau, S., Thomson, S., & Ring, U. (2010). Thermochronometric constraints on the tectonic evolution of the Serifos detachment, Aegean Sea, Greece. *International Journal of Earth Sciences*, *99*(2), 379–393. https://doi.org/10.1007/s00531-008-0386-0

Bröcker, M. (1990). Blueschist-to-greenschist transition in metabasites from Tinos Island, Cyclades, Greece: Compositional control or fluid infiltration? *Lithos*, *25*, 25–39.

Bröcker, M., & Franz, L. (1998). Rb-Sr isotope studies on Tinos Island (Cyclades, Greece): Additional time constraints for metamorphism, extent of infiltration-controlled overprinting and deformational activity. *Geological Magazine*, *135*(3), 369–382. https://doi.org/10.1017/S0016756898008681

Bröcker, M., & Franz, L. (2006). Dating metamorphism and tectonic juxtaposition on Andros Island (Cyclades, Greece): Results of a Rb - Sr study. *Geological Magazine*, *143*(5), 609–620. https://doi.org/10.1017/S001675680600241X

Bröcker, M., & Pidgeon, R. T. (2007). Protolith ages of meta-igneous and metatuffaceous rocks from the Cycladic Blueschist Unit, Greece: Results of a reconnaissance U-Pb zircon study. *Journal of Geology*, *115*(1), 83–98. https://doi.org/10.1086/509269

Bröcker, M., Kreuzer, H., Matthews, A., & Okrusch, M. (1993). 40Ar/39Ar and oxygen isotope studies of polymetamorphism from Tinos Island, Cycladic blueschist belt, Greece. *Journal of Metamorphic Geology*, *11*(2), 223–240. https://doi.org/10.1111/j.1525-1314.1993.tb00144.x

Bröcker, M., Bieling, D., Hacker, B., & Gans, P. (2004). High-Si phengite records the time of greenschist facies overprinting: implications for models suggesting mega-detachments in the Aegean Sea. *Journal of Metamorphic Geology*, *22*, 427–442. https://doi.org/10.1111/j.1525-1314.2004.00524.x

Bröcker, M., Huyskens, M., & Berndt, J. (2016). U–Pb dating of detrital zircons from Andros, Greece: constraints for the time of sediment accumulation in the northern part of the Cycladic blueschist belt. *Geological Journal*, *367*, 354–367. https://doi.org/10.1002/gj

Brodie, K. H., & Rutter, E. H. (2000). Deformation mechanisms and rheology: Why marble is weaker than quartzite. *Journal of the Geological Society*, *157*(6), 1093–1096. https://doi.org/10.1144/jgs.157.6.1093

Brun, J. P., & Faccenna, C. (2008). Exhumation of high-pressure rocks driven by slab rollback. *Earth and Planetary Science Letters*, *272*(1–2), 1–7. https://doi.org/10.1016/j.epsl.2008.02.038

Brun, J. P., Sokoutis, D., & Van Den Driessche, J. (1995). Analogue modeling of detachment fault systems and core complexes: Comment and reply. *Geology*, *12*, 95–98. https://doi.org/10.1130/0091-7613(1994)022<0319

Brunn, J. H. (1956). Contributions a l'etude geologique du Pinde septentrional et d'une partie de la Macedonie occidentale. *Annales Géologiques Des Pays Helléniques*, *7*, 1–358.

Buick, I. S. (1991). Mylonite fabric development on Naxos, Greece. *Journal of Structural Geology*, *13*(6), 643–655.

Burns, S. J., Mckenzie, J. A., & Vasconcelos, C. (2000). Dolomite formation and biogeochemical cycles in the Phanerozoic. *Sedimentology*, *47*, 49–61. https://doi.org/10.1046/j.1365-3091.2000.00004.x

Candan, O., Dora, O., Oberhansli, R., Oelsner, F., & Dürr, S. (1997). Blueschist relicts in the Mesozoic cover series of the Menderes Massif and correlations with Samos Island, Cyclades. *Schweizerische Mineralogische Und Petrographische Mitteilungen*, *77*, 95–99.

Cao, S., Neubauer, F., Bernroider, M., & Genser, J. (2018). Eocene high-pressure metamorphism and Oligocene retrogression on Naxos, Cyclades, Greece: Significance for Aegean tectonics and 40Ar/39Ar dating in polyphase metamorphic rocks. *Tectonophysics*, *745*, 66–94. https://doi.org/10.1016/j.tecto.2018.08.009

Cardozo, N., & Allmendinger, R. W. (2013). Spherical projections with OSXStereonet. *Computers and Geosciences*, *51*, 193–205.

Carlslaw, H. S., & Jaeger, J. C. (1959). Conduction of heat in solids. *Oxford: Clarendon Press*.

Casey, M., & Mcgrew, A. J. (1999). One-dimensional kinematic model of preferred orientation development. *Tectonophysics*, *303*, 131–140.

Cetinkaplan, M., Candan, O., Oberhansli, R., Sudo, M., & Cenki-Tok, B. (2020). P–T–t evolution of the Cycladic Blueschist Unit in Western Anatolia/Turkey: Geodynamic implications for the Aegean region. *Journal of Metamorphic Geology*, (March), 1–41. https://doi.org/10.1111/jmg.12526

Chadwick, B. (1968). Deformation and metamorphism in the Lukmanier region, central Switzerland. *Bulletin of the Geological Society of America*, *79*, 1123–1150.

Chatzaras, V., Dörr, W., Finger, F., Xypolias, P., & Zulauf, G. (2013). Tectonophysics U–Pb single

zircon ages and geochemistry of metagranitoid rocks in the Cycladic Blueschists (Evia Island): Implications for the Triassic tectonic setting of Greece. *Tectonophysics*, *595–596*, 125–139. https://doi.org/10.1016/j.tecto.2012.05.016

Chatzaras, V., Dörr, W., Gerdes, A., Krahl, J., Xypolias, P., & Zulauf, G. (2016). Tracking the late Paleozoic to early Mesozoic margin of northern Gondwana in the Hellenides: Paleotectonic constraints from U–Pb detrital zircon ages. *International Journal of Earth Sciences*, *105*(7), 1881–1899. https://doi.org/10.1007/s00531-016-1298-z

Clayton, R. N., Skinner, H. C. W., Berner, R. A., & Rubinson, M. (1968). Isotopic compositions of recent South Australian lagoonal carbonates. *Geochimica et Cosmochimica Acta*, *32*(9), 983–988.

Clerc, C., Ringenbach, J. C., Jolivet, L., & Ballard, J. F. (2018). Rifted margins: Ductile deformation, boudinage, continentward-dipping normal faults and the role of the weak lower crust. *Gondwana Research*. https://doi.org/10.1016/j.gr.2017.04.030

Cliff, R. A., Butler, R. W. H., & Bond, C. E. (2016). Geochronological challenges posed by continuously developing tectonometamorphic systems; insights from Rb-Sr mica ages from the Cycladic Blueschist Belt, Syros (Greece). *Journal of Metamorphic Geology*, 1–16. https://doi.org/10.1111/jmg.12228

Clift, P. D. (1996). Accretion tectonics of the Neotethyan Ermioni Complex, Peloponessos, Greece. *Journal of the Geological Society, London*, *153*, 745–757.

Coleman, M., Dubosq, R., Schneider, D. A., Grasemann, B., & Soukis, K. (2019). Along-strike consistency of an extensional detachment system, West Cyclades, Greece. *Terra Nova*, 1–14. https://doi.org/10.1111/ter.12388

Coleman, M., Schneider, D. A., Grasemann, B., Soukis, K., Lozios, S., & Hollinetz, M. S. (2020). Lateral termination of a Cycladic-style detachment system (Hymittos, Greece). *Tectonics*, *39*, 30. https://doi.org/10.1029/2020TC006128

Collettini, C. (2011). The mechanical paradox of low-angle normal faults: Current understanding and open questions. *Tectonophysics*, *510*(3–4), 253–268. https://doi.org/10.1016/j.tecto.2011.07.015

Collettini, C., & Sibson, R. H. (2001). Normal faults, normal friction? *Geology*, *29*(10), 927–930.

Compton, R. R., Todd, V. R., Zartman, R., & Naeser, C. (1977). Oligocene and Miocene metamorphism, folding, and low-angle faulting in northwestern Utah. *Bulletin of the Geological Society of America*, *88*, 1237–1250. https://doi.org/10.1130/0016-7606(1979)90<307:OAMMFA>2.0.CO;2

Coney, P. (1980). Cordilleran metamorphic core complexes: An overview. In M. Crittenden, P. Coney, & G. Davis (Eds.), *Cordilleran Metamorphic Core Complexes* (p. 491). Boulder, Colorado: The Geological Society of America.

Corfu, F., Hanchar, J. M., Hoskin, P. W. O., & Kinny, P. (2003). Atlas of zircon textures. *Reviews in Mineralogy and Geochemistry*, *53*(1), 469–500. https://doi.org/10.2113/0530469

Cossette, É., Schneider, D. A., Warren, C. J., & Grasemann, B. (2015). Lithological, rheological, and fluid infiltration control on ^{40}Ar/^{39}Ar ages in polydeformed rocks from the West Cycladic detachment system, Greece. *Lithosphere*, *7*(2), 189–205. https://doi.org/10.1130/L416.1

Coutts, D. S., Matthews, W. A., & Hubbard, S. M. (2019). Assessment of widely used methods to derive depositional ages from detrital zircon populations. *Geoscience Frontiers*, *10*(4), 1421–1435. https://doi.org/10.1016/j.gsf.2018.11.002

Cowie, P. A., & Scholz, C. H. (1992). Physical explanation for the displacement-length relationship of faults using a post-yield fracture mechanics model. *Journal of Structural Geology*, *14*(10), 1133–1148.

Craddock, J. P., Klein, T., Kowalczyk, G., & Zulauf, G. (2009). Calcite twinning strains in Alpine orogen flysch: Implications for thrust-nappe mechanics and the geo dynamics of Crete. *Lithosphere*, *1*(3), 174–191. https://doi.org/10.1130/L31.1

Czaplińska, D., Piazolo, S., & Zibra, I. (2015). The influence of phase and grain size distribution on the dynamics of strain localization in polymineralic rocks. *Journal of Structural Geology*, *72*, 15–32. https://doi.org/10.1016/j.jsg.2015.01.001

Davis, E., & Bastas, C. (1978). Petrology and geochemistry of the metamorphic system of Santorini. In C. Doumas (Ed.), *Proceedings of the Second Internation Congress "Thera and the Aegean World."* London: The Thera Foundation.

Davis, G. (1983). Shear-zone model for the origin of metamorphic core complexes. *Geology*, *11*(6), 342–347.

Davis, G., & Coney, P. J. (1979). Geologic development of the Cordilleran metamorphic core complexes. *Geology*, *7*(3), 120–124. https://doi.org/10.1130/0091-7613(1979)7<120:GDOTCM>2.0.CO;2

Davis, N., Kronenberg, A. K., & Newman, J. (2008). Plasticity and diffusion creep of dolomite. *Tectonophysics*, *456*, 127–146. https://doi.org/10.1016/j.tecto.2008.02.002

Davis, N., Newman, J., Wheelock, P. B., & Kronenberg, A. K. (2011). Grain growth kinetics of dolomite, magnesite and calcite: a comparative study. *Physics and Chemistry of Minerals*, *38*, 123–138. https://doi.org/10.1007/s00269-010-0389-9

Dazé, A., Lee, J. K. W., & Villeneuve, M. (2003). An intercalibration study of the Fish Canyon sanidine and biotite 40Ar/39Ar standards and some comments on the age of the Fish Canyon Tuff. *Chemical Geology*, *199*, 111–127.

Degnan, P. J., & Robertson, A. H. F. (1998). Mesozoic-early Tertiary passive margin evolution of the Pindos ocean (NW Peloponnese, Greece). *Sedimentary Geology*, *117*, 33–70.

Degnan, P. J., & Robertson, A. H. F. (2006). Synthesis of the tectonic-sedimentary evolution of the Mesozoic-Early Cenozoic Pindos ocean: evidence from the NW Peloponnese, Greece. *Geological Society, London, Special Publications*, *260*, 467–491.

Delle Piane, C., Burlini, L., Kunze, K., Brack, P., & Burg, J. P. (2008). Rheology of dolomite: Large strain torsion experiments and natural examples. *Journal of Structural Geology*, *30*, 767–776. https://doi.org/10.1016/j.jsg.2008.02.018

Delle Piane, C., Clennell, M. Ben, Keller, J. V. A., Giwelli, A., & Luzin, V. (2017). Carbonate hosted fault rocks: A review of structural and microstructural characteristic with implications for seismicity in the upper crust. *Journal of Structural Geology*, *103*, 17–36. https://doi.org/10.1016/j.jsg.2017.09.003

Diamantopoulos, A., Krohe, A., & Mposkos, E. (2009a). Kinematics of conjugate shear zones, displacement partitioning and fragmentation of the upper rigid crust during denudation of high-P rocks (Pelagonian and Sub-Pelagonian Zones, Greece). *Tectonophysics*, *473*(1–2), 84–98. https://doi.org/10.1016/j.tecto.2008.05.028

Diamantopoulos, A., Krohe, A., & Mposkos, E. (2009b). Kinematics of conjugate shear zones, displacement partitioning and fragmentation of the upper rigid crust during denudation of high-P

rocks (Pelagonian and Sub-Pelagonian Zones, Greece). *Tectonophysics*, *473*(1–2), 84–98. https://doi.org/10.1016/j.tecto.2008.05.028

Dickinson, W. R., & Gehrels, G. E. (2009). Use of U–Pb ages of detrital zircons to infer maximum depositional ages of strata: A test against a Colorado Plateau Mesozoic database. *Earth and Planetary Science Letters*, *288*(1–2), 115–125. https://doi.org/10.1016/j.epsl.2009.09.013

Dilalos, S., Alexopoulos, J. D., & Lozios, S. (2019). New insights on subsurface geological and tectonic structure of the Athens basin (Greece), derived from urban gravity measurements. *Journal of Applied Geophysics*, *167*, 73–105. https://doi.org/10.1016/j.jappgeo.2019.04.024

Dilek, Y., & Altunkaynak, Ş. (2007). Cenozoic crustal evolution and mantle dynamics of post-collisional magmatism in Western Anatolia. *International Geology Review*, *49*(5), 431–453. https://doi.org/10.2747/0020-6814.49.5.431

Dinter, D. A., Macfarlane, A., Hames, W., Isachsen, C., Bowring, S., & Royden, L. (1995). U-Pb and 40Ar/39Ar geochronology of the Symvolon granodiorite: Implications for the thermal and structural evolution of the Rhodope metamorphic core complex, northeastern Greece. *Tectonics*, *14*(4), 886–908. https://doi.org/10.1029/95TC00926

Dodson, M. H. (1973). Closure Temperature in Cooling Geochronological and Petrological Systems. *Contributions to Mineralogy and Petrology*, *40*, 259–274.

Doglioni, C. (1987). Tectonics of the Dolomites (Southern Alps, Northern Italy). *Journal of Structural Geology*, *9*(2), 181–193.

Doutsos, T., Pe-Piper, G., Boronkay, K., & Koukouvelas, I. (1993). Kinematics of the Central Hellenides. *Tectonics*, *12*(4), 936–953.

Dragovic, B., Baxter, E. F., & Caddick, M. J. (2015). Pulsed dehydration and garnet growth during subduction revealed by zoned garnet geochronology and thermodynamic modeling, Sifnos, Greece. *Earth and Planetary Science Letters*, *413*, 111–122. https://doi.org/10.1016/j.epsl.2014.12.024

Dürr, S., Altherr, R., Keller, J., Okrusch, M., & Seidel, E. (1978). The median Aegean Crystalline Belt: Stratigraphy structure, metamorphism, magmatism. In H. Cloos, D. Roeder, & K. Schmidt (Eds.), *Alps, Apennines, Hellenides* (pp. 455–477). Stuttgart: Schweiz Bartsche Verlag.

Ehlers, T. A. (2005). Crustal Thermal Processes and the Interpretation of Thermochronometer Data. *Reviews in Mineralogy and Geochemistry*, *58*(1), 315–350. https://doi.org/10.2138/rmg.2005.58.12

Ehlers, T. A., Chaudhri, T., Kumar, S., Fuller, C. W., Willett, S. D., Ketcham, R. A., et al. (2005). Computational Tools for Low-Temperature Thermochronometer Interpretation. *Reviews in Mineralogy and Geochemistry*, *58*(1), 589–622. https://doi.org/10.2138/rmg.2005.58.22

El-Shazly, A. K., & Liou, J. G. (1991). Glaucophane chloritoid-bearing assemblages from NE Oman: petrologic significance and a petrogenetic grid for high P metapelites. *Contributions to Mineralogy and Petrology*, *107*(2), 180–201.

Elliot, D. (1976). The energy balance and deformation mechanisms of thrust sheets. *Philosophical Transactions of the Royal Society, London*, *283*, 289–312.

Engel, M., & Reischmann, T. (1998). Single zircon geochronology of orthogneisses from Paros, Greece. *Bulletin of the Geological Society of Greece*, *32*(3), 91–99.

Eskola, P. (1949). The problem of mantled gneiss domes. *Geological Society of London, Quarterly Journal*, *90*, 291–308.

Farley, K. A., Shuster, D. L., Watson, E. B., Wanser, K. H., & Balco, G. (2010). Numerical investigations of apatite 4He/3He thermochronometry. *Geochemistry Geophysics Geosystems*, *11*(10), 1–18. https://doi.org/10.1029/2010GC003243

Faupl, P., Pavlopoulos, A., Klötzli, U., & Petrakakis, K. (2006). On the provenance of mid-Cretaceous turbidites of the Pindos zone (Greece): Implications from heavy mineral distribution, detrital zircon ages and chrome spinel chemistry. *Geological Magazine*, *143*(3), 329–342. https://doi.org/10.1017/S001675680600197X

Ferrière, J., Chanier, F., & Ditbanjong, P. (2012). The Hellenic ophiolites: eastward or westward obduction of the Maliac Ocean, a discussion. *International Journal of Earth Sciences*, *101*, 1559–1580. https://doi.org/10.1007/s00531-012-0797-9

Flansburg, M. E., Stockli, D. F., Poulaki, E. M., & Soukis, K. (2019). Tectono-magmatic and stratigraphic evolution of the Cycladic Basement, Ios Island, Greece. *Tectonics*, *38*, 2291–2316. https://doi.org/10.1029/2018TC005436

Fletcher, J. M., & Bartley, J. M. (1994). Constrictional strain in a non-coaxial shear zone: Implications for fold and rock fabric development, Central Mojave metamorphic core complex, California. *Journal of Structural Geology*, *16*(4), 555–570. https://doi.org/10.1016/0191-8141(94)90097-3

Fleury, J. J. (1980). Evolution d'une platforme et d'un bassin dans leur cadre Alpin: les zones de Gavrovo-Tripolitza et du Pinde-Olonos. *Societé Géologique Du Nord, Special Publication*, *4*, 897–898.

Fondriest, M., Smith, S. A. F., Di Toro, G., Zampieri, D., & Mittempergher, S. (2012). Fault zone structure and seismic slip localization in dolostones, an example from the Southern Alps, Italy. *Journal of Structural Geology*, *45*, 52–67. https://doi.org/10.1016/j.jsg.2012.06.014

Forster, M., & Lister, G. S. (2009). Core-complex-related extension of the Aegean lithosphere initiated at the Eocene-Oligocene transition. *Journal of Geophysical Research*, *114*, 1–36.

Foster, D. A., & Fanning, C. M. (1997). Geochronology of the northern Idaho batholith and the bitterroot metamorphic core complex: Magmatism preceding and contemporaneous with extension. *Bulletin of the Geological Society of America*, *109*(4), 379–394. https://doi.org/10.1130/0016-7606(1997)109<0379:GOTNIB>2.3.CO;2

Freeman, S. R., Inger, S., Butler, R. W. H., & Cliff, R. A. (1997). Dating deformation using Rb-Sr in white mica: Greenschist facies deformation ages from the Entrelor shear zone, Italian Alps. *Tectonics*, *16*(1), 57–76. https://doi.org/10.1029/96TC02477

Friedrich, W., Kromer, B., Friedrich, M., Heinemeier, J., Pfeiffer, T., & Talamo, S. (2006). Santorini eruption radiocarbon dated to 1627-1600 B.C. *Science*, *312*, 548.

Frisch, W., Meschede, M., & Blakey, R. (2011). *Plate tectonics: Continental drift and mountain building*. Berlin: Springer.

Fytikas, M., Innocenti, F., Manetti, P., Mazzuoli, R., Peccerilio, A., & Villari, L. (1984). Tertiary to Quaternary evolution of volcanism in the Aegean region. *Geological Society of London Special Publication*, *17*, 689–699.

Gallagher, K. (2012). Transdimensional inverse thermal history modeling for quantitative thermochronology. *Journal of Geophysical Research*, *117*, 1–16. https://doi.org/10.1029/2011JB008825

Ganor, J., Matthews, A., & Paldor, N. (1989). Constraints on effective diffusivity during oxygen isotope

exchange at a marble-schist contact, Sifnos (Cyclades), Greece. *Earth and Planetary Science Letters*, *94*(3–4), 208–216. https://doi.org/10.1016/0012-821X(89)90140-4

Gartrell, A. P. (1997). Evolution of rift basins and low-angle detachments in multilayer analog models. *Geology*, *25*(7), 615–618.

Gautheron, C., & Tassan-got, L. (2010). A Monte Carlo approach to diffusion applied to noble gas/helium thermochronology. *Chemical Geology*, *273*(3–4), 212–224. https://doi.org/10.1016/j.chemgeo.2010.02.023

Gebauer, D. (1993). The pre-Alpine evolution of the continental crust of the Central Alps - An overview. In J. F. Raumer & F. Neubauer (Eds.), *Pre-Mesozoic geology in the Alps* (pp. 93–117). Berlin: Springer-Verlag.

Gehrels, G. (2014). Detrital zircon U-Pb geochronology applied to tectonics. *Annual Review of Earth and Planetary Sciences*, *42*, 127–149. https://doi.org/10.1146/annurev-earth-050212-124012

Gerogiannis, N., Xypolias, P., Chatzaras, V., Aravadinou, E., & Papapavlou, K. (2019). Deformation within the Cycladic subduction–exhumation channel: New insights from the enigmatic Makrotantalo nappe (Andros, Aegean). *International Journal of Earth Sciences*, *108*(3), 817–843. https://doi.org/10.1007/s00531-019-01680-3

Grasemann, B., & Dabrowski, M. (2015). Winged inclusions: Pinch-and-swell objects during high-strain simple shear. *Journal of Structural Geology*, *70*, 78–94. https://doi.org/10.1016/j.jsg.2014.10.017

Grasemann, B., & Petrakakis, K. (2007). Evolution of the Serifos metamorphic core complex. *Journal of the Virtual Explorer*, *27*, 1–17.

Grasemann, B., Schneider, D. A., Stockli, D. F., & Iglseder, C. (2012). Miocene bivergent crustal extension in the Aegean: Evidence from the western Cyclades (Greece). *Lithosphere*, *4*(1), 23–39. https://doi.org/10.1130/L164.1

Grasemann, B., Huet, B., Schneider, D. A., Rice, A. H. N., Lemonnier, N., & Tschegg, C. (2018). Miocene postorogenic extension of the Eocene synorogenic imbricated Hellenic subduction channel: New constraints from Milos (Cyclades, Greece). *Bulletin of the Geological Society of America*, *130*(1–2), 238–262. https://doi.org/10.1130/B31731.1

Grasemann, B., Schneider, D. A., Soukis, K., Roche, V., & Hubmann, B. (2021). Paleogeographic position of the central Dodecanese Islands, southeastern Greece: The push-pull of Pelagonia. *Bulletin of the Geological Society of America*, *134*(5–6), 1506–1528. https://doi.org/10.1130/b36095.1

Grujic, D., & Mancktelow, N. S. (1995). Folds with axes parallel to the extension direction: An experimental study. *Journal of Structural Geology*, *17*(2), 279–291. https://doi.org/10.1016/0191-8141(94)E0048-4

Guenthner, W. R., Reiners, P. W., Ketcham, R. A., Nasdala, L., & Giester, G. (2013). Helium diffusion in natural zircon: radiation damage, anisotropy, and the interpretation of zircon (U-TH)/He thermochronology. *American Journal of Science*, *313*(3), 145–198. https://doi.org/10.2475/03.2013.01

Guenthner, W. R., Reiners, P. W., & Tian, Y. (2014). Interpreting date–eU correlations in zircon (U-Th)/He datasets: A case study from the Longmen Shan, China. *Earth and Planetary Science Letters*, *403*, 328–339. https://doi.org/10.1016/j.epsl.2014.06.050

Guenthner, W. R., Reiners, P. W., Decelles, P. G., & Kendall, J. (2015). Sevier belt exhumation in central

Utah constrained from complex zircon (U-Th)/He data sets: Radiation damage and He inheritance effects on partially reset detrital zircons. *Bulletin of the Geological Society of America*, (3), 323–348. https://doi.org/10.1130/B31032.1

Gutiérrez-Alonso, G., Fernández-Suárez, J., Collins, A. S., Abad, I., & Nieto, F. (2005). Amazonian Mesoproterozoic basement in the core of the Ibero-Armorican Arc: 40Ar/39Ar detrital mica ages complement the zircon's tale. *Geology*, *33*(8), 637–640.

Handin, J., & Hager, R. V. (1958). Experimental deformation of sedimentary rocks under confining pressure: Tests at high temperature. *AAPG Bulletin*, *42*(12), 2892–2934.

Harrison, T. M., Célérier, J., Aikman, A. B., Hermann, J., & Heizler, M. T. (2009). Diffusion of 40Ar in muscovite. *Geochimica et Cosmochimica Acta*, *73*(4), 1039–1051. https://doi.org/10.1016/j.gca.2008.09.038

Heineke, C., Hetzel, R., Nilius, N., Zwingmann, H., Todd, A., Mulch, A., et al. (2019). Detachment faulting in a bivergent core complex constrained by fault gouge dating and low-temperature thermochronology. *Journal of Structural Geology*, *127*(January), 1–15. https://doi.org/10.1016/j.jsg.2019.103865

van Hinsbergen, D. J. J., Hafkenscheid, E., Spakman, W., Meulenkamp, J. E., & Wortel, R. (2005). Nappe stacking resulting from subduction of oceanic and continental lithosphere below Greece. *Geology*, *33*(4), 325–328. https://doi.org/10.1130/G20878.1

Hinsken, T., Bröcker, M., Berndt, J., & Gärtner, C. (2016). Maximum sedimentation ages and provenance of metasedimentary rocks from Tinos Island, Cycladic blueschist belt, Greece. *International Journal of Earth Sciences*, *105*(7), 1923–1940. https://doi.org/10.1007/s00531-015-1258-z

Holyoke, C. W., Kronenberg, A. K., & Newman, J. (2013). Dislocation creep of polycrystalline dolomite. *Tectonophysics*, *590*, 72–82. https://doi.org/10.1016/j.tecto.2013.01.011

Holyoke, C. W., Kronenberg, A. K., & Newman, J. (2014). Microstructural evolution during strain localization in dolomite aggregates. *Journal of Structural Geology*, *69*, 449–464. https://doi.org/10.1016/j.jsg.2014.04.008

Huet, B., Labrousse, L., & Jolivet, L. (2009). Thrust or detachment? Exhumation processes in the Aegean: Insight from a field study on Ios (Cyclades, Greece). *Tectonics*, *28*, 1–27. https://doi.org/10.1029/2008TC002397

Huet, B., Labrousse, L., Monié, P., Malvoisin, B., & Jolivet, L. (2015). Coupled phengite ^{40}Ar-^{39}Ar geochronology and thermobarometry: P-T-t evolution of Andros Island (Cyclades, Greece). *Geological Magazine*, *152*(4), 711–727. https://doi.org/10.1017/S0016756814000661

Huyskens, M. H., & Bröcker, M. (2014). The status of the makrotantalon unit (Andros, Greece) within the structural framework of the Attic-Cycladic Crystalline Belt. *Geological Magazine*, *151*(3), 430–446. https://doi.org/10.1017/S0016756813000307

Iglseder, C., Grasemann, B., Schneider, D. A., Petrakakis, K., Miller, C., Klötzli, U. S., et al. (2009). I and S-type plutonism on Serifos (W-Cyclades, Greece). *Tectonophysics*, *473*(1–2), 69–83. https://doi.org/10.1016/j.tecto.2008.09.021

Iglseder, C., Grasemann, B., Rice, A. H. N., Petrakakis, K., & Schneider, D. A. (2011). Miocene south directed low-angle normal fault evolution on Kea Island (West Cycladic Detachment System, Greece). *Tectonics*, *30*(4), 1–31. https://doi.org/10.1029/2010TC002802

Jackson, J. A. (1987). Active normal faulting and crustal extension. *Geological Society Special*

Publication, *28*(28), 3–17. https://doi.org/10.1144/GSL.SP.1987.028.01.02

Jackson, J. A., & White, N. J. (1989). Normal faulting in the upper continental crust: Observations from regions of active extension. *Journal of Structural Geology*, *11*(1/2), 15–36.

Jacobshagen, V. (1986). *Geologie von Griechenland* (1st ed.). Berlin: Gebrüder Borntraeger.

Janney, D. E., & Wenk, H.-R. (1994). Some typical microstructures in deformed rocks. *Materials Science & Engineering*, *175*, 201–208.

Jenkyns, H. C., & Winterer, E. L. (1982). Palaeoceanography of Mesozoic ribbon radiolarites. *Earth and Planetary Science Letters*, *60*, 351–375.

Jolivet, L., & Brun, J. P. (2010). Cenozoic geodynamic evolution of the Aegean. *International Journal of Earth Sciences*, *99*(1), 109–138. https://doi.org/10.1007/s00531-008-0366-4

Jolivet, L., & Faccenna, C. (2000). Mediterranean extension and the Africa-Eurasia collision. *Tectonics*, *19*(6), 1095–1106.

Jolivet, L., Faccenna, C., Goffe, B., Burov, E., & Agard, P. (2003). Subduction tectonics and exhumation of high-pressure metamorphic rocks in the Mediterranean orogens. *American Journal of Science*, *303*, 353–409.

Jolivet, L., Famin, V., Mehl, C., Parra, T., Aubourg, C., Hebert, R., & Philippot, P. (2004). Strain localization during crustal-scale boudinage to form extensional metamorphic domes in the Aegean Sea. In D. L. Whitney, C. Teyssier, & C. S. Siddoway (Eds.), *Gneiss domes in orogeny: Geological Society of America, Special Paper 380* (pp. 185–210). Boulder, Colorado: Geological Society of America. https://doi.org/10.1130/0-8137-2380-9.185

Jolivet, L., Lecomte, E., Huet, B., Denèle, Y., Lacombe, O., Labrousse, L., et al. (2010). The North Cycladic Detachment System. *Earth and Planetary Science Letters*, *289*(1–2), 87–104.

Jolivet, L., Faccenna, C., Huet, B., Labrousse, L., Le Pourhiet, L., Lacombe, O., et al. (2013). Aegean tectonics: Strain localisation, slab tearing and trench retreat. *Tectonophysics*, *597–598*, 1–33. https://doi.org/10.1016/j.tecto.2012.06.011

Jolivet, L., Menant, A., Sternai, P., Rabillard, A., Arbaret, L., Augier, R., et al. (2015). The geological signature of a slab tear below the Aegean. *Tectonophysics*, *659*, 166–182. https://doi.org/10.1016/j.tecto.2015.08.004

Katsiavrias, N., Solakius, N., & Salaj, J. (1991). The age of the Agios Konstantinos limestone at Lavrion, southeastern Attica, Greece. *Geologica Carpathica*, *42*, 303–309.

Katzir, Y., Avigad, D., Matthews, A., Garfunkel, Z., & Evans, B. (2000). Origin, HP/LT metamorphism and cooling of ophiolitic melanges in southern Evia (NW Cyclades), Greece. *Journal of Metamorphic Geology*, *18*, 699–718.

Keay, S., & Lister, G. S. (2002). African provenance for the metasediments and metaigneous rocks of the Cyclades, Aegean Sea, Greece. *Geology*, *30*(3), 235–238.

Keiter, M., Ballhaus, C., & Tomaschek, F. (2011). A new geological map of the Island of Syros (Aegean Sea, Greece): Implications for lithostratigraphy and structural history of the Cycladic Blueschist Unit. *The Geological Society of America*, *481*, 1–50.

Kellett, D. A., Warren, C., Larson, K. P., Zwingmann, H., van Staal, C. R., & Rogers, N. (2016). Influence of deformation and fluids on Ar retention in white mica: Dating the Dover Fault, Newfoundland Appalachians. *Lithos*, *254–255*, 1–17. https://doi.org/10.1016/j.lithos.2016.03.003

Kendall, J. (2016). *Sm/Nd garnet geochronology and pressure-temperature paths of eclogites from Syros, Greece: Implications for subduction zone process and water loss from the subducting slab (Unpublished doctoral dissertation)*. Boston College.

Kennedy, L. A., & White, J. C. (2001). Low-temperature recrystallization in calcite: Mechanisms and consequences. *Geology*, *29*(11), 1027–1030. https://doi.org/10.1130/0091-7613(2001)029<1027:LTRICM>2.0.CO;2

Kerrich, R., & Allison, I. (1978). Flow mechanisms in rocks: Microscopic and mesoscoplc structures, and their relation to physical conditions of deformation in the crust. *Geoscience Canada*, *5*(3), 109–118.

Ketcham, R. A. (2005). Forward and inverse modeling of low-temperature thermochronometry data. *Reviews in Mineralogy and Geochemistry*, *58*(1), 275–314. https://doi.org/10.2138/rmg.2005.58.11

Ketcham, R. A., & Brichau, S. (2008). The unroofing history of Naxos and Paros: Constraints and questions from thermochronology and thermal modeling. *IOP Science*, (July), 1–6. https://doi.org/10.1088/1755-1307/2/1/012019

Ketcham, R. A., Gautheron, C., & Tassan-got, L. (2011). Accounting for long alpha-particle stopping distances in (U–Th–Sm)/He geochronology: Refinement of the baseline case. *Geochimica et Cosmochimica Acta*, *75*(24), 7779–7791. https://doi.org/10.1016/j.gca.2011.10.011

Kilias, A., Tranos, M. D., & Pavlides, S. (1998). The prevolcanic metamorphic rocks of Santorini island: Structural evolution and kinematics during the Tertiary (South Aegean, Greece). In R. Casale, M. Fytikas, G. Sigvaldasson, & G. Vougioukalakis (Eds.), *Volcanic risk. The European laboratory volcanoes, 2nd workshop* (pp. 23–36). Computer Science Research Development.

Kim, Y., & Sanderson, D. J. (2006). Structural similarity and variety at the tips in a wide range of strike–slip faults: A review. *Terra Nova*, *18*, 330–344. https://doi.org/10.1111/j.1365-3121.2006.00697.x

Kolodner, K., Avigad, D., McWilliams, M., Wooden, J. L., Weissbrod, T., & Feinstein, S. (2006). Provenance of north Gondwana Cambrian-Ordovician sandstone: U-Pb SHRIMP dating of detrital zircons from Israel and Jordan. *Geological Magazine*, *143*(3), 367–391. https://doi.org/10.1017/S0016756805001640

Konstantinos, S., & Papanikolaou, D. (2004). Contrasting geometry between Alpine and late-to-postalpine tectonic structures in Anafi Island (Cyclades). *Bulletin of the Geological Society of Greece*, *36*(4), 1688–1696. https://doi.org/10.12681/bgsg.16575

Kotowski, A. J., & Behr, W. M. (2019). Length scales and types of heterogeneities along the deep subduction interface: Insights from exhumed rocks on Syros Island, Greece. *Geosphere*, *15*, 1–28. https://doi.org/10.1130/GES02037.1

Kotowski, A. J., Cisneros, M., Behr, W. M., Stockli, D. F., Soukis, K., Barnes, J. D., & Ortega-arroyo, D. (2021). Subduction, underplating, and return flow recorded in the Cycladic Blueschist Unit exposed on Syros, Greece. *Tectonics*, *41*(6), 1–41.

Koutsovitis, P., Soukis, K., Voudouris, P., Ntaflos, T., Stouraiti, C., Koukouzas, N., & Stouraiti, C. (2021). The Late Cretaceous magmatic arc of the south Aegean: Geodynamic implications from petrological and geochemical studies of granitoids from Anafi island (Cyclades – Greece). *International Geology Review*, *64*(6), 1–24. https://doi.org/10.1080/00206814.2021.1884906

Krogh, T. E., & Keppie, J. (1990). Age of detrital zircon and titanite in the Meguma Group, southern Nova Scotia, Canada: Clues to the origin of the Meguma Terrane. *Tectonophysics*, *177*(1), 307–323. https://doi.org/10.1016/0040-1951(90)90287-I

Krohe, A., Mposkos, E., Diamantopoulos, A., & Kaouras, G. (2010). Formation of basins and mountain ranges in Attica (Greece): The role of Miocene to recent low-angle normal detachment faults. *Earth-Science Reviews*, *98*(1–2), 81–104. https://doi.org/10.1016/j.earscirev.2009.10.005

Kuiper, K. F., Deino, A., Hilgen, F. J., Krijgsman, W., Renne, P. R., & Wijbrans, J. R. (2008). Synchronizing rock clocks of Earth history. *Science*, *320*, 500–504.

Kushnir, A. R. L., Kennedy, L. A., Misra, S., Benson, P., & White, J. C. (2015). The mechanical and microstructural behaviour of calcite-dolomite composites: An experimental investigation. *Journal of Structural Geology*, *70*, 200–216. https://doi.org/10.1016/j.jsg.2014.12.006

Lacassin, R. (1988). Large-scale foliation boudinage in gneisses. *Journal of Structural Geology*, *10*(6), 643–647. https://doi.org/10.1016/0191-8141(88)90030-2

Lagos, M., Scherer, E. E., Tomaschek, F., Münker, C., Keiter, M., Berndt, J., & Ballhaus, C. (2007). High precision Lu–Hf geochronology of Eocene eclogite-facies rocks from Syros, Cyclades, Greece. *Chemical Geology*, *243*, 16–35. https://doi.org/10.1016/j.chemgeo.2007.04.008

Lamont, T. N., Roberts, N. M. W., Searle, M. P., Gopon, P., Waters, D. J., & Millar, I. (2019). The Age, origin, and emplacement of the Tsiknias Ophiolite, Tinos, Greece. *Tectonics*, *39*, 1–45. https://doi.org/10.1029/2019TC005677

Laskari, S., Soukis, K., Lozios, S., Stockli, D. F., Poulaki, E. M., & Stouraiti, C. (2022). Structural study and detrital zircon provenance analysis of the Cycladic Blueschist Unit rocks from Iraklia Island: From the Paleozoic basement unroofing to the Cenozoic exhumation. *Minerals*, *12*, 1–20. https://doi.org/10.3390/min12010083

Laurent, V., Beaudoin, A., Jolivet, L., Arbaret, L., Augier, R., Rabillard, A., & Menant, A. (2015). Interrelations between extensional shear zones and synkinematic intrusions: The example of Ikaria Island (NE Cyclades, Greece). *Tectonophysics*, *651*, 152–171. https://doi.org/10.1016/j.tecto.2015.03.020

Laurent, V., Jolivet, L., Roche, V., Augier, R., Scaillet, S., & Cardello, G. L. (2016). Strain localization in a fossilized subduction channel: Insights from the Cycladic Blueschist Unit (Syros, Greece). *Tectonophysics*, *672–673*, 150–169. https://doi.org/10.1016/j.tecto.2016.01.036

Laurent, V., Huet, B., Labrousse, L., Jolivet, L., Monié, P., & Augier, R. (2017). Extraneous argon in high-pressure metamorphic rocks: Distribution, origin and transport in the Cycladic Blueschist Unit (Greece). *Lithos*, *272–273*, 315–335. https://doi.org/10.1016/j.lithos.2016.12.013

Laurent, V., Lanari, P., Naïr, I., Augier, R., Lahfid, A., & Jolivet, L. (2018). Exhumation of eclogite and blueschist (Cyclades, Greece): Pressure–temperature evolution determined by thermobarometry and garnet equilibrium modelling. *Journal of Metamorphic Geology*, *36*(6). https://doi.org/10.1111/jmg.12309

Leiss, B., & Barber, D. J. (1999). Mechanisms of dynamic recrystallization in naturally deformed dolomite inferred from EBSP analyses. *Tectonophysics*, *303*, 51–69.

Leiss, B., & Molli, G. (2003). "High-temperature" texture in naturally deformed Carrara marble from the Alpi Apuane, Italy. *Journal of Structural Geology*, *25*(4), 649–658. https://doi.org/10.1016/S0191-8141(02)00148-7

Leiss, B., Helming, K., Siegesmund, S., & Weber, K. (1994). Quantitative texture analysis of naturally deformed polyphase dolomite marbles and its kinematic significance. *Materials Science Forum*, *157–162*, 789–794. https://doi.org/10.4028/www.scientific.net/msf.157-162.789

Leiss, B., Siegesmund, S., & Weber, K. (1999). Texture asymmetries as shear sense indicators in naturally deformed mono- and polyphase carbonate Rocks. *Textures and Microstructures*, *33*(1–4), 61–74. https://doi.org/10.1155/tsm.33.61

Lekkas, S., & Lozios, S. (2000). Tectonic structure of Mt. Hymittos. *Annales Géologiques Des Pays Helléniques2*, *38*, 47–62.

Leleu, M., & Neumann, M. (1969). Age of the Attic formations (Greece): From Palaeozoic to Mesozoic. *Comptes Rendus Hebdomadaires Des Seances de l'Académie Des Sciences Série D*, *268*, 1361–1363.

Lepsius, R. (1893). *Geologie von Attika* (4th ed.). Berlin: Zeitsch. F. Praktische Geologie.

Lewis, S., Holness, M., & Graham, C. (1998). Ion microprobe study of marble from Naxos, Greece: Grain-scale fluid pathways and stable isotope equilibration during metamorphism. *Geology*, *26*(10), 935–938. https://doi.org/10.1130/0091-7613(1998)026<0935:IMSOMF>2.3.CO;2

Liati, A., Skarpelis, N., & Pe-Piper, G. (2009). Late Miocene magmatic activity in the Attic-Cycladic Belt of the Aegean (Lavrion, SE Attica, Greece): Implications for the geodynamic evolution and timing of ore deposition. *Geological Magazine*, *146*(5), 732–742. https://doi.org/10.1017/S0016756809006438

Liati, A., Skarpelis, N., & Fanning, M. C. (2013). Late Permian-Early Triassic igneous activity in the Attic Cycladic Belt (Attica): New geochronological data and geodynamic implications. *Tectonophysics*, *595–596*, 140–147. https://doi.org/10.1016/j.tecto.2012.05.009

Lion, A. (2018). *Thermochronologic and geochronologic investigations of the pre-volcanic crystalline basement of Thera (Santorini), Greece: Determining the tectonostratigraphy and deformational history of the metamorphic core*. University of Ottawa.

Lips, A. L. W., White, S. H., & Wijbrans, J. R. (1998). 40Ar/39Ar laserprobe direct dating of discrete deformational events: A continuous record of early Alpine tectonics in the Pelagonian Zone, NW Aegean area, Greece. *Tectonophysics*, *298*, 133–153.

Lister, G. S., & Davis, G. A. (1989). The origin of metamorphic core complexes and detachment faults formed during Tertiary continental extension in the northern Colorado River region, U.S.A. *Journal of Structural Geology*, *11*(1/2), 65–94.

Lister, G. S., & Forster, M. (2005). Several distinct tectono-metamorphic slices in the Cycladic eclogite–blueschist belt, Greece. *Contributions to Mineralogy and Petrology*, *150*, 523–545. https://doi.org/10.1007/s00410-005-0032-9

Lister, G. S., & Forster, M. (2016). White mica 40Ar/39Ar age spectra and the timing of multiple episodes of high-P metamorphic mineral growth in the Cycladic eclogite-blueschist belt, Syros, Aegean Sea, Greece. *Journal of Metamorphic Geology*, *34*(5), 401–421. https://doi.org/10.1111/jmg.12178

Lister, G. S., & Williams, P. F. (1979). Fabric development in shear zones: Theoretical controls and observed phenomena. *Journal of Structural Geology*, *1*(4), 283–297. https://doi.org/10.1016/0191-8141(79)90003-8

Lister, G. S., Banga, G., & Feenstra, A. (1984). Metamorphic core complexes of Cordilleran type in the Cyclades, Aegean Sea, Greece. *Geology*, *12*(4), 221–225. https://doi.org/10.1130/0091-7613(1984)12<221:MCCOCT>2.0.CO;2

Lister, G. S., Etheridge, M. A., & Symonds, P. A. (1986). Detachment faulting and the evolution of

passsive margins. *Geology*, (March), 246–250. https://doi.org/10.1130/0091-7613(1986)14<246:DFATEO>2.0.CO;2

Lloyd, G. E., Farmer, A. B., & Mainprice, D. (1997). Misorientation analysis and the formation and orientation of subgrain and grain boundaries. *Tectonophysics*, *279*(1–4), 55–78. https://doi.org/10.1016/S0040-1951(97)00115-7

Löwen, K., Bröcker, M., & Berndt, J. (2015). Depositional ages of clastic metasediments from Samos and Syros, Greece: Results of a detrital zircon study. *International Journal of Earth Sciences*, *104*(1), 205–220. https://doi.org/10.1007/s00531-014-1058-x

Lozios, S., Soukis, K., Antoniou, V., Lozios, S., Soukis, K., & Antoniou, V. (2019). A guide to lithostratigraphy and structural inventory of the Cycladic Blueschist Unit rocks of NE Attica (Greece). *Journal of the Virtual Explorer*, *50*, 1–30. https://doi.org/10.3809/jvirtex.2016.08691

Lü, Z., Bucher, K., & Zhang, L. (2013). Omphacite-bearing calcite marble and associated coesite-bearing pelitic schist from the meta-ophiolitic belt of Chinese western Tianshan. *Journal of Asian Earth Sciences*, *76*, 37–47. https://doi.org/10.1016/j.jseaes.2013.07.034

Ludwig, K. R. (2003). Isoplot 3.00: A geochronological toolkit for Microsoft Excel. *Berkeley Geochronology Center, Berkeley*, *70*.

Ma, Z., Zhang, C., Pathegama Gamage, R., & Zhang, G. (2022). Uncovering the creep deformation mechanism of rock-forming minerals using nanoindentation. *International Journal of Mining Science and Technology*, *32*(2), 283–294. https://doi.org/10.1016/j.ijmst.2021.11.010

Maffione, M., & van Hinsbergen, D. J. J. (2018). Reconstructing plate boundaries in the Jurassic Neo-Tethys From the East and West Vardar Ophiolites (Greece and Serbia). *Tectonics*, *37*, 858–887.

Maluski, H., Vergely, P., Bavay, P., & Katsikatsos, G. (1981). 40Ar/39Ar dating of glaucophane and phengites in southern Euboa (Greece), geodynamic implications. *Bulletin de La Société Géologique de France*, *5*, 469–476.

Maluski, H., Bonneau, M., & Kienast, J. R. (1987). Dating the metamorphic events in the Cycladic area: 39Ar/40Ar data from metamorphic rocks of the island of Syros (Greece). *Bulletin de La Société Géologique de France*, *8*, 833–842.

Mancktelow, N. S., & Pavlis, T. L. (1994). Fold-fault relationships in low-angle detachment systems. *Tectonics*, *13*(2), 668–685.

Marinos, G., & Petrascheck, W. (1956). Laurium. I.G.M.E. *Geological & Geophysical Research*, *1*, 247.

Marinos, G., & Symeonidis, N. (1974). Neue Funde aus Pikermi (Attika, Griechenland) und eine allgemeine geologische Übersicht des paläontologischen Raumes. *Annales Geologique Des Pays Hellenique*, *XXVI*, 1–20.

Martel, S. J. (1997). Effects of cohesive zones on small faults and implications for secondary fracturing and fault trace geometry. *Journal of Structural Geology*, *19*(6), 835–847.

Massonne, H., & Schreyer, W. (1987). Phengite geobarometry based on the limiting assemblage with K-feldspar, phlogopite and quartz. *Contributions to Mineralogy and Petrology*, *96*(2), 212–224.

McDougall, I., & Harrison, T. M. (1999). *Geochronology and thermochronology by the 40Ar/39Ar method*. Oxford University Press.

Mcfarlane, C. R. M., & Luo, Y. (2012). U-Pb geochronology using 193 nm Excimer LA-ICP-MS optimized for in situ accessory mineral dating in thin sections. *Geoscience Canada*, *39*, 158–172.

Meesters, A. G. C. A., & Dunai, T. J. (2002). Solving the production–diffusion equation for finite diffusion domains of various shapes Part I. Implications for low-temperature (U–Th)/He thermochronology. *Chemical Geology*, *186*, 333–344.

Meinhold, G., & Frei, D. (2008). Detrital zircon ages from the islands of Inousses and Psara, Aegean Sea, Greece: Constraints on depositional age and provenance. *Geological Magazine*, *145*(6), 886–891. https://doi.org/10.1017/S0016756808005505

Meinhold, G., Reischmann, T., Kostopoulos, D., Lehnert, O., & Matukov, D. (2008). Provenance of sediments during subduction of Palaeotethys: Detrital zircon ages and olistolith analysis in Palaeozoic sediments from Chios Island, Greece. *Palaeogeography, Palaeoclimatology, Palaeoecology*, *263*, 71–91. https://doi.org/10.1016/j.palaeo.2008.02.013

Meinhold, G., Kostopoulos, D., Reischmann, T., Frei, D., & BouDagher-Fadel, M. K. (2009). Geochemistry, provenance and stratigraphic age of metasedimentary rocks from the eastern Vardar suture zone, northern Greece. *Palaeogeography, Palaeoclimatology, Palaeoecology*, *277*(3–4), 199–225. https://doi.org/10.1016/j.palaeo.2009.04.005

Meinhold, G., Reischmann, T., Kostopoulos, D., Frei, D., & Larionov, A. N. (2010). Mineral chemical and geochronological constraints on the age and provenance of the eastern Circum-Rhodope Belt low-grade metasedimentary rocks, NE Greece. *Sedimentary Geology*, *229*(4), 207–223. https://doi.org/10.1016/j.sedgeo.2010.06.007

Mercier, J. L., Vergely, P., & Bebien, J. (1975). Les ophiolites Helleniques obductees au Jurassique superier sont-elles les vestiges d'un Ocean Tethysien ou d'une mer marginale peri-Europeene? *Comptes Rendus Geosciences*, (November 1975).

Min, K., Mundil, R., Renne, P. R., & Ludwig, K. R. (2000). A test for systematic errors in 40Ar/39Ar geochronology through comparison with U/Pb analysis of a 1.1-Ga rhyolite. *Geochimica et Cosmochimica Acta*, *64*, 73–98.

Moecher, D. P., & Samson, S. D. (2006). Differential zircon fertility of source terranes and natural bias in the detrital zircon record: Implications for sedimentary provenance analysis. *Earth and Planetary Science Letters*, *247*, 252–266. https://doi.org/10.1016/j.epsl.2006.04.035

Mountrakis, D. (1986). The Pelagonian Zone in Greece: A polyphase-deformed fragment of the Cimmerian Continent and its role in the geotectonic evolution of the Eastern Mediterranean. *Journal of Geology*, *94*(3), 335–347.

Mountrakis, D., Sapountzis, E., Kilias, A., Eleftheriadis, G., & Christofides, G. (1983). Paleogeographic conditions in the western Pelagonian margin in Greece during the initial rifting of the continental area. *Canadian Journal of Earth Science*, *20*, 1673–1681.

Nance, R. D., & Murphy, J. B. (1994). Contrasting basement isotopic signatures and the palinspastic restoration of peripheral orogens: Example from the Neoproterozoic Avalonian-Cadomian belt. *Geology*, *22*(7), 617–620. https://doi.org/10.1130/0091-7613(1994)022<0617:CBISAT>2.3.CO;2

Nance, R. D., Murphy, J. B., Strachan, R. A., Keppie, J. D., Gutierrez-Alonso, G., Fernandez-Suarez, J., et al. (2008). Neoproterozoic–early Palaeozoic tectonostratigraphy and palaeogeography of the peri-Gondwanan terranes: Amazonian v. West African connections. *Geological Society of London Special Publication*, *297*, 345–383.

Nania, L. (2021). Unravelling the evolution of regional-scale shear zones with the aid of microstructures and textural analysis: an example from the central Himalaya. *Rendiconti Online Della Società Geologica Italiana*, *54*, 32–40. https://doi.org/10.3301/rol.2021.07

Negris, P., & Meunier, S. (1915). *Roches cristallphylliennes et tectonique de la Grece*. Athens: Imprimerie PD Sakellarios.

Oesterling, N., Heilbronner, R., Stunitz, H., Barnhoorn, A., & Molli, G. (2007). Strain dependent variation of microstructure and texture in naturally deformed Carrara marble. *Journal of Structural Geology*, *29*, 681–686. https://doi.org/10.1016/j.jsg.2006.10.007

Ohl, M., Nzogang, B., Mussi, A., Wallis, D., Drury, M., & Plümper, O. (2021). Crystal-Plastic Deformation in Seismically Active Carbonate Fault Rocks. *Journal of Geophysical Research: Solid Earth*, *126*(4), 1–20. https://doi.org/10.1029/2020JB020626

Okrusch, M., & Bröcker, M. (1990). Eclogites associated with high-grade blueschists in the Cyclades archipelago, Greece: A review. *European Journal of Mineralogy*, *2*(4), 451–478.

Oner, Z., Dilek, Y., & Kadioglu, Y. K. (2010). Geology and geochemistry of the synextensional Salihli granitoid in the Menderes core complex, western Anatolia, Turkey. *International Geology Review*, *52*(2–3), 336–368. https://doi.org/10.1080/00206810902815871

Papanikolaou, D. (1984). The three metamorphic belts of the Hellenides: a review and a kinematic interpretation. In J. E. Dixon & A. H. F. Robertson (Eds.), *The Geological Evolution of the Eastern Mediterranean* (pp. 551–561). Geological Society of London, Special Publication.

Papanikolaou, D. (1987a). Contribution to the geology of Aegean Sea: The island of Andros. *Annales Géologiques Des Pays Helléniques*, *29*, 477–533.

Papanikolaou, D. (1987b). Tectonic Evolution ofthe Cycladic Blueschist Belt (Aegean Sea, Greece). In *Chemical Transport in Metasomatic Processes* (pp. 429–450). Dordrecth, Netherlands: Springer.

Papanikolaou, D. (2009). Timing of tectonic emplacement of the ophiolites and terrane paleogeography in the Hellenides. *Lithos*, *108*(1–4), 262–280. https://doi.org/10.1016/j.lithos.2008.08.003

Papanikolaou, D. (2021). *The Geology of Greece*. (R. Oberhansli, M. de Wit, & F. Roure, Eds.). Cham, Switzerland: Springer.

Papanikolaou, D., & Papanikolaou, I. (2007). Geological, geomorphological and tectonic structure of the NE Attica and seismic hazard implications for the northern edge of the Athens plain. *Bulletin of the Geological Society of Greece*, 425–438.

Papanikolaou, D., & Royden, L. H. (2007). Disruption of the Hellenic arc: Late Miocene extensional detachment faults and steep Pliocene-Quaternary normal faults — Or what happened at Corinth? *Tectonics*, *26*, 1–16. https://doi.org/10.1029/2006TC002007

Papanikolaou, D., Bassi, E. K., Kranis, H., & Danamos, G. (2004). Paleogeographic evolution of the Athens Basin from Upper Miocene to present. *Bulletin of the Geological Society of Greece*, *36*(2), 816–825.

Park, R. G. (1969). Structural correlation in metamorphic belts. *Tectonophysics*, *7*, 323–338.

Parra, T., Vidal, O., & Agard, P. (2002). A thermodynamic model for Fe-Mg dioctahedral K white micas using data from phase-equilibrium experiments and natural pelitic assemblages. *Contributions to Mineralogy and Petrology*, *143*(6), 706–732. https://doi.org/10.1007/s00410-002-0373-6

Parra, T., Vidal, O., & Jolivet, L. (2002). Relation between the intensity of deformation and retrogression in blueschist metapelites of Tinos Island (Greece) evidenced by chlorite-mica local equilibria. *Lithos*, *63*(1–2), 41–66. https://doi.org/10.1016/S0024-4937(02)00115-9

Parsons, A. J., Law, R. D., Lloyd, G. E., Phillips, R. J., & Searle, M. P. (2016). Thermo-kinematic

evolution of the Annapurna-Dhaulagiri Himalaya, central Nepal: The Composite Orogenic System. *Geochemistry, Geophysics, Geosystems*, *17*(4), 1511–1539. https://doi.org/10.1002/2015GC006184

Parsons, A. J., Coleman, M., Ryan, J. J., & Zagorevski, A. (2018). Structural evolution of a crustal-scale shear zone through a decreasing temperature regime: The Yukon River shear zone, Yukon-Tanana terrane, Northern Cordillera. *Lithosphere*, *10*, 1–23. https://doi.org/10.1130/L724.1/4520588/l724.pdf

Paton, C., Hellstrom, J., Paul, B., Woodhead, J., & Hergt, J. (2011). Iolite: Freeware for the visualisation and processing of mass spectrometric data. *Journal of Analytical Atomic Spectrometry*, *26*, 2508–2518.

Patzak, M., Okrusch, M., & Kreuzer, H. (1994). The Akrotiri Unit on the island of Tinos, Cyclades, Greece: Witness to a lost terrane of Late Cretaceous age. *Neues Jahrbuch Fur Mineralogie*, *194*(2), 211–252.

Pe-Piper, G., & Piper, D. (2002). *The Igneous Rocks of Greece. The Anatomy of an Orogen* (1st ed.). Michigan: Gebr. Borntraeger.

Peillod, A. (2018). *The metamorphic history of Naxos (central Cyclades, Greece)*. Stockholm University.

Peillod, A., Ring, U., Glodny, J., & Skelton, A. (2017). An Eocene/Oligocene blueschist-/greenschist facies P – T loop from the Cycladic Blueschist Unit on Naxos Island, Greece: Deformation-related re-equilibration vs . thermal relaxation. *Journal of Metamorphic Geology*, *35*, 805–830. https://doi.org/10.1111/jmg.12256

Petrus, J. A., & Kamber, B. S. (2012). VizualAge: A novel approach to laser ablation ICP-MS U-Pb geochronology data reduction. *Geostandards and Geoanalytical Research*, *36*(3), 247–270. https://doi.org/10.1111/j.1751-908X.2012.00158.x

Photiades, A., & Carras, N. (2001). Stratigraphy and geological structure of the Lavrion area (Attica, Greece). *Bulletin of the Geological Society of Greece*, *34*(1), 103–109.

Photiades, A., & Saccani, E. (2006). Geochemistry and tectono-magmatic significance of HP/LT metaophiolites of the Attic-Cycladic Zone in the Lavrion area (Attica, Greece). *Ofioliti*, *31*(2), 89–102.

Platt, J. P., & Behrmann, J. H. (1986). Structures and fabrics in a crustal-scale shear zone, Betic Cordillera, SE Spain. *Journal of Structural Geology*, *8*(1), 15–33. https://doi.org/10.1016/0191-8141(86)90014-3

Porkolab, K., Willingshofer, E., Sokoutis, D., Creton, I., Kostopoulos, D., & Wijbrans, J. (2019). Cretaceous-Paleogene tectonics of the Pelagonian Zone: Inferences from Skopelos Island (Greece). *Tectonics*, *38*, 1–28. https://doi.org/10.1029/2018TC005331

Poulaki, E. M., Stockli, D. F., Flansburg, M. E., & Soukis, K. (2019). Zircon U-Pb chronostratigraphy and provenance of the Cycladic Blueschist Unit and the nature of the contact with the Cycladic Basement on Sikinos and Ios Islands, Greece. *Tectonics*, *38*, 1–28. https://doi.org/10.1029/2018TC005403

Poulaki, E. M., Stockli, D. F., Flansburg, M. E., Gevedon, M. L., Stockli, L. D., Barnes, J. D., et al. (2021). Zircon U-Pb and geochemical signatures in high-pressure, low-temperature metamorphic rocks as recorders of subduction zone processes, Sikinos and Ios islands, Greece. *Chemical Geology*, *582*, 1–22. https://doi.org/10.1016/j.chemgeo.2021.120447

Powell, J., Schneider, D., Stockli, D., & Fallas, K. (2016). Zircon (U-Th)/He thermochronology of

Neoproterozoic strata from the Mackenzie Mountains, Canada: Implications for the Phanerozoic exhumation and deformation history of the northern Canadian Cordillera. *Tectonics*, *35*(3), 663–689. https://doi.org/10.1002/2015TC003989

Prikryl, R. (2001). Some microstructural aspects of strength variation in rocks. *International Journal of Rock Mechanics and Mining Sciences*, *38*, 671–682.

Prior, D. J., Boyle, Alan, P., Brenker, F., Cheadle, M. C., Aay, A., Lopez, G., et al. (1999). The application of electron backscatter diffraction and orientation contrast imaging in the SEM to textural problems in rocks. *American Mineralogist*, *84*, 1741–1759.

Rabillard, A., Arbaret, L., Jolivet, L., Breton, N. Le, Gumiaux, C., Augier, R., & Grasemann, B. (2015). Interactions between plutonism and detachments during metamorphic core complex formation, Serifos Island (Cyclades, Greece), 1080–1106. https://doi.org/10.1002/2014TC003650

Rabillard, A., Jolivet, L., Arbaret, L., & Bessière, E. (2018). Synextensional granitoids and detachment systems within Cycladic Metamorphic Core Complexes (Aegean Sea, Greece): Toward a regional tectonomagmatic model. *Tectonics*, 2328–2362. https://doi.org/10.1029/2017TC004697

Reinecke, T., Altherr, R., Hartung, B., Hatzipanagiotou, K., Kreuzer, H., Harre, W., et al. (1982). Remnants of a Late Cretaceous high tempearture belt on the island of Anafi (Cyclades, Greece). *Neues Jahrbuch Fur Mineralogie*, *145*, 157–182.

Reiners, P. W., & Brandon, M. T. (2006). Using Thermochronology to Understand Orogenic Erosion. *Annu*, *34*, 419–466. https://doi.org/10.1146/annurev.earth.34.031405.125202

Reiners, P. W., Farley, K. A., & Hickes, H. J. (2002). He diffusion and (U–Th)/He thermochronometry of zircon: Initial results from Fish Canyon Tuff and Gold Butte. *Tectonophysics*, *349*, 297–308.

Reiners, P. W., Spell, T. L., Nicolescu, S., & Zanetti, Kathleen, A. (2004). Zircon (U-Th)/He thermochronometry: He diffusion and comparisons with 40Ar/39Ar dating. *Geochimica et Cosmochimica Acta*, *68*(8), 1857–1887. https://doi.org/10.1016/j.gca.2003.10.021

Reischmann, T. (1998). Pre-Alpine origin of tectonic units from the metamorphic complex of Naxos, Greece, identified by single zircon Pb/Pb dating. *Bulletin of the Geological Society of Greece*, *XXXII*(3), 101–111.

Renne, P. R., & Norman, E. B. (2001). Determination of the half-life of 37Ar by mass spectrometry. *Physical Review C Nuclear Physics*, *63*, 1–3.

Renne, P. R., Swisher, C. C., Deino, A. L., Karner, D. B., Owens, T. L., & DePaolo, D. J. (1998). Intercalibration of standards, absolute ages and uncertainties in 40Ar/39Ar dating. *Chemical Geology*, *145*, 117–152.

Reynolds, S., & Rehrig, W. (1980). Mid-Tertiary plutonism and mylonitization, South Mountains, central Arizona. In M. Crittenden, P. Coney, & G. Davis (Eds.), *Cordilleran metamorphic core complexes* (pp. 159–175). Boulder, Colorado.

Ricou, L. E., Dercourt, J., Geyssant, J., Grandjacquet, C., Lepvrier, C., & Biju-Duval, B. (1986). Geological constraints on the Alpine evolution of the Mediterranean Tethys. *Tectonophysics*, *123*, 83–122.

Ricou, L. E., Burg, J., Godfriaux, I., & Ivanov, Z. (1998). Rhodope and Vardar: The metamorphic and the olistostromic paired belts related to the Cretaceous subduction under Europe. *Geodinamica Acta*, *11*(6), 285–309. https://doi.org/10.1080/09853111.1998.11105326

Ring, U., & Layer, P. W. (2003). High-pressure metamorphism in the Aegean, eastern Mediterranean: Underplating and exhumation from the Late Cretaceous until the Miocene to recent above the retreating Hellenic subduction zone. *Tectonics*, *22*(3), 1–23. https://doi.org/10.1029/2001TC001350

Ring, U., Glodny, J., Will, T., & Thomson, S. (2007). An Oligocene extrusion wedge of blueschist-facies nappes on Evia, Aegean Sea, Greece: Implications for the early exhumation of high-pressure rocks. *Journal of the Geological Society*, *164*(3), 637–652. https://doi.org/10.1144/0016-76492006-041

Ring, U., Will, T., Glodny, J., Kumerics, C., Gessner, K., Thomson, S., et al. (2007). Early exhumation of high-pressure rocks in extrusion wedges: Cycladic blueschist unit in the eastern Aegean, Greece, and Turkey. *Tectonics*, *26*, 1–23.

Ring, U., Glodny, J., Will, T., & Thomson, S. (2010). The Hellenic Subduction System: High-pressure metamorphism, exhumation, normal faulting, and large-scale extension. *Annual Reviews in Earth and Planetary Sceince*, *38*, 45–70. https://doi.org/10.1146/annurev.earth.050708.170910

Robertson, A. H. F. (2002). Overview of the genesis and emplacement of Mesozoic ophiolites in the Eastern Mediterranean Tethyan region. *Lithos*, *65*, 1–67.

Robertson, A. H. F., & Dixon, J. E. (1984). Introduction: Aspects of the geological evolution of the Eastern Mediterranean. *Geological Society Special Publication*, *17*, 1–74. https://doi.org/10.1144/GSL.SP.1984.017.01.02

Robertson, A. H. F., Clift, P. D., Degnan, P. J., & Jones, G. (1991). Palaeogeographic and palaeotectonic evolution of the Eastern Mediterranean Neotethys. *Palaeogeography, Palaeoclimatology, Palaeoecology*, *87*, 289–343.

Robertson, S. (1999). BGS rock classification scheme volume 2: Classification of metamorphic rocks. *British Geological Survey Research Report*, *RR 99–02*.

Roche, V., Sternai, P., Guillou-frottier, L., & Menant, A. (2018). Emplacement of metamorphic core complexes and associated geothermal systems controlled by slab dynamics Emplacement of metamorphic core complexes and associated geothermal systems controlled by slab dynamics. *Earth and Planetary Science Letters*, *498*, 322–333. https://doi.org/10.1016/j.epsl.2018.06.043

Roche, V., Jolivet, L., Papanikolaou, D., Bozkurt, E., Menant, A., & Rimmele, G. (2019). Slab fragmentation beneath the Aegean/Anatolia transition zone: Insights from the tectonic and metamorphic evolution of the Eastern Aegean region. *Tectonophysics*, *754*, 101–129.

Roddick. (1983). High precision intercalibration of 40Ar-39Ar standards. *Geochimica et Cosmochimica Acta*, *47*, 887–898.

Rogowitz, A., White, J. C., & Grasemann, B. (2016). Strain localization in ultramylonitic marbles by simultaneous activation of dislocation motion and grain boundary sliding (Syros, Greece). *Solid Earth*, *7*(2), 355–366. https://doi.org/10.5194/se-7-355-2016

Rohrmeier, M. K., von Quadt, A., Driesner, T., Heinrich, C. A., Handler, R., Ovtcharova, M., et al. (2013). Post-orogenic extension and hydrothermal ore formation: High-precision geochronology of the central rhodopian metamorphic core complex. *Economic Geology*, *106*, 691–718.

Ross, J. (2019). Pychron. https://doi.org/doi:10.5281/zenodo.9884.

Royden, L. H. (1993). The tectonic expression of slab pull at continental convergent boundaries. *Tectonics*, *12*(2), 303–325.

Rutter, E. H., & Brodie, K. H. (1988). The role of tectonic grain size reduction in the rheological

stratification of the lithosphere. *Geologische Rundschau*, *77*(1), 295–308. https://doi.org/10.1007/BF01848691

Rutter, E. H., & Casey, M. (1994). Preferred crystallographic orientation development during the plastic and superplastic flow of calcite rocks. *Journal of Structural Geology*, *16*(10), 1430–1446.

Rybacki, E., Wirth, R., & Dresen, G. (2003). Rheology of calcite–quartz aggregates deformed to large strain in torsion. *Journal of Geophysical Research*, *108*, 1–24. https://doi.org/10.1029/2002JB001833

Rybacki, E., Janssen, C., Wirth, R., Chen, K., Wenk, H. R., Stromeyer, D., & Dresen, G. (2011). Low-temperature deformation in calcite veins of SAFOD core samples (San Andreas Fault)-Microstructural analysis and implications for fault rheology. *Tectonophysics*, *509*(1–2), 107–119. https://doi.org/10.1016/j.tecto.2011.05.014

Sanchez-Gomez, M., Avigad, D., & Heimann, A. (2002). Geochronology of clasts in allochthonous Miocene sedimentary sequences on Mykonos and Paros Islands: Implications for back-arc extension in the Aegean Sea. *Journal of the Geological Society*, *159*, 45–60. https://doi.org/10.1144/0016-764901031

Scheffer, C., Vanderhaeghe, O., Lanari, P., Tarantola, A., Ponthus, L., Photiades, A., & France, L. (2016). Syn- to post-orogenic exhumation of metamorphic nappes: Structure and thermobarometry of the western Attic-Cycladic metamorphic complex (Lavrion, Greece). *Journal of Geodynamics*, *96*, 174–193. https://doi.org/10.1016/j.jog.2015.08.005

Schenker, F. L., Burg, J., Kostopoulos, D., Moulas, E., Larionov, A., Quadt, A., et al. (2014). From Mesoproterozoic magmatism to collisional Cretaceous anatexis: Tectonomagmatic history of the Pelagonian Zone, Greece. *Tectonics*, *33*, 1–25. https://doi.org/10.1002/2014TC003563

Schenker, F. L., Fellin, M. G., & Burg, J. P. (2015). Polyphase evolution of Pelagonia (northern Greece) revealed by geological and fission-track data. *Solid Earth*, *6*(1), 285–302. https://doi.org/10.5194/se-6-285-2015

Schermer, E. R., Lux, D. R., & Burchfiel, B. C. (1990). Temperature-time history of subducted continetal crust, Mount Olympos region, Greece. *Tectonics*, *9*(5), 1165–1195.

Scherreiks, R., Zone, P., & Evvoia, N. E. (2000). Platform margin and oceanic sedimentation in a divergent and convergent plate setting (Jurassic, Pelagonian Zone, NE Evvoia, Greece). *International Journal of Earth Sciences*, *89*, 90–107.

Scherreiks, R., Meléndez, G., BouDagher-Fadel, M., Fermeli, G., & Bosence, D. (2014). Stratigraphy and tectonics of a time-transgressive ophiolite obduction onto the eastern margin of the Pelagonian platform from Late Bathonian until Valanginian time, exemplified in northern Evvoia, Greece. *International Journal of Earth Sciences*, *103*(8), 2191–2216. https://doi.org/10.1007/s00531-014-1036-3

Schliestedt, M., & Matthews, A. (1987). Transformation of blueschist to greenschist facies rocks as a consequence of fluid infiltration, Sifnos (Cyclades), Greece. *Contributions to Mineralogy and Petrology*, *97*, 237–250.

Schmid, S. M. (1982). Microfabric studies as indicators of deformation mechanisms and flow laws operative. In K. J. Hsu (Ed.), *Mountain building processes* (pp. 95–110). London: Academic Press.

Schmid, S. M. (1983). Microfabric studies as indicators of deformation mechanisms and flow laws operative in mountain building. *Mountain Building Processes*, (May), 95–110.

Schmid, S. M., Panozzot, R., & Bauer, S. (1987). Simple shear experiments on calcite rocks: rheology and microfabric. *Journal of Structural Geology*, *9*(5), 747–778.

Schmid, S. M., Fügenschuh, B., Kounov, A., Mat, L., Pleuger, J., Schefer, S., et al. (2020). Tectonic units of the Alpine collision zone between Eastern Alps and western Turkey, *78*, 308–374. https://doi.org/10.1016/j.gr.2019.07.005

Schmitz, M. D., Bowring, S. A., & Ireland, T. R. (2003). Evaluation of Duluth Complex anorthositic series (AS3) zircon as a U-Pb geochronological standard: New high-precision isotope dilution thermal ionization mass spectrometry results. *Geochimica et Cosmochimica Acta*, *67*(19), 3665–3672. https://doi.org/10.1016/S0016-7037(03)00200-X

Schneider, D. A., Senkowski, C., Vogel, H., Grasemann, B., Iglseder, C., & Schmitt, A. K. (2011). Eocene tectonometamorphism on Serifos (western Cyclades) deduced from zircon depth-profiling geochronology and mica thermochronology. *Lithos*, *125*(1–2), 151–172. https://doi.org/10.1016/j.lithos.2011.02.005

Schneider, D. A., Grasemann, B., Lion, A., Soukis, K., & Draganits, E. (2018). Geodynamic significance of the Santorini Detachment System (Cyclades, Greece). *Terra Nova*, *00*(March), 1–9. https://doi.org/10.1111/ter.12357

Schöpfer, M. P. J., Childs, C., Manzocchi, T., Walsh, J. J., Nicol, A., & Grasemann, B. (2017). The emergence of asymmetric normal fault systems under symmetric boundary conditions. *Journal of Structural Geology*, *104*, 159–171. https://doi.org/10.1016/j.jsg.2017.10.006

Schulmann, K., Maierová, P., Jeřábek, P., Lexa, O., Ulrich, S., Hobbs, B., & Ord, A. (2023). Deformation mechanisms and rheology inversion of jointly deformed marble and quartzite in natural thermal gradient. *Journal of Structural Geology*, *173*(October 2022). https://doi.org/10.1016/j.jsg.2023.104892

Seck, H., Kotz, J., Okrusch, M., Seidel, E., & Stosch, H. G. (1996). Geochemistry of a meta-ophiolite suite: An association of metagabbros, eclogites and glaucophanites on the island of Syros, Greece. *European Journal of Mineralogy*, *8*(3), 607–623.

Seman, S. M. (2016). *The tectonostratigraphy of the Cycladic Blueschist Unit and new garnet geo/thermochronology techniques (unpublished thesis)*. University of Texas at Austin.

Seman, S. M., Stockli, D. F., & Soukis, K. (2017). The provenance and internal structure of the Cycladic Blueschist Unit revealed by detrital zircon geochronology, Western Cyclades, Greece. *Tectonics*, *36*(7), 1407–1429. https://doi.org/10.1002/2016TC004378

Sharp, I. R., & Robertson, A. H. F. (2006). Tectonic-sedimentary evolution of the western margin of the Mesozoic Vardar Ocean: Evidence from the Pelagonian and Almopias zones, northern Greece. *Geological Society Special Publication*, *260*, 373–412. https://doi.org/10.1144/GSL.SP.2006.260.01.16

Sibson, R. H. (1977). Fault rocks and fault mechanisms. *Journal of the Geological Society*, *133*(3), 191–213. https://doi.org/10.1144/gsjgs.133.3.0191

Siivola, J., & Schmid, R. (2007). Recommendations by the IUGS subcommission on the Systematics of metamorphic rocks: web version 01.02.07. *BGS*.

Skarpelis, N. (2002). Geodynamics and evolution of the Miocene mineralization in the Cycladic-Pelagonian Belt, Hellenides. *Bulletin of the Geological Society of Greece*, *34*(6), 2191–2206.

Skarpelis, N., & Liati, A. (1990). The prevolcanic basement of Thera at Athinios: Metamorphism,

plutonism and mineralization. In D. Hardy (Ed.), *Proceedings of the Third International Congress "Thera and the Aegean World"* (pp. 172–182). London: The Thera Foundation.

Skourlis, K., & Doutsos, T. (2003). The Pindos Fold-and-thrust belt (Greece): Inversion kinematics of a passive continental margin. *International Journal of Earth Sciences*, *92*, 891–903. https://doi.org/10.1007/s00531-003-0365-4

Slama, J., Kosler, J., Condon, D. J., Crowley, J. L., Gerdes, A., Hancher, J. M., et al. (2008). Plešovice zircon — A new natural reference material for U–Pb and Hf isotopic microanalysis. *Chemical Geology*, *249*, 1–35. https://doi.org/10.1016/j.chemgeo.2007.11.005

Smith, A. (1993). Tectonic significance of the Hellenic-Dinaric ophiolites. *Geological Society Special Publication*, *76*, 213–243.

Smith, A., Hynes, A. J., Menzies, M., Nisber, E. G., Price, I., Welland, M. J., & Ferriere, J. (1975). The stratigraphy of the Othris Mountains, eastern Central Greece: A deformed Mesozoic continental margin sequence. *Eclogae Geologicae Helvetiae*, *68*(3), 463–481.

Soukis, K., & Stockli, D. F. (2013). Structural and thermochronometric evidence for multi-stage exhumation of southern Syros, Cycladic islands, Greece. *Tectonophysics*, *595–596*, 148–164. https://doi.org/10.1016/j.tecto.2012.05.017

Spanos, D., Xypolias, P., & Koukouvelas, I. (2015). Vorticity analysis in calcite tectonites: An example from the Attico-Cycladic massif (Attica , Greece). *Journal of Structural Geology*, *80*, 120–132. https://doi.org/10.1016/j.jsg.2015.08.014

Spear, F. S., & Cheney, J. T. (1989). A petrogenetic grid for pelitic schists in the system SiO2-Al2O3-FeO-MgO-K2O-H2O. *Contributions to Mineralogy and Petrology1*, *101*, 149–164.

Stampfli, G. M., Vavassis, I., de Bono, A., & Rosselet, F. (2003). Remnants of the Paleotethys oceanic suture-zone in the western Tethyan area. *Bulletin of the Geological Society of Italy*, *2*, 1–23.

Steiger, R. H., & Jäger, E. (1977). Subcommission on geochronology: Convention on the use of decay constants in geo- and cosmochronology. *Earth and Planetary Science Letters*, *36*, 359–362.

Stouraiti, C., Lekkas, S., Lozios, S., & Kanellopoulos, C. (2016). Iron-oxide mineralization of Sesi, Koropi (S . Hymittos, Greece): Mineralization within a detachment zone. *Bulletin of the Geological Society of Greece*, 1–13. https://doi.org/10.12681/bgsg.11949

Stouraiti, C., Soukis, K., Voudouris, P., Mavrogonatos, C., Stylianos, L., Lekkas, S., et al. (2019). Silver-rich sulfide mineralization in the northwestern termination of the Western Cycladic Detachment System, at Agios Ioannis Kynigos, Hymittos Mt. (Attica, Greece): A mineralogical, geochemical and stable isotope study. *Ore Geology Reviews*, *111*(June), 1–16. https://doi.org/10.1016/j.oregeorev.2019.102992

Terry, J., & Mercier, M. (1971). Sur l'existence d'une série détritique berriasienne intercalée entre la nappe des ophiolites et le flysch éocène de la nappe du Pinde (Pinde septentrional, Grèce). *Congress of the Geological Society of France*, *2*, 71–73.

Tobisch, O. T., & Paterson, S. R. (1988). Analysis and interpretation of composite foliations in areas of progressive deformation. *Journal of Structural Geology*, *10*(7), 745–754.

Tomaschek, F., Kennedy, A. K., Villa, I. M., Lagos, M., & Ballhaus, C. (2003). Zircons from Syros, Cyclades, Greece: Recrystallization and mobilization of zircon during high-pressure metamorphism. *Journal of Petrology*, *44*(11), 1977–2002. https://doi.org/10.1093/petrology/egg067

Tschegg, C., & Grasemann, B. (2009). Deformation and alteration of a granodiorite during low-angle normal faulting (Serifos, Greece). *Lithosphere*, *1*(3), 139–154. https://doi.org/10.1130/L33.1

Turner, F. J., & Weiss, L. E. (1963). *Structural analysis of metamorphic tectonites*. New York: McGraw-Hill.

Ulrich, S., Schulmann, K., & Casey, M. (2002). Microstructural evolution and rheological behaviour of marbles deformed at different crustal levels. *Journal of Structural Geology*, *24*, 979–995.

Ulrich, S., Hobbs, B. E., Ord, A., & Schulmann, K. (2020). The relative strengths of deforming mineral phase assemblages: Geometrically necessary deformation mechanisms. *Journal of Structural Geology*, *137*(March), 1–16. https://doi.org/10.1016/j.jsg.2020.104056

Urai, J. L., Schuiling, R. D., & Jansen, J. B. H. (1990). Alpine deformation on Naxos (Greece). In R. J. Knipe & E. H. Rutter (Eds.), *Deformation Mechanisms, Rheology and Tectonics* (pp. 509–522). Geological Society Special Publication.

Uunk, B., Brouwer, F., ter Voorde, M., & Wijbrans, J. (2018). Understanding phengite argon closure using single grain fusion age distributions in the Cycladic Blueschist Unit on Syros, Greece. *Earth and Planetary Science Letters*, *484*, 192–203. https://doi.org/10.1016/j.epsl.2017.12.031

Uunk, B., Brouwer, F., Paz-álvarez, M. De, & Zuilen, K. Van. (2022). Consistent detachment of supracrustal rocks from a fixed subduction depth in the Cyclades. *Earth and Planetary Science Letters*, *584*, 1–16. https://doi.org/10.1016/j.epsl.2022.117479

Vanderhaeghe, O. (2004). Structural development of the Naxos migmatite dome. In D. L. Whitney, C. Teyssier, & C. S. Siddoway (Eds.), *Gneiss domes in orogeny: Geological Society of America, Special Paper 380* (pp. 211–228). Boulder, Colorado. https://doi.org/10.1130/0-8137-2380-9.211

Vasconcelos, C., Mckenzie, J. A., Bernasconi, S., Grujic, D., & Tien, A. J. (1995). Microbial mediation as a possible mechanism for natural dolomite formation at low temperatures. *Nature*, *377*(September), 220–222.

Vermeesch, P. (2012). On the visualisation of detrital age distributions. *Chemical Geology*, *312–313*, 190–194. https://doi.org/10.1016/j.chemgeo.2012.04.021

Vermeesch, P. (2018). IsoplotR: A free and open toolbox for geochronology. *Geoscience Frontiers*, *9*(5). https://doi.org/10.1016/j.gsf.2018.04.001

Vermeesch, P. (2021). Maximum depositional age estimation revisited. *Geoscience Frontiers*, *12*(2), 843–850. https://doi.org/10.1016/j.gsf.2020.08.008

Vidal, O., & Parra, T. (2000). Exhumation paths of high-pressure metapelites obtained from local equilibria for chlorite-phengite assemblages. *Geological Journal*, *35*(3–4), 139–161. https://doi.org/10.1002/gj.856

Vidal, O., Theye, T., & Chopin, C. (1994). Experimental study of chloritoid stability at high pressure and various fO2 conditions. *Contributions to Mineralogy and Petrology*, *118*(3), 256–270.

Di Vincenzo, G., Ghiribelli, B., Giorgetti, G., & Palmeri, R. (2001). Evidence of a close link between petrology and isotope records: constraints from SEM, EMP, TEM and in situ 40Ar-39Ar laser analyses on multiple generations of white micas (Lanterman Range, Antarctica). *Earth and Planetary Science Letters*, *192*, 389–405.

Voudouris, P., Melfos, V., Spry, P., & Economou-Eliopoulos, M. (2008). Mineralogical and fluid inclusion constraints on the evolution of the Plaka intrusion-related ore system, Lavrion, Greece.

Mineralogy and Petrology, *93*, 79–110. https://doi.org/10.1007/s00710-007-0218-0

Warren, C. J., Hanke, F., & Kelley, S. P. (2012). When can muscovite 40Ar/39Ar dating constrain the timing of metamorphic exhumation? *Chemical Geology*, *291*, 79–86. https://doi.org/10.1016/j.chemgeo.2011.09.017

Warren, J. M., & Hirth, G. (2006). Grain size sensitive deformation mechanisms in naturally deformed peridotites. *Earth and Planetary Science Letters*, *248*, 438–450. https://doi.org/10.1016/j.epsl.2006.06.006

Watson, E. B., Wanser, K. H., & Farley, K. A. (2010). Anisotropic diffusion in a finite cylinder, with geochemical applications. *Geochimica et Cosmochimica Acta*, *74*, 614–633. https://doi.org/10.1016/j.gca.2009.10.013

Wenk, H.-R., & Christie, J. M. (1991). Comments on the interpretation of deformation textures in rocks. *Journal of Structural Geology*, *13*(10), 1091–1110.

Wernicke, B. (1981). Low-angle normal faults in the Basin and Range Province: Nappe tectonics in an extending orogen. *Nature*, *291*, 645–648.

Wernicke, B. (1985). Uniform-sense normal simple shear of the continental lithosphere. *Canadian Journal of Earth Sciences*, *22*(1), 108–125. https://doi.org/10.1139/e85-009

Wernicke, B., & Axen, G. J. (1988). On the role of isostasy in the evolution of normal fault systems. *Geology*, *16*, 848–851.

Wernicke, B., & Burchfiel, B. C. (1982). Modes of extensional tectonics. *Journal of Structural Geology*, *4*(2), 105–115. https://doi.org/10.1016/0191-8141(82)90021-9

Wheeler, J., Prior, D. J., Jiang, Z., Spiess, R., & Trimby, P. W. (2001). The petrological significance of misorientations between grains. *Contributions to Mineralogy and Petrology*, *141*, 109–124. https://doi.org/10.1007/s004100000225

White, J. C., & White, S. H. (1980). High-voltage transmission electron microscopy of naturally deformed polycrystalline dolomite. *Tectonophysics*, *66*, 35–54.

Wiedenbeck, M., Griffin, W. L., & von Quadt, A. (2007). Three natural zircon standards for U-Th-Pb, Lu-Hf, trace element and REE analyses. *Geostandards and Geoanalytical Research*, *19*(1), 1–23. https://doi.org/10.1111/j.1751-908X.1995.tb00147.x

Wiesmayr, G., & Grasemann, B. (2005). Sense and non-sense of shear in flanking structures with layer-parallel shortening: Implications for fault-related folds. *Journal of Structural Geology*, *27*, 249–264. https://doi.org/10.1016/j.jsg.2004.09.001

Wijbrans, J. R., & McDougall, I. (1986). 40Ar/39Ar dating of white micas from an Alpine high-pressure metamorphic belt on Naxos (Greece): The resetting of the argon isotopic system. *Contributions to Mineralogy and Petrology*, *93*(2), 187–194. https://doi.org/10.1007/BF00371320

Wijbrans, J. R., & McDougall, I. (1988). Metamorphic evolution of the Attic Cycladic Metamorphic Belt. *Journal of Metamorphic Geology*, *6*, 571–594.

Wijbrans, J. R., Schliestedt, M., & York, D. (1990). Single grain argon laser probe dating of phengites from the blueschist to greenschist transition on Sifnos (Cyclades, Greece). *Contributions to Mineralogy and Petrology*, *104*(5), 582–593. https://doi.org/10.1007/BF00306666

Wind, S. C., Schneider, D. A., Hannington, M. D., & McFarlane, C. R. M. (2020). Regional similarities in lead isotopes and trace elements in galena of the Cyclades Mineral District, Greece with

implications for the underlying basement. *Lithos*, *366–367*, 1–27. https://doi.org/10.1016/j.lithos.2020.105559

Wolfe, M. R., & Stockli, D. F. (2010). Zircon (U–Th)/He thermochronometry in the KTB drill hole, Germany, and its implications for bulk He diffusion kinetics in zircon. *Earth and Planetary Science Letters*, *295*(1–2), 69–82. https://doi.org/10.1016/j.epsl.2010.03.025

Woodward, N. B., Wojtal, S., Paul, J. B., & Zadins, Z. Z. (1988). Partitioning of deformation within several external thrust zones of the Appalachian orogen. *Journal of Geology*, *96*(3), 351–361. https://doi.org/10.1086/629225

Xypolias, P., Kokkalas, S., & Skourlis, K. (2003). Upward extrusion and subsequent transpression as a possible mechanism for the exhumation of HP/LT rocks in Evia Island (Aegean Sea, Greece). *Journal of Geodynamics*, *35*(3), 303–332. https://doi.org/10.1016/S0264-3707(02)00131-X

Xypolias, P., Iliopoulos, I., Chatzaras, V., & Kokkalas, S. (2012). Subduction- and exhumation-related structures in the Cycladic Blueschists: Insights from south Evia Island (Aegean region, Greece). *Tectonics*, *31*, 1–22. https://doi.org/10.1029/2011TC002946

Yarwood, G. A., & Aftalion, M. (1976). Field relations and U-Pb geochronology of a granite from the Pelagonian Zone of the Hellenides (High Pieira, Greece). *Bulletin de La Société Géologique de France*, *18*(2), 259–264.

Zak, J., Svojtka, M., Gerdjikov, I., Kounov, A., & Vangelov, D. A. (2021). The Balkan terranes: A missing link between the eastern and western segments of the Avalonian-Cadomian orogenic belt? *International Geology Review*, *64*(17), 2389–2415. https://doi.org/10.1080/00206814.2020.1861486

Zlatkin, O., Avigad, D., & Gerdes, A. (2014). Peri-Amazonian provenance of the proto-Pelagonian basement (Greece), from zircon U-Pb geochronology and Lu-Hf isotopic geochemistry. *Lithos*, *184–187*, 379–392. https://doi.org/10.1016/j.lithos.2013.11.010

Zlatkin, O., Avigad, D., & Gerdes, A. (2017). The Pelagonian terrane of Greece in the peri-Gondwanan mosaic of the Eastern Mediterranean: Implications for the geological evolution of Avalonia. *Precambrian Research*, *290*, 163–183. https://doi.org/10.1016/j.precamres.2017.01.005

Zlatkin, O., Avigad, D., & Gerdes, A. (2018). New detrital zircon geochronology from the Cycladic Basement (Greece): Implications for the Paleozoic accretion of peri-Gondwanan terranes to Laurussia. *Tectonics*, *37*(12), 4679–4699. https://doi.org/10.1029/2018TC005046

Supplementary information

SI Chapter 2

This data repository includes: A detailed description of the methodology for each of the analytical processes (**S2.1**), a brief review of zircon (U-Th)/He versus effective spherical radius (ESR) and effective uranium (eU) plots (**S2.2**) along with the figure (**Figure S2.3**), their results and interpretation. Additional figures comprise a map of $^{40}Ar/^{39}Ar$ and (U-Th)/He ages (**Figure S2.1**), white mica EDS maps (**Figure S2.2**) thin section photomicrographs (Figure S2.4), age vs. ^{39}Ar graphs (**Figure S2.5**) and representative white mica from characterized populations (**Figure S2.6**). Tables include: thin section petrography (**Table S2.1**), electron microprobe analysis (EMPA) results (**Table S2.2**), white mica $^{40}Ar/^{39}Ar$ analysis results (**Table S2.3**), and zircon (U-Th)/He analysis results (**Table S2.4**).

S2.1 Methodology

S2.1.1 Sampling Strategy

Sampling for this study was conducted throughout the ~ 200 km^2 study area in Attica, Greece (**Figure 2.1**; **Figure 2.2**). The bedrock geology of the study area is characterized by several major low-angle detachments, petrological samples were collected to fully characterize the lithologies and tectonostratigraphy of Mt. Hymittos and the surrounding lowlands. Geochronological samples were selected from white mica and/or zircon bearing lithologies within the 3 tectonostratigraphic packages to determine a thermochronologic history. Samples were not selected as a series of vertical transects as the wavelengths of the detachments are long enough to invalidate age-elevation thermochronology (Ehlers, 2005).

S2.1.2 Petrographic Methods

Oriented and non-oriented thin sections were produced in the XZ plane of the kinematic reference frame with respect to the dominant deformation fabric. In this system, X points downdip and is parallel to mineral lineation azimuths parallel to the plane of the foliation; Z is normal to the foliation plane (Lister & Williams, 1979). Rock samples from the Upper (n: 15) Middle (n: 43) and Lower Unit (n: 27) were analyzed by plane- and cross-polarized light microscopy. Analysis focused on mineralogy, microstructures, and kinematic indicators. Metamorphic rocks are classified according to Robertson (1999). Petrographic observations are briefly summarized in Table S2.1.

S2.1.3 White mica $^{40}Ar/^{39}Ar$ Geochronology

White mica is susceptible to both chemical and physical weathering; thus, detrital white mica are unlikely to survive multiple episodes of uplift, erosion and deposition and are useful for examining the most recent tectonic events in polydeformed terranes (Gutiérrez-Alonso et al., 2005; Uunk et al., 2018). In low-grade metamorphic rocks (never heated above 350°C) white mica $^{40}Ar/^{39}Ar$ geochronology may preserve a detrital source terrane history or reflect in-situ white mica formation below the closure temperature of white mica. In medium-to-high grade metamorphic or igneous rocks white mica $^{40}Ar/^{39}Ar$ geochronology is influenced by many parameters, including rate of cooling, diffusion domain and grain size, degree of neocrystallization, pressure, and chemical composition (Dodson, 1973; Harrison et al., 2009; Warren et al., 2012). For example, Mg and/or Fe substitution in phengite has been shown to have an effect on the closure temperature of white mica; muscovitic end-members exhibit closure temperatures of 400±50 °C (Harrison et al., 2009), whereas phengitic closure temperatures may range as high as 600±50°C (Augier et al., 2005; Laurent et al., 2017; Di Vincenzo et al., 2001).

25 new multiple single-grain fusion $^{40}Ar/^{39}Ar$ analyses were conducted on white mica from Mount Hymittos. The advantage of multiple single-grain fusion is that it constrains age heterogeneity within a sample (meso-scale), and across multiple samples (macro-scale). As such this technique is particularly useful for polydeformed terranes as age variations within samples may be the product of repeated heating, metamorphism and deformation that is not captured by the step-heating method (e.g. Uunk et al., 2018; Schneider et al., 2018; Coleman et al., 2019). After mechanical mineral separation from the host rock to achieve 99% purity, white mica with grain sizes between 106 and 250 μm were picked and washed with dilute HCl. Up to 8 individual grains were analyzed per sample. All $^{40}Ar/^{39}Ar$ analytical work was performed at the University of Manitoba using a multi-collector Thermo Fisher Scientific ARGUSVI mass spectrometer, linked to a stainless steel Thermo Fisher Scientific extraction/purification line and Photon Machines (55 W) Fusions 10.6 CO_2 laser. Argon isotopes were measured using the following configuration:

For samples analyzed in 2017 (Irradiation 1)

^{40}Ar (H1; 1 x 10^{12} Ω resistor), ^{39}Ar (AX; 1 x 10^{12} Ω resistor), ^{38}Ar (L1; 1 x 10^{12} Ω resistor), ^{37}Ar (L2; 1 x 10^{12} Ω resistor) and ^{36}Ar (compact discrete dynode [CDD]).

For samples analyzed in 2019 (Irradiation 2)

^{40}Ar (H1; 1 x 10^{12} Ω resistor), ^{39}Ar (AX; 1 x 10^{13} Ω resistor), ^{38}Ar (L1; 1 x 10^{13} Ω resistor), ^{37}Ar (L2; 1 x 10^{13} Ω resistor) and ^{36}Ar (CDD).

The sensitivity for argon measurements is ~6.3 x 10^{17} moles/fA as determined from measured aliquots of Fish Canyon Sanidine (Dazé et al., 2003; Kuiper et al., 2008).

Standards and unknowns were placed in 2 mm deep wells in 18 mm diameter aluminium disks, with standards placed strategically so that the lateral neutron flux gradients across the disk

could be evaluated. Planar regressions were fit to the standard data, and the $^{40}Ar/^{39}Ar$ neutron fluence parameter, J, interpolated for the unknowns. All specimens were irradiated in the Cadmium-lined, in-core CLICIT facility of the Oregon State University TRIGA reactor. Samples with the prefix 17MC and 18MC were irradiated for 10 hours and 70 hours, respectively. In both irradiations the flux monitor used was Fish Canyon sanidine (Kuiper et al., 2008).

Irradiated samples were placed in a Cu sample tray, with a KBr cover slip, in a stainless-steel high vacuum extraction line and baked with an infrared lamp for 24 hours. Single crystals were either fused or step-heated using the laser, and reactive gases were removed, after ~ 3 minutes, by three NP-10 SAES getters (two at room temperature and one at 450 °C) prior to being admitted to an ARGUSVI mass spectrometer by expansion. Five argon isotopes were measured simultaneously over a period of 6 minutes. Measured isotope abundances were corrected for extraction-line blanks, which were determined before every sample analysis. For samples irradiated in the first irradiation, measured extraction line blanks averaged ~6 fA for mass 40 and ~0.004 fA for mass 36.

Detector intercalibration (IC) between the different faraday cups was monitored (in Qtegra) every two days by peak hopping ^{40}Ar. The intercalibration factor between H1 and the CDD was measured with the unknowns by online analysis of air pipettes. For the first irradiation, detector IC values are ICH1: 1.0000, ICAX: 1.0745, ICL1: 1.0637, and ICL2: 1.0534, with an error of ~0.2%. The intercalibration factor between H1 and the CDD was measured using 50 air aliquots interspersed with the unknowns resulting in ICCDD: 1.0054 ± 0.0005 per amu.

A value of 295.5 was used for the atmospheric $^{40}Ar/^{36}Ar$ ratio (Steiger & Jäger, 1977) for the purposes of routine measurement of mass spectrometer discrimination using air aliquots, and correction for atmospheric argon in the $^{40}Ar/^{39}Ar$ age calculation. Corrections are made for

neutron-induced ^{40}Ar from potassium, ^{39}Ar and ^{36}Ar from calcium, and ^{36}Ar from chlorine (Renne et al., 1998; Renne & Norman, 2001; Roddick, 1983). For the first irradiation, data collection was performed using the Pychron software, whereas data reduction, error propagation, age calculation, and plotting were performed using MassSpec software (version 8.091). The decay constants used were those recommended by Min et al. (2000). For the second irradiation, data collection and reduction was performed using Pychron (Ross, 2019). The decay constants used were those recommended by Min et al. (2000).

S2.1.4 Zircon (U-Th)/He Thermochronology

In the zircon-helium system, ^{4}He is produced by α-emission during decay of uranium and thorium. At temperatures above 180-200°C zircon acts as an open system, and He diffuses out of the crystal (Reiners et al., 2002, 2004). For temperatures between 180°C and 130°C a partial retention zone exists wherein a portion of radiogenic He will accumulate within the zircon (Wolfe & Stockli, 2010). At temperatures below 130°C zircon is a fully closed system to He. Thus, for rapidly cooling rocks zircon (U-Th)/He thermochronology records the time at which a rock passed below 180-200°C; for slow cooling rocks, the partial retention zone may produce a spread of ages reflecting partial retention of He during residence within the partial retention zone. If rocks are heated to temperatures between 130-180°C some He will escape from zircon, if the rock subsequently cools below 130°C a partially reset age will be produced (Guenthner et al., 2015).

Zircon (U-Th)/He analyses carried out at the University of Colorado Boulder TRaIL (Thermochronology Research and Instrumentation Lab) used the following methods. Individual mineral grains are handpicked using a Leica M165 binocular microscope equipped with a calibrated digital camera and capable of both reflected and transmitted, polarized light. The grains are screened for quality, including crystal size, shape, and the presence of inclusions. After

characterization, grains are placed into small Nb tubes that are then crimped on both ends. This Nb packet is then loaded into an ASI Alphachron He extraction and measurement line. The packet is placed in the UHV extraction line (~3 X 10^{-8} torr) and heated with a 25W diode laser to ~800-1100°C for 5 to 10 minutes to extract the radiogenic ^{4}He. The degassed ^{4}He is then spiked with approximately 13 ncc of pure ^{3}He, cleaned via interaction with two SAES getters, and analyzed on a Balzers PrismaPlus QME 220 quadrupole mass spectrometer. This procedure is repeated at least once to ensure complete mineral degassing. Degassed grains are then removed from the line and taken to a Class 10 clean lab for dissolution.

Zircon are dissolved using Parr large-capacity dissolution vessels in a multi-step acid-vapor dissolution process. Grains (including the Nb tube) are placed in Ludwig-style Savillex vials, spiked with a ^{235}U - ^{230}Th - ^{145}Nd tracer, and mixed with 200 µl of Optima grade HF. The vials are then capped, stacked in a 125 mL Teflon liner, placed in a Parr dissolution vessel, and baked at 220°C for 72 hours. After cooling, the vials are uncapped and dried down on a 90°C hot plate until dry. The vials then undergo a second round of acid-vapor dissolution, this time with 200 µl of 6N Optima grade HCl in each vial that is baked at 200°C for 24 hours. Vials are then dried down a second time on a hot plate. Once dry, 200 µl of a 7:1 HNO_3:HF mixture is added to each vial, the vial is capped, and cooked on the hot plate at 90°C for 4 hours. Once the zircon are dissolved they are diluted with 1 to 3 mL of doubly-deionized water, and taken to the ICP-MS lab for analysis. Sample solutions, along with normal solutions and blanks, are analyzed for U, Th, and Sm content using either a Thermo Element 2 magnetic sector ICP-MS or an Agilent 7900 quadrupole ICP-MS. After the U, Th, and Sm contents are measured, He dates and all associated data are calculated on a custom spreadsheet using the methods described in Ketcham et al. (2011). Every batch of samples includes standards run sporadically throughout the process to monitor procedures and

maintain consistency from run to run. Long term averages of Fish Canyon Tuff zircons run in the CU TRaIL are 28.7 ± 1.8 Ma (n=150).

S2.1.5 EMPA methods

Detailed investigation of textures, microstructures, and related variations of chemistry in chlorite was conducted using optical microscopy and scanning electron microscope (SEM) coupled with energy-dispersive X-ray spectroscopy (EDS) analyses. Quantitative chemical analyses were performed by electron probe micro-analysis (EPMA).

Following optical petrography, white mica were investigated more fully using a JEOL 6610LV scanning electron microscope (SEM) at the University of Ottawa (Ottawa, Canada). BSE images were produced for white mica in all samples to investigate textures and microstructures. Energy dispersive spectrometer (EDS) chemical maps of Fe, Mg, Mn, Cr, Ni, Na, K, Ca, Ti, Si, Al, O, C, Cl, F, S, and P in white mica were produced to better resolve the distribution of the chemical variation within single mica crystals. An accelerating voltage of 20 kV and a beam current of 200 nA were combined with a spot size of 1 μm to produce maps with a 20 μm pixel size and 100 ms dwell time on each pixel.

Wavelength dispersive X-ray spectroscopy (WDS) was used to determine quantitative mineral chemical composition for eleven samples using the JEOL JXA-8230 SuperProbe at the University of Ottawa (Ottawa, Canada). Analyses were conducted with an accelerating voltage of 20 kV and probe current of 20 nA to focus and concentrate the beam diameter to 5 μm. 2-3 grains of mica per polished section were analyzed to quantify all observable white mica populations. 2-4 points were probed on each mica, more spot analyses were run when mica showed evidence of chemically heterogeneity i.e. core-rim relationships, or intergrowth of several phyllosilicate phases. Analyzed elements and associated standards were: K-sanidine, Ca-diopside, Na-albite, Al-

sanidine, Fe-hematite, Mn-tephroite, Ti-rutile, Si-sanidine, Mg-diopside, Cr-chromite, F-flourite and Cl-tugtupite. Count times were 20 ms/element save for F and Cl which were 40 ms/element.

White mica compositions were calculated following the methodology of Parra, Vidal, & Agard (2002) and Vidal & Parra (2000). In order to discard contaminated analyses, only EMP analyses with oxygen sum between 92-96 wt% and <0.5 wt% TiO_2 + MnO + CaO were retained. Structural formulae were calculated assuming 11 oxygen and that all iron is divalent. Molar fractions of seven end members (Mg- and Fe-Al-celadonite, muscovite, annite, phlogopite, paragonite and pyrophyllite) were calculated by 6 equations assuming the sum of all seven end members is equal to 1. For the result of these calculations see table S2.2.

S2.2 eU vs age vs ESR

As a general rule larger crystals tend to be more retentive than smaller crystals, In (U-Th)/He thermochronology, a sphere is thought to provide a sufficiently accurate estimate of crystal size provided the radius of the model sphere has the same surface to volume ratio as the analyzed crystal (Carlslaw & Jaeger, 1959; Dodson, 1973; Farley et al., 2010; Gautheron & Tassan-got, 2010; Meesters & Dunai, 2002; Watson et al., 2010). This approximation is termed the effective spherical radius (ESR) value and is a first order estimate of the size of a specific crystal. Positive date-ESR trend may indicate that for these zircon populations crystal size is a major control on closure temperature and thus the determined age.

Effective uranium (eU: uranium + thorium) may be a useful proxy for the degree of accumulated radiation damage and therefore retentivity (Guenthner et al., 2013). Radiation damage produces tracks that initially inhibit diffusion; at a critical point these tracks link up and serve as pathways that enhance diffusion, producing an age-eU turnover point (Guenthner et al., 2014). Slow cooled zircon populations exhibit well developed age-eU turnovers, rapidly cooled

zircon populations exhibit less pronounced or not observable turnovers (Guenthner et al., 2013). Thus, age vs. eU plots are an effective method for evaluating the geologic history of zircon, particularly for zircon (and samples) that spent significant time in the partial retention zone (Guenthner et al., 2015; Powell et al., 2016).

Zircon (U-Th)/He date vs. ESR plots were produced for Lower-, Middle- and Upper-Unit zircon (U-Th)/He populations (**Figure S2.3a, b, c**). A single Upper Unit sample displays a strong positive date-ESR trend (17mC045A1; **Figure S2.3a**); a second Upper Unit sample displays a weakly positive date-ESR trend (17MC030A1; **Figure S2.3a**). All other Upper Unit samples exhibit weak-to-moderately negative date-ESR trends (17MC019A1, 17MC050A1, 18MC116A1, 18MC142A1; **Figure S2.3a**). Upper Unit samples display a series of weakly positive date-eU trends at eU values below 350 ppm (**Figure S2.3d**). Samples 17MC019A1, 17MC045A1, 17MC050A1 and 18MC116A2 may exhibit an age-eU turnover point between 200-350 ppm eU, at higher eU values the age-eU trends are dominantly negative before converging towards c. 37 Ma.

7 Middle Unit samples display positive date-ESR trends; 5 are weak positive trends (17MC024B3, 17MC032A1, 18MC083A1, 18MC121A1, 18MC125B1, 17MC060A1; **Figure S2.3b**), 17MC059A1 displays the only strong date-ESR trend, which is heavily controlled by an outlier age of 15.18 Ma. 5 other Middle Unit age populations display weak negative age-ESR trends (17MC045RA2, 17MC046A1, 18MC020B1, 18MC047B1, 18MC055B1; **Figure S2.3b**). Middle Unit date-eU trends are dominantly negative (17MC032A1, 17MC045RA2, 17MC046A1, 17MC059A1, 18MC020A1, 18MC047B1, 18MC055B1, 18MC121A1, and 18MC125B1) or weakly positive (17MC024B3, and 18MC083A1; **Figure S2.3e**). Sample 18MC125B1 analyses had unusually high levels of eU and strongly affects the appearance of the populations on Figure

12b. Overall the negative trends may converge towards a minimum age of 8 Ma save for 17MC024B3 which hosts the mid-Miocene age population.

Two Lower Unit samples (17MC003B2, and 18MC005B1) show weak positive date-ESR trends, though individual outliers may disrupt this (**Figure S2.3c**). A third Lower Unit sample (18MC089A1) displays a weak negative date-ESR trend (**Figure S2.3c**). Lower Unit date-eU trends are all negative trends that converge towards 7.5 Ma with increasing eU (**Figure S2.3f**).

S2.3 Figures:

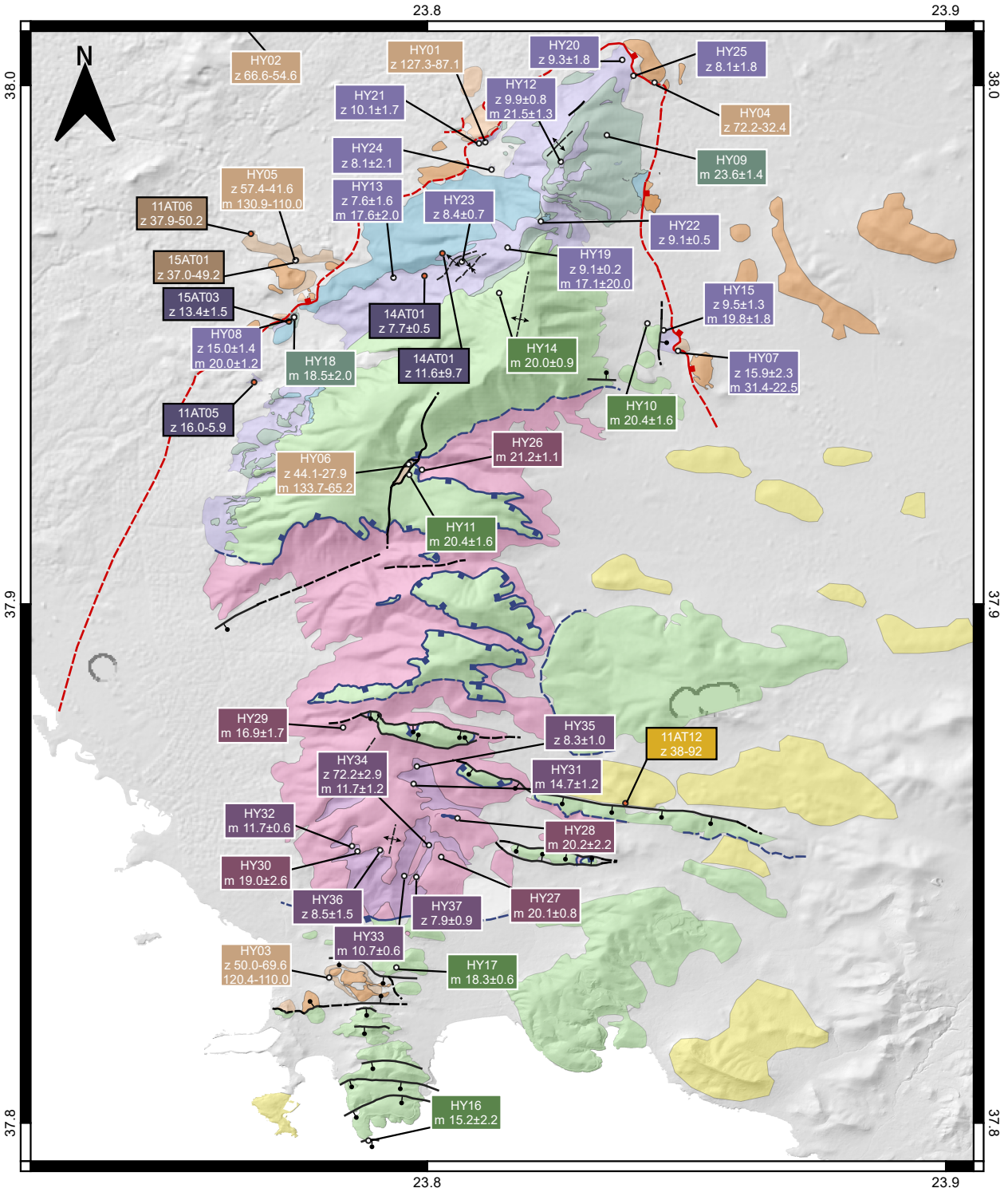

Figure S2.1. Spatial distribution of geochronological data overlain on the bedrock geological map of Mt. Hymittos, Greece. Sample locations are indicated by white dots, geochronological data includes new white mica (m) 40Ar/39Ar and zircon (z) (U-Th)/He ages, as well as previous zircon (U-Th)/He ages (Seman, 2016). Grey regions of the map represent areas of no or limited data, typically obscured by the city of Athens.

Given the number and file size of these maps they have not been included in this thesis document; they are archived in the Mendeley data repository: DOI: 10.17632/zjhdtsnm4z.1

Figure S2.2. Cation compositional EDS maps, with WDS point locations. See table S2 for the results of WDS analyses.

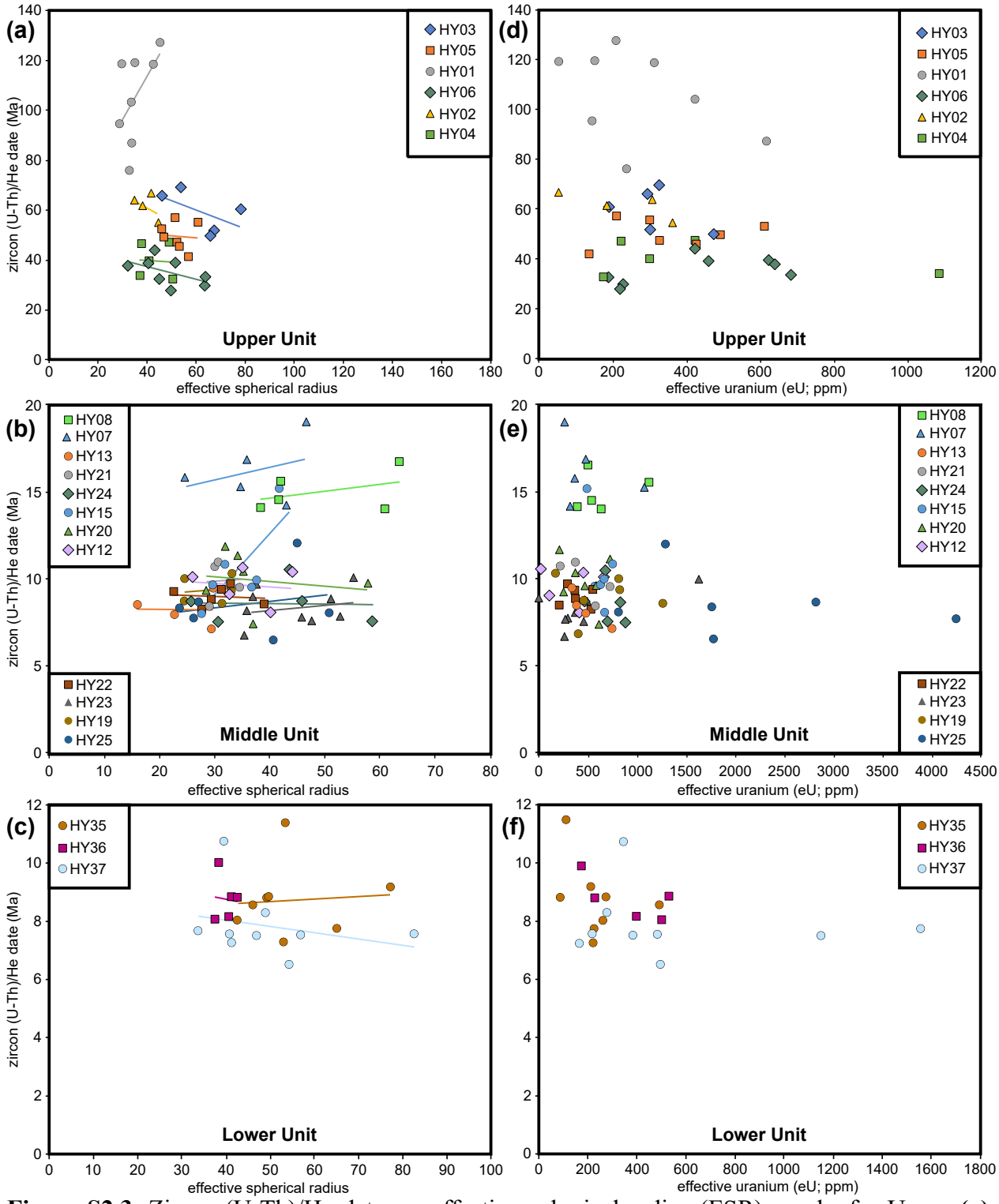

Figure S2.3. Zircon (U-Th)/He date vs. effective spherical radius (ESR) graphs for Upper **(a)**, Middle **(b)** and Lower **(c)** Unit samples examined in this study. Typically, trends are typically close to flat, and may be positive or negative. Graphs of zircon (U-Th)/He age vs. effective uranium for Upper **(d)**, Middle **(e)** and Lower **(f)** Unit samples examined in this study. Upper Unit analyses may display an age-eU turnover indicating residence time in the partial retention zone. Middle- and Lower-Unit analyses do not display an age-eU turnover.

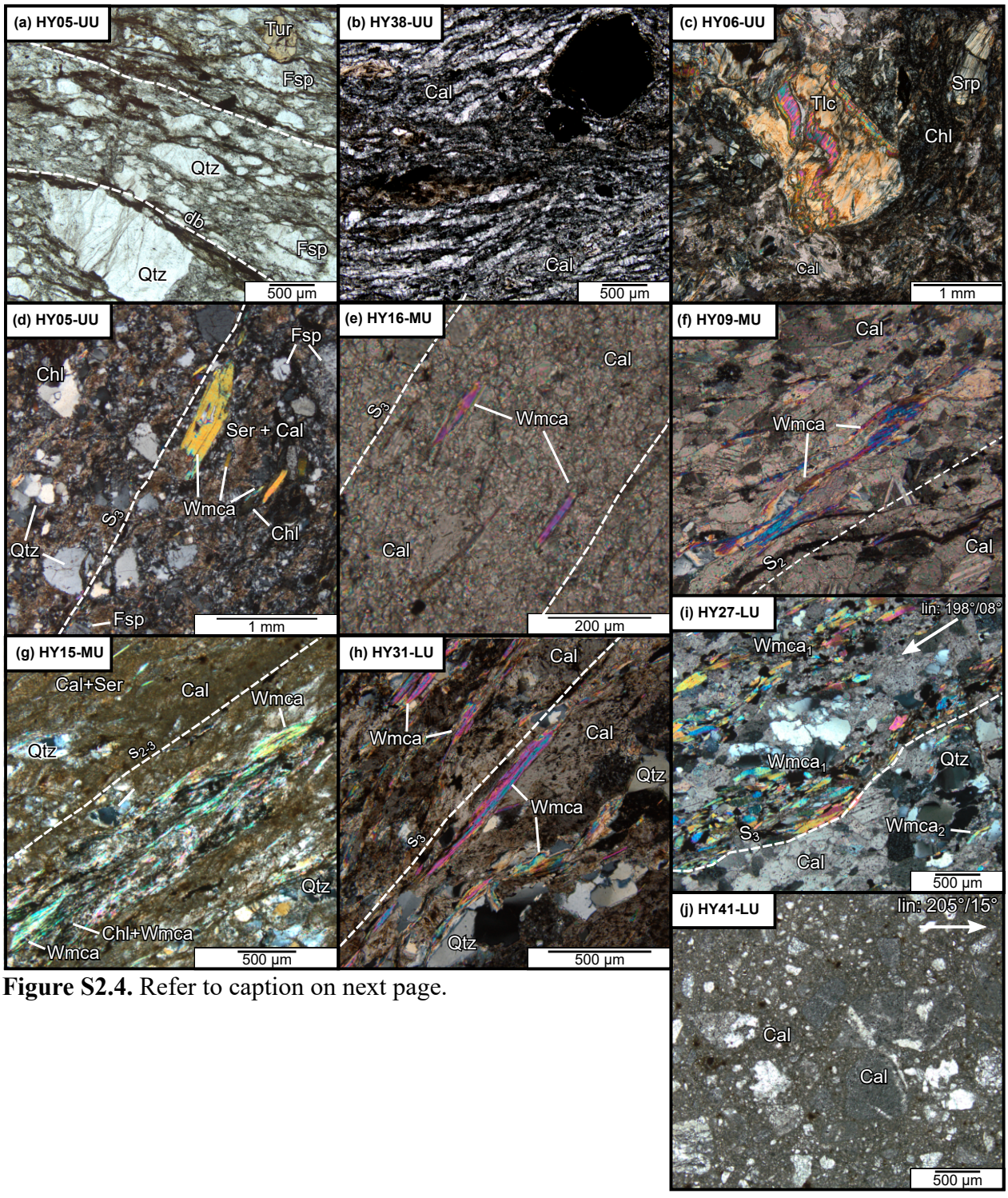

Figure S2.4. Refer to caption on next page.

Figure S2.4. (previous page) Thin section photomicrographs of selected bedrock samples from Mt. Hymittos, Greece. **(a; HY05, 37.966245°N; 23.774561°E)** plane polarized light (PPL) photomicrograph of Upper Unit tourmaline, chlorite, calcite feldspar, quartz, low metamorphic grade metasedimentary phyllite. Dissolution bands (db) form a weak foliation reflecting flattening strain and pressure dissolution. **(b: HY38: 37.958704°N; 23.778339°E)** cross-polarized light (XPL) photomicrograph of Upper Unit low metamorphic grade calcitic marble. Calcite aligned in ribbons. **(c: HY06; 37.927279°N; 23.796349°E)** XPL photomicrograph of Upper Unit serpentinized melange. Sample contains multiple generations of serpentinite, talc veins, deformed calcite veins and chlorite. **(d: HY05: 37.96625°N; 23.774561°E)** Upper Unit metasedimentary phyllite, white mica form a single population of 100-1000 μm-long, brittlely deformed, kinked, subhedral to anhedral crystals. **(e: HY16: 37.79659°N; 23.78864°E)** Middle Unit marble mylonite white mica are 50-100 μm-long euhedral crystals oriented parallel to the foliation. **(f: HY09: 37.98527°N; 23.82573°E)** Coarser grained Middle Unit marble mylonite, white mica are 200-500 μm-long, anhedral to euhedral and are not strongly sheared, compositionally they are comprised of phengite with minor muscovite both aligned with the S_2 foliation. **(g: HY15: 37.95278°N; 23.84557°E)** Middle Unit mylonitic calc-schist, white mica are anhedral, 50-500 μm-long phengite cored mica fish and are strongly sheared. **(h: HY31: 37.86536°N; 23.79734°E)** Lower Unit mylonitic calc-schist, white mica are 100-800 μm-long subhedral to anhedral moderately deformed crystals. **(i: HY27: 37.85127°N; 23.80268°E)** Lower Unit calcitic marble mylonite, white mica comprise two populations: Wmca1 200-800 μm-long euhedral crystals oriented parallel to the foliation and aligned in shear bands (sensu lato). Wmca2 50-250 μm-long euhedral crystals oriented parallel to the foliation. **(j: HY41: 37.850627°N; 23.82965°E)** XPL photomicrograph of calcite cataclasite from the lower detachment. Cal: calcite, Chl: chlorite, Fsp: felsdpar, Qtz: quartz, Ser: sericite, Srp: serpentine, Tlc: talc, Tur: tourmaline, Wmca: white mica (mineral abbreviations from Siivola, & Schmid; 2007).

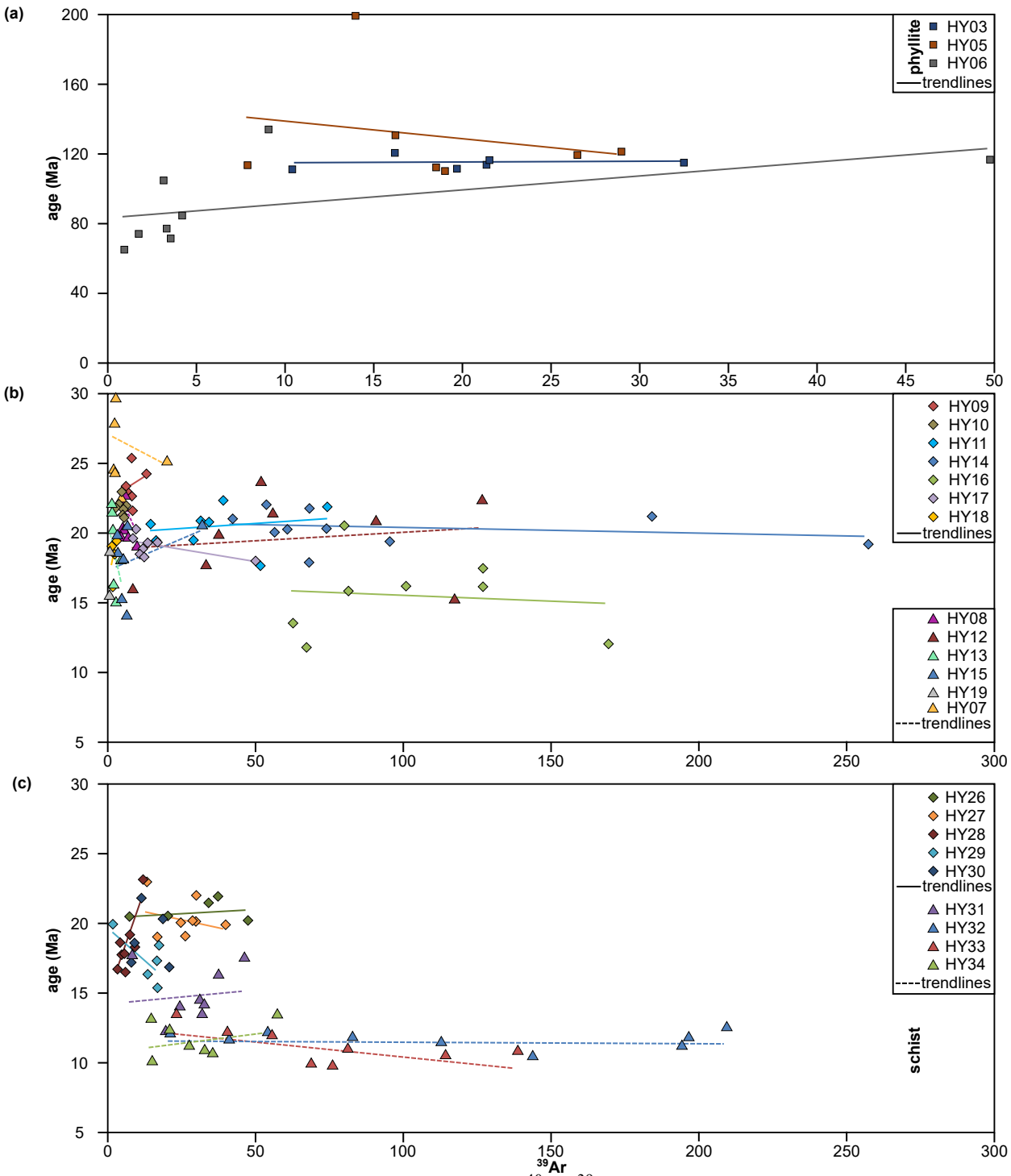

Figure S2.5. Age vs. 39Ar graphs for white mica $^{40}Ar/^{39}Ar$ analyses from the Upper **(a)**, Middle **(b)**, and Lower **(c)** units of Hymittos. ^{39}Ar in white mica can be a proxy for grain size, as the total fusion technique does not provide grain size information. Graphs do not show a consistent relationship between age and ^{39}Ar. That being said, in certain samples (e.g. HY12, HY11, HY06, HY31, HY34) the dominant group of analyses does appear to exhibit a positive age-^{39}Ar trend. This may indicate that grain size is a control on some mica ages. Though the randomness of the rest of the rest of the analyses suggests grain size is not a consistent control on $^{40}Ar/^{39}Ar$ ages in these samples.

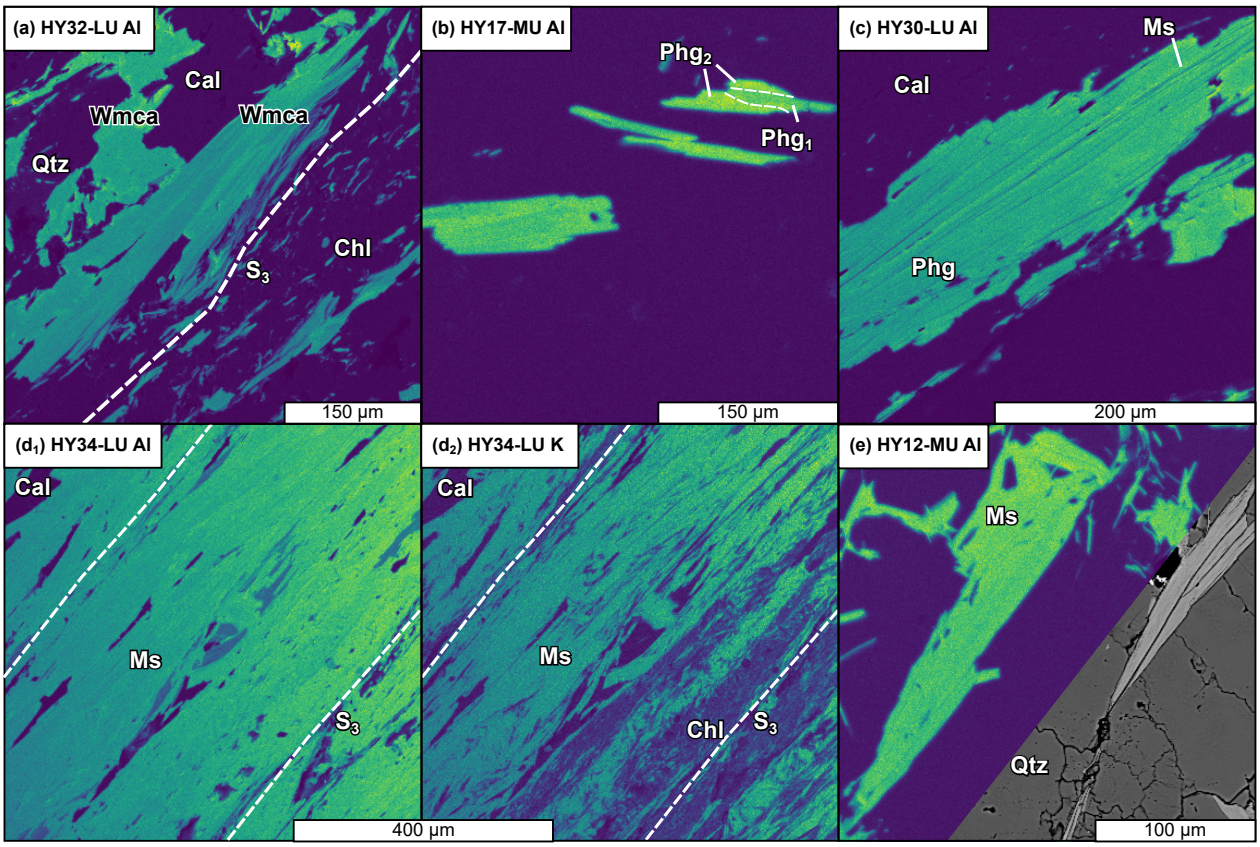

Figure S2.6. Select white mica compositional maps from Figure S2. **(a: HY32)** Al zoning depicts phengite-muscovite intergrowths in S3 aligned moderately sheared white mica. This mica is from the edge of a calcite-rich portion of the sample, and is less sheared and deformed than mica in interlinked shear bands. **(b: HY17)** High-Al cores (Phg1) and moderate-Al (Phg2) rim compositional zoning in white mica from Middle Unit marble. **(c: Hy30)** Moderate-Si phengite with minor muscovite intergrowths in Lower Unit calcitic marble. **(d1 & d2: Hy34)** Al (d1) and K (d2) maps reveal chlorite and muscovitic white mica in intermeshed within S3 parallel shear bands. **(e: Hy12)** Subhedral muscovite in quartz rich microlithons. Mica outside the microlithons have the same composition (Figure 7b, d; S2), but are pervasively sheared and deformed.

S2.4 Tables:

Table S2.1. Sample coordinates and summary of results from optical petrography conducted on select Upper, Middle and Lower Unit samples From Mt. Hymittos, Attica

Unit	Sample	Rock Classification	Latitude (°N)	Longitude (°E)	Elevation (m)	Thermochronology
Upper Unit	**HY01-17MC045A1**	Graphite, chlorite, calcite, quartz, phyllite	37.98904	23.81117	296	(U-Th)/He
	HY02-18MC142A2	Tourmaline, white mica, quartz, calcite, sericite phyllite	38.02367	23.76793	301	(U-Th)/He
	HY03-17MC019A1	Tourmaline, chlorite, plagioclase, white mica, quartz, phyllite	37.82802	23.78105	50	$^{40}Ar/^{39}Ar$, (U-Th)/He
	HY04-18MC116A2	Chlorite, epidote, sericite, plagioclase, serpentinite, phyllite	38.00055	23.84381	105	(U-Th)/He
	HY05-17MC030A1	Tourmaline, chlorite, white mica, calcite, feldspar, quartz phyllite	37.96625	23.77456	196	$^{40}Ar/^{39}Ar$, (U-Th)/He
	HY06-17MC050A1	Talc, chlorite, serpentinite, epidote calcite, white mica, quartz, phyllite	37.92694	23.79639	461	$^{40}Ar/^{39}Ar$, (U-Th)/He
	HY38-17MC028A1	Quartz, calcite, marble	37.95870	23.77834	305	
Middle Unit	**HY07-17MC060A1**	Serpentinite, chlorite, epidote, white mica, quartz, feldspar, cataclased schist	37.94881	23.84833	223	$^{40}Ar/^{39}Ar$, (U-Th)/He
	HY08-17MC024B3	Quartz, calcite, graphite, white mica, plagioclase feldspar, white mica, ultramylonitic schist	37.95529	23.77431	242	$^{40}Ar/^{39}Ar$, (U-Th)/He
	HY09-17MC047A1	White mica, calcite, mylonitic marble	37.99040	23.83462	410	$^{40}Ar/^{39}Ar$
	HY10-17MC058A1	White mica, quartz, plagioclase feldspar, calcite, mylonitic marble	37.95411	23.84243	233	$^{40}Ar/^{39}Ar$
	HY11-17MC052A1	White mica, calcite, mylonitic marble	37.92494	23.79651	483	$^{40}Ar/^{39}Ar$
	HY12-18MC047B1	Calcite, plagioclase feldspar, quartz, chlorite, white mica schist	37.98527	23.82573	719	$^{40}Ar/^{39}Ar$, (U-Th)/He
	HY13-17MC032A1	Chloritoid, chlorite, graphite, white mica, calcite, quartz, schist	37.96293	23.79347	307	$^{40}Ar/^{39}Ar$, (U-Th)/He
	HY14-18MC119A1	White mica, calcite, mylonitic marble	37.95997	23.81384	811	$^{40}Ar/^{39}Ar$
	HY15-17MC059A1	Quartz, white mica, graphite, calcite, calc-schist	37.95278	23.84557	219	$^{40}Ar/^{39}Ar$, (U-Th)/He
	HY16-18MC246A1	White mica, calcite, ultramylonitic marble	37.79659	23.78864	47	$^{40}Ar/^{39}Ar$
	HY17-17MC021A1	White mica, calcite mylonitic marble	37.82996	23.79402	83	$^{40}Ar/^{39}Ar$
	HY18-17MC024A2	White mica, calcite, ultramlyonitic marble	37.95529	23.77431	242	$^{40}Ar/^{39}Ar$
	HY19-18MC121A1	Calcite, chlorite, white mica, quartz schist	37.96438	23.81716	770	$^{40}Ar/^{39}Ar$, (U-Th)/He
	HY20-18MC020B1	Chlorite, graphite, quartz, white mica schist	38.00491	23.83758	336	(U-Th)/He

Unit	Sample	Rock Classification	Latitude (°N)	Longitude (°E)	Elevation (m)	Thermochronology
	HY21-17MC045RA2	Chlorite, white mica, calcite, quartz, mylonitic schist	37.98882	23.80995	285	(U-Th)/He
	HY22-18MC055B1	White mica, graphite, quartz phyllonite	37.97378	23.82188	678	(U-Th)/He
	HY23-18MC083A1	Chlorite, graphite, white mica, plagioclase feldspar, quartz, calcite schist	37.96600	23.80664	505	(U-Th)/He
	HY24-17MC046A1	Chlorite, quartz, calcite, white mica, graphite, mylonitic schist	37.98376	23.81238	330	(U-Th)/He
	HY25-18MC125B1	White mica, quartz, calcite mylonitic marble	38.00185	23.83975	347	(U-Th)/He
	HY39-18MC081A2	Glaucophane, white mica, quartz, chlorite, albite epidote, graphite, metabasic schist	37.96368	23.80796	483	
	HY40-18MC078A1	Quartz, albite, graphite, white mica schist	37.963923	23.803121	384	
Lower Unit	**HY26-17MC053B1**	White mica, dolomite, ultramylonitic marble	37.92590	23.79896	451	$^{40}Ar/^{39}Ar$
	HY27-17MC007A2	Amphibole, quartz, white mica, calcite, mylonitic marble	37.85127	23.80268	163	$^{40}Ar/^{39}Ar$
	HY28-17MC005B1	Quartz, white mica, calcite, mylonitic marble	37.85873	23.80580	240	$^{40}Ar/^{39}Ar$
	HY29-18MC155A1	Quartz, chlorite, white mica, dolomite, marble	37.87622	23.78374	381	$^{40}Ar/^{39}Ar$
	HY30-18MC003B1	Graphite, white mica, dolomite, calcite, carbonaceous ultramylonitic marble	37.85234	23.78653	245	$^{40}Ar/^{39}Ar$
	HY31-17MC003A1	Chloritoid, white mica, quartz, calcite, calc-schist	37.86536	23.79734	306	$^{40}Ar/^{39}Ar$
	HY32-18MC001A1	Tourmaline, chlorite, graphite, quartz, white mica schist	37.85336	23.78547	226	$^{40}Ar/^{39}Ar$
	HY33-18MC086A1	Graphite, chlorite, quartz, sericite, white mica, mylonitic schist	37.84760	23.79554	190	$^{40}Ar/^{39}Ar$
	HY34-17MC001A1	Quartz, sericite, calcite, graphite, white mica, mylonitic schist	37.85355	23.80030	176	$^{40}Ar/^{39}Ar$
	HY35-17MC003B2	Tourmaline, graphite, mylonitic quartzite	37.86872	23.79798	305	(U-Th)/He
	HY36-18MC005B1	Tourmaline, white mica, graphite, hematite quartzite	37.85258	23.79088	244	(U-Th)/He
	HY37-18MC089A1	Quartz, sericite, calcite, graphite, white mica, mylonitic schist	37.84741	23.79787	142	(U-Th)/He
	HY41-17MC048A1	White mica, dolomite, calcite, marble cataclasite	37.85063	23.82965	76	

Table S2.2. Results of white mica EMPA analysis from Mt. Hymittos

		structural formulae calculation assuming 11 O (a.p.f.u.)											site occupancies by element												end-member and XMg calculations							
Unit	Sample/Grain #	Si	Ti	Al	Fe	Mn	Mg	Ca	Na	K	F	Cl	Si(T2)	Ti(T2)	Al_{IV} (T2)	Al_{VI} (M2	Mg(M2)	Fe(M2)	Fe+Mg (M2)	Mn(M2)	Mg(M1)	Fe(M1)	v(M1)	K(A)	Na(A)	v(A)	Para	Phlog	Annite	Mg-Cel	Fe-Cel	Pyr	Musc	XMg
Lower Unit schist	**HY32-18MC001A1**																															
	grain 1, spot 1	3.3051	0.0046	2.3888	0.1203	-0.0002	0.2475	0.0092	0.0357	0.8058	1.39E-01	-3.42E-04	3.3051	0.0046	0.6903	1.6984	0.2031	0.0987	0.3018	-0.0002	0.0446	0.0216	0.9340	0.8058	0.0357	0.1585	0.036	0.044	0.022	0.114	0.056	0.158	0.570	0.673
	grain 1, spot 2	3.0386	0.0062	2.9160	0.0280	0.0002	0.0682	0.0070	0.1490	0.7169	4.92E-02	-1.96E-04	3.0386	0.0062	0.9551	1.9609	0.0276	0.0113	0.0389	0.0002	0.0406	0.0166	0.9428	0.7169	0.1490	0.1341	0.149	0.041	0.017	-0.054	-0.022	0.134	0.735	0.709
	grain 1, spot 3	2.9668	0.0069	2.9945	0.0203	0.0006	0.0480	0.0772	0.2173	0.6122	3.71E-02	1.49E-04	2.9668	0.0069	1.0263	1.9682	0.0219	0.0093	0.0312	0.0006	0.0261	0.0110	0.9629	0.6122	0.2173	0.1705	0.217	0.026	0.011	-0.030	-0.013	0.171	0.618	0.703
	grain 1, spot 4	3.2278	0.0036	2.5373	0.0914	0.0002	0.2165	0.0056	0.0500	0.7848	1.05E-01	-5.30E-04	3.2278	0.0036	0.7686	1.7688	0.1625	0.0686	0.2310	0.0002	0.0541	0.0228	0.9231	0.7848	0.0500	0.1651	0.050	0.054	0.023	0.054	0.023	0.165	0.631	0.703
	grain 1, spot 5	3.0244	0.0099	2.9350	0.0343	0.0009	0.0568	0.0080	0.1534	0.7044	2.42E-02	-3.76E-05	3.0244	0.0099	0.9657	1.9693	0.0186	0.0112	0.0298	0.0009	0.0382	0.0230	0.9387	0.7044	0.1534	0.1422	0.153	0.038	0.023	-0.058	-0.035	0.142	0.736	0.624
	grain 2, spot 1	3.1159	0.0040	2.7795	0.0371	-0.0007	0.1261	0.0036	0.1096	0.7402	5.88E-02	-1.85E-04	3.1159	0.0040	0.8801	1.8994	0.0783	0.0231	0.1013	-0.0007	0.0478	0.0141	0.9381	0.7402	0.1096	0.1502	0.110	0.048	0.014	-0.017	-0.005	0.150	0.701	0.772
	grain 2, spot 2	3.2291	0.0068	2.5623	0.0750	0.0011	0.1984	0.0033	0.0789	0.7599	3.59E-02	-1.39E-04	3.2291	0.0068	0.7709	1.7914	0.1430	0.0569	0.2000	0.0011	0.0417	0.0145	0.9381	0.7599	0.0789	0.1673	0.050	0.045	0.018	0.052	0.021	0.167	0.646	0.715
	grain 2, spot 3	3.0787	0.0041	2.8302	0.0442	0.0000	0.1182	0.0022	0.1156	0.7335	7.40E-02	3.15E-04	3.0787	0.0041	0.9172	1.9130	0.0633	0.0237	0.0870	0.0000	0.0549	0.0205	0.9246	0.7335	0.1156	0.1509	0.116	0.055	0.021	-0.046	-0.017	0.151	0.722	0.728
	grain 2, spot 4	3.1988	0.0030	2.6687	0.0325	0.0002	0.1245	0.0083	0.1173	0.7386	6.31E-02	-2.25E-04	3.1988	0.0030	0.7982	1.8705	0.1026	0.0268	0.1293	0.0002	0.0219	0.0057	0.9724	0.7386	0.1173	0.1441	0.117	0.022	0.006	0.059	0.015	0.144	0.637	0.793
	HY33-18MC086A1																															
	grain 1, spot 1	3.1869	0.0064	2.6340	0.0818	0.0002	0.1565	0.0014	0.0607	0.7840	1.15E-01	3.28E-04	3.1869	0.0064	0.8066	1.8274	0.1132	0.0592	0.1724	0.0002	0.0432	0.0226	0.9342	0.7840	0.0607	0.1552	0.061	0.043	0.023	0.027	0.014	0.155	0.677	0.657
	grain 1, spot 2	3.2223	0.0060	2.5391	0.1149	0.0000	0.2001	0.0045	0.0455	0.7994	2.15E-02	-3.76E-05	3.2223	0.0060	0.7777	1.7625	0.1459	0.0862	0.2321	0.0000	0.0488	0.0200	0.9227	0.7994	0.0455	0.1502	0.045	0.049	0.029	0.049	0.029	0.150	0.650	0.629
	grain 1, spot 3	3.0613	0.0076	2.8443	0.0539	-0.0001	0.0982	0.0021	0.1224	0.7612	8.35E-02	-7.52E-05	3.0613	0.0076	0.9312	1.9131	0.0561	0.0308	0.0870	-0.0001	0.0421	0.0231	0.9348	0.7612	0.1224	0.1165	0.122	0.042	0.023	-0.028	-0.015	0.116	0.739	0.646
	grain 1, spot 4	3.3470	0.0083	2.3256	0.1440	0.0011	0.2373	-0.0001	0.0285	0.8091	7.53E-02	2.43E-04	3.3470	0.0083	0.6448	1.6809	0.1979	0.1201	0.3180	0.0011	0.0394	0.0239	0.9367	0.8091	0.0285	0.1624	0.029	0.039	0.024	0.119	0.072	0.162	0.554	0.622
	grain 2, spot 1	3.2276	0.0071	2.5588	0.0978	0.0005	0.1628	0.0031	0.0550	0.8016	8.82E-02	4.14E-04	3.2276	0.0071	0.7653	1.7935	0.1287	0.0774	0.2060	0.0005	0.0341	0.0205	0.9454	0.8016	0.0550	0.1434	0.055	0.034	0.020	0.060	0.036	0.143	0.650	0.625
	grain 2, spot 2	3.1154	0.0055	2.7907	0.0442	0.0005	0.0961	-0.0008	0.1339	0.7305	5.75E-02	-3.67E-05	3.1154	0.0055	0.8791	1.9116	0.0602	0.0277	0.0879	0.0005	0.0359	0.0165	0.9476	0.7305	0.1339	0.1356	0.134	0.036	0.017	-0.012	-0.005	0.136	0.695	0.685
	grain 2, spot 3	3.0801	0.0095	2.8398	0.0440	-0.0001	0.1083	0.0057	0.1183	0.7597	4.69E-02	-1.46E-04	3.0801	0.0095	0.9199	1.9104	0.0463	0.0244	0.0707	-0.0001	0.0352	0.0166	0.9432	0.7597	0.1183	0.1322	0.108	0.037	0.020	-0.028	-0.015	0.132	0.745	0.656
	grain 2, spot 4	3.2856	0.0074	2.4230	0.1254	-0.0006	0.2265	0.0000	0.0350	0.8217	1.01E-01	2.65E-04	3.2856	0.0074	0.7070	1.7160	0.1832	0.1014	0.2846	-0.0006	0.0433	0.0239	0.9328	0.8217	0.0350	0.1433	0.035	0.043	0.024	0.097	0.054	0.143	0.604	0.644
	grain 3, spot 1	3.0917	0.0079	2.8130	0.0480	0.0013	0.0966	0.0006	0.1267	0.7428	7.22E-02	4.50E-05	3.0917	0.0079	0.9004	1.9126	0.0575	0.0286	0.0860	0.0013	0.0391	0.0194	0.9414	0.7428	0.1267	0.1305	0.127	0.039	0.019	-0.021	-0.010	0.131	0.715	0.668
	grain 3, spot 2	3.0447	0.0068	2.8975	0.0426	-0.0003	0.0661	0.0046	0.2857	0.5894	5.42E-02	5.16E-05	3.0447	0.0068	0.9484	1.9491	0.0311	0.0201	0.0512	-0.0003	0.0350	0.0232	0.9424	0.5894	0.2857	0.1249	0.286	0.035	0.023	-0.039	-0.025	0.125	0.596	0.608
	grain 3, spot 3	2.9570	0.0234	3.0368	0.0145	-0.0002	0.0143	0.0201	0.7401	0.1303	2.52E-02	-1.32E-04	2.9570	0.0234	1.0196	2.0173	-0.0085	-0.0086	-0.0171	-0.0002	0.0227	0.0232	0.9541	0.1303	0.7401	0.1297	0.740	0.023	0.023	-0.054	-0.055	0.130	0.193	0.496
	grain 3, spot 4	3.1004	0.0108	2.7939	0.0475	-0.0010	0.0329	0.0014	0.1389	0.7534	3.59E-02	2.45E-04	3.1004	0.0108	0.8996	1.9051	0.0634	0.0325	0.0959	-0.0010	0.0150	0.0557	0.7534	0.1389	0.0207	0.1475	0.139	0.029	0.015	0.005	0.002	0.148	0.750	0.661
	grain 3, spot 5	2.9846	0.0045	3.0284	0.0122	-0.0004	0.0165	0.0189	0.7336	0.1304	5.12E-02	2.18E-04	2.9846	0.0045	1.0109	2.0175	-0.0099	-0.0072	-0.0171	-0.0004	0.0264	0.0194	0.9542	0.1304	0.7336	0.1360	0.734	0.026	0.019	-0.063	-0.046	0.136	0.193	0.576
	HY34-17MC001A1																															
	grain 1, spot 1	3.0963	0.0031	2.8189	0.0408	-0.0011	0.1078	-0.0003	0.0980	0.7538	2.58E-02	6.18E-04	3.0963	0.0031	0.9006	1.9183	0.0601	0.0228	0.0828	-0.0011	0.0477	0.0181	0.9342	0.7538	0.0980	0.1487	0.098	0.048	0.018	-0.035	-0.013	0.149	0.736	0.725
	grain 2, spot 1	3.1076	0.0040	2.7980	0.0406	0.0007	0.1154	0.0002	0.0957	0.7504	4.60E-02	2.68E-04	3.1076	0.0040	0.8884	1.9096	0.0664	0.0233	0.0898	0.0007	0.0490	0.0172	0.9338	0.7504	0.0957	0.1539	0.096	0.049	0.017	-0.032	-0.011	0.154	0.727	0.740
	grain 2, spot 2	3.0416	0.0044	2.9258	0.0277	-0.0010	0.0682	0.0001	0.1320	0.7197	2.99E-02	1.25E-04	3.0416	0.0044	0.9584	1.9717	0.0332	0.0086	0.0292	-0.0010	0.0460	0.0095	0.9349	0.7197	0.1320	0.1486	0.132	0.046	0.019	-0.071	-0.030	0.148	0.756	0.707
	grain 2, spot 3	3.0856	0.0038	2.8324	0.0449	0.0004	0.0945	0.0002	0.0910	0.7737	6.26E-02	1.26E-04	3.0856	0.0038	0.9105	1.9218	0.0527	0.0250	0.0777	0.0004	0.0419	0.0199	0.9382	0.7737	0.0910	0.1353	0.091	0.042	0.020	-0.031	-0.015	0.135	0.758	0.678
	grain 2, spot 4	3.0857	0.0035	2.8276	0.0346	0.0003	0.1045	0.0003	0.1112	0.7699	4.21E-02	-3.20E-04	3.0857	0.0035	0.9109	1.9168	0.0623	0.0206	0.0830	0.0003	0.0422	0.0140	0.9439	0.7699	0.1112	0.1189	0.111	0.042	0.014	-0.022	-0.007	0.119	0.743	0.751
	grain 3, spot 1	3.1216	0.0053	2.7655	0.0455	-0.0006	0.1216	0.0008	0.0963	0.7649	6.06E-02	3.77E-04	3.1216	0.0053	0.8731	1.8925	0.0987	0.0295	0.1082	-0.0006	0.0429	0.0161	0.9411	0.7649	0.0963	0.1388	0.096	0.043	0.016	-0.007	-0.003	0.139	0.716	0.728
	grain 2, spot 4	3.1238	0.0059	2.7592	0.0487	0.0015	0.1124	0.0024	0.0760	0.7975	3.83E-02	-1.04E-04	3.1238	0.0059	0.8703	1.8889	0.0765	0.0331	0.1096	0.0015	0.0359	0.0156	0.9485	0.7975	0.0760	0.1264	0.076	0.036	0.016	0.005	0.002	0.126	0.739	0.698
	grain 3, spot 1	3.0854	0.0041	2.8285	0.0375	0.0002	0.0994	0.0002	0.1326	0.7606	3.76E-02	6.73E-04	3.0854	0.0041	0.9105	1.9180	0.0584	0.0234	0.0818	0.0002	0.0352	0.0141	0.9507	0.7606	0.1326	0.1068	0.133	0.035	0.014	-0.012	-0.005	0.107	0.782	0.714
	grain 3, spot 2	3.1285	0.0042	2.7749	0.0431	-0.0001	0.0951	0.0011	0.1221	0.7439	2.52E-02	-2.94E-04	3.1285	0.0042	0.8673	1.9076	0.0636	0.0288	0.0924	-0.0001	0.0315	0.0143	0.9543	0.7439	0.1221	0.1340	0.122	0.031	0.014	0.001	0.000	0.134	0.697	0.688
	grain 3, spot 3	3.1419	0.0053	2.7382	0.0425	0.0015	0.1185	0.0000	0.0875	0.7845	6.65E-02	-1.80E-04	3.1419	0.0053	0.8529	1.8854	0.0833	0.0299	0.1132	0.0015	0.0352	0.0126	0.9522	0.7845	0.0875	0.1281	0.087	0.035	0.013	0.013	0.005	0.128	0.719	0.736
	HY31-17MC003A1																															
	grain 1, spot 1	3.3512	0.0085	2.3066	0.1402	0.0013	0.2513	0.0077	0.0443	0.7966	1.05E-01	4.19E-05	3.3512	0.0085	0.6404	1.6662	0.2134	0.1191	0.3325	0.0013	0.0378	0.0211	0.9411	0.7966	0.0443	0.1590	0.044	0.038	0.021	0.138	0.077	0.159	0.523	0.642
	grain 1, spot 2	3.0748	0.0074	2.8519	0.0374	-0.0010	0.0831	0.0118	0.1176	0.7338	1.37E-02	8.39E-06	3.0748	0.0074	0.9178	1.9341	0.0456	0.0205	0.0661	-0.0002	0.0375	0.0093	0.9349	0.7338	0.1176	0.1486	0.118	0.037	0.017	-0.029	-0.013	0.149	0.722	0.689
	grain 1, spot 3	3.2779	0.0052	2.4270	0.1225	0.0004	0.2316	0.0144	0.0263	0.8224	1.01E-01	1.26E-04	3.2779	0.0052	0.7169	1.7101	0.1893	0.1002	0.2895	0.0004	0.0423	0.0224	0.9354	0.8224	0.0263	0.1513	0.026	0.042	0.022	0.105	0.055	0.151	0.598	0.654
	grain 1, spot 4	3.1072	0.0031	2.7826	0.0406	0.0003	0.1249	0.0216	0.0940	0.7420	1.03E-01	-4.85E-04	3.1072	0.0031	0.8897	1.8929	0.0806	0.0262	0.1067	0.0003	0.0443	0.0144	0.9413	0.7420	0.0940	0.1640	0.094	0.044	0.014	-0.008	-0.003	0.164	0.694	0.755
	grain 2, spot 1	3.1034	0.0052	2.7734	0.0463	-0.0001	0.1306	0.0112	0.0678	0.8015	6.62E-02	-2.44E-04	3.1034	0.0052	0.8914	1.8820	0.0872	0.0309	0.1181	-0.0001	0.0404	0.0154	0.9412	0.8015	0.0678	0.1307	0.068	0.043	0.015	0.000	0.000	0.131	0.742	0.738
	grain 2, spot 2	3.2149	0.0055	2.5671	0.0824	0.0013	0.1973	0.0069	0.0783	0.7630	9.99E-02	8.15E-05	3.2149	0.0055	0.7796	1.7875	0.1490	0.0622	0.2112	0.0013	0.0483	0.0202	0.9315	0.7630	0.0783	0.1588	0.078	0.048	0.020	0.052	0.022	0.159	0.620	0.705
	grain 2, spot 3	3.1974	0.0059	2.6019	0.0774	0.0007	0.1662	0.0050	0.0593	0.7803	1.09E-01	-1.84E-04	3.1974	0.0059	0.8026	1.8052	0.1372	0.0570	0.1941	0.0007	0.0403	0.0205	0.9303	0.7803	0.0593	0.1604	0.059	0.049	0.020	0.039	0.016	0.160	0.656	0.707
	grain 2, spot 4	3.0717	0.0053	2.8117	0.0397	0.0006	0.0969	0.0635	0.1121	0.7435	3.11E-02	-1.12E-04	3.0717	0.0053	0.9231	1.8886	0.0786	0.0322	0.1108	0.0006	0.0184	0.0084	0.0075	0.9741	0.7435	0.1121	0.1444	0.112	0.018	0.008	0.042	0.017	0.144	0.659	0.709
	grain 3, spot 1	3.3075	0.0087	2.3810	0.1337	0.0000	0.2371	0.0030	0.0251	0.8192	9.16E-02	1.07E-04	3.3075	0.0087	0.6838	1.6972	0.1935	0.1092	0.3027	0.0000	0.0435	0.0246	0.9319	0.8192	0.0251	0.1557	0.025	0.044	0.025	0.106	0.060	0.156	0.585	0.639
	grain 3, spot 2	3.0780	0.0056	2.8309	0.0445	-0.0003	0.0970	0.0075	0.1159	0.7601	3.44E-02	-8.50E-05	3.0780	0.0056	0.9165	1.9144	0.0589	0.0270	0.0859	-0.0003	0.0381	0.0175	0.9444	0.7601	0.1159	0.1240	0.116	0.038	0.017	-0.017	-0.008	0.124	0.730	0.685
	grain 3, spot 3	3.0708	0.0030	2.8360	0.0426	-0.0003	0.1115	0.0003	0.1021	0.7862	5.55E-02	-3.98E-04	3.0708	0.0030	0.9261	1.9098	0.0654	0.0250	0.0904	-0.0003	0.0461	0.0176	0.9363	0.7862	0.1021	0.1117	0.102	0.046	0.018	-0.027	-0.010	0.112	0.759	0.723
	grain 3, spot 4	3.2993	0.0068	2.4074	0.1222	0.0008	0.2139	0.0098	0.0398	0.8086	1.08E-01	1.58E-04	3.2993	0.0068	0.7007	1.6942	0.1732	0.1869	0.0995	0.2864	0.0008	0.0426	0.0181	0.9521	0.8086	0.0398	0.1516	0.040	0.043	0.023	0.102	0.054	0.152	0.567	0.653
	grain 3, spot 5	3.1153	0.0040	2.7795	0.0372	0.0005	0.1220	0.0078	0.0309	0.7455	5.98E-02	1.70E-04	3.1153	0.0040	0.8807	1.8988	0.0772	0.0235	0.1007	0.0005	0.0448	0.0136	0.9416	0.7455	0.1039	0.1506	0.104	0.045	0.014	-0.012	-0.004	0.151	0.703	0.766
	grain 3, spot 6	3.3582	0.0086	2.2910	0.1689	0.0008	0.2431	0.0050	0.0206	0.8037	1.16E-01	-5.71E-04	3.3582	0.0086	0.6331	1.6578	0.2014	0.1399	0.3414	0.0008	0.0416	0.0289	0.9294	0.8037	0.0206	0.1757	0.021	0.042	0.029	0.118	0.082	0.176	0.533	0.590
Lower Unit marble	**HY29-18MC155A1**																															
	grain 1, spot 1	3.3807	0.0053	2.2205	0.0002	-0.0001	0.4599	0.0025	0.0202	0.8435	1.99E-01	2.79E-04	3.3807	0.0074	0.6120	1.6085	0.3915	0.0001	0.3916	-0.0001	0.0634	0.0000	0.9316	0.8435	0.0202	0.1363	0.020	0.068	0.000	0.255	0.000	0.136	0.520	1.000
	grain 1, spot 2	3.3330	0.0153	2.3042	-0.0001	0.0001	0.4145	0.0025	0.0224	0.8458	1.89E-01	-3.40E-04	3.3330	0.0153	0.6517	1.6525	0.3475	-0.0001	0.3474	0.0001	0.0431	0.0000	0.9227	0.8458	0.0224	0.1318	0.022	0.063	0.000	0.221	0.000	0.132	0.561	1.000
	grain 3, spot 1	3.2248	0.0259	2.5042	-0.0007	0.0000	0.2870	0.0036	0.0317	0.8730	1.45E-01	-1.27E-04	3.2248	0.0259	0.7492	1.7549	0.2456	-0.0006	0.2450	0.0000	0.0414	-0.0001	0.9587	0.8730	0.0317	0.0953	0.032	0.041	0.000	0.163	0.000	0.095	0.669	1.002
	grain 3, spot 2	3.2090	0.0208	2.5408	-0.0004	0.0001	0.2666	0.0000	0.0391	0.8866	1.24E-01	-1.64E-04	3.2090	0.0208	0.7702	1.7706	0.2296	-0.0003	0.2293	0.0001	0.0370	0.0000	0.9631	0.8866	0.0391	0.0744	0.039	0.037	0.000	0.156	0.000	0.074	0.694	1.001
	grain 2, spot 1	3.3546	0.0032	2.2777	0.0010	-0.0006	0.4210	0.0016	0.0200	0.8695	2.64E-01	-2.63E-04	3.3546	0.0032	0.6422	1.6356	0.3642	0.0009	0.3650	-0.0006	0.0568	0.0001	0.9430	0.8695	0.0200	0.1105	0.020	0.057	0.000	0.250	0.001	0.111	0.561	0.998
	grain 2, spot 2	3.3621	0.0051	2.2602	0.0016	0.0006	0.4284	0.0012	0.0201	0.8671	2.19E-01	-1.21E-04	3.3621	0.0051	0.6329	1.6273	0.3707	0.0014	0.3721	0.0006	0.0577	0.0002	0.9421	0.8671	0.0201	0.1128	0.020	0.058	0.000	0.255	0.001	0.113	0.553	0.996
	grain 2, spot 3	3.2128	0.0215	2.5266	0.0007	-0.0002	0.2694	0.0105	0.0303	0.8915	1.90E-01	6.48E-04	3.2128	0.0215	0.7656	1.7610	0.2385	0.0006	0.2392	-0.0002	0.0308	0.0001	0.9491	0.8915	0.0303	0.0782	0.030	0.031	0.000	0.177	0.000	0.078	0.683	0.997
	grain 2, spot 4	3.1747	0.0284	2.5808	0.0037	-0.0006	0.2461	0.0044	0.0343	0.9038	1.51E-01	4.07E-04	3.1747	0.0284	0.7969	1.7839	0.2135	0.0032	0.2167	-0.0006	0.0326	0.0005	0.9669	0.9038	0.0343	0.0620	0.034	0.033	0.000	0.148	0.002	0.062	0.720	0.985
	grain 3, spot 1	3.4064	0.0024	2.1898	0.0011	0.0003	0.4625	0.0003	0.0186	0.8481	2.10E-01	-4.00E-04	3.4064	0.0024	0.5912	1.5986	0.4000	0.0010	0.4010	0.0003	0.0625	0.0002	0.9374	0.8481	0.0186	0.1333	0.019	0.062	0.000	0.275	0.001	0.133	0.510	0.998
	grain 3, spot 2	3.4220	0.0022	2.1600	-0.0008	0.0002	0.4797	-0.0003	0.0175	0.8478	2.65E-01	-2.22E-04	3.4220	0.0022	0.5757	1.5842	0.4162	-0.0007	0.4155	0.0002	0.0635	-0.0001	0.9366	0.8478	0.0175	0.1346	0.018	0.063	0.000	0.289	0.000	0.135	0.496	1.002
	grain 3, spot 3	3.1540	0.0213	2.6381	0.0057	-0.0004	0.2195	0.0004	0.0421	0.8923	1.83E-01	1.67E-04	3.1540	0.0213	0.8247	1.8134	0.1823	0.0047	0.1870	-0.0004	0.0371	0.0010	0.9619	0.8923	0.0421	0.0656	0.042	0.037	0.001	0.108	0.003	0.066	0.743	0.975
	grain 3, spot 4	3.1760	0.0273	2.5984	0.0013	-0.0001	0.2292	0.0005	0.0337	0.9042	1.38E-01	3.61E-04	3.1760	0.0273	0.7967	1.8017	0.1973	0.0011	0.1984	-0.0001	0.0281	0.0002	0.9718	0.9042	0.0337	0.0621	0.034	0.028	0.000	0.141	0.001	0.062	0.734	0.994
	grain 3, spot 5	3.3239	0.0126	2.3335	0.0030	0.0010	0.3589	0.0116	0.0258	0.8786	2.64E-01	8.21E-04	3.3239	0.0126	0.6635	1.6700	0.3262	0.0028	0.3290	0.0010	0.0327	0.0003	0.9670	0.8786	0.0258	0.0956	0.026	0.033	0.000	0.261	0.002	0.096	0.583	0.992
	HY27-17MC007A2																															
	grain 1, spot 1	3.3077	0.0058	2.3499	0.0032	0.0006	0.3895	0.0054	0.0045	0.8947	1.59E-01	-5.64E-04	3.3077	0.0058	0.6866	1.6633	0.3333	0.0028	0.3361	0.0006	0.0562	0.0005	0.9433	0.8947	0.0045	0.1008	0.004	0.056	0.000	0.221	0.002	0.101	0.615	0.992
	grain 1, spot 2	3.2014	0.0385	2.5189	-0.0002	-0.0002	0.2715	0.0032	0.0007	0.9343	1.70E-01	2.50E-04	3.2014	0.0385	0.7601	1.7588	0.2416	-0.0002	0.2414	-0.0002	0.0300	0.0000	0.9701	0.9343	0.0007	0.0651	0.001	0.030	0.000	0.182	0.000	0.065	0.723	1.001
	grain 3, spot 1	3.2801	0.0169	2.3842	0.0002	-0.0008	0.3355	0.0127	0.0028	0.9110	1.76E-01	1.87E-04	3.2801	0.0169	0.7029	1.6813	0.3193	0.0002	0.3195	-0.0008	0.0162	0.0000	0.9838	0.9110	0.0028	0.0822	0.003	0.016	0.000	0.287	0.000	0.082	0.658	1.000
	grain 3, spot 2	3.2259	0.0327	2.4789	0.0009	0.0005	0.2862	0.0033	0.0024	0.9447	1.56E-01	1.21E-04	3.2259	0.0327	0.7414	1.7375	0.2612	0.0008	0.2620	0.0005	0.0250	0.0001	0.9749	0.9447	0.0024	0.0529	0.002	0.025	0.000	0.211	0.001	0.053	0.708	0.997
	grain 3, spot 3	3.2599	0.0339	2.4091	0.0007	-0.0007	0.3318	0.0012	-0.0018	0.9330	1.48E-01	6.86E-05	3.2599	0

Table S2.2. Results of white mica EMPA analysis from Mt. Hymittos

		structural formulae calculation assuming 11 O (a.p.f.u.)											site occupancies by element												end-member and XMg calculations							
Unit	Sample/Grain #	Si	Ti	Al	Fe	Mn	Mg	Ca	Na	K	F	Cl	Si(T2)	Ti(T2)	Al_{IV} (T2)	Al_{VI} (M2	Mg(M2)	Fe(M2)	Fe+Mg (M2)	Mn(M2)	Mg(M1)	Fe(M1)	v(M1)	K(A)	Na(A)	v(A)	Para	Phlog	Annite	Mg-Cel	Fe-Cel	Pyr	Musc	XMg
Middle Unit Schist	grain 2, spot 3	3.1956	0.0142	2.5832	-0.0001	0.0010	0.2379	0.0113	0.0497	0.8614	1.86E-01	-4.01E-04	3.1956	0.0142	0.7902	1.7930	0.2061	-0.0001	0.2060	0.0010	0.0318	0.0000	0.9682	0.8614	0.0497	0.0889	0.050	0.032	0.000	0.142	0.000	0.089	0.687	1.000
	grain 2, spot 4	3.2869	0.0041	2.4021	0.0005	0.0018	0.3553	0.0124	0.0394	0.8504	3.41E-01	6.79E-04	3.2869	0.0041	0.7090	1.6931	0.3047	0.0004	0.3051	0.0018	0.0506	0.0001	0.9493	0.8504	0.0394	0.1102	0.039	0.051	0.000	0.203	0.000	0.110	0.596	0.999
	grain 3, spot 1	3.2520	0.0094	2.3156	0.0005	-0.0002	0.3623	0.2108	0.0343	0.8266	3.63E-01	-1.66E-04	3.2520	0.0094	0.7387	1.5769	0.4227	0.0005	0.4232	-0.0002	-0.0604	-0.0001	1.0604	0.8266	0.0343	0.1390	0.034	-0.060	0.000	0.543	0.001	0.139	0.343	0.999
	grain 3, spot 2	3.3254	0.0069	2.3221	0.0006	0.0005	0.3917	0.0308	0.0369	0.8202	3.08E-01	-7.48E-05	3.3254	0.0069	0.6677	1.6545	0.3445	0.0006	0.3450	0.0005	0.0472	0.0001	0.9527	0.8202	0.0369	0.1429	0.037	0.047	0.000	0.250	0.000	0.143	0.522	0.998
	grain 3, spot 3	3.2437	0.0087	2.4008	0.0004	0.0012	0.3280	0.1196	0.0325	0.8571	3.01E-01	-2.87E-04	3.2437	0.0087	0.7476	1.6532	0.3452	0.0004	0.3456	0.0012	-0.0172	0.0000	1.0172	0.8571	0.0325	0.1104	0.033	-0.017	0.000	0.380	0.000	0.110	0.494	0.999
	HY12-18MC047B1																																	
	grain 1, spot 1	3.0891	0.0062	2.8158	0.0487	-0.0005	0.0903	-0.0003	0.0807	0.8142	6.43E-02	1.85E-04	3.0891	0.0062	0.9047	1.9111	0.0581	0.0313	0.0894	-0.0005	0.0322	0.0174	0.9504	0.8142	0.0807	0.1051	0.081	0.032	0.017	-0.006	-0.003	0.105	0.774	0.650
	grain 1, spot 2	3.1375	0.0053	2.7345	0.0499	0.0004	0.1165	0.0005	0.0938	0.7973	9.56E-02	3.39E-04	3.1375	0.0053	0.8572	1.8772	0.0857	0.0367	0.1223	0.0004	0.0308	0.0132	0.9560	0.7973	0.0938	0.1089	0.094	0.031	0.013	0.024	0.010	0.109	0.719	0.700
	grain 1, spot 3	3.1315	0.0032	2.7482	0.0411	0.0002	0.1183	0.0014	0.0968	0.7982	6.26E-02	-7.09E-04	3.1315	0.0032	0.8653	1.8828	0.0868	0.0302	0.1170	0.0002	0.0314	0.0109	0.9576	0.7982	0.0968	0.1049	0.097	0.031	0.011	0.024	0.008	0.105	0.724	0.742
	grain 1, spot 4	3.0875	0.0036	2.8146	0.0492	-0.0004	0.0857	0.0001	0.0950	0.8272	3.93E-02	3.15E-04	3.0875	0.0036	0.9088	1.9058	0.0601	0.0345	0.0946	-0.0004	0.0256	0.0147	0.9597	0.8272	0.0950	0.0778	0.095	0.026	0.015	0.009	0.005	0.078	0.773	0.635
	grain 2, spot 1	3.1492	0.0043	2.6943	0.0687	0.0013	0.1255	0.0005	0.0668	0.8445	6.36E-02	8.67E-05	3.1492	0.0043	0.8465	1.8478	0.0975	0.0534	0.1509	0.0013	0.0280	0.0153	0.9567	0.8445	0.0668	0.0887	0.067	0.028	0.015	0.042	0.023	0.089	0.737	0.646
	grain 2, spot 2	3.1388	0.0036	2.7365	0.0441	-0.0011	0.0997	-0.0002	0.1317	0.8045	7.39E-02	4.22E-04	3.1388	0.0036	0.8576	1.8788	0.0848	0.0375	0.1223	-0.0011	0.0149	0.0066	0.9785	0.8045	0.1317	0.0638	0.132	0.015	0.007	0.055	0.024	0.064	0.704	0.693
	grain 2, spot 3	3.0810	0.0092	2.8326	0.0445	-0.0002	0.0776	0.0003	0.1232	0.7741	1.73E-02	2.67E-05	3.0810	0.0092	0.9098	1.9228	0.0492	0.0282	0.0775	-0.0002	0.0283	0.0163	0.9554	0.7741	0.1232	0.1027	0.123	0.028	0.016	-0.007	-0.004	0.103	0.741	0.635
	grain 3, spot 1	3.1235	0.0046	2.7457	0.0636	0.0008	0.1081	-0.0003	0.0765	0.8295	4.03E-02	-8.43E-05	3.1235	0.0046	0.8719	1.8738	0.0789	0.0464	0.1253	0.0008	0.0292	0.0172	0.9536	0.8295	0.0765	0.0940	0.076	0.029	0.017	0.021	0.012	0.094	0.751	0.630
	grain 3, spot 2	3.1158	0.0048	2.7544	0.0682	0.0004	0.1123	0.0007	0.0683	0.8229	4.04E-02	1.80E-04	3.1158	0.0048	0.8794	1.8750	0.0775	0.0471	0.1246	0.0004	0.0348	0.0211	0.9441	0.8229	0.0683	0.1088	0.068	0.035	0.021	0.008	0.005	0.109	0.754	0.622
	grain 3, spot 3	3.1103	0.0047	2.7718	0.0398	0.0000	0.1184	0.0001	0.0889	0.8189	4.28E-02	2.81E-04	3.1103	0.0047	0.8849	1.8868	0.0847	0.0285	0.1132	0.0000	0.0337	0.0113	0.9550	0.8189	0.0889	0.0922	0.089	0.034	0.011	0.017	0.006	0.092	0.751	0.748
	grain 3, spot 4	2.9877	0.0025	2.9972	0.0199	0.0003	0.0257	0.0036	0.7243	0.2242	2.07E-02	6.87E-04	2.9877	0.0025	1.0098	1.9875	0.0069	0.0053	0.0122	0.0003	0.0188	0.0145	0.9667	0.2242	0.7243	0.0515	0.724	0.019	0.015	-0.031	-0.024	0.051	0.245	0.564
	HY13-17MC032A2																																	
	grain 1, spot 1	3.0651	0.0066	2.8461	0.0712	0.0000	0.0780	-0.0009	0.0929	0.7852	1.92E-02	1.36E-04	3.0651	0.0066	0.9283	1.9178	0.0429	0.0392	0.0822	0.0000	0.0351	0.0320	0.9329	0.7852	0.0929	0.1219	0.093	0.035	0.032	-0.027	-0.025	0.122	0.770	0.523
	grain 1, spot 2	3.1754	0.0044	2.6299	0.1106	0.0001	0.1409	0.0007	0.0577	0.8289	2.19E-02	-2.76E-04	3.1754	0.0044	0.8202	1.8097	0.1066	0.0836	0.1903	0.0001	0.0343	0.0269	0.9388	0.8289	0.0577	0.1134	0.058	0.034	0.027	0.038	0.030	0.113	0.700	0.560
	grain 1, spot 3	3.0720	0.0043	2.8203	0.0778	0.0011	0.0832	-0.0007	0.1060	0.8052	2.68E-02	6.11E-05	3.0720	0.0043	0.9236	1.8966	0.0529	0.0494	0.1023	0.0011	0.0303	0.0283	0.9414	0.8052	0.1060	0.0888	0.106	0.030	0.028	-0.008	-0.007	0.089	0.762	0.517
	grain 2, spot 1	3.0625	0.0064	2.8770	0.0630	-0.0011	0.0627	0.0009	0.1258	0.7163	2.83E-02	2.58E-04	3.0625	0.0064	0.9310	1.9460	0.0275	0.0276	0.0551	-0.0011	0.0352	0.0354	0.9294	0.7163	0.1258	0.1579	0.126	0.035	0.035	-0.043	-0.043	0.158	0.732	0.499
	grain 2, spot 2	3.1117	0.0075	2.4411	0.1241	0.0001	0.1813	0.0218	0.0444	0.7012	8.74E-02	5.32E-04	3.1117	0.0075	0.6809	1.7602	0.1423	0.0974	0.2397	0.0001	0.0390	0.0267	0.9343	0.7012	0.0444	0.2543	0.044	0.039	0.027	0.064	0.044	0.254	0.527	0.594
	grain 2, spot 3	3.3237	0.0072	2.4241	0.1631	0.0000	0.1799	0.0164	0.0941	0.5913	1.13E-01	1.72E-03	3.3237	0.0072	0.6692	1.7550	0.1285	0.1165	0.2450	0.0000	0.0514	0.0466	0.9020	0.5913	0.0941	0.3146	0.094	0.051	0.047	0.026	0.023	0.315	0.444	0.525
	HY19-18MC121A1																																	
	grain 1, spot 1	3.0907	0.0052	2.8440	0.0627	-0.0004	0.0789	-0.0005	0.0710	0.7321	3.25E-02	-5.37E-04	3.0907	0.0052	0.9041	1.9399	0.0337	0.0268	0.0606	-0.0004	0.0451	0.0359	0.9190	0.7321	0.0710	0.1968	0.071	0.045	0.036	-0.057	-0.045	0.197	0.753	0.557
	grain 1, spot 2	3.2415	0.0065	2.5148	0.1212	0.0014	0.1837	0.0003	0.0411	0.8094	5.62E-02	-4.63E-05	3.2415	0.0065	0.7520	1.7627	0.1421	0.0938	0.2358	0.0014	0.0416	0.0275	0.9309	0.8094	0.0411	0.1495	0.041	0.042	0.027	0.059	0.039	0.149	0.643	0.602
	grain 2, spot 1	3.0147	0.0015	2.9321	0.0949	0.0006	0.0373	0.0026	0.7178	0.1503	5.66E-02	4.50E-05	3.0147	0.0015	0.9837	1.9483	0.0144	0.0367	0.0511	0.0006	0.0229	0.0582	0.9189	0.1503	0.7178	0.1319	0.718	0.023	0.058	-0.031	-0.080	0.132	0.180	0.282
	grain 2, spot 2	3.1933	0.0032	2.6552	0.0893	0.0000	0.1192	0.0025	0.4547	0.3717	5.42E-02	-7.44E-04	3.1933	0.0032	0.8035	1.8517	0.0848	0.0635	0.1483	0.0000	0.0345	0.0258	0.9398	0.3717	0.4547	0.1737	0.455	0.034	0.026	0.016	0.012	0.174	0.284	0.572
	grain 2, spot 3	3.1545	0.0050	2.7139	0.0859	0.0003	0.0968	0.0021	0.4516	0.3986	3.78E-02	1.86E-04	3.1545	0.0050	0.8405	1.8734	0.0669	0.0594	0.1263	0.0003	0.0299	0.0265	0.9436	0.3986	0.4516	0.1499	0.452	0.030	0.027	0.007	0.006	0.150	0.329	0.530
	grain 2, spot 4	3.1010	0.0107	2.8127	0.0731	-0.0007	0.0625	0.0011	0.0958	0.7472	-3.87E-03	-4.07E-04	3.1010	0.0107	0.8883	1.9244	0.0351	0.0411	0.0762	-0.0007	0.0273	0.0320	0.9406	0.7472	0.0958	0.1570	0.096	0.027	0.032	-0.020	-0.023	0.157	0.730	0.461
	grain 3, spot 2	3.2228	0.0061	2.6231	0.1219	-0.0002	0.1249	0.0073	0.0701	0.6372	3.67E-02	-1.22E-04	3.2228	0.0061	0.7710	1.8520	0.0750	0.0732	0.1482	-0.0002	0.0499	0.0487	0.9014	0.6372	0.0701	0.2928	0.070	0.050	0.049	-0.025	-0.024	0.293	0.588	0.506
	grain 3, spot 3	3.2115	0.0087	2.5802	0.1162	0.0007	0.1427	0.0006	0.0467	0.8116	7.51E-02	3.46E-04	3.2115	0.0087	0.7798	1.8004	0.1096	0.0893	0.1989	0.0007	0.0331	0.0269	0.9400	0.8116	0.0467	0.1417	0.047	0.033	0.027	0.043	0.035	0.142	0.673	0.551
	grain 3, spot 4	3.3805	0.0055	2.3043	0.1942	0.0002	0.2024	0.0114	0.0161	0.7105	9.40E-02	9.36E-06	3.3805	0.0055	0.6139	1.6904	0.1580	0.1515	0.3095	0.0002	0.0444	0.0426	0.9129	0.7105	0.0161	0.2734	0.016	0.044	0.043	0.069	0.066	0.273	0.488	0.510
	grain 3, spot 5	3.0567	0.0047	2.8946	0.0580	-0.0001	0.0576	0.0015	0.1697	0.6671	2.78E-02	2.40E-04	3.0567	0.0047	0.9386	1.9560	0.0220	0.0222	0.0442	-0.0001	0.0356	0.0358	0.9286	0.6671	0.1697	0.1631	0.170	0.036	0.036	-0.049	-0.050	0.163	0.694	0.498
	grain 3, spot 6	3.4649	0.0065	2.1293	0.3406	0.0004	0.1766	0.0056	0.0463	0.6340	3.28E-02	2.15E-04	3.4649	0.0065	0.5286	1.6006	0.1362	0.2627	0.3990	0.0004	0.0404	0.0779	0.8817	0.6340	0.0463	0.3198	0.046	0.040	0.078	0.055	0.107	0.320	0.353	0.341
	HY15-17MC059A1																																	
	grain 1, spot 1	3.3585	0.0048	2.3156	0.1046	-0.0002	0.2444	0.0073	0.0273	0.8604	8.00E-02	-9.60E-05	3.3585	0.0048	0.6368	1.6789	0.2250	0.0963	0.3213	-0.0002	0.0194	0.0083	0.9723	0.8604	0.0273	0.1123	0.027	0.019	0.008	0.186	0.080	0.112	0.567	0.700
	grain 1, spot 2	3.0774	0.0027	2.8548	0.0244	0.0003	0.0793	0.0161	0.1650	0.7102	6.70E-02	-3.36E-04	3.0774	0.0027	0.9199	1.9349	0.0496	0.0153	0.0648	0.0003	0.0297	0.0091	0.9612	0.7102	0.1650	0.1248	0.165	0.030	0.009	-0.010	-0.003	0.125	0.684	0.765
	grain 1, spot 3	3.1627	0.0034	2.6801	0.0382	0.0003	0.1503	0.0050	0.0817	0.8258	1.19E-01	1.29E-03	3.1627	0.0034	0.8339	1.8462	0.1223	0.0311	0.1535	0.0003	0.0279	0.0071	0.9650	0.8258	0.0817	0.0924	0.082	0.028	0.007	0.066	0.017	0.092	0.707	0.797
	grain 1, spot 4	3.1312	0.0045	2.7482	0.0334	0.0009	0.1122	0.0026	0.0958	0.8182	9.93E-02	-8.55E-05	3.1312	0.0045	0.8642	1.8839	0.0888	0.0264	0.1152	0.0009	0.0235	0.0070	0.9695	0.8182	0.0958	0.0860	0.096	0.023	0.007	0.042	0.012	0.086	0.734	0.771
	grain 2, spot 1	3.3335	0.0069	2.3031	0.1319	0.0001	0.2673	0.0183	0.0265	0.8675	1.75E-01	-2.94E-05	3.3335	0.0069	0.6596	1.6435	0.2387	0.1177	0.3564	0.0001	0.0287	0.0141	0.9572	0.8675	0.0265	0.1060	0.026	0.029	0.014	0.181	0.089	0.106	0.554	0.670
	grain 2, spot 2	3.1081	0.0051	2.7581	0.0309	-0.0004	0.1189	0.0213	0.1035	0.8278	6.55E-02	-6.66E-05	3.1081	0.0051	0.8868	1.8713	0.1024	0.0267	0.1291	-0.0004	0.0165	0.0043	0.9793	0.8278	0.1035	0.0686	0.104	0.016	0.004	0.069	0.018	0.069	0.720	0.793
	grain 2, spot 3	3.1415	0.0070	2.6962	0.0453	-0.0002	0.1425	0.0163	0.0758	0.8339	4.91E-02	1.31E-04	3.1415	0.0070	0.8515	1.8446	0.1180	0.0375	0.1555	-0.0002	0.0245	0.0078	0.9677	0.8339	0.0758	0.0903	0.076	0.024	0.008	0.069	0.022	0.090	0.711	0.759
	grain 2, spot 4	3.2985	0.0072	2.4002	0.0933	-0.0003	0.2308	0.0186	0.0471	0.8447	1.50E-01	2.69E-04	3.2985	0.0072	0.6942	1.7059	0.2096	0.0848	0.2944	-0.0003	0.0211	0.0086	0.9703	0.8447	0.0471	0.1082	0.047	0.021	0.009	0.167	0.068	0.108	0.580	0.712
	grain 3, spot 1	3.1467	0.0042	2.7098	0.0420	0.0009	0.1248	0.0125	0.0808	0.8256	7.33E-02	1.64E-04	3.1467	0.0042	0.8490	1.8608	0.1035	0.0348	0.1383	0.0009	0.0213	0.0072	0.9715	0.8256	0.0808	0.0936	0.081	0.021	0.007	0.061	0.021	0.094	0.716	0.748
	grain 3, spot 2	3.1865	0.0049	2.6307	0.0541	-0.0003	0.1612	0.0031	0.0738	0.8324	7.27E-02	5.39E-04	3.1865	0.0049	0.8086	1.8221	0.1334	0.0448	0.1782	-0.0003	0.0278	0.0093	0.9629	0.8324	0.0738	0.0939	0.074	0.028	0.009	0.078	0.026	0.094	0.691	0.749
	grain 3, spot 3	3.2713	0.0059	2.4536	0.0915	-0.0011	0.2188	0.0025	0.0509	0.8558	1.19E-01	-1.24E-04	3.2713	0.0059	0.7227	1.7309	0.1905	0.0797	0.2702	-0.0011	0.0283	0.0118	0.9599	0.8558	0.0509	0.0933	0.051	0.028	0.012	0.134	0.056	0.093	0.626	0.705
	HY08-17MC024B2																																	
	grain 1, spot 1	3.3540	0.0080	2.2560	0.0934	0.0017	0.3273	0.0062	0.0230	0.9038	3.27E-02	8.64E-04	3.3540	0.0080	0.6380	1.6180	0.2959	0.0845	0.3804	0.0017	0.0314	0.0090	0.9596	0.9038	0.0230	0.0732	0.023	0.031	0.009	0.233	0.067	0.073	0.564	0.778
	grain 1, spot 2	3.3272	0.0101	2.2847	0.0902	0.0012	0.3266	0.0110	0.0179	0.9209	6.16E-02	1.61E-03	3.3272	0.0101	0.6627	1.6220	0.2953	0.0815	0.3768	0.0012	0.0313	0.0086	0.9601	0.9209	0.0179	0.0612	0.018	0.031	0.009	0.233	0.064	0.061	0.584	0.784
	grain 1, spot 3	3.3617	0.0063	2.2372	0.0986	0.0004	0.3419	0.0018	0.0271	0.9037	6.90E-02	5.50E-05	3.3617	0.0063	0.6320	1.6053	0.3061	0.0883	0.3944	0.0004	0.0358	0.0103	0.9538	0.9037	0.0271	0.0692	0.027	0.036	0.010	0.234	0.068	0.069	0.555	0.776
	grain 1, spot 4	3.3517	0.0093	2.2488	0.1027	-0.0002	0.3364	0.0046	0.0233	0.8993	8.21E-02	4.31E-04	3.3517	0.0093	0.6390	1.6098	0.2991	0.0913	0.3904	-0.0002	0.0373	0.0114	0.9513	0.8993	0.0233	0.0774	0.023	0.037	0.011	0.224	0.069	0.077	0.558	0.766
	grain 2, spot 1	3.3368	0.0138	2.2367	0.1279	0.0008	0.3528	0.0009	0.0095	0.9133	6.64E-02	1.21E-04	3.3368	0.0138	0.6494	1.5873	0.3024	0.1096	0.4120	0.0008	0.0504	0.0183	0.9313	0.9133	0.0095	0.0772	0.010	0.050	0.018	0.201	0.073	0.077	0.570	0.734
	grain 2, spot 2	3.3323	0.0081	2.2812	0.1121	0.0010	0.3178	-0.0005	0.0269	0.9068	4.86E-02	4.58E-04	3.3323	0.0081	0.6596	1.6216	0.2789	0.0984	0.3774	0.0010	0.0389	0.0137	0.9474	0.9068	0.0269	0.0663	0.027	0.039	0.014	0.201	0.071	0.066	0.582	0.739
	grain 2, spot 3	3.3686	0.0086	2.2330	0.1061	0.0010	0.3205	0.0010	0.0187	0.9163	2.89E-02	1.04E-03	3.3686	0.0086	0.6229	1.6102	0.2921	0.0967	0.3888	0.0010	0.0284	0.0094	0.9622	0.9163	0.0187	0.0650	0.019	0.028	0.009	0.235	0.078	0.065	0.565	0.751
	grain 2, spot 4	3.3085	0.0116	2.2813	0.1451	0.0012	0.3236	0.0025	0.0166	0.9141	6.53E-02	1.90E-03	3.3085	0.0116	0.6799	1.6015	0.2743	0.1230	0.3974	0.0012	0.0493	0.0221	0.9286	0.9141	0.0166	0.0693	0.017	0.049	0.022	0.176	0.079	0.069	0.588	0.690
	grain 3, spot 1	3.3300	0.0175	2.2471	0.1309	0.0003	0.3342	0.0068	0.0139	0.9104	4.01E-02	3.39E-04	3.3300	0.0175	0.6525	1.5946	0.2911	0.1140	0.4051	0.0003	0.0431	0.0169	0.9401	0.9104	0.0139	0.0756	0.014	0.043	0.017	0.205	0.080	0.076	0.565	0.719
	grain 3, spot 2	3.3380	0.0188	2.2370	0.1186	-0.0002	0.3435	0.0077	0.0194	0.9030	1.59E-02	-4.99E-04	3.3380	0.0188	0.6432	1.5938	0.3021	0.1043	0.4064	-0.0002	0.0414	0.0143	0.9443	0.9030	0.0194	0.0776	0.019	0.041	0.014	0.219	0.076	0.078	0.552	0.743
	grain 3, spot 3	3.3180	0.0152	2.2709	0.1214	-0.0006	0.3358	0.0034	0.0163	0.9182	6.86E-02	6.81E-04	3.3180	0.0152	0.6668	1.6041	0.2912	0.1053	0.3965	-0.0006	0.0446	0.0161	0.9393	0.9182	0.0163	0.0655	0.016	0.045	0.016	0.202	0.073	0.066	0.582	0.734
	grain 3, spot 4	3.3125	0.0171	2.3017	0.1078	0.0005	0.3064	0.0012	0.0158	0.9291	5.06E-02	-3.17E-04	3.3125	0.0171	0.6704	1.6312	0.2724	0.0959	0.3682	0.0005	0.0340	0.0120	0.9540	0.9291	0.0158	0.0551	0.016	0.034	0.012	0.204	0.072	0.055	0.607	0.740

[1] red values are rejected by exlusion criteria (Parra et al., 2002).

Table S2.3. Results of $^{40}Ar/^{39}Ar$ total fusion analysis of white mica from the Upper Middle and Lower Units of Mt. Hymittos, Attica; values corrected for blank, mass discrimination and radioactive decay

Unit	Sample/Grain #	Ar^{40} (fA)	±1σ	Ar^{39} (fA)	±1σ	Ar^{38} (fA)	±1σ	Ar^{37} (fA)	±1σ	Ar^{36} (fA)	±1σ	Ca/K	±1σ	Cl/K	±1σ	$^{40}Ar^*/^{39}Ar_{(K)}$	±1σ	$^{40}Ar^*$	Age (Ma)[1]	±1σ
Upper Unit	**HY03-17MC019A1**																			
	Grain 1	541.653	0.1181	21.5054	0.0631	0.310	0.030	-0.019	0.024	0.027	0.001	-0.018	0.022	0.006	0.004	24.795	0.079	98.528	**116.290**	**0.359**
	Grain 2	254.235	0.0876	10.4013	0.0641	0.142	0.030	-0.018	0.029	0.028	0.001	-0.035	0.055	0.003	0.008	23.627	0.154	96.746	**110.976**	**0.702**
	Grain 3	2261.472	0.2151	29.0645	0.0668	0.393	0.029	-0.090	0.028	0.111	0.002	-0.061	0.019	0.002	0.003	76.616	0.192	98.551	**337.527**	**0.773**
	Grain 4	816.749	0.1309	32.4503	0.0756	0.390	0.029	-0.003	0.027	0.075	0.002	-0.002	0.016	-0.002	0.003	24.464	0.065	97.282	**114.788**	**0.294**
	Grain 5	446.774	0.1114	16.1810	0.0652	0.244	0.032	-0.034	0.028	0.103	0.002	-0.041	0.035	0.005	0.006	25.708	0.113	93.189	**120.433**	**0.513**
	Grain 6	518.887	0.1088	21.3691	0.0608	0.224	0.033	0.027	0.026	0.009	0.001	0.025	0.025	-0.005	0.005	24.138	0.074	99.492	**113.305**	**0.335**
	Grain 7	473.223	0.1028	19.6458	0.0618	0.183	0.031	0.047	0.028	0.020	0.001	0.046	0.028	-0.009	0.005	23.769	0.081	98.758	**111.622**	**0.367**
	HY05-17MC030A1																			
	Grain 1	686.396	0.1145	26.4796	0.0637	0.275	0.031	-0.002	0.028	0.041	0.001	-0.012	0.188	-0.006	0.003	25.417	0.068	98.213	**118.983**	**0.306**
	Grain 2	447.590	0.1101	18.4905	0.0674	0.226	0.031	0.006	0.027	0.020	0.001	0.058	0.256	-0.001	0.005	23.850	0.093	98.687	**111.872**	**0.421**
	Grain 3	465.481	0.1052	16.1873	0.0646	0.188	0.032	0.018	0.027	0.036	0.001	0.196	0.298	-0.003	0.006	28.054	0.119	97.711	**130.890**	**0.537**
	Grain 4	192.861	0.0795	7.8742	0.0627	0.112	0.031	0.062	0.027	0.008	0.001	1.417	0.610	0.005	0.012	24.211	0.204	98.961	**113.510**	**0.925**
	Grain 5	616.090	0.1284	14.0017	0.0577	0.098	0.032	0.002	0.029	0.014	0.001	0.024	0.377	-0.016	0.007	43.643	0.188	99.347	**199.718**	**0.813**
	Grain 6	751.529	0.1137	28.9529	0.0678	0.330	0.031	0.019	0.025	0.011	0.001	0.117	0.154	-0.003	0.003	25.809	0.065	99.591	**120.761**	**0.294**
	Grain 7	449.477	0.0999	18.9917	0.0622	0.219	0.031	-0.095	0.027	0.010	0.001	-0.908	0.262	-0.002	0.005	23.431	0.082	99.198	**109.965**	**0.375**
	Grain 8	1080.027	0.1421	12.6156	0.0642	0.249	0.029	0.009	0.027	0.034	0.001	0.128	0.384	0.020	0.007	84.676	0.443	99.065	**369.252**	**1.748**
	HY06-17MC050A1																			
	Grain 1	266.230	0.0917	9.0858	0.0709	0.058	0.028	-0.029	0.026	0.018	0.001	-0.115	0.103	-0.018	0.009	28.683	0.233	97.997	**133.659**	**1.047**
	Grain 2	1255.216	0.1651	49.7197	0.0635	0.597	0.027	-0.008	0.027	0.072	0.002	-0.006	0.019	-0.001	0.002	24.788	0.042	98.293	**116.081**	**0.189**
	Grain 3	24.585	0.0684	0.9181	0.0724	0.002	0.031	-0.058	0.027	0.040	0.001	-2.265	1.057	-0.053	0.098	13.724	1.191	51.348	**65.191**	**5.557**
	Grain 4	66.453	0.0706	3.3113	0.0625	0.032	0.030	0.043	0.027	0.043	0.001	0.459	0.288	-0.015	0.027	16.236	0.341	80.977	**76.869**	**1.581**
	Grain 5	85.415	0.0744	3.1029	0.0644	0.094	0.029	-0.010	0.027	0.054	0.002	-0.111	0.309	0.043	0.027	22.335	0.498	81.226	**104.919**	**2.271**
	Grain 6	85.623	0.0706	4.1971	0.0641	0.064	0.030	0.007	0.026	0.035	0.001	0.063	0.224	0.005	0.021	17.893	0.294	87.803	**84.535**	**1.358**
	Grain 7	35.685	0.0666	1.7249	0.0632	0.093	0.031	0.041	0.025	0.030	0.001	0.859	0.534	0.112	0.053	15.567	0.628	75.305	**73.767**	**2.915**
	Grain 8	61.249	0.0682	3.5336	0.0637	0.011	0.028	0.007	0.025	0.028	0.001	0.069	0.256	-0.030	0.023	15.006	0.299	86.665	**71.160**	**1.393**
Middle Unit	**HY07-17MC060A1**																			
	Grain 1	14.478	0.0630	2.0363	0.0612	0.047	0.029	-0.080	0.025	0.014	0.001	-0.598	0.190	0.028	0.042	5.077	0.229	71.490	**24.267**	**1.085**
	Grain 2	17.419	0.0641	2.2793	0.0627	0.066	0.027	0.030	0.028	0.011	0.001	0.201	0.187	0.046	0.035	6.217	0.233	81.421	**29.671**	**1.105**
	Grain 3	30.947	0.0684	2.9870	0.0603	-0.037	0.030	0.007	0.026	0.038	0.001	0.035	0.135	-0.078	0.029	6.585	0.194	63.609	**31.410**	**0.916**
	Grain 4	10.701	0.0654	1.6635	0.0604	0.099	0.031	-0.045	0.028	0.007	0.001	-0.420	0.258	0.134	0.054	5.131	0.270	79.849	**24.523**	**1.282**
	Grain 5	24.392	0.0720	4.5089	0.0632	0.063	0.032	0.097	0.028	0.011	0.001	0.331	0.096	0.004	0.021	4.699	0.102	86.935	**22.472**	**0.487**
	Grain 6	118.773	0.0843	19.6503	0.0599	0.252	0.032	0.073	0.026	0.052	0.002	0.057	0.021	0.000	0.005	5.253	0.030	86.982	**25.101**	**0.145**
	Grain 7	11.715	0.0662	2.0157	0.0635	0.021	0.030	0.008	0.027	0.000	0.001	0.061	0.218	-0.005	0.044	5.822	0.240	100.257	**27.892**	**1.139**
	HY08-17MC024B2																			
	Grain 1	29.993	0.0679	5.6059	0.0657	0.043	0.032	-0.010	0.027	0.012	0.001	-0.322	0.859	-0.014	0.017	4.717	0.088	88.320	**22.701**	**0.419**
	Grain 2	41.408	0.0674	5.4285	0.0613	0.048	0.029	-0.022	0.023	0.014	0.001	-0.732	0.765	-0.011	0.016	6.823	0.105	89.620	**32.747**	**0.500**
	Grain 3	17.303	0.0678	3.6869	0.0637	0.137	0.033	0.001	0.026	0.001	0.001	0.071	1.234	0.072	0.026	4.574	0.130	97.623	**22.017**	**0.622**
	Grain 4	29.573	0.0673	6.6449	0.0598	0.056	0.032	0.018	0.027	0.009	0.001	0.476	0.724	-0.012	0.014	4.069	0.067	91.583	**19.603**	**0.321**
	Grain 5	19.615	0.0651	4.2257	0.0572	0.050	0.031	0.015	0.026	0.008	0.001	0.612	1.108	-0.002	0.021	4.083	0.103	88.098	**19.669**	**0.495**
	Grain 6	23.503	0.0705	4.9941	0.0610	0.077	0.031	-0.019	0.026	0.008	0.001	-0.687	0.935	0.008	0.018	4.211	0.090	89.657	**20.281**	**0.430**
	Grain 7	24.763	0.0601	5.2187	0.0659	0.044	0.029	0.051	0.028	0.011	0.001	1.770	0.955	-0.012	0.016	4.186	0.089	88.309	**20.160**	**0.427**
	Grain 8	44.673	0.0756	9.5897	0.0629	0.071	0.030	-0.010	0.028	0.022	0.001	-0.189	0.536	-0.015	0.009	3.954	0.047	85.037	**19.051**	**0.226**
	HY09-17MC047A1																			
	Grain 1	72.268	0.0631	13.0225	0.0607	0.124	0.031	0.084	0.027	0.022	0.001	0.232	0.075	-0.009	0.007	5.055	0.037	91.185	**24.274**	**0.178**
	Grain 2	44.680	0.0714	7.8261	0.0598	0.089	0.030	-0.015	0.026	0.011	0.001	-0.071	0.120	-0.003	0.011	5.290	0.058	92.770	**25.395**	**0.278**
	Grain 3	40.188	0.0640	7.8990	0.0604	0.136	0.028	0.000	0.028	0.010	0.001	-0.002	0.128	0.014	0.010	4.718	0.057	92.843	**22.667**	**0.273**
	Grain 4	31.003	0.0720	6.0891	0.0622	0.125	0.031	0.011	0.027	0.004	0.001	0.067	0.159	0.024	0.015	4.872	0.074	95.802	**23.402**	**0.356**
	Grain 5	34.823	0.0713	6.1274	0.0627	0.174	0.029	0.001	0.028	0.018	0.001	0.008	0.166	0.045	0.014	4.804	0.078	84.637	**23.079**	**0.373**
	Grain 6	39.643	0.0608	8.1198	0.0651	0.118	0.030	0.062	0.027	0.011	0.001	0.277	0.121	0.006	0.011	4.498	0.054	92.230	**21.616**	**0.260**
	HY10-17MC058A1																			
	Grain 1	18.901	0.0671	3.4201	0.0603	0.013	0.030	0.017	0.026	0.011	0.001	0.170	0.268	-0.026	0.026	4.581	0.135	82.975	**22.067**	**0.647**
	Grain 2	27.521	0.0649	5.2023	0.0678	0.046	0.030	-0.044	0.023	0.016	0.001	-0.298	0.156	-0.011	0.017	4.379	0.091	82.886	**21.102**	**0.435**
	Grain 3	35.500	0.0641	5.7851	0.0701	0.129	0.030	-0.017	0.028	0.031	0.001	-0.101	0.170	0.027	0.015	4.559	0.087	74.386	**21.965**	**0.414**
	Grain 4	26.957	0.0686	5.1303	0.0635	0.127	0.029	0.021	0.026	0.013	0.001	0.140	0.175	0.035	0.017	4.502	0.089	85.785	**21.693**	**0.425**
	Grain 5	25.338	0.0602	4.5469	0.0666	0.045	0.029	0.016	0.027	0.012	0.001	0.123	0.205	-0.008	0.019	4.772	0.103	85.729	**22.984**	**0.494**
	Grain 6	12.975	0.0687	2.5229	0.0622	-0.023	0.029	-0.049	0.027	0.005	0.001	-0.681	0.377	-0.062	0.034	4.528	0.176	88.169	**21.816**	**0.842**
	Grain 7	24.191	0.0715	4.8100	0.0638	0.078	0.030	-0.043	0.027	0.010	0.001	-0.315	0.199	0.011	0.018	4.412	0.098	87.842	**21.260**	**0.467**
	HY11-17MC052A1																			
	Grain 1	65.472	0.0688	14.0732	0.0664	0.155	0.030	0.072	0.027	0.017	0.001	0.180	0.068	-0.004	0.006	4.302	0.033	92.581	**20.684**	**0.159**
	Grain 2	73.233	0.0713	16.0612	0.0675	0.262	0.029	0.064	0.024	0.028	0.001	0.141	0.054	0.011	0.005	4.049	0.030	88.894	**19.471**	**0.146**
	Grain 3	124.745	0.0808	28.7662	0.0653	0.368	0.032	0.065	0.025	0.027	0.001	0.079	0.031	0.001	0.003	4.053	0.019	93.576	**19.493**	**0.092**
	Grain 4	147.745	0.0822	31.3355	0.0610	0.364	0.031	-0.009	0.028	0.038	0.001	-0.011	0.031	-0.002	0.003	4.353	0.017	92.440	**20.928**	**0.083**
	Grain 5	158.184	0.0867	33.9675	0.0671	0.365	0.028	0.055	0.029	0.037	0.001	0.057	0.031	-0.005	0.002	4.333	0.017	93.152	**20.831**	**0.079**
	Grain 6	201.413	0.0809	51.2361	0.0618	0.626	0.031	0.127	0.028	0.043	0.001	0.087	0.020	0.000	0.002	3.680	0.011	93.723	**17.707**	**0.051**
	Grain 7	356.898	0.1017	74.0005	0.0712	0.908	0.032	0.187	0.028	0.065	0.002	0.090	0.014	0.000	0.001	4.561	0.010	94.672	**21.919**	**0.049**
	Grain 8	189.312	0.0843	38.6616	0.0737	0.402	0.029	0.027	0.029	0.031	0.002	0.024	0.027	-0.006	0.002	4.656	0.016	95.199	**22.375**	**0.076**
	HY12-18MC047B1																			
	Grain 1	90.882	0.0572	126.4776	0.0295	1.500	0.016	0.062	0.014	0.022	0.001	0.004	0.001	0.000	0.000	0.660	0.002	91.869	**22.276**	**0.058**
	Grain 2	19.016	0.0557	33.0498	0.0252	0.405	0.017	-0.012	0.013	0.005	0.001	-0.003	0.003	0.001	0.001	0.525	0.005	91.257	**17.740**	**0.176**
	Grain 3	24.807	0.0497	37.2633	0.0255	0.438	0.016	0.039	0.014	0.009	0.001	0.008	0.003	-0.001	0.001	0.587	0.005	88.233	**19.834**	**0.161**
	Grain 4	57.768	0.0560	117.2275	0.0295	1.421	0.017	0.025	0.014	0.015	0.001	0.001	0.001	0.000	0.000	0.449	0.002	91.099	**15.178**	**0.061**
	Grain 5	5.338	0.0505	8.2742	0.0229	0.096	0.016	0.011	0.013	0.005	0.001	0.011	0.013	-0.001	0.006	0.472	0.023	73.239	**15.973**	**0.762**
	Grain 6	39.524	0.0528	51.5815	0.0253	0.637	0.016	0.021	0.013	0.010	0.001	0.003	0.002	0.001	0.001	0.699	0.004	91.311	**23.601**	**0.133**
	Grain 7	38.321	0.0549	55.8011	0.0242	0.691	0.016	0.029	0.014	0.009	0.001	0.004	0.002	0.001	0.001	0.632	0.003	92.124	**21.354**	**0.105**
	Grain 8	60.813	0.0541	90.5466	0.0284	1.063	0.015	0.028	0.014	0.015	0.001	0.002	0.001	-0.001	0.000	0.614	0.002	91.509	**20.748**	**0.081**
	HY13-17MC032A2																			
	Grain 1	10.587	0.0587	1.6140	0.0543	0.059	0.029	-0.001	0.027	0.017	0.001	-0.037	0.689	0.065	0.052	3.387	0.196	51.700	**16.298**	**0.940**
	Grain 2	8.347	0.0667	1.0108	0.0588	0.059	0.033	0.028	0.025	0.013	0.001	1.146	1.018	0.128	0.097	4.601	0.423	55.752	**22.102**	**2.021**
	Grain 3	7.653	0.0677	1.4022	0.0668	-0.070	0.030	-0.099	0.028	0.005	0.001	-2.910	0.839	-0.183	0.063	4.190	0.309	76.959	**20.142**	**1.477**
	Grain 4	19.422	0.0664	4.4399	0.0606	0.054	0.029	0.016	0.028	0.009	0.001	0.146	0.259	-0.001	0.019	3.756	0.090	85.967	**18.064**	**0.431**
	Grain 5	9.974	0.0623	2.2648	0.0629	0.024	0.028	0.032	0.028	0.010	0.001	0.590	0.507	-0.007	0.036	3.111	0.158	70.715	**14.975**	**0.759**
	Grain 6	6.893	0.0613	1.2564	0.0614	-0.043	0.029	0.013	0.027	0.005	0.001	1.822	3.949	-0.136	0.067	4.469	0.369	81.557	**21.476**	**1.762**
	HY14-18MC119A1																			
	Grain 1	178.634	0.0392	257.4379	0.0298	3.110	0.017	50.565	0.018	0.185	0.001	2.420	0.001	0.000	0.000	0.573	0.001	82.493	**19.223**	**0.044**
	Grain 2	63.679	0.0333	95.3663	0.0206	1.168	0.014	1.186	0.014	0.028	0.001	0.153	0.002	0.001	0.000	0.580	0.002	86.863	**19.461**	**0.062**
	Grain 3	174.054	0.0416	184.3395	0.0252	2.261	0.017	0.321	0.013	0.190	0.001	0.021	0.001	0.000	0.000	0.632	0.002	66.978	**21.208**	**0.063**
	Grain 4	39.944	0.0361	67.9025	0.0192	0.778	0.016	1.481	0.014	0.013	0.000	0.269	0.003	-0.002	0.001	0.534	0.002	90.774	**17.925**	**0.063**
	Grain 5	52.802	0.0339	73.7795	0.0200	0.891	0.017	0.151	0.014	0.026	0.000	0.025	0.002	0.000	0.001	0.605	0.002	84.641	**20.319**	**0.068**
	Grain 6	43.504	0.0354	53.4860	0.0169	0.675	0.016	0.130	0.014	0.027	0.001	0.030	0.003	0.002	0.001	0.657	0.003	80.879	**22.056**	**0.096**
	Grain 7	39.316	0.0326	60.3928	0.0183	0.750	0.017	0.722	0.015	0.009	0.000	0.148	0.003	0.001	0.001	0.605	0.002	92.919	**20.292**	**0.069**
	Grain 8	48.263	0.0364	56.2888	0.0188	0.688	0.016	2.378	0.014	0.052	0.001	0.524	0.003	0.000	0.001	0.598	0.003	69.826	**20.087**	**0.110**
	Grain 9	28.994	0.0311	41.9798	0.0170	0.518	0.014	0.676	0.014	0.009	0.000	0.202	0.004	0.001	0.001	0.628	0.003	91.025	**21.085**	**0.103**
	Grain 10	53.047	0.0381	68.0248	0.0185	0.822	0.014	2.055	0.014	0.032	0.001	0.379	0.003	0.000	0.001	0.650	0.002	83.370	**21.802**	**0.082**
	HY15-17MC059A1																			
	Grain 1	149.430	0.0753	31.7334	0.0652	0.410	0.032	0.049	0.027	0.048	0.001	0.053	0.030	0.001	0.003	4.255	0.016	90.459	**20.494**	**0.079**
	Grain 2	19.616	0.0643	4.6108	0.0659	0.109	0.029	-0.001	0.029	0.008	0.001	-0.005	0.214	0.032	0.019	3.744	0.092	88.118	**18.047**	**0.443**
	Grain 3	18.838	0.0664	3.2622	0.0558	0.015	0.028	0.025	0.029	0.018	0.001	0.263	0.304	-0.026	0.025	4.117	0.125	71.366	**19.832**	**0.600**
	Grain 4	73.042	0.0702	6.4522	0.0605	0.112	0.029	0.040	0.028	0.009	0.001	0.215	0.148	0.014	0.013	10.911	0.121	96.478	**52.093**	**0.568**
	Grain 5	20.830	0.0588	6.2379	0.0592	0.057	0.029	0.017	0.029	0.009	0.001	0.092	0.159	-0.010	0.014	2.909	0.058	87.222	**14.037**	**0.277**
	Grain 6	20.177	0.0627	3.1867	0.0579	0.091	0.029	0.000	0.030	0.027	0.001	0.004	0.324	0.043	0.027	3.842	0.135	60.744	**18.514**	**0.649**
	Grain 7	17.812	0.0677	4.4339	0.0608	0.066	0.028	0.017	0.027	0.013	0.001	0.133	0.215	0.006	0.019	3.165	0.092	78.887	**15.269**	**0.444**
	Grain 8	39.201	0.0689	6.3242	0.0674	0.121	0.031	-0.102	0.028	0.041	0.001	-0.555	0.151	0.017	0.015	4.255	0.075	68.735	**20.494**	**0.360**
	HY16-18MC246A1																			
	Grain 1	60.718	0.0361	100.8088	0.0213	1.229	0.015	0.216	0.013	0.038	0.001	0.026	0.002	0.000	0.000	0.485	0.002	80.506	**16.237**	**0.062**
	Grain 2	61.984	0.0370	79.8831	0.0185	0.972	0.016	0.087	0.014	0.042	0.001	0.013	0.002	0.000	0.001	0.615	0.002	79.269	**20.571**	**0.076**
	Grain 3	30.776	0.0339	62.4154	0.0176	0.738	0.015	0.440	0.014	0.018	0.000	0.086	0.003	-0.001	0.001	0.404	0.002	82.069	**13.561**	**0.070**
	Grain 4	27.770	0.0359	66.8622	0.0199	0.796	0.015	5.102	0.014	0.021	0.000	0.932	0.003	0.000	0.001	0.353	0.002	84.914	**11.827**	**0.069**
	Grain 5	69.085	0.0367	169.3153	0.0285	2.046	0.016	16.719	0.016	0.052	0.001	1.207	0.001	0.000	0.000	0.360	0.001	88.192	**12.068**	**0.037**
	Grain 6	70.078	0.0362	126.6750	0.0220	1.525	0.016	0.187	0.013	0.027	0.000	0.018	0.001	0.000	0.000	0.483	0.001	87.275	**16.167**	**0.039**
	Grain 7	75.378	0.0362	126.8583	0.0200	1.515	0.015	0.113	0.013	0.028	0.001	0.010	0.001	0.000	0.000	0.522	0.001	87.920	**17.487**	**0.043**
	Grain 8	44.056	0.0359	81.0083	0.0181	0.986	0.016	0.155	0.014	0.017	0.000	0.023	0.002	0.000	0.001	0.474	0.002	87.198	**15.881**	**0.053**
	HY17-17MC021A1																			
	Grain 1	65.894	0.0641	13.4657	0.0623	0.143	0.028	0.073	0.028	0.040	0.001	0.106	0.041	-0.006	0.006	4.023	0.037	82.282	**19.390**	**0.179**
	Grain 2	200.946	0.0884	50.5506	0.0752	0.642	0.031	0.065	0.027	0.044	0.001	0.025	0.010	0.001	0.002	3.716	0.011	93.580	**17.920**	**0.053**
	Grain 3	48.520	0.0706	11.5013	0.0674	0.117	0.030	0.023	0.028	0.011	0.001	0.039	0.048	-0.007	0.008	3.921	0.040	93.037	**18.903**	**0.192**
	Grain 4	45.459	0.0735	10.8108	0.0673	0.170	0.029	0.047	0.028	0.013	0.001	0.086	0.052	0.010	0.008	3.847	0.040	91.575	**18.548**	**0.193**
	Grain 5	47.801	0.0700	9.3878	0.0624	0.110	0.030	0.065	0.028	0.028	0.001	0.136	0.059	-0.003	0.009	4.224	0.054	83.030	**20.355**	**0.260**
	Grain 6	38.770	0.0730	8.0862	0.0645	0.136	0.032	1.322	0.029	0.023	0.001	3.249	0.077	0.012	0.012	4.073	0.062	84.946	**19.634**	**0.298**
	Grain 7	78.805	0.0767	16.3375	0.0622	0.213	0.029	0.131	0.028	0.044	0.002	0.159	0.034	0.001	0.005	4.038	0.032	83.785	**19.462**	**0.155**
	Grain 8	50.839	0.0680	11.9519	0.0659	0.166	0.031	-0.037	0.027	0.018	0.001	-0.062	0.046	0.004	0.007	3.804	0.036	89.514	**18.340**	**0.175**
	HY18-17MC024A2																			
	Grain 1	12.711	0.0657	2.6589	0.0591	0.105	0.029	0.003	0.028	0.007	0.001	0.030	0.320	0.078	0.032	4.040	0.163	84.597	**19.450**	**0.782**
	Grain 2	5.382	0.0606	1.1630	0.0579	0.060	0.032	0.043	0.029	0.003	0.001	1.103	0.738	0.112	0.081	3.961	0.343	85.644	**19.071**	**1.642**
	Grain 3	8.944	0.0503	2.1160	0.0444	0.022	0.029	-0.049	0.025	0.002	0.001	-0.943	0.498	-0.006	0.040	3.844	0.142	91.082	**18.510**	**0.679**
	Grain 4	6.271	0.0642	1.5087	0.0562	0.033	0.031	0.030	0.026	0.004	0.001	0.817	0.703	0.027	0.061	3.360	0.231	80.925	**16.193**	**1.109**

Unit	Sample/Grain #	Ar^{40} (fA)	±1σ	Ar^{39} (fA)	±1σ	Ar^{38} (fA)	±1σ	Ar^{37} (fA)	±1σ	Ar^{36} (fA)	±1σ	Ca/K	±1σ	Cl/K	±1σ	$^{40}Ar^*/^{39}Ar_{(K)}$	±1σ	$^{40}Ar^*$	Age (Ma)[1]	±1σ
	HY19-18MC121A1																			
	Grain 01	2.416	0.0331	4.4510	0.0136	0.043	0.016	0.005	0.013	0.001	0.000	0.014	0.034	-0.007	0.010	0.460	0.026	84.743	**15.446**	**0.870**
	Grain 02	3.645	0.0324	4.3838	0.0129	0.061	0.016	-0.009	0.014	0.004	0.000	-0.026	0.038	0.005	0.011	0.554	0.025	66.630	**18.585**	**0.846**
	Grain 03	0.778	0.0315	0.4818	0.0127	0.028	0.015	0.011	0.013	0.001	0.000									
	HY26-17MC053B1																			
	Grain 1	153.749	0.0770	19.8851	0.0665	0.271	0.030	-0.026	0.027	0.233	0.002	-0.047	0.049	-0.002	0.004	4.261	0.044	55.175	**20.515**	**0.210**
	Grain 2	71.221	0.0727	6.9844	0.0625	0.114	0.031	-0.003	0.025	0.140	0.002	-0.014	0.127	0.001	0.013	4.251	0.097	41.736	**20.467**	**0.462**
	Grain 3	212.499	0.0813	33.7717	0.0647	0.363	0.029	0.061	0.027	0.208	0.003	0.064	0.028	-0.008	0.003	4.467	0.027	71.078	**21.501**	**0.131**
	Grain 4	222.966	0.0690	36.9139	0.0506	0.459	0.022	0.022	0.019	0.185	0.002	0.021	0.018	-0.002	0.002	4.558	0.021	75.551	**21.936**	**0.100**
	Grain 5	279.869	0.0883	47.1323	0.0715	0.593	0.031	-0.009	0.027	0.277	0.003	-0.007	0.021	-0.002	0.002	4.194	0.023	70.712	**20.193**	**0.109**
	HY27-17MC007A2																			
	Grain 1	146.163	0.0820	29.3098	0.0634	0.399	0.029	-0.039	0.026	0.080	0.002	-0.026	0.017	0.003	0.003	4.180	0.020	83.901	**20.141**	**0.096**
	Grain 2	76.480	0.0748	16.2027	0.0685	0.226	0.032	0.037	0.028	0.042	0.001	0.043	0.034	0.004	0.006	3.949	0.032	83.739	**19.033**	**0.153**
	Grain 3	111.835	0.0779	25.8803	0.0681	0.340	0.031	0.007	0.026	0.031	0.001	0.005	0.019	0.002	0.004	3.966	0.019	91.874	**19.116**	**0.091**
	Grain 4	169.654	0.0872	39.3961	0.0642	0.462	0.032	0.004	0.028	0.023	0.001	0.002	0.014	-0.002	0.002	4.131	0.013	96.029	**19.908**	**0.065**
	Grain 5	73.032	0.0777	12.9822	0.0717	0.135	0.030	0.011	0.026	0.038	0.002	0.016	0.039	-0.007	0.007	4.764	0.049	84.771	**22.939**	**0.237**
	Grain 6	175.020	0.0840	29.5203	0.0618	0.389	0.028	-0.020	0.027	0.136	0.002	-0.014	0.018	0.000	0.003	4.566	0.024	77.090	**21.991**	**0.114**
	Grain 7	113.944	0.0730	24.4161	0.0669	0.348	0.032	0.084	0.028	0.041	0.001	0.066	0.022	0.005	0.004	4.169	0.022	89.430	**20.091**	**0.103**
	Grain 8	129.510	0.0744	28.4142	0.0687	0.335	0.035	-0.001	0.026	0.034	0.001	-0.001	0.018	-0.002	0.004	4.196	0.018	92.159	**20.220**	**0.087**
	HY28-17MC005B1																			
	Grain 1	21.428	0.0658	5.6103	0.0659	0.107	0.031	0.008	0.029	0.007	0.001	0.027	0.098	0.019	0.016	3.430	0.070	89.902	**16.553**	**0.338**
	Grain 2	63.566	0.0729	8.5938	0.0639	0.140	0.031	0.072	0.028	0.105	0.002	0.159	0.062	0.005	0.010	3.788	0.079	51.252	**18.269**	**0.378**
	Grain 3	24.013	0.0631	5.3078	0.0689	0.100	0.030	0.032	0.027	0.015	0.001	0.114	0.099	0.018	0.017	3.697	0.083	81.804	**17.836**	**0.397**
	Grain 4	57.444	0.0668	11.1286	0.0628	0.168	0.031	0.030	0.026	0.014	0.001	0.051	0.045	0.008	0.008	4.787	0.039	92.828	**23.059**	**0.186**
	Grain 5	29.417	0.0717	3.6869	0.0595	0.041	0.029	-0.052	0.027	0.051	0.001	-0.272	0.140	-0.011	0.023	3.869	0.121	48.536	**18.658**	**0.581**
	Grain 6	22.432	0.0690	4.5249	0.0604	0.074	0.028	0.019	0.027	0.019	0.001	0.081	0.116	0.010	0.018	3.688	0.096	74.462	**17.791**	**0.460**
	Grain 7	34.545	0.0661	6.9221	0.0619	0.093	0.032	-0.020	0.026	0.023	0.001	-0.055	0.073	0.002	0.013	3.990	0.057	80.038	**19.242**	**0.273**
	Grain 8	14.127	0.0670	3.1363	0.0622	0.048	0.031	0.032	0.028	0.011	0.001	0.198	0.170	0.007	0.028	3.471	0.126	77.127	**16.748**	**0.604**
	HY29-18MC155A1																			
	Grain 1	13.328	0.0481	22.1496	0.0214	0.298	0.017	0.002	0.014	0.008	0.001	0.000	0.005	0.004	0.002	0.485	0.009	80.602	**16.375**	**0.290**
	Grain 2	16.374	0.0519	22.4655	0.0233	0.302	0.016	0.004	0.014	0.016	0.001	0.001	0.005	0.004	0.002	0.515	0.009	70.743	**17.402**	**0.296**
	Grain 3	1.448	0.0494	2.6538	0.0213	0.042	0.015	-0.004	0.013	0.000	0.001	-0.013	0.039	0.012	0.017	0.592	0.066	108.600	**19.980**	**2.209**
	Grain 4	150.125	0.0560	43.6176	0.0258	0.544	0.015	0.189	0.014	0.160	0.001	0.034	0.003	-0.001	0.001	2.351	0.009	68.348	**78.089**	**0.306**
	Grain 5	16.413	0.0547	29.6132	0.0236	0.382	0.017	2.296	0.013	0.012	0.001	0.619	0.004	0.003	0.002	0.457	0.007	82.530	**15.450**	**0.240**
	Grain 6	17.058	0.0519	25.0405	0.0245	0.255	0.017	-0.005	0.014	0.011	0.001	-0.002	0.004	-0.005	0.002	0.546	0.008	80.212	**18.437**	**0.260**
	HY30-18MC003B1																			
	Grain 1	4.869	0.0653	7.5009	0.0214	0.105	0.016	0.010	0.014	0.003	0.001	0.010	0.015	0.006	0.006	0.511	0.025	78.696	**17.243**	**0.842**
	Grain 2	6.288	0.0539	8.4449	0.0243	0.124	0.018	0.010	0.014	0.005	0.001	0.009	0.013	0.008	0.006	0.551	0.021	74.067	**18.608**	**0.712**
	Grain 3	8.798	0.0537	10.9322	0.0219	0.121	0.017	-0.001	0.013	0.006	0.001	-0.001	0.010	-0.003	0.005	0.647	0.015	80.391	**21.811**	**0.516**
	Grain 4	13.682	0.0528	18.2320	0.0220	0.191	0.017	0.013	0.014	0.009	0.001	0.005	0.006	-0.005	0.003	0.603	0.010	80.384	**20.343**	**0.333**
	Grain 5	12.731	0.0481	20.5891	0.0236	0.257	0.018	0.026	0.014	0.008	0.001	0.010	0.005	0.001	0.002	0.501	0.009	81.012	**16.910**	**0.318**
	HY31-17MC003A1																			
	Grain 01	14.618	0.0313	32.2452	0.0161	0.361	0.015	-0.005	0.013	0.003	0.000	-0.002	0.005	-0.002	0.001	0.422	0.003	93.207	**14.153**	**0.107**
	Grain 02	17.757	0.0324	31.4396	0.0152	0.364	0.016	-0.002	0.013	0.016	0.000	-0.001	0.005	-0.001	0.002	0.403	0.005	71.334	**13.497**	**0.156**
	Grain 03	58.932	0.0354	45.8936	0.0173	0.590	0.016	-0.011	0.013	0.117	0.001	-0.003	0.003	0.001	0.001	0.523	0.006	40.757	**17.514**	**0.199**
	Grain 04	15.788	0.0317	30.6462	0.0160	0.359	0.018	0.037	0.014	0.008	0.000	0.014	0.005	-0.001	0.002	0.433	0.004	84.134	**14.517**	**0.125**
	Grain 05	8.147	0.0349	7.7977	0.0133	0.087	0.016	0.088	0.013	0.014	0.000	0.134	0.021	-0.003	0.006	0.527	0.016	50.510	**17.660**	**0.546**
	Grain 06	23.257	0.0340	37.1879	0.0155	0.461	0.016	-0.008	0.015	0.016	0.000	-0.003	0.005	0.001	0.001	0.489	0.004	78.209	**16.373**	**0.125**
	Grain 07	13.125	0.0331	24.0587	0.0156	0.267	0.016	-0.004	0.014	0.010	0.000	-0.003	0.007	-0.003	0.002	0.420	0.006	77.122	**14.092**	**0.189**
	Grain 08	10.244	0.0348	19.8470	0.0146	0.253	0.017	-0.004	0.013	0.009	0.000	-0.003	0.008	0.002	0.002	0.368	0.006	71.436	**12.356**	**0.195**
	HY32-18MC001A1																			
	Grain 1	12.844	0.0324	20.6929	0.0143	0.252	0.016	1.524	0.015	0.020	0.000	0.914	0.009	0.000	0.002	0.359	0.007	57.885	**12.101**	**0.232**
	Grain 2	83.188	0.0393	196.4877	0.0252	2.375	0.016	2.605	0.014	0.047	0.001	0.164	0.001	0.000	0.000	0.352	0.001	83.267	**11.871**	**0.036**
	Grain 3	50.296	0.0389	143.7078	0.0241	1.715	0.015	0.950	0.013	0.017	0.000	0.082	0.001	0.000	0.000	0.311	0.001	88.867	**10.477**	**0.034**
	Grain 4	77.116	0.0369	194.2121	0.0255	2.340	0.016	1.395	0.013	0.039	0.001	0.089	0.001	0.000	0.000	0.334	0.001	84.057	**11.241**	**0.031**
	Grain 5	84.520	0.0353	209.1621	0.0279	2.475	0.016	0.434	0.014	0.017	0.000	0.025	0.001	0.000	0.000	0.374	0.001	92.519	**12.586**	**0.024**
	Grain 6	41.006	0.0372	112.6789	0.0239	1.347	0.016	0.653	0.013	0.007	0.000	0.072	0.001	0.000	0.000	0.341	0.001	93.773	**11.492**	**0.034**
	Grain 7	15.542	0.0328	40.6677	0.0173	0.506	0.016	0.109	0.015	0.004	0.000	0.033	0.004	0.001	0.001	0.347	0.002	90.829	**11.689**	**0.081**
	Grain 8	31.018	0.0369	82.5978	0.0199	0.980	0.015	0.555	0.014	0.006	0.000	0.084	0.002	0.000	0.001	0.351	0.001	93.581	**11.834**	**0.049**
	Grain 9	21.000	0.0324	53.8427	0.0175	0.607	0.016	0.141	0.014	0.004	0.000	0.032	0.003	-0.002	0.001	0.363	0.002	93.103	**12.226**	**0.072**
	HY33-18MC086A1																			
	Grain 1	26.434	0.0333	75.7119	0.0187	0.897	0.015	0.146	0.014	0.013	0.000	0.023	0.002	0.000	0.001	0.293	0.002	83.991	**9.834**	**0.050**
	Grain 2	19.615	0.0319	39.8986	0.0172	0.476	0.016	0.102	0.014	0.016	0.000	0.031	0.004	0.000	0.001	0.365	0.003	74.368	**12.253**	**0.109**
	Grain 3	42.485	0.0344	114.1153	0.0205	1.360	0.016	0.300	0.013	0.020	0.001	0.031	0.001	0.000	0.000	0.314	0.001	84.377	**10.532**	**0.046**
	Grain 4	31.560	0.0326	80.8007	0.0201	0.978	0.016	1.442	0.013	0.017	0.000	0.216	0.002	0.000	0.001	0.329	0.002	84.289	**11.037**	**0.055**
	Grain 5	23.537	0.0338	68.3114	0.0176	0.806	0.016	0.111	0.013	0.010	0.000	0.019	0.002	-0.001	0.001	0.297	0.002	86.127	**9.951**	**0.058**
	Grain 6	49.035	0.0363	138.4263	0.0230	1.660	0.017	0.358	0.013	0.011	0.000	0.031	0.001	0.000	0.000	0.325	0.001	91.735	**10.894**	**0.029**
	Grain 7	23.347	0.0316	55.1598	0.0182	0.668	0.016	0.131	0.015	0.011	0.000	0.028	0.003	0.000	0.001	0.358	0.002	84.613	**12.003**	**0.083**
	Grain 8	10.362	0.0319	22.9573	0.0144	0.256	0.015	0.069	0.013	0.003	0.000	0.036	0.007	-0.002	0.002	0.404	0.005	89.475	**13.529**	**0.163**
	HY34-17MC001A1																			
	Grain 1	42.844	0.0709	14.4294	0.0615	0.167	0.030	0.010	0.026	0.011	0.001	0.012	0.034	-0.002	0.006	2.732	0.027	92.122	**13.199**	**0.128**
	Grain 2	80.323	0.0777	34.9754	0.0625	0.403	0.032	0.168	0.027	0.010	0.001	0.090	0.014	-0.002	0.003	2.216	0.012	96.617	**10.714**	**0.058**
	Grain 3	32.216	0.0657	14.5251	0.0698	0.196	0.032	0.052	0.026	0.006	0.001	0.068	0.033	0.004	0.006	2.099	0.026	94.739	**10.148**	**0.124**
	Grain 4	85.167	0.0722	32.5372	0.0722	0.473	0.032	0.295	0.026	0.039	0.001	0.172	0.015	0.006	0.003	2.266	0.013	86.671	**10.954**	**0.065**
	Grain 5	74.173	0.0733	27.1801	0.0690	0.319	0.031	0.133	0.029	0.037	0.001	0.093	0.021	-0.002	0.003	2.327	0.016	85.368	**11.248**	**0.078**
	Grain 6	179.395	0.0900	56.8846	0.0830	0.632	0.033	0.954	0.024	0.072	0.002	0.318	0.008	-0.004	0.002	2.789	0.012	88.520	**13.471**	**0.058**
	Grain 7	74.129	0.0691	20.4834	0.0767	0.235	0.031	0.085	0.026	0.073	0.002	0.079	0.024	-0.004	0.004	2.571	0.030	71.125	**12.424**	**0.146**

Lower Unit

[1] red values are rejected

Table S2.4. Results of (U-Th)/He analysis of zircon from the Upper, Middle and Lower Units of Mt. Hymittos, Attica

Unit	Sample/Grain #	length 1 (mm)	width 1 (mm)	length 2 (mm)	width 2 (mm)	Terms	Dim Mass (mg)	ESR (mm)	4He (nmol/g)	±2σ	U[1] (ppm)	±2σ	Th (ppm)	±2σ	Sm (ppm)	±2σ	eU	4He[1] (ncc)	±2σ	Re (%)	U[1] (ng)	±2σ	Th (ng)	±2σ	Sm[1] (ng)	±2σ	Th/U	Raw Date ft (Ma)	±2σ	Ft[2]	Corrected Date (Ma)*	Analytic Unc. (Ma)2σ
Upper Unit	**HY01-17MC045A1**																														
	Grain 01	165.6	78.7	165.4	73.2	2	3.08	45.61	108.530	0.302	188.971	2.883	79.294	2.494	0.687	0.266	207.605	7.481	0.021	99.994	581.91	0.009	244.04	0.008	BDL	BDL	0.420	96.170	1.349	0.753	**127.28**	**3.58**
	Grain 02	152.0	78.7	152.4	66.6	2	2.52	42.84	25.537	0.116	44.502	1.762	38.848	1.601	1.251	0.177	53.631	1.442	0.007	99.966	0.112	0.004	0.098	0.004	BDL	BDL	0.873	87.611	2.879	0.735	**118.86**	**7.79**
	Grain 03	118.7	51.1	119.5	59.7	2	1.16	32.98	65.184	0.271	209.613	4.261	118.217	1.667	0.624	0.500	237.394	1.698	0.007	99.981	0.244	0.005	0.137	0.002	BDL	BDL	0.564	50.705	0.910	0.665	**76.02**	**2.71**
	Grain 04	117.3	68.2	116.9	57.0	2	1.36	35.50	150.150	0.300	128.943	2.209	113.546	1.833	1.365	0.693	155.626	2.102	0.009	99.987	0.175	0.003	0.154	0.002	BDL	BDL	0.881	81.805	1.200	0.685	**119.07**	**3.45**
	Grain 05	102.4	62.9	101.0	42.3	2	0.80	29.03	46.419	0.224	128.115	4.966	67.483	2.491	0.774	0.315	143.973	0.836	0.004	99.984	0.103	0.004	0.054	0.002	BDL	BDL	0.527	59.495	2.021	0.624	**95.01**	**6.22**
	Grain 06	124.9	47.6	125.6	47.8	2	0.99	30.02	128.294	0.262	289.363	9.356	95.136	2.660	1.446	0.485	311.720	2.838	0.006	99.992	0.286	0.009	0.094	0.003	BDL	BDL	0.329	75.856	2.215	0.624	**118.45**	**6.94**
	Grain 07	110.8	66.9	111.2	52.9	2	1.16	33.60	161.574	0.441	411.892	16.517	147.398	1.187	0.944	1.100	423.031	4.196	0.011	99.998	0.477	0.019	0.055	0.001	BDL	BDL	0.115	70.450	2.672	0.676	**103.88**	**7.77**
	Grain 08	130.4	48.9	127.5	63.8	1	1.59	34.00	198.342	0.759	601.775	6.890	54.846	1.048	0.865	0.234	614.664	7.085	0.027	99.998	0.959	0.011	0.087	0.002	BDL	BDL	0.091	59.582	0.686	0.682	**87.07**	**1.96**
	HY02-18MC142A2																														
	Grain 01	189.1	77.0	187.9	66.4	2	3.34	44.91	79.903	0.238	334.958	4.872	107.975	2.098	0.363	0.525	360.332	5.979	0.018	99.989	1.118	0.016	0.360	0.007	BDL	BDL	0.322	40.999	0.553	0.750	**54.56**	**1.48**
	Grain 02	124.5	61.0	124.9	57.0	2	1.38	35.12	71.920	0.213	249.076	5.519	238.824	10.283	0.093	1.259	305.199	2.224	0.007	99.994	0.344	0.008	0.329	0.014	BDL	BDL	0.959	43.520	0.847	0.681	**63.80**	**2.47**
	Grain 03	130.4	68.1	124.3	65.6	2	1.72	38.50	43.069	0.157	183.613	2.134	76.956	1.313	0.747	0.786	181.958	1.660	0.006	99.972	0.282	0.004	0.132	0.002	BDL	BDL	0.470	43.741	0.527	0.711	**61.42**	**1.47**
	Grain 04	166.7	66.2	168.1	68.7	1	3.06	42.03	14.213	0.074	51.646	2.109	7.142	0.333	BDL	BDL	53.325	0.976	0.005	99.978	0.158	0.006	0.022	0.001	BDL	BDL	0.138	49.258	1.906	0.738	**66.61**	**5.20**
	Grain 05	171.0	69.5	169.4	39.6	2	1.66	32.52	4.651	0.038	2.207	0.401	6.572	0.208	BDL	BDL	3.751	0.174	0.001	99.742	0.004	0.001	0.011	0.000	BDL	BDL	2.978	225.841	23.541	0.643	**348.29**	**69.81**
	Grain 06	155.6	56.4	152.2	59.0	1	2.08	36.43	14.717	0.058	0.971	0.283	6.941	0.481	BDL	BDL	2.602	0.687	0.003	97.328	0.002	0.001	0.014	0.001	BDL	BDL	7.146	989.231	112.439	0.673	**1430.23**	**332.06**
	HY03-17MC019A1																														
	Grain 01	259.6	137.0	255.9	136.4	2	14.48	78.46	52.635	0.162	177.799	2.620	40.714	1.497	0.269	0.020	187.367	17.080	0.053	99.997	2.574	0.038	0.589	0.022	BDL	BDL	0.229	51.897	0.727	0.854	**60.71**	**1.70**
	Grain 02	238.2	119.8	234.5	109.1	2	9.71	67.56	70.166	0.234	276.184	4.024	104.613	7.814	0.582	0.141	300.768	15.277	0.051	99.995	2.683	0.039	1.016	0.076	BDL	BDL	0.379	43.121	0.635	0.830	**51.88**	**1.53**
	Grain 03	194.2	101.2	192.8	82.8	2	5.12	54.14	96.494	0.310	310.308	4.850	53.487	0.483	0.327	0.052	322.878	11.080	0.036	99.992	1.590	0.025	0.274	0.002	BDL	BDL	0.172	55.199	0.823	0.792	**69.60**	**2.07**
	Grain 04	195.2	124.7	194.0	124.8	2	8.06	65.96	105.813	0.330	445.217	6.456	117.337	8.337	0.588	0.053	472.791	19.125	0.060	99.996	3.590	0.052	0.946	0.067	BDL	BDL	0.264	41.383	0.588	0.827	**49.97**	**1.41**
	Grain 05	242.3	157.9	37.5	143.4	2	4.13	46.30	78.762	0.236	230.255	4.564	263.955	5.515	1.627	0.325	292.285	7.293	0.022	99.992	0.951	0.019	1.091	0.023	0.007	**0.001**	1.146	49.729	0.797	0.752	**65.99**	**1.85**
	Grain 06	162.6	58.8	162.0	64.7	1	2.51	38.82	0.840	0.011	0.165	0.041	0.953	0.036	0.000	0.000	0.385	0.047	0.001	99.823	BDL	BDL	BDL	0.000	BDL	BDL	5.759	389.466	40.811	0.693	**555.85**	**117.15**
	Grain 07	189.5	47.9	193.5	69.4	2	2.34	37.19	1.584	0.012	1.456	2.615	6.414	0.114	0.000	0.000	2.963	0.083	0.001	100.000	0.003	0.006	0.015	0.000	BDL	BDL	4.406	98.168	83.506	0.680	**143.81**	**241.05**
	HY04-18MC116A2																														
	Grain 01	158.0	74.3	159.5	60.2	2	2.36	40.82	46.850	0.160	272.339	3.831	117.921	2.642	0.284	0.616	300.051	2.476	0.008	99.732	0.642	0.009	0.278	0.006	BDL	BDL	0.433	28.894	0.375	0.726	**39.75**	**1.03**
	Grain 02	116.4	75.2	119.0	60.0	1	1.99	38.23	40.111	0.111	200.705	2.909	91.808	4.779	0.100	0.224	222.280	1.789	0.005	99.985	0.399	0.006	0.183	0.010	BDL	BDL	0.457	33.380	0.465	0.712	**46.82**	**1.30**
	Grain 03	165.0	81.1	169.4	91.2	1	4.76	50.65	23.700	0.106	159.508	4.954	61.283	1.753	0.298	0.096	173.910	2.528	0.011	99.990	0.759	0.024	0.292	0.008	BDL	BDL	0.384	25.229	0.707	0.778	**32.38**	**1.82**
	Grain 04	162.8	82.0	163.0	90.0	2	3.62	49.33	13.283	0.194	389.264	4.943	143.811	1.436	0.375	0.319	423.059	6.755	0.016	99.994	1.409	0.018	0.520	0.005	BDL	BDL	0.369	36.409	0.422	0.771	**47.15**	**1.09**
	Grain 05	105.7	79.6	101.9	74.8	2	1.45	37.27	140.684	0.375	1028.379	19.763	238.409	5.985	0.925	0.389	1084.406	4.564	0.012	99.997	1.489	0.029	0.345	0.009	BDL	BDL	0.232	24.027	0.430	0.705	**34.03**	**1.17**
	Grain 06	151.0	82.0	153.4	62.8	2	2.47	42.22	9.090	0.054	1.224	0.305	6.714	0.125	BDL	BDL	2.802	0.502	0.003	99.982	0.003	0.001	0.017	0.000	BDL	BDL	5.486	579.509	61.184	0.714	**800.13**	**168.16**
	Grain 07	209.5	121.8	237.3	100.9	2	7.63	63.98	64.639	0.139	186.574	2.983	74.457	0.626	0.286	0.106	214.071	11.732	0.024	99.975	1.499	0.023	0.568	0.005	BDL	BDL	0.379	59.182	0.808	0.819	**72.17**	**1.96**
	HY05-17MC030A1																														
	Grain 01	273.9	78.6	273.8	77.3	2	6.27	51.68	51.476	0.125	185.906	1.536	112.645	5.651	1.754	0.279	212.378	7.233	0.018	99.996	1.166	0.010	0.706	0.035	0.011	**0.002**	0.606	44.777	0.436	0.779	**57.39**	**1.13**
	Grain 02	172.3	88.2	168.5	85.1	1	5.45	53.37	83.233	0.176	387.566	7.417	165.502	2.680	1.260	0.150	426.470	10.171	0.021	99.998	2.113	0.040	0.903	0.015	0.007	**0.001**	0.427	36.094	0.615	0.789	**45.71**	**1.56**
	Grain 03	253.7	112.6	248.3	71.1	2	4.89	52.39	64.759	0.184	306.106	4.521	91.211	5.431	1.083	0.133	327.541	7.104	0.020	99.996	1.498	0.022	0.446	0.027	BDL	BDL	0.298	36.571	0.520	0.775	**47.14**	**1.28**
	Grain 04	259.9	102.0	261.8	90.9	2	8.46	60.91	73.242	0.271	275.882	4.757	106.076	1.561	0.769	0.256	300.810	13.895	0.051	99.996	2.335	0.040	0.898	0.013	0.007	**0.002**	0.384	44.997	0.711	0.813	**55.31**	**1.76**
	Grain 05	175.4	74.8	176.2	75.9	2	3.31	46.16	131.911	0.402	556.736	8.294	224.404	3.387	1.195	0.389	609.941	9.800	0.030	99.996	1.845	0.027	0.750	0.011	BDL	BDL	0.407	39.984	0.543	0.756	**52.81**	**1.44**
	Grain 06	183.8	99.4	184.4	101.9	2	5.51	57.11	24.495	0.113	120.784	2.971	64.227	2.017	1.588	0.116	135.878	3.025	0.014	99.873	0.665	0.016	0.354	0.011	0.009	**0.001**	0.532	33.339	0.731	0.800	**41.64**	**1.82**
	Grain 07	190.7	73.6	192.5	77.3	2	3.74	47.15	100.193	0.432	473.816	6.090	75.477	1.927	0.490	0.110	491.553	8.398	0.036	99.998	1.772	0.023	0.282	0.007	BDL	BDL	0.159	37.708	0.482	0.763	**49.36**	**1.27**
	Grain 08	220.5	61.1	219.7	59.1	1	3.02	40.06	0.639	0.009	0.143	0.119	0.409	0.207	BDL	BDL	1.197	0.064	0.001	99.848	BDL	BDL	0.015	0.001	BDL	BDL	34.248	132.527	12.798	0.685	**192.98**	**36.96**
	HY06-17MC050A1																														
	Grain 01	200.5	112.4	197.8	118.2	2	7.55	63.90	30.011	0.092	218.900	4.730	31.808	0.772	0.925	0.085	226.375	5.080	0.016	99.992	1.653	0.036	0.240	0.006	0.007	0.001	0.145	24.555	0.503	0.823	**29.83**	**1.22**
	Grain 02	207.0	93.9	206.2	74.6	1	5.80	51.74	75.937	0.224	433.461	13.481	102.687	1.677	0.777	0.192	457.592	9.873	0.029	99.996	2.515	0.078	0.596	0.010	BDL	BDL	0.237	30.715	0.881	0.783	**39.16**	**2.26**
	Grain 03	198.1	112.6	196.5	54.5	1	4.69	45.27	24.605	0.102	167.862	3.438	75.944	0.853	0.607	0.179	185.708	2.584	0.011	99.987	0.787	0.016	0.356	0.004	BDL	BDL	0.452	24.527	0.452	0.752	**32.60**	**1.16**
	Grain 04	190.8	140.3	189.8	104.2	2	7.59	64.12	100.711	0.333	576.519	13.535	443.914	6.607	2.055	0.259	680.839	17.134	0.057	99.805	4.376	0.103	3.369	0.050	0.016	0.002	0.770	27.361	0.538	0.820	**33.36**	**1.29**
	Grain 05	168.2	54.2	165.8	44.8	2	1.51	32.33	86.950	0.248	525.689	8.071	31.312	0.863	1.416	0.497	537.747	2.944	0.008	100.000	1.945	0.012	0.078	0.001	BDL	BDL	0.062	25.255	0.318	0.664	**37.99**	**0.96**
	Grain 06	157.5	72.0	158.8	72.0	2	2.65	43.38	74.682	0.139	403.059	4.398	77.543	1.304	0.386	0.193	421.281	4.440	0.008	99.999	1.069	0.012	0.206	0.003	BDL	BDL	0.192	32.808	0.338	0.743	**44.08**	**0.91**
	Grain 07	159.0	66.7	157.6	65.2	2	2.31	40.67	95.951	0.212	590.403	10.710	131.442	3.866	0.673	0.193	621.292	4.969	0.011	99.649	1.364	0.025	0.304	0.009	BDL	BDL	0.223	28.591	0.483	0.727	**39.27**	**1.33**
	Grain 08	168.7	108.4	154.4	78.6	2	5.82	50.07	25.576	0.093	208.076	3.549	74.453	1.597	0.538	0.184	218.644	2.188	0.009	99.995	0.794	0.015	0.172	0.006	BDL	BDL	0.216	21.670	0.380	0.778	**27.92**	**0.99**
Middle Unit	**HY07-17MC060A1**																														
	Grain 01	137.6	66.7	131.3	37.0	1	1.32	29.96	0.392	0.025	0.153	0.192	0.807	0.038	0.295	0.333	0.343	0.012	0.001	97.061	BDL	0.000	BDL	0.000	BDL	BDL	5.270					
	Grain 02	127.3	88.1	119.8	67.6	2	1.79	43.05	17.228	0.065	295.690	5.672	64.956	2.097	0.271	0.222	310.955	0.691	0.003	99.980	0.529	0.010	0.116	0.004	BDL	BDL	0.220	10.274	0.186	0.728	**14.11**	**0.50**
	Grain 03	83.0	73.5	82.8	62.4	2	0.93	35.83	28.826	0.151	452.080	10.654	85.347	1.044	0.876	0.638	472.136	0.598	0.003	99.987	0.419	0.010	0.079	0.001	BDL	BDL	0.189	11.322	0.255	0.675	**16.76**	**0.71**
	Grain 04	109.0	92.5	114.5	81.6	2	2.05	46.61	19.182	0.059	228.200	3.396	100.715	1.131	0.752	0.226	251.868	0.882	0.003	100.000	0.468	0.007	0.207	0.002	BDL	BDL	0.441	14.111	0.190	0.746	**18.90**	**0.49**
	Grain 05	73.6	43.5	73.1	50.1	2	0.43	24.67	17.461	0.073	315.534	10.509	91.766	1.384	0.000	0.000	361.099	0.167	0.001	100.000	0.145	0.004	0.039	0.001	BDL	BDL	0.270	8.967	0.256	0.571	**15.69**	**0.85**
	Grain 06	116.6	55.6	103.0	65.1	1	1.51	34.78	60.108	0.167	954.528	11.089	487.473	7.400	0.965	0.429	1069.084	2.030	0.006	99.987	1.438	0.017	0.734	0.011	BDL	BDL	0.511	10.420	0.110	0.685	**15.19**	**0.32**
	HY08-17MC024B3																														
	Grain 01	206.5	112.7	209.0	105.8	2	6.03	63.43	35.809	0.064	463.934	5.829	102.838	1.725	0.875	0.136	488.101	4.842	0.009	99.995	2.799	0.035	0.620	0.010	BDL	BDL	0.222	13.600	0.160	0.814	**16.70**	**0.39**
	Grain 02	147.9	81.4	145.2	62.4	2	2.31	41.52	30.826	0.163	526.785	8.614	45.199	1.778	0.291	0.142	537.407	1.593	0.008	99.996	1.215	0.020	0.104	0.004	BDL	BDL	0.086	10.640	0.175	0.734	**14.49**	**0.47**
	Grain 03	189.2	51.7	190.2	68.0	2	2.44	38.35	21.119	0.101	354.752	5.420	157.568	5.016	0.697	0.218	391.781	1.155	0.006	99.992	0.866	0.013	0.384	0.012	BDL	BDL	0.444	9.992	0.145	0.709	**14.08**	**0.41**
	Grain 04	241.7	111.2	241.7	88.2	2	7.95	60.77	88.828	0.101	598.581	8.642	148.126	7.205	0.496	0.101	633.391	6.917	0.018	99.997	4.757	0.070	1.177	0.057	BDL	BDL	0.247	11.366	0.159	0.813	**13.97**	**0.39**
	Grain 05	127.6	81.4	129.0	66.6	2	1.69	41.91	67.580	0.173	1078.323	12.660	165.174	2.867	0.707	0.234	1117.139	2.566	0.007	99.979	1.826	0.021	0.280	0.005	BDL	BDL	0.153	11.219	0.127	0.721	**15.54**	**0.34**
	HY12-18MC047B1																														
	Grain 01	72.8	67.6	81.6	65.8	1	1.14	32.69	3.055	0.087	89.918	3.602	13.083	0.502	BDL	BDL	BDL	92.993	0.078	0.002	95.910	0.102	0.004	0.015	0.001	BDL	BDL	0.145	6.096	0.287	0.673	**9.05**	**0.85**
	Grain 02	142.1	72.3	158.6	79.3	2	2.66	44.18	18.855	0.097	432.806	18.244	77.361	7.217	1.312	0.619	450.986	1.123	0.006	99.799	1.151	0.049	0.206	0.019	BDL	BDL	0.179	7.755	0.308	0.748	**10.36**	**0.82**
	Grain 03	98.9	47.1	97.4	47.3	2	0.69	27.99	0.010	0.068	30.393	8.008	410.736	122.918	26.203	24.326	126.916	BDL	0.001	100.000	0.007	0.006	0.284	0.085	0.018	0.017	39.521					
	Grain 04	115.3	58.3	109.3	59.6	0	1.81	35.02	0.106	0.026	0.811	0.533	8.454	0.837	0.342	0.099	2.798	BDL	0.001	100.000	0.001	0.001	0.015	0.002	BDL	BDL	10.420	6.973	2.182	0.661	**10.54**	**6.57**
	Grain 05	74.3	50.6	74.5	42.9	1	0.59	25.86	21.092	0.133	609.011	27.261	185.925	6.422	BDL	BDL	652.704	0.280	0.002	100.000	0.361	0.016	0.110	0.004	BDL	BDL	0.305	5.994	0.246	0.594	**10.08**	**0.82**
	Grain 06	94.3	83.9	100.5	76.7	1	2.11	40.16	12.355	0.091	347.824	219.846	198.390	140.715	5.172	10.381	394.445	0.585	0.004	100.000	0.735	0.464	0.419	0.297	BDL	BDL	0.570	5.806	3.170	0.725	**8.01**	**8.67**
	HY13-17MC032A1																														
	Grain 01	66.4	42.0	64.0	39.5	1	0.40	22.70	11.184	0.076	463.292	14.062	59.993	2.072	0.000	0.000	477.390	0.100	0.001	99.685	0.184	0.006	0.024	0.001	BDL	BDL	0.129	4.348	0.128	0.549	**7.92**	**0.46**
	Grain 02	84.2	57.1	85.7	55.9	2	0.70	29.29	18.003	0.135	720.940	7.897	98.129	2.209	3.085	0.865	744.000	0.283	0.002	99.974	0.506	0.006	0.069	0.002	BDL	BDL	0.136	4.490	0.057	0.634	**7.08**	**0.17**
	Grain 03	93.5	58.2	93.5	50.2	2	0.78	29.85	10.887	0.073	299.954	6.075	154.660	4.746	0.222	0.442	336.299	0.189	0.001	99.843	0.233	0.005	0.120	0.004	BDL	BDL	0.516	6.002	0.114	0.635	**9.45**	**0.35**
	Grain 04	46.1	31.2	44.8	32.6	2	0.11	16.02	6.672	0.171	356.110	11.689	107.566	3.925	0.000	0.000	381.388	0.017	0.000	97.466	0.041	0.001	0.012	0.000	BDL	BDL	0.302	3.246	0.127	0.384	**8.44**	**0.57**
	Grain 05	95.0	63.8	95.9	52.6	1	1.18	32.42	40.974	0.126	202.253	4.921	107.404	2.150	0.498	0.621	227.493	1.086	0.003	99.975	0.239	0.006	0.127	0.003	BDL	BDL	0.531	33.312	0.709	0.665	**49.99**	**2.12**
	HY15-17MC059A1																														
	Grain 01	100.3	44.7	99.1	46.2	2	0.67	27.38	17.699	0.169	660.119	11.004	41.620	0.700	BDL	BDL	669.899	0.264	0.003	99.942	0.440	0.007	0.028	0.000	BDL	BDL	0.063	4.903	0.091	0.610	**8.03**	**0.30**
	Grain 02	109.3	77.8	109.2	73.1	2	1.51	41.67	27.529	0.089	466.126	10.468	28.065	1.827	0.500	0.206	472.721	0.945	0.003	99.987	0.705	0.016	0.042	0.003	BDL	BDL	0.060	10.951	0.238	0.721	**15.18**	**0.65**
	Grain 03	92.6	59.9	88.4	68.3	2	0.90	31.84	28.684	0.187	705.314	13.922	172.299	5.419	0.325	0.522	745.804	0.582	0.004	99.996	0.638	0.013	0.156	0.005	BDL	BDL	0.244	7.134	0.138	0.659	**10.81**	**0.40**
	Grain 04	114.4	59.9	114.4	66.7	1	1.73	36.52	20.638	0.082	555.323	11.006	80.120	0.861	0.654	0.346	574.151	0.801	0.003	99.985	0.962	0.019	0.139	0.001	BDL	BDL	0.144	6.669	0.127	0.703	**9.48**	**0.36**
	Grain 05	88.3	69.2	87.1	50.2	2	0.76	29.49	20.059	0.147	2375.423	16.295	209.628	4.738	BDL	BDL	622.685	0.346	0.002	99.962	0.433	0.012	0.158	0.004	BDL	BDL	0.066	6.090	0.161	0.632	**9.62**	**0.48**
	Grain 06	85.4	86.8	101.7	82.7	2	1.63	43.70	0.042	0.011	0.000	#DIV/0!	0.792	0.037	0.160	0.505	0.186	BDL	0.000	92.599	BDL	BDL	BDL	BDL	BDL	BDL	N/A	6.090				
	Grain 07	84.9	68.5	82.0	75.2	2	1.05	37.54	24.444	0.104	597.826	9.053	286.830	4.554	4.459	0.638	665.231	0.573	0.002	99.980	0.626	0.009	0.300	0.005	BDL	BDL	0.480	6.812	0.095	0.686	**9.92**	**0.27**
	HY19-18MC121A1																														
	Grain 01	115.8	41.1	114.3	35.1	2	0.60	24.50	11.905	0.066	417.745	11.162	138.258	2.848	0.670	1.185	450.235	0.160	0.001	99.822	0.251	0.007	0.083	0.002	BDL	BDL	0.331	4.904	0.101	0.585	**8.67**	**0.42**
	Grain 02	122.2	61.8	120.3	49.8	2	1.20	33.10	6.253	0.033	152.695	3.618	69.589	2.874	0.431	0.836	169.048	0.168	0.001	99.938	0.183	0.004	0.083	0.003	BDL	BDL	0.456	6.858	0.149	0.667	**10.27**	**0.44**
	Grain 03	108.0	46.4	103.5	40.7	0	0.93	26.99	0.410	0.031	1.376	1.615	6.090	0.028	0.028	0.000	0.416	BDL	0.000	97.827	BDL	BDL	BDL	BDL	BDL	BDL	4.250	5.952	42.867	57.486	**5.22**	**131.16**
	Grain 04	83.4	65.1	85.9	56.2	2	0.75	33.09	26.220	0.063	635.496	10.604	777.009	3.158	4.106	1.539	818.093	0.443	0.001	99.965	0.479	0.008	0.586	0.002	BDL	BDL	1.223	5.934	0.076	0.638	**9.29**	**0.23**
	Grain 05	81.6	66.3	83.0	50.2	1	0.67	31.42	36.640	0.209	1225.835	15.231	145.368	5.276	7.837	1.218	1259.996	0.548	0.003	99.954	0.818	0.010	0.097	0.004	BDL	BDL	0.119	5.396	0.070	0.632	**8.53**	**0.21**
	Grain 06	115.8	41.1	114.3	35.1	2	0.60	24.50	24.849	0.106	773.510	14.322	178.193	5.946	BDL	BDL	815.385	0.334	0.001	99.990	0.464	0.009	0.107	0.004	BDL	BDL	0.230	5.654	0.100	0.566	**9.97**	**0.35**
	HY20-18MC020B1																														
	Grain 01	171.5	117.5	169.2	90.3	2	4.40	57.83	19.076	0.128	444.350	8.137	78.596

SI Chapter 3

This supplementary information includes: A detailed description of the methodology for the analytical processes (**S3.1**), a more detailed description of the samples, their zircon morphologies, ages and textures (**S3.2**) as well as SEM-CL images of all imaged zircon (**Figure S3.1**) from chapter three. Tables include detailed detrital zircon analyses from all samples (**Table S3.1**).

S3.1. Methodology

S3.1.1 Zircon U-Pb geochronology

Samples were disaggregated using a jaw crusher followed by sieving and heavy mineral density separation using 3.0 g/cm^3 methylene triiodide. A Franz magnetic separator was used to separate magnetic fractions. Zircon grains were then hand-picked and polished grain mounts were prepared. Zircon textures and compositional zoning were imaged using back-scattered electron (BSE) and scanning electron microscopy cathode luminescence (SEM-CL) imaging using a JEOL 6610LV SEM at the University of Ottawa. SEM images were used to target analytical laser spots in order to avoid cracks, inclusions, and other potential sources of common lead, as well as to avoid overlapping age zones so as to prevent a composite age. LA-ICPMS U-Pb analysis of zircon in grain mounts was conducted at the University of New Brunswick (Attica) and the University of Ottawa (Santorini).

Analyses conducted at the University of New Brunswick, Fredericton, Canada, utilized a Resonetics 193 nm Excimer laser ablation system coupled to an Agilent 7700x quadrupole ICP-MS. A Laurin Technic Pty. 'squid' sample smoothing device was used to improve the measurement quality for the single spot analyses between the sample and the ICPMS. Individual analyses consist of 30 s of ablation per 24 μm spot followed by 25 s of a gas background under a

fluence of 3 J/cm^2. Carrier gases are 300 ml/min helium, 2 ml/min nitrogen, and 930 ml/min argon. The ICPMS was tuned using a continuous raster along the surface of a NIST610 standard, and fine-tuned for maximum sensitivity across the heavy element mass spectrum (Pb, Th, U) following the procedure of (Mcfarlane & Luo, 2012). Atomic masses and ratios monitored for tuning include: 207, 238, 248/232, and 238/232. Isotopes and collection times include: ^{90}Zr: 0.01 s; ^{202}Hg: 0.01 s; ^{204}Pb: 0.04 s; ^{206}Pb: 0.05 s; ^{207}Pb: 0.07 s; ^{208}Pb: 0.01 s; ^{232}Th: 0.01 s; ^{238}U: 0.02 s. Laser-induced Pb/U fractionation corrections, corrected isotope ratios and elemental abundances were calculated offline using Iolite™ version 2.15 (Paton et al., 2011) running as a plug-in for Wavemetrics Igor Pro™ 6.22 and VizualAge™ (Petrus & Kamber, 2012). Reference material FC-1 (1099.1 ± 1.2 Ma; Schmitz et al., 2003) was used as a geochronology standard with Plesovice as a quality control (337.13 ± 0.37 Ma; Slama et al., 2008). Samples 17MC019, 18MC116, 18MC136, 18MC005, and 18MC089 were analysed in two batches, noted on table S3.1.

Analyses conducted at the University of Ottawa, Ottawa, Canada, utilized a Photon Machines Analyte Excite 193 nm excimer laser ablation system coupled to an Agilent 7700x quadrupole ICP-MS. Individual analyses consist of a sequence of 30 s background acquisition, 30 s of ablation time and 40 s of flush per 32 μm spot. The laser was operating at a fluence of 4.9 J/cm^2, and a repetition rate of 6 Hz. Carrier gases are 985 ml/min helium and 710 ml/min argon. The ICPMS was tuned using a continuous raster along the surface of a NIST610 standard, and fine-tuned for maximum sensitivity across the heavy element mass spectrum (Pb, Th, U). Atomic masses and ratios monitored for tuning include: 207, 238, 232/248, 238/232, 89, 175, 232. Isotopes and collection times include: ^{90}Zr: 0.005 s; ^{204}Pb: 0.01 s; ^{206}Pb: 0.02 s; ^{207}Pb: 0.02 s; ^{208}Pb: 0.02 s; ^{232}Th: 0.02 s; ^{238}U: 0.02 s. Data reduction was accomplished using Glitter v4.4 (Griffin et al., 2008) using reference material 91500 (1065 Ma; Wiedenbeck et al., 2007) for ratio calibration and

reference material Plesovice as a secondary standard. Each reference zircon was run every 8 unknowns. Following data reduction and integration, plotting of U-Pb data and kernel density estimates for both data sets was performed using IsoplotR^{TM} 4.0 (Ludwig, 2003; Vermeesch, 2018).

S3.1.2 SEM-CL imaging

Polished zircon mounted in pucks were imaged by SEM-CL using a JEOL 6610LV scanning electron microscope at the University of Ottawa Microanalysis Laboratory (Ottawa, Canada). Imaging was conducted under high vacuum at an acceleration voltage of 15 kV and working distance of 46 mm. Zircon microstructures are described below (**S3.2**) as well as in **Table 3.1**; zircon images are in **Figures S3.1, S3.2**.

S3.2 Detailed sample descriptions and results

The results of 1422 new laser spot analyses (**Table S3.1**) are presented in **Figures 3.4**, and **3.5** within the main manuscript, which also incorporate previous detrital zircon U-Pb analyses from Attica and Santorini in **Figure 3.6** (Lion, 2018; Seman, 2016; Seman et al., 2017). **Table 3.1** provides sample and zircon descriptions, and synthesizes age analyses. Analyses that are >10% discordant, >5% reversely discordant or have >10% 2σ uncertainty are not considered in the following sections. Analyses younger than 900 Ma were not discordance filtered. $^{206}Pb/^{238}U$ ages are considered for apparent ages <1000 Ma, $^{207}Pb/^{206}Pb$ ages are used for analyses >1000 Ma. In cases where $^{206}Pb/^{238}U$ and $^{207}Pb/^{206}Pb$ ages straddle 1000 Ma, the age with lower uncertainty is considered. Select SEM-BSE images of zircon are displayed in **Figure 3.7**. Below is a detailed description of all rock samples analyzed in this study. Zircon textures are described using the nomenclature of Corfu et al. (2003).

3.2.1 Attic Peninsula samples

17MC019A1

Sample 17MC019A1 is a foliated, metasedimentary calcite-sericite-plagioclase feldspar-chlorite-white mica-quartz phyllite collected from an exposure of the Alepovouni Unit in southern Hymittos (**Figure 3.2**). The zircon recovered from this sample comprise euhedral to subrounded, equant (1:1) to elongate grains (up to 6:1) of 90-400 μm lengths. Zircon regularly exhibit oscillatory zoning and rare 1-10 μm thick CL-bright overgrowths (**Figure 3.7; S3.1**). Subrounded zircon boundaries commonly truncate the internal zoning. LA-ICPM spot analyses were conducted on 264 zircon grains; 41 analyses were discarded (**Table S3.1**). The remaining 223 grains yielded concordant ages with distributions ranging between the Neoarchean to early Paleoproterozoic, middle Paleoproterozoic, and late Mesoproterozoic to early Mesozoic with major populations in the Ediacaran, Ordovician, and Devonian (**Figure 3.4**). Sparse late Paleoproterozoic to early Mesoproterozoic analyses occur in the gap between the two older age distributions. Concentrations of U range between 48-1836 ppm and show no correlation with age (**Figure S3.2**). Ratios of Th/U generally range from 0.00-1.00; 13 analyses exhibit ratios of Th/U greater than 1.5; Th/U ratios <0.2 cluster in the Carboniferous to Silurian, and Neoproterozoic.

18MC116A3

Sample 18MC116A3 (**Figure 3.3b**) is a foliated, cataclased calcite-quartz-white mica-chlorite-epidote-serpentinite phyllite collected from an exposure of the Alepovouni Unit directly above the Cycladic Blueschist Unit in northern Hymittos (**Figure 3.2**). The zircon within this sample are typically subhedral to rounded and generally 50-150 μm in length with L:W ratios ranging from 1:1 to 5:1. Zircon grains display a range of CL-brightness, occasional inherited cores, and regularly exhibit oscillatory zoning (**Figure S3.1**). Subrounded to rounded zircon boundaries

truncate the internal zoning. Thin 1-8 μm thick CL-bright overgrowths are rarely observed (**Figure 3.7; S3.1**). LA-ICPM spot analyses were conducted on 241 zircon grains; 19 analyses were discarded (**Table S3.1**). The remaining 222 grains yielded concordant ages with distributions ranging from the early to middle Paleoproterozoic with a cluster in the Orosirian, and late Mesoproterozoic to late Mesozoic with major populations in the Ediacaran, Silurian, and Permian (**Figure 3.4**). Sparse analyses occur in the Neo- and Mesoarchean and the Cretaceous. Uranium concentrations range from 22-828 ppm. Zircon Th/U ratios range from 0.03 to 3.08; zircon analyses with Th/U <0.2 exhibit a cluster in the Late Ordovician. Zircon from this sample commonly exhibit two sets of zoning. The first set surrounds a subrounded to rounded core and is overgrown by a second set of zoning that is itself truncated by the current grain boundary (**Figure 3.7; S3.1**).

18MC136A1

Sample 18MC136A1 (**Figure 3.3d**) is a foliated, L>S tectonite white mica quartzite from a high structural level within the Cheroma Unit in southern Hymittos (**Figure 3.2**). Zircon are typically 50-200 μm in length, with habits generally ranging from rounded to subhedral (**Figure 3.7; S3.1**); larger crystals typically display a greater degree of rounding. Zircon L:W ratios range from 1.2:1 to 4.5:1. Zircon often exhibit oscillatory zoning, and/or CL-bright or CL-dark inherited cores. Incomplete CL-bright rims ranging from 1-5 μm thick are exhibited by rare grains. Spot analyses were conducted on 288 zircon grains; 13 analyses were discarded (**Table S3.1**). The remaining 275 grains yielded concordant ages with distributions ranging from the Neoarchean to middle Paleoproterozoic, and late Mesoproterozoic to the Ordovician with major populations in the Stenian, and Ediacaran (**Figure 3.4**). Sparse analyses yield early Mesoproterozoic and Triassic ages. Concentrations of U range from 26-709 ppm and show no obvious correlation with age

(**Figure S3.2**). Zircon Th/U ratios are 0.03-2.06 with clusters in the Neoproterozoic and middle Paleoproterozoic.

18MC005B1

Sample 18MC005B1 is a foliated hematite quartzite from immediately below the Pyrnari marble in southern Hymittos (**Figure 3.2**). Zircon from this sample range in length from 90-190 μm in length and range from euhedral to subrounded crystals; L:W rations range from 1:1 to 5.5:1. Magmatic oscillatory zoning is common and CL-bright or CL-dark inherited cores are rarely observed (**Figure 3.7; S3.1**). Rounded grain boundaries regularly truncate internal zoning patterns and incomplete, CL-bright rims are rarely observed. Spot analyses were conducted on 261 zircon grains; 42 analyses were discarded (**Table S3.1**). The remaining 219 grains yielded concordant ages with distributions in the Neoarchean, Middle Paleoproterozoic, and Mesoproterozoic to early Paleozoic with major populations in the Stenian, Tonian, and Ediacaran (**Figure 3.4**). Sparse analyses occur in the Calymmian, Mississippian and Triassic. Concentrations of U range from 1675-41 ppm and show no correlation with age. Zircon Th/U values range from 2.15-0.05; analyses of Th/U <0.2 cluster at c. 600 Ma.

18MC089A1

Sample 18MC089A1 is a foliated, lineated, SCC' banded, chloritoid-graphite-quartz-chlorite-white mica schist sampled from the structurally lowest exposure of Cheroma Unit schist in southern Hymittos (**Figure 3.2; 3.3a**). Zircon from this sample are subhedral to anhedral and range in length from 65-190 μm; L:W ratios range from 1:1 to 5:1 (**Figure S3.1**). Crystals regularly exhibit oscillatory zoning, sometimes two generations, and CL-bright or CL-dark inherited cores (**Figure 3.7; S3.1**). Spot analyses were conducted on 255 zircon grains; 26 analyses were discarded (**Table S3.1**). The remaining 229 grains yielded concordant ages with distributions in the

Neoarchean to early Paleoproterozoic, middle Paleoproterozoic and late Mesoproterozoic to early Paleozoic with populations in the Tonian and Ediacaran. Sparse analyses occur in the Mesoarchean (**Figure 3.4**). Concentrations of U range from 1638 to 23 ppm with no obvious relationship to age (**Figure S3.2**). Zircon Th/U values range from 2.75 to 0.02; values <0.2 cluster in the Neoproterozoic.

18MC175A1

Sample 18MC175A1 is a foliated, refolded, lineated calcite-white mica-quartz schist sampled from the Kamariza Unit in central Lavrion (**Figure 3.2**). Zircon from this sample are 70-170 μm in length, and range from equant and anhedral to elongate and prismatic subhedral crystals with 1:1 to 3:1 size ratios. Zircon commonly exhibit one or more generations of oscillatory zoning, and CL-bright inherited cores; rounding of some cores suggest that they were eroded prior to further growth of new oscillatory zones (**Figure S3.1**). Discontinuous 1-5 μm thick, CL- bright rims are interpreted to reflect metamorphic growth of zircon. Recrystallized domains are visible at the margins of some euhedral zircon. LA-ICPM spot analyses were conducted on 113 zircon grains; 43 analyses were discarded (**Table S3.1**). The remaining 70 grains yielded concordant ages with distributions in the late Neoarchean to middle Paleoproterozoic, and Mesoproterozoic to Mesozoic with a distinct population in the Mississippian and a minor cluster in the Silurian (**Figure 3.5**). Uranium concentrations range from 1390 to 45 ppm; Mesoproterozoic and younger analyses exhibit a weak negative correlation with age (**Figure S3.2**). Zircon Th/U ratios range from 1.87 to 0.00 and do not display any relationship with age; ratios <0.2 cluster in the Carboniferous to Cambrian.

S3.2.2 Santorini samples

ALS16

Sample ALS16 is a metasedimentary graphite-white mica-calcite-quartz schist sampled from the Paleogene metaflysch of the hanging wall (**Figure 3.2**). Zircon from this sample are 75-200 μm in length with L:W ratios of 1.1:1 to 4.5:1. Morphologically, zircon range from euhedral to subhedral with blocky, tabular and prismatic habits, less common grains are subrounded to rounded and more equant to elongate (**Figure S3.2**). Texturally zircon grains exhibit oscillatory, sector and patchy zoning, and uncommon chaotic alteration patterns. Multi-stage zoning and CL-bright or CL-dark cores are also observed. Of the 52 analyses that were conducted, 5 were rejected (**Table S3.2**); the remaining 47 grains yielded concordant ages with distributions in the late Neoproterozoic to early Mesozoic, with a major population in the Carboniferous and a minor cluster in the Triassic (**Figure 3.6**). Sparse analyses occur throughout the Proterozoic and the Neoarchean. Zircon Th/U ratios range from 1.64 to 0.07 and do not display any relationship with age; ratios <0.2 cluster in the Ordovician to Mississippian.

ALS17

Sample ALS17 is a metasedimentary, foliated, calcite-alkali feldspar-graphite-white mica-quartz schist from the Paleogene metaflysch of the hanging wall (**Figure 3.2**). Zircon from this sample are 55-180 μm in length with 2:1 to 4:1 L:W ratios, they range in habit from euhedral prismatic crystals, to rounded, and equant grains (**Figure S3.2**). Grains dominantly exhibit oscillatory zoning, commonly multi-stage. Uncommonly zircon may exhibit patchy zoning, sector zoning, or chaotic alteration patterns. Parallel partings, and CL-bright or CL-dark cores are rarely observed. Of the 112 analyses conducted, 16 were rejected (**Table S3.2**); the remaining 96 grains yielded concordant ages with distributions in the middle Mesoproterozoic to early Mesozoic, a major population in the Carboniferous and minor clusters in the Triassic and Cryogenian (**Figure 3.6**). Smaller age distributions occur in the middle Paleoproterozoic and Neoarchean. Zircon Th/U

ratios range from 1.88 to 0.05 and do not display any simple relationship with age; ratios <0.2 cluster in the Silurian to Ediacaran.

ALS13

Sample ALS13 is a feldspar-calcite-quartz metaconglomerate from the Paleogene metaflysch of the hanging wall (**Figure 3.2**). Zircon from this sample are 50-210 μm in length with L:W ratios of 1.5:1 to 4.5:1. Morphologies range from euhedral, prismatic crystals to blocky and anhedral to subhedral grains (**Figure S3.2**). Zircon exhibit oscillatory and patchy multi-stage zoning, resorption textures and rare sector zoning and CL-bright overgrowths. Rare complex alteration patterns may be observed. Of the 96 analyses that were conducted, 16 were rejected (**Table S3.2**); the remaining 80 grains yielded concordant ages error with a main distribution in the middle Neoproterozoic to the early Mesozoic, a major population in the Permo-Carboniferous and a minor cluster in the Ediacaran (**Figure 3.6**). A minor age distribution occurs in the Paleoproterozoic, with sparse analyses in the Neo- and Mesoarchean. Zircon Th/U ratios range from 1.61 to 0.02 and overall do not display any linear relationship with age.

ALS11

Sample ALS11 is a foliated, lineated chlorite-white mica-biotite metarhyolite sampled from the CBU (**Figure 3.2**). Zircon from this sample are 75-200 μm in length with L:W ratios of 1:1 to 3.5:1, and range in morphology from blocky to prismatic and euhedral crystals to subhedral, equant, elongate or tabular grains. Zircon commonly exhibit oscillatory, multi-stage or sector zoning, resorption textures, rare patchy zoning, and CL-bright or CL-dark inherited cores (**Figure S3.2**). Rare parallel parting in zircon crystals may also be observed. Spot analyses were conducted on 96 zircon grains; 8 analyses were discarded (**Table S3.2**). The remaining 88 grains yielded concordant ages with a distribution from the late Stenian to Ediacaran, a distinct population in the

Triassic and sparse ages in the Paleoproterozoic and Neoarchean (**Figure 3.6**). Zircon Th/U ratios range from 1.45 to 0.02 and do not display any relationship with age; ratios <0.2 cluster in the Ediacaran to Cryogenian.

ALS08

Sample ALS08 is a foliated, lineated white mica-biotite-quartz schist sampled from the structurally highest levels of the CBU (**Figure 3.2**). Zircon from this sample are 75-195 μm in length with 1:1 to 3.5:1 L:W ratios, and range from equant and blocky anhedral grains to elongate or prismatic subhedral crystals. Zircon commonly exhibit one or more generations of oscillatory or sector zoning, uncommon patchy zoning, and uncommon CL-bright inherited cores (**Figure 3.7; S3.2**). Spot analyses were conducted on 100 zircon grains; 4 analyses were discarded (**Table S3.2**). The remaining 96 grains yielded concordant ages error with distributions in the late Neoarchean to Siderian, Orosirian to Stathian and Ectasian to Ediacaran with major populations in the Ediacaran and Stenian and minor clusters in the Cryogenian (**Figure 3.6**). Zircon Th/U ratios range from 2.85 to 0.02 and do not display any relationship with age; ratios <0.2 cluster in the Cambrian to Cryogenian.

ALS02

Sample ALS02 is a foliated, lineated mica-quartz calc-schist with well-developed quartz ribbons sampled from a structurally intermediate level of the CBU (**Figure 3.2**). Zircon from this sample are 65-255 μm in length with L:W ratios of 1:1 to 4:1, and range from equant and rounded to elongate or prismatic subhedral crystals with rare euhedral forms. Zircon may exhibit one or more generations of oscillatory zoning, sector zoning or patchy zoning. Unzoned CL-bright overgrowths and CL-bright or CL-dark inherited cores are also common (**Figure S3.1**). Circa 30 Ma discontinuous 1-15 μm thick, CL-bright rims are observed on some samples. LA-ICPM spot

analyses were conducted on 98 zircon grains; 5 analyses were discarded (**Table S3.1**). The remaining 93 grains yielded concordant ages with distributions in the late Neoarchean to early Paleoproterozoic, and late Mesoproterozoic to early Paleozoic with a distinct population in the Ediacaran and minor clusters in the Cryogenian and Stenian (**Figure 3.6**). Zircon Th/U ratios range from 2.19 to 0.01 and do not display any relationship with age; ratios <0.2 cluster in the Cryogenian to Tonian.

ALS05

Sample ALS05 is a foliated, lineated metasedimentary graphite-feldspar-mica-quartz calc-schist sampled from the structurally lowest levels of the CBU (**Figure 3.2**). Zircon from this sample are 90-170 μm in length with 1:1 to 3:1 L:W ratios, and range from equant or blocky to tabular euhedral and prismatic subhedral crystals. Zircon commonly exhibit one to two generations of oscillatory and/or patchy zoning, resorption textures and CL-bright or CL-dark inherited cores (**Figure S3.1**). Partially abraded 1-10 μm thick, CL-white rims are observed on several crystals. Spot analyses were conducted on 62 zircon grains; 9 analyses were discarded (**Table S3.2**). The remaining 53 grains yielded concordant ages with distributions in the late Neoarchean to early Paleoproterozoic, and Stenian to Cambrian with a distinct population in the Cryogenian and a minor cluster in the Tonian (**Figure 3.6**). Zircon Th/U ratios range from 1.51 to 0.01 and do not display any relationship with age; ratios <0.2 cluster in the Ordovician to Cryogenian.

S3.3 Figures

Given the file size of these figures they have not been included in this thesis document; they are archived in the Mendeley data repository: DOI: 10.17632/zjhdtsnm4z.1

Figure S3.1. SEM-CL images of all zircon from the Attic Peninsula imaged prior to analysis. White circles are the locations of targeted spots. Yellow X mark grains that were not analyzed or were plucked out during polishing.

Given the number and file size of these figures they have not been included in this thesis document; they are archived in the Mendeley data repository: DOI: 10.17632/zjhdtsnm4z.1

Figure S3.2. SEM-CL images of all zircon from Santorini imaged prior to analysis. Zircon for several samples were analyzed in two batches, grain identifiers are specific to zircon analyzed in each batch.

S3.4 Tables

Table S3.1 Results of single grain zircon U-Pb ICP-MS analysis from Attica, Greece

				Measured values and ratios							Apparent Ages					
Batch & Grain no.	U (ppm)	Th (ppm)	U/Th	$^{207}Pb/^{206}Pb$	2σ	$^{206}Pb/^{238}U$	2σ	$^{207}Pb/^{235}U$	2σ	Discordance (%)	$^{207}Pb/^{206}Pb$	2σ	$^{207}Pb/^{235}U$	2σ	$^{206}Pb/^{238}U$	2σ
17MC019A1																
1-1	765.7	128.0	5.98	0.0710	0.0018	0.0466	0.0007	0.4560	0.0130	23.0	945	51	382	9	294	5
1-2	136.7	100.1	1.37	0.0852	0.0034	0.1793	0.0034	2.0710	0.0910	19.8	1296	77	1140	30	1063	18
1-3	140.8	130.7	1.08	0.0624	0.0032	0.1069	0.0021	0.9120	0.0460	0.4	630	110	657	24	654	12
1-4	395.0	400.0	0.99	0.0556	0.0027	0.0516	0.0010	0.3890	0.0180	3.7	410	100	337	14	325	6
1-5	328.2	182.8	1.80	0.1790	0.0180	0.0458	0.0015	1.1900	0.1500	62.3	2510	160	765	65	289	10
1-6	1659.0	431.0	3.85	0.0585	0.0009	0.0665	0.0012	0.5370	0.0130	4.8	553	32	436	9	415	7
1-7	419.9	83.8	5.01	0.0718	0.0015	0.1614	0.0027	1.6090	0.0420	0.8	979	45	972	16	964	15
1-8	226.9	73.9	3.07	0.1602	0.0014	0.4558	0.0066	10.1030	0.1800	1.3	2456	15	2444	16	2423	29
1-9	453.0	380.0	1.19	0.0542	0.0024	0.0608	0.0010	0.4550	0.0220	-0.2	381	97	380	15	381	6
1-10	267.2	159.3	1.68	0.0595	0.0016	0.0931	0.0015	0.7660	0.0230	0.6	590	57	577	14	574	9
1-11	577.0	85.5	6.75	0.0919	0.0016	0.1439	0.0024	1.8130	0.0420	43.5	1459	32	1050	15	866	14
1-12	77.5	56.1	1.38	0.0605	0.0039	0.0852	0.0021	0.7260	0.0460	4.9	600	130	554	26	527	12
1-13	506.1	177.9	2.84	0.0544	0.0021	0.0425	0.0007	0.3200	0.0130	4.6	379	84	281	10	268	5
1-14	318.8	153.4	2.08	0.0745	0.0015	0.1723	0.0025	1.7750	0.0470	3.7	1061	40	1036	17	1024	14
1-15	1811.0	695.5	2.60	0.0558	0.0008	0.0567	0.0008	0.4394	0.0099	4.0	440	32	370	7	355	5
1-16	1836.0	1604.0	1.14	0.0516	0.0018	0.0388	0.0006	0.2784	0.0100	1.5	258	77	249	8	245	4
1-17	244.8	92.4	2.65	0.0743	0.0017	0.1466	0.0023	1.5020	0.0400	14.9	1033	46	929	16	882	13
1-18	272.0	134.0	2.03	0.0568	0.0022	0.0736	0.0017	0.5760	0.0220	1.4	456	84	464	14	458	10
1-19	429.0	10.3	41.69	0.0552	0.0017	0.0737	0.0012	0.5630	0.0190	-1.2	417	66	453	12	459	7
1-20	1128.0	240.8	4.68	0.0553	0.0011	0.0596	0.0009	0.4582	0.0110	2.7	429	43	383	8	373	5
1-21	469.0	95.0	4.94	0.0814	0.0013	0.2052	0.0032	2.3040	0.0530	1.7	1226	31	1212	16	1203	17
1-22	182.3	247.5	0.74	0.0619	0.0020	0.0939	0.0016	0.8140	0.0300	4.6	691	73	606	17	578	9
1-23	215.3	57.0	3.78	0.0561	0.0024	0.0722	0.0012	0.5670	0.0260	1.2	457	94	455	17	450	7
1-24	382.2	174.0	2.20	0.0602	0.0014	0.0977	0.0015	0.8130	0.0220	0.4	605	51	603	12	601	9
1-25	798.0	42.0	19.01	0.1608	0.0011	0.3850	0.0069	8.5500	0.1900	17.2	2465	12	2290	20	2099	32
1-26	817.9	3.2	258.01	0.0530	0.0013	0.0524	0.0008	0.3865	0.0110	0.7	319	57	331	8	329	5
1-27	209.1	155.9	1.34	0.0669	0.0026	0.1031	0.0017	0.9480	0.0370	7.1	824	80	681	19	633	10
1-28	696.0	526.0	1.32	0.0592	0.0012	0.0931	0.0013	0.7640	0.0190	0.6	582	42	577	11	574	8
1-29	733.6	690.1	1.06	0.0675	0.0018	0.1164	0.0017	1.0930	0.0330	5.5	854	55	751	16	710	10
1-30	342.3	167.4	2.04	0.0570	0.0019	0.0605	0.0010	0.4760	0.0170	3.9	463	75	394	12	379	6
1-31	1131.4	161.7	7.00	0.0709	0.0007	0.1548	0.0021	1.5180	0.0290	1.8	949	21	937	12	928	12
1-32	145.8	454.9	0.32	0.1516	0.0024	0.3644	0.0066	7.6800	0.1800	17.1	2365	28	2193	21	2002	31
1-33	310.1	113.8	2.72	0.0633	0.0016	0.1167	0.0018	1.0240	0.0290	0.4	717	53	714	15	712	10
1-34	236.9	416.8	0.57	0.0765	0.0017	0.1389	0.0023	1.4670	0.0400	26.9	1118	47	917	16	839	13
1-35	76.4	47.6	1.61	0.0594	0.0041	0.0990	0.0023	0.8300	0.0550	1.0	610	160	615	32	609	14
1-36	121.4	51.8	2.35	0.0873	0.0046	0.1170	0.0024	1.4110	0.0770	19.7	1330	110	888	33	713	14
1-37	1542.0	773.4	1.99	0.0519	0.0009	0.0436	0.0006	0.3121	0.0074	0.8	267	40	277	6	275	4
1-38	143.0	91.9	1.56	0.0524	0.0041	0.0420	0.0010	0.3040	0.0220	1.1	290	150	268	17	265	6
1-39	136.6	49.5	2.76	0.1374	0.0021	0.3876	0.0062	7.4300	0.1600	3.3	2195	27	2165	19	2111	29
1-40	190.9	136.4	1.40	0.1284	0.0015	0.3610	0.0056	6.4240	0.1300	4.6	2077	21	2034	17	1986	27
1-41	481.0	211.6	2.27	0.0706	0.0018	0.0901	0.0015	0.8830	0.0250	13.6	930	55	644	14	557	9
1-42	993.4	437.3	2.27	0.0555	0.0013	0.0416	0.0006	0.3197	0.0096	6.8	421	54	282	7	263	4
1-43	101.5	44.1	2.30	0.0589	0.0039	0.0925	0.0021	0.7570	0.0500	0.2	500	140	571	29	570	13
1-44	871.4	392.7	2.22	0.0775	0.0044	0.0630	0.0012	0.6800	0.0480	24.3	1070	110	520	28	394	8
1-45	710.0	360.3	1.97	0.0548	0.0016	0.0542	0.0009	0.4110	0.0120	2.8	395	62	350	9	340	5
1-46	641.0	378.9	1.69	0.0582	0.0014	0.0835	0.0014	0.6620	0.0190	-0.2	522	53	516	12	517	8
1-47	1096.0	839.0	1.31	0.0735	0.0008	0.1383	0.0019	1.4090	0.0270	19.2	1025	22	893	11	835	11
1-48	282.6	134.1	2.11	0.0566	0.0021	0.0738	0.0012	0.5690	0.0220	-0.4	440	79	457	14	459	7
1-49	1231.3	220.0	5.60	0.0603	0.0014	0.0580	0.0009	0.4880	0.0130	9.8	612	49	403	9	364	5
1-50	234.2	126.4	1.85	0.0624	0.0018	0.1085	0.0019	0.9440	0.0310	1.6	687	61	675	16	664	11
1-51	432.5	175.1	2.47	0.0697	0.0014	0.1224	0.0018	1.1870	0.0310	6.5	935	43	796	14	744	11
1-52	189.2	64.3	2.94	0.0585	0.0022	0.0727	0.0014	0.5840	0.0240	3.5	538	86	469	16	453	8
1-53	615.0	1039.0	0.59	0.0649	0.0017	0.0967	0.0015	0.8710	0.0300	6.2	767	52	634	16	595	9
1-54	106.3	65.4	1.63	0.0649	0.0036	0.1177	0.0023	1.0490	0.0570	0.6	690	110	721	27	717	13
1-55	230.0	98.3	2.34	0.0631	0.0019	0.0885	0.0016	0.7680	0.0260	5.4	690	62	578	15	547	10
1-56	1190.0	45.2	26.33	0.1303	0.0013	0.3363	0.0054	6.0420	0.1300	13.6	2111	18	1983	19	1868	26
1-57	320.0	276.0	1.16	0.0601	0.0015	0.0869	0.0013	0.7290	0.0220	3.3	613	59	555	13	537	8
1-58	587.0	176.2	3.33	0.0547	0.0013	0.0609	0.0010	0.4590	0.0130	0.4	383	53	383	9	381	6
1-59	370.0	247.0	1.50	0.0520	0.0026	0.0450	0.0009	0.3260	0.0170	1.1	280	100	287	13	284	6
1-60	442.7	58.5	7.57	0.1280	0.0013	0.3470	0.0050	6.1180	0.1100	8.4	2070	18	1994	16	1920	24
1-61	164.6	112.3	1.47	0.0716	0.0021	0.1523	0.0030	1.5030	0.0490	6.0	970	60	934	21	913	17
1-62	84.5	62.5	1.35	0.0666	0.0040	0.1015	0.0024	0.9270	0.0570	6.2	760	130	664	31	623	14
1-63	204.0	112.5	1.81	0.0711	0.0037	0.0435	0.0009	0.4270	0.0230	23.3	930	110	358	17	275	5
1-64	160.0	114.9	1.39	0.1261	0.0032	0.2806	0.0085	4.9700	0.1600	24.2	2054	48	1812	27	1599	42
1-65	684.8	274.5	2.49	0.1716	0.0013	0.4437	0.0065	10.4840	0.1800	9.7	2574	13	2478	16	2367	29
1-66	171.1	42.0	4.07	0.1867	0.0075	0.1063	0.0027	2.7380	0.0930	51.3	2709	63	1336	25	651	15
1-67	1088.0	2300.0	0.47	0.0616	0.0013	0.0961	0.0017	0.8190	0.0220	2.6	650	47	607	12	591	10
1-68	119.9	90.7	1.32	0.1110	0.0130	0.3495	0.0095	5.8500	0.7400	-13.4	2080	140	1900	110	1928	45
1-69	484.3	173.7	2.79	0.0709	0.0012	0.1397	0.0020	1.3580	0.0310	11.7	946	34	872	14	843	12
1-70	182.6	71.0	2.57	0.0622	0.0020	0.1092	0.0017	0.9300	0.0310	-0.4	664	68	665	16	668	10
1-71	73.6	117.9	0.62	0.1123	0.0027	0.3180	0.0054	4.9000	0.1400	2.4	1823	44	1798	24	1780	27
1-72	562.0	439.0	1.28	0.0567	0.0014	0.0606	0.0009	0.4730	0.0140	3.6	460	55	394	10	380	6
1-73	321.5	219.3	1.47	0.1389	0.0016	0.2922	0.0054	5.6180	0.1200	28.7	2217	19	1919	18	1652	27
1-74	918.0	173.8	5.28	0.1745	0.0009	0.3997	0.0063	9.6300	0.1900	19.4	2601	8	2399	18	2169	29
1-75	2290.0	1830.0	1.25	0.0526	0.0009	0.0421	0.0006	0.3070	0.0071	2.1	302	38	272	6	266	4
1-76	1138.6	268.4	4.24	0.0543	0.0011	0.0593	0.0009	0.4456	0.0110	0.6	377	44	374	8	371	6
1-77	370.8	103.1	3.60	0.1318	0.0011	0.3711	0.0055	6.7430	0.1200	4.8	2122	15	2078	16	2034	26
1-78	162.3	62.5	2.60	0.0661	0.0024	0.1223	0.0021	1.1180	0.0420	2.2	837	72	760	21	744	12
1-79	273.0	74.9	3.64	0.0993	0.0020	0.1772	0.0030	2.4280	0.0650	37.1	1605	39	1249	19	1052	16
1-80	892.0	236.9	3.77	0.0545	0.0012	0.0589	0.0009	0.4416	0.0120	0.5	382	50	371	8	369	5
1-81	125.8	44.9	2.80	0.0694	0.0030	0.1119	0.0022	1.0830	0.0500	7.6	896	93	740	24	684	13
1-82	1326.0	702.0	1.89	0.0880	0.0040	0.0428	0.0007	0.5210	0.0270	36.0	1351	84	422	18	270	4

				Measured values and ratios								Apparent Ages					
Batch & Grain no.	U (ppm)	Th (ppm)	U/Th	$^{207}Pb/^{206}Pb$	2σ	$^{206}Pb/^{238}U$	2σ	$^{207}Pb/^{235}U$	2σ	Discordance (%)	$^{207}Pb/^{206}Pb$	2σ	$^{207}Pb/^{235}U$	2σ	$^{206}Pb/^{238}U$	2σ
1-83	519.3	362.8	1.43	0.1014	0.0026	0.1118	0.0018	1.5800	0.0470	28.9	1647	49	961	19	683	10
1-84	359.0	137.9	2.60	0.0570	0.0020	0.0603	0.0010	0.4790	0.0190	4.6	479	77	396	13	378	6
1-85	655.7	289.6	2.26	0.0580	0.0012	0.0847	0.0012	0.6780	0.0180	0.1	525	46	524	11	524	7
1-86	150.1	256.0	0.59	0.0617	0.0034	0.1074	0.0023	0.9110	0.0460	0.0	620	120	658	26	658	14
1-87	312.0	193.7	1.61	0.0664	0.0022	0.0951	0.0017	0.8830	0.0330	8.5	812	68	643	18	588	10
1-88	44.3	36.7	1.21	0.0737	0.0054	0.1006	0.0024	1.0220	0.0760	14.2	1040	150	720	38	618	14
1-89	242.2	154.0	1.57	0.0780	0.0033	0.1024	0.0016	1.1160	0.0490	16.9	1165	82	756	24	629	10
1-90	584.4	169.2	3.45	0.0593	0.0012	0.0932	0.0014	0.7630	0.0190	0.3	583	40	577	10	575	8
1-91	1136.5	414.3	2.74	0.1138	0.0011	0.2272	0.0035	3.5610	0.0690	32.3	1862	17	1540	15	1320	18
1-92	800.2	200.5	3.99	0.0546	0.0014	0.0603	0.0009	0.4580	0.0130	1.4	396	55	383	10	378	6
1-93	411.4	63.3	6.50	0.0780	0.0018	0.0949	0.0016	1.0200	0.0320	18.0	1146	45	713	16	584	10
1-94	175.7	146.5	1.20	0.0953	0.0016	0.2473	0.0038	3.2690	0.0740	6.5	1526	31	1471	18	1424	19
1-95	996.0	550.0	1.81	0.0480	0.0220	0.0503	0.0021	0.3900	0.1900	-31.7	1580	330	240	160	316	13
1-96	525.9	279.9	1.88	0.1364	0.0012	0.3841	0.0055	7.2020	0.1300	4.8	2181	15	2136	16	2095	26
1-97	101.0	100.8	1.00	0.1124	0.0026	0.2900	0.0056	4.5200	0.1300	10.8	1831	41	1733	23	1643	28
1-98	873.0	286.0	3.05	0.0637	0.0014	0.0971	0.0014	0.8620	0.0220	5.2	718	47	630	12	597	9
1-99	299.0	413.4	0.72	0.0534	0.0026	0.0606	0.0011	0.4560	0.0230	0.0	340	100	379	16	379	7
1-100	165.6	138.7	1.19	0.1311	0.0051	0.1743	0.0032	3.1700	0.1500	53.1	2080	67	1445	33	1035	17
1-101	109.6	63.8	1.72	0.0640	0.0036	0.0842	0.0016	0.7410	0.0410	7.8	710	110	565	24	521	10
1-102	129.0	39.3	3.28	0.0625	0.0031	0.0921	0.0019	0.8020	0.0430	4.6	660	100	595	24	568	11
1-103	457.0	46.1	9.91	0.0649	0.0013	0.1250	0.0018	1.1210	0.0280	1.2	757	41	762	13	759	10
1-104	207.8	117.3	1.77	0.0599	0.0021	0.0929	0.0017	0.7780	0.0300	2.3	577	77	586	16	573	10
1-105	1414.0	805.7	1.75	0.0544	0.0010	0.0587	0.0009	0.4418	0.0110	1.0	376	44	371	8	367	5
1-106	341.0	158.0	2.16	0.0562	0.0023	0.0437	0.0009	0.3470	0.0150	8.3	458	85	301	11	276	6
1-107	142.4	34.3	4.15	0.1287	0.0024	0.3792	0.0080	6.6900	0.1800	0.3	2074	33	2075	23	2071	37
1-108	202.1	154.9	1.30	0.0635	0.0022	0.0977	0.0016	0.8490	0.0300	3.9	693	75	625	17	601	10
1-109	147.1	338.3	0.43	0.0715	0.0045	0.0692	0.0016	0.6890	0.0440	18.6	960	130	530	26	432	10
1-110	no value	no value	no value	no value	no value	no value	no value	no value	no value	no value	no value	no value	no value	no value	no value	no value
1-111	1794.0	1878.0	0.96	0.0760	0.0012	0.0434	0.0008	0.4599	0.0100	28.8	1096	32	385	7	274	5
1-112	59.3	27.1	2.19	0.0905	0.0045	0.1407	0.0036	1.7130	0.0960	43.4	1414	92	1023	35	848	21
1-113	485.0	345.0	1.41	0.0555	0.0015	0.0565	0.0009	0.4380	0.0130	4.0	442	64	369	9	354	5
1-114	2183.0	1546.0	1.41	0.0564	0.0008	0.0569	0.0008	0.4429	0.0090	4.2	467	32	373	6	357	5
1-115	54.0	73.0	0.74	0.0684	0.0048	0.1044	0.0025	0.9750	0.0680	7.4	830	140	691	35	640	14
1-116	48.4	77.6	0.62	0.1749	0.0036	0.4822	0.0096	11.5900	0.3000	3.1	2601	34	2570	24	2535	42
1-117	103.0	34.7	2.97	0.1868	0.0018	0.4977	0.0076	12.9200	0.2600	4.9	2721	17	2675	18	2603	33
1-118	127.0	56.4	2.25	0.1740	0.0180	0.0905	0.0037	2.3100	0.3300	51.4	2580	180	1148	94	558	22
1-119	582.1	554.7	1.05	0.0607	0.0014	0.0967	0.0014	0.8130	0.0230	1.5	625	51	604	13	595	8
2-1	37.2	42.9	0.87	0.0703	0.0035	0.1128	0.0025	1.0840	0.0560	7.9	910	100	748	28	689	15
2-2	520.0	175.0	2.97	0.0540	0.0013	0.0519	0.0008	0.3880	0.0120	1.7	384	54	332	9	326	5
2-3	140.6	95.4	1.47	0.0644	0.0020	0.1184	0.0027	1.0450	0.0430	0.3	751	63	723	21	721	16
2-4	259.5	120.9	2.15	0.1978	0.0015	0.5517	0.0086	14.9800	0.2900	-0.6	2808	13	2813	18	2832	36
2-5	188.8	165.0	1.14	0.1378	0.0069	0.1004	0.0019	1.9100	0.0820	43.2	2212	82	1085	28	617	11
2-6	116.5	67.0	1.74	0.0581	0.0021	0.0934	0.0015	0.7480	0.0290	-2.1	500	79	564	17	576	9
2-7	286.1	75.0	3.81	0.0642	0.0015	0.1233	0.0021	1.0810	0.0290	-0.9	743	50	743	14	750	12
2-8	127.0	17.8	7.14	0.0598	0.0017	0.1013	0.0016	0.8230	0.0260	-2.2	578	61	609	15	622	9
2-9	182.3	39.6	4.60	0.0537	0.0019	0.0616	0.0010	0.4550	0.0170	-1.4	344	76	380	12	385	6
2-10	392.0	694.0	0.56	0.0561	0.0011	0.0701	0.0011	0.5400	0.0140	0.4	455	41	439	9	437	7
2-11	46.3	28.1	1.65	0.0694	0.0027	0.1492	0.0026	1.4340	0.0600	0.1	897	82	898	25	897	14
2-12	944.0	31.5	29.97	0.1700	0.0008	0.4341	0.0065	10.0900	0.1800	11.5	2557	8	2443	16	2324	29
2-13	346.0	131.0	2.64	0.0551	0.0020	0.0414	0.0006	0.3110	0.0120	4.5	378	77	274	9	262	4
2-14	150.4	70.4	2.14	0.0623	0.0019	0.1093	0.0016	0.9310	0.0290	0.1	689	65	669	15	669	9
2-15	251.0	94.3	2.66	0.0622	0.0017	0.1038	0.0017	0.8810	0.0290	0.9	666	55	642	15	636	10
2-16	192.6	29.2	6.60	0.0552	0.0018	0.0740	0.0011	0.5580	0.0180	-2.0	414	68	451	11	460	7
2-17	773.0	438.0	1.76	0.0545	0.0011	0.0599	0.0008	0.4449	0.0100	-0.3	387	44	374	7	375	5
2-18	744.0	179.0	4.16	0.0540	0.0011	0.0433	0.0006	0.3187	0.0081	2.8	361	46	281	6	273	4
2-19	294.0	170.5	1.72	0.0596	0.0012	0.0890	0.0014	0.7290	0.0170	1.2	578	43	556	10	549	8
2-20	114.6	47.1	2.43	0.1806	0.0018	0.5061	0.0073	12.4600	0.2200	-1.7	2656	17	2639	17	2640	31
2-21	870.0	344.0	2.53	0.0534	0.0012	0.0399	0.0006	0.2911	0.0075	2.8	339	50	259	6	252	4
2-22	58.2	48.6	1.20	0.1706	0.0022	0.4617	0.0069	10.8400	0.2000	5.9	2566	21	2513	18	2448	31
2-23	587.6	341.3	1.72	0.0556	0.0011	0.0577	0.0008	0.4363	0.0120	1.6	430	46	367	8	361	5
2-24	1023.0	253.0	4.04	0.0544	0.0010	0.0482	0.0007	0.3596	0.0080	2.7	384	41	312	6	303	4
2-25	421.0	76.4	5.51	0.0563	0.0011	0.0718	0.0010	0.5530	0.0130	0.0	462	43	447	8	447	6
2-26	678.0	442.0	1.53	0.0700	0.0010	0.1519	0.0020	1.4630	0.0290	0.3	931	28	915	12	912	11
2-27	93.0	62.1	1.50	0.0632	0.0017	0.1063	0.0020	0.9240	0.0290	2.0	705	61	664	15	651	11
2-28	799.0	145.0	5.51	0.0545	0.0012	0.0599	0.0008	0.4474	0.0110	0.0	384	49	375	8	375	5
2-29	177.9	93.9	1.89	0.0745	0.0014	0.1609	0.0024	1.6380	0.0400	2.2	1058	38	983	15	961	13
2-30	154.7	27.3	5.67	0.0548	0.0020	0.0530	0.0010	0.4070	0.0160	3.5	406	78	345	12	333	6
2-31	322.0	76.3	4.22	0.0781	0.0016	0.1907	0.0047	2.0520	0.0560	2.6	1151	43	1132	19	1125	25
2-32	53.9	46.1	1.17	0.0620	0.0026	0.1043	0.0020	0.8880	0.0390	1.0	652	89	646	21	639	11
2-33	239.0	226.7	1.05	0.0544	0.0015	0.0605	0.0009	0.4520	0.0140	-0.3	388	63	378	10	379	6
2-34	264.4	115.6	2.29	0.0554	0.0015	0.0721	0.0010	0.5520	0.0160	-0.8	424	58	445	10	449	6
2-35	207.4	75.1	2.76	0.0563	0.0015	0.0754	0.0012	0.5840	0.0180	-0.5	436	60	466	12	469	7
2-36	257.8	79.1	3.26	0.0703	0.0010	0.1414	0.0020	1.3670	0.0260	2.5	932	30	874	11	852	12
2-37	246.9	159.4	1.55	0.0743	0.0013	0.1664	0.0022	1.6930	0.0350	1.4	1044	33	1006	13	992	12
2-38	185.4	149.2	1.24	0.0521	0.0021	0.0420	0.0007	0.2970	0.0120	0.6	292	84	266	10	265	5
2-39	249.6	31.4	7.95	0.0565	0.0013	0.0714	0.0010	0.5510	0.0140	0.3	471	50	446	10	445	6
2-40	1527.4	437.0	3.50	0.0513	0.0008	0.0392	0.0005	0.2757	0.0056	-0.3	251	34	247	4	248	3
2-41	368.5	190.7	1.93	0.0533	0.0012	0.0593	0.0008	0.4330	0.0120	-1.4	340	52	366	8	371	5
2-42	334.9	48.2	6.95	0.0538	0.0014	0.0590	0.0008	0.4340	0.0130	-0.7	343	58	367	9	369	5
2-43	180.6	67.0	2.70	0.0611	0.0016	0.1065	0.0016	0.8980	0.0240	-0.1	647	59	652	13	652	9
2-44	347.0	67.2	5.16	0.0531	0.0013	0.0629	0.0009	0.4570	0.0120	-2.8	320	54	382	8	393	6
2-45	99.3	54.1	1.84	0.1776	0.0019	0.4633	0.0067	11.2400	0.1900	9.1	2633	17	2543	16	2454	29
2-46	69.6	163.6	0.43	0.1038	0.0021	0.2668	0.0040	3.7760	0.0850	12.4	1695	38	1591	19	1524	20
2-47	146.7	70.2	2.09	0.0571	0.0017	0.0720	0.0011	0.5670	0.0190	1.7	478	65	456	13	448	7

				Measured values and ratios								Apparent Ages					
Batch & Grain no.	U (ppm)	Th (ppm)	U/Th	$^{207}Pb/^{206}Pb$	2σ	$^{206}Pb/^{238}U$	2σ	$^{207}Pb/^{235}U$	2σ	Discordance (%)	$^{207}Pb/^{206}Pb$	2σ	$^{207}Pb/^{235}U$	2σ	$^{206}Pb/^{238}U$	2σ
2-48	43.6	38.9	1.12	0.0733	0.0034	0.1589	0.0028	1.5960	0.0760	0.5	1005	93	957	30	952	16
2-49	362.7	132.9	2.73	0.0594	0.0010	0.0928	0.0013	0.7540	0.0160	-0.3	578	37	571	9	572	8
2-50	345.0	71.9	4.80	0.0545	0.0013	0.0622	0.0011	0.4640	0.0120	-0.4	374	53	387	8	389	6
2-51	95.3	90.6	1.05	0.0539	0.0045	0.0511	0.0012	0.3750	0.0320	2.3	320	170	329	24	322	8
2-52	631.4	599.9	1.05	0.0615	0.0008	0.1079	0.0014	0.9120	0.0170	-0.1	655	28	660	10	661	8
2-53	216.3	110.3	1.96	0.0528	0.0020	0.0470	0.0008	0.3410	0.0140	1.1	320	83	299	10	296	5
2-54	189.4	86.8	2.18	0.0646	0.0017	0.0953	0.0014	0.8490	0.0230	5.9	736	56	623	13	587	8
2-55	48.0	20.5	2.35	0.0670	0.0030	0.1318	0.0024	1.1930	0.0530	-0.3	812	90	796	25	798	14
2-56	185.0	86.4	2.14	0.0539	0.0015	0.0564	0.0009	0.4220	0.0140	0.7	358	63	356	10	354	6
2-57	387.0	442.0	0.88	0.0550	0.0011	0.0587	0.0009	0.4431	0.0110	1.0	406	48	372	8	368	5
2-58	212.2	125.2	1.69	0.0588	0.0015	0.0918	0.0015	0.7380	0.0220	-0.9	544	56	561	13	566	9
2-59	207.9	83.6	2.49	0.0613	0.0013	0.1066	0.0015	0.8990	0.0220	-0.2	657	49	651	12	653	9
2-60	323.0	254.0	1.27	0.0535	0.0013	0.0579	0.0008	0.4300	0.0120	0.1	332	54	363	8	363	5
2-61	239.8	178.2	1.35	0.0532	0.0017	0.0508	0.0008	0.3710	0.0130	0.5	324	72	321	10	319	5
2-62	347.0	156.1	2.22	0.0605	0.0012	0.0890	0.0013	0.7340	0.0180	1.5	619	42	558	10	549	8
2-63	100.3	46.9	2.14	0.0614	0.0018	0.1063	0.0017	0.8930	0.0310	-0.7	630	66	647	16	651	10
2-64	160.5	88.5	1.81	0.0754	0.0014	0.1704	0.0024	1.7640	0.0410	6.7	1078	39	1032	15	1014	13
2-65	1360.0	687.0	1.98	0.0566	0.0010	0.0755	0.0010	0.5870	0.0130	0.0	486	43	469	8	469	6
2-66	185.9	49.8	3.73	0.0549	0.0016	0.0729	0.0011	0.5550	0.0180	-1.2	391	65	448	12	454	7
2-67	101.5	16.4	6.19	0.0615	0.0029	0.0837	0.0015	0.7090	0.0340	3.3	595	92	536	19	518	9
2-68	206.9	90.6	2.28	0.0541	0.0016	0.0568	0.0010	0.4210	0.0140	-0.2	356	63	356	10	356	6
2-69	148.3	26.1	5.68	0.0608	0.0023	0.0693	0.0012	0.5820	0.0230	7.4	636	74	467	14	432	7
2-70	198.7	80.5	2.47	0.0577	0.0017	0.0431	0.0008	0.3410	0.0120	9.0	517	70	299	9	272	5
2-71	310.0	478.0	0.65	0.0551	0.0018	0.0654	0.0010	0.4990	0.0170	1.1	438	66	413	11	408	6
2-72	276.7	159.5	1.73	0.0543	0.0021	0.0579	0.0010	0.4300	0.0170	-0.2	366	84	362	12	363	6
2-73	183.0	86.2	2.12	0.0554	0.0020	0.0630	0.0010	0.4750	0.0180	0.4	412	79	395	12	394	6
2-74	455.3	220.8	2.06	0.0614	0.0009	0.0978	0.0013	0.8320	0.0170	2.2	650	31	615	9	602	8
2-75	88.7	23.2	3.83	0.0619	0.0018	0.1119	0.0018	0.9520	0.0310	-0.9	692	58	678	16	684	10
2-76	295.7	38.8	7.63	0.0560	0.0014	0.0791	0.0012	0.6160	0.0180	-0.9	448	58	487	11	491	7
2-77	218.0	57.3	3.80	0.0603	0.0013	0.0999	0.0015	0.8270	0.0210	-0.3	610	47	612	12	614	9
2-78	266.6	339.7	0.78	0.0597	0.0012	0.0997	0.0014	0.8210	0.0210	-0.7	592	43	608	11	613	8
2-79	261.8	160.0	1.64	0.0562	0.0015	0.0711	0.0010	0.5510	0.0160	0.7	450	58	446	10	443	6
2-80	317.4	79.2	4.01	0.0596	0.0012	0.0950	0.0013	0.7780	0.0180	0.0	575	45	585	11	585	8
2-81	631.9	71.0	8.90	0.0544	0.0010	0.0596	0.0008	0.4462	0.0099	0.3	372	43	374	7	373	5
2-82	155.4	29.1	5.33	0.0601	0.0015	0.0987	0.0017	0.8050	0.0250	-1.1	592	55	600	14	607	10
2-83	463.1	83.7	5.53	0.0561	0.0010	0.0787	0.0011	0.6086	0.0120	-0.9	457	38	484	8	488	6
2-84	682.0	499.0	1.37	0.0531	0.0009	0.0527	0.0008	0.3820	0.0078	-0.9	328	37	328	6	331	5
2-85	1560.0	137.0	11.39	0.0552	0.0007	0.0553	0.0009	0.4186	0.0079	2.2	413	27	355	6	347	5
2-86	85.3	36.5	2.34	0.1384	0.0016	0.3927	0.0058	7.5360	0.1300	3.1	2206	20	2178	16	2135	27
2-87	235.5	124.1	1.90	0.0527	0.0020	0.0374	0.0006	0.2690	0.0110	2.6	290	78	243	9	237	4
2-88	459.8	47.5	9.68	0.0569	0.0012	0.0713	0.0010	0.5590	0.0130	1.4	478	44	451	8	444	6
2-89	305.0	16.9	18.07	0.0576	0.0015	0.0720	0.0011	0.5710	0.0180	2.2	513	59	458	12	448	7
2-90	47.6	15.7	3.04	0.0673	0.0031	0.1313	0.0025	1.2230	0.0550	2.0	863	93	811	25	795	14
2-91	148.7	71.1	2.09	0.0684	0.0016	0.1294	0.0019	1.2180	0.0330	3.1	882	47	809	15	784	11
2-92	782.0	49.8	15.70	0.0610	0.0010	0.1061	0.0015	0.8940	0.0190	-0.1	634	35	649	10	650	9
2-93	36.2	23.7	1.53	0.0628	0.0039	0.0866	0.0020	0.7460	0.0450	6.8	660	120	574	25	535	12
2-94	543.0	257.6	2.11	0.0520	0.0013	0.0403	0.0006	0.2903	0.0083	1.5	274	56	258	7	255	4
2-95	57.3	85.1	0.67	0.0705	0.0025	0.1559	0.0027	1.5420	0.0560	1.1	937	76	944	22	934	15
2-96	500.4	242.3	2.07	0.1246	0.0010	0.3045	0.0058	5.2370	0.1100	17.2	2022	15	1858	18	1713	29
2-97	587.0	113.1	5.19	0.1192	0.0008	0.3037	0.0045	4.9810	0.0890	13.7	1942	12	1816	15	1711	22
2-98	83.8	46.2	1.81	0.0645	0.0020	0.1340	0.0023	1.1940	0.0410	-1.8	756	69	796	19	811	13
2-99	188.9	117.2	1.61	0.0530	0.0023	0.0476	0.0008	0.3450	0.0150	1.1	302	89	303	11	300	5
2-100	536.4	126.0	4.26	0.0598	0.0010	0.0905	0.0012	0.7460	0.0160	1.2	588	34	565	9	558	7
2-101	240.7	45.5	5.29	0.0555	0.0015	0.0751	0.0011	0.5760	0.0170	-1.3	425	61	461	11	467	7
2-102	705.0	179.7	3.92	0.0541	0.0009	0.0591	0.0008	0.4414	0.0093	0.2	371	37	371	7	370	5
2-103	426.3	183.6	2.32	0.0549	0.0017	0.0738	0.0012	0.5620	0.0190	-1.0	407	67	454	12	459	8
2-104	474.0	236.0	2.01	0.0568	0.0013	0.0567	0.0008	0.4433	0.0110	4.4	470	48	372	8	356	5
2-105	1251.0	201.2	6.22	0.0545	0.0007	0.0578	0.0009	0.4333	0.0093	0.8	389	31	365	7	362	6
2-106	235.9	149.4	1.58	0.0594	0.0012	0.0892	0.0013	0.7400	0.0180	1.9	582	44	561	10	551	7
2-107	817.0	957.0	0.85	0.0598	0.0007	0.0958	0.0013	0.7930	0.0140	0.6	599	28	593	8	590	7
2-108	630.0	15.5	40.75	0.0625	0.0014	0.1101	0.0032	0.9490	0.0250	0.6	694	47	677	13	673	19
2-109	86.0	69.2	1.24	0.0767	0.0024	0.1496	0.0024	1.6000	0.0520	7.2	1110	65	968	20	899	14
2-110	345.0	57.5	6.00	0.0570	0.0012	0.0722	0.0013	0.5730	0.0150	2.2	475	47	459	10	449	8
2-111	305.8	240.0	1.27	0.0584	0.0014	0.0679	0.0010	0.5470	0.0140	4.6	546	54	444	9	424	6
2-112	261.3	100.7	2.59	0.0571	0.0017	0.0697	0.0010	0.5450	0.0170	2.1	477	63	444	11	435	6
2-113	407.7	6.7	60.76	0.0555	0.0019	0.0705	0.0011	0.5300	0.0180	-1.2	415	71	434	13	439	7
2- 113core	78.4	16.8	4.67	0.1781	0.0045	0.4172	0.0094	10.2900	0.3300	17.3	2638	43	2468	28	2247	43
2-114	177.9	88.8	2.00	0.0541	0.0019	0.0589	0.0009	0.4380	0.0160	-0.4	368	75	367	11	369	6
2-115	293.6	102.8	2.86	0.0607	0.0011	0.0988	0.0014	0.8300	0.0190	1.2	636	39	615	10	608	8
2-116	334.0	180.0	1.86	0.0573	0.0013	0.0707	0.0010	0.5620	0.0140	2.8	485	49	453	9	440	6
2-117	239.8	118.1	2.03	0.1598	0.0011	0.4285	0.0057	9.4980	0.1500	6.8	2452	11	2388	14	2299	26
2-118	685.0	162.0	4.23	0.0539	0.0009	0.0603	0.0008	0.4504	0.0098	-0.1	357	38	377	7	377	5
2-119	143.6	46.8	3.07	0.0560	0.0020	0.0723	0.0012	0.5600	0.0200	0.2	415	75	451	13	450	7
2-120	167.5	176.6	0.95	0.0809	0.0020	0.1377	0.0021	1.5340	0.0420	11.6	1213	49	941	17	832	12
2-121	469.0	477.0	0.98	0.0562	0.0012	0.0579	0.0008	0.4510	0.0120	3.8	463	51	377	8	363	5
2-122	227.0	439.0	0.52	0.0617	0.0013	0.1048	0.0015	0.8880	0.0230	0.2	654	46	644	12	643	9
2-123	397.8	71.2	5.59	0.0531	0.0012	0.0510	0.0007	0.3750	0.0098	0.6	338	49	323	7	321	5
2-124	513.5	105.1	4.89	0.0717	0.0008	0.1598	0.0021	1.5890	0.0280	1.0	976	22	966	11	956	12
2-125	423.9	42.8	9.90	0.0563	0.0011	0.0726	0.0010	0.5630	0.0140	0.4	448	45	454	9	452	6
2-126	164.6	45.0	3.66	0.0553	0.0017	0.0720	0.0011	0.5530	0.0180	-0.3	416	69	447	12	448	7
2-127	243.4	60.9	4.00	0.0557	0.0018	0.0724	0.0011	0.5520	0.0190	-1.1	415	70	446	13	451	7
2-128	210.5	46.1	4.57	0.0630	0.0017	0.0856	0.0017	0.7430	0.0250	5.8	711	57	563	15	530	10
2-129	340.8	105.6	3.23	0.0543	0.0015	0.0575	0.0008	0.4310	0.0130	0.9	358	60	363	9	360	5
2-130	544.0	117.7	4.62	0.0547	0.0011	0.0577	0.0008	0.4350	0.0100	1.5	394	45	367	7	361	5

				Measured values and ratios								Apparent Ages					
Batch & Grain no.	U (ppm)	Th (ppm)	U/Th	$^{207}Pb/^{206}Pb$	2σ	$^{206}Pb/^{238}U$	2σ	$^{207}Pb/^{235}U$	2σ	Discordance (%)	$^{207}Pb/^{206}Pb$	2σ	$^{207}Pb/^{235}U$	2σ	$^{206}Pb/^{238}U$	2σ
2-131	95.0	33.8	2.81	0.0557	0.0022	0.0842	0.0014	0.6550	0.0290	-2.4	408	86	509	17	521	8
2-132	1206.7	325.0	3.71	0.0537	0.0007	0.0549	0.0007	0.4097	0.0080	1.2	355	32	348	6	344	4
2-133	80.9	32.9	2.46	0.0545	0.0024	0.0599	0.0012	0.4500	0.0210	0.1	380	95	375	15	375	7
2-134	437.0	48.0	9.10	0.0563	0.0011	0.0704	0.0010	0.5490	0.0140	1.3	467	46	444	9	439	6
2-135	68.0	43.3	1.57	0.0509	0.0040	0.0406	0.0009	0.2930	0.0220	2.1	270	150	262	17	256	5
2-136	336.9	224.3	1.50	0.1409	0.0010	0.3784	0.0048	7.3590	0.1100	8.7	2238	13	2156	14	2069	23
2-137	247.5	99.8	2.48	0.0667	0.0011	0.1291	0.0018	1.1910	0.0260	1.5	822	36	795	12	783	10
2-138	243.0	66.6	3.65	0.0558	0.0015	0.0717	0.0012	0.5580	0.0180	0.6	433	56	449	12	446	7
2-139	301.6	29.7	10.15	0.0567	0.0015	0.0707	0.0010	0.5620	0.0160	2.6	488	55	452	10	440	6
2-140	229.8	44.5	5.16	0.0556	0.0016	0.0703	0.0011	0.5460	0.0170	0.7	422	64	441	11	438	6
2-141	250.8	92.7	2.71	0.0563	0.0015	0.0685	0.0011	0.5340	0.0150	1.6	439	59	434	10	427	6
2-142	200.6	81.8	2.45	0.0615	0.0015	0.1010	0.0015	0.8630	0.0240	1.7	658	53	631	13	620	9
2-143	304.0	103.1	2.95	0.1677	0.0015	0.4516	0.0069	10.5400	0.2000	5.2	2533	15	2484	18	2402	31
2-144	483.8	58.3	8.30	0.0565	0.0010	0.0719	0.0010	0.5612	0.0120	0.9	465	40	452	8	448	6
18MC116A3																
1-1	828.0	67.5	12.27	0.0542	0.0016	0.0530	0.0009	0.3950	0.0130	1.4	369	56	338	9	333	6
1-2	428.0	49.6	8.63	0.0608	0.0027	0.0662	0.0016	0.5550	0.0390	8.2	614	77	450	19	413	9
1-3	160.6	197.3	0.81	0.0593	0.0063	0.0450	0.0010	0.3670	0.0570	10.2	500	160	316	31	284	6
1-4	103.4	107.6	0.96	0.0650	0.0043	0.1006	0.0021	0.8950	0.0660	4.9	743	110	650	31	618	12
1-5	1203.0	1990.0	0.60	0.0663	0.0021	0.0677	0.0010	0.6160	0.0230	13.4	808	58	487	14	422	6
1-6	597.0	149.1	4.00	0.0556	0.0020	0.0690	0.0011	0.5290	0.0220	0.1	426	66	430	13	430	6
1-7	136.0	34.8	3.91	0.0562	0.0040	0.0713	0.0014	0.5520	0.0420	-0.5	410	120	442	25	444	9
1-8	225.1	27.9	8.07	0.0650	0.0023	0.1290	0.0020	1.1580	0.0440	-1.5	773	69	778	18	782	11
1-9	479.0	342.0	1.40	0.0557	0.0022	0.0463	0.0008	0.3580	0.0180	5.9	456	80	310	12	292	5
1-10	132.7	81.9	1.62	0.0567	0.0049	0.0494	0.0011	0.3860	0.0370	5.8	450	140	330	24	311	7
1-11	36.7	29.6	1.24	0.0743	0.0066	0.1806	0.0046	1.8500	0.2100	-3.6	1040	120	1063	43	1069	25
1-12	814.0	280.5	2.90	0.1282	0.0019	0.0895	0.0072	1.5980	0.1200	43.2	2080	25	973	40	553	41
1-13	242.0	133.9	1.81	0.0626	0.0042	0.0790	0.0016	0.6780	0.0620	6.8	667	94	526	26	490	10
1-14	744.0	711.0	1.05	0.0525	0.0025	0.0464	0.0007	0.3330	0.0170	0.1	297	79	293	12	292	5
1-15	340.3	235.5	1.45	0.0491	0.0039	0.0242	0.0005	0.1640	0.0160	0.1	160	130	154	13	154	3
1-16	454.0	226.0	2.01	0.0524	0.0035	0.0379	0.0006	0.2700	0.0200	0.5	280	110	241	15	240	4
1-17	293.0	155.2	1.89	0.0564	0.0030	0.0480	0.0008	0.3700	0.0210	5.6	450	100	320	15	302	5
1-18	69.1	31.2	2.21	0.0648	0.0061	0.0874	0.0023	0.7800	0.1000	6.7	690	150	579	40	540	13
1-19	161.3	56.1	2.87	0.0732	0.0027	0.1675	0.0027	1.6780	0.0650	0.8	995	67	1002	22	999	15
1-20	158.5	129.9	1.22	0.0611	0.0063	0.0464	0.0012	0.3930	0.0580	11.9	590	160	332	30	292	7
1-21	183.0	78.7	2.33	0.0560	0.0038	0.0717	0.0014	0.5530	0.0420	-0.8	450	110	443	25	447	8
1-22	77.3	101.9	0.76	0.0655	0.0049	0.0974	0.0022	0.8910	0.0760	6.8	750	120	643	31	599	13
1-23	95.8	27.5	3.49	0.0622	0.0059	0.0681	0.0017	0.5820	0.0810	8.8	630	140	466	30	425	11
1-24	594.0	39.5	15.05	0.0579	0.0016	0.0722	0.0011	0.5800	0.0190	3.1	515	56	463	12	449	7
1-25	178.3	94.4	1.89	0.0605	0.0030	0.0961	0.0016	0.8030	0.0410	0.5	594	87	594	22	591	9
1-26	75.3	49.5	1.52	0.0599	0.0042	0.0953	0.0020	0.7800	0.0660	-0.2	560	130	586	30	587	12
1-27	582.1	470.0	1.24	0.0538	0.0020	0.0463	0.0007	0.3490	0.0160	4.1	367	74	304	10	292	4
1-28	741.0	1253.0	0.59	0.0592	0.0014	0.0767	0.0012	0.6270	0.0180	3.3	582	51	493	11	477	7
1-29	143.9	6.2	23.21	0.0659	0.0029	0.1059	0.0019	0.9810	0.0430	6.0	820	82	690	22	649	11
1-30	60.1	36.3	1.66	0.0654	0.0047	0.0892	0.0020	0.7880	0.0660	6.9	710	130	594	32	553	12
1-31	69.6	44.9	1.55	0.0654	0.0092	0.0385	0.0014	0.3340	0.0650	16.6	630	230	292	39	244	9
1-32	69.8	186.2	0.37	0.0743	0.0039	0.1365	0.0028	1.3880	0.0780	20.8	1028	92	885	31	825	16
1-33	368.2	220.1	1.67	0.0617	0.0019	0.1085	0.0016	0.9250	0.0300	0.0	678	60	664	15	664	9
1-34	755.5	355.2	2.13	0.0588	0.0014	0.0868	0.0012	0.7030	0.0180	0.8	548	49	541	11	537	7
1-35	178.0	106.7	1.67	0.0752	0.0023	0.1748	0.0028	1.8130	0.0630	2.5	1067	54	1047	21	1039	15
1-36	49.6	110.1	0.45	0.0580	0.0120	0.0483	0.0021	0.3530	0.1400	1.6	330	260	309	56	304	13
1-37	241.0	139.8	1.72	0.0609	0.0038	0.0462	0.0010	0.3850	0.0310	12.2	622	110	332	17	291	6
1-38	59.6	63.2	0.94	0.1413	0.0035	0.3618	0.0065	6.9600	0.2200	12.8	2229	41	2117	27	1990	31
1-39	397.7	244.5	1.63	0.0700	0.0012	0.1522	0.0022	1.4570	0.0360	2.2	926	35	915	14	913	13
1-40	531.0	315.0	1.69	0.0629	0.0018	0.1024	0.0018	0.8870	0.0220	2.6	715	53	645	12	629	11
1-41	118.1	25.6	4.62	0.0642	0.0038	0.0961	0.0025	0.8270	0.0470	3.6	750	110	613	26	591	15
1-42	649.0	1149.0	0.56	0.0612	0.0014	0.0963	0.0015	0.8100	0.0240	1.4	639	48	601	13	593	9
1-43	744.5	259.1	2.87	0.0699	0.0009	0.1610	0.0022	1.5520	0.0280	-4.7	923	26	951	11	962	12
1-44	422.1	105.6	4.00	0.0556	0.0022	0.0647	0.0011	0.4950	0.0220	1.2	408	72	409	14	404	7
1-45	462.2	276.8	1.67	0.0544	0.0023	0.0493	0.0008	0.3650	0.0190	2.6	372	80	319	12	310	5
1-46	256.8	222.0	1.16	0.0733	0.0024	0.1453	0.0023	1.4520	0.0500	16.9	1026	58	911	20	874	13
1-47	513.0	27.2	18.86	0.0557	0.0016	0.0721	0.0011	0.5550	0.0180	0.0	424	61	448	12	449	7
1-48	49.5	BDL	NA	0.0667	0.0140	0.0263	0.0015	0.2280	0.0860	20.1	670	280	209	39	167	9
1-49	690.0	183.3	3.76	0.0590	0.0013	0.0904	0.0012	0.7330	0.0190	-0.1	552	47	557	11	558	7
1-50	335.1	187.8	1.78	0.0848	0.0013	0.2311	0.0031	2.7300	0.0570	-3.1	1314	30	1335	14	1340	16
1-51	100.6	119.1	0.84	0.1207	0.0029	0.3381	0.0057	5.6700	0.1600	4.9	1970	41	1930	23	1879	27
1-52	124.8	56.7	2.20	0.1492	0.0024	0.3569	0.0056	7.3500	0.1600	18.2	2337	28	2152	19	1967	27
1-53	60.9	47.7	1.28	0.1212	0.0030	0.3584	0.0067	6.0100	0.1900	0.8	1970	41	1979	25	1974	31
1-54	352.5	49.2	7.16	0.0564	0.0021	0.0726	0.0011	0.5610	0.0250	0.0	432	75	452	14	452	7
1-55	115.1	65.3	1.76	0.0699	0.0070	0.0392	0.0012	0.3690	0.0590	24.3	890	160	327	27	248	7
1-56	229.6	148.6	1.55	0.0842	0.0110	0.1273	0.0027	1.4730	0.2500	39.3	1250	160	907	70	772	15
1-57	263.7	180.0	1.47	0.0614	0.0018	0.1052	0.0016	0.8900	0.0280	0.2	656	56	646	15	645	9
1-58	558.0	171.2	3.26	0.0559	0.0015	0.0711	0.0011	0.5500	0.0180	0.5	454	53	445	11	443	7
1-59	21.7	42.0	0.52	0.1196	0.0069	0.3417	0.0089	5.6500	0.3300	2.4	1945	85	1927	44	1897	43
1-60	269.1	33.7	8.00	0.0564	0.0025	0.0723	0.0012	0.5640	0.0280	0.7	449	83	453	16	450	7
1-61	226.7	162.2	1.40	0.0634	0.0032	0.0884	0.0015	0.7610	0.0460	5.8	725	91	580	22	546	9
1-62	220.2	70.1	3.14	0.0676	0.0029	0.1134	0.0019	1.0620	0.0520	5.4	866	80	732	23	692	11
1-63	537.0	69.7	7.70	0.0578	0.0022	0.0698	0.0011	0.5550	0.0260	3.4	519	72	450	14	435	7
1-64	265.9	167.6	1.59	0.0552	0.0043	0.0480	0.0009	0.3660	0.0350	5.0	390	120	318	17	302	6
1-65	482.0	143.2	3.37	0.0702	0.0014	0.1452	0.0020	1.4040	0.0350	6.5	931	41	889	14	874	11
1-66	766.0	228.5	3.35	0.0628	0.0011	0.1083	0.0015	0.9440	0.0210	1.8	701	36	675	11	663	9
1-67	272.0	158.6	1.72	0.0797	0.0040	0.1382	0.0023	1.5100	0.0920	30.8	1175	69	932	30	835	13
1-68	1164.0	413.2	2.82	0.0730	0.0250	0.0314	0.0013	0.3200	0.1300	29.9	2140	190	285	88	200	8
1-69	142.0	88.5	1.60	0.1022	0.0069	0.1094	0.0022	1.5390	0.1300	28.1	1643	110	931	41	669	13

				Measured values and ratios								Apparent Ages				
Batch & Grain no.	U (ppm)	Th (ppm)	U/Th	$^{207}Pb/^{206}Pb$	2σ	$^{206}Pb/^{238}U$	2σ	$^{207}Pb/^{235}U$	2σ	Discordance (%)	$^{207}Pb/^{206}Pb$	2σ	$^{207}Pb/^{235}U$	2σ	$^{206}Pb/^{238}U$	2σ
1-70	718.0	129.0	5.57	0.1217	0.0009	0.3587	0.0054	6.0190	0.0960	0.2	1980	13	1978	14	1976	26
1-71	320.1	257.5	1.24	0.0547	0.0044	0.0392	0.0008	0.2970	0.0260	6.2	380	120	264	17	248	5
1-72	229.4	92.6	2.48	0.0668	0.0025	0.1029	0.0016	0.9440	0.0350	5.9	804	75	671	18	632	9
1-73	1794.0	1386.0	1.29	0.0545	0.0011	0.0436	0.0008	0.3274	0.0099	4.0	394	44	287	7	276	5
1-74	272.0	94.4	2.88	0.0662	0.0030	0.1212	0.0019	1.1120	0.0540	2.6	797	69	757	21	738	11
1-75	556.8	282.0	1.97	0.0553	0.0180	0.0420	0.0016	0.3340	0.1600	9.1	390	240	292	77	265	10
1-76	690.7	356.0	1.94	0.0592	0.0014	0.0884	0.0013	0.7200	0.0200	0.8	568	47	550	11	546	8
1-77	185.0	84.9	2.18	0.0573	0.0040	0.0753	0.0015	0.5980	0.0630	1.2	460	110	474	26	468	9
1-78	524.0	294.5	1.78	0.0609	0.0014	0.0972	0.0014	0.8080	0.0230	0.6	634	46	602	12	598	8
1-79	2361.0	1475.0	1.60	0.0582	0.0008	0.0780	0.0011	0.6232	0.0120	1.5	538	27	492	7	484	6
1-80	564.0	14.9	37.85	0.0561	0.0035	0.0547	0.0009	0.4160	0.0260	3.3	433	100	355	17	343	6
1-81	1245.6	497.0	2.51	0.0543	0.0016	0.0476	0.0007	0.3514	0.0120	1.8	369	58	305	8	300	4
1-82	204.7	132.2	1.55	0.1597	0.0022	0.3530	0.0057	7.7500	0.1700	23.9	2452	22	2199	20	1948	27
1-83	278.1	2695.0	0.10	0.1455	0.0048	0.0577	0.0013	1.1440	0.0490	53.2	2284	57	772	22	362	8
1-84	238.0	182.0	1.31	0.0524	0.0059	0.0474	0.0010	0.3430	0.0540	-0.8	280	140	297	25	300	6
1-85	229.0	706.0	0.32	0.0628	0.0029	0.1120	0.0017	0.9720	0.0600	0.7	688	81	689	20	684	10
1-86	206.9	174.7	1.18	0.0543	0.0052	0.0495	0.0011	0.3620	0.0490	3.1	360	130	321	23	311	7
1-87	195.2	273.4	0.71	0.0641	0.0077	0.0396	0.0010	0.3480	0.0530	17.4	710	160	303	32	250	6
1-88	242.8	60.4	4.02	0.0569	0.0036	0.0715	0.0013	0.5640	0.0470	1.5	494	99	452	20	445	8
1-89	506.2	238.6	2.12	0.0531	0.0031	0.0497	0.0008	0.3610	0.0240	-0.2	314	96	312	15	313	5
1-90	212.6	129.9	1.64	0.1284	0.0018	0.4110	0.0060	7.2270	0.1400	-8.1	2071	29	2140	16	2219	27
1-91	389.0	127.2	3.06	0.0544	0.0047	0.0471	0.0013	0.3540	0.0790	3.8	347	120	308	25	296	8
1-92	234.7	100.3	2.34	0.0592	0.0030	0.0725	0.0013	0.5880	0.0500	4.0	552	93	470	23	451	8
1-93	526.9	706.0	0.75	0.0682	0.0044	0.0386	0.0006	0.3630	0.0220	22.0	872	100	313	15	244	4
1-94	906.0	749.0	1.21	0.0541	0.0019	0.0377	0.0006	0.2835	0.0099	5.8	372	71	253	8	238	4
1-95	145.9	69.0	2.11	0.0606	0.0042	0.0841	0.0015	0.7020	0.0570	3.1	604	110	537	24	520	9
1-96	457.0	172.3	2.65	0.0541	0.0021	0.0609	0.0010	0.4510	0.0180	-0.9	381	74	378	12	382	6
1-97	227.4	66.9	3.40	0.0604	0.0022	0.1011	0.0016	0.8460	0.0330	0.0	595	75	621	18	621	9
1-98	311.3	217.6	1.43	0.1736	0.0015	0.4628	0.0064	11.1140	0.1700	6.0	2591	14	2533	15	2451	28
1-99	79.7	37.1	2.15	0.2159	0.0028	0.5621	0.0091	16.7900	0.3400	2.9	2951	21	2920	19	2874	38
1-100	547.0	575.7	0.95	0.0527	0.0026	0.0469	0.0008	0.3420	0.0180	1.6	304	91	300	13	295	5
1-101	82.4	68.5	1.20	0.1776	0.0028	0.4803	0.0084	11.6600	0.2800	5.3	2629	25	2577	21	2530	36
2-2	299.4	135.9	2.20	0.0523	0.0016	0.0462	0.0009	0.3337	0.0110	0.5	286	66	293	9	291	5
2-3	1074.0	666.0	1.61	0.0537	0.0008	0.0494	0.0009	0.3638	0.0083	1.4	355	31	315	6	311	5
2-4	242.1	26.3	9.22	0.0588	0.0015	0.0734	0.0015	0.5980	0.0190	3.8	548	54	475	12	457	9
2-5	252.2	52.1	4.84	0.0565	0.0015	0.0719	0.0013	0.5610	0.0170	0.8	479	56	451	11	448	8
2-6	637.9	62.4	10.22	0.0579	0.0014	0.0793	0.0016	0.6350	0.0190	1.6	512	54	500	12	492	10
2-7	250.0	442.0	0.57	0.0654	0.0018	0.0655	0.0017	0.5840	0.0180	12.3	783	58	466	12	409	11
2-8	328.6	387.4	0.85	0.0543	0.0024	0.0291	0.0007	0.2166	0.0099	6.8	340	89	198	8	185	5
2-9	918.0	574.0	1.60	0.0595	0.0007	0.0819	0.0015	0.6703	0.0140	2.6	588	26	521	9	507	9
2-10	734.6	14.6	50.28	0.0540	0.0013	0.0562	0.0010	0.4230	0.0130	2.0	374	55	359	9	352	6
2-11	448.8	52.1	8.61	0.0581	0.0015	0.0806	0.0017	0.6410	0.0200	0.5	526	58	502	13	500	10
2-12	306.6	165.7	1.85	0.0541	0.0017	0.0424	0.0010	0.3150	0.0120	3.7	355	69	278	9	268	6
2-13	230.7	74.0	3.12	0.0591	0.0014	0.0661	0.0018	0.5400	0.0200	5.9	567	50	438	13	412	11
2-14	835.0	63.3	13.19	0.0533	0.0009	0.0489	0.0009	0.3599	0.0089	1.4	333	39	312	7	308	5
2-15	936.9	370.0	2.53	0.0551	0.0010	0.0528	0.0011	0.4013	0.0100	3.1	412	40	342	8	332	7
2-16	737.0	376.0	1.96	0.0575	0.0007	0.0861	0.0015	0.6862	0.0150	-0.3	513	29	531	9	532	9
2-17	351.0	78.9	4.45	0.0568	0.0013	0.0613	0.0011	0.4760	0.0140	3.0	471	48	395	10	383	7
2-18	205.9	260.0	0.79	0.0799	0.0024	0.1465	0.0031	1.6120	0.0470	9.6	1200	61	975	18	881	17
2-19	342.0	74.5	4.59	0.0625	0.0028	0.0527	0.0022	0.4420	0.0260	10.5	669	98	370	18	331	14
2-20	372.0	102.0	3.65	0.0560	0.0013	0.0700	0.0013	0.5390	0.0150	0.5	456	54	438	10	436	8
2-21	469.0	88.0	5.33	0.0744	0.0008	0.1638	0.0029	1.6830	0.0350	2.3	1055	20	1001	13	978	16
2-22	216.8	159.9	1.36	0.0601	0.0012	0.0951	0.0017	0.7930	0.0210	1.2	610	44	593	12	586	10
2-23	629.9	396.0	1.59	0.0536	0.0011	0.0441	0.0008	0.3283	0.0083	3.5	358	46	289	6	278	5
2-24	710.0	63.8	11.13	0.0560	0.0008	0.0573	0.0010	0.4425	0.0100	3.4	457	30	372	7	359	6
2-25	558.4	4.7	119.06	0.0529	0.0014	0.0473	0.0009	0.3444	0.0110	0.8	339	64	300	8	298	6
2-26	233.3	61.3	3.81	0.0571	0.0014	0.0709	0.0014	0.5520	0.0170	0.9	485	54	446	11	442	8
2-27	118.6	153.5	0.77	0.0686	0.0019	0.1150	0.0023	1.0870	0.0370	6.1	874	59	747	18	702	13
2-28	434.3	108.5	4.00	0.0533	0.0017	0.0457	0.0009	0.3350	0.0110	1.7	320	70	293	9	288	5
2-29	98.9	66.7	1.48	0.0584	0.0029	0.0820	0.0021	0.6650	0.0360	1.9	510	110	518	23	508	13
2-30	120.0	92.5	1.30	0.1269	0.0014	0.3720	0.0070	6.4740	0.1400	1.4	2055	19	2041	19	2038	33
2-31	2050.0	782.0	2.62	0.0648	0.0017	0.0420	0.0012	0.3795	0.0120	18.7	763	54	327	9	265	8
2-32	82.3	99.1	0.83	0.0606	0.0020	0.0946	0.0019	0.7880	0.0300	1.3	619	69	591	17	583	11
2-33	785.0	722.0	1.09	0.0517	0.0010	0.0371	0.0007	0.2638	0.0069	1.3	270	43	238	6	235	4
2-34	62.4	19.3	3.24	0.0563	0.0030	0.0822	0.0019	0.6220	0.0330	-3.9	410	110	490	21	509	11
2-35	531.0	808.0	0.66	0.0653	0.0009	0.1280	0.0022	1.1520	0.0250	0.2	789	28	778	12	776	13
2-36	482.4	8.5	56.49	0.0544	0.0012	0.0509	0.0009	0.3798	0.0110	2.0	376	51	326	8	320	6
2-37	67.8	47.4	1.43	0.0634	0.0030	0.0923	0.0021	0.8030	0.0390	6.0	690	100	605	22	569	12
2-38	568.0	371.0	1.53	0.0526	0.0010	0.0471	0.0008	0.3423	0.0086	0.8	302	43	299	6	297	5
2-39	766.0	356.0	2.15	0.0594	0.0031	0.0370	0.0010	0.3010	0.0160	11.9	570	120	266	12	234	6
2-40	357.0	74.9	4.76	0.0556	0.0012	0.0485	0.0010	0.3669	0.0110	4.1	432	49	318	8	305	6
2-41	341.2	276.3	1.23	0.0547	0.0015	0.0449	0.0008	0.3384	0.0110	4.3	394	60	296	8	283	5
2-42	881.0	103.5	8.51	0.0530	0.0008	0.0494	0.0009	0.3615	0.0082	0.8	329	33	313	6	311	5
2-43	401.2	217.4	1.85	0.0555	0.0010	0.0741	0.0013	0.5710	0.0140	-0.6	436	42	458	9	461	8
2-44	362.6	251.6	1.44	0.0513	0.0017	0.0348	0.0007	0.2479	0.0094	1.6	236	71	224	8	221	4
2-45	324.4	38.9	8.33	0.0130	0.0360	0.0512	0.0025	0.1500	0.2600	13.0	2180	320	370	160	322	15
2-46	257.1	194.9	1.32	0.0578	0.0013	0.0865	0.0016	0.6940	0.0200	-0.1	517	50	534	12	535	10
2-47	264.5	155.9	1.70	0.1245	0.0014	0.2384	0.0071	4.0500	0.1300	35.7	2018	20	1639	28	1376	37
2-48	148.7	59.6	2.49	0.0979	0.0012	0.2654	0.0048	3.6020	0.0770	4.1	1583	23	1550	17	1517	25
2-49	542.4	84.4	6.43	0.0544	0.0018	0.0391	0.0010	0.2957	0.0110	5.8	370	72	262	9	247	6
2-50	1041.0	151.7	6.86	0.1460	0.0017	0.2678	0.0051	5.3950	0.1700	37.5	2300	19	1888	28	1529	26
2-51	201.0	159.0	1.26	0.0676	0.0014	0.1370	0.0024	1.2790	0.0340	1.6	865	42	841	15	827	14
2-52	244.4	108.1	2.26	0.0676	0.0028	0.0589	0.0018	0.5500	0.0240	17.1	845	85	445	16	369	11
2-53	463.0	404.0	1.15	0.0507	0.0014	0.0386	0.0007	0.2695	0.0086	-0.8	215	58	242	7	244	4

	Measured values and ratios											Apparent Ages					
Batch & Grain no.	U (ppm)	Th (ppm)	U/Th	$^{207}Pb/^{206}Pb$	2σ	$^{206}Pb/^{238}U$	2σ	$^{207}Pb/^{235}U$	2σ	Discordance (%)	$^{207}Pb/^{206}Pb$	2σ	$^{207}Pb/^{235}U$	2σ	$^{206}Pb/^{238}U$	2σ
2-54	390.0	532.0	0.73	0.0524	0.0012	0.0470	0.0009	0.3426	0.0094	1.0	288	51	299	7	296	5
2-55	363.0	124.7	2.91	0.0528	0.0013	0.0488	0.0009	0.3543	0.0110	0.0	301	56	307	8	307	6
2-56	520.6	126.2	4.13	0.0574	0.0016	0.0720	0.0014	0.5710	0.0180	2.3	508	60	459	12	448	9
2-57	801.0	33.7	23.79	0.0587	0.0015	0.0563	0.0011	0.4560	0.0140	7.5	549	58	382	10	353	7
2-58	399.5	133.6	2.99	0.0522	0.0012	0.0476	0.0009	0.3423	0.0096	-0.5	287	52	299	7	300	5
2-59	994.0	592.0	1.68	0.0513	0.0009	0.0405	0.0007	0.2879	0.0069	0.4	246	39	257	6	256	4
2-60	230.0	100.3	2.29	0.0636	0.0011	0.1194	0.0022	1.0590	0.0260	0.7	726	37	732	13	727	12
2-61	542.0	53.6	10.11	0.0612	0.0016	0.0581	0.0013	0.4900	0.0180	9.9	635	56	404	13	364	8
2-62	526.0	165.0	3.19	0.0565	0.0015	0.0327	0.0019	0.2550	0.0170	10.0	467	62	230	13	207	12
2-63	525.0	221.0	2.38	0.0587	0.0011	0.0824	0.0017	0.6680	0.0160	1.8	558	40	520	10	510	10
2-64	469.2	74.1	6.33	0.0522	0.0011	0.0452	0.0008	0.3264	0.0086	0.5	293	48	287	7	285	5
2-65	413.9	159.8	2.59	0.0598	0.0011	0.0702	0.0013	0.5750	0.0160	5.3	608	42	462	10	437	8
2-66	364.0	435.0	0.84	0.0523	0.0013	0.0471	0.0011	0.3427	0.0110	0.9	290	53	299	8	297	7
2-67	568.0	68.3	8.32	0.0601	0.0013	0.0659	0.0012	0.5480	0.0160	7.3	610	50	443	11	411	7
2-68	353.0	258.0	1.37	0.0532	0.0013	0.0475	0.0009	0.3499	0.0100	1.5	326	53	304	8	299	6
2-69	138.0	27.9	4.95	0.0649	0.0016	0.1060	0.0026	0.9610	0.0330	5.0	778	52	683	17	649	15
2-70	220.0	159.8	1.38	0.0600	0.0016	0.0856	0.0017	0.7110	0.0230	2.8	599	60	545	14	530	10
2-71	71.3	47.2	1.51	0.0590	0.0021	0.0975	0.0019	0.7920	0.0320	-0.9	567	74	594	18	600	11
2-72	769.0	623.0	1.23	0.0522	0.0011	0.0464	0.0008	0.3335	0.0089	-0.1	287	46	292	7	292	5
2-73	491.0	469.0	1.05	0.0534	0.0014	0.0481	0.0009	0.3540	0.0110	1.3	323	57	307	8	303	5
2-74	232.0	15.0	15.50	0.0844	0.0036	0.0706	0.0016	0.8230	0.0360	27.7	1305	88	608	20	440	10
2-75	412.0	266.0	1.55	0.0523	0.0015	0.0480	0.0010	0.3451	0.0120	-0.7	286	62	300	9	302	6
2-76	104.4	66.2	1.58	0.0782	0.0016	0.1840	0.0035	1.9750	0.0520	4.6	1139	40	1108	18	1089	19
2-77	117.6	81.3	1.45	0.0708	0.0018	0.1501	0.0029	1.4480	0.0450	0.5	945	51	906	19	901	16
2-78	233.8	124.4	1.88	0.0945	0.0011	0.2530	0.0045	3.2970	0.0700	4.2	1514	23	1479	17	1454	23
2-79	47.4	42.2	1.12	0.0618	0.0031	0.0912	0.0022	0.7770	0.0410	2.9	620	100	580	23	563	13
2-80	843.0	1281.0	0.66	0.0547	0.0011	0.0454	0.0008	0.3443	0.0094	4.8	390	45	301	7	286	5
2-81	340.0	285.3	1.19	0.0528	0.0013	0.0488	0.0009	0.3545	0.0110	1.2	315	56	311	8	307	5
2-82	838.0	255.7	3.28	0.0512	0.0016	0.0371	0.0009	0.2598	0.0110	-0.3	230	72	234	9	235	6
2-83	447.4	120.1	3.73	0.0528	0.0013	0.0402	0.0008	0.2974	0.0085	3.7	333	60	264	7	254	5
2-84	380.0	29.8	12.76	0.0552	0.0011	0.0702	0.0013	0.5370	0.0150	-0.5	416	45	435	10	437	8
2-85	139.5	75.5	1.85	0.0627	0.0021	0.0564	0.0022	0.4850	0.0230	12.2	702	72	403	16	354	14
2-86	484.1	122.6	3.95	0.0601	0.0009	0.1007	0.0017	0.8360	0.0190	-0.3	613	30	617	10	619	10
2-87	1205.0	548.7	2.20	0.0617	0.0008	0.0757	0.0020	0.6500	0.0210	7.4	664	28	508	13	470	12
2-88	187.0	67.7	2.76	0.0605	0.0016	0.0474	0.0017	0.3940	0.0170	11.8	600	57	338	12	298	10
2-89	152.2	213.3	0.71	0.0532	0.0033	0.0424	0.0010	0.3150	0.0190	3.4	320	130	277	14	268	6
2-90	56.5	40.8	1.38	0.1269	0.0023	0.3366	0.0063	5.8460	0.1400	10.4	2049	32	1952	20	1870	30
2-91	218.4	144.4	1.51	0.0740	0.0011	0.1759	0.0032	1.7990	0.0440	1.7	1034	31	1045	16	1044	18
2-92	269.0	191.0	1.41	0.0520	0.0016	0.0451	0.0009	0.3255	0.0110	0.4	292	65	286	8	285	6
2-93	415.0	20.4	20.33	0.0570	0.0011	0.0741	0.0015	0.5820	0.0160	1.2	492	43	466	10	460	9
2-94	899.0	5.0	179.44	0.0547	0.0009	0.0470	0.0008	0.3554	0.0086	4.0	408	34	309	6	296	5
2-95	305.0	104.7	2.91	0.0608	0.0013	0.0960	0.0019	0.8090	0.0220	1.7	638	47	601	12	591	11
2-96	809.0	1241.0	0.65	0.0532	0.0010	0.0418	0.0010	0.3050	0.0079	2.3	330	43	270	6	264	6
2-97	729.0	91.4	7.98	0.0554	0.0087	0.0504	0.0017	0.3940	0.0650	6.5	1200	180	339	47	317	10
2-98	120.4	64.9	1.86	0.0565	0.0029	0.0415	0.0009	0.3230	0.0180	7.0	430	110	282	13	262	6
2-99	314.0	232.0	1.35	0.0528	0.0017	0.0446	0.0009	0.3280	0.0120	2.0	296	67	287	9	281	5
2-100	149.1	99.5	1.50	0.0572	0.0017	0.0840	0.0016	0.6600	0.0220	-0.5	488	68	517	14	520	10
2-101	149.1	114.3	1.30	0.0517	0.0019	0.0551	0.0011	0.3970	0.0170	-2.6	267	79	337	12	346	7
2-102	362.8	270.9	1.34	0.0611	0.0010	0.0983	0.0018	0.8260	0.0190	1.1	640	34	612	11	605	10
2-103	171.8	187.4	0.92	0.1428	0.0020	0.1882	0.0058	3.7200	0.1400	54.9	2259	24	1573	31	1110	32
2-104	853.0	86.4	9.87	0.0547	0.0011	0.0391	0.0008	0.2930	0.0081	5.4	384	43	261	6	247	5
2-105	316.7	156.9	2.02	0.0523	0.0012	0.0482	0.0010	0.3508	0.0110	0.4	282	51	305	8	303	6
2-106	180.1	29.8	6.04	0.0557	0.0018	0.0712	0.0013	0.5480	0.0190	0.6	462	69	446	13	444	8
2-107	179.4	93.2	1.92	0.0608	0.0015	0.0891	0.0017	0.7550	0.0230	3.3	627	54	569	14	550	10
2-108	657.0	62.2	10.56	0.0774	0.0015	0.1042	0.0024	1.1180	0.0410	15.7	1127	38	758	19	639	14
2-109	48.4	44.2	1.09	0.0536	0.0039	0.0442	0.0012	0.3280	0.0230	3.8	340	140	290	17	279	7
2-110	309.9	304.8	1.02	0.0552	0.0011	0.0722	0.0013	0.5510	0.0140	-1.1	416	46	445	9	450	8
2-111	762.0	588.0	1.30	0.0532	0.0010	0.0362	0.0007	0.2630	0.0063	3.3	333	40	237	5	229	4
2-112	3720.0	966.0	3.85	0.0455	0.0074	0.0150	0.0004	0.0970	0.0240	-3.9	930	170	92	23	96	3
2-113	147.2	124.0	1.19	0.0529	0.0026	0.0366	0.0009	0.2670	0.0140	2.8	330	100	239	11	232	5
2-114	165.7	35.8	4.63	0.0644	0.0016	0.1287	0.0030	1.1500	0.0390	-0.3	757	58	778	19	780	17
2-115	756.0	493.0	1.53	0.0535	0.0010	0.0437	0.0009	0.3212	0.0081	2.7	348	43	283	6	276	6
2-116	449.3	259.7	1.73	0.0570	0.0012	0.0680	0.0012	0.5320	0.0140	1.9	473	45	432	9	424	7
2-117	105.2	53.6	1.96	0.0623	0.0018	0.1030	0.0021	0.8960	0.0300	2.6	695	60	649	16	632	12
2-118	236.0	101.2	2.33	0.0584	0.0014	0.0812	0.0031	0.6330	0.0270	-0.6	540	51	500	18	503	18
2-119	150.4	55.2	2.73	0.0607	0.0016	0.0904	0.0018	0.7540	0.0240	2.2	609	57	570	14	558	11
2-120	281.0	30.3	9.27	0.0594	0.0018	0.0691	0.0013	0.5670	0.0190	5.3	573	63	455	12	431	8
2-121	209.6	81.5	2.57	0.0559	0.0028	0.0483	0.0011	0.3740	0.0200	6.7	460	120	326	16	304	7
2-122	501.0	330.0	1.52	0.0530	0.0010	0.0494	0.0009	0.3618	0.0099	1.0	314	42	314	7	311	6
2-123	85.1	53.7	1.58	0.0937	0.0017	0.2603	0.0048	3.3850	0.0810	0.6	1496	33	1500	19	1491	24
2-124	83.7	76.4	1.10	0.0512	0.0029	0.0452	0.0010	0.3180	0.0190	-1.1	250	120	282	15	285	6
2-125	2275.0	857.0	2.65	0.0545	0.0006	0.0354	0.0008	0.2649	0.0064	5.9	392	26	238	5	224	5
2-126	208.0	67.8	3.07	0.0545	0.0013	0.0816	0.0020	0.6140	0.0210	-4.2	376	52	485	13	505	12
2-127	1085.0	14.2	76.41	0.0539	0.0008	0.0615	0.0018	0.4600	0.0140	0.0	360	35	385	10	385	11
2-128	387.3	109.3	3.54	0.0595	0.0016	0.0686	0.0015	0.5640	0.0200	6.4	583	55	457	13	428	9
2-129	325.0	80.5	4.04	0.0549	0.0011	0.0728	0.0016	0.5520	0.0160	-1.5	398	46	446	10	453	9
2-130	586.0	44.9	13.04	0.0523	0.0020	0.0510	0.0011	0.3720	0.0160	-0.2	308	93	320	12	321	7
2-131	694.0	35.1	19.79	0.0554	0.0007	0.0595	0.0011	0.4546	0.0099	2.2	424	29	381	7	373	7
2-132	434.0	304.0	1.43	0.0488	0.0017	0.0252	0.0005	0.1724	0.0069	0.3	152	72	161	6	161	3
2-133	1007.0	27.1	37.20	0.0544	0.0007	0.0494	0.0009	0.3688	0.0084	2.5	384	31	319	6	311	5
2-134	544.3	153.4	3.55	0.0570	0.0010	0.0604	0.0011	0.4751	0.0120	4.0	486	36	394	8	378	7
2-135	252.6	75.8	3.33	0.0563	0.0012	0.0684	0.0014	0.5290	0.0150	0.9	448	48	430	10	426	9
2-136	174.1	127.0	1.37	0.0512	0.0017	0.0470	0.0009	0.3310	0.0120	-1.9	229	69	291	9	296	6
2-137	490.0	22.9	21.42	0.0542	0.0011	0.0569	0.0010	0.4276	0.0110	1.4	370	45	362	8	357	6

				Measured values and ratios								Apparent Ages					
Batch & Grain no.	U (ppm)	Th (ppm)	U/Th	$^{207}Pb/^{206}Pb$	2σ	$^{206}Pb/^{238}U$	2σ	$^{207}Pb/^{235}U$	2σ	Discordance (%)	$^{207}Pb/^{206}Pb$	2σ	$^{207}Pb/^{235}U$	2σ	$^{206}Pb/^{238}U$	2σ
2-138	49.9	51.1	0.98	0.0532	0.0045	0.0455	0.0012	0.3290	0.0270	1.4	290	160	291	21	287	8
2-139	599.5	65.3	9.18	0.0548	0.0021	0.0447	0.0011	0.3450	0.0140	6.1	388	86	300	10	282	7
2-140	709.7	825.0	0.86	0.0527	0.0009	0.0464	0.0008	0.3381	0.0083	1.2	318	40	296	6	292	5
2-141	249.8	38.8	6.44	0.0586	0.0017	0.0701	0.0014	0.5680	0.0190	4.2	533	65	456	12	437	9
18MC136A1																
1-1	52.7	51.1	1.03	0.0576	0.0033	0.0910	0.0019	0.7100	0.0420	-3.1	470	110	545	25	562	11
1-2	115.4	60.7	1.90	0.1283	0.0026	0.3770	0.0063	6.6980	0.2000	0.5	2077	35	2073	26	2064	29
1-3	106.1	116.7	0.91	0.0591	0.0022	0.0967	0.0018	0.7930	0.0340	-0.7	569	83	591	20	595	11
1-4	142.8	27.4	5.21	0.0726	0.0020	0.1414	0.0026	1.3930	0.0500	3.5	987	57	885	21	854	15
1-5	374.6	81.4	4.60	0.0620	0.0014	0.1010	0.0018	0.8690	0.0280	2.2	683	48	634	15	620	11
1-6	337.0	37.4	9.00	0.0622	0.0019	0.1089	0.0020	0.9300	0.0340	0.7	686	65	671	18	666	11
1-7	90.5	89.9	1.01	0.0610	0.0026	0.1030	0.0020	0.8710	0.0380	0.3	607	87	634	21	632	12
1-8	235.3	126.8	1.86	0.0507	0.0020	0.0368	0.0007	0.2537	0.0110	-1.6	211	79	229	9	233	5
1-9	34.1	17.4	1.96	0.0569	0.0039	0.0944	0.0025	0.7470	0.0530	-2.7	490	140	566	29	581	15
1-10	224.8	393.0	0.57	0.1821	0.0032	0.4311	0.0075	11.0800	0.3100	13.9	2670	29	2529	26	2310	34
1-11	148.2	129.4	1.15	0.0609	0.0020	0.0966	0.0018	0.8190	0.0310	2.4	624	72	609	17	595	10
1-12	154.9	276.0	0.56	0.0780	0.0020	0.1516	0.0041	1.6470	0.0600	8.1	1140	49	989	23	909	23
1-13	79.3	70.9	1.12	0.1840	0.0033	0.4777	0.0081	12.3200	0.3600	5.8	2685	29	2627	27	2517	35
1-14	125.4	56.2	2.23	0.0609	0.0021	0.0943	0.0019	0.7910	0.0310	1.9	606	74	592	17	581	11
1-15	143.1	101.6	1.41	0.0599	0.0021	0.0948	0.0017	0.7890	0.0310	1.3	577	77	591	18	584	10
1-16	148.0	38.4	3.85	0.1805	0.0031	0.4854	0.0084	12.1500	0.3400	4.2	2656	29	2618	26	2550	36
1-17	84.8	26.9	3.15	0.0720	0.0020	0.1583	0.0028	1.6090	0.0580	2.5	978	57	972	23	947	16
1-18	106.1	64.2	1.65	0.0596	0.0021	0.0987	0.0018	0.8220	0.0330	0.2	573	74	608	18	607	11
1-19	105.5	40.7	2.59	0.0609	0.0023	0.1027	0.0019	0.8750	0.0380	0.7	614	82	635	20	630	11
1-20	327.8	196.3	1.67	0.0621	0.0014	0.0953	0.0016	0.8170	0.0260	3.2	664	49	607	15	587	9
1-21	132.7	97.1	1.37	0.0627	0.0020	0.1084	0.0020	0.9320	0.0350	1.3	702	65	672	19	663	12
1-22	63.8	57.9	1.10	0.0716	0.0026	0.1536	0.0029	1.5080	0.0590	1.2	981	72	932	23	921	16
1-23	134.8	179.7	0.75	0.1762	0.0028	0.4741	0.0077	11.4100	0.3200	6.2	2617	27	2556	26	2503	33
1-24	312.7	218.3	1.43	0.1743	0.0026	0.4628	0.0074	11.0570	0.3000	7.2	2598	25	2529	24	2452	33
1-25	260.4	113.4	2.30	0.0635	0.0016	0.1085	0.0018	0.9450	0.0310	1.8	722	55	676	17	664	11
1-26	82.5	54.4	1.52	0.0751	0.0022	0.1730	0.0033	1.7780	0.0630	1.8	1049	57	1034	23	1029	18
1-27	64.7	63.4	1.02	0.0734	0.0037	0.1619	0.0038	1.6110	0.0850	0.4	1040	100	971	33	967	21
1-28	267.1	714.0	0.37	0.0608	0.0016	0.0776	0.0015	0.6430	0.0220	4.3	621	58	503	14	482	9
1-29	146.9	75.6	1.94	0.1080	0.0020	0.3019	0.0050	4.4580	0.1300	4.7	1763	34	1723	23	1700	25
1-30	37.1	26.0	1.42	0.0612	0.0037	0.0948	0.0021	0.7860	0.0510	-0.2	600	120	583	28	584	13
1-31	253.2	362.0	0.70	0.0737	0.0016	0.1692	0.0028	1.7180	0.0520	2.0	1028	42	1016	19	1008	15
1-32	88.0	42.5	2.07	0.1290	0.0024	0.3709	0.0065	6.5660	0.1900	3.1	2083	33	2054	25	2033	30
1-33	220.7	59.8	3.69	0.1322	0.0022	0.3884	0.0063	7.0720	0.1900	1.2	2131	29	2120	24	2116	29
1-34	252.2	305.1	0.83	0.0594	0.0017	0.0954	0.0017	0.7790	0.0280	-0.1	580	59	587	16	587	10
1-35	164.7	145.6	1.13	0.0733	0.0022	0.1585	0.0030	1.6080	0.0570	2.5	1028	61	972	22	948	17
1-36	258.7	95.7	2.70	0.1723	0.0025	0.4551	0.0077	10.8420	0.3000	7.2	2579	25	2511	26	2418	34
1-37	186.6	108.6	1.72	0.0607	0.0018	0.0780	0.0019	0.6520	0.0260	5.0	626	64	509	15	484	11
1-38	206.0	524.0	0.39	0.1624	0.0025	0.4744	0.0087	10.7000	0.3100	-1.9	2480	26	2496	27	2502	38
1-39	95.8	184.5	0.52	0.0746	0.0023	0.1653	0.0030	1.7030	0.0650	2.0	1049	61	1007	24	987	16
1-40	472.9	248.9	1.90	0.0661	0.0014	0.1331	0.0024	1.2160	0.0380	0.2	806	42	807	17	805	14
1-41	105.2	145.8	0.72	0.0587	0.0022	0.0974	0.0018	0.7870	0.0360	-2.4	525	80	585	21	599	10
1-42	57.4	32.8	1.75	0.0702	0.0023	0.1624	0.0035	1.5700	0.0630	-0.6	960	66	964	26	970	19
1-43	212.0	195.1	1.09	0.0729	0.0015	0.1601	0.0027	1.6060	0.0480	1.5	1014	43	971	19	957	15
1-44	373.8	279.2	1.34	0.0747	0.0016	0.1508	0.0028	1.5330	0.0470	4.1	1057	43	944	19	905	16
1-45	260.0	121.3	2.14	0.0740	0.0016	0.1685	0.0029	1.6980	0.0510	4.7	1039	44	1007	19	1004	16
1-46	99.0	145.9	0.68	0.1782	0.0029	0.4975	0.0083	12.1700	0.3400	1.9	2636	27	2617	27	2603	36
1-47	295.2	135.7	2.18	0.1160	0.0018	0.3222	0.0052	5.1230	0.1400	6.6	1898	28	1840	23	1800	25
1-48	99.3	75.6	1.31	0.0742	0.0026	0.1620	0.0029	1.6320	0.0640	1.5	1029	70	982	24	968	16
1-49	202.0	103.7	1.95	0.0749	0.0025	0.1752	0.0035	1.7840	0.0670	-1.6	1050	68	1038	24	1040	19
1-50	96.9	114.5	0.85	0.0596	0.0023	0.1014	0.0019	0.8380	0.0360	-0.1	605	81	622	20	622	11
1-51	196.0	141.9	1.38	0.0601	0.0016	0.0965	0.0017	0.7920	0.0270	-0.5	608	59	591	15	594	10
1-52	262.6	141.0	1.86	0.0723	0.0015	0.1247	0.0023	1.2430	0.0380	7.7	998	44	821	17	758	13
1-53	169.5	96.1	1.76	0.0641	0.0019	0.1068	0.0018	0.9410	0.0330	2.5	725	64	671	18	654	11
1-54	324.4	258.0	1.26	0.0748	0.0015	0.1765	0.0029	1.8080	0.0540	2.2	1063	40	1048	20	1048	16
1-55	154.3	146.3	1.05	0.0654	0.0019	0.1250	0.0023	1.1360	0.0400	1.7	785	60	773	18	760	13
1-56	116.3	66.1	1.76	0.0608	0.0023	0.1005	0.0018	0.8360	0.0360	-0.6	610	83	614	20	618	11
1-57	213.6	97.4	2.19	0.0666	0.0017	0.1129	0.0022	1.0310	0.0360	3.8	811	55	717	18	690	12
1-58	53.0	10.9	4.86	0.0930	0.0024	0.2601	0.0048	3.3390	0.1100	-0.4	1487	50	1488	27	1490	25
1-59	79.1	95.5	0.83	0.0713	0.0023	0.1696	0.0031	1.6670	0.0630	-4.1	971	66	1002	24	1010	17
1-60	200.2	119.3	1.68	0.1232	0.0020	0.3699	0.0061	6.2650	0.1700	-1.0	2005	28	2013	25	2029	29
1-61	230.7	274.5	0.84	0.1781	0.0027	0.4834	0.0082	11.9200	0.3300	4.0	2636	25	2598	26	2543	35
1-62	115.1	51.6	2.23	0.0613	0.0020	0.0962	0.0021	0.8050	0.0320	0.9	678	68	597	18	592	12
1-63	147.6	24.3	6.07	0.1667	0.0028	0.4150	0.0075	9.5800	0.2800	12.9	2523	29	2394	27	2240	35
1-64	301.7	264.5	1.14	0.0629	0.0033	0.0918	0.0033	0.7830	0.0510	3.1	670	110	584	28	566	19
1-65	344.9	66.3	5.20	0.0615	0.0014	0.1105	0.0018	0.9340	0.0290	-0.9	657	48	670	15	676	10
1-66	283.5	146.7	1.93	0.0644	0.0013	0.1195	0.0020	1.0520	0.0320	0.2	747	43	729	16	728	11
1-67	516.1	159.6	3.23	0.0606	0.0014	0.0955	0.0017	0.7870	0.0250	0.3	630	50	590	15	588	10
1-68	131.9	75.8	1.74	0.1834	0.0030	0.4638	0.0081	11.6000	0.3400	11.1	2683	26	2573	26	2456	36
1-69	239.1	126.2	1.89	0.1210	0.0019	0.3454	0.0056	5.7380	0.1600	3.5	1968	28	1936	24	1913	27
1-70	458.0	137.4	3.33	0.0730	0.0013	0.1505	0.0025	1.4940	0.0420	2.5	1007	37	927	17	904	14
1-71	232.9	266.5	0.87	0.0603	0.0024	0.0916	0.0018	0.7520	0.0340	1.4	605	89	573	21	565	11
1-72	131.1	60.8	2.16	0.0614	0.0020	0.0890	0.0017	0.7470	0.0300	3.2	628	73	568	17	550	10
1-73	38.7	18.0	2.15	0.0655	0.0032	0.1381	0.0030	1.2560	0.0650	-0.8	770	100	826	29	833	17
1-74	142.7	102.0	1.40	0.1208	0.0021	0.3565	0.0059	5.9110	0.1600	-0.4	1966	31	1962	24	1967	27
1-75	545.4	214.8	2.54	0.0615	0.0010	0.1065	0.0017	0.8946	0.0250	-0.6	657	37	649	13	652	10
1-76	107.7	55.1	1.95	0.0697	0.0018	0.1562	0.0028	1.5020	0.0520	-0.6	922	54	930	21	935	16
1-77	35.6	10.5	3.40	0.0651	0.0028	0.1313	0.0027	1.1610	0.0570	-2.2	765	94	778	27	795	16
1-78	236.4	395.4	0.60	0.1236	0.0019	0.3517	0.0057	5.9470	0.1600	4.9	2012	27	1967	24	1943	27
1-79	159.6	212.9	0.75	0.0588	0.0017	0.0950	0.0016	0.7590	0.0280	-2.1	544	66	573	16	585	10

				Measured values and ratios								Apparent Ages					
Batch & Grain no.	U (ppm)	Th (ppm)	U/Th	$^{207}Pb/^{206}Pb$	2σ	$^{206}Pb/^{238}U$	2σ	$^{207}Pb/^{235}U$	2σ	Discordance (%)	$^{207}Pb/^{206}Pb$	2σ	$^{207}Pb/^{235}U$	2σ	$^{206}Pb/^{238}U$	2σ
1-80	687.0	113.7	6.04	0.0729	0.0014	0.1136	0.0026	1.1360	0.0380	9.9	1011	37	769	18	693	15
1-81	135.5	92.5	1.46	0.0728	0.0019	0.1728	0.0030	1.7120	0.0590	-0.2	1013	52	1014	22	1027	16
1-82	105.4	22.3	4.72	0.0733	0.0020	0.1694	0.0030	1.7040	0.0600	-1.4	1001	56	1007	22	1009	16
1-83	249.2	91.2	2.73	0.1372	0.0021	0.4040	0.0067	7.5800	0.2100	-1.1	2192	28	2183	25	2187	31
1-84	119.3	67.0	1.78	0.0662	0.0020	0.1187	0.0020	1.0850	0.0410	3.1	823	61	746	20	723	12
1-85	214.3	433.1	0.49	0.0601	0.0018	0.0951	0.0016	0.7850	0.0290	0.6	607	65	589	17	585	10
1-86	74.6	34.4	2.17	0.0629	0.0028	0.1093	0.0021	0.9460	0.0460	-0.2	641	96	668	23	670	12
1-87	179.3	123.5	1.45	0.1385	0.0024	0.3628	0.0073	6.9500	0.2100	10.6	2205	30	2106	27	1994	34
1-88	134.1	100.5	1.33	0.0737	0.0016	0.1749	0.0031	1.7820	0.0580	0.5	1042	45	1040	22	1039	17
1-89	113.4	98.0	1.16	0.1159	0.0022	0.3434	0.0059	5.4980	0.1600	-1.4	1888	34	1902	25	1903	28
1-90	110.0	113.7	0.97	0.0676	0.0020	0.1306	0.0023	1.2270	0.0450	2.9	843	61	815	20	791	13
1-91	99.9	44.1	2.26	0.0646	0.0024	0.1108	0.0020	0.9830	0.0420	2.3	781	75	693	21	677	11
1-92	272.9	81.4	3.35	0.0600	0.0016	0.0993	0.0017	0.8350	0.0280	0.9	589	57	616	16	610	10
1-93	135.2	49.9	2.71	0.0654	0.0020	0.1244	0.0023	1.1200	0.0420	0.8	791	63	763	20	757	13
1-94	211.9	188.7	1.12	0.0614	0.0017	0.0975	0.0017	0.8320	0.0300	2.1	641	61	613	17	600	10
1-95	34.5	0.6	60.16	0.0819	0.0034	0.2049	0.0044	2.3080	0.1000	1.6	1226	79	1212	33	1203	24
1-96	55.2	23.3	2.37	0.0622	0.0028	0.1151	0.0026	0.9990	0.0500	0.1	657	100	703	26	702	15
1-97	310.0	46.6	6.66	0.1225	0.0020	0.3270	0.0053	5.5480	0.1500	9.2	1992	29	1907	24	1824	26
1-98	230.6	232.9	0.99	0.0598	0.0016	0.0889	0.0015	0.7370	0.0250	1.9	590	63	560	15	549	9
1-99	76.0	84.0	0.90	0.1594	0.0029	0.4571	0.0076	10.1400	0.3000	0.3	2450	30	2448	27	2426	34
1-100	184.9	28.0	6.60	0.0615	0.0017	0.1075	0.0019	0.9210	0.0330	0.6	645	58	662	18	658	11
1-101	157.5	71.6	2.20	0.0633	0.0019	0.0990	0.0018	0.8620	0.0320	3.3	706	68	629	18	609	10
1-102	84.1	63.8	1.32	0.0740	0.0025	0.1677	0.0031	1.7220	0.0650	0.5	1020	67	1015	25	1000	17
1-103	331.2	282.2	1.17	0.2162	0.0032	0.4839	0.0110	14.5400	0.4600	16.2	2954	25	2781	31	2542	47
1-104	54.3	54.1	1.00	0.0618	0.0029	0.0945	0.0020	0.8030	0.0410	2.2	631	100	595	24	582	12
1-105	22.9	27.9	0.82	0.0549	0.0044	0.0965	0.0026	0.7430	0.0570	-7.0	400	160	554	35	593	15
1-106	149.4	87.4	1.71	0.0611	0.0017	0.1116	0.0020	0.9470	0.0330	-1.1	638	62	675	18	682	12
1-107	190.1	169.1	1.12	0.0611	0.0017	0.1052	0.0019	0.8840	0.0300	-0.4	639	57	642	16	645	11
1-108	103.2	72.3	1.43	0.0597	0.0021	0.0946	0.0018	0.7700	0.0330	-0.3	566	79	581	19	583	10
1-109	110.4	86.0	1.28	0.1180	0.0023	0.3267	0.0057	5.3160	0.1600	6.5	1929	35	1869	26	1822	28
1-110	368.0	243.9	1.51	0.0596	0.0014	0.0852	0.0015	0.7000	0.0220	2.0	590	50	538	13	527	9
1-111	128.1	38.8	3.30	0.0629	0.0018	0.1132	0.0020	0.9750	0.0370	-0.2	693	61	690	19	691	12
1-112	124.9	103.0	1.21	0.0599	0.0020	0.1042	0.0020	0.8570	0.0350	-0.3	591	73	637	19	639	12
1-113	177.8	164.7	1.08	0.0733	0.0017	0.1697	0.0030	1.7030	0.0530	0.4	1012	48	1013	19	1010	16
1-114	104.6	102.3	1.02	0.0653	0.0019	0.1216	0.0024	1.0990	0.0430	1.8	772	62	753	21	739	14
1-115	43.2	37.6	1.15	0.0747	0.0032	0.1777	0.0037	1.8470	0.0860	5.9	1025	88	1056	31	1055	20
1-116	118.4	80.9	1.46	0.0611	0.0032	0.0953	0.0020	0.8010	0.0470	1.2	630	120	594	27	587	12
1-117	500.3	203.3	2.46	0.0673	0.0014	0.0966	0.0026	0.8930	0.0300	8.2	836	44	647	16	594	15
1-118	63.2	14.4	4.38	0.0626	0.0030	0.1073	0.0023	0.9320	0.0490	1.8	669	100	669	26	657	13
1-119	167.2	103.8	1.61	0.0732	0.0016	0.1666	0.0029	1.6810	0.0520	1.0	1012	45	1003	19	993	16
1-120	60.6	33.7	1.80	0.0578	0.0031	0.0917	0.0019	0.7290	0.0400	-0.3	500	110	564	22	566	11
1-121	80.7	97.9	0.82	0.0622	0.0026	0.0950	0.0019	0.8210	0.0390	4.2	662	98	611	22	585	11
1-122	186.3	116.9	1.59	0.0772	0.0015	0.1905	0.0032	2.0260	0.0610	0.8	1130	39	1124	21	1124	18
1-123	259.0	75.6	3.43	0.0626	0.0016	0.0993	0.0017	0.8580	0.0290	3.0	686	54	629	16	610	10
1-124	263.2	59.7	4.41	0.0727	0.0015	0.1674	0.0031	1.6890	0.0530	0.4	1003	44	1002	20	998	17
1-125	10.1	16.1	0.62	0.0617	0.0073	0.1033	0.0038	0.8880	0.1000	0.6	570	230	637	57	633	22
1-126	126.3	160.4	0.79	0.0612	0.0020	0.0995	0.0019	0.8410	0.0350	1.2	635	73	619	19	611	11
1-127	43.4	135.3	0.32	0.0749	0.0031	0.1685	0.0033	1.7570	0.0780	7.4	1080	86	1025	29	1003	18
1-128	82.1	67.5	1.22	0.1299	0.0023	0.3753	0.0066	6.6760	0.1900	2.8	2095	32	2068	25	2054	31
1-129	56.8	33.5	1.70	0.0754	0.0023	0.1715	0.0033	1.7780	0.0660	7.4	1088	63	1038	25	1020	18
1-130	102.6	146.3	0.70	0.0638	0.0023	0.1068	0.0021	0.9360	0.0390	1.7	712	69	665	19	654	12
1-131	324.5	128.7	2.52	0.0569	0.0016	0.0715	0.0013	0.5610	0.0200	1.5	494	63	452	13	445	8
1-132	125.0	111.4	1.12	0.0750	0.0019	0.1640	0.0030	1.6710	0.0590	1.8	1082	49	998	22	980	17
1-133	289.0	31.6	9.15	0.0684	0.0037	0.0339	0.0016	0.3120	0.0220	21.7	850	110	274	17	215	10
1-134	344.0	312.0	1.10	0.0587	0.0015	0.0943	0.0016	0.7590	0.0250	-1.5	539	55	572	14	581	10
1-135	239.1	106.5	2.24	0.1721	0.0026	0.4484	0.0072	10.6370	0.2800	9.0	2580	25	2492	25	2388	32
1-136	99.3	61.4	1.62	0.0804	0.0049	0.1079	0.0021	1.2000	0.0840	16.4	1180	120	790	37	661	12
1-137	515.0	326.0	1.58	0.0536	0.0019	0.0488	0.0009	0.3580	0.0150	1.3	340	78	311	11	307	6
1-138	605.7	538.1	1.13	0.0687	0.0011	0.1381	0.0022	1.3030	0.0370	1.5	888	33	846	16	834	12
1-139	123.8	79.3	1.56	0.0765	0.0020	0.1655	0.0028	1.7390	0.0580	3.4	1095	54	1022	22	987	15
1-140	81.9	48.2	1.70	0.1832	0.0032	0.4947	0.0085	12.4500	0.3600	4.2	2679	29	2640	28	2590	37
1-141	116.0	24.6	4.72	0.0601	0.0017	0.1018	0.0019	0.8430	0.0320	-0.9	606	65	619	17	625	11
1-142	438.6	174.8	2.51	0.0608	0.0013	0.0920	0.0015	0.7730	0.0240	2.3	620	45	581	14	567	9
1-143	95.3	206.0	0.46	0.1278	0.0024	0.3765	0.0065	6.6380	0.2000	0.1	2065	33	2062	26	2060	31
1-144	237.0	63.5	3.73	0.0744	0.0017	0.1857	0.0031	1.9050	0.0590	-5.4	1048	44	1083	20	1098	17
2-1	52.7	51.1	1.03	0.0576	0.0033	0.0910	0.0019	0.7100	0.0420	-3.1	470	110	545	25	562	11
2-2	115.4	60.7	1.90	0.1283	0.0026	0.3770	0.0063	6.6980	0.2000	0.5	2077	35	2073	26	2064	29
2-3	106.1	116.7	0.91	0.0591	0.0022	0.0967	0.0018	0.7930	0.0340	-0.7	569	83	591	20	595	11
2-4	142.8	27.4	5.21	0.0726	0.0020	0.1414	0.0026	1.3930	0.0500	3.5	987	57	885	21	854	15
2-5	374.6	81.4	4.60	0.0620	0.0014	0.1010	0.0018	0.8690	0.0280	2.2	683	48	634	15	620	11
2-6	337.0	37.4	9.00	0.0622	0.0019	0.1089	0.0020	0.9300	0.0340	0.7	686	65	671	18	666	11
2-7	90.5	89.9	1.01	0.0610	0.0026	0.1030	0.0020	0.8710	0.0380	0.3	607	87	634	21	632	12
2-8	235.3	126.8	1.86	0.0507	0.0020	0.0368	0.0007	0.2537	0.0110	-1.6	211	79	229	9	233	5
2-9	34.1	17.4	1.96	0.0569	0.0039	0.0944	0.0025	0.7470	0.0530	-2.7	490	140	566	29	581	15
2-10	224.8	393.0	0.57	0.1821	0.0032	0.4311	0.0075	11.0800	0.3100	13.9	2670	29	2529	26	2310	34
2-11	148.2	129.4	1.15	0.0609	0.0020	0.0966	0.0018	0.8190	0.0310	2.4	624	72	609	17	595	10
2-12	154.9	276.0	0.56	0.0780	0.0020	0.1516	0.0041	1.6470	0.0600	8.1	1140	49	989	23	909	23
2-13	79.3	70.9	1.12	0.1840	0.0033	0.4777	0.0081	12.3200	0.3600	5.8	2685	29	2627	27	2517	35
2-14	125.4	56.2	2.23	0.0609	0.0021	0.0943	0.0019	0.7910	0.0310	1.9	606	74	592	17	581	11
2-15	143.1	101.6	1.41	0.0599	0.0021	0.0948	0.0017	0.7890	0.0310	1.3	577	77	591	18	584	10
2-16	148.0	38.4	3.85	0.1805	0.0031	0.4854	0.0084	12.1500	0.3400	4.2	2656	29	2618	26	2550	36
2-17	84.8	26.9	3.15	0.0720	0.0020	0.1583	0.0028	1.6090	0.0580	2.5	978	57	972	23	947	16
2-18	106.1	64.2	1.65	0.0596	0.0021	0.0987	0.0018	0.8220	0.0330	0.2	573	74	608	18	607	11
2-19	105.5	40.7	2.59	0.0609	0.0023	0.1027	0.0019	0.8750	0.0380	0.7	614	82	635	20	630	11

				Measured values and ratios								Apparent Ages					
Batch & Grain no.	U (ppm)	Th (ppm)	U/Th	$^{207}Pb/^{206}Pb$	2σ	$^{206}Pb/^{238}U$	2σ	$^{207}Pb/^{235}U$	2σ	Discordance (%)	$^{207}Pb/^{206}Pb$	2σ	$^{207}Pb/^{235}U$	2σ	$^{206}Pb/^{238}U$	2σ
2-20	327.8	196.3	1.67	0.0621	0.0014	0.0953	0.0016	0.8170	0.0260	3.2	664	49	607	15	587	9
2-21	132.7	97.1	1.37	0.0627	0.0020	0.1084	0.0020	0.9320	0.0350	1.3	702	65	672	19	663	12
2-22	63.8	57.9	1.10	0.0716	0.0026	0.1536	0.0029	1.5080	0.0590	1.2	981	72	932	23	921	16
2-23	134.8	179.7	0.75	0.1762	0.0028	0.4741	0.0077	11.4100	0.3200	6.2	2617	27	2556	26	2503	33
2-24	312.7	218.3	1.43	0.1743	0.0026	0.4628	0.0074	11.0570	0.3000	7.2	2598	25	2529	24	2452	33
2-25	260.4	113.4	2.30	0.0635	0.0016	0.1085	0.0018	0.9450	0.0310	1.8	722	55	676	17	664	11
2-26	82.5	54.4	1.52	0.0751	0.0022	0.1730	0.0033	1.7780	0.0630	1.8	1049	57	1034	23	1029	18
2-27	64.7	63.4	1.02	0.0734	0.0037	0.1619	0.0038	1.6110	0.0850	0.4	1040	100	971	33	967	21
2-28	267.1	714.0	0.37	0.0608	0.0016	0.0776	0.0015	0.6430	0.0220	4.3	621	58	503	14	482	9
2-29	146.9	75.6	1.94	0.1080	0.0020	0.3019	0.0050	4.4580	0.1300	4.7	1763	34	1723	23	1700	25
2-30	37.1	26.0	1.42	0.0612	0.0037	0.0948	0.0021	0.7860	0.0510	-0.2	600	120	583	28	584	13
2-31	253.2	362.0	0.70	0.0737	0.0016	0.1692	0.0028	1.7180	0.0520	2.0	1028	42	1016	19	1008	15
2-32	88.0	42.5	2.07	0.1290	0.0024	0.3709	0.0065	6.5660	0.1900	3.1	2083	33	2054	25	2033	30
2-33	220.7	59.8	3.69	0.1322	0.0022	0.3884	0.0063	7.0720	0.1900	1.2	2131	29	2120	24	2116	29
2-34	252.2	305.1	0.83	0.0594	0.0017	0.0954	0.0017	0.7790	0.0280	-0.1	580	59	587	16	587	10
2-35	164.7	145.6	1.13	0.0733	0.0022	0.1585	0.0030	1.6080	0.0570	2.5	1028	61	972	22	948	17
2-36	258.7	95.7	2.70	0.1723	0.0025	0.4551	0.0077	10.8420	0.3000	7.2	2579	25	2511	26	2418	34
2-37	186.6	108.6	1.72	0.0607	0.0018	0.0780	0.0019	0.6520	0.0260	5.0	626	64	509	15	484	11
2-38	206.0	524.0	0.39	0.1624	0.0025	0.4744	0.0087	10.7000	0.3100	-1.9	2480	26	2496	27	2502	38
2-39	95.8	184.5	0.52	0.0746	0.0023	0.1653	0.0030	1.7030	0.0650	2.0	1049	61	1007	24	987	16
2-40	472.9	248.9	1.90	0.0661	0.0014	0.1331	0.0024	1.2160	0.0380	0.2	806	42	807	17	805	14
2-41	105.2	145.8	0.72	0.0587	0.0022	0.0974	0.0018	0.7870	0.0360	-2.4	525	80	585	21	599	10
2-42	57.4	32.8	1.75	0.0702	0.0023	0.1624	0.0035	1.5700	0.0630	-0.6	960	66	964	26	970	19
2-43	212.0	195.1	1.09	0.0729	0.0015	0.1601	0.0027	1.6060	0.0480	1.5	1014	43	971	19	957	15
2-44	373.8	279.2	1.34	0.0747	0.0016	0.1508	0.0028	1.5330	0.0470	4.1	1057	43	944	19	905	16
2-45	260.0	121.3	2.14	0.0740	0.0016	0.1685	0.0029	1.6980	0.0510	4.7	1039	44	1007	19	1004	16
2-46	99.0	145.9	0.68	0.1782	0.0029	0.4975	0.0083	12.1700	0.3400	1.9	2636	27	2617	27	2603	36
2-47	295.2	135.7	2.18	0.1160	0.0018	0.3222	0.0052	5.1230	0.1400	6.6	1898	28	1840	23	1800	25
2-48	99.3	75.6	1.31	0.0742	0.0026	0.1620	0.0029	1.6320	0.0640	1.5	1029	70	982	24	968	16
2-49	202.0	103.7	1.95	0.0749	0.0025	0.1752	0.0035	1.7840	0.0670	-1.6	1050	68	1038	24	1040	19
2-50	96.9	114.5	0.85	0.0596	0.0023	0.1014	0.0019	0.8380	0.0360	-0.1	605	81	622	20	622	11
2-51	196.0	141.9	1.38	0.0601	0.0016	0.0965	0.0017	0.7920	0.0270	-0.5	608	59	591	15	594	10
2-52	262.6	141.0	1.86	0.0723	0.0015	0.1247	0.0023	1.2430	0.0380	7.7	998	44	821	17	758	13
2-53	169.5	96.1	1.76	0.0641	0.0019	0.1068	0.0018	0.9410	0.0330	2.5	725	64	671	18	654	11
2-54	324.4	258.0	1.26	0.0748	0.0015	0.1765	0.0029	1.8080	0.0540	2.2	1063	40	1048	20	1048	16
2-55	154.3	146.3	1.05	0.0654	0.0019	0.1250	0.0023	1.1360	0.0400	1.7	785	60	773	18	760	13
2-56	116.3	66.1	1.76	0.0608	0.0023	0.1005	0.0018	0.8360	0.0360	-0.6	610	83	614	20	618	11
2-57	213.6	97.4	2.19	0.0666	0.0017	0.1129	0.0022	1.0310	0.0360	3.8	811	55	717	18	690	12
2-58	53.0	10.9	4.86	0.0930	0.0024	0.2601	0.0048	3.3390	0.1100	-0.4	1487	50	1488	27	1490	25
2-59	79.1	95.5	0.83	0.0713	0.0023	0.1696	0.0031	1.6670	0.0630	-4.1	971	66	1002	24	1010	17
2-60	200.2	119.3	1.68	0.1232	0.0020	0.3699	0.0061	6.2650	0.1700	-1.0	2005	28	2013	25	2029	29
2-61	230.7	274.5	0.84	0.1781	0.0027	0.4834	0.0082	11.9200	0.3300	4.0	2636	25	2598	26	2543	35
2-62	115.1	51.6	2.23	0.0613	0.0020	0.0962	0.0021	0.8050	0.0320	0.9	678	68	597	18	592	12
2-63	147.6	24.3	6.07	0.1667	0.0028	0.4150	0.0075	9.5800	0.2800	12.9	2523	29	2394	27	2240	35
2-64	301.7	264.5	1.14	0.0629	0.0033	0.0918	0.0033	0.7830	0.0510	3.1	670	110	584	28	566	19
2-65	344.9	66.3	5.20	0.0615	0.0014	0.1105	0.0018	0.9340	0.0290	-0.9	657	48	670	15	676	10
2-66	283.5	146.7	1.93	0.0644	0.0013	0.1195	0.0020	1.0520	0.0320	0.2	747	43	729	16	728	11
2-67	516.1	159.6	3.23	0.0606	0.0014	0.0955	0.0017	0.7870	0.0250	0.3	630	50	590	15	588	10
2-68	131.9	75.8	1.74	0.1834	0.0030	0.4638	0.0081	11.6000	0.3400	11.1	2683	26	2573	26	2456	36
2-69	239.1	126.2	1.89	0.1210	0.0019	0.3454	0.0056	5.7380	0.1600	3.5	1968	28	1936	24	1913	27
2-70	458.0	137.4	3.33	0.0730	0.0013	0.1505	0.0025	1.4940	0.0420	2.5	1007	37	927	17	904	14
2-71	232.9	266.5	0.87	0.0603	0.0024	0.0916	0.0018	0.7520	0.0340	1.4	605	89	573	21	565	11
2-72	131.1	60.8	2.16	0.0614	0.0020	0.0890	0.0017	0.7470	0.0300	3.2	628	73	568	17	550	10
2-73	38.7	18.0	2.15	0.0655	0.0032	0.1381	0.0030	1.2560	0.0650	-0.8	770	100	826	29	833	17
2-74	142.7	102.0	1.40	0.1208	0.0021	0.3565	0.0059	5.9110	0.1600	-0.4	1966	31	1962	24	1967	27
2-75	545.4	214.8	2.54	0.0615	0.0010	0.1065	0.0017	0.8946	0.0250	-0.6	657	37	649	13	652	10
2-76	107.7	55.1	1.95	0.0697	0.0018	0.1562	0.0028	1.5020	0.0520	-0.6	922	54	930	21	935	16
2-77	35.6	10.5	3.40	0.0651	0.0028	0.1313	0.0027	1.1610	0.0570	-2.2	765	94	778	27	795	16
2-78	236.4	395.4	0.60	0.1236	0.0019	0.3517	0.0057	5.9470	0.1600	4.9	2012	27	1967	24	1943	27
2-79	159.6	212.9	0.75	0.0588	0.0017	0.0950	0.0016	0.7590	0.0280	-2.1	544	66	573	16	585	10
2-80	687.0	113.7	6.04	0.0729	0.0014	0.1136	0.0026	1.1360	0.0380	9.9	1011	37	769	18	693	15
2-81	135.5	92.5	1.46	0.0728	0.0019	0.1728	0.0030	1.7120	0.0590	-0.2	1013	52	1014	22	1027	16
2-82	105.4	22.3	4.72	0.0733	0.0020	0.1694	0.0030	1.7040	0.0600	-1.4	1001	56	1007	22	1009	16
2-83	249.2	91.2	2.73	0.1372	0.0021	0.4040	0.0067	7.5800	0.2100	-1.1	2192	28	2183	25	2187	31
2-84	119.3	67.0	1.78	0.0662	0.0020	0.1187	0.0020	1.0850	0.0410	3.1	823	61	746	20	723	12
2-85	214.3	433.1	0.49	0.0601	0.0018	0.0951	0.0016	0.7850	0.0290	0.6	607	65	589	17	585	10
2-86	74.6	34.4	2.17	0.0629	0.0028	0.1093	0.0021	0.9460	0.0460	-0.2	641	96	668	23	670	12
2-87	179.3	123.5	1.45	0.1385	0.0024	0.3628	0.0073	6.9500	0.2100	10.6	2205	30	2106	27	1994	34
2-88	134.1	100.5	1.33	0.0737	0.0016	0.1749	0.0031	1.7820	0.0580	0.5	1042	45	1040	22	1039	17
2-89	113.4	98.0	1.16	0.1159	0.0022	0.3434	0.0059	5.4980	0.1600	-1.4	1888	34	1902	25	1903	28
2-90	110.0	113.7	0.97	0.0676	0.0020	0.1306	0.0023	1.2270	0.0450	2.9	843	61	815	20	791	13
2-91	99.9	44.1	2.26	0.0646	0.0024	0.1108	0.0020	0.9830	0.0420	2.3	781	75	693	21	677	11
2-92	272.9	81.4	3.35	0.0600	0.0016	0.0993	0.0017	0.8350	0.0280	0.9	589	57	616	16	610	10
2-93	135.2	49.9	2.71	0.0654	0.0020	0.1244	0.0023	1.1200	0.0420	0.8	791	63	763	20	757	13
2-94	211.9	188.7	1.12	0.0614	0.0017	0.0975	0.0017	0.8320	0.0300	2.1	641	61	613	17	600	10
2-95	34.5	0.6	60.16	0.0819	0.0034	0.2049	0.0044	2.3080	0.1000	1.6	1226	79	1212	33	1203	24
2-96	55.2	23.3	2.37	0.0622	0.0028	0.1151	0.0026	0.9990	0.0500	0.1	657	100	703	26	702	15
2-97	310.0	46.6	6.66	0.1225	0.0020	0.3270	0.0053	5.5480	0.1500	9.2	1992	29	1907	24	1824	26
2-98	230.6	232.9	0.99	0.0598	0.0016	0.0889	0.0015	0.7370	0.0250	1.9	590	63	560	15	549	9
2-99	76.0	84.0	0.90	0.1594	0.0029	0.4571	0.0076	10.1400	0.3000	0.3	2450	30	2448	27	2426	34
2-100	184.9	28.0	6.60	0.0615	0.0017	0.1075	0.0019	0.9210	0.0330	0.6	645	58	662	18	658	11
2-101	157.5	71.6	2.20	0.0633	0.0019	0.0990	0.0018	0.8620	0.0320	3.3	706	68	629	18	609	10
2-102	84.1	63.8	1.32	0.0740	0.0025	0.1677	0.0031	1.7220	0.0650	0.5	1020	67	1015	25	1000	17
2-103	331.2	282.2	1.17	0.2162	0.0032	0.4839	0.0110	14.5400	0.4600	16.2	2954	25	2781	31	2542	47

				Measured values and ratios								Apparent Ages					
Batch & Grain no.	U (ppm)	Th (ppm)	U/Th	$^{207}Pb/^{206}Pb$	2σ	$^{206}Pb/^{238}U$	2σ	$^{207}Pb/^{235}U$	2σ	Discordance (%)	$^{207}Pb/^{206}Pb$	2σ	$^{207}Pb/^{235}U$	2σ	$^{206}Pb/^{238}U$	2σ
2-104	54.3	54.1	1.00	0.0618	0.0029	0.0945	0.0020	0.8030	0.0410	2.2	631	100	595	24	582	12
2-105	22.9	27.9	0.82	0.0549	0.0044	0.0965	0.0026	0.7430	0.0570	-7.0	400	160	554	35	593	15
2-106	149.4	87.4	1.71	0.0611	0.0017	0.1116	0.0020	0.9470	0.0330	-1.1	638	62	675	18	682	12
2-107	190.1	169.1	1.12	0.0611	0.0017	0.1052	0.0019	0.8840	0.0300	-0.4	639	57	642	16	645	11
2-108	103.2	72.3	1.43	0.0597	0.0021	0.0946	0.0018	0.7700	0.0330	-0.3	566	79	581	19	583	10
2-109	110.4	86.0	1.28	0.1180	0.0023	0.3267	0.0057	5.3160	0.1600	6.5	1929	35	1869	26	1822	28
2-110	368.0	243.9	1.51	0.0596	0.0014	0.0852	0.0015	0.7000	0.0220	2.0	590	50	538	13	527	9
2-111	128.1	38.8	3.30	0.0629	0.0018	0.1132	0.0020	0.9750	0.0370	-0.2	693	61	690	19	691	12
2-112	124.9	103.0	1.21	0.0599	0.0020	0.1042	0.0020	0.8570	0.0350	-0.3	591	73	637	19	639	12
2-113	177.8	164.7	1.08	0.0733	0.0017	0.1697	0.0030	1.7030	0.0530	0.4	1012	48	1013	19	1010	16
2-114	104.6	102.3	1.02	0.0653	0.0019	0.1216	0.0024	1.0990	0.0430	1.8	772	62	753	21	739	14
2-115	43.2	37.6	1.15	0.0747	0.0032	0.1777	0.0037	1.8470	0.0860	5.9	1025	88	1056	31	1055	20
2-116	118.4	80.9	1.46	0.0611	0.0032	0.0953	0.0020	0.8010	0.0470	1.2	630	120	594	27	587	12
2-117	500.3	203.3	2.46	0.0673	0.0014	0.0966	0.0026	0.8930	0.0300	8.2	836	44	647	16	594	15
2-118	63.2	14.4	4.38	0.0626	0.0030	0.1073	0.0023	0.9320	0.0490	1.8	669	100	669	26	657	13
2-119	167.2	103.8	1.61	0.0732	0.0016	0.1666	0.0029	1.6810	0.0520	1.0	1012	45	1003	19	993	16
2-120	60.6	33.7	1.80	0.0578	0.0031	0.0917	0.0019	0.7290	0.0400	-0.3	500	110	564	22	566	11
2-121	80.7	97.9	0.82	0.0622	0.0026	0.0950	0.0019	0.8210	0.0390	4.2	662	98	611	22	585	11
2-122	186.3	116.9	1.59	0.0772	0.0015	0.1905	0.0032	2.0260	0.0610	0.8	1130	39	1124	21	1124	18
2-123	259.0	75.6	3.43	0.0626	0.0016	0.0993	0.0017	0.8580	0.0290	3.0	686	54	629	16	610	10
2-124	263.2	59.7	4.41	0.0727	0.0015	0.1674	0.0031	1.6890	0.0530	0.4	1003	44	1002	20	998	17
2-125	10.1	16.1	0.62	0.0617	0.0073	0.1033	0.0038	0.8880	0.1000	0.6	570	230	637	57	633	22
2-126	126.3	160.4	0.79	0.0612	0.0020	0.0995	0.0019	0.8410	0.0350	1.2	635	73	619	19	611	11
2-127	43.4	135.3	0.32	0.0749	0.0031	0.1685	0.0033	1.7570	0.0780	7.4	1080	86	1025	29	1003	18
2-128	82.1	67.5	1.22	0.1299	0.0023	0.3753	0.0066	6.6760	0.1900	2.8	2095	32	2068	25	2054	31
2-129	56.8	33.5	1.70	0.0754	0.0023	0.1715	0.0033	1.7780	0.0660	7.4	1088	63	1038	25	1020	18
2-130	102.6	146.3	0.70	0.0638	0.0023	0.1068	0.0021	0.9360	0.0390	1.7	712	69	665	19	654	12
2-131	324.5	128.7	2.52	0.0569	0.0016	0.0715	0.0013	0.5610	0.0200	1.5	494	63	452	13	445	8
2-132	125.0	111.4	1.12	0.0750	0.0019	0.1640	0.0030	1.6710	0.0590	1.8	1082	49	998	22	980	17
2-133	289.0	31.6	9.15	0.0684	0.0037	0.0339	0.0016	0.3120	0.0220	21.7	850	110	274	17	215	10
2-134	344.0	312.0	1.10	0.0587	0.0015	0.0943	0.0016	0.7590	0.0250	-1.5	539	55	572	14	581	10
2-135	239.1	106.5	2.24	0.1721	0.0026	0.4484	0.0072	10.6370	0.2800	9.0	2580	25	2492	25	2388	32
2-136	99.3	61.4	1.62	0.0804	0.0049	0.1079	0.0021	1.2000	0.0840	16.4	1180	120	790	37	661	12
2-137	515.0	326.0	1.58	0.0536	0.0019	0.0488	0.0009	0.3580	0.0150	1.3	340	78	311	11	307	6
2-138	605.7	538.1	1.13	0.0687	0.0011	0.1381	0.0022	1.3030	0.0370	1.5	888	33	846	16	834	12
2-139	123.8	79.3	1.56	0.0765	0.0020	0.1655	0.0028	1.7390	0.0580	3.4	1095	54	1022	22	987	15
2-140	81.9	48.2	1.70	0.1832	0.0032	0.4947	0.0085	12.4500	0.3600	4.2	2679	29	2640	28	2590	37
2-141	116.0	24.6	4.72	0.0601	0.0017	0.1018	0.0019	0.8430	0.0320	-0.9	606	65	619	17	625	11
2-142	438.6	174.8	2.51	0.0608	0.0013	0.0920	0.0015	0.7730	0.0240	2.3	620	45	581	14	567	9
2-143	95.3	206.0	0.46	0.1278	0.0024	0.3765	0.0065	6.6380	0.2000	0.1	2065	33	2062	26	2060	31
2-144	237.0	63.5	3.73	0.0744	0.0017	0.1857	0.0031	1.9050	0.0590	-5.4	1048	44	1083	20	1098	17
18MC005B1																
1-1	125.8	81.1	1.55	0.0722	0.0030	0.1631	0.0031	1.6230	0.0710	2.5	995	83	975	28	974	17
1-2	167.1	65.9	2.54	0.0755	0.0017	0.1607	0.0023	1.6820	0.0460	9.7	1068	46	1004	17	960	13
1-3	106.9	84.6	1.26	0.0699	0.0043	0.0976	0.0021	0.9610	0.0620	12.3	900	130	684	31	600	12
1-4	84.5	76.1	1.11	0.0650	0.0030	0.0953	0.0021	0.8590	0.0440	6.4	771	95	626	24	586	12
1-5	151.0	54.4	2.78	0.0400	0.0560	0.0803	0.0059	0.7500	0.6300	44.2	2270	410	890	280	497	35
1-6	53.6	102.3	0.52	0.2470	0.0310	0.1214	0.0068	4.3100	0.7400	54.8	3070	200	1630	140	737	39
1-7	175.1	155.1	1.13	0.0738	0.0017	0.1711	0.0026	1.7360	0.0510	1.7	1033	44	1023	19	1018	15
1-8	309.7	66.8	4.64	0.1642	0.0015	0.4170	0.0053	9.4400	0.1700	11.6	2496	16	2381	16	2247	24
1-9	69.1	55.6	1.24	0.0730	0.0033	0.1198	0.0025	1.2170	0.0560	10.1	1005	93	811	26	729	14
1-10	284.0	159.6	1.78	0.1781	0.0018	0.5087	0.0077	12.6300	0.2600	2.0	2634	17	2656	19	2651	33
1-11	138.0	53.8	2.57	0.0656	0.0025	0.1067	0.0017	0.9720	0.0370	5.4	801	77	692	19	654	10
1-12	135.1	94.8	1.43	0.0705	0.0024	0.1351	0.0024	1.3360	0.0500	13.0	945	71	864	22	817	13
1-13	472.5	498.0	0.95	0.0601	0.0017	0.0774	0.0011	0.6490	0.0200	5.4	608	61	508	12	481	7
1-14	8.5	1.0	8.55	0.1580	0.0330	0.1113	0.0069	2.5200	0.6200	36.0	1740	430	1060	160	678	40
1-15	335.8	210.6	1.59	0.1227	0.0018	0.3607	0.0053	6.1500	0.1300	0.1	1997	26	1996	19	1985	25
1-16	412.0	354.9	1.16	0.0606	0.0016	0.0944	0.0014	0.7900	0.0250	1.5	626	58	590	14	581	8
1-17	83.3	119.1	0.70	0.0621	0.0034	0.0946	0.0021	0.8310	0.0480	4.4	680	120	611	26	584	13
1-18	220.9	258.2	0.86	0.0657	0.0028	0.1230	0.0021	1.1150	0.0480	1.3	758	89	757	23	748	12
1-19	102.0	107.8	0.95	0.1137	0.0027	0.2816	0.0046	4.5200	0.1300	13.8	1860	43	1732	24	1601	23
1-20	773.0	807.0	0.96	0.0682	0.0018	0.0782	0.0013	0.7270	0.0190	12.4	876	53	554	11	485	8
1-21	81.2	40.5	2.00	0.0663	0.0036	0.0934	0.0018	0.8620	0.0470	9.4	830	120	635	25	576	11
1-22	194.5	227.0	0.86	0.1254	0.0017	0.3554	0.0046	6.1720	0.1200	3.8	2034	23	2001	16	1960	22
1-23	1960.0	962.0	2.04	0.0579	0.0017	0.0215	0.0020	0.1730	0.0150	14.4	508	61	160	13	137	13
1-24	161.9	160.1	1.01	0.0610	0.0019	0.0970	0.0015	0.8130	0.0270	1.4	619	68	605	15	597	9
1-25	478.4	189.4	2.53	0.0608	0.0014	0.0944	0.0012	0.7930	0.0210	1.9	625	48	593	12	582	7
1-26	160.1	116.0	1.38	0.0688	0.0024	0.1188	0.0018	1.1350	0.0430	6.6	879	75	775	19	724	10
1-27	97.9	123.4	0.79	0.1796	0.0027	0.4863	0.0069	11.9700	0.2400	5.2	2652	25	2601	19	2554	30
1-28	171.9	106.0	1.62	0.1134	0.0021	0.3195	0.0045	4.9620	0.1100	5.5	1861	35	1811	19	1787	22
1-29	68.6	28.9	2.37	0.1970	0.0038	0.4963	0.0098	13.3100	0.3700	11.1	2813	34	2700	26	2596	42
1-30	42.2	34.5	1.22	0.0771	0.0042	0.1586	0.0037	1.6720	0.0940	10.5	1070	110	996	35	948	20
1-31	124.1	80.2	1.55	0.0629	0.0028	0.1009	0.0019	0.8890	0.0400	4.0	679	92	645	22	620	11
1-32	51.3	44.0	1.17	0.0683	0.0052	0.0947	0.0024	0.8860	0.0690	9.6	830	160	645	38	583	14
1-33	1239.0	433.0	2.86	0.0564	0.0015	0.0307	0.0014	0.2380	0.0110	9.7	449	58	216	9	195	9
1-34	449.6	23.3	19.27	0.0630	0.0012	0.1074	0.0014	0.9430	0.0230	2.4	705	43	674	12	657	8
1-35	42.8	29.0	1.48	0.0629	0.0063	0.1070	0.0035	0.9570	0.0900	3.7	740	200	680	46	655	20
1-36	26.9	92.2	0.29	0.0781	0.0069	0.1545	0.0044	1.7000	0.1500	15.6	1120	180	1010	57	926	25
1-37	156.8	81.7	1.92	0.1898	0.0019	0.5301	0.0068	13.8700	0.2400	0.1	2740	16	2742	17	2741	29
1-38	199.8	245.4	0.81	0.0649	0.0024	0.0979	0.0015	0.8910	0.0350	7.1	771	83	648	19	602	9
1-39	89.8	46.7	1.92	0.0665	0.0041	0.1059	0.0024	0.9840	0.0620	5.7	780	140	689	32	650	14
1-40	200.1	146.4	1.37	0.0638	0.0021	0.1040	0.0015	0.9130	0.0320	3.1	705	72	658	17	638	9
1-41	741.0	292.0	2.54	0.1912	0.0051	0.3044	0.0077	8.1400	0.3700	41.8	2748	40	2220	40	1710	38
1-42	193.8	273.1	0.71	0.1836	0.0018	0.4894	0.0064	12.4300	0.2200	4.8	2684	16	2636	17	2567	28

				Measured values and ratios								Apparent Ages					
Batch & Grain no.	U (ppm)	Th (ppm)	U/Th	$^{207}Pb/^{206}Pb$	2σ	$^{206}Pb/^{238}U$	2σ	$^{207}Pb/^{235}U$	2σ	Discordance (%)	$^{207}Pb/^{206}Pb$	2σ	$^{207}Pb/^{235}U$	2σ	$^{206}Pb/^{238}U$	2σ
1-43	498.6	337.5	1.48	0.2586	0.0016	0.3969	0.0049	14.2900	0.2300	38.6	3238	10	2769	15	2155	23
1-44	1225.0	796.0	1.54	0.0598	0.0009	0.0865	0.0011	0.7220	0.0160	3.0	591	33	552	10	535	7
1-45	224.0	161.0	1.39	0.0672	0.0019	0.1161	0.0017	1.0760	0.0340	4.2	826	59	739	17	708	10
1-46	158.6	146.9	1.08	0.0627	0.0028	0.0950	0.0018	0.8400	0.0430	6.1	690	100	623	24	585	11
1-47	111.0	116.7	0.95	0.0603	0.0033	0.0963	0.0020	0.8010	0.0450	0.5	620	110	596	26	593	12
1-48	84.5	181.6	0.47	0.0753	0.0029	0.1653	0.0032	1.7220	0.0710	6.2	1058	77	1015	26	986	18
1-49	113.7	94.8	1.20	0.0604	0.0045	0.0995	0.0022	0.8380	0.0660	0.0	570	160	611	37	611	13
1-50	358.2	115.2	3.11	0.1235	0.0011	0.2881	0.0045	4.9420	0.0940	20.6	2008	16	1811	16	1632	22
1-51	558.4	132.6	4.21	0.0686	0.0014	0.1320	0.0017	1.2560	0.0320	8.9	880	41	825	14	799	10
1-52	130.7	117.2	1.12	0.0758	0.0019	0.1784	0.0028	1.8490	0.0530	4.3	1092	49	1064	18	1058	15
1-53	162.4	113.7	1.43	0.1751	0.0018	0.4136	0.0053	9.9800	0.1900	16.8	2604	17	2433	17	2231	24
1-54	175.3	44.4	3.95	0.0754	0.0028	0.1837	0.0029	1.9160	0.0770	-3.6	1063	76	1086	27	1087	16
1-55	85.7	88.7	0.97	0.1211	0.0024	0.3653	0.0054	6.0800	0.1500	-1.4	1975	35	1989	22	2009	25
1-56	478.0	437.0	1.09	0.0648	0.0019	0.0631	0.0022	0.5640	0.0210	13.0	748	63	453	14	394	13
1-57	227.9	74.7	3.05	0.0630	0.0017	0.1114	0.0016	0.9830	0.0300	1.8	707	58	693	15	681	9
1-58	96.0	36.6	2.62	0.1804	0.0050	0.2639	0.0045	6.5800	0.2200	47.3	2641	46	2049	29	1509	23
1-59	92.1	38.4	2.40	0.0736	0.0027	0.1703	0.0029	1.7170	0.0650	0.3	1017	74	1019	24	1013	16
1-60	27.0	22.6	1.20	0.0728	0.0073	0.0934	0.0034	0.9530	0.0950	12.3	920	210	656	51	575	20
1-61	161.5	154.8	1.04	0.1238	0.0016	0.3642	0.0050	6.2120	0.1200	0.3	2009	23	2005	17	2003	24
1-62	245.6	129.6	1.90	0.0955	0.0012	0.2690	0.0034	3.5510	0.0680	0.7	1533	24	1538	15	1536	18
1-63	94.0	49.1	1.92	0.0560	0.0044	0.0547	0.0014	0.4160	0.0330	2.5	370	150	352	24	343	8
1-64	638.0	386.0	1.65	0.0734	0.0011	0.1529	0.0020	1.5600	0.0300	10.4	1024	30	955	12	917	11
1-65	41.0	47.0	0.87	0.0724	0.0044	0.1620	0.0037	1.6040	0.0940	-7.0	930	130	964	37	967	20
1-66	185.7	179.3	1.04	0.0617	0.0022	0.0955	0.0016	0.8310	0.0290	4.3	651	76	614	16	588	9
1-67	128.4	171.4	0.75	0.0608	0.0038	0.0960	0.0018	0.8030	0.0480	0.6	600	120	594	27	591	11
1-68	163.4	210.8	0.78	0.0629	0.0034	0.0977	0.0017	0.8550	0.0430	3.9	680	120	625	24	601	10
1-69	211.7	136.4	1.55	0.0513	0.0028	0.0412	0.0008	0.2940	0.0170	-0.5	250	110	259	13	260	5
1-70	381.8	156.5	2.44	0.0787	0.0014	0.1919	0.0024	2.0910	0.0500	3.0	1167	34	1144	16	1132	13
1-71	354.6	116.7	3.04	0.0584	0.0015	0.0872	0.0013	0.7060	0.0220	0.4	553	55	541	13	539	8
1-72	478.8	180.6	2.65	0.0621	0.0014	0.0982	0.0013	0.8340	0.0220	2.0	677	47	616	12	604	8
1-73	233.6	219.6	1.06	0.1272	0.0017	0.3729	0.0048	6.4790	0.1300	-1.3	2055	24	2042	17	2043	22
1-74	99.3	49.7	2.00	0.0682	0.0029	0.1307	0.0021	1.2600	0.0510	10.0	889	84	828	23	792	12
1-75	128.1	87.3	1.47	0.1766	0.0018	0.4841	0.0064	11.7500	0.2100	3.7	2620	17	2583	17	2548	27
1-76	291.3	176.6	1.65	0.0783	0.0028	0.0997	0.0016	1.0630	0.0400	16.8	1135	74	736	19	612	9
1-77	176.7	139.0	1.27	0.0554	0.0046	0.0367	0.0008	0.2760	0.0210	5.1	330	160	245	17	232	5
1-78	214.0	123.4	1.73	0.0613	0.0019	0.1114	0.0018	0.9530	0.0320	-0.3	632	67	679	17	681	10
1-79	122.2	75.2	1.63	0.1229	0.0020	0.3478	0.0048	5.9150	0.1300	3.9	1998	29	1961	19	1924	23
1-80	283.4	115.2	2.46	0.1333	0.0020	0.3813	0.0047	6.9600	0.1400	3.5	2138	26	2106	18	2082	22
1-81	309.7	107.6	2.88	0.0609	0.0016	0.0937	0.0013	0.7900	0.0230	2.3	643	60	591	14	577	8
1-82	89.4	89.0	1.00	0.0647	0.0032	0.0990	0.0018	0.9010	0.0440	5.9	740	100	647	24	609	10
1-83	175.6	163.0	1.08	0.0944	0.0054	0.0978	0.0016	1.2780	0.0760	27.5	1470	100	830	32	602	9
1-84	558.8	198.4	2.82	0.0758	0.0009	0.1752	0.0021	1.8330	0.0340	4.8	1090	25	1059	12	1040	11
1-85	282.0	63.3	4.45	0.0765	0.0021	0.1640	0.0034	1.6870	0.0550	13.8	1101	58	1008	21	979	19
1-86	76.4	73.8	1.03	0.0601	0.0037	0.0895	0.0019	0.7480	0.0460	1.6	550	130	562	26	553	11
1-87	278.1	444.0	0.63	0.0608	0.0021	0.0874	0.0015	0.7460	0.0290	4.7	639	75	567	17	540	9
1-88	209.9	115.2	1.82	0.0761	0.0019	0.1706	0.0024	1.7980	0.0530	5.4	1081	50	1046	19	1015	13
1-89	777.9	44.8	17.36	0.0616	0.0010	0.0983	0.0012	0.8370	0.0180	2.1	671	36	617	10	604	7
1-90	103.9	52.2	1.99	0.0682	0.0034	0.1137	0.0019	1.0560	0.0530	5.2	820	100	732	26	694	11
1-91	544.0	336.0	1.62	0.0638	0.0017	0.0761	0.0012	0.6680	0.0190	9.4	744	54	522	12	473	7
1-92	147.8	130.7	1.13	0.0880	0.0056	0.0988	0.0023	1.1810	0.0790	22.9	1350	120	787	36	607	13
1-93	282.0	135.0	2.09	0.0760	0.0014	0.1699	0.0023	1.7790	0.0450	8.0	1093	36	1040	17	1011	13
1-94	244.0	181.4	1.35	0.0840	0.0050	0.0389	0.0008	0.4530	0.0280	35.5	1270	120	381	20	246	5
1-95	134.3	102.8	1.31	0.0597	0.0025	0.0980	0.0017	0.8040	0.0350	-0.3	585	91	601	19	603	10
1-96	361.7	318.9	1.13	0.0611	0.0016	0.0929	0.0012	0.7880	0.0250	3.4	641	59	593	14	573	7
1-97	83.6	57.5	1.45	0.1190	0.0021	0.3525	0.0056	5.8300	0.1400	0.7	1957	32	1955	22	1950	27
1-98	381.1	409.6	0.93	0.1152	0.0012	0.3264	0.0041	5.2140	0.0920	2.9	1880	18	1854	15	1821	20
1-99	128.4	175.3	0.73	0.1302	0.0023	0.3703	0.0051	6.6100	0.1400	4.5	2101	31	2062	18	2030	24
1-100	576.0	262.0	2.20	0.0647	0.0011	0.1159	0.0014	1.0400	0.0230	2.3	764	36	724	12	707	8
1-101	359.8	203.4	1.77	0.0670	0.0017	0.0837	0.0013	0.7720	0.0240	10.6	833	50	579	14	518	8
1-102	353.0	52.1	6.78	0.0636	0.0016	0.1136	0.0018	0.9890	0.0300	0.6	729	53	698	16	694	10
1-103	227.1	151.8	1.50	0.0682	0.0021	0.0997	0.0016	0.9440	0.0310	9.1	899	66	674	16	613	10
1-104	155.8	104.3	1.49	0.0770	0.0022	0.1666	0.0024	1.7450	0.0560	10.8	1101	57	1026	21	993	13
1-105	95.3	44.8	2.13	0.0733	0.0024	0.1577	0.0028	1.6000	0.0580	7.7	1021	71	971	24	944	16
1-106	1674.7	148.5	11.28	0.0610	0.0007	0.0983	0.0011	0.8286	0.0150	1.4	639	26	613	8	604	7
1-107	282.2	476.0	0.59	0.0617	0.0018	0.0897	0.0013	0.7720	0.0260	4.8	651	66	582	15	554	8
1-108	117.3	66.2	1.77	0.1178	0.0069	0.1558	0.0033	2.5200	0.1300	52.1	1862	97	1257	35	933	18
1-109	439.0	500.0	0.88	0.0618	0.0013	0.1010	0.0013	0.8730	0.0220	2.7	679	43	637	12	620	8
1-110	164.5	136.1	1.21	0.0687	0.0022	0.1146	0.0019	1.1000	0.0340	6.9	903	66	751	16	700	11
1-111	235.3	64.9	3.63	0.0760	0.0016	0.1680	0.0023	1.7750	0.0460	9.3	1101	42	1034	17	1001	13
1-112	276.9	388.0	0.71	0.0607	0.0022	0.0932	0.0016	0.7810	0.0290	1.7	637	79	584	16	574	10
1-113	248.3	256.4	0.97	0.0619	0.0027	0.0938	0.0016	0.8130	0.0380	4.3	668	94	604	21	578	10
1-114	92.0	87.0	1.06	0.0745	0.0029	0.1525	0.0026	1.5750	0.0590	12.0	1042	75	961	23	915	15
1-115	110.3	176.1	0.63	0.0634	0.0025	0.0963	0.0016	0.8490	0.0370	4.7	710	87	622	20	593	10
1-116	580.0	420.0	1.38	0.0632	0.0013	0.0859	0.0016	0.7590	0.0180	7.2	711	45	573	10	531	10
1-117	496.6	432.8	1.15	0.0629	0.0011	0.0944	0.0013	0.8230	0.0190	4.8	696	39	611	10	581	8
1-118	85.7	170.0	0.50	0.0595	0.0055	0.0918	0.0030	0.7640	0.0740	0.7	620	190	570	42	566	18
1-119	104.8	100.7	1.04	0.0794	0.0031	0.1652	0.0027	1.8150	0.0700	16.4	1172	78	1048	25	985	15
1-120	148.5	80.3	1.85	0.0711	0.0025	0.1559	0.0031	1.5210	0.0580	1.8	950	71	939	23	936	17
2-1	408.0	93.1	4.38	0.0601	0.0011	0.0925	0.0012	0.7600	0.0230	0.7	603	40	574	13	570	7
2-2	269.7	69.4	3.89	0.0665	0.0013	0.1329	0.0018	1.2090	0.0370	-0.1	812	40	804	17	804	10
2-3	391.7	286.4	1.37	0.1683	0.0020	0.4370	0.0055	10.0740	0.2700	10.0	2540	20	2442	24	2337	25
2-4	62.6	44.3	1.41	0.0608	0.0026	0.0983	0.0019	0.8280	0.0390	1.7	629	91	615	21	605	11
2-5	407.0	108.0	3.77	0.0735	0.0014	0.1185	0.0015	1.1900	0.0350	9.3	1030	37	796	16	722	9
2-6	149.4	130.2	1.15	0.0572	0.0020	0.0810	0.0012	0.6290	0.0250	-1.6	483	73	494	16	502	7

				Measured values and ratios								Apparent Ages				
Batch & Grain no.	U (ppm)	Th (ppm)	U/Th	$^{207}Pb/^{206}Pb$	2σ	$^{206}Pb/^{238}U$	2σ	$^{207}Pb/^{235}U$	2σ	Discordance (%)	$^{207}Pb/^{206}Pb$	2σ	$^{207}Pb/^{235}U$	2σ	$^{206}Pb/^{238}U$	2σ
2-7	134.7	144.9	0.93	0.1606	0.0023	0.4411	0.0056	9.7300	0.2700	5.3	2460	24	2409	25	2355	25
2-8	163.7	123.8	1.32	0.0614	0.0021	0.0923	0.0014	0.7790	0.0310	2.5	629	73	583	18	569	8
2-9	108.1	106.1	1.02	0.1083	0.0019	0.3131	0.0041	4.6640	0.1400	1.3	1772	31	1760	24	1756	20
2-10	73.3	50.3	1.46	0.0671	0.0023	0.1182	0.0024	1.0810	0.0480	2.6	829	72	739	23	720	14
2-11	176.0	60.3	2.92	0.0626	0.0016	0.1068	0.0015	0.9170	0.0310	1.5	689	57	664	17	654	9
2-12	307.0	401.0	0.77	0.0615	0.0014	0.0879	0.0013	0.7380	0.0250	3.4	642	49	562	14	543	8
2-13	94.9	86.1	1.10	0.0604	0.0024	0.0959	0.0015	0.7990	0.0370	1.0	576	87	596	21	590	9
2-14	152.9	48.7	3.14	0.0719	0.0021	0.1324	0.0026	1.2900	0.0500	4.8	987	65	842	23	802	15
2-15	95.2	38.2	2.50	0.0591	0.0024	0.0935	0.0016	0.7670	0.0360	-0.1	562	87	576	20	576	9
2-16	86.1	67.6	1.27	0.0646	0.0022	0.1181	0.0018	1.0520	0.0430	1.1	785	74	728	22	720	10
2-17	59.1	45.9	1.29	0.0588	0.0027	0.0943	0.0018	0.7720	0.0390	0.3	570	100	582	22	581	11
2-18	480.0	166.9	2.88	0.0618	0.0013	0.1024	0.0013	0.8730	0.0270	1.9	670	44	640	15	628	8
2-19	354.7	226.4	1.57	0.1765	0.0022	0.4296	0.0057	10.4890	0.2900	14.0	2619	20	2478	25	2305	26
2-20	33.2	45.1	0.74	0.1722	0.0035	0.4686	0.0079	11.1400	0.3500	4.1	2574	34	2530	31	2476	35
2-21	110.0	131.0	0.84	0.0658	0.0021	0.0938	0.0016	0.8530	0.0340	7.5	819	69	625	18	578	9
2-22	510.5	306.0	1.67	0.0577	0.0012	0.0850	0.0011	0.6790	0.0210	-0.1	534	44	525	13	526	6
2-23	204.0	170.0	1.20	0.1757	0.0023	0.4626	0.0063	11.2100	0.3100	7.3	2612	22	2541	26	2451	28
2-24	221.5	162.3	1.36	0.0504	0.0023	0.0362	0.0006	0.2519	0.0120	-0.6	211	91	228	10	230	4
2-25	324.5	222.1	1.46	0.1474	0.0020	0.3526	0.0059	7.1800	0.2200	18.3	2316	24	2132	27	1946	28
2-26	560.4	76.8	7.30	0.0678	0.0013	0.1185	0.0015	1.1180	0.0340	5.2	862	41	761	17	722	9
2-27	192.4	200.0	0.96	0.0590	0.0017	0.0968	0.0014	0.7820	0.0290	-0.9	566	59	590	17	596	8
2-28	232.0	334.0	0.69	0.0600	0.0015	0.0966	0.0014	0.8050	0.0260	0.7	597	52	599	15	594	8
2-29	72.3	54.4	1.33	0.0572	0.0021	0.0955	0.0016	0.7650	0.0340	-2.2	483	84	577	19	590	9
2-30	469.3	401.0	1.17	0.0713	0.0019	0.1217	0.0019	1.1950	0.0410	7.5	957	53	800	20	740	11
2-31	75.3	39.0	1.93	0.0611	0.0024	0.0983	0.0016	0.8380	0.0400	2.3	655	85	619	22	605	9
2-32	113.6	72.3	1.57	0.0602	0.0020	0.0899	0.0014	0.7490	0.0300	1.8	594	71	565	17	555	8
2-33	137.3	93.0	1.48	0.0749	0.0019	0.1799	0.0026	1.8640	0.0650	2.5	1052	50	1067	23	1066	14
2-34	345.2	206.0	1.68	0.0591	0.0015	0.0945	0.0012	0.7750	0.0260	0.0	562	54	582	15	582	7
2-35	402.0	81.0	4.96	0.0648	0.0022	0.1017	0.0015	0.9030	0.0350	4.3	757	70	653	19	625	9
2-36	95.4	94.3	1.01	0.0608	0.0024	0.0893	0.0015	0.7400	0.0350	2.3	607	85	564	19	551	9
2-37	211.6	61.1	3.46	0.0672	0.0016	0.1339	0.0020	1.2170	0.0410	-0.1	845	49	809	18	810	12
2-38	247.3	142.4	1.74	0.0700	0.0015	0.1398	0.0018	1.3410	0.0410	2.3	925	42	864	18	843	10
2-39	177.9	98.5	1.81	0.0694	0.0015	0.1501	0.0021	1.4220	0.0440	0.0	907	44	901	18	901	12
2-40	210.3	87.5	2.40	0.0631	0.0015	0.1050	0.0015	0.9160	0.0310	2.5	710	53	660	17	644	9
2-41	267.2	148.0	1.81	0.0601	0.0014	0.0992	0.0013	0.8240	0.0270	0.0	611	52	610	15	610	8
2-42	97.4	48.2	2.02	0.1893	0.0034	0.5280	0.0110	13.7700	0.4200	0.0	2734	30	2732	29	2732	44
2-43	95.2	83.8	1.14	0.0810	0.0230	0.0961	0.0020	1.1000	0.3200	2.3	660	100	605	18	591	12
2-44	164.2	45.1	3.64	0.0768	0.0015	0.1819	0.0023	1.9090	0.0580	4.5	1115	40	1084	20	1077	13
2-45	673.0	408.0	1.65	0.0665	0.0011	0.0910	0.0016	0.8260	0.0260	8.2	827	36	611	15	561	10
2-46	216.5	152.9	1.42	0.0513	0.0019	0.0368	0.0006	0.2566	0.0110	-0.8	234	75	231	9	233	4
2-47	203.9	47.1	4.33	0.0633	0.0017	0.1021	0.0015	0.8780	0.0300	2.3	709	57	641	16	626	9
2-48	520.0	231.9	2.24	0.0629	0.0081	0.1518	0.0032	1.3200	0.2800	-8.5	890	190	840	120	911	18
2-49	92.2	36.9	2.50	0.0637	0.0021	0.1188	0.0019	1.0230	0.0430	-0.9	732	69	717	22	723	11
2-50	145.3	90.8	1.60	0.0719	0.0017	0.1576	0.0022	1.5370	0.0520	0.0	992	47	944	21	944	12
2-51	229.0	181.1	1.26	0.0764	0.0015	0.1709	0.0023	1.7940	0.0550	8.1	1099	39	1045	19	1017	13
2-52	163.3	312.0	0.52	0.0601	0.0019	0.0938	0.0015	0.7670	0.0300	-0.2	589	71	577	17	578	9
2-53	189.8	177.2	1.07	0.1157	0.0018	0.3314	0.0042	5.2810	0.1500	3.2	1894	29	1865	24	1845	20
2-54	94.9	76.8	1.24	0.2900	0.1700	0.0760	0.0190	1.4000	1.3000	63.2	3210	300	1170	240	430	66
2-55	167.5	137.5	1.22	0.0634	0.0045	0.1028	0.0021	0.9060	0.0640	3.1	606	96	646	26	626	8
2-56	135.3	46.7	2.89	0.1730	0.0032	0.2207	0.0059	5.2800	0.2200	55.5	2593	29	1862	36	1285	31
2-57	525.1	307.9	1.71	0.1736	0.0021	0.4626	0.0057	10.9690	0.2900	7.4	2593	20	2522	26	2451	25
2-58	302.0	111.2	2.72	0.0600	0.0016	0.0898	0.0014	0.7310	0.0260	0.3	597	62	556	15	554	8
2-59	83.8	117.1	0.72	0.0721	0.0021	0.1651	0.0024	1.6320	0.0600	-0.2	983	58	983	24	985	13
2-61	121.5	169.0	0.72	0.0600	0.0020	0.0851	0.0013	0.6950	0.0290	2.2	580	74	538	18	526	8
2-62	187.3	3.6	52.03	0.1155	0.0017	0.3197	0.0042	5.0550	0.1400	6.5	1886	27	1829	24	1788	20
2-63	187.9	97.8	1.92	0.0893	0.0016	0.2336	0.0029	2.8650	0.0840	4.2	1405	34	1373	22	1353	15
2-64	335.0	201.8	1.66	0.0727	0.0027	0.0545	0.0008	0.5450	0.0230	22.5	1004	79	441	16	342	5
2-65	240.4	197.4	1.22	0.0593	0.0013	0.0934	0.0013	0.7560	0.0240	-0.5	562	49	573	14	576	8
2-66	192.0	96.3	1.99	0.0514	0.0033	0.0378	0.0008	0.2640	0.0180	0.9	250	120	241	14	239	5
2-67	99.9	69.2	1.44	0.0629	0.0037	0.0951	0.0020	0.8200	0.0480	3.1	690	110	604	27	585	12
2-68	101.1	37.0	2.73	0.0707	0.0018	0.1619	0.0023	1.5820	0.0540	-0.6	933	54	962	21	967	13
2-69	230.9	141.0	1.64	0.1192	0.0019	0.2982	0.0051	4.8800	0.1500	15.4	1942	29	1797	26	1682	25
2-70	98.8	74.3	1.33	0.0740	0.0018	0.1675	0.0024	1.7100	0.0570	1.2	1038	52	1010	22	998	13
2-71	203.1	45.9	4.42	0.0585	0.0017	0.0906	0.0013	0.7270	0.0270	-1.1	531	66	553	16	559	7
2-72	292.1	138.8	2.10	0.0650	0.0012	0.1247	0.0016	1.1160	0.0340	0.7	770	40	763	16	758	9
2-73	282.1	58.0	4.86	0.0658	0.0018	0.1121	0.0018	1.0220	0.0390	4.1	790	58	714	19	685	10
2-74	57.4	40.0	1.44	0.0635	0.0031	0.0917	0.0017	0.7900	0.0410	3.8	660	100	588	23	565	10
2-75	83.3	119.6	0.70	0.0632	0.0025	0.0923	0.0017	0.8070	0.0380	4.7	688	88	597	21	569	10
2-76	223.6	88.6	2.52	0.1195	0.0017	0.3489	0.0043	5.7860	0.1600	0.7	1950	26	1943	24	1929	21
2-77	66.8	14.8	4.51	0.0656	0.0025	0.1195	0.0019	1.0780	0.0480	1.9	789	82	742	24	728	11
2-78	64.7	42.9	1.51	-0.3000	0.2200	0.0800	0.0120	-0.9100	1.3100	42.7	3160	270	860	490	493	73
2-79	230.4	70.6	3.26	0.1329	0.0021	0.3478	0.0066	6.4400	0.2000	10.8	2139	27	2036	28	1923	31
2-80	342.4	175.8	1.95	0.0743	0.0014	0.1427	0.0020	1.4660	0.0450	6.1	1045	38	916	19	860	11
2-81	168.7	156.5	1.08	0.0597	0.0018	0.0914	0.0019	0.7540	0.0310	0.8	578	65	568	18	564	11
2-82	400.0	180.7	2.21	0.1136	0.0015	0.2908	0.0047	4.5600	0.1300	12.7	1856	24	1743	25	1645	23
2-83	204.0	144.9	1.41	0.0630	0.0019	0.0638	0.0019	0.5420	0.0260	8.9	702	66	437	17	398	12
2-84	148.7	156.6	0.95	0.0651	0.0033	0.0764	0.0016	0.6840	0.0410	9.8	730	100	526	25	475	10
2-85	269.2	268.6	1.00	0.0610	0.0013	0.0985	0.0013	0.8280	0.0260	1.1	634	47	612	15	605	8
2-86	129.5	133.6	0.97	0.0590	0.0020	0.0930	0.0014	0.7560	0.0320	0.1	550	77	574	18	573	8
2-87	162.8	84.8	1.92	0.1328	0.0025	0.3935	0.0053	7.2100	0.2200	-0.6	2132	32	2136	27	2141	25
2-88	127.1	249.5	0.51	0.0641	0.0025	0.0921	0.0015	0.8050	0.0340	5.2	716	78	599	19	568	9
2-89	56.2	52.8	1.06	0.0607	0.0026	0.1035	0.0019	0.8700	0.0440	0.8	631	96	640	24	635	11
2-90	52.5	43.4	1.21	0.0566	0.0028	0.0945	0.0018	0.7410	0.0360	-3.0	470	100	565	21	582	11
2-91	266.7	186.6	1.43	0.0606	0.0016	0.0648	0.0011	0.5440	0.0190	8.2	625	60	441	13	405	7

Batch & Grain no.	U (ppm)	Th (ppm)	U/Th	Measured values and ratios							Apparent Ages					
				$^{207}Pb/^{206}Pb$	2σ	$^{206}Pb/^{238}U$	2σ	$^{207}Pb/^{235}U$	2σ	Discordance (%)	$^{207}Pb/^{206}Pb$	2σ	$^{207}Pb/^{235}U$	2σ	$^{206}Pb/^{238}U$	2σ
2-92	157.1	106.0	1.48	0.0717	0.0017	0.1360	0.0019	1.3420	0.0460	5.1	988	50	866	20	822	11
2-93	237.7	109.6	2.17	0.0749	0.0013	0.1695	0.0021	1.7380	0.0510	5.4	1059	36	1022	19	1010	12
2-94	209.1	91.9	2.28	0.0687	0.0017	0.1386	0.0019	1.3020	0.0430	1.0	898	51	845	19	837	11
2-95	134.7	249.0	0.54	0.0649	0.0019	0.1155	0.0017	1.0230	0.0380	1.6	761	63	716	19	704	10
2-96	215.6	235.4	0.92	0.0603	0.0015	0.0945	0.0013	0.7780	0.0270	0.3	613	52	584	16	582	8
2-97	589.0	16.1	36.63	0.0982	0.0016	0.2507	0.0041	3.3700	0.1000	10.9	1589	30	1497	24	1442	21
2-98	160.3	42.9	3.74	0.1191	0.0019	0.3302	0.0044	5.3970	0.1500	6.4	1941	28	1884	24	1840	21
2-99	218.0	51.7	4.22	0.0611	0.0016	0.1007	0.0014	0.8410	0.0290	0.6	643	54	622	15	618	8
2-100	123.8	62.2	1.99	0.0633	0.0021	0.1007	0.0018	0.8780	0.0350	3.2	729	73	639	19	618	10
2-101	323.0	212.4	1.52	0.0694	0.0014	0.1234	0.0023	1.1640	0.0400	4.6	909	41	786	19	750	13
2-102	194.0	70.6	2.75	0.0762	0.0018	0.1449	0.0024	1.5260	0.0560	7.3	1091	47	941	22	872	13
2-103	104.1	95.0	1.10	0.0608	0.0020	0.0945	0.0014	0.7880	0.0300	1.6	616	71	592	17	582	9
2-104	175.7	50.1	3.51	0.0690	0.0016	0.1325	0.0019	1.2620	0.0440	2.8	889	49	826	20	803	11
2-105	101.8	46.9	2.17	0.0672	0.0020	0.1268	0.0020	1.1640	0.0450	2.0	844	61	786	20	770	11
2-106	147.6	125.6	1.18	0.1197	0.0018	0.2955	0.0051	4.8730	0.1500	16.3	1950	28	1797	25	1668	26
2-107	691.0	296.0	2.33	0.0661	0.0084	0.1290	0.0029	1.1700	0.2300	-2.0	970	210	767	110	782	17
2-108	443.0	199.9	2.22	0.0597	0.0013	0.0973	0.0013	0.7950	0.0240	-0.7	584	46	594	14	598	7
2-110	1719.0	361.0	4.76	0.1452	0.0027	0.2136	0.0062	4.2800	0.1800	49.7	2287	32	1679	36	1246	33
2-111	164.5	27.7	5.94	0.1783	0.0024	0.4776	0.0063	11.5800	0.3200	6.8	2637	22	2571	26	2516	28
2-112	146.3	77.0	1.90	0.1150	0.0019	0.3131	0.0042	4.9090	0.1400	8.3	1877	30	1805	24	1757	21
2-113	119.5	30.8	3.88	0.0624	0.0016	0.1169	0.0017	0.9910	0.0350	-1.9	674	56	699	18	713	10
2-114	145.5	94.4	1.54	0.0536	0.0032	0.0370	0.0007	0.2740	0.0170	3.9	350	120	244	14	235	5
2-115	62.5	31.0	2.02	0.0751	0.0024	0.1761	0.0029	1.8160	0.0670	3.8	1077	64	1053	24	1045	16
2-116	220.7	554.9	0.40	0.0599	0.0016	0.0940	0.0013	0.7660	0.0250	-0.3	600	58	577	14	579	8
2-117	119.1	62.2	1.91	0.0613	0.0023	0.0959	0.0014	0.7990	0.0330	0.7	632	78	594	19	590	8
2-118	401.0	458.0	0.88	0.0581	0.0013	0.0833	0.0013	0.6590	0.0220	-0.4	524	48	513	13	516	8
2-119	195.7	209.0	0.94	0.0610	0.0018	0.0956	0.0014	0.7920	0.0290	0.3	635	64	590	16	589	8
2-120	455.5	190.8	2.39	0.0625	0.0012	0.1056	0.0014	0.9070	0.0280	1.1	699	40	655	15	647	8
2-121	240.7	184.0	1.31	0.0747	0.0016	0.1791	0.0026	1.8380	0.0630	-1.6	1049	42	1056	22	1062	14
2-122	99.7	34.6	2.88	0.0726	0.0020	0.1589	0.0026	1.5570	0.0570	0.5	996	54	957	23	952	14
2-123	139.3	133.2	1.05	0.0613	0.0021	0.0962	0.0014	0.8060	0.0330	0.8	658	69	597	18	592	8
2-124	142.0	79.3	1.79	0.1756	0.0025	0.4668	0.0068	11.1900	0.3200	7.2	2609	24	2537	27	2469	30
2-125	56.1	43.3	1.30	0.0574	0.0029	0.0995	0.0017	0.7770	0.0430	-5.4	490	110	580	24	611	10
2-126	81.2	166.9	0.49	0.0784	0.0020	0.1955	0.0028	2.0960	0.0710	-0.4	1150	47	1145	23	1151	15
2-127	1052.0	221.6	4.75	0.0583	0.0009	0.0823	0.0010	0.6585	0.0180	0.7	541	36	514	11	510	6
2-128	109.0	87.8	1.24	0.0759	0.0037	0.1377	0.0048	1.4220	0.0770	7.0	1079	95	894	32	831	27
2-129	41.3	55.8	0.74	0.1262	0.0029	0.3671	0.0057	6.3300	0.2100	1.2	2033	42	2019	29	2015	27
2-130	116.2	76.0	1.53	0.0640	0.0020	0.1100	0.0017	0.9690	0.0380	1.9	721	66	687	19	674	10
2-131	348.7	176.2	1.98	0.0667	0.0013	0.1338	0.0017	1.2280	0.0370	0.3	824	41	812	17	810	10
2-132	447.0	53.2	8.40	0.0762	0.0011	0.1721	0.0024	1.7940	0.0520	7.8	1097	30	1043	18	1024	13
2-133	99.2	53.9	1.84	0.0756	0.0022	0.1699	0.0027	1.7760	0.0690	5.0	1070	62	1038	24	1012	14
2-134	1130.0	235.0	4.81	0.0616	0.0010	0.0720	0.0011	0.6112	0.0180	7.3	661	36	484	12	448	7
2-135	140.0	86.6	1.62	0.0725	0.0016	0.1691	0.0023	1.6950	0.0530	-0.4	1009	43	1006	20	1007	13
2-136	85.2	33.8	2.52	0.0646	0.0023	0.1162	0.0021	1.0170	0.0410	0.4	741	73	711	20	709	12
2-137	130.0	121.6	1.07	0.0596	0.0020	0.0957	0.0014	0.7940	0.0320	0.6	588	71	593	18	589	8
2-139	178.5	127.7	1.40	0.0603	0.0017	0.0937	0.0013	0.7890	0.0280	2.2	605	63	590	16	577	8
2-140	247.2	105.5	2.34	0.0789	0.0014	0.1860	0.0027	2.0240	0.0620	7.6	1178	33	1124	21	1100	15
2-141	140.7	138.3	1.02	0.0929	0.0025	0.1659	0.0033	2.1130	0.0910	14.2	1486	49	1154	30	990	18
2-142	162.7	113.4	1.43	0.1077	0.0019	0.2544	0.0035	3.7680	0.1100	19.2	1761	33	1587	24	1461	18
2-143	501.0	612.0	0.82	0.0735	0.0012	0.1581	0.0021	1.5930	0.0460	2.1	1028	33	967	18	946	12
2-144	180.9	26.5	6.82	0.0890	0.0015	0.2355	0.0032	2.9020	0.0840	2.9	1405	33	1384	21	1363	17
18MC089A1																
1-1	190.4	352.9	0.54	0.0674	0.0021	0.0935	0.0020	0.8630	0.0320	8.6	843	67	630	17	576	12
1-2	506.6	355.2	1.43	0.1187	0.0012	0.3120	0.0059	5.1120	0.1100	10.6	1934	18	1838	18	1750	29
1-3	80.2	64.5	1.24	0.0634	0.0042	0.0968	0.0026	0.8370	0.0540	3.2	640	140	616	31	596	15
1-4	350.4	11.6	30.18	0.0635	0.0015	0.1037	0.0020	0.9110	0.0270	3.0	717	50	656	14	636	11
1-5	408.1	275.4	1.48	0.0604	0.0016	0.0933	0.0017	0.7820	0.0240	1.7	615	59	585	14	575	10
1-6	159.3	82.2	1.94	0.0739	0.0021	0.1698	0.0033	1.7220	0.0530	4.3	1045	57	1014	20	1011	18
1-7	252.9	260.2	0.97	0.1202	0.0018	0.3494	0.0065	5.7980	0.1300	1.2	1957	26	1946	19	1931	31
1-8	682.0	1011.0	0.67	0.0613	0.0013	0.0824	0.0020	0.6860	0.0210	3.7	640	45	530	13	511	12
1-9	74.4	66.2	1.12	0.1243	0.0027	0.3667	0.0069	6.2600	0.1700	-0.2	2015	38	2009	24	2013	33
1-10	112.2	88.4	1.27	0.1281	0.0021	0.3770	0.0075	6.6800	0.1700	0.2	2072	31	2070	22	2061	35
1-11	101.2	7.3	13.92	0.0665	0.0029	0.1330	0.0029	1.1980	0.0510	-3.0	817	92	804	24	805	17
1-12	61.1	45.3	1.35	0.0598	0.0045	0.0948	0.0030	0.8000	0.0670	1.7	570	160	593	37	583	17
1-13	345.4	408.0	0.85	0.0607	0.0012	0.1061	0.0020	0.9000	0.0230	0.3	636	45	652	12	650	12
1-14	118.7	58.9	2.02	0.0749	0.0030	0.1638	0.0032	1.6870	0.0700	10.0	1072	76	1002	27	978	18
1-15	283.7	50.5	5.62	0.0585	0.0016	0.0834	0.0017	0.6720	0.0210	0.7	521	62	520	13	516	10
1-16	133.9	83.4	1.61	0.0694	0.0025	0.1370	0.0028	1.3220	0.0510	6.2	893	74	851	22	830	16
1-17	117.1	2.0	57.97	0.0669	0.0029	0.0968	0.0021	0.8940	0.0390	7.6	818	90	644	21	595	13
1-18	299.0	85.0	3.52	0.0662	0.0019	0.0809	0.0018	0.7410	0.0250	10.9	798	60	563	14	502	11
1-19	237.2	165.9	1.43	0.0812	0.0030	0.0877	0.0021	0.9740	0.0390	21.5	1212	68	690	19	542	12
1-20	1468.0	902.0	1.63	0.1458	0.0013	0.1762	0.0039	3.5730	0.0920	58.4	2296	15	1541	20	1046	21
1-21	36.1	62.8	0.58	0.0648	0.0065	0.0914	0.0030	0.8300	0.0850	7.6	720	190	609	44	563	17
1-22	145.0	235.2	0.62	0.0599	0.0028	0.0949	0.0020	0.7920	0.0370	1.0	604	94	590	21	584	12
1-23	113.9	73.7	1.55	0.0610	0.0054	0.0358	0.0010	0.2960	0.0260	14.6	540	180	265	21	226	6
1-24	20.8	0.2	137.62	0.0701	0.0091	0.0975	0.0041	0.9100	0.1100	10.6	800	250	670	61	599	24
1-25	462.0	382.7	1.21	0.0622	0.0015	0.0982	0.0018	0.8580	0.0230	4.3	693	53	631	13	604	11
1-26	575.6	76.5	7.52	0.0604	0.0014	0.0932	0.0017	0.7810	0.0220	1.8	608	49	585	12	574	10
1-27	185.3	307.7	0.60	0.0734	0.0021	0.1639	0.0032	1.6680	0.0520	3.0	1016	59	994	20	978	18
1-28	468.3	285.6	1.64	0.0699	0.0013	0.1386	0.0026	1.3470	0.0350	9.1	923	37	866	15	837	15
1-29	749.0	305.0	2.46	0.0529	0.0019	0.0375	0.0007	0.2742	0.0100	3.3	318	78	246	8	238	5
1-30	131.0	131.7	0.99	0.0778	0.0025	0.1709	0.0033	1.8290	0.0680	9.8	1125	64	1053	24	1018	18
1-31	165.2	245.3	0.67	0.0779	0.0022	0.1665	0.0033	1.7890	0.0580	13.2	1136	54	1037	21	992	18
1-32	159.3	95.9	1.66	0.0601	0.0028	0.0901	0.0020	0.7490	0.0370	1.9	558	99	567	21	556	12

				Measured values and ratios								Apparent Ages					
Batch & Grain no.	U (ppm)	Th (ppm)	U/Th	$^{207}Pb/^{206}Pb$	2σ	$^{206}Pb/^{238}U$	2σ	$^{207}Pb/^{235}U$	2σ	Discordance (%)	$^{207}Pb/^{206}Pb$	2σ	$^{207}Pb/^{235}U$	2σ	$^{206}Pb/^{238}U$	2σ
1-33	178.6	31.8	5.62	0.0649	0.0026	0.1101	0.0023	0.9670	0.0440	2.3	757	84	689	23	673	14
1-34	101.1	114.0	0.89	0.0723	0.0035	0.1055	0.0026	1.0310	0.0520	11.1	974	98	727	25	646	15
1-35	760.0	116.9	6.50	0.1775	0.0014	0.4146	0.0074	10.1270	0.1900	17.8	2629	13	2446	17	2236	34
1-36	179.8	63.5	2.83	0.1300	0.0020	0.3598	0.0067	6.4990	0.1500	5.9	2099	27	2045	20	1981	32
1-37	176.5	100.6	1.75	0.0612	0.0025	0.0930	0.0021	0.7800	0.0330	1.7	632	91	583	19	573	12
1-38	46.4	28.3	1.64	0.0684	0.0057	0.0906	0.0029	0.8570	0.0710	10.1	810	170	622	39	559	17
1-39	173.3	170.5	1.02	0.0642	0.0022	0.0984	0.0020	0.8670	0.0330	4.1	772	72	631	18	605	12
1-40	858.0	122.2	7.02	0.0603	0.0010	0.1009	0.0018	0.8390	0.0200	0.0	606	37	620	11	620	10
1-41	193.8	126.7	1.53	0.0749	0.0018	0.1702	0.0032	1.7530	0.0500	4.9	1061	47	1028	19	1013	18
1-42	52.7	67.4	0.78	0.0602	0.0047	0.0968	0.0030	0.8180	0.0640	1.5	600	160	604	36	595	17
1-43	166.2	135.2	1.23	0.0605	0.0026	0.0935	0.0021	0.7760	0.0340	1.0	580	92	582	20	576	12
1-44	451.4	859.0	0.53	0.0683	0.0019	0.0887	0.0016	0.8330	0.0250	11.0	866	59	615	14	548	10
1-45	133.6	132.9	1.01	0.0625	0.0028	0.0975	0.0021	0.8440	0.0380	2.7	651	100	617	21	601	13
1-46	18.3	17.7	1.03	0.2494	0.0066	0.5620	0.0170	19.6300	0.6500	12.5	3203	43	3068	33	2877	69
1-47	76.4	38.0	2.01	0.0647	0.0041	0.1108	0.0028	1.0100	0.0610	4.1	750	140	706	32	677	16
1-48	266.9	192.6	1.39	0.0616	0.0017	0.0967	0.0018	0.8230	0.0260	2.3	680	58	609	14	595	11
1-49	471.4	77.2	6.11	0.1150	0.0011	0.3213	0.0056	5.1160	0.0980	4.7	1880	18	1838	16	1796	27
1-50	446.4	159.2	2.80	0.0622	0.0020	0.0447	0.0010	0.3860	0.0160	14.6	668	66	330	11	282	6
1-51	576.9	141.4	4.08	0.0730	0.0011	0.1673	0.0029	1.6940	0.0370	1.8	1018	30	1005	14	997	16
1-52	552.0	35.3	15.63	0.0626	0.0013	0.1143	0.0021	0.9840	0.0250	-0.2	681	44	696	13	698	12
1-53	110.9	240.0	0.46	0.0637	0.0037	0.0939	0.0023	0.8070	0.0510	6.1	720	130	616	29	579	13
1-54	542.8	90.6	5.99	0.0680	0.0012	0.1293	0.0024	1.2050	0.0290	10.2	864	36	803	13	784	14
1-55	890.7	467.5	1.91	0.0610	0.0011	0.0963	0.0017	0.8090	0.0190	1.9	638	39	604	10	593	10
1-56	1284.0	785.0	1.64	0.0600	0.0120	0.0479	0.0029	0.3600	0.0960	8.2	1610	210	330	73	303	18
1-57	43.4	29.5	1.47	0.0710	0.0040	0.1496	0.0040	1.4980	0.0910	1.6	920	120	920	36	902	21
1-58	84.7	52.3	1.62	0.1344	0.0028	0.3850	0.0080	7.2300	0.2000	2.0	2158	35	2137	25	2101	38
1-59	132.4	68.8	1.92	0.0627	0.0038	0.0890	0.0020	0.7740	0.0480	4.4	610	130	575	28	550	12
1-60	143.3	87.6	1.64	0.0634	0.0041	0.0400	0.0010	0.3590	0.0240	18.8	670	140	311	18	253	6
1-61	96.7	77.3	1.25	0.0642	0.0037	0.0959	0.0021	0.8450	0.0490	5.1	710	120	622	27	590	13
1-62	62.3	43.4	1.43	0.0742	0.0048	0.0913	0.0026	0.9420	0.0620	15.7	970	130	668	32	563	15
1-63	433.0	224.9	1.93	0.0743	0.0014	0.1567	0.0029	1.6170	0.0390	11.1	1052	37	977	15	938	16
1-64	201.6	164.0	1.23	0.1179	0.0020	0.3305	0.0060	5.4060	0.1200	4.5	1925	31	1886	19	1841	29
1-65	384.8	524.8	0.73	0.0660	0.0019	0.0809	0.0017	0.7370	0.0270	10.3	796	61	559	16	502	10
1-66	41.4	24.8	1.67	0.0743	0.0052	0.1050	0.0033	1.1060	0.0800	14.8	1030	150	755	38	643	19
1-67	106.3	92.7	1.15	0.1670	0.0190	0.1157	0.0054	2.9900	0.5000	44.1	2350	200	1260	110	704	31
1-68	1.0	0.1	16.70	0.2900	0.1800	0.1400	0.0260	4.9000	1.8000	1313.2	300	1900	2130	200	830	140
1-69	196.9	162.1	1.21	0.0742	0.0025	0.1687	0.0033	1.6920	0.0660	8.9	1066	64	1020	26	1005	18
1-70	106.9	76.5	1.40	0.0680	0.0028	0.1239	0.0026	1.1540	0.0520	13.1	858	86	778	24	753	15
1-71	60.9	80.1	0.76	0.0641	0.0042	0.0968	0.0027	0.8500	0.0540	4.5	690	140	623	31	595	16
1-72	243.8	164.9	1.48	0.0674	0.0022	0.1253	0.0025	1.1490	0.0410	9.3	831	69	778	19	761	14
1-73	276.6	190.7	1.45	0.0635	0.0019	0.0973	0.0019	0.8480	0.0300	4.1	714	67	624	17	599	11
1-74	34.2	19.1	1.79	0.0653	0.0072	0.1088	0.0035	1.0000	0.1100	4.3	750	220	698	56	668	21
1-75	249.5	217.7	1.15	0.0623	0.0021	0.1027	0.0020	0.8840	0.0320	2.3	698	71	645	17	630	12
1-76	527.9	570.4	0.93	0.0610	0.0016	0.0956	0.0018	0.8000	0.0250	1.6	634	56	598	14	589	11
1-77	285.9	238.5	1.20	0.0577	0.0020	0.0822	0.0016	0.6530	0.0250	0.1	513	80	510	15	509	10
1-78	8.6	9.6	0.89	0.3070	0.0380	0.2560	0.0260	12.6000	2.7000	55.0	3420	220	2430	210	1450	130
1-79	208.4	339.5	0.61	0.0851	0.0040	0.1030	0.0023	1.1980	0.0620	20.6	1268	90	796	27	632	13
1-80	278.3	194.1	1.43	0.0661	0.0019	0.1260	0.0024	1.1550	0.0380	4.9	807	59	777	18	765	14
1-81	773.1	280.2	2.76	0.0790	0.0011	0.1649	0.0029	1.8160	0.0390	16.1	1170	27	1050	14	984	16
1-82	1002.1	593.0	1.69	0.1623	0.0012	0.4222	0.0075	9.4380	0.1800	10.0	2479	12	2382	17	2270	34
1-83	187.1	158.8	1.18	0.0749	0.0019	0.1437	0.0028	1.5090	0.0480	19.6	1073	51	933	20	865	16
1-84	60.4	38.5	1.57	0.0771	0.0041	0.1381	0.0033	1.4770	0.0840	24.0	1096	97	918	33	834	19
1-85	195.7	53.9	3.63	0.1165	0.0018	0.3079	0.0055	4.9770	0.1100	10.1	1906	28	1815	18	1730	27
1-86	633.2	11.9	53.25	0.0629	0.0014	0.0931	0.0017	0.8110	0.0220	4.8	710	47	603	12	574	10
1-87	580.7	12.8	45.44	0.0632	0.0014	0.0982	0.0018	0.8600	0.0240	4.5	719	49	632	13	604	11
1-88	268.3	180.0	1.49	0.1289	0.0015	0.3524	0.0062	6.3030	0.1300	7.1	2084	21	2018	18	1946	30
1-89	188.2	170.5	1.10	0.1238	0.0016	0.3442	0.0063	5.8740	0.1300	5.8	2009	23	1962	19	1908	30
1-90	76.5	41.6	1.84	0.0645	0.0041	0.0802	0.0020	0.7120	0.0460	8.6	750	140	544	27	497	12
1-91	186.4	83.5	2.23	0.0623	0.0029	0.0940	0.0021	0.7950	0.0350	3.5	669	93	600	21	579	12
1-92	57.4	121.5	0.47	0.0694	0.0056	0.0900	0.0026	0.8660	0.0750	10.9	790	160	623	39	555	15
1-93	469.6	20.0	23.48	0.0668	0.0018	0.0981	0.0022	0.9020	0.0260	7.6	837	59	653	14	603	13
1-94	175.7	243.0	0.72	0.0608	0.0027	0.0919	0.0023	0.7670	0.0360	2.1	597	94	579	20	567	14
1-95	44.1	42.7	1.03	0.0717	0.0054	0.1247	0.0034	1.2070	0.0870	14.0	890	150	803	39	757	20
1-96	419.9	142.3	2.95	0.0657	0.0013	0.1143	0.0021	1.0370	0.0260	3.5	793	41	723	13	698	12
1-97	34.1	16.0	2.13	0.0754	0.0072	0.1123	0.0039	1.1500	0.1000	11.4	930	180	774	48	686	23
1-98	526.0	273.4	1.92	0.2062	0.0018	0.4907	0.0092	13.9400	0.2700	12.7	2875	14	2745	18	2573	40
1-99	654.6	523.4	1.25	0.0625	0.0016	0.0693	0.0015	0.5880	0.0190	8.1	690	54	470	12	432	9
1-100	137.3	94.1	1.46	0.0784	0.0021	0.1670	0.0036	1.8020	0.0610	13.5	1143	52	1042	22	997	20
1-101	375.0	232.0	1.62	0.0580	0.0016	0.0843	0.0016	0.6750	0.0230	0.0	512	62	522	14	522	9
1-102	145.7	79.0	1.84	0.0760	0.0021	0.1727	0.0033	1.8020	0.0570	5.9	1086	56	1047	21	1027	18
1-103	285.0	125.8	2.27	0.0608	0.0018	0.0979	0.0018	0.8090	0.0280	0.3	618	64	604	16	602	11
1-104	451.3	152.0	2.97	0.0750	0.0013	0.1602	0.0029	1.6490	0.0390	10.4	1060	36	989	15	959	16
1-105	192.4	177.9	1.08	0.1228	0.0019	0.3503	0.0064	5.8870	0.1300	4.0	1995	27	1962	19	1936	31
1-106	210.4	192.1	1.10	0.0633	0.0023	0.0994	0.0020	0.8820	0.0350	4.6	718	80	641	19	611	11
1-107	149.3	182.6	0.82	0.0645	0.0024	0.1135	0.0023	1.0110	0.0380	2.2	751	73	708	19	693	13
1-108	37.0	36.6	1.01	0.1442	0.0059	0.2406	0.0058	4.7200	0.2100	43.0	2262	72	1768	37	1389	30
1-109	125.9	72.3	1.74	0.0619	0.0030	0.0957	0.0022	0.8040	0.0410	1.9	620	100	600	23	589	13
1-110	257.8	223.5	1.15	0.0603	0.0022	0.0965	0.0020	0.8000	0.0290	0.4	579	78	596	17	594	11
1-111	219.3	177.8	1.23	0.1767	0.0019	0.4645	0.0083	11.3400	0.2200	7.1	2620	17	2552	18	2460	36
1-112	208.4	123.5	1.69	0.0621	0.0025	0.0984	0.0020	0.8420	0.0350	3.2	662	86	625	19	605	12
1-113	77.1	48.3	1.60	0.0825	0.0031	0.1910	0.0042	2.1790	0.0850	14.6	1287	72	1173	27	1127	23
1-114	217.2	103.2	2.10	0.1171	0.0017	0.3291	0.0060	5.3590	0.1200	5.0	1922	27	1878	18	1834	29
1-115	148.1	177.2	0.84	0.0636	0.0029	0.0920	0.0019	0.8140	0.0380	5.4	711	95	600	21	567	11
1-116	166.5	204.5	0.81	0.0738	0.0019	0.1679	0.0032	1.7310	0.0540	0.9	1026	54	1017	20	1001	18

				Measured values and ratios								Apparent Ages				
Batch & Grain no.	U (ppm)	Th (ppm)	U/Th	$^{207}Pb/^{206}Pb$	2σ	$^{206}Pb/^{238}U$	2σ	$^{207}Pb/^{235}U$	2σ	Discordance (%)	$^{207}Pb/^{206}Pb$	2σ	$^{207}Pb/^{235}U$	2σ	$^{206}Pb/^{238}U$	2σ
1-117	368.7	35.8	10.30	0.0604	0.0014	0.1022	0.0019	0.8540	0.0260	0.0	616	51	627	14	627	11
1-118	166.6	121.9	1.37	0.1125	0.0018	0.3142	0.0061	4.9200	0.1200	3.5	1836	28	1803	21	1761	30
1-119	928.9	364.4	2.55	0.0743	0.0011	0.1715	0.0030	1.7690	0.0390	2.0	1047	30	1033	14	1020	17
1-120	233.1	94.2	2.47	0.0612	0.0021	0.0962	0.0019	0.8080	0.0280	1.5	636	70	601	16	592	11
1-121	228.9	96.2	2.38	0.2171	0.0021	0.5621	0.0100	16.9300	0.3400	2.8	2958	16	2929	19	2875	42
2-1	113.9	27.6	4.13	0.0687	0.0019	0.1472	0.0023	1.3820	0.0430	-0.7	883	58	879	18	885	13
2-2	59.3	59.1	1.00	0.0684	0.0028	0.1473	0.0027	1.3900	0.0580	-0.7	861	89	881	25	887	16
2-3	78.2	72.5	1.08	0.0608	0.0026	0.1032	0.0018	0.8630	0.0380	-0.6	623	92	629	21	633	10
2-4	114.5	39.2	2.92	0.1873	0.0036	0.5285	0.0079	13.6400	0.3200	-0.3	2722	31	2725	22	2735	33
2-5	177.4	125.4	1.41	0.0587	0.0021	0.0990	0.0016	0.8030	0.0310	-1.9	557	76	597	18	609	9
2-6	318.7	64.0	4.98	0.0738	0.0019	0.1665	0.0026	1.7030	0.0500	1.5	1033	55	1008	19	993	14
2-9	279.0	767.0	0.36	0.0602	0.0017	0.0983	0.0016	0.8220	0.0260	0.7	604	63	609	15	605	10
2-10	426.0	140.7	3.03	0.0644	0.0014	0.1109	0.0015	0.9880	0.0250	2.8	751	48	698	13	678	9
2-11	163.0	112.5	1.45	0.0501	0.0027	0.0365	0.0007	0.2540	0.0130	-1.3	180	110	228	10	231	4
2-12	120.2	44.8	2.68	0.0684	0.0020	0.1318	0.0020	1.2550	0.0380	3.3	897	57	825	17	798	11
2-13	194.2	166.6	1.17	0.0621	0.0027	0.0880	0.0016	0.7630	0.0330	5.8	687	93	577	19	544	9
2-14	192.6	146.3	1.32	0.0736	0.0019	0.1618	0.0023	1.6430	0.0450	1.8	1019	52	985	17	968	13
2-15	131.2	116.1	1.13	0.0721	0.0025	0.1643	0.0029	1.6530	0.0600	1.0	980	72	991	23	981	16
2-16	171.0	91.6	1.87	0.0666	0.0020	0.1305	0.0019	1.2110	0.0360	1.6	818	61	804	17	792	11
2-17	386.3	237.0	1.63	0.0608	0.0015	0.0954	0.0013	0.8020	0.0210	1.8	624	53	598	12	588	8
2-18	386.9	137.6	2.81	0.0664	0.0019	0.1218	0.0020	1.1240	0.0320	3.0	811	63	764	15	741	11
2-19	53.3	63.1	0.84	0.0647	0.0044	0.0928	0.0030	0.8110	0.0600	5.1	740	130	603	34	572	18
2-20	121.7	196.9	0.62	0.0602	0.0021	0.0929	0.0015	0.7650	0.0280	0.6	606	73	576	16	573	9
2-21	235.8	97.2	2.43	0.0615	0.0017	0.1032	0.0015	0.8840	0.0260	1.4	652	59	642	14	633	9
2-22	139.0	174.3	0.80	0.0621	0.0022	0.1048	0.0017	0.8940	0.0310	1.1	670	76	649	17	642	10
2-23	121.2	79.1	1.53	0.0517	0.0040	0.0371	0.0008	0.2640	0.0200	0.5	220	150	236	16	235	5
2-24	403.0	282.8	1.43	0.1200	0.0022	0.3375	0.0046	5.5740	0.1200	5.0	1956	33	1912	19	1875	22
2-25	35.5	30.4	1.17	0.1852	0.0042	0.5119	0.0084	13.0700	0.3400	1.8	2702	39	2683	25	2664	36
2-26	116.8	103.4	1.13	0.0630	0.0024	0.0814	0.0024	0.6880	0.0330	4.7	677	86	529	20	504	14
2-27	43.8	24.8	1.77	0.0682	0.0035	0.1464	0.0032	1.3720	0.0750	-0.8	860	110	873	33	880	18
2-29	241.0	66.8	3.61	0.0654	0.0018	0.1170	0.0018	1.0560	0.0300	2.7	795	59	733	15	713	10
2-30	196.0	259.0	0.76	0.0616	0.0020	0.1002	0.0015	0.8550	0.0280	1.9	677	66	627	15	615	9
2-31	231.1	58.5	3.95	0.0648	0.0018	0.1179	0.0019	1.0510	0.0320	1.2	775	57	727	16	718	11
2-32	529.0	13.0	40.60	0.1188	0.0022	0.3301	0.0045	5.3840	0.1200	6.3	1938	34	1882	18	1839	22
2-33	121.7	78.1	1.56	0.0741	0.0022	0.1674	0.0025	1.7100	0.0520	1.3	1027	61	1011	19	998	14
2-34	48.1	51.6	0.93	0.0602	0.0031	0.0964	0.0019	0.8010	0.0410	1.7	600	110	603	23	593	11
2-35	27.6	26.4	1.05	0.0616	0.0045	0.0945	0.0022	0.8230	0.0610	4.0	650	150	606	33	582	13
2-36	67.7	33.4	2.03	0.0734	0.0026	0.1707	0.0027	1.7030	0.0590	-0.9	1004	71	1012	21	1016	15
2-37	51.8	61.7	0.84	0.0622	0.0045	0.0908	0.0020	0.7750	0.0550	2.6	620	150	575	32	560	12
2-38	336.0	266.0	1.26	0.1708	0.0031	0.4400	0.0075	10.4200	0.2500	9.6	2567	31	2473	22	2349	34
2-39	366.8	246.8	1.49	0.0608	0.0017	0.0957	0.0015	0.8010	0.0240	1.3	629	62	597	14	589	9
2-41	362.9	238.0	1.52	0.0597	0.0015	0.0992	0.0014	0.8230	0.0220	-0.1	590	51	609	12	610	8
2-42	377.3	311.0	1.21	0.0683	0.0015	0.1418	0.0019	1.3400	0.0330	0.9	874	46	863	14	855	11
2-43	212.6	159.6	1.33	0.0656	0.0019	0.1366	0.0020	1.2440	0.0360	-0.7	786	60	819	16	825	11
2-44	163.4	88.6	1.84	0.0605	0.0022	0.0951	0.0015	0.7910	0.0290	1.4	606	77	594	17	586	9
2-45	198.7	93.1	2.13	0.0613	0.0018	0.1169	0.0019	0.9890	0.0320	-2.4	627	61	696	16	712	11
2-46	93.1	118.0	0.79	0.0582	0.0024	0.0981	0.0018	0.7840	0.0330	-2.9	503	92	586	19	603	10
2-47	114.4	51.6	2.22	0.0621	0.0023	0.0934	0.0018	0.7910	0.0300	3.1	652	81	594	17	576	11
2-48	201.1	208.0	0.97	0.0588	0.0017	0.0961	0.0014	0.7780	0.0240	-1.2	539	64	584	14	591	8
2-49	203.9	77.8	2.62	0.0570	0.0019	0.0882	0.0013	0.6970	0.0240	-1.8	470	73	535	14	545	8
2-50	362.0	150.4	2.41	0.0511	0.0017	0.0380	0.0006	0.2665	0.0094	0.1	239	72	241	8	241	4
2-52	71.6	55.1	1.30	0.0609	0.0026	0.1034	0.0022	0.8710	0.0410	0.2	582	92	635	21	634	13
2-53	194.3	189.7	1.02	0.0711	0.0018	0.1588	0.0028	1.5590	0.0440	0.3	956	50	953	18	950	16
2-54	73.4	55.3	1.33	0.0652	0.0033	0.0918	0.0017	0.8270	0.0410	6.9	720	110	608	23	566	10
2-55	102.3	123.2	0.83	0.0732	0.0022	0.1644	0.0028	1.6720	0.0550	1.3	999	62	994	21	981	16
2-56	30.4	53.0	0.57	0.0985	0.0036	0.2485	0.0057	3.3600	0.1400	11.7	1594	68	1498	32	1429	30
2-57	184.5	121.1	1.52	0.1302	0.0026	0.3635	0.0051	6.5640	0.1500	5.2	2102	35	2055	20	1998	24
2-58	114.4	73.8	1.55	0.1631	0.0033	0.4750	0.0066	10.6700	0.2400	-0.6	2489	32	2494	21	2505	29
2-59	289.1	63.6	4.55	0.0717	0.0017	0.1645	0.0023	1.6220	0.0420	-0.2	967	49	980	17	982	13
2-60	182.9	74.0	2.47	0.1036	0.0024	0.2103	0.0034	2.9720	0.0840	30.6	1690	45	1401	22	1230	18
2-61	1424.0	754.0	1.89	0.0619	0.0013	0.0518	0.0014	0.4420	0.0140	12.3	672	42	371	10	326	8
2-62	175.9	249.5	0.71	0.0592	0.0020	0.0976	0.0015	0.7910	0.0270	-1.4	543	73	592	15	600	9
2-63	360.0	89.5	4.02	0.0615	0.0015	0.1012	0.0015	0.8610	0.0240	1.3	649	52	630	13	621	9
2-65	66.8	101.5	0.66	0.1214	0.0029	0.3556	0.0054	5.9700	0.1600	0.3	1969	42	1970	23	1961	26
2-66	129.8	138.9	0.93	0.0640	0.0023	0.1242	0.0019	1.0960	0.0390	-0.9	706	74	748	19	755	11
2-67	336.9	172.1	1.96	0.0605	0.0014	0.0972	0.0015	0.8140	0.0220	1.1	622	53	605	13	598	9
2-68	154.0	167.3	0.92	0.1146	0.0024	0.3356	0.0047	5.3420	0.1300	0.2	1874	38	1875	20	1865	23
2-69	172.4	90.6	1.90	0.0583	0.0018	0.0975	0.0017	0.7910	0.0270	-1.1	527	68	594	15	601	10
2-70	131.9	64.3	2.05	0.0660	0.0023	0.1214	0.0021	1.1220	0.0450	2.9	802	74	761	21	739	12
2-71	114.3	130.0	0.88	0.0600	0.0023	0.1123	0.0018	0.9240	0.0360	-2.7	610	81	668	19	686	11
2-72	237.0	40.1	5.91	0.0635	0.0017	0.1175	0.0017	1.0270	0.0280	0.1	721	53	717	14	717	10
2-73	119.5	111.5	1.07	0.0562	0.0028	0.0547	0.0010	0.4200	0.0200	3.8	405	100	357	15	343	6
2-74	94.2	134.3	0.70	0.0593	0.0024	0.0952	0.0017	0.7930	0.0330	1.2	571	91	593	19	586	10
2-75	157.8	46.1	3.42	0.0665	0.0020	0.1139	0.0021	1.0530	0.0330	4.8	824	63	730	16	695	12
2-76	234.0	117.4	1.99	0.0648	0.0027	0.0657	0.0018	0.5740	0.0270	10.1	766	86	457	17	411	11
2-77	278.6	173.4	1.61	0.0603	0.0016	0.0984	0.0014	0.8290	0.0240	1.4	633	60	613	13	605	8
2-78	22.9	38.2	0.60	0.0652	0.0051	0.0998	0.0025	0.8920	0.0680	6.0	720	160	652	37	613	15
2-79	382.7	42.4	9.03	0.0636	0.0017	0.1165	0.0016	1.0220	0.0300	0.6	736	59	715	15	710	10
2-80	28.2	55.9	0.50	0.0568	0.0046	0.0821	0.0021	0.6450	0.0510	-2.4	440	160	496	31	508	13
2-81	61.1	39.9	1.53	0.0733	0.0026	0.1690	0.0029	1.7300	0.0640	0.5	1023	74	1019	23	1006	16
2-82	228.8	130.1	1.76	0.0579	0.0025	0.0362	0.0007	0.2890	0.0120	11.1	513	93	258	10	229	4
2-83	222.3	61.6	3.61	0.0747	0.0018	0.1786	0.0027	1.8430	0.0480	-0.4	1058	48	1059	17	1059	15
2-84	157.6	60.4	2.61	0.0750	0.0019	0.1874	0.0027	1.9450	0.0550	-4.2	1069	51	1096	19	1107	15
2-85	90.9	96.4	0.94	0.0598	0.0028	0.0881	0.0015	0.7350	0.0340	2.3	562	99	557	20	544	9

				Measured values and ratios								Apparent Ages				
Batch & Grain no.	U (ppm)	Th (ppm)	U/Th	$^{207}Pb/^{206}Pb$	2σ	$^{206}Pb/^{238}U$	2σ	$^{207}Pb/^{235}U$	2σ	Discordance (%)	$^{207}Pb/^{206}Pb$	2σ	$^{207}Pb/^{235}U$	2σ	$^{206}Pb/^{238}U$	2σ
2-86	207.8	102.3	2.03	0.0718	0.0017	0.1636	0.0025	1.6070	0.0420	0.1	979	46	977	16	977	14
2-87	317.6	364.7	0.87	0.0741	0.0017	0.1638	0.0023	1.6730	0.0440	2.1	1037	45	998	17	978	13
2-88	159.8	96.5	1.66	0.0736	0.0018	0.1751	0.0025	1.7670	0.0470	-1.8	1022	51	1032	17	1040	14
2-89	62.1	105.7	0.59	0.0651	0.0026	0.1354	0.0023	1.2120	0.0500	-1.7	745	83	805	23	818	13
2-90	89.9	142.2	0.63	0.0522	0.0036	0.0384	0.0009	0.2770	0.0190	2.8	280	130	250	15	243	5
2-91	55.8	103.4	0.54	0.0587	0.0034	0.0961	0.0019	0.7760	0.0420	-1.4	510	120	584	24	592	11
2-92	361.1	185.2	1.95	0.0681	0.0015	0.1462	0.0020	1.3700	0.0320	-0.4	871	44	876	14	880	11
2-93	114.9	79.3	1.45	0.1129	0.0025	0.3058	0.0046	4.7480	0.1200	7.9	1845	41	1776	20	1721	22
2-94	90.7	24.9	3.65	0.0529	0.0061	0.0300	0.0015	0.2250	0.0300	5.7	290	230	202	25	191	9
2-95	71.4	64.2	1.11	0.0584	0.0029	0.0955	0.0017	0.7760	0.0390	-0.5	550	110	585	22	588	10
2-96	186.8	150.5	1.24	0.0618	0.0020	0.1031	0.0016	0.8840	0.0300	1.5	663	71	642	16	633	9
2-97	118.6	132.1	0.90	0.1272	0.0027	0.3640	0.0055	6.3780	0.1600	3.4	2060	38	2029	23	2003	27
2-98	751.0	584.0	1.29	0.0601	0.0013	0.0992	0.0015	0.8240	0.0200	0.3	607	47	611	12	609	9
2-99	192.7	109.6	1.76	0.0730	0.0018	0.1696	0.0025	1.7200	0.0450	2.1	1030	52	1017	17	1010	14
2-100	511.0	152.1	3.36	0.0767	0.0015	0.1818	0.0025	1.9190	0.0450	4.1	1116	41	1087	16	1077	14
2-101	1638.0	165.8	9.88	0.0589	0.0012	0.0804	0.0013	0.6548	0.0160	2.4	564	43	511	10	499	8
2-102	49.3	64.1	0.77	0.0561	0.0036	0.0841	0.0020	0.6520	0.0380	-3.4	430	130	503	23	520	12
2-103	119.2	53.2	2.24	0.0622	0.0021	0.1099	0.0017	0.9420	0.0340	0.1	662	72	673	17	672	10
2-104	81.3	38.7	2.10	0.0705	0.0024	0.1550	0.0025	1.4950	0.0530	0.1	929	71	930	22	929	14
2-105	244.8	208.5	1.17	0.0602	0.0016	0.0971	0.0015	0.7990	0.0230	-0.4	610	57	595	13	597	9
2-106	64.1	48.6	1.32	0.1170	0.0029	0.3519	0.0056	5.6500	0.1600	-2.3	1904	46	1920	24	1943	27
2-107	273.0	247.1	1.10	0.0592	0.0017	0.0739	0.0011	0.6000	0.0190	3.6	559	64	477	12	460	7
2-108	81.1	61.0	1.33	0.0602	0.0023	0.1062	0.0025	0.8790	0.0360	-1.2	589	82	642	19	650	15
2-109	141.3	90.6	1.56	0.2168	0.0046	0.5805	0.0085	17.3500	0.4200	0.4	2958	35	2955	23	2950	35
2-110	32.8	34.9	0.94	0.0620	0.0043	0.0964	0.0020	0.8100	0.0550	1.1	600	140	600	30	593	12
2-111	257.2	148.0	1.74	0.0591	0.0016	0.0968	0.0014	0.7920	0.0220	-0.5	581	60	592	13	596	9
2-112	217.1	102.2	2.12	0.0498	0.0026	0.0359	0.0006	0.2410	0.0130	-3.7	175	100	219	10	227	4
2-113	353.8	170.1	2.08	0.1770	0.0033	0.3526	0.0080	8.5700	0.2400	30.3	2627	31	2292	26	1945	38
2-114	249.5	147.2	1.69	0.1607	0.0033	0.4628	0.0081	10.2140	0.2300	0.6	2460	36	2454	21	2451	35
2-115	72.0	102.6	0.70	0.1938	0.0041	0.5247	0.0080	13.8400	0.3400	3.5	2773	34	2746	23	2719	34
2-116	459.2	92.4	4.97	0.0598	0.0014	0.0992	0.0013	0.8210	0.0210	-0.3	593	52	608	11	610	8
2-117	138.3	82.4	1.68	0.0522	0.0029	0.0378	0.0008	0.2700	0.0160	0.8	280	110	241	13	239	5
2-118	184.9	120.8	1.53	0.1403	0.0029	0.4170	0.0072	8.0200	0.2200	-0.2	2235	36	2231	24	2246	33
2-119	137.5	16.0	8.58	0.0616	0.0021	0.1201	0.0019	1.0230	0.0360	-2.5	656	75	713	18	731	11
2-120	166.0	95.0	1.75	0.1121	0.0023	0.3370	0.0054	5.2270	0.1300	-3.0	1832	38	1858	21	1872	26
2-121	76.7	51.9	1.48	0.0593	0.0026	0.0998	0.0020	0.8130	0.0350	-0.7	571	92	609	20	613	12
2-122	106.7	66.7	1.60	0.0726	0.0021	0.1719	0.0026	1.7160	0.0520	-2.3	1000	58	1016	19	1023	14
2-123	188.5	118.5	1.59	0.1248	0.0027	0.3695	0.0068	6.3300	0.1800	-0.1	2022	38	2023	24	2026	32
2-124	216.0	278.0	0.78	0.0616	0.0019	0.0949	0.0016	0.7990	0.0260	2.0	641	70	596	15	584	10
2-125	555.0	213.3	2.60	0.1621	0.0029	0.4465	0.0063	9.9910	0.2200	4.5	2477	31	2434	21	2379	28
2-126	153.0	44.2	3.46	0.0611	0.0018	0.0999	0.0015	0.8470	0.0260	1.1	643	63	621	14	614	9
2-127	147.9	91.2	1.62	0.0609	0.0035	0.0340	0.0007	0.2810	0.0160	15.1	600	120	254	13	216	5
2-128	183.0	88.6	2.07	0.0526	0.0024	0.0479	0.0009	0.3500	0.0170	1.5	289	96	306	12	302	5
2-129	143.2	70.4	2.03	0.0590	0.0020	0.0986	0.0016	0.8040	0.0270	-0.5	552	70	603	16	606	9
2-130	187.9	102.3	1.84	0.0683	0.0019	0.1394	0.0022	1.3170	0.0400	1.3	880	56	852	17	841	12
2-131	103.3	125.1	0.83	0.0748	0.0025	0.1557	0.0027	1.5990	0.0510	4.3	1067	68	975	22	933	15
2-132	90.8	20.6	4.41	0.0595	0.0022	0.0966	0.0019	0.7920	0.0320	0.3	588	83	597	18	595	11
2-133	78.4	96.1	0.82	0.0611	0.0028	0.0964	0.0016	0.8240	0.0360	2.6	627	92	610	20	594	9
2-134	77.0	153.4	0.50	0.0726	0.0027	0.1481	0.0026	1.4980	0.0580	3.9	981	77	926	23	890	14
2-135	96.5	111.7	0.86	0.1169	0.0026	0.3385	0.0051	5.5070	0.1400	0.9	1909	40	1901	21	1879	25
2-136	203.0	62.3	3.26	0.1054	0.0030	0.1800	0.0089	2.5300	0.1600	42.0	1705	55	1268	45	1062	49
2-137	377.0	48.0	7.85	0.0765	0.0019	0.1499	0.0031	1.5950	0.0580	6.7	1101	49	965	23	900	17
2-138	449.0	522.0	0.86	0.0598	0.0015	0.0938	0.0013	0.7780	0.0210	0.9	586	56	584	12	578	8
2-139	188.5	30.8	6.12	0.0692	0.0023	0.1482	0.0024	1.4410	0.0540	1.5	901	71	904	23	891	14
2-140	775.4	62.8	12.35	0.0592	0.0013	0.0928	0.0013	0.7666	0.0180	0.9	574	47	577	11	572	7
18MC175A1																
1-1	312.0	29.4	10.60	0.0576	0.0023	0.0773	0.0015	0.6080	0.0260	0.2	488	85	481	16	480	9
1-2	81.4	51.0	1.60	0.0605	0.0031	0.1032	0.0024	0.8790	0.0470	1.4	640	110	643	24	634	14
1-3	263.5	160.1	1.65	0.0542	0.0024	0.0539	0.0010	0.4040	0.0190	1.4	355	95	344	14	339	6
1-4	185.5	85.5	2.17	0.0542	0.0029	0.0513	0.0011	0.3800	0.0190	1.2	350	110	327	14	323	7
1-5	739.0	123.0	6.01	0.0545	0.0023	0.0514	0.0011	0.3760	0.0140	0.1	363	93	323	10	323	7
1-6	1006.0	575.0	1.75	0.0844	0.0071	0.0181	0.0005	0.2110	0.0170	40.5	1230	170	194	14	116	3
1-7	626.6	484.4	1.29	0.0513	0.0021	0.0343	0.0007	0.2421	0.0100	1.1	238	84	220	8	217	4
1-8	301.0	140.5	2.14	0.0530	0.0025	0.0506	0.0009	0.3750	0.0170	1.1	310	100	322	13	318	6
1-9	685.2	344.6	1.99	0.0608	0.0012	0.0777	0.0013	0.6520	0.0170	5.1	624	42	509	11	483	8
1-10	46.6	36.3	1.28	0.0718	0.0042	0.1662	0.0042	1.6800	0.1100	-13.9	920	120	989	39	990	23
1-11	217.5	17.2	12.65	0.0570	0.0024	0.0619	0.0014	0.4890	0.0220	3.7	472	93	402	15	387	8
1-12	188.4	73.3	2.57	0.0554	0.0032	0.0518	0.0012	0.3960	0.0240	3.4	400	120	337	18	326	8
1-13	513.1	194.4	2.64	0.0685	0.0016	0.1054	0.0017	0.9890	0.0260	7.7	870	50	700	14	646	10
1-14	611.2	123.3	4.96	0.1627	0.0011	0.4070	0.0071	9.1060	0.1600	13.7	2485	11	2348	17	2203	33
1-15	150.8	77.6	1.94	0.0645	0.0027	0.1210	0.0023	1.0790	0.0470	0.7	724	92	741	23	736	13
1-16	451.5	35.9	12.58	0.1067	0.0019	0.1826	0.0038	2.7040	0.0670	40.9	1745	32	1330	18	1081	20
1-17	272.2	89.8	3.03	0.0808	0.0030	0.1494	0.0042	1.6700	0.0850	27.7	1215	70	993	32	897	24
1-18	767.7	463.2	1.66	0.0581	0.0016	0.0770	0.0014	0.6170	0.0190	2.0	526	61	488	12	478	8
1-19	383.3	261.6	1.47	0.0719	0.0031	0.0560	0.0010	0.5550	0.0250	21.2	982	89	446	16	351	6
1-20	961.0	284.5	3.38	0.0566	0.0011	0.0743	0.0012	0.5770	0.0140	0.2	480	39	463	9	462	7
1-21	105.8	46.3	2.29	0.0567	0.0046	0.0543	0.0015	0.4190	0.0340	4.1	400	170	355	25	341	10
1-22	358.0	244.0	1.47	0.0537	0.0022	0.0540	0.0011	0.4090	0.0180	2.6	347	86	348	13	339	7
1-23	231.9	32.5	7.14	0.0632	0.0025	0.0845	0.0016	0.7260	0.0300	5.6	682	85	554	17	523	10
1-24	658.0	54.3	12.12	0.0540	0.0012	0.0599	0.0011	0.4450	0.0120	-0.5	353	50	373	8	375	7
1-25	350.7	154.8	2.27	0.0610	0.0024	0.0636	0.0013	0.5300	0.0240	7.8	607	83	431	16	398	8
1-26	65.2	38.7	1.68	0.0610	0.0041	0.0699	0.0019	0.6170	0.0410	10.6	660	140	487	27	435	11
1-27	242.5	104.0	2.33	0.0827	0.0017	0.1717	0.0029	1.9610	0.0500	19.6	1254	41	1101	17	1022	16
1-28	498.3	213.7	2.33	0.0552	0.0019	0.0674	0.0012	0.5200	0.0200	1.1	426	74	425	13	420	7

				Measured values and ratios								Apparent Ages				
Batch & Grain no.	U (ppm)	Th (ppm)	U/Th	$^{207}Pb/^{206}Pb$	2σ	$^{206}Pb/^{238}U$	2σ	$^{207}Pb/^{235}U$	2σ	Discordance (%)	$^{207}Pb/^{206}Pb$	2σ	$^{207}Pb/^{235}U$	2σ	$^{206}Pb/^{238}U$	2σ
1-29	1045.2	610.9	1.71	0.0624	0.0009	0.0968	0.0016	0.8350	0.0170	3.3	691	29	616	10	595	9
1-30	217.6	89.0	2.44	0.0702	0.0028	0.0824	0.0016	0.8010	0.0320	14.3	939	83	596	18	511	9
1-31	213.8	110.8	1.93	0.0544	0.0041	0.0560	0.0014	0.4240	0.0300	1.6	350	160	357	22	351	9
1-32	398.4	168.5	2.36	0.0580	0.0019	0.0665	0.0013	0.5320	0.0190	4.4	510	70	434	12	415	8
1-33	75.4	56.8	1.33	0.1000	0.1000	0.1170	0.0110	2.2000	1.6000	54.1	2970	340	1550	230	712	65
1-34	546.4	303.2	1.80	0.0531	0.0016	0.0547	0.0010	0.3980	0.0140	-0.7	325	65	341	10	344	6
1-35	1068.0	321.0	3.33	0.0526	0.0013	0.0486	0.0008	0.3509	0.0100	-0.3	314	53	305	8	306	5
1-36	1207.0	362.5	3.33	0.0537	0.0012	0.0517	0.0008	0.3786	0.0100	0.4	352	51	326	8	325	5
1-37	653.6	305.4	2.14	0.0553	0.0013	0.0572	0.0010	0.4280	0.0120	0.7	409	54	361	9	359	6
1-38	545.3	227.0	2.40	0.0571	0.0014	0.0749	0.0013	0.5850	0.0170	0.4	487	56	467	11	466	8
1-39	1112.0	306.0	3.63	0.0538	0.0013	0.0475	0.0008	0.3507	0.0093	1.9	375	52	305	7	299	5
1-40	251.1	83.3	3.01	0.0629	0.0020	0.1117	0.0019	0.9610	0.0330	0.1	717	68	683	17	682	11
1-41	417.5	243.9	1.71	0.0556	0.0028	0.0500	0.0010	0.3770	0.0190	3.0	410	110	324	14	314	6
1-42	462.0	222.6	2.08	0.0630	0.0015	0.1119	0.0019	0.9560	0.0260	-0.2	699	51	682	14	684	11
1-43	927.0	84.5	10.97	0.0564	0.0015	0.0683	0.0013	0.5280	0.0170	0.8	459	61	429	11	426	8
1-44	188.0	73.5	2.56	0.0550	0.0033	0.0576	0.0012	0.4210	0.0260	-1.6	340	120	355	19	361	7
1-45	250.9	112.0	2.24	0.0558	0.0027	0.0559	0.0011	0.4300	0.0220	3.6	420	100	364	15	351	7
1-46	74.6	58.8	1.27	0.1345	0.0027	0.3954	0.0070	7.3200	0.1800	0.6	2157	35	2152	21	2147	33
1-47	38.6	39.1	0.99	0.0678	0.0087	0.0588	0.0021	0.5690	0.0760	16.6	730	280	441	51	368	13
1-48	498.0	207.0	2.41	0.0544	0.0019	0.0553	0.0010	0.4070	0.0150	-0.3	381	78	346	11	347	6
1-49	284.0	143.8	1.97	-0.0060	0.0500	0.0539	0.0030	0.3000	0.3200	41.7	2320	220	580	170	338	18
1-50	216.0	71.0	3.04	0.0588	0.0024	0.0731	0.0014	0.5880	0.0240	2.9	533	89	469	15	456	9
1-51	267.1	56.4	4.74	0.0866	0.0025	0.1554	0.0032	1.8480	0.0560	32.9	1343	54	1060	20	933	18
1-52	635.7	254.1	2.50	0.0602	0.0015	0.0772	0.0013	0.6430	0.0190	4.9	615	52	504	12	479	8
1-53	540.0	128.7	4.20	0.0583	0.0015	0.0829	0.0014	0.6660	0.0190	0.7	525	55	517	12	513	8
1-54	865.9	122.0	7.10	0.1678	0.0009	0.4095	0.0065	9.4640	0.1600	15.1	2535	9	2384	15	2212	30
1-55	1030.0	132.1	7.80	0.0639	0.0013	0.0831	0.0019	0.7380	0.0250	8.1	733	43	560	15	515	11
1-56	386.2	61.0	6.33	0.1034	0.0018	0.1939	0.0037	2.7700	0.0630	35.2	1688	32	1346	17	1144	19
1-57	113.6	44.3	2.56	0.1676	0.0025	0.4517	0.0079	10.5500	0.2200	5.4	2536	25	2485	20	2402	35
1-58	758.0	121.0	6.26	0.0579	0.0013	0.0602	0.0012	0.4820	0.0140	6.2	520	49	402	10	377	7
1-59	586.4	747.0	0.79	0.0594	0.0016	0.0832	0.0015	0.6850	0.0200	2.6	565	58	529	12	515	9
1-60	439.0	13.0	33.77	0.0531	0.0019	0.0515	0.0011	0.3850	0.0160	2.5	342	83	332	12	324	7
1-61	44.7	42.1	1.06	0.0598	0.0052	0.0905	0.0030	0.7410	0.0610	2.4	560	170	572	36	558	17
1-62	268.0	173.9	1.54	0.0649	0.0023	0.0910	0.0017	0.8120	0.0290	7.4	727	75	606	17	561	10
1-63	830.7	196.2	4.23	0.0624	0.0010	0.1053	0.0017	0.9180	0.0200	2.5	683	33	662	11	645	10
1-64	319.3	167.1	1.91	0.0521	0.0031	0.0468	0.0010	0.3390	0.0210	0.1	270	130	295	16	295	6
1-65	714.0	454.0	1.57	0.0534	0.0015	0.0470	0.0008	0.3492	0.0110	2.5	353	66	304	8	296	5
1-66	316.2	31.2	10.13	0.0561	0.0027	0.0582	0.0010	0.4530	0.0220	3.8	423	95	379	15	365	6
1-67	58.3	29.2	2.00	0.0666	0.0044	0.0828	0.0022	0.7690	0.0530	10.5	750	140	573	30	513	13
1-68	341.3	177.4	1.92	0.0567	0.0030	0.0377	0.0008	0.2980	0.0150	9.7	440	110	264	12	238	5
1-69	1404.4	1605.0	0.88	0.0548	0.0010	0.0492	0.0008	0.3729	0.0091	3.8	397	42	322	7	309	5
1-70	241.8	174.9	1.38	0.0729	0.0018	0.1428	0.0025	1.4600	0.0440	14.7	1013	51	913	18	860	14
1-71	384.4	38.9	9.87	0.0543	0.0020	0.0545	0.0010	0.4070	0.0160	0.8	353	79	345	11	342	6
1-72	326.4	101.1	3.23	0.0693	0.0021	0.1136	0.0021	1.0790	0.0360	6.6	905	61	743	17	694	12
1-73	977.0	88.9	10.99	0.0612	0.0010	0.0920	0.0015	0.7800	0.0180	3.0	638	34	585	10	567	9
1-74	522.2	171.0	3.05	0.0520	0.0019	0.0472	0.0009	0.3410	0.0140	0.6	296	80	299	11	297	5
1-75	11.0	0.0	249.77	0.1340	0.0390	0.0414	0.0032	0.6600	0.1500	35.9	890	630	410	110	263	19
1-76	604.4	311.1	1.94	0.0593	0.0018	0.0486	0.0009	0.3960	0.0130	9.8	573	63	339	9	306	5
1-77	504.5	320.9	1.57	0.0627	0.0028	0.0511	0.0011	0.4370	0.0210	12.4	710	110	367	15	321	7
1-78	810.0	28.1	28.82	0.0539	0.0016	0.0542	0.0009	0.4020	0.0120	0.6	368	65	342	9	340	6
1-79	280.0	116.5	2.40	0.1603	0.0017	0.4447	0.0078	9.8600	0.1900	3.7	2457	18	2421	17	2371	35
1-80	236.7	31.1	7.60	0.1548	0.0028	0.3213	0.0059	6.8600	0.1500	28.5	2396	31	2093	20	1796	29
1-81	341.5	160.8	2.12	0.1354	0.0012	0.3674	0.0058	6.8370	0.1200	8.3	2168	15	2090	16	2017	27
1-82	188.5	162.5	1.16	0.0711	0.0030	0.1130	0.0025	1.0900	0.0470	7.4	941	87	745	23	690	15
1-83	246.0	11.1	22.18	0.0559	0.0025	0.0582	0.0013	0.4430	0.0210	3.1	432	98	376	16	364	8
1-84	1242.0	456.0	2.72	0.0607	0.0020	0.0592	0.0011	0.4960	0.0180	8.9	612	67	407	12	371	7
1-85	86.7	76.9	1.13	0.0609	0.0044	0.0927	0.0025	0.7660	0.0490	0.2	570	150	572	28	571	15
1-86	406.4	157.3	2.58	0.0778	0.0016	0.1860	0.0033	2.0120	0.0460	3.2	1142	43	1118	16	1100	18
1-87	181.2	21.7	8.36	0.0541	0.0029	0.0569	0.0012	0.4300	0.0260	1.5	350	110	362	18	357	7
1-88	678.3	100.5	6.75	0.0716	0.0012	0.1367	0.0023	1.3430	0.0320	17.1	978	35	864	14	826	13
1-89	361.4	358.0	1.01	0.0650	0.0016	0.0967	0.0018	0.8760	0.0240	6.9	770	53	639	13	595	11
1-90	346.8	533.1	0.65	0.0600	0.0018	0.0772	0.0014	0.6440	0.0210	4.9	614	63	504	13	480	9
1-91	810.0	428.5	1.89	0.0579	0.0012	0.0692	0.0012	0.5500	0.0140	3.0	527	43	445	9	431	7
1-92	747.0	7.9	94.68	0.0552	0.0023	0.0535	0.0011	0.4010	0.0170	1.8	419	94	342	12	336	7
1-93	133.2	110.6	1.20	0.0736	0.0022	0.1581	0.0031	1.5990	0.0540	7.6	1020	63	971	21	947	18
1-94	179.1	233.0	0.77	0.0715	0.0021	0.1472	0.0026	1.4530	0.0480	8.4	965	60	910	20	885	15
1-95	203.9	114.1	1.79	0.0583	0.0029	0.0533	0.0011	0.4340	0.0230	8.2	520	110	365	16	335	7
1-96	222.0	92.0	2.41	0.1824	0.0026	0.3755	0.0076	9.3600	0.2300	27.5	2673	23	2373	23	2055	36
1-97	504.0	243.1	2.07	0.0548	0.0019	0.0615	0.0011	0.4650	0.0180	0.3	385	77	386	12	385	7
1-98	771.0	416.3	1.85	0.0581	0.0010	0.0799	0.0013	0.6410	0.0150	1.5	538	39	503	10	495	8
1-99	452.6	259.0	1.75	0.0740	0.0012	0.1682	0.0027	1.7120	0.0370	3.5	1036	33	1012	14	1002	15
1-100	1390.0	981.0	1.42	0.0564	0.0010	0.0694	0.0013	0.5420	0.0130	1.7	463	40	440	9	432	8
1-101	203.0	155.4	1.31	0.0613	0.0021	0.1058	0.0019	0.8900	0.0330	-0.5	624	74	645	18	648	11
1-102	388.1	128.8	3.01	0.3003	0.0027	0.4062	0.0069	16.9000	0.3200	42.8	3471	14	2928	18	2197	32
1-103	150.5	99.1	1.52	0.0568	0.0042	0.0673	0.0019	0.5320	0.0400	2.2	460	150	429	27	420	11
1-104	114.6	84.8	1.35	0.0740	0.0039	0.0954	0.0022	0.9660	0.0490	14.9	970	110	690	26	587	13
1-105	538.0	4.0	135.18	0.0555	0.0029	0.0565	0.0012	0.4370	0.0250	4.2	430	120	370	18	354	7
1-106	376.9	213.8	1.76	0.0563	0.0020	0.0492	0.0009	0.3760	0.0140	4.9	439	76	326	11	310	6
1-107	589.7	294.9	2.00	0.0522	0.0019	0.0472	0.0009	0.3430	0.0140	0.6	286	80	299	11	297	6
1-108	87.7	56.7	1.55	0.0685	0.0044	0.0902	0.0021	0.8320	0.0520	10.4	820	130	621	28	556	13
1-109	309.0	577.0	0.54	0.0695	0.0023	0.0716	0.0014	0.6980	0.0280	17.8	958	70	542	17	446	8
1-110	850.0	212.5	4.00	0.0569	0.0014	0.0493	0.0009	0.3819	0.0110	5.6	479	53	329	8	310	5
1-111	215.8	69.1	3.12	0.0697	0.0028	0.0768	0.0015	0.7350	0.0310	14.9	909	82	560	18	477	9
1-112	170.7	88.9	1.92	0.0685	0.0037	0.1409	0.0030	1.3370	0.0720	1.4	870	120	858	31	850	17

	Measured values and ratios										Apparent Ages					
Batch & Grain no.	U (ppm)	Th (ppm)	U/Th	$^{207}Pb/^{206}Pb$	2σ	$^{206}Pb/^{238}U$	2σ	$^{207}Pb/^{235}U$	2σ	Discordance (%)	$^{207}Pb/^{206}Pb$	2σ	$^{207}Pb/^{235}U$	2σ	$^{206}Pb/^{238}U$	2σ
1-113	1928.0	2258.0	0.85	0.0534	0.0012	0.0463	0.0008	0.3394	0.0087	1.6	335	49	297	7	292	5

Table S3.2 Results of single grain zircon U-Pb ICP-MS analysis from Thera (Santorini), Greece

Grain no.	Measured ratios									Apparent ages (Ma)					
	$^{207}Pb/^{206}Pb$	2σ	$^{206}Pb/^{238}U$	2σ	$^{207}Pb/^{235}U$	2σ	$^{208}Pb/^{232}Th$	2σ	Discordance (%)	$^{207}Pb/^{206}Pb$	1σ	$^{206}Pb/^{238}U$	1σ	$^{207}Pb/^{235}U$	1σ
ALS02, 359540 E, 4027830 N															
1	0.0700	0.0028	0.1454	0.0036	1.4029	0.0563	0.0460	0.0014	1.7	927.9	40.0	875.0	10.1	890.1	11.9
2a	0.1822	0.0055	0.4334	0.0105	10.8892	0.3407	0.1359	0.00394	8.3	2673.2	24.6	2321.0	23.6	2513.7	14.6
02b	0.1813	0.0053	0.5319	0.0127	13.2982	0.4053	0.1415	0.00406	1.8	2665.1	23.9	2749.3	26.6	2701.1	14.4
3	0.1635	0.0053	0.4496	0.0110	10.1360	0.3397	0.1312	0.0038	2.2	2492.2	27.1	2393.5	24.4	2447.3	15.5
5	0.0618	0.0040	0.1006	0.0027	0.8566	0.0554	0.0338	0.00118	1.7	666.1	68.4	617.8	8.1	628.3	15.2
6	0.0670	0.0037	0.0985	0.0026	0.9097	0.0502	0.0337	0.0011	8.5	837.5	56.7	605.5	7.6	656.9	13.4
7	0.0740	0.0024	0.1664	0.0040	1.6970	0.0566	0.0528	0.00142	1.5	1040.5	32.2	992.2	11.0	1007.4	10.7
8	0.0724	0.0023	0.1581	0.0038	1.5776	0.0525	0.0467	0.00134	1.6	997.0	32.3	946.0	10.5	961.4	10.3
9	0.1685	0.0050	0.4682	0.0112	10.8782	0.3399	0.1404	0.00374	1.5	2543.1	24.8	2475.4	24.7	2512.8	14.5
10	0.0666	0.0022	0.1389	0.0033	1.2750	0.0433	0.0444	0.00124	0.5	824.5	33.9	838.4	9.4	834.6	9.7
11	0.0601	0.0021	0.1031	0.0025	0.8541	0.0303	0.0315	0.00172	0.9	607.1	36.9	632.3	7.2	626.9	8.3
12	0.0614	0.0022	0.1010	0.0024	0.8549	0.0308	0.0304	0.0014	1.2	653.8	37.2	620.0	7.1	627.3	8.4
13	0.0631	0.0029	0.1175	0.0030	1.0218	0.0477	0.0393	0.0012	0.2	710.6	48.7	716.1	8.5	714.8	12.0
14	0.0603	0.0034	0.0862	0.0023	0.7165	0.0407	0.0275	0.00078	3.0	614.8	60.5	532.7	6.7	548.6	12.0
15	0.0621	0.0023	0.1027	0.0025	0.8791	0.0332	0.0316	0.00094	1.6	676.3	39.1	630.4	7.3	640.5	9.0
16	0.0586	0.0040	0.1157	0.0032	0.9356	0.0637	0.0376	0.0019	5.0	553.7	73.2	705.8	9.2	670.5	16.7
18	0.0703	0.0024	0.1528	0.0037	1.4819	0.0521	0.0486	0.00146	0.7	938.1	34.7	916.6	10.2	923.0	10.7
20	0.0687	0.0024	0.1432	0.0034	1.3556	0.0481	0.0459	0.00132	0.9	888.9	35.3	862.6	9.7	870.0	10.4
21	0.0714	0.0024	0.1657	0.0040	1.6317	0.0558	0.0518	0.00146	0.6	970.1	33.5	988.1	10.9	982.5	10.8
22	0.0683	0.0036	0.1319	0.0034	1.2420	0.0649	0.0446	0.0018	2.7	877.7	53.3	798.6	9.8	819.8	14.7
23	0.0665	0.0024	0.1286	0.0031	1.1779	0.0440	0.0410	0.00114	1.4	820.9	37.8	779.6	8.9	790.3	10.3
24	0.0587	0.0024	0.0915	0.0023	0.7412	0.0311	0.0295	0.0008	0.3	557.1	44.6	564.6	6.6	563.1	9.1
25	0.0649	0.0073	0.0964	0.0033	0.8626	0.0958	0.0308	0.00156	6.4	769.9	114.6	593.5	9.6	631.6	26.1
26	0.1836	0.0057	0.4875	0.0117	12.3398	0.3981	0.1402	0.00396	2.8	2685.4	25.6	2560.0	25.4	2630.6	15.2
27	0.0719	0.0029	0.1658	0.0041	1.6434	0.0666	0.0519	0.00172	0.2	982.7	40.3	988.9	11.3	987.0	12.8
29	0.0644	0.0038	0.1061	0.0028	0.9418	0.0550	0.0317	0.00156	3.6	753.1	60.9	650.3	8.3	673.8	14.4
30	0.0778	0.0034	0.1730	0.0044	1.8555	0.0827	0.0542	0.00178	3.6	1141.0	43.4	1028.4	12.2	1065.4	14.7
31	0.0625	0.0024	0.1195	0.0029	1.0302	0.0399	0.0385	0.00132	1.2	692.1	40.1	727.7	8.3	719.0	10.0
32	0.0736	0.0028	0.1738	0.0043	1.7632	0.0691	0.0533	0.0017	0.1	1030.4	38.6	1032.7	11.7	1032.0	12.7
33	0.0660	0.0043	0.1449	0.0040	1.3192	0.0850	0.0425	0.00208	2.1	806.8	66.7	872.5	11.3	854.1	18.6
34	0.0728	0.0023	0.1577	0.0038	1.5835	0.0524	0.0522	0.00174	2.1	1008.5	31.8	944.0	10.6	963.7	10.3
35	0.0717	0.0022	0.1572	0.0037	1.5533	0.0499	0.0510	0.00134	1.1	976.5	31.3	941.0	10.4	951.8	9.9
36	0.0727	0.0029	0.1702	0.0042	1.7069	0.0687	0.0510	0.00156	0.2	1006.6	39.9	1013.2	11.5	1011.1	12.9
37	0.1253	0.0043	0.2636	0.0065	4.5552	0.1615	0.0929	0.00298	15.4	2033.5	30.4	1508.1	16.5	1741.1	14.8
38	0.0626	0.0026	0.1173	0.0029	1.0125	0.0431	0.0390	0.00158	0.7	693.7	44.1	715.0	8.4	710.2	10.9
41	0.0593	0.0026	0.1050	0.0026	0.8587	0.0383	0.0332	0.00104	2.3	577.2	47.2	643.9	7.6	629.4	10.5
42	0.0735	0.0019	0.1112	0.0026	1.1272	0.0317	0.0363	0.0009	12.8	1027.9	25.8	679.7	7.6	766.4	7.6
43	0.1144	0.0028	0.2861	0.0067	4.5122	0.1222	0.0944	0.00264	6.9	1869.8	22.3	1621.8	16.9	1733.2	11.3
44	0.0685	0.0030	0.1404	0.0036	1.3264	0.0596	0.0478	0.00278	1.3	884.1	45.3	846.7	10.1	857.3	13.0
45	0.0702	0.0023	0.1489	0.0036	1.4426	0.0494	0.0360	0.001	1.3	935.3	33.5	894.9	10.1	906.8	10.3
46	0.0718	0.0022	0.1643	0.0039	1.6270	0.0531	0.0512	0.0013	0.0	979.9	31.4	980.8	10.9	980.7	10.3
47	0.0749	0.0036	0.1737	0.0045	1.7935	0.0860	0.0564	0.00206	1.1	1064.8	47.3	1032.2	12.4	1043.1	15.6
48	0.0988	0.0027	0.2906	0.0069	3.9610	0.1155	0.0866	0.0024	1.1	1602.2	25.2	1644.5	17.3	1626.2	11.8
50	0.1667	0.0042	0.4379	0.0103	10.0664	0.2744	0.1294	0.00316	4.3	2524.5	21.0	2341.3	23.2	2440.9	12.6
51	0.0521	0.0020	0.0500	0.0012	0.3595	0.0143	0.0166	0.00048	0.9	289.6	43.6	314.8	3.7	311.9	5.3
54	0.0612	0.0040	0.1059	0.0029	0.8936	0.0585	0.0357	0.00154	0.1	645.9	69.3	648.7	8.5	648.3	15.7
56	0.1517	0.0039	0.3656	0.0087	7.6488	0.2134	0.1112	0.00272	9.1	2364.8	22.0	2008.6	20.5	2190.6	12.5
58	0.0665	0.0024	0.0791	0.0019	0.7252	0.0268	0.0358	0.00096	12.8	820.7	37.0	490.9	5.8	553.8	7.9
59	0.0933	0.0037	0.1035	0.0026	1.3307	0.0538	0.0465	0.00142	35.4	1492.9	37.3	634.7	7.6	859.2	11.7
61	0.0749	0.0032	0.1453	0.0037	1.5001	0.0657	0.0486	0.00132	6.4	1064.9	42.9	874.4	10.4	930.4	13.3
62	0.0590	0.0041	0.0909	0.0025	0.7395	0.0506	0.0285	0.00088	0.2	566.4	73.3	560.8	7.5	562.1	14.8
63	0.1505	0.0046	0.3569	0.0088	7.4092	0.2358	0.1238	0.00332	9.9	2351.9	25.8	1967.4	20.9	2162.1	14.2
64	0.1106	0.0036	0.3339	0.0082	5.0943	0.1717	0.1012	0.00266	1.2	1809.6	29.1	1857.3	19.9	1835.2	14.3
65	0.0680	0.0024	0.1407	0.0034	1.3200	0.0478	0.0449	0.0012	0.7	868.9	35.9	848.7	9.7	854.5	10.5
66	0.0659	0.0040	0.1363	0.0037	1.2396	0.0746	0.0448	0.00176	0.6	804.2	62.1	823.9	10.5	818.7	16.9
67	0.0807	0.0023	0.1018	0.0024	1.1335	0.0341	0.0405	0.00102	23.1	1214.4	27.5	625.1	7.1	769.4	8.1
68	0.1705	0.0049	0.5008	0.0123	11.7791	0.3588	0.1520	0.00378	1.2	2562.9	23.9	2617.2	26.4	2587.0	14.3
71	0.0696	0.0020	0.1555	0.0037	1.4914	0.0464	0.0485	0.00132	0.5	915.6	30.0	931.5	10.3	926.9	9.5
72	0.0616	0.0022	0.1144	0.0028	0.9715	0.0358	0.0362	0.00098	1.3	658.6	37.8	698.5	8.1	689.3	9.2
73	0.0597	0.0023	0.1037	0.0025	0.8534	0.0334	0.0338	0.00088	1.5	592.9	40.3	635.9	7.4	626.5	9.2
74	0.1727	0.0045	0.4584	0.0109	10.9154	0.3063	0.1290	0.00326	3.4	2583.5	21.6	2432.5	24.1	2516.0	13.1
75	0.0757	0.0029	0.1962	0.0049	2.0465	0.0801	0.0574	0.00202	2.0	1086.0	37.9	1154.6	13.1	1131.1	13.4
76	0.0738	0.0021	0.1254	0.0030	1.2756	0.0391	0.0434	0.00112	9.7	1035.5	28.8	761.4	8.6	834.9	8.7
80	0.0565	0.0034	0.1044	0.0028	0.8129	0.0482	0.0329	0.00102	5.6	470.2	64.7	640.0	8.1	604.1	13.5
81	0.0608	0.0026	0.0962	0.0024	0.8065	0.0347	0.0309	0.00078	1.4	631.2	45.0	592.3	7.0	600.5	9.8
82	0.0666	0.0023	0.1309	0.0032	1.2018	0.0436	0.0414	0.00118	1.0	824.2	36.2	793.1	9.1	801.4	10.1
85	0.0559	0.0030	0.0975	0.0025	0.7518	0.0404	0.0309	0.00118	5.1	447.8	58.3	599.9	7.4	569.2	11.7
86	0.0661	0.0022	0.1336	0.0032	1.2173	0.0417	0.0413	0.00112	0.0	808.7	34.0	808.3	9.2	808.5	9.5
88	0.0513	0.0058	0.0046	0.0001	0.0325	0.0036	0.0015	0.00008	10.2	256.0	123.7	29.5	0.5	32.5	1.8
89	0.0647	0.0043	0.1202	0.0033	1.0722	0.0703	0.0401	0.00246	1.1	763.7	68.2	731.9	9.6	739.8	17.2
90	0.0578	0.0116	0.1123	0.0049	0.8958	0.1780	-0.0062	0.10424	5.3	523.2	206.9	686.2	14.3	649.5	47.7
91	0.1669	0.0045	0.4226	0.0101	9.7260	0.2804	0.1264	0.00346	6.0	2526.9	22.5	2272.1	22.9	2409.2	13.3
93	0.0621	0.0021	0.1066	0.0026	0.9129	0.0325	0.0326	0.0009	0.8	676.8	36.2	653.2	7.5	658.6	8.6
94	0.0579	0.0020	0.0902	0.0022	0.7197	0.0252	0.0281	0.0008	1.1	525.1	36.8	556.5	6.4	550.5	7.4
95	0.0525	0.0040	0.0045	0.0001	0.0326	0.0024	0.0016	0.00006	12.4	305.1	83.7	29.0	0.4	32.6	1.2
96	0.1305	0.0034	0.2590	0.0061	4.6590	0.1319	0.0896	0.00226	18.5	2104.1	22.9	1484.7	15.7	1759.9	11.8
97	0.0607	0.0017	0.1029	0.0025	0.8611	0.0263	0.0236	0.00074	0.1	629.0	30.6	631.2	7.2	630.7	7.2
98	0.0650	0.0064	0.1043	0.0033	0.9354	0.0901	0.0327	0.00112	4.8	775.8	99.6	639.5	9.8	670.5	23.6
99	0.2723	0.0068	0.5002	0.0118	18.7819	0.5099	0.1286	0.00314	15.9	3319.3	19.4	2614.6	25.4	3030.7	13.1
100	0.3201	0.0079	0.6631	0.0157	29.2644	0.7948	0.1791	0.00432	5.6	3570.1	19.0	3279.2	30.5	3462.4	13.3
102	0.0633	0.0034	0.1112	0.0029	0.9706	0.0524	0.0361	0.00146	1.3	718.0	56.3	679.7	8.5	688.8	13.5
103	0.0612	0.0025	0.1001	0.0025	0.8442	0.0356	0.0335	0.00098	1.1	645.8	43.9	614.7	7.3	621.4	9.8
104	0.0666	0.0025	0.1426	0.0035	1.3091	0.0504	0.0474	0.00144	1.1	824.2	38.6	859.5	9.9	849.7	11.1
108	0.0688	0.0027	0.1641	0.0041	1.5571	0.0624	0.0513	0.00148	2.6	893.8	40.0	979.2	11.3	953.3	12.4
109	0.0619	0.0023	0.1061	0.0026	0.9063	0.0352	0.0369	0.00134	0.8	672.2	40.1	650.1	7.6	655.1	9.4
110	0.1672	0.0049	0.4644	0.0113	10.7055	0.3285	0.1394	0.00354	1.6	2529.9	24.1	2458.8	25.0	2497.9	14.3

Table S3.2 Results of single grain zircon U-Pb ICP-MS analysis from Thera (Santorini), Greece

Grain no.	Measured ratios									Apparent ages (Ma)					
	$^{207}Pb/^{206}Pb$	2σ	$^{206}Pb/^{238}U$	2σ	$^{207}Pb/^{235}U$	2σ	$^{208}Pb/^{232}Th$	2σ	Discordance (%)	$^{207}Pb/^{206}Pb$	1σ	$^{206}Pb/^{238}U$	1σ	$^{207}Pb/^{235}U$	1σ
111	0.1355	0.0038	0.2535	0.0061	4.7346	0.1405	0.1006	0.00274	21.8	2170.0	24.1	1456.4	15.6	1773.4	12.4
112	0.0621	0.0020	0.0903	0.0022	0.7726	0.0258	0.0312	0.00084	4.3	675.8	33.6	557.3	6.4	581.2	7.4
114	0.0609	0.0023	0.0641	0.0016	0.5387	0.0205	0.0226	0.00066	9.2	637.2	39.3	400.6	4.7	437.6	6.8
116	0.0771	0.0024	0.1802	0.0043	1.9147	0.0625	0.0572	0.00166	1.7	1123.0	30.7	1067.9	11.8	1086.2	10.9
117	0.0848	0.0025	0.1643	0.0039	1.9195	0.0600	0.0550	0.00138	11.0	1309.8	28.5	980.4	10.9	1087.9	10.4
118	0.0732	0.0030	0.1779	0.0044	1.7954	0.0741	0.0543	0.00178	1.1	1019.6	40.5	1055.3	12.2	1043.8	13.5
119	0.0650	0.0028	0.1298	0.0033	1.1642	0.0508	0.0402	0.00106	0.4	775.3	44.6	787.0	9.3	783.9	11.9
125	0.0751	0.0022	0.1786	0.0043	1.8491	0.0571	0.0560	0.00178	0.4	1071.0	29.0	1059.3	11.7	1063.1	10.2
127	0.0790	0.0024	0.0963	0.0023	1.0497	0.0336	0.0348	0.00088	22.9	1172.7	29.8	592.9	6.8	728.7	8.3
128	0.0695	0.0024	0.1311	0.0032	1.2567	0.0452	0.0422	0.00126	4.1	914.2	35.4	794.1	9.1	826.4	10.2
129	0.0575	0.0032	0.0975	0.0025	0.7733	0.0428	0.0313	0.00144	3.0	511.2	60.1	599.7	7.5	581.6	12.3
130	0.0590	0.0019	0.1041	0.0025	0.8468	0.0285	0.0320	0.00092	2.4	567.1	34.6	638.4	7.3	622.9	7.8
ALS05, 358981 E, 4027944 N															
2	0.0641	0.0022	0.1120	0.0028	0.9893	0.0353	0.0394	0.00108	2.1	743.7	35.3	684.3	8.1	698.4	9.0
4a	0.0684	0.0025	0.1026	0.0026	0.9673	0.0370	0.0454	0.00144	9.2	880.3	37.5	629.5	7.6	687.1	9.6
4b	0.0617	0.0025	0.0990	0.0025	0.8418	0.0345	0.0355	0.00124	1.9	663.0	42.0	608.4	7.3	620.2	9.5
5	0.0667	0.0024	0.1514	0.0038	1.3934	0.0519	0.0524	0.0016	2.5	829.7	36.8	908.8	10.6	886.1	11.0
6	0.0952	0.0028	0.1011	0.0025	1.3260	0.0417	0.0513	0.00138	38.1	1531.0	27.3	620.6	7.2	857.1	9.1
7	0.0580	0.0024	0.0859	0.0022	0.6863	0.0295	0.0395	0.00594	0.1	527.8	45.7	531.1	6.4	530.6	8.9
8	0.0721	0.0021	0.1603	0.0039	1.5930	0.0511	0.0570	0.00156	0.9	987.5	29.9	958.7	11.0	967.5	10.0
9	0.0622	0.0033	0.0571	0.0015	0.4892	0.0264	0.0268	0.00094	13.0	679.4	56.2	357.8	4.6	404.4	9.0
10	0.1595	0.0046	0.4625	0.0113	10.1740	0.3144	0.1392	0.00386	0.0	2450.7	24.1	2450.5	24.9	2450.7	14.3
11	0.0623	0.0019	0.1043	0.0026	0.8962	0.0297	0.0362	0.00108	1.6	685.5	32.9	639.4	7.5	649.7	8.0
12	0.0700	0.0039	0.1093	0.0030	1.0555	0.0592	0.3339	0.00932	9.4	928.8	56.4	668.9	8.6	731.6	14.6
13	0.1689	0.0049	0.4514	0.0111	10.5125	0.3287	0.1486	0.00416	3.3	2546.9	24.2	2401.2	24.6	2481.0	14.5
14	0.1826	0.0053	0.5166	0.0128	13.0091	0.4063	0.1569	0.00448	0.2	2676.7	23.7	2684.9	27.3	2680.3	14.7
15	0.0576	0.0020	0.0893	0.0022	0.7089	0.0262	0.0316	0.00092	1.3	512.7	38.7	551.5	6.6	544.1	7.8
16	0.0770	0.0035	0.1690	0.0044	1.7944	0.0825	0.0621	0.00198	3.6	1121.0	44.5	1006.8	12.2	1043.4	15.0
17	0.0682	0.0021	0.1443	0.0035	1.3577	0.0439	0.0500	0.0014	0.2	875.9	30.9	868.8	10.0	870.9	9.5
18	0.1626	0.0052	0.4760	0.0120	10.6709	0.3588	0.1481	0.0053	0.6	2482.9	26.6	2509.6	26.1	2494.9	15.6
19	0.1752	0.0050	0.4278	0.0104	10.3335	0.3162	0.1317	0.00362	7.4	2607.8	23.4	2295.8	23.6	2465.1	14.2
21	0.0624	0.0045	0.0768	0.0022	0.6605	0.0471	0.0107	0.00228	7.9	687.1	74.7	477.0	6.6	514.9	14.4
23	0.0722	0.0054	0.1766	0.0053	1.7577	0.1295	0.0626	0.00256	1.8	990.7	73.9	1048.5	14.5	1030.0	23.9
25	0.0598	0.0020	0.0929	0.0023	0.7658	0.0267	0.0331	0.00096	0.8	596.2	35.4	572.6	6.8	577.4	7.7
26	0.0613	0.0023	0.1037	0.0026	0.8760	0.0342	0.0366	0.00112	0.5	649.4	39.9	635.8	7.6	638.8	9.3
27	0.0684	0.0050	0.1053	0.0031	0.9932	0.0719	0.0375	0.00224	8.6	882.0	73.7	645.1	9.0	700.4	18.3
30	0.1128	0.0034	0.3059	0.0075	4.7590	0.1518	0.1051	0.003	3.3	1845.2	26.7	1720.7	18.5	1777.7	13.4
31	0.0998	0.0033	0.2837	0.0071	3.9027	0.1357	0.0998	0.0029	0.3	1619.7	30.5	1610.1	17.8	1614.2	14.1
32	0.0658	0.0031	0.1312	0.0034	1.1905	0.0572	0.0446	0.00184	0.2	800.8	48.9	794.5	9.8	796.2	13.3
33	0.0663	0.0046	0.1489	0.0043	1.3603	0.0941	0.0535	0.00268	2.5	814.6	71.1	894.7	12.1	872.0	20.2
34	0.1588	0.0051	0.4307	0.0107	9.4291	0.3192	0.1446	0.00436	3.1	2442.5	27.0	2309.0	24.2	2380.7	15.5
36	0.1098	0.0040	0.1141	0.0029	1.7268	0.0650	0.0616	0.00192	46.3	1795.6	32.8	696.4	8.4	1018.5	12.1
37	0.0663	0.0025	0.1402	0.0035	1.2805	0.0498	0.0455	0.00138	1.0	814.4	38.9	845.7	9.9	837.1	11.1
38	0.0755	0.0040	0.1799	0.0049	1.8721	0.0990	0.0599	0.00202	0.4	1080.8	51.9	1066.6	13.4	1071.3	17.5
39	0.0629	0.0028	0.1060	0.0027	0.9193	0.0410	0.0362	0.00182	1.9	703.9	45.9	649.7	7.9	662.0	10.8
40	0.1147	0.0037	0.2414	0.0060	3.8158	0.1296	0.0793	0.00234	14.5	1874.7	28.7	1393.7	15.6	1596.1	13.7
41	0.1675	0.0064	0.1168	0.0031	2.6975	0.1048	0.0723	0.00222	86.5	2533.0	31.7	712.0	8.8	1327.8	14.4
42	0.0666	0.0024	0.1241	0.0031	1.1389	0.0427	0.0418	0.00132	2.4	824.2	37.2	754.1	8.9	772.0	10.1
43	0.0718	0.0027	0.1692	0.0043	1.6756	0.0648	0.0638	0.0021	0.8	980.9	37.5	1007.8	11.8	999.3	12.3
45	0.0674	0.0032	0.1210	0.0032	1.1250	0.0540	0.0440	0.00172	4.0	851.5	48.5	736.1	9.1	765.3	12.9
46	0.1644	0.0051	0.4567	0.0113	10.3517	0.3432	0.1419	0.00418	1.7	2501.1	26.1	2425.1	25.0	2466.7	15.4
48	0.0644	0.0025	0.0959	0.0024	0.8513	0.0341	0.0302	0.0011	5.9	753.8	40.7	590.5	7.1	625.3	9.4
49	0.0621	0.0038	0.1129	0.0031	0.9664	0.0591	0.0425	0.00162	0.4	677.2	64.1	689.5	9.1	686.6	15.3
50	0.1476	0.0046	0.3088	0.0076	6.2852	0.2079	0.0999	0.0032	16.2	2318.4	26.5	1735.0	18.8	2016.4	14.5
51	0.1776	0.0055	0.5179	0.0128	12.6848	0.4192	0.1592	0.00472	1.3	2631.0	25.6	2690.3	27.2	2656.5	15.6
52	0.0544	0.0070	0.0043	0.0001	0.0321	0.0041	0.0016	0.00012	16.7	385.6	137.6	27.5	0.5	32.1	2.0
53a	0.0629	0.0026	0.1149	0.0029	0.9964	0.0415	0.0415	0.00138	0.1	704.6	42.7	701.1	8.4	702.0	10.6
53b	0.0677	0.0030	0.1232	0.0032	1.1497	0.0511	0.0464	0.0017	3.8	858.6	44.7	749.0	9.1	777.1	12.1
54	0.0705	0.0038	0.1518	0.0041	1.4768	0.0796	0.0605	0.00214	1.1	944.2	54.2	911.3	11.5	920.9	16.3
55	0.1148	0.0039	0.3243	0.0081	5.1351	0.1806	0.1050	0.00324	1.7	1877.2	30.0	1810.7	19.7	1841.9	14.9
56a	0.0603	0.0027	0.1123	0.0029	0.9341	0.0420	0.0369	0.00126	2.4	615.3	47.0	686.1	8.4	669.8	11.0
56b	0.0638	0.0031	0.0592	0.0016	0.5206	0.0258	0.0174	0.00064	14.8	735.3	51.2	370.6	4.7	425.6	8.6
57	0.0652	0.0032	0.0674	0.0018	0.6052	0.0295	0.0242	0.00086	14.3	779.2	50.0	420.3	5.3	480.5	9.3
58	0.0847	0.0033	0.1931	0.0049	2.2561	0.0900	0.0659	0.00238	5.3	1309.0	37.3	1138.3	13.3	1198.7	14.0
59	0.0587	0.0025	0.0863	0.0022	0.6980	0.0299	0.0309	0.00116	0.8	555.0	45.1	533.5	6.5	537.6	8.9
60	0.0639	0.0029	0.1253	0.0033	1.1043	0.0511	0.0455	0.00158	0.7	738.5	47.4	761.1	9.3	755.4	12.3
61	0.0595	0.0024	0.1057	0.0027	0.8664	0.0357	0.0367	0.00164	2.2	583.9	43.1	647.6	7.8	633.6	9.7
63	0.0633	0.0028	0.1194	0.0031	1.0424	0.0476	0.0393	0.00206	0.2	719.8	47.0	726.8	8.9	725.1	11.8
65	0.0739	0.0027	0.1765	0.0044	1.7977	0.0682	0.0568	0.00188	0.3	1038.4	36.6	1047.6	12.1	1044.6	12.4
66	0.1783	0.0060	0.4485	0.0111	11.0217	0.3859	0.1201	0.00378	5.7	2636.8	27.6	2388.4	24.7	2525.0	16.3
67	0.0607	0.0025	0.0964	0.0024	0.8064	0.0334	0.0374	0.0032	1.2	628.1	43.0	593.1	7.2	600.4	9.4
68	0.0648	0.0024	0.1322	0.0033	1.1813	0.0453	0.0450	0.0016	1.1	768.0	38.6	800.4	9.4	791.9	10.6
70	0.0625	0.0026	0.1018	0.0026	0.8768	0.0370	0.0330	0.00114	2.3	689.6	43.5	625.1	7.6	639.3	10.0
71	0.1299	0.0051	0.3909	0.0102	7.0004	0.2829	0.1310	0.00422	0.7	2096.3	34.2	2127.0	23.7	2111.5	18.0
72	0.1664	0.0062	0.4856	0.0126	11.1381	0.4292	0.1430	0.00504	0.7	2521.4	31.1	2551.5	27.4	2534.8	18.0
ALS08, 360641 E, 4025605 N															
1	0.0699	0.0021	0.1482	0.0036	1.4285	0.0459	0.0428	0.00112	1.1	925.4	30.8	890.8	10.0	900.9	9.6
2	0.0721	0.0024	0.1654	0.0040	1.6442	0.0565	0.0502	0.00134	0.0	987.8	33.1	986.9	11.1	987.3	10.8
4	0.0733	0.0027	0.1800	0.0045	1.8184	0.0701	0.0582	0.00182	1.4	1021.1	37.1	1067.0	12.2	1052.1	12.6
5	0.0679	0.0024	0.1225	0.0030	1.1468	0.0426	0.0386	0.00118	4.1	864.9	36.7	745.1	8.6	775.7	10.1
6	0.0662	0.0022	0.1264	0.0031	1.1536	0.0405	0.0531	0.00158	1.5	811.7	34.8	767.5	8.8	778.9	9.6
7	0.0739	0.0023	0.1689	0.0041	1.7209	0.0567	0.0509	0.00136	1.0	1038.3	31.3	1006.2	11.2	1016.4	10.6
8	0.0591	0.0035	0.1063	0.0028	0.8665	0.0513	0.0317	0.00084	2.7	570.6	63.1	651.4	8.3	633.7	13.9
9	0.0825	0.0024	0.1970	0.0047	2.2412	0.0683	0.0629	0.0015	3.0	1258.0	27.5	1159.0	12.7	1194.0	10.7
10	0.0594	0.0027	0.0892	0.0022	0.7310	0.0335	0.0284	0.00072	0.3	583.2	48.4	550.7	6.6	557.1	9.8
11	0.0731	0.0022	0.1689	0.0040	1.7013	0.0535	0.0514	0.00138	5.1	1015.3	29.8	1006.1	11.1	1009.0	10.1
12	0.0693	0.0029	0.1250	0.0031	1.1948	0.0511	0.0424	0.00116	2.8	908.6	42.7	759.2	9.0	798.2	11.8

Table S3.2 Results of single grain zircon U-Pb ICP-MS analysis from Thera (Santorini), Greece

Grain no.	Measured ratios									Apparent ages (Ma)					
	$^{207}Pb/^{206}Pb$	2σ	$^{206}Pb/^{238}U$	2σ	$^{207}Pb/^{235}U$	2σ	$^{208}Pb/^{232}Th$	2σ	Discordance (%)	$^{207}Pb/^{206}Pb$	1σ	$^{206}Pb/^{238}U$	1σ	$^{207}Pb/^{235}U$	1σ
13	0.0591	0.0024	0.1068	0.0027	0.8699	0.0367	0.0322	0.00146	1.0	570.6	44.3	653.9	7.7	635.5	10.0
14	0.0695	0.0031	0.1575	0.0040	1.5082	0.0677	0.0490	0.00184	1.5	912.2	44.9	942.8	11.1	933.7	13.7
15	0.0601	0.0021	0.0917	0.0022	0.7594	0.0275	0.0574	0.00328	0.1	606.5	37.1	565.3	6.6	573.7	7.9
16	0.0710	0.0019	0.1608	0.0038	1.5738	0.0450	0.0537	0.00136	3.0	956.8	26.8	961.2	10.6	959.9	8.9
17	0.0640	0.0034	0.1069	0.0028	0.9429	0.0498	0.0356	0.00134	2.3	741.3	54.6	654.5	8.1	674.4	13.0
18	0.0598	0.0019	0.0862	0.0021	0.7109	0.0242	0.0305	0.00144	5.6	596.2	34.8	533.1	6.1	545.3	7.2
19	0.0658	0.0037	0.1050	0.0028	0.9530	0.0535	0.0334	0.00112	3.3	800.9	57.8	643.6	8.1	679.6	13.9
20	0.0632	0.0032	0.1014	0.0026	0.8842	0.0444	0.0324	0.00112	7.5	715.8	52.1	622.8	7.6	643.3	12.0
21	0.0672	0.0025	0.1040	0.0025	0.9638	0.0366	0.0334	0.0009	2.6	844.7	37.9	637.7	7.4	685.3	9.5
22	0.0646	0.0026	0.1395	0.0035	1.2432	0.0517	0.0423	0.0013	2.6	761.6	42.3	842.1	9.8	820.3	11.7
24	0.0653	0.0025	0.1434	0.0035	1.2902	0.0500	0.0496	0.00152	3.9	782.4	39.0	863.7	10.0	841.4	11.1
25	0.0642	0.0035	0.1042	0.0027	0.9232	0.0509	0.0320	0.001	0.9	749.4	57.2	639.1	8.0	664.0	13.5
26	0.0591	0.0022	0.0965	0.0023	0.7853	0.0301	0.0313	0.00092	0.0	568.8	40.0	593.6	6.9	588.5	8.6
28	0.0695	0.0024	0.1522	0.0037	1.4575	0.0526	0.0461	0.0013	4.3	912.2	35.4	913.2	10.4	913.0	10.9
29	0.0686	0.0036	0.1729	0.0045	1.6349	0.0862	0.0500	0.00268	0.4	886.0	53.4	1028.1	12.5	983.7	16.6
30a	0.0969	0.0031	0.2775	0.0067	3.7062	0.1221	0.0837	0.00204	17.2	1564.6	29.3	1578.8	17.0	1572.7	13.2
30b	0.0810	0.0024	0.1237	0.0029	1.3824	0.0435	0.0619	0.00162	4.3	1222.4	29.0	751.9	8.5	881.5	9.3
31	0.0723	0.0028	0.1439	0.0035	1.4350	0.0562	0.0493	0.00144	0.5	995.3	38.4	866.6	10.0	903.7	11.7
32	0.0647	0.0019	0.1238	0.0029	1.1045	0.0341	0.0389	0.00096	4.4	765.5	30.3	752.1	8.4	755.5	8.2
33	0.0576	0.0017	0.0851	0.0020	0.6756	0.0211	0.0271	0.00066		513.6	32.4	526.4	6.0	524.1	6.4
34	0.0896	0.0036	0.2180	0.0055	2.6935	0.1099	0.0693	0.00224	0.6	1417.3	37.8	1271.2	14.6	1326.7	15.1
35	0.0747	0.0021	0.1751	0.0042	1.8026	0.0537	0.0561	0.0014	0.5	1058.9	28.1	1040.2	11.4	1046.4	9.7
37a	0.1634	0.0040	0.4671	0.0110	10.5248	0.2841	0.1396	0.0032	2.6	2491.4	20.7	2470.8	24.1	2482.1	12.5
37b	0.1664	0.0041	0.4529	0.0106	10.3919	0.2801	0.1327	0.00306	0.7	2521.9	20.6	2408.3	23.5	2470.3	12.5
38	0.0666	0.0025	0.1331	0.0033	1.2225	0.0467	0.0413	0.0011	5.2	825.9	38.2	805.4	9.3	810.9	10.7
39	0.0736	0.0032	0.1450	0.0037	1.4712	0.0649	0.0525	0.0015	1.5	1030.4	43.5	872.8	10.3	918.6	13.3
40	0.0612	0.0018	0.0983	0.0023	0.8293	0.0260	0.0311	0.00076	0.1	645.8	31.5	604.4	6.9	613.2	7.2
42	0.0698	0.0029	0.1543	0.0039	1.4849	0.0636	0.0504	0.00154	0.9	921.7	42.7	925.3	10.8	924.2	13.0
44	0.0618	0.0023	0.1136	0.0028	0.9682	0.0363	0.0347	0.0009	3.0	667.6	38.5	693.7	8.0	687.5	9.4
46	0.0650	0.0023	0.1123	0.0027	1.0055	0.0367	0.0361	0.00116	1.4	772.8	36.7	685.9	7.9	706.6	9.3
47	0.0741	0.0022	0.1678	0.0040	1.7153	0.0543	0.0518	0.00152	1.2	1045.1	30.0	1000.0	11.1	1014.3	10.2
48	0.0698	0.0021	0.1468	0.0035	1.4123	0.0442	0.0461	0.0012	4.9	921.6	30.4	883.1	9.8	894.1	9.3
49	0.0543	0.0040	0.0854	0.0023	0.6398	0.0470	0.0281	0.00096	3.1	384.9	80.2	528.3	7.0	502.2	14.5
50	0.0699	0.0028	0.1380	0.0034	1.3303	0.0536	0.0427	0.00122	6.3	925.9	40.1	833.4	9.7	859.0	11.7
51	0.0639	0.0026	0.0916	0.0023	0.8066	0.0336	0.0301	0.00128	2.1	736.9	42.7	565.0	6.7	600.6	9.4
52	0.0618	0.0026	0.0990	0.0024	0.8432	0.0357	0.0314	0.00096	1.4	667.0	44.0	608.3	7.2	620.9	9.8
53	0.0607	0.0020	0.1098	0.0026	0.9187	0.0317	0.0337	0.00086	0.8	628.8	35.3	671.3	7.6	661.7	8.4
54a	0.0649	0.0022	0.1226	0.0030	1.0965	0.0383	0.0412	0.00132	0.1	769.7	34.8	745.5	8.6	751.7	9.3
54b	0.0666	0.0035	0.1372	0.0036	1.2601	0.0669	0.0419	0.00156	0.7	826.2	54.3	828.6	10.2	828.0	15.0
55	0.0601	0.0021	0.0953	0.0023	0.7890	0.0289	0.0298	0.00086	1.3	605.7	37.9	586.7	6.8	590.6	8.2
56	0.0609	0.0022	0.0974	0.0024	0.8183	0.0308	0.0311	0.00084	1.0	636.5	38.9	599.3	6.9	607.1	8.6
57	0.1068	0.0040	0.3031	0.0076	4.4605	0.1690	0.0932	0.00244	0.6	1744.6	33.6	1706.5	18.8	1723.7	15.7
58	0.0720	0.0024	0.1691	0.0041	1.6791	0.0587	0.0524	0.00174	0.4	987.2	33.6	1007.0	11.3	1000.7	11.1
59	0.0678	0.0039	0.1454	0.0039	1.3599	0.0779	0.0439	0.00162	0.0	863.2	58.5	875.2	11.0	871.8	16.8
60	0.0722	0.0025	0.1665	0.0041	1.6576	0.0603	0.0498	0.0013	5.4	991.5	35.4	992.9	11.2	992.5	11.5
61	0.1745	0.0048	0.4434	0.0107	10.6713	0.3112	0.1314	0.00314	0.1	2601.5	22.6	2366.0	23.8	2494.9	13.5
62	0.0675	0.0020	0.1410	0.0033	1.3115	0.0409	0.0420	0.0011	1.6	852.1	30.4	850.2	9.4	850.8	9.0
63	0.0709	0.0035	0.1689	0.0044	1.6516	0.0827	0.0516	0.00148	0.1	955.5	50.2	1005.8	12.1	990.1	15.8
64	0.0734	0.0026	0.1725	0.0042	1.7453	0.0640	0.0522	0.00128	6.4	1024.1	35.6	1026.1	11.6	1025.4	11.8
65	0.0646	0.0044	0.0950	0.0027	0.8462	0.0576	0.0307	0.00094	3.4	761.6	70.8	584.9	7.8	622.5	15.9
66	0.0680	0.0024	0.1268	0.0031	1.1895	0.0432	0.0403	0.00118	0.2	869.1	36.1	769.8	8.8	795.7	10.0
67	0.0602	0.0024	0.0981	0.0024	0.8143	0.0333	0.0313	0.00096	2.4	610.3	42.9	603.4	7.0	604.9	9.3
68	0.0621	0.0027	0.0995	0.0025	0.8517	0.0379	0.0310	0.0009	3.5	678.0	46.3	611.2	7.3	625.6	10.4
69	0.0561	0.0021	0.0905	0.0022	0.7003	0.0270	0.0285	0.00084	2.7	457.4	41.0	558.4	6.5	539.0	8.1
70	0.0609	0.0028	0.0909	0.0023	0.7635	0.0352	0.0288	0.00078	2.4	637.0	48.4	560.7	6.7	576.0	10.1
71	0.0725	0.0027	0.1548	0.0038	1.5483	0.0598	0.0503	0.00126	1.3	1001.0	37.9	927.9	10.6	949.8	11.9
72	0.0628	0.0026	0.1086	0.0027	0.9406	0.0395	0.0341	0.00096	6.8	701.9	43.3	664.5	7.9	673.2	10.3
73	0.0725	0.0026	0.1326	0.0032	1.3254	0.0490	0.0421	0.00124	4.1	1000.3	36.2	802.5	9.2	856.9	10.7
74	0.0677	0.0037	0.1216	0.0032	1.1349	0.0617	0.0383	0.00116	5.7	859.7	55.5	739.5	9.2	770.1	14.7
75	0.1078	0.0036	0.2734	0.0067	4.0649	0.1419	0.0937	0.00268	1.3	1762.8	30.6	1558.2	17.0	1647.3	14.2
76	0.0601	0.0025	0.1055	0.0026	0.8744	0.0372	0.0323	0.00108	1.0	608.6	44.7	646.3	7.6	637.9	10.1
77	0.0643	0.0019	0.1181	0.0028	1.0466	0.0323	0.0368	0.0009	4.3	750.1	30.7	719.8	8.0	727.2	8.0
78	0.0485	0.0055	0.0043	0.0001	0.0290	0.0032	0.0013	0.00008	1.9	124.0	127.3	27.9	0.4	29.1	1.6
79	0.0687	0.0027	0.1378	0.0034	1.3052	0.0517	0.0435	0.00126	9.6	889.3	39.5	832.2	9.7	848.0	11.4
80	0.1054	0.0029	0.2417	0.0057	3.5119	0.1030	0.0704	0.00182	5.1	1721.2	25.2	1395.3	14.8	1529.9	11.6
81	0.1101	0.0030	0.2848	0.0067	4.3241	0.1247	0.0850	0.00214	3.4	1801.3	24.4	1615.4	16.8	1698.0	11.9
82	0.0634	0.0021	0.1017	0.0024	0.8886	0.0301	0.0332	0.0009	1.9	719.9	34.2	624.6	7.1	645.6	8.1
83	0.0614	0.0032	0.0976	0.0025	0.8261	0.0434	0.0304	0.00096	0.4	653.9	55.4	600.0	7.4	611.5	12.1
84	0.0632	0.0027	0.1157	0.0029	1.0083	0.0436	0.0409	0.00154	0.3	715.7	44.8	705.5	8.3	708.0	11.0
85	0.0620	0.0026	0.1088	0.0027	0.9305	0.0390	0.0331	0.00098	1.8	675.0	43.5	665.7	7.8	667.9	10.3
86	0.0749	0.0046	0.1694	0.0047	1.7494	0.1066	0.0506	0.00194	1.4	1065.2	60.6	1009.0	13.0	1026.9	19.7
87	0.0598	0.0023	0.1042	0.0026	0.8596	0.0342	0.0334	0.00108	0.6	597.6	41.6	638.9	7.5	629.9	9.3
88	0.0603	0.0045	0.0973	0.0027	0.8091	0.0592	0.0296	0.00116	4.9	615.0	78.0	598.5	8.1	601.9	16.6
90	0.0685	0.0038	0.1221	0.0032	1.1533	0.0642	0.0386	0.00158	0.6	884.6	56.7	742.4	9.3	778.8	15.1
91	0.0667	0.0024	0.1340	0.0032	1.2321	0.0450	0.0397	0.00146	7.2	827.9	36.6	810.7	9.2	815.3	10.2
92	0.0651	0.0023	0.0939	0.0023	0.8422	0.0312	0.0275	0.00074	0.5	776.0	37.5	578.5	6.7	620.4	8.6
93	0.0609	0.0026	0.1012	0.0025	0.8497	0.0362	0.0313	0.00096	0.5	635.7	44.6	621.4	7.3	624.5	9.9
95	0.0608	0.0027	0.1003	0.0025	0.8403	0.0375	0.0316	0.00092	18.8	631.3	46.9	616.0	7.3	619.3	10.3
96	0.1599	0.0044	0.3175	0.0075	7.0009	0.2047	0.1017	0.00258	1.0	2454.9	23.1	1777.4	18.4	2111.5	13.0
97a	0.1280	0.0037	0.3702	0.0088	6.5324	0.1998	0.1097	0.00286	10.3	2070.5	25.4	2030.1	20.7	2050.3	13.5
97b	0.1256	0.0037	0.3723	0.0090	6.4476	0.1997	0.1059	0.0029	1.2	2037.6	25.7	2040.0	21.1	2038.8	13.6
99	0.0827	0.0037	0.1595	0.0041	1.8196	0.0821	0.0547	0.00196	0.4	1263.2	43.2	954.0	11.3	1052.5	14.8
100	0.1866	0.0058	0.5194	0.0127	13.3638	0.4307	0.1448	0.00368	0.3	2712.6	25.3	2696.5	27.0	2705.7	15.2
102	0.0605	0.0043	0.1031	0.0029	0.8605	0.0607	0.0327	0.00126	2.5	623.1	75.0	632.4	8.4	630.4	16.6
103	0.1147	0.0033	0.3182	0.0075	5.0314	0.1524	0.0966	0.00256	3.6	1875.1	25.8	1780.8	18.3	1824.6	12.8
104	0.1798	0.0052	0.4716	0.0112	11.6925	0.3564	0.1384	0.00362	1.0	2651.1	24.0	2490.7	24.5	2580.1	14.3
105	0.0649	0.0035	0.1215	0.0032	1.0866	0.0583	0.0395	0.00134	6.3	769.5	55.6	739.3	9.1	746.9	14.2

Table S3.2 Results of single grain zircon U-Pb ICP-MS analysis from Thera (Santorini), Greece

Grain no.	Measured ratios									Apparent ages (Ma)					
	$^{207}Pb/^{206}Pb$	2σ	$^{206}Pb/^{238}U$	2σ	$^{207}Pb/^{235}U$	2σ	$^{208}Pb/^{232}Th$	2σ	Discordance (%)	$^{207}Pb/^{206}Pb$	1σ	$^{206}Pb/^{238}U$	1σ	$^{207}Pb/^{235}U$	1σ
106	0.1233	0.0036	0.3151	0.0075	5.3567	0.1634	0.0881	0.00226	0.3	2004.2	25.5	1765.9	18.3	1878.0	13.1
107	0.0585	0.0020	0.0873	0.0021	0.7036	0.0245	0.0276	0.0008	0.3	547.1	36.5	539.4	6.2	540.9	7.3
ALS11, 360636 E, 4025605 N															
1	0.0497	0.0029	0.0374	0.0010	0.2563	0.0151	0.0127	0.00036	2.1	182.3	67.4	236.6	3.0	231.7	6.1
02a	0.0512	0.0021	0.0351	0.0009	0.2480	0.0104	0.0117	0.00034	1.1	250.4	46.6	222.5	2.7	225.0	4.2
02b	0.0524	0.0032	0.0378	0.0010	0.2732	0.0164	0.0117	0.00036	2.4	301.6	67.1	239.5	3.1	245.3	6.5
3	0.0514	0.0028	0.0366	0.0009	0.2594	0.0143	0.0122	0.00036	1.0	257.1	62.0	231.9	2.9	234.2	5.8
4	0.1139	0.0033	0.3420	0.0082	5.3730	0.1637	0.1072	0.0029	0.8	1863.0	25.7	1896.5	19.7	1880.6	13.0
5	0.0506	0.0022	0.0382	0.0009	0.2663	0.0119	0.0129	0.00034	0.7	224.1	49.9	241.4	2.9	239.7	4.8
7	0.0666	0.0038	0.0380	0.0010	0.3487	0.0199	0.0128	0.00038	26.4	825.1	58.7	240.3	3.2	303.8	7.5
8	0.0568	0.0021	0.0359	0.0009	0.2807	0.0107	0.0123	0.00032	10.6	481.2	40.8	227.2	2.7	251.2	4.2
9	0.0524	0.0023	0.0368	0.0009	0.2659	0.0122	0.0135	0.00038	2.8	304.4	50.2	232.8	2.9	239.4	4.9
10	0.0498	0.0025	0.0370	0.0009	0.2539	0.0129	0.0117	0.00034	1.9	184.3	57.8	234.2	2.9	229.8	5.2
11	0.0661	0.0025	0.1288	0.0032	1.1750	0.0462	0.0399	0.00114	1.0	810.8	39.7	781.3	9.1	789.0	10.8
12a	0.0674	0.0023	0.0947	0.0023	0.8803	0.0307	0.0370	0.00104	9.9	849.9	34.5	583.5	6.7	641.1	8.3
12b	0.0515	0.0019	0.0380	0.0009	0.2698	0.0102	0.0126	0.0004	1.0	264.4	41.5	240.3	2.9	242.6	4.1
13	0.0523	0.0033	0.0380	0.0010	0.2738	0.0171	0.0123	0.00038	2.3	299.5	69.6	240.1	3.1	245.7	6.8
15	0.0699	0.0028	0.1650	0.0041	1.5899	0.0650	0.0494	0.00162	1.9	925.0	40.6	984.5	11.4	966.2	12.7
18	0.0615	0.0019	0.1022	0.0024	0.8670	0.0281	0.0334	0.00092	1.0	657.1	32.7	627.4	7.1	633.9	7.6
19	0.0582	0.0047	0.0880	0.0026	0.7056	0.0560	0.0270	0.0013	0.3	535.7	85.9	543.6	7.6	542.1	16.7
20	0.0619	0.0022	0.1061	0.0026	0.9053	0.0330	0.0326	0.00096	0.7	671.0	37.3	649.9	7.5	654.5	8.8
21	0.0479	0.0033	0.0372	0.0010	0.2450	0.0168	0.0116	0.00036	5.4	90.6	80.5	235.1	3.1	222.5	6.8
22	0.0746	0.0026	0.1719	0.0042	1.7675	0.0641	0.0548	0.00152	1.1	1057.4	35.2	1022.4	11.6	1033.6	11.8
23	0.0503	0.0031	0.0370	0.0010	0.2568	0.0160	0.0120	0.00038	1.0	209.2	71.0	234.4	3.1	232.1	6.5
24	0.0622	0.0022	0.1187	0.0029	1.0174	0.0373	0.0366	0.00108	1.5	679.8	37.4	723.2	8.4	712.6	9.4
25	0.0710	0.0035	0.1502	0.0039	1.4693	0.0721	0.0463	0.00142	1.8	956.3	49.2	901.9	10.9	917.8	14.8
26	0.0502	0.0020	0.0381	0.0009	0.2641	0.0107	0.0122	0.00034	1.4	205.3	45.2	241.3	2.9	237.9	4.3
27	0.0517	0.0026	0.0371	0.0009	0.2646	0.0133	0.0120	0.00034	1.4	271.8	56.3	235.1	2.9	238.4	5.4
28	0.0512	0.0021	0.0370	0.0009	0.2611	0.0107	0.0120	0.00032	0.7	251.5	45.5	234.0	2.8	235.6	4.3
29	0.0498	0.0032	0.0361	0.0010	0.2477	0.0157	0.0120	0.0004	1.7	185.6	72.2	228.5	3.0	224.7	6.4
30	0.0496	0.0021	0.0369	0.0009	0.2521	0.0109	0.0120	0.00034	2.3	173.8	48.7	233.6	2.8	228.3	4.4
31	0.0819	0.0031	0.1089	0.0027	1.2287	0.0480	0.0649	0.00224	22.1	1241.9	36.8	666.3	7.9	813.8	10.9
32	0.0498	0.0020	0.0372	0.0009	0.2558	0.0105	0.0119	0.00032	1.9	187.5	46.1	235.7	2.9	231.3	4.3
33	0.0669	0.0027	0.1263	0.0032	1.1643	0.0488	0.0444	0.00262	2.3	834.6	42.3	766.4	9.0	783.9	11.4
34	0.0513	0.0020	0.0375	0.0009	0.2649	0.0104	0.0120	0.00032	0.6	253.6	43.2	237.1	2.8	238.6	4.2
35	0.0538	0.0023	0.0365	0.0009	0.2707	0.0116	0.0118	0.00034	5.2	361.6	46.8	231.2	2.8	243.3	4.6
36	0.0558	0.0042	0.0362	0.0010	0.2788	0.0206	0.0119	0.0004	8.8	444.9	80.9	229.4	3.1	249.7	8.2
37	0.1771	0.0053	0.4783	0.0116	11.6797	0.3688	0.1402	0.00408	2.3	2626.3	24.7	2519.9	25.4	2579.1	14.8
38	0.0527	0.0026	0.0369	0.0009	0.2683	0.0135	0.0122	0.00036	3.3	317.4	55.7	233.6	2.9	241.3	5.4
39a	0.0531	0.0037	0.0367	0.0010	0.2686	0.0184	0.0122	0.00042	4.0	332.6	76.4	232.4	3.1	241.6	7.4
39b	0.0490	0.0029	0.0375	0.0010	0.2534	0.0148	0.0124	0.00038	3.4	147.7	67.0	237.4	3.0	229.3	6.0
40	0.0640	0.0028	0.1131	0.0028	0.9980	0.0442	0.0378	0.0014	1.8	742.7	45.5	690.5	8.2	702.8	11.2
41	0.0762	0.0037	0.1800	0.0047	1.8911	0.0911	0.0530	0.00216	1.1	1101.3	47.2	1066.7	12.9	1078.0	16.0
42a	0.0570	0.0025	0.0903	0.0023	0.7098	0.0319	0.0284	0.00134	2.3	491.6	48.2	557.3	6.7	544.6	9.5
42b	0.0586	0.0019	0.0936	0.0023	0.7562	0.0258	0.0297	0.0018	0.9	552.3	35.3	576.9	6.6	571.8	7.5
43a	0.1762	0.0051	0.4955	0.0119	12.0365	0.3713	0.1390	0.00382	0.5	2617.6	24.0	2594.2	25.6	2607.3	14.5
43b	0.1805	0.0052	0.4946	0.0119	12.3078	0.3792	0.1437	0.00386	1.5	2657.6	23.8	2590.5	25.7	2628.2	14.5
44	0.0672	0.0023	0.1303	0.0032	1.2068	0.0423	0.0422	0.00122	1.8	843.5	34.7	789.6	9.0	803.7	9.7
45	0.0659	0.0034	0.0369	0.0010	0.3357	0.0172	0.0132	0.0004	25.7	804.1	52.7	233.9	3.0	293.9	6.6
46	0.2937	0.0090	0.7023	0.0173	28.4348	0.9182	0.1852	0.00564	0.1	3437.4	23.6	3429.4	32.7	3434.2	15.8
47	0.0520	0.0024	0.0377	0.0009	0.2701	0.0128	0.0122	0.00036	1.8	283.4	52.8	238.6	2.9	242.8	5.1
48	0.0517	0.0021	0.0370	0.0009	0.2635	0.0109	0.0121	0.00034	1.5	271.4	45.6	234.1	2.8	237.5	4.4
49	0.0513	0.0030	0.0365	0.0010	0.2582	0.0149	0.0118	0.00036	0.9	254.6	64.8	231.2	3.0	233.2	6.0
51	0.0505	0.0026	0.0376	0.0010	0.2615	0.0136	0.0119	0.00036	0.7	219.0	58.9	237.6	3.0	235.9	5.5
52	0.0588	0.0028	0.0380	0.0010	0.3079	0.0146	0.0125	0.00036	13.4	560.4	50.4	240.3	3.0	272.6	5.7
53	0.0509	0.0023	0.0369	0.0009	0.2585	0.0119	0.0120	0.00036	0.0	235.8	51.5	233.3	2.9	233.4	4.8
54	0.0543	0.0033	0.0373	0.0010	0.2789	0.0169	0.0117	0.00038	5.9	383.9	66.6	235.8	3.1	249.8	6.7
55	0.0536	0.0028	0.0369	0.0009	0.2723	0.0143	0.0118	0.00036	4.8	353.8	58.0	233.4	2.9	244.6	5.7
56	0.0497	0.0027	0.0383	0.0010	0.2620	0.0144	0.0122	0.00038	2.4	179.9	62.4	242.1	3.1	236.3	5.8
57	0.0503	0.0026	0.0366	0.0009	0.2537	0.0133	0.0119	0.00036	0.9	208.9	59.3	231.6	2.9	229.6	5.4
58	0.0528	0.0030	0.0376	0.0010	0.2733	0.0154	0.0121	0.00036	3.2	320.0	62.7	237.7	3.0	245.3	6.1
59	0.0519	0.0025	0.0376	0.0009	0.2690	0.0130	0.0120	0.00034	1.7	281.7	53.9	237.9	2.9	241.9	5.2
60	0.0522	0.0025	0.0378	0.0010	0.2721	0.0130	0.0121	0.00036	2.1	293.1	53.3	239.3	3.0	244.3	5.2
61	0.0708	0.0031	0.1510	0.0038	1.4748	0.0655	0.0474	0.00168	1.5	952.8	44.2	906.7	10.8	920.1	13.4
62	0.0508	0.0024	0.0370	0.0009	0.2592	0.0125	0.0119	0.00034	0.0	233.7	54.1	234.1	2.9	234.0	5.0
64	0.0622	0.0025	0.1141	0.0028	0.9779	0.0401	0.0366	0.0012	0.6	680.3	42.3	696.5	8.2	692.5	10.3
65	0.0661	0.0035	0.0990	0.0026	0.9023	0.0473	0.0314	0.00132	7.3	810.9	53.8	608.3	7.6	653.0	12.6
67	0.0508	0.0019	0.0377	0.0009	0.2634	0.0103	0.0123	0.00038	0.3	230.0	43.5	238.2	2.9	237.4	4.2
70	0.0519	0.0028	0.0376	0.0010	0.2687	0.0144	0.0119	0.00036	1.6	279.5	60.0	237.9	3.0	241.7	5.8
71	0.0498	0.0030	0.0380	0.0010	0.2605	0.0159	0.0130	0.00042	2.1	185.6	69.7	240.2	3.1	235.1	6.4
72	0.0710	0.0031	0.1089	0.0028	1.0649	0.0466	0.0325	0.00136	10.5	956.3	43.5	666.3	8.0	736.2	11.5
73	0.1717	0.0053	0.4398	0.0107	10.4060	0.3389	0.1228	0.00346	5.2	2573.9	25.6	2349.9	23.9	2471.6	15.1
74	0.0496	0.0031	0.0393	0.0010	0.2681	0.0168	0.0121	0.0004	2.8	174.4	71.9	248.2	3.2	241.2	6.7
75	0.0506	0.0029	0.0373	0.0010	0.2599	0.0149	0.0118	0.00038	0.6	221.7	64.8	235.9	3.0	234.6	6.0
76	0.0539	0.0029	0.0360	0.0009	0.2669	0.0143	0.0118	0.00038	5.5	365.3	59.2	227.7	2.9	240.2	5.7
77	0.0510	0.0033	0.0372	0.0010	0.2618	0.0169	0.0120	0.0004	0.2	242.7	72.9	235.6	3.1	236.1	6.8
81	0.0646	0.0037	0.1187	0.0032	1.0559	0.0606	0.0413	0.00164	1.2	759.9	59.5	722.9	9.2	731.8	15.0
82	0.0640	0.0028	0.0972	0.0025	0.8568	0.0382	0.0319	0.00098	5.1	740.2	45.8	597.9	7.2	628.4	10.5
83	0.0520	0.0023	0.0376	0.0009	0.2693	0.0121	0.0122	0.00038	1.8	284.9	49.7	237.8	2.9	242.1	4.8
84	0.0675	0.0035	0.1645	0.0043	1.5301	0.0798	0.0506	0.00186	4.0	853.3	53.1	981.7	12.0	942.5	16.0
86	0.0566	0.0021	0.0935	0.0023	0.7291	0.0284	0.0298	0.00088	3.5	473.8	41.7	576.3	6.8	556.0	8.3
87	0.0521	0.0021	0.0364	0.0009	0.2615	0.0109	0.0117	0.00034	2.2	288.2	45.8	230.7	2.8	235.8	4.4
88	0.0718	0.0024	0.1602	0.0039	1.5839	0.0558	0.0531	0.00174	0.6	979.4	34.1	957.7	10.8	963.9	11.0
89	0.0536	0.0027	0.0386	0.0010	0.2853	0.0145	0.0126	0.00038	4.3	352.8	56.2	244.3	3.1	254.8	5.7
90	0.1215	0.0046	0.1987	0.0050	3.3271	0.1290	0.1163	0.0037	27.3	1978.3	33.4	1168.3	13.5	1487.4	15.1
91	0.0640	0.0037	0.0376	0.0010	0.3314	0.0189	0.0134	0.00046	22.2	741.1	59.5	237.8	3.1	290.7	7.2
92	0.0548	0.0020	0.0343	0.0008	0.2593	0.0098	0.0122	0.00038	7.6	404.0	40.4	217.6	2.6	234.1	4.0

Table S3.2 Results of single grain zircon U-Pb ICP-MS analysis from Thera (Santorini), Greece

Grain no.	Measured ratios									Apparent ages (Ma)					
	$^{207}Pb/^{206}Pb$	2σ	$^{206}Pb/^{238}U$	2σ	$^{207}Pb/^{235}U$	2σ	$^{208}Pb/^{232}Th$	2σ	Discordance (%)	$^{207}Pb/^{206}Pb$	1σ	$^{206}Pb/^{238}U$	1σ	$^{207}Pb/^{235}U$	1σ
93	0.0600	0.0026	0.1039	0.0026	0.8592	0.0372	0.0327	0.00098	1.2	603.0	45.5	637.4	7.6	629.7	10.2
94	0.0509	0.0031	0.0379	0.0010	0.2660	0.0162	0.0122	0.00042	0.2	234.8	68.9	240.1	3.1	239.5	6.5
97	0.0514	0.0026	0.0384	0.0010	0.2720	0.0138	0.0124	0.0004	0.6	257.8	57.0	242.9	3.1	244.3	5.5
99	0.0508	0.0024	0.0366	0.0009	0.2561	0.0123	0.0113	0.00036	0.1	231.7	54.0	231.7	2.9	231.5	5.0
100	0.0503	0.0021	0.0390	0.0010	0.2705	0.0117	0.0122	0.0004	1.5	209.3	48.4	246.7	3.0	243.1	4.7
101	0.0515	0.0029	0.0371	0.0010	0.2633	0.0146	0.0120	0.00038	1.1	263.6	62.3	234.8	3.0	237.3	5.9
102	0.0535	0.0032	0.0360	0.0010	0.2651	0.0158	0.0129	0.00042	4.8	347.8	66.2	227.9	3.0	238.8	6.4
103	0.0534	0.0026	0.0362	0.0009	0.2663	0.0129	0.0129	0.0004	4.7	347.1	53.0	228.9	2.9	239.7	5.2
104	0.0539	0.0028	0.0367	0.0009	0.2727	0.0144	0.0128	0.00042	5.4	368.5	58.1	232.3	3.0	244.9	5.8
105	0.0502	0.0028	0.0375	0.0010	0.2594	0.0145	0.0123	0.0004	1.3	202.8	63.6	237.4	3.0	234.2	5.9
106	0.0744	0.0030	0.1765	0.0045	1.8094	0.0755	0.0566	0.00192	0.1	1052.6	40.6	1047.7	12.2	1048.8	13.7
107	0.0531	0.0028	0.0360	0.0009	0.2633	0.0138	0.0123	0.00038	4.2	334.5	58.2	227.7	2.9	237.3	5.6
ALS13, 363067 E, 4025097 N															
1a	0.0641	0.0041	0.0823	0.0023	0.7265	0.0468	0.0305	0.00138	8.8	743.3	66.7	509.6	7.0	554.5	13.8
1b	0.0541	0.0023	0.0619	0.0016	0.4623	0.0205	0.0174	0.0013	0.4	376.4	47.8	387.4	4.9	385.9	7.1
2	0.0662	0.0029	0.1203	0.0032	1.0978	0.0501	0.0421	0.00166	2.7	812.2	45.9	732.3	9.1	752.3	12.1
3	0.0556	0.0039	0.0424	0.0012	0.3250	0.0225	0.0145	0.00064	6.8	437.6	75.3	267.5	3.7	285.8	8.6
5	0.0570	0.0030	0.0507	0.0014	0.3989	0.0210	0.0180	0.00074	6.8	491.5	56.9	319.1	4.2	340.9	7.6
6	0.1212	0.0051	0.3627	0.0096	6.0636	0.2642	0.1156	0.00436	0.5	1974.6	37.0	1994.9	22.6	1985.0	19.0
8	0.0548	0.0025	0.0626	0.0017	0.4731	0.0221	0.0218	0.00084	0.5	403.8	49.8	391.5	5.0	393.3	7.6
9	0.1759	0.0074	0.4737	0.0125	11.4881	0.5013	0.1447	0.0054	2.6	2614.4	34.6	2499.7	27.3	2563.6	20.4
11	0.0540	0.0090	0.0156	0.0006	0.1162	0.0191	0.0061	0.00046	11.7	369.7	177.6	99.9	2.0	111.6	8.7
12	0.0564	0.0026	0.0971	0.0025	0.7555	0.0351	0.0320	0.00106	4.4	468.6	50.2	597.6	7.4	571.4	10.2
13	0.0494	0.0021	0.0414	0.0011	0.2815	0.0122	0.0143	0.00042	3.6	165.4	48.4	261.2	3.3	251.8	4.8
14	0.0755	0.0030	0.1787	0.0046	1.8593	0.0760	0.0574	0.0019	0.6	1081.0	39.3	1059.9	12.6	1066.7	13.5
15	0.0374	0.0062	0.0044	0.0002	0.0229	0.0038	0.0015	0.0001	19.6	0.1	0.0	28.6	0.5	23.0	1.9
16	0.0583	0.0033	0.0878	0.0024	0.7056	0.0397	0.0306	0.00136	0.0	541.0	60.7	542.4	7.1	542.2	11.8
17	0.0570	0.0027	0.0704	0.0018	0.5530	0.0266	0.0246	0.00096	2.0	491.0	52.2	438.4	5.5	447.0	8.7
18	0.0602	0.0064	0.0155	0.0005	0.1286	0.0134	0.0064	0.00034	23.9	611.2	110.5	99.1	1.6	122.8	6.0
19	0.0503	0.0020	0.0468	0.0012	0.3248	0.0133	0.0157	0.00048	3.2	209.7	45.6	295.0	3.6	285.6	5.1
20	0.0538	0.0019	0.0465	0.0012	0.3450	0.0130	0.0160	0.00046	2.6	361.3	40.5	293.3	3.6	301.0	4.9
22	0.0493	0.0038	0.0175	0.0005	0.1187	0.0090	0.0067	0.0003	2.1	163.2	86.6	111.6	1.6	113.9	4.1
23	0.0599	0.0022	0.1150	0.0029	0.9490	0.0359	0.0376	0.00122	3.4	599.1	39.0	701.5	8.3	677.6	9.4
24	0.0521	0.0026	0.0509	0.0013	0.3653	0.0187	0.0181	0.00066	1.2	288.3	56.8	320.0	4.1	316.2	6.9
25	0.0542	0.0024	0.0516	0.0013	0.3857	0.0173	0.0167	0.00062	2.1	379.2	48.8	324.4	4.1	331.2	6.3
26	0.0553	0.0029	0.0495	0.0013	0.3771	0.0199	0.0177	0.00074	4.4	423.7	56.9	311.3	4.0	324.9	7.3
27	0.0516	0.0028	0.0353	0.0009	0.2511	0.0136	0.0130	0.00046	1.7	267.6	60.7	223.6	2.9	227.4	5.5
29	0.0527	0.0024	0.0515	0.0013	0.3741	0.0170	0.0192	0.0006	0.4	314.1	50.0	323.9	4.0	322.7	6.3
30	0.0532	0.0026	0.0513	0.0013	0.3766	0.0187	0.0151	0.00058	0.6	337.8	54.8	322.7	4.1	324.6	6.9
31	0.0484	0.0044	0.0182	0.0005	0.1216	0.0110	0.0057	0.00032	0.0	117.4	104.4	116.5	1.7	116.5	5.0
32	0.0595	0.0021	0.1012	0.0025	0.8303	0.0303	0.0317	0.00096	1.2	586.3	37.6	621.4	7.3	613.8	8.4
33	0.0521	0.0025	0.0405	0.0010	0.2911	0.0139	0.0137	0.00054	1.4	291.5	52.9	256.0	3.3	259.5	5.5
35	0.0619	0.0023	0.0516	0.0013	0.4401	0.0170	0.0188	0.00056	14.3	671.3	39.6	324.1	3.9	370.3	6.0
36	0.0534	0.0020	0.0520	0.0013	0.3824	0.0147	0.0176	0.00056	0.7	344.5	41.5	326.6	4.0	328.8	5.4
37	0.0528	0.0026	0.0393	0.0010	0.2860	0.0143	0.0136	0.00046	2.8	319.7	55.3	248.5	3.2	255.4	5.7
38	0.0531	0.0021	0.0535	0.0013	0.3914	0.0161	0.0181	0.00058	0.1	332.6	44.8	335.8	4.1	335.4	5.9
39	0.0532	0.0022	0.0574	0.0014	0.4208	0.0176	0.0196	0.00066	0.9	336.4	45.4	359.8	4.4	356.6	6.3
40	0.0552	0.0030	0.0478	0.0013	0.3642	0.0201	0.0151	0.00054	4.7	421.4	59.7	301.2	3.9	315.4	7.5
41	0.0575	0.0027	0.0666	0.0018	0.5279	0.0255	0.0327	0.00122	3.5	509.8	52.0	415.7	5.3	430.4	8.5
42	0.0506	0.0031	0.0378	0.0010	0.2636	0.0162	0.0127	0.00054	0.7	222.2	69.6	239.2	3.2	237.6	6.5
43	0.0504	0.0029	0.0390	0.0010	0.2706	0.0154	0.0140	0.00056	1.3	212.4	64.4	246.4	3.2	243.1	6.1
44	0.0518	0.0039	0.0478	0.0014	0.3414	0.0254	0.0155	0.0007	1.0	275.4	83.6	301.2	4.2	298.2	9.6
45	0.0603	0.0132	0.0289	0.0014	0.2402	0.0520	0.0124	0.00146	19.0	614.8	221.0	183.6	4.3	218.5	21.3
46	0.0562	0.0029	0.0404	0.0011	0.3129	0.0165	0.0115	0.00044	8.3	458.9	57.6	255.3	3.3	276.5	6.4
47	0.0545	0.0028	0.0498	0.0013	0.3738	0.0196	0.0165	0.0007	3.0	390.1	57.3	313.2	4.1	322.5	7.2
48	0.1269	0.0057	0.3965	0.0107	6.9366	0.3190	0.1210	0.0047	2.3	2055.0	39.0	2153.0	24.8	2103.3	20.4
49	0.0613	0.0027	0.0998	0.0026	0.8441	0.0376	0.0349	0.00124	1.3	651.1	46.3	613.4	7.5	621.4	10.4
51	0.0533	0.0037	0.0485	0.0012	0.3564	0.0244	0.0155	0.00066	1.4	342.7	76.4	305.2	3.8	309.5	9.1
52	0.0536	0.0031	0.0451	0.0011	0.3334	0.0190	0.0141	0.0005	2.7	353.8	63.9	284.4	3.4	292.1	7.3
53	0.1333	0.0037	0.3760	0.0084	6.9128	0.1952	0.1125	0.0027	2.1	2142.3	24.0	2057.6	19.7	2100.3	12.5
54	0.0804	0.0044	0.0524	0.0013	0.5810	0.0313	0.0224	0.00082	41.2	1205.8	53.0	329.4	4.1	465.1	10.0
55	0.0531	0.0044	0.0900	0.0024	0.6595	0.0538	0.0265	0.00122	7.5	334.5	90.8	555.7	7.2	514.3	16.5
56	0.0413	0.0045	0.0171	0.0005	0.0973	0.0105	0.0050	0.00022	13.7	0.1	0.0	109.2	1.5	94.2	4.8
57	0.0679	0.0052	0.0469	0.0013	0.4393	0.0328	0.0187	0.00086	25.0	865.0	76.9	295.7	3.9	369.7	11.6
58	0.0559	0.0023	0.0515	0.0012	0.3967	0.0164	0.0139	0.00044	4.9	449.0	45.1	323.4	3.7	339.2	6.0
59	0.1306	0.0034	0.3617	0.0081	6.5115	0.1748	0.1155	0.00288	2.9	2105.8	22.5	1990.4	19.1	2047.5	11.8
60	0.0549	0.0023	0.0736	0.0017	0.5564	0.0228	0.0229	0.00092	1.8	406.6	45.0	457.6	5.1	449.2	7.4
63	0.1124	0.0037	0.2801	0.0065	4.3417	0.1448	0.0878	0.0022	6.9	1838.8	29.7	1591.8	16.4	1701.3	13.8
64	0.0516	0.0016	0.0538	0.0012	0.3824	0.0118	0.0155	0.00038	2.6	266.5	34.3	337.7	3.7	328.8	4.3
65	0.0525	0.0024	0.0509	0.0012	0.3686	0.0171	0.0157	0.00052	0.5	307.7	52.1	320.2	3.6	318.6	6.3
66	0.0523	0.0017	0.0520	0.0012	0.3751	0.0124	0.0159	0.0004	1.0	299.2	36.6	326.8	3.6	323.4	4.6
67	0.0516	0.0025	0.0439	0.0010	0.3121	0.0151	0.0128	0.00038	0.4	265.7	54.7	277.0	3.2	275.8	5.8
68	0.0738	0.0023	0.1503	0.0034	1.5295	0.0481	0.0497	0.0014	4.4	1037.0	30.9	902.4	9.5	942.3	9.7
69	0.0621	0.0047	0.0459	0.0012	0.3929	0.0291	0.0169	0.00074	16.3	677.0	78.3	289.3	3.8	336.5	10.6
70	0.0505	0.0029	0.0423	0.0010	0.2945	0.0170	0.0129	0.0005	1.8	219.2	66.0	266.9	3.2	262.1	6.7
71	0.0519	0.0041	0.0333	0.0009	0.2384	0.0184	0.0104	0.00064	2.7	280.4	86.9	211.3	2.7	217.1	7.5
72	0.0535	0.0017	0.0544	0.0012	0.4012	0.0129	0.0166	0.00042	0.2	348.4	35.5	341.7	3.7	342.5	4.7
73	0.0569	0.0065	0.0496	0.0015	0.3894	0.0439	0.0159	0.00094	7.0	488.3	122.0	312.1	4.6	333.9	16.0
74	0.0489	0.0029	0.0524	0.0013	0.3535	0.0210	0.0156	0.00056	6.6	144.7	68.7	329.2	3.9	307.4	7.9
75	0.0552	0.0025	0.0716	0.0017	0.5445	0.0243	0.0229	0.00074	0.9	419.4	48.7	445.5	5.0	441.4	8.0
77	0.0519	0.0032	0.0430	0.0011	0.3076	0.0188	0.0128	0.0004	0.4	282.2	68.8	271.2	3.3	272.3	7.3
78	0.0741	0.0020	0.0453	0.0010	0.4626	0.0130	0.0205	0.0005	35.1	1042.7	27.4	285.7	3.1	386.1	4.5
79	0.0487	0.0040	0.0455	0.0012	0.3060	0.0247	0.0145	0.0006	5.6	134.4	93.0	287.1	3.7	271.0	9.6
80	0.0557	0.0064	0.0443	0.0014	0.3405	0.0389	0.0143	0.00082	6.4	440.6	124.1	279.6	4.2	297.5	14.7
81	0.0547	0.0031	0.0446	0.0011	0.3368	0.0192	0.0136	0.00046	4.7	400.1	63.1	281.6	3.4	294.8	7.3
82	0.0538	0.0031	0.0441	0.0011	0.3268	0.0184	0.0135	0.00046	3.2	361.6	62.9	278.1	3.3	287.1	7.0
83	0.0542	0.0033	0.0441	0.0011	0.3297	0.0196	0.0140	0.00052	4.0	380.3	66.1	278.2	3.4	289.3	7.5

Table S3.2 Results of single grain zircon U-Pb ICP-MS analysis from Thera (Santorini), Greece

Grain no.	Measured ratios									Apparent ages (Ma)					
	$^{207}Pb/^{206}Pb$	2σ	$^{206}Pb/^{238}U$	2σ	$^{207}Pb/^{235}U$	2σ	$^{208}Pb/^{232}Th$	2σ	Discordance (%)	$^{207}Pb/^{206}Pb$	1σ	$^{206}Pb/^{238}U$	1σ	$^{207}Pb/^{235}U$	1σ
84	0.0395	0.0089	0.0443	0.0015	0.2412	0.0541	0.0133	0.0009	21.6	0.1	0.0	279.7	4.8	219.4	22.1
85	0.0553	0.0041	0.0458	0.0012	0.3485	0.0252	0.0147	0.00064	5.3	422.8	79.5	288.4	3.7	303.6	9.5
86	0.1076	0.0030	0.2451	0.0054	3.6374	0.1027	0.0841	0.00204	10.2	1759.8	24.9	1412.9	14.1	1557.7	11.2
87	0.1168	0.0042	0.1730	0.0041	2.7841	0.1008	0.0872	0.00248	31.4	1907.0	32.2	1028.4	11.3	1351.3	13.5
88	0.0525	0.0024	0.0495	0.0012	0.3583	0.0163	0.0156	0.00044	0.2	305.6	51.0	311.6	3.6	310.9	6.1
89	0.0585	0.0019	0.0947	0.0021	0.7639	0.0254	0.0324	0.00118	1.2	547.5	35.7	583.4	6.2	576.2	7.3
90	0.0593	0.0087	0.0850	0.0029	0.6939	0.1003	0.0266	0.00232	1.8	576.5	151.6	525.6	8.7	535.1	30.1
91	0.0598	0.0032	0.1037	0.0025	0.8549	0.0456	0.0312	0.00084	1.4	595.3	57.9	636.1	7.4	627.3	12.5
92	0.0581	0.0026	0.0953	0.0023	0.7635	0.0347	0.0283	0.00076	1.9	532.5	49.5	587.0	6.7	576.0	10.0
93	0.0508	0.0029	0.0432	0.0010	0.3029	0.0169	0.0130	0.00042	1.5	233.3	63.5	272.8	3.2	268.7	6.6
94	0.0595	0.0023	0.0452	0.0010	0.3705	0.0141	0.0164	0.00052	12.4	586.3	40.7	284.7	3.2	320.0	5.2
95	0.1967	0.0052	0.4851	0.0108	13.1528	0.3572	0.1366	0.00346	5.5	2798.7	21.3	2549.5	23.5	2690.7	12.8
96	0.0569	0.0033	0.0560	0.0014	0.4393	0.0252	0.0163	0.00068	5.2	485.9	63.5	351.4	4.2	369.8	8.9
97	0.1946	0.0050	0.5214	0.0115	13.9867	0.3693	0.1352	0.00318	1.6	2781.2	20.7	2705.1	24.3	2748.8	12.5
100	0.0483	0.0049	0.0335	0.0009	0.2234	0.0224	0.0101	0.00042	3.7	114.4	115.5	212.6	2.9	204.7	9.3
101	-0.0241	0.1144	0.0187	0.0073	-0.0612	0.2899	0.0224	0.01826	153.6	0.1	0.0	119.5	23.0	-64.1	156.8
102	0.0660	0.0084	0.1059	0.0035	0.9636	0.1214	0.0338	0.00208	5.6	807.3	128.3	648.6	10.3	685.1	31.4
103	0.0524	0.0044	0.0494	0.0013	0.3564	0.0299	0.0163	0.00074	0.4	301.6	94.1	310.6	4.1	309.5	11.2
104	0.0521	0.0026	0.0452	0.0011	0.3245	0.0163	0.0139	0.00042	0.2	289.0	56.7	284.9	3.3	285.4	6.3
105	0.1298	0.0034	0.3952	0.0088	7.0732	0.1939	0.1066	0.00274	1.2	2095.4	23.1	2147.0	20.4	2120.7	12.2
115	0.1272	0.0043	0.3209	0.0079	5.6272	0.1979	0.0779	0.00244	7.0	2059.4	29.3	1794.2	19.4	1920.3	15.2
116	0.0742	0.0036	0.0405	0.0011	0.4148	0.0203	0.0206	0.00084	37.6	1047.9	47.6	256.1	3.4	352.3	7.3
ALS16, 363102 E, 4025730 N															
3	0.0580	0.0115	0.0367	0.0015	0.2931	0.0578	0.0123	0.00132	12.5	528.1	204.9	232.1	4.6	261.0	22.7
4	0.0566	0.0026	0.1057	0.0027	0.8248	0.0385	0.0378	0.0013	5.7	474.1	50.2	647.8	7.9	610.7	10.7
5	0.0661	0.0026	0.1095	0.0028	0.9974	0.0406	0.0395	0.00136	4.9	807.9	40.6	669.8	8.1	702.5	10.3
6	0.0599	0.0027	0.0853	0.0022	0.7039	0.0328	0.0351	0.00124	2.6	598.4	48.6	527.5	6.5	541.1	9.8
7	0.0523	0.0031	0.0357	0.0010	0.2571	0.0155	0.0128	0.00042	2.9	297.9	66.8	225.9	3.0	232.4	6.3
8	0.0561	0.0019	0.0676	0.0017	0.5232	0.0189	0.0228	0.0007	1.3	455.5	37.3	421.9	5.0	427.3	6.3
13	0.0818	0.0044	0.1898	0.0052	2.1395	0.1162	0.0703	0.00272	3.7	1239.5	52.0	1120.2	14.2	1161.7	18.8
14	0.0755	0.0075	0.1738	0.0059	1.8090	0.1781	0.0597	0.0016	1.5	1081.4	97.0	1032.8	16.3	1048.7	32.2
15	0.0515	0.0030	0.0526	0.0014	0.3735	0.0217	0.0189	0.00072	2.4	263.8	64.9	330.3	4.3	322.3	8.0
16	0.0516	0.0039	0.0474	0.0013	0.3371	0.0255	0.0182	0.00082	1.2	265.8	84.7	298.6	4.1	295.0	9.7
17	0.1270	0.0036	0.3814	0.0094	6.6806	0.2057	0.1363	0.00392	0.6	2057.0	24.9	2083.0	21.9	2070.1	13.6
21	0.0554	0.0025	0.0517	0.0013	0.3953	0.0180	0.0183	0.00054	4.1	428.7	48.4	325.1	4.1	338.3	6.6
22	0.1863	0.0049	0.4882	0.0120	12.5420	0.3662	0.1477	0.00378	3.2	2709.7	21.7	2562.8	26.0	2645.9	13.7
23	0.0547	0.0018	0.0524	0.0013	0.3952	0.0141	0.0199	0.00054	2.8	400.1	37.5	329.1	4.0	338.2	5.1
30	0.0714	0.0056	0.0378	0.0011	0.3725	0.0289	0.0160	0.00072	34.3	968.1	78.2	239.4	3.5	321.5	10.7
32	0.0584	0.0030	0.0767	0.0020	0.6174	0.0325	0.0279	0.0011	2.4	542.8	56.0	476.6	6.0	488.2	10.2
33	0.0614	0.0028	0.1046	0.0027	0.8849	0.0407	0.0385	0.00114	0.4	652.1	47.6	641.1	7.9	643.6	11.0
34	0.0560	0.0037	0.0517	0.0014	0.3989	0.0265	0.0173	0.0009	5.0	452.5	72.4	324.6	4.4	340.9	9.6
35	0.0594	0.0127	0.1172	0.0053	0.9600	0.2032	0.0398	0.00738	4.3	582.5	217.0	714.1	15.3	683.3	52.6
36	0.0630	0.0020	0.1152	0.0028	1.0013	0.0336	0.0382	0.00122	0.2	709.6	33.2	702.8	8.2	704.5	8.5
37	0.0688	0.0024	0.1504	0.0038	1.4261	0.0524	0.0502	0.00142	0.3	892.3	35.8	902.9	10.5	899.9	11.0
39	0.0566	0.0022	0.0670	0.0017	0.5222	0.0212	0.0232	0.00084	2.1	473.4	43.3	417.9	5.1	426.6	7.1
40	0.0576	0.0029	0.0543	0.0014	0.4312	0.0219	0.0186	0.00062	6.9	515.8	54.6	340.6	4.3	364.0	7.8
41	0.0541	0.0019	0.0634	0.0016	0.4727	0.0177	0.0213	0.00064	0.7	375.4	39.8	396.0	4.7	393.1	6.1
42	0.0572	0.0019	0.0531	0.0013	0.4187	0.0150	0.0187	0.00062	6.6	499.8	36.9	333.2	4.0	355.1	5.4
43	0.0509	0.0025	0.0555	0.0014	0.3896	0.0196	0.0179	0.00086	4.0	237.9	56.3	348.0	4.4	334.1	7.2
44	0.0760	0.0034	0.0684	0.0018	0.7170	0.0330	0.0330	0.00118	28.7	1094.8	44.6	426.6	5.4	548.9	9.8
45	0.0535	0.0022	0.0544	0.0014	0.4017	0.0171	0.0178	0.00054	0.4	351.1	46.2	341.6	4.2	342.9	6.2
46a	0.0532	0.0033	0.0538	0.0015	0.3946	0.0249	0.0187	0.00078	0.1	335.5	69.8	338.0	4.5	337.7	9.1
46b	0.0531	0.0026	0.0531	0.0014	0.3884	0.0196	0.0186	0.00064	0.0	332.0	55.4	333.3	4.2	333.2	7.2
47	0.0553	0.0025	0.0509	0.0013	0.3884	0.0183	0.0171	0.00064	4.0	423.9	50.1	320.3	4.0	333.2	6.7
52	0.1032	0.0031	0.2192	0.0054	3.1196	0.1018	0.0954	0.00282	12.5	1682.3	27.9	1277.9	14.4	1437.5	12.5
53	0.0536	0.0026	0.0534	0.0014	0.3944	0.0194	0.0183	0.0006	0.7	352.7	53.7	335.3	4.2	337.6	7.1
54	0.0539	0.0019	0.0544	0.0013	0.4041	0.0152	0.0186	0.00054	1.0	367.3	40.0	341.2	4.1	344.6	5.5
55	0.0595	0.0021	0.1054	0.0026	0.8655	0.0314	0.0375	0.00106	2.0	586.8	37.0	646.1	7.6	633.1	8.5
56	0.0539	0.0037	0.0386	0.0011	0.2863	0.0194	0.0136	0.0005	4.8	364.4	74.6	243.9	3.3	255.7	7.7
61	0.0520	0.0019	0.0527	0.0013	0.3778	0.0146	0.0208	0.00062	1.8	283.1	42.0	331.3	4.0	325.4	5.4
62	0.0495	0.0029	0.0372	0.0010	0.2540	0.0152	0.0159	0.00056	2.5	170.0	68.1	235.7	3.1	229.9	6.2
63	0.1809	0.0049	0.5203	0.0128	12.9801	0.3840	0.1861	0.00492	0.8	2661.4	22.2	2700.3	27.0	2678.2	13.9
64	0.0531	0.0021	0.0550	0.0014	0.4024	0.0166	0.0192	0.0006	0.4	333.3	44.5	344.8	4.2	343.4	6.0
65	0.0516	0.0030	0.0527	0.0014	0.3749	0.0219	0.0189	0.00066	2.3	269.2	65.3	330.8	4.3	323.3	8.1
66	0.0532	0.0025	0.0526	0.0014	0.3862	0.0187	0.0199	0.00076	0.3	338.7	52.9	330.5	4.2	331.6	6.8
67	0.0519	0.0035	0.0378	0.0010	0.2699	0.0183	0.0154	0.00068	1.6	279.1	75.7	238.8	3.2	242.6	7.3
68	0.0562	0.0021	0.0525	0.0013	0.4071	0.0160	0.0206	0.00066	5.2	461.0	41.6	329.8	4.0	346.8	5.8
72	0.0511	0.0020	0.0415	0.0010	0.2926	0.0117	0.0143	0.00046	0.6	245.1	43.8	262.3	3.2	260.6	4.6
73	0.0509	0.0032	0.0377	0.0010	0.2644	0.0168	0.0132	0.0005	0.1	235.1	71.6	238.5	3.2	238.2	6.7
76	0.0548	0.0025	0.0524	0.0013	0.3956	0.0186	0.0177	0.0006	2.8	402.7	50.7	329.1	4.1	338.4	6.8
77	0.1114	0.0032	0.2561	0.0063	3.9363	0.1230	0.0997	0.00276	10.3	1823.0	26.0	1470.1	16.2	1621.2	12.7
81	0.0496	0.0021	0.0238	0.0006	0.1626	0.0072	0.0083	0.00022	1.1	178.0	49.5	151.4	1.9	153.0	3.1
82	0.0537	0.0017	0.0668	0.0016	0.4946	0.0168	0.0233	0.0007	2.1	357.7	35.8	416.9	5.0	408.1	5.7
83	0.0573	0.0021	0.0717	0.0018	0.5660	0.0218	0.0291	0.00128	2.1	501.6	39.8	446.2	5.4	455.4	7.1
84	0.0531	0.0025	0.0390	0.0010	0.2859	0.0136	0.0149	0.00048	3.4	333.1	51.9	246.9	3.1	255.3	5.4
ALS17, 363135 E, 4025970 N															
1	0.0568	0.0028	0.0735	0.0018	0.5754	0.0283	0.0227	0.00086	0.9	481.4	53.8	457.4	5.3	461.5	9.1
2	0.0517	0.0022	0.0512	0.0012	0.3642	0.0157	0.0161	0.0005	1.9	269.8	48.6	321.6	3.7	315.4	5.8
3	0.0534	0.0028	0.0518	0.0012	0.3816	0.0198	0.0172	0.0006	0.8	346.0	58.0	325.7	3.8	328.2	7.3
4	0.0686	0.0025	0.1413	0.0032	1.3356	0.0484	0.0442	0.0013	1.1	885.4	36.8	852.0	9.1	861.3	10.5
5	0.0713	0.0028	0.1398	0.0032	1.3737	0.0538	0.0434	0.00126	4.1	965.5	39.5	843.2	9.2	877.7	11.5
6	0.0621	0.0021	0.1112	0.0025	0.9527	0.0332	0.0333	0.00094	0.1	678.1	36.5	679.9	7.3	679.5	8.6
7	0.0616	0.0027	0.1109	0.0026	0.9415	0.0417	0.0332	0.00122	0.7	658.6	46.9	678.2	7.6	673.7	10.9
8	0.0538	0.0024	0.0554	0.0013	0.4112	0.0186	0.0168	0.00056	0.6	364.1	50.4	347.6	4.0	349.8	6.7
9	0.0562	0.0021	0.0774	0.0018	0.5994	0.0227	0.0234	0.00084	0.8	458.5	41.2	480.6	5.3	476.9	7.2
10	0.0565	0.0026	0.0486	0.0011	0.3783	0.0172	0.0148	0.0005	6.6	470.9	50.4	305.7	3.5	325.8	6.3
11	0.0528	0.0024	0.0512	0.0012	0.3726	0.0169	0.0156	0.0005	0.1	319.0	50.8	321.9	3.7	321.6	6.3

Table S3.2 Results of single grain zircon U-Pb ICP-MS analysis from Thera (Santorini), Greece

Grain no.	Measured ratios									Apparent ages (Ma)					
	$^{207}Pb/^{206}Pb$	2σ	$^{206}Pb/^{238}U$	2σ	$^{207}Pb/^{235}U$	2σ	$^{208}Pb/^{232}Th$	2σ	Discordance (%)	$^{207}Pb/^{206}Pb$	1σ	$^{206}Pb/^{238}U$	1σ	$^{207}Pb/^{235}U$	1σ
12	0.0795	0.0040	0.0477	0.0012	0.5228	0.0260	0.0168	0.00056	42.2	1185.7	49.0	300.2	3.6	427.0	8.7
13	0.0558	0.0029	0.0604	0.0015	0.4649	0.0237	0.0185	0.0006	2.5	444.6	55.8	378.1	4.4	387.6	8.2
14	0.0742	0.0028	0.1704	0.0040	1.7444	0.0670	0.0508	0.00152	1.0	1047.6	38.2	1014.5	10.9	1025.1	12.4
15	0.1113	0.0042	0.0592	0.0014	0.9088	0.0341	0.0540	0.00166	77.0	1820.7	33.8	370.8	4.2	656.4	9.1
16	0.0685	0.0029	0.0508	0.0012	0.4798	0.0202	0.0240	0.00076	24.6	884.7	43.1	319.3	3.7	397.9	6.9
18	0.0519	0.0021	0.0522	0.0012	0.3740	0.0153	0.0165	0.0005	1.7	282.0	46.0	328.3	3.7	322.6	5.7
19	0.0823	0.0031	0.2013	0.0047	2.2835	0.0866	0.0578	0.00188	2.1	1252.7	36.4	1182.0	12.6	1207.2	13.4
20	0.0726	0.0028	0.1653	0.0038	1.6549	0.0637	0.0499	0.00152	0.5	1003.2	38.5	986.1	10.6	991.4	12.2
21	0.0519	0.0028	0.0362	0.0009	0.2592	0.0138	0.0114	0.00038	2.0	281.2	60.3	229.4	2.8	234.1	5.6
22	0.1034	0.0045	0.1567	0.0038	2.2340	0.0958	0.0686	0.00222	27.0	1685.7	39.4	938.5	10.6	1191.8	15.0
23	0.2848	0.0099	0.0824	0.0019	3.2363	0.1131	0.1483	0.00432	187.1	3389.2	26.9	510.6	5.7	1465.9	13.6
24	0.0620	0.0028	0.1038	0.0025	0.8880	0.0393	0.0313	0.00098	1.4	675.6	46.7	636.6	7.2	645.3	10.6
25	0.0624	0.0034	0.0986	0.0025	0.8492	0.0461	0.0302	0.00122	2.9	689.1	57.4	606.4	7.2	624.2	12.7
26	0.0559	0.0024	0.0620	0.0015	0.4776	0.0205	0.0202	0.00074	2.2	446.6	46.8	387.8	4.4	396.4	7.0
27	0.0838	0.0030	0.2204	0.0051	2.5460	0.0915	0.0640	0.00194	0.1	1287.1	34.3	1284.2	13.4	1285.3	13.1
28	0.1187	0.0044	0.3396	0.0079	5.5597	0.2070	0.0973	0.00308	1.3	1937.3	32.8	1884.7	19.1	1909.9	16.0
29	0.0660	0.0042	0.1075	0.0028	0.9787	0.0613	0.0308	0.00112	5.2	806.6	65.0	658.4	8.2	692.9	15.7
30	0.0652	0.0028	0.0775	0.0018	0.6972	0.0295	0.0299	0.00114	11.6	782.2	44.0	481.2	5.5	537.1	8.8
31	0.0760	0.0037	0.0573	0.0014	0.6000	0.0288	0.0245	0.00088	32.9	1093.8	47.9	359.1	4.2	477.2	9.1
33	0.0526	0.0028	0.0365	0.0009	0.2644	0.0140	0.0115	0.0004	3.2	311.9	59.6	230.8	2.7	238.2	5.6
34	0.0589	0.0035	0.0993	0.0025	0.8066	0.0468	0.0309	0.0011	1.6	563.9	62.6	610.3	7.3	600.6	13.2
35	0.0541	0.0024	0.0564	0.0013	0.4208	0.0186	0.0171	0.00054	0.8	375.4	49.1	353.7	4.1	356.6	6.7
38	0.0778	0.0035	0.1717	0.0041	1.8408	0.0829	0.0538	0.00178	3.8	1140.8	44.4	1021.4	11.4	1060.1	14.8
51	0.0598	0.0036	0.0427	0.0011	0.3520	0.0208	0.0143	0.00046	13.7	597.7	63.5	269.4	3.3	306.2	7.8
52	0.1198	0.0033	0.3626	0.0081	5.9871	0.1675	0.1039	0.0025	1.0	1952.7	24.1	1994.5	19.1	1974.0	12.2
53	0.0480	0.0029	0.0332	0.0008	0.2195	0.0133	0.0103	0.00028	4.2	97.3	72.0	210.4	2.5	201.5	5.6
54	0.0514	0.0028	0.0515	0.0012	0.3650	0.0194	0.0164	0.00058	2.4	259.4	60.4	323.7	3.8	316.0	7.2
55	0.0532	0.0033	0.0372	0.0009	0.2727	0.0166	0.0118	0.0004	4.0	336.0	68.0	235.5	2.9	244.9	6.6
56	0.0503	0.0028	0.0529	0.0013	0.3667	0.0203	0.0167	0.0006	4.6	207.0	63.3	332.4	3.9	317.2	7.5
57	0.0652	0.0024	0.0662	0.0015	0.5944	0.0220	0.0354	0.00106	14.7	779.1	38.2	413.1	4.6	473.7	7.0
58	0.0550	0.0027	0.0558	0.0013	0.4232	0.0204	0.0194	0.00076	2.4	413.3	52.6	349.9	4.1	358.3	7.3
60	0.0720	0.0029	0.1536	0.0036	1.5259	0.0605	0.0466	0.00166	2.1	987.3	39.6	921.3	10.0	940.8	12.2
61	0.0743	0.0026	0.1793	0.0041	1.8377	0.0644	0.0540	0.00148	0.4	1050.5	34.5	1063.2	11.3	1059.0	11.5
62	0.0614	0.0024	0.0975	0.0022	0.8252	0.0317	0.0311	0.0008	1.9	653.7	40.6	599.5	6.6	611.0	8.8
63	0.0577	0.0023	0.1041	0.0024	0.8283	0.0332	0.0318	0.00098	4.0	518.5	43.4	638.4	7.1	612.7	9.2
64	0.0554	0.0022	0.0630	0.0015	0.4817	0.0194	0.0200	0.00066	1.3	429.5	43.8	394.0	4.4	399.2	6.7
65	0.0506	0.0046	0.0360	0.0010	0.2508	0.0227	0.0110	0.0004	0.2	221.6	102.6	227.7	3.1	227.2	9.2
66	0.0571	0.0030	0.0973	0.0024	0.7662	0.0401	0.0301	0.00086	3.5	495.0	57.7	598.7	6.9	577.6	11.5
67	0.0540	0.0021	0.0521	0.0012	0.3884	0.0151	0.0162	0.00052	1.7	372.1	43.0	327.7	3.7	333.2	5.5
68	0.0575	0.0028	0.0822	0.0020	0.6521	0.0312	0.0315	0.00132	0.1	511.9	52.3	509.2	5.9	509.8	9.6
69	0.0521	0.0019	0.0515	0.0012	0.3698	0.0139	0.0166	0.0005	1.2	291.4	42.1	323.4	3.6	319.5	5.2
70	0.0661	0.0026	0.1193	0.0028	1.0866	0.0428	0.0373	0.00104	2.8	808.9	40.7	726.3	8.0	746.8	10.4
71	0.0545	0.0024	0.0498	0.0012	0.3747	0.0164	0.0151	0.00044	3.1	393.4	48.0	313.5	3.6	323.1	6.0
72	0.0603	0.0029	0.1110	0.0027	0.9223	0.0437	0.0324	0.001	2.2	614.0	50.6	678.2	7.7	663.5	11.5
73	0.0572	0.0031	0.0527	0.0013	0.4162	0.0224	0.0184	0.00072	6.6	500.2	59.1	331.3	3.9	353.3	8.0
74	0.0528	0.0063	0.0365	0.0011	0.2652	0.0310	0.0114	0.0005	3.5	318.6	129.0	230.8	3.4	238.9	12.5
75	0.0607	0.0022	0.1049	0.0024	0.8783	0.0325	0.0353	0.0016	0.5	628.8	39.3	643.2	6.9	640.1	8.8
76	0.0562	0.0025	0.0500	0.0012	0.3872	0.0172	0.0158	0.0005	5.7	460.0	49.1	314.3	3.6	332.3	6.3
77	0.0636	0.0021	0.1138	0.0026	0.9990	0.0331	0.0336	0.0009	1.2	729.7	34.3	695.0	7.4	703.3	8.4
78	0.1736	0.0054	0.4742	0.0111	11.3496	0.3619	0.1329	0.00424	2.0	2592.9	25.9	2501.8	24.2	2552.3	14.9
79	0.0595	0.0044	0.0512	0.0014	0.4194	0.0308	0.0162	0.00084	10.6	584.1	78.6	321.6	4.1	355.6	11.0
80	0.0520	0.0022	0.0501	0.0012	0.3589	0.0155	0.0157	0.00048	1.2	283.5	48.7	315.1	3.6	311.4	5.8
81	0.0568	0.0020	0.0729	0.0017	0.5709	0.0201	0.0227	0.00062	1.1	484.2	38.5	453.4	5.0	458.6	6.5
82	0.0564	0.0025	0.0724	0.0017	0.5627	0.0253	0.0227	0.00072	0.6	466.0	49.6	450.7	5.1	453.3	8.2
83	0.0525	0.0032	0.0506	0.0013	0.3664	0.0220	0.0167	0.00068	0.4	307.1	67.5	318.3	3.9	316.9	8.2
84	0.1794	0.0061	0.4840	0.0117	11.9737	0.4100	0.1306	0.00354	2.3	2647.6	28.0	2544.8	25.3	2602.4	16.1
85	0.0534	0.0032	0.0517	0.0013	0.3802	0.0227	0.0160	0.0006	0.8	344.6	66.9	324.7	3.9	327.2	8.4
86	0.0510	0.0032	0.0518	0.0013	0.3643	0.0228	0.0161	0.00054	3.1	240.8	71.3	325.6	4.0	315.4	8.5
87	0.0523	0.0047	0.0362	0.0010	0.2607	0.0231	0.0119	0.0005	2.7	298.0	99.1	229.0	3.1	235.2	9.3
89	0.1321	0.0045	0.3800	0.0089	6.9230	0.2360	0.1072	0.00316	1.2	2126.4	29.3	2076.4	20.8	2101.6	15.1
90	0.0658	0.0053	0.0953	0.0026	0.8650	0.0684	0.0354	0.00164	7.8	800.1	81.9	587.1	7.7	632.8	18.6
91	0.0538	0.0026	0.0508	0.0012	0.3770	0.0179	0.0160	0.00052	1.7	362.8	52.9	319.5	3.7	324.8	6.6
92	0.0496	0.0065	0.0506	0.0016	0.3458	0.0447	0.0155	0.00144	5.2	173.8	145.7	318.3	4.8	301.6	16.9
93	0.0651	0.0028	0.1304	0.0031	1.1695	0.0510	0.0401	0.00134	0.5	776.4	45.3	790.0	8.8	786.4	11.9
94	0.0735	0.0024	0.1720	0.0039	1.7423	0.0570	0.0507	0.00152	0.1	1027.3	31.8	1023.0	10.8	1024.3	10.5
95	0.0547	0.0036	0.0524	0.0013	0.3946	0.0259	0.0170	0.00074	2.7	398.8	72.0	328.9	4.1	337.7	9.4
96	0.0580	0.0025	0.0914	0.0021	0.7312	0.0309	0.0284	0.00088	1.2	529.6	46.1	564.0	6.3	557.3	9.1
97	0.1164	0.0037	0.3320	0.0076	5.3269	0.1718	0.0936	0.00266	1.4	1901.2	28.3	1848.0	18.4	1873.2	13.8
98	0.0554	0.0031	0.0515	0.0013	0.3932	0.0217	0.0165	0.00058	4.1	428.9	60.5	323.5	3.9	336.7	7.9
99	0.0529	0.0022	0.0522	0.0012	0.3803	0.0155	0.0163	0.00054	0.2	322.4	45.6	327.9	3.7	327.3	5.7
100	0.0555	0.0021	0.0586	0.0013	0.4481	0.0171	0.0180	0.00052	2.5	432.3	41.4	366.8	4.1	375.9	6.0
101	0.0607	0.0023	0.0674	0.0015	0.5641	0.0214	0.0641	0.0022	8.1	629.9	40.1	420.3	4.7	454.2	6.9
102	0.0536	0.0022	0.0510	0.0012	0.3771	0.0155	0.0164	0.00052	1.3	355.1	45.0	320.7	3.6	324.9	5.7
103	0.0728	0.0027	0.1577	0.0036	1.5822	0.0583	0.0498	0.00152	2.0	1007.8	36.8	943.9	10.1	963.2	11.5
104a	0.1262	0.0039	0.3578	0.0080	6.2237	0.1934	0.0943	0.00282	1.8	2045.3	26.7	1971.5	19.1	2007.8	13.6
104b	0.1240	0.0040	0.3529	0.0081	6.0333	0.1960	0.1008	0.0028	1.7	2014.7	28.2	1948.2	19.3	1980.7	14.2
105	0.0518	0.0026	0.0513	0.0012	0.3667	0.0181	0.0162	0.00054	1.7	277.6	55.7	322.6	3.8	317.2	6.7
107	0.0536	0.0025	0.0521	0.0012	0.3846	0.0178	0.0166	0.00064	1.0	353.8	51.6	327.1	3.8	330.4	6.5
109	0.0680	0.0030	0.0890	0.0021	0.8341	0.0369	0.0271	0.00088	12.1	867.7	45.4	549.6	6.3	615.9	10.2
111	0.0618	0.0032	0.0393	0.0010	0.3351	0.0172	0.0129	0.00042	18.0	667.8	54.5	248.6	3.0	293.4	6.6
112	0.0533	0.0040	0.0348	0.0009	0.2560	0.0190	0.0110	0.0004	4.8	340.9	82.9	220.8	2.8	231.4	7.7
113	0.0608	0.0025	0.0945	0.0022	0.7915	0.0327	0.0293	0.00084	1.7	631.1	43.8	582.0	6.5	592.0	9.3
114	0.0692	0.0033	0.1477	0.0036	1.4099	0.0669	0.0450	0.00172	0.6	905.7	48.5	888.0	10.1	893.1	14.1
115	0.1605	0.0051	0.1007	0.0023	2.2287	0.0714	0.0580	0.00154	92.3	2460.4	26.5	618.8	6.8	1190.1	11.2
116	0.0590	0.0027	0.0776	0.0019	0.6313	0.0292	0.0228	0.00092	3.1	566.4	49.8	482.0	5.5	496.9	9.1
117	0.0611	0.0036	0.0997	0.0025	0.8399	0.0493	0.0303	0.00138	1.1	642.8	62.6	612.6	7.4	619.1	13.6
118	0.0568	0.0023	0.0636	0.0015	0.4979	0.0205	0.0195	0.00062	3.3	484.2	45.2	397.2	4.5	410.3	7.0

Table S3.2 Results of single grain zircon U-Pb ICP-MS analysis from Thera (Santorini), Greece

Grain no.	Measured ratios									Apparent ages (Ma)					
	$^{207}Pb/^{206}Pb$	2σ	$^{206}Pb/^{238}U$	2σ	$^{207}Pb/^{235}U$	2σ	$^{208}Pb/^{232}Th$	2σ	Discordance (%)	$^{207}Pb/^{206}Pb$	1σ	$^{206}Pb/^{238}U$	1σ	$^{207}Pb/^{235}U$	1σ
119	0.0595	0.0054	0.0336	0.0009	0.2756	0.0247	0.0111	0.00044	16.1	586.3	95.9	212.9	3.0	247.2	9.9
120	0.1346	0.0046	0.3561	0.0082	6.6096	0.2275	0.1099	0.00326	4.9	2158.7	29.6	1963.8	19.5	2060.6	15.2
121	0.0544	0.0024	0.0357	0.0008	0.2676	0.0120	0.0122	0.00044	6.6	388.3	49.3	225.9	2.6	240.8	4.8
122	0.0555	0.0023	0.0502	0.0012	0.3838	0.0158	0.0159	0.00048	4.5	431.5	44.8	315.6	3.6	329.9	5.8
123	0.0575	0.0023	0.0770	0.0018	0.6106	0.0249	0.0264	0.00158	1.1	509.8	44.6	478.4	5.4	483.9	7.9
124	0.1176	0.0037	0.3466	0.0078	5.6217	0.1779	0.0986	0.00268	0.1	1920.7	27.6	1918.1	18.7	1919.4	13.6
125	0.1801	0.0054	0.4673	0.0105	11.6036	0.3575	0.1289	0.00346	4.1	2653.6	24.9	2471.9	23.0	2573.0	14.4
126	0.0542	0.0020	0.0514	0.0012	0.3844	0.0144	0.0152	0.00044	2.2	379.1	41.2	323.3	3.6	330.3	5.3
127	0.0527	0.0022	0.0357	0.0008	0.2598	0.0110	0.0111	0.00044	3.6	316.8	47.4	226.4	2.6	234.5	4.4
128	0.0562	0.0029	0.0539	0.0013	0.4171	0.0214	0.0171	0.00056	4.7	458.0	56.3	338.2	4.0	354.0	7.7
129	0.0583	0.0023	0.0626	0.0014	0.5031	0.0201	0.0220	0.00082	5.8	541.6	43.7	391.1	4.4	413.8	6.8
130	0.0686	0.0029	0.0659	0.0015	0.6233	0.0261	0.0287	0.00098	19.5	886.0	42.9	411.5	4.7	491.9	8.2
133	0.0790	0.0031	0.0674	0.0016	0.7337	0.0291	0.0407	0.0014	32.9	1171.9	38.7	420.3	4.8	558.7	8.5
134	0.0630	0.0023	0.1093	0.0025	0.9494	0.0345	0.0333	0.0011	1.3	707.3	38.1	668.9	7.2	677.8	9.0

SI Chapter 4

This data repository comprises a table of dolomite and calcite chemical composition (**Table S4.1**).

S4.1 Tables:

Table S4.1. Results of dolomite and calcite EMPA analysis from Mt. Hymittos

			structural formulae calculation assuming 3 O (a.p.f.u.)					
Sample	EBSD map	Mineral	Ca	Mg	Fe	Mn	Sr	Si
19MC017A1	subfigure 4.4f	dolomite	0.5035	0.4958	0.0001	0.0002	0.0000	0.0001
		dolomite	0.5063	0.5045	0.0000	0.0001	0.0003	0.0000
		dolomite	0.5057	0.5070	0.0001	0.0000	0.0005	0.0000
		dolomite	0.5138	0.5022	0.0000	0.0000	0.0000	0.0000
		dolomite	0.5048	0.5100	0.0013	0.0002	0.0000	0.0006
		dolomite	0.5182	0.4957	0.0000	0.0000	0.0000	0.0002
		dolomite	0.5118	0.5020	0.0000	0.0005	0.0001	0.0000
		dolomite	0.5024	0.5004	0.0008	0.0000	0.0000	0.0000
		dolomite	0.5127	0.5018	0.0000	0.0005	0.0000	0.0000
		dolomite	0.5121	0.5037	0.0000	0.0000	0.0001	0.0000
		dolomite	0.5127	0.4989	0.0000	0.0000	0.0000	0.0000
		dolomite	0.4954	0.5041	0.0002	0.0000	0.0000	0.0000
		dolomite	0.5069	0.4993	0.0005	0.0005	0.0001	0.0000
		dolomite	0.5101	0.5009	0.0000	0.0000	0.0001	0.0002
		dolomite	0.5127	0.5054	0.0011	0.0000	0.0001	0.0000
		dolomite	0.5151	0.5044	0.0008	0.0006	0.0000	0.0000
		dolomite	0.5153	0.5100	0.0002	0.0002	0.0000	0.0001
		calcite	1.0085	0.0081	0.0000	0.0009	0.0000	0.0000
		calcite	1.0265	0.0046	0.0000	0.0000	0.0000	0.0000
		calcite	1.0174	0.0127	0.0000	0.0000	0.0000	0.0000
		calcite	1.0234	0.0126	0.0003	0.0010	0.0000	0.0003
		calcite	1.0243	0.0110	0.0000	0.0007	0.0000	0.0000
19MC015	subfigure 4.2c	calcite	1.0190	0.0047	0.0000	0.0000	0.0001	0.0000
		calcite	1.0130	0.0054	0.0000	0.0003	0.0008	0.0000
		calcite	1.0118	0.0027	0.0004	0.0000	0.0003	0.0001
		calcite	1.0263	0.0031	0.0000	0.0000	0.0000	0.0002
		dolomite	0.5116	0.5106	0.0000	0.0006	0.0003	0.0000
		dolomite	0.5132	0.5060	0.0002	0.0000	0.0000	0.0000
		dolomite	0.5203	0.5073	0.0000	0.0004	0.0000	0.0002
		dolomite	0.5079	0.5068	0.0002	0.0004	0.0000	0.0002
		dolomite	0.5010	0.5116	0.0002	0.0000	0.0001	0.0000
		dolomite	0.5096	0.5189	0.0003	0.0004	0.0006	0.0000
		dolomite	0.4994	0.5035	0.0000	0.0008	0.0002	0.0000
		dolomite	0.5005	0.5073	0.0005	0.0001	0.0002	0.0000
		dolomite	0.5058	0.5167	0.0001	0.0002	0.0000	0.0001
		dolomite	0.5186	0.5122	0.0000	0.0000	0.0000	0.0000
		dolomite	0.5162	0.4974	0.0000	0.0002	0.0001	0.0000
		dolomite	0.5089	0.5159	0.0005	0.0000	0.0002	0.0001
		dolomite	0.5086	0.5183	0.0000	0.0000	0.0000	0.0001
		dolomite	0.5138	0.5052	0.0000	0.0000	0.0000	0.0000
		dolomite	0.5181	0.5106	0.0007	0.0000	0.0003	0.0000
		dolomite	0.5103	0.5119	0.0002	0.0000	0.0000	0.0000
		dolomite	0.5030	0.5077	0.0000	0.0000	0.0000	0.0001
		dolomite	0.5091	0.5051	0.0000	0.0001	0.0000	0.0002
		dolomite	0.4941	0.5194	0.0000	0.0005	0.0000	0.0000
		dolomite	0.5075	0.5037	0.0000	0.0005	0.0000	0.0000
		dolomite	0.4975	0.5059	0.0000	0.0000	0.0000	0.0000
		dolomite	0.5104	0.5058	0.0000	0.0001	0.0000	0.0000
		dolomite	0.5035	0.5117	0.0007	0.0004	0.0000	0.0001
		dolomite	0.4996	0.5000	0.0000	0.0004	0.0000	0.0000
		dolomite	0.5095	0.4990	0.0000	0.0000	0.0000	0.0000
		dolomite	0.5084	0.5057	0.0000	0.0000	0.0000	0.0000
		dolomite	0.5071	0.5101	0.0003	0.0004	0.0000	0.0000
		dolomite	0.5144	0.5035	0.0000	0.0001	0.0002	0.0000
		dolomite	0.5035	0.5233	0.0000	0.0000	0.0000	0.0004
	subfigure 4.2f	dolomite	0.4902	0.5167	0.0001	0.0000	0.0000	0.0000
		dolomite	0.5070	0.5129	0.0004	0.0004	0.0000	0.0000
		dolomite	0.5101	0.5040	0.0000	0.0002	0.0005	0.0000
		dolomite	0.5122	0.5100	0.0000	0.0000	0.0000	0.0000
		dolomite	0.5021	0.5068	0.0000	0.0000	0.0001	0.0001
		dolomite	0.5055	0.5087	0.0000	0.0002	0.0000	0.0001
		dolomite	0.5039	0.5052	0.0000	0.0000	0.0002	0.0001
		dolomite	0.5041	0.5081	0.0000	0.0000	0.0001	0.0000
		dolomite	0.5088	0.5061	0.0000	0.0004	0.0000	0.0001
		dolomite	0.5115	0.5044	0.0000	0.0000	0.0000	0.0000
		dolomite	0.5080	0.5073	0.0000	0.0006	0.0000	0.0000
		dolomite	0.5105	0.5044	0.0000	0.0001	0.0000	0.0000
		calcite	1.0098	0.0095	0.0000	0.0000	0.0000	0.0001
		calcite	0.9998	0.0050	0.0001	0.0000	0.0000	0.0001
		calcite	1.0244	0.0027	0.0000	0.0000	0.0000	0.0000
18MC130	subfigure 4.3c	dolomite	0.5040	0.5177	0.0000	0.0000	0.0000	0.0002
		dolomite	0.5149	0.5069	0.0001	0.0004	0.0000	0.0000
		dolomite	0.5135	0.4999	0.0033	0.0005	0.0000	0.0002
		dolomite	0.5105	0.5021	0.0000	0.0000	0.0000	0.0000
		dolomite	0.5062	0.5024	0.0000	0.0002	0.0000	0.0006
		dolomite	0.5098	0.5040	0.0001	0.0000	0.0000	0.0000
		dolomite	0.5057	0.5104	0.0006	0.0000	0.0000	0.0005
		dolomite	0.5142	0.5086	0.0000	0.0007	0.0000	0.0001
		dolomite	0.5103	0.5080	0.0003	0.0001	0.0000	0.0000
		dolomite	0.5085	0.5212	0.0000	0.0000	0.0000	0.0002
		dolomite	0.5162	0.5003	0.0005	0.0000	0.0000	0.0003
		dolomite	0.5089	0.5196	0.0000	0.0004	0.0001	0.0000
		dolomite	0.5067	0.4963	0.0051	0.0010	0.0000	0.0002
		calcite	0.9944	0.0223	0.0000	0.0000	0.0000	0.0004
		calcite	1.0176	0.0109	0.0000	0.0000	0.0000	0.0000
		calcite	1.0228	0.0076	0.0002	0.0006	0.0000	0.0000
		calcite	0.9668	0.0009	0.0000	0.0000	0.0000	0.0000
	subfigure 4.3f	dolomite	0.5139	0.5106	0.0003	0.0000	0.0000	0.0000
		dolomite	0.5155	0.5133	0.0000	0.0002	0.0000	0.0000
		dolomite	0.5170	0.5028	0.0002	0.0000	0.0001	0.0002
		dolomite	0.5180	0.5099	0.0000	0.0000	0.0003	0.0000
		dolomite	0.5114	0.5054	0.0001	0.0007	0.0000	0.0000
		dolomite	0.5134	0.5059	0.0000	0.0001	0.0000	0.0000
		dolomite	0.5109	0.5190	0.0006	0.0000	0.0000	0.0000
		dolomite	0.5127	0.5033	0.0000	0.0002	0.0001	0.0001
		dolomite	0.5083	0.5159	0.0009	0.0001	0.0000	0.0006
		dolomite	0.5091	0.5131	0.0000	0.0000	0.0004	0.0002
		dolomite	0.4992	0.5019	0.0007	0.0002	0.0000	0.0000